Modélisation statistique de la solidification colonnaire/équiaxe des alliages binaires

Alexandru Ciobanas

INSTITUT NATIONAL POLYTECHNIQUE DE GRENOBLE

N° attribué par la bibliothèque
|__|__|__|__|__|__|__|__|__|__|

T H E S E

pour obtenir le grade de

DOCTEUR DE L'INP Grenoble

***Spécialité* : MECANIQUE DES FLUIDES ET TRANSFERTS**

préparée au laboratoire : **ELABORATION PAR PROCEDES MAGNETIQUE**

dans le cadre de **l'Ecole Doctorale : MECANIQUE ET ENERGETIQUE**

présentée et soutenue publiquement

par

Alexandru CIOBANAS

le 15 septembre 2006

Modélisation statistique de la solidification colonnaire/équiaxe des alliages binaires

Directeur de thèse:

Yves FAUTRELLE

JURY

M.	H. COMBEAU	, Président
M.	CH.-A. GANDIN	, Rapporteur
M.	D. GOBIN	, Rapporteur
M.	Y. FAUTRELLE	, Directeur de thèse
Mme.	A.M. BIANCHI	, Examinateur

à ma chère Nicole

« Savoir que l'on sait ce que l'on sait, et savoir que l'on ne sait pas ce que l'on ne sait pas: voilà la véritable science. »

(Confucius)

« La statistique est la première des sciences inexactes. »

les frères Goncourt

Remerciements

Aucun manuscrit de thèse ne serait complet sans les mots de remerciements apportés aux personnes qui ont contribué à son accomplissement. Car une chose est sûre, tout au long de ces longues années je n'étais pas seul derrière ce projet de thèse. De nombreuses personnes ont été à mes côtés, m'ont encouragé et m'ont finalement aidées à accomplir un travail difficile.

Mes plus vifs remerciements vont à Yves Fautrelle pour son soutien inconditionnel dans tout ce que j'ai entrepris. Vous m'avez toujours fais confiance et vous avez su diriger mon travail avec une grande compétence. Merci pour tout Yves.

Je remercie Madame Ana-Maria Bianchi qui m'a toujours soutenu dans mes démarches et qui a toujours cru en moi. Sans votre soutien ce projet de thèse n'aurait certainement pas existé.

Je remercie aussi Adrian Bejan pour avoir accepté de réviser une partie de mon travail et pour les très bonnes critiques apportées. Heureusement que la théorie constructale existe !

Merci à Christian Trassy qui m'a accueilli au sein du laboratoire et ceci depuis mon DEA puis pour l'ensemble de cette thèse.

Mes remerciements vont aussi à chacun des membres du jury et plus particulièrement à Charles André Gandin et Dominique Gobin pour avoir accepté d'être les rapporteurs de ce travail.

Merci à tout celles et ceux qui ont été à mes côtes tout au long de cette thèse. Je remercie Anne Noeppel pour son aide précieuse et sa grande patience, Ghislain Quillet pour mes premières leçons de Fluent, Fouad Khaldi pour les agréables moments passés ensemble, Yves Delannoy pour ses conseils utiles, Yves Duterrail pour sa disponibilité et sa bonne humeur, Anne et Pascale pour leur aide dans mes démarches administratives. Je tiens à remercier aussi Monsieur René Moreau pour ses mots d'encouragement et pour ses conseils scientifiques pertinents.

Mais s'il y a des personnes que je voudrais remercier particulièrement, ce sont sans doute les membres de ma famille. Je remercie de tout mon cœur Nicole pour les si beaux mots d'encouragement qu'elle a su m'apporter dans les moments difficiles de ces dernières années et pour son soutien permanent dans tous mes projets. Je voudrais aussi remercier mes parents qui, malgré la grande distance qui nous a séparé, ont été à côté de moi tout au long de ces cinq dernières années.

Merci à tout celles et ceux que j'aurais pu oublier mais qui ont eux aussi apporté une contribution à l'accomplissement de cette thèse.

Table des matières

1 Contexte de l'étude

1.1 Généralités

Les alliages métalliques sont presque toujours élaborés à l'état liquide, et ils doivent donc subir une solidification pour prendre les formes solides désirées. Les transformations subies par l'alliage lors du processus de solidification ont une influence extrêmement importante sur les propriétés d'usages mécaniques et électriques/électroniques du solide final.

Les processus de solidification utilisés dans l'industrie pour l'élaboration des alliages sont dans leur majorité assez rapides, voire très rapides, ce qui favorise les phénomènes de déstabilisation de l'interface solide-liquide plane. Les conséquences de ces déstabilisations donnent naissance à des structures solides très spécifiques aux phénomènes de solidification, nommés *structures dendritiques*. Elles peuvent prendre la forme de colonnes orientées le long de la direction de l'extraction du flux de chaleur : dans ce cas on les appelle dendrites colonnaires ou bien la forme des grains quasi-sphériques distribués de façon plus ou moins homogène dans le creuset : ce sont les dendrites équiaxes (voir Figure 1).

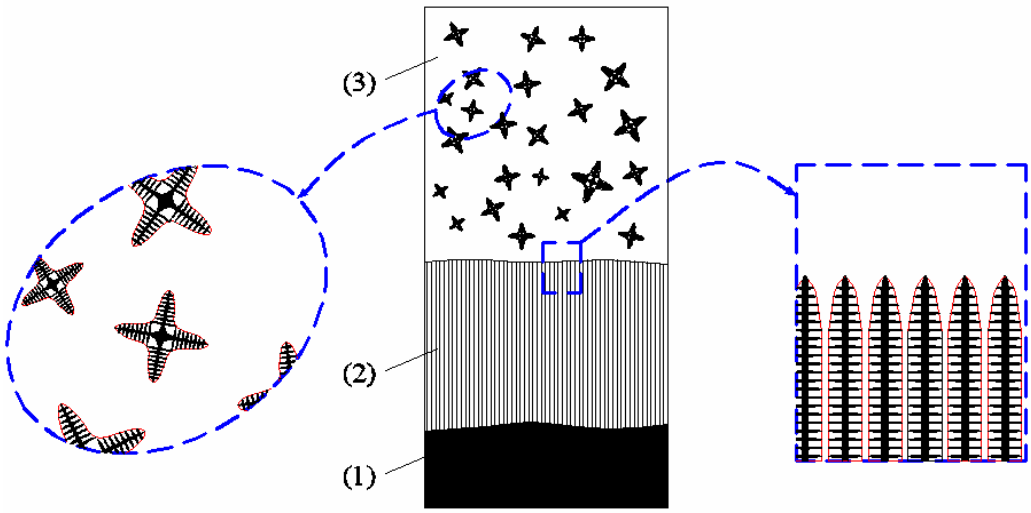

Figure 1 : Les trois zones caractéristiques qui peuvent apparaître pendant la solidification d'un alliage binaire: 1-le solide ; 2-la zone colonnaire ; 3-la zone équiaxe.

Prenons par exemple le cas d'un alliage Al-Si très utilisé dans l'industrie aéronautique là où les propriétés mécaniques ont un enjeu très important. Parce que les propriétés mécaniques d'un alliage dépendent fortement de sa microstructure (les microstructures du type équiaxe ont une meilleure résistance et élasticité que celles du type colonnaire) on comprend l'intérêt de l'obtention d'un alliage à structure équiaxe et en particulier une structure équiaxe plus affinée (avec des grains dendritiques nombreux et petits).

En outre, les corps solides finaux présentent aussi des défauts qui se manifestent sous la forme d'hétérogénéités de la concentration du soluté. Les écarts de concentration du soluté se manifestent à l'échelle des dendrites - 10 $\mu m \div 100$ μm - (les *« ségrégations dendritiques »),* mais aussi à l'échelle du lingot (des *« macroségrégations »* ou des *« mesoségrégations »)*. Si les premiers défauts peuvent être éliminés par un traitement

thermique post-solidification, les derniers persistent encore et font que la composition locale de l'alliage peut sensiblement s'écarter de la composition nominale. En particulier dans certains produits (lingots de refusion à l'arc sous vide, ou aubes de turbine unidirectionnelle) les macroségrégations peuvent apparaître sous forme de « canaux ». Certaines sections du produit présentent des taches isolées dites « freckles » (taches de rousseur) (voir Figure 2). Les alliages obtenus deviennent de cette manière impropres pour des applications à hautes caractéristiques.

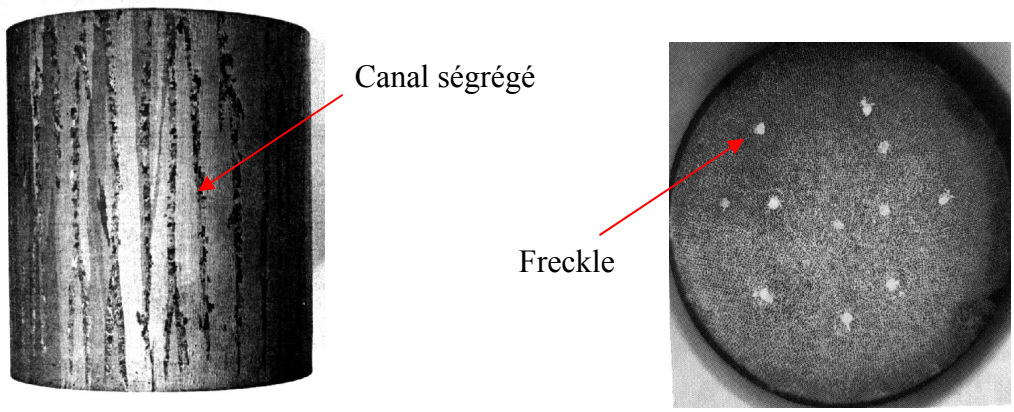

Figure 2 : Les canaux ségrégés et les freckles correspondants dans lingot d'un alliage Pb-Sn 10% en masse, Sarazin et Hellawel [1]

À cause des différents phénomènes de transport qui apparaissent et qui sont fortement couplés, la solidification des alliages même binaires se trouve être un problème très difficile à résoudre. La solidification représente un carrefour pour différentes disciplines et c'est ici qu'on retrouve à la fois des écoulements laminaires ou turbulents, des transferts de masse et de chaleur, des changements de phase et des réactions chimiques. De plus il y a toujours les contraintes d'équilibre thermodynamique aux interfaces (le diagramme de phase), une forte variation des propriétés physiques des métaux liquides avec la température et l'opacité des matériaux. On s'aperçoit vite que, étant donné la complexité des différents processus physiques qui entrent en jeu dans la solidification, les analyses expérimentales et théoriques deviennent très difficiles à aborder, sauf pour des cas simples et/ou des matériaux particuliers.

Dans cette optique, l'existence d'un modèle numérique de la solidification fournissant des prédictions aux macro-échelles du procédé est indispensable. Il peut apporter des informations nouvelles sur la solidification des matériaux multi-constitués, notamment sur les effets des phénomènes de transport (soluté, masse) qui entrent en jeu tout au long du processus de solidification. Ainsi, on peut espérer mieux comprendre les phénomènes complexes qui donnent naissance à la coexistence de dendrites colonnaires et équiaxes dans le même lingot, les facteurs qui influencent *la transition colonnaire-équiaxe* et les *macroségrégations*. En effet, toutes les informations utiles obtenues avec cette analyse auront des conséquences directes sur la qualité des matériaux alliés obtenus.

1.2 Le projet MAP MICAST

Ce travail entre dans le cadre d'un projet européen nommé MAP MICAST (*Microgravity Application Program « Microstructure formation in CASTing »*), soutenu par l'Agence Spatiale Européenne. Ce programme se situe dans la perspective d'améliorer à terme la maîtrise des microstructures de solidification grâce à un brassage contrôlé obtenu par

application de champs magnétiques tournants ou glissants. Son objectif est d'élaborer un modèle global du processus en s'appuyant sur des démarches expérimentales conjointes en microgravité et au sol. En effet, alors qu'au sol la convection forcée est couplée de façon complexe à la convection naturelle (thermique et surtout solutale), ainsi qu'aux mouvements de décantation des particules et des cristaux dans le cas de la solidification équiaxe, la microgravité offre une possibilité unique de séparer les mécanismes mis en jeu, en partant d'une situation contrôlée par la diffusion, puis en appliquant des niveaux de brassage croissants.

La contribution du laboratoire EPM dans ce programme MICAST concerne la modélisation de la macroségrégation et de la convection forcée (brassage électromagnétique) dans des creusets rectangulaires et cylindriques, ainsi que la réalisation des expériences capables d'apporter des éléments de validation au modèle numérique.

Plus particulièrement, le travail de cette thèse porte sur la création d'un modèle mathématique multiphasique du type Euler-Euler qui soit capable de modéliser à la fois la solidification colonnaire (c) et celle équiaxe (e), mais aussi les éventuelles zones mixtes c/e qui peuvent apparaître lors des solidifications dirigées. Un intérêt particulier sera mis sur la transition colonnaire-équiaxe (voir références II et III, Annexe 7.2) mais aussi sur l'effet de la convection forcée sur les macroségrégations. Le modèle mathématique valide pour une solidification colonnaire a été ensuite implémenté dans le module diphasique du logiciel commercial Fluent. En utilisant les résultats expérimentaux obtenus dans le cadre du même projet MICAST on a aussi effectué une première validation semi-quantitative du modèle mathématique développé.

2 Problématique

Avant de passer à l'énumération des objectifs de ce travail je présenterai quelques détails sur les problèmes auxquels on veut traiter. Je commencerai tout d'abord par une brève caractérisation des microstructures colonnaires/équiaxe, je poursuivrai ensuite par une présentation des causes principales des macroségrégations et terminerai enfin par la description de l'approche utilisée dans la modélisation numérique des phénomènes de solidification.

2.1 La microstructure : colonnaire/équiaxe

Comme nous avons pu l'observer, lors d'un processus de solidification on peut distinguer dans le creuset plusieurs zones spécifiques : le solide, la zone colonnaire ainsi que la zone équiaxe (voir Figure 1). Les deux dernières nous intéressent particulièrement car c'est dans ces deux zones que les macroségrégations prennent naissance. Les zones colonnaires et équiaxes se caractérisent par la présence à la fois du liquide et du solide. On a donc à traiter des milieux diphasiques.

Ces deux zones ont comme point de départ un même phénomène de nucléation. En effet, en fonction des contraintes géométriques auxquelles les nuclei initiaux sont soumis juste après leur naissance dans le liquide en surfusion, les germes peuvent évoluer sous forme de *dendrites colonnaires* ou *équiaxes*.

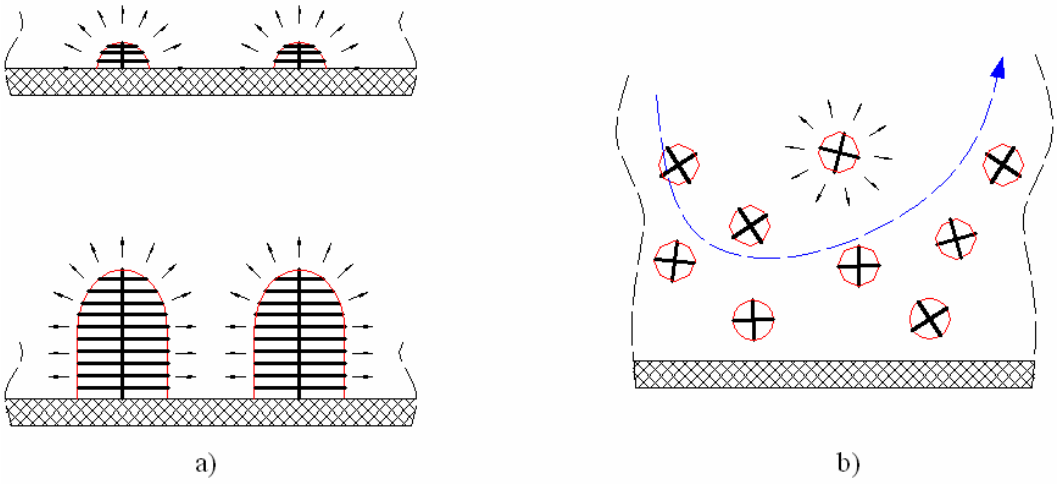

Figure 3 : L'évolution des germes colonnaires (a) et équiaxes (b)

Les dendrites colonnaires qui naissent à partir de petits germes sur la paroi et puis évoluent sous des contraintes géométriques provenant du fait que le solide reste « collé » à la paroi. En effet pour les germes colonnaires qui restent collés à des structures solides stationnaires (les parois) le champ de croissance est implicitement réduit à un angle solide de 2π (voir Figure 3a). Ainsi les dendrites colonnaires évolueront vers des structures ayant une dimension beaucoup plus grande que les deux autres, presque unidimensionnelles, si on les rapporte à la dimension caractéristique du lingot (voir le zoom de la zone 2, Figure 1). Il est important de noter que cette direction caractéristique des dendrites colonnaires correspond à la direction de l'extraction du flux de chaleur dans le lingot.

D'autre part il existe dans le liquide des germes équiaxes qui, pour des raisons diverses (germination dans le liquide en surfusion se trouvant devant les dendrites

colonnaires ou fragmentation des dendrites colonnaires), arrivent à être emportés dans le bain liquide et ainsi auront la possibilité de croître sous un angle solide de 4π (voir Figure 3b).

Les caractéristiques de ces deux structures vont déterminer des comportements hydrodynamiques très différents. Le solide colonnaire est stationnaire, étant bloqué à la vitesse des parois (dans la plus part des cas nulle), tandis que le solide équiaxe subit un transport, produit à la fois par une éventuelle sédimentation mais aussi par les courants convectifs dans le creuset. Dans le cas des structures colonnaires, étant donné qu'elles restent collées à des structures stationnaires, il ne faudra pas résoudre une équation de transport pour le solide. Par contre les choses se compliquent bien plus pour le cas des structures équiaxes. Pour celles-ci, il est obligatoire de prendre en compte le transport de solide équiaxe. A ce transport de masse il faut aussi coupler l'interaction solutale entre le solide et le liquide l'entourant.

2.1.1 La transition colonnaire-équiaxe

Dans la plupart des cas de solidification des alliages les deux structures colonnaire et équiaxe coexistent dans le lingot. En effet deux mécanismes principaux ont été identifiés pour expliquer la coexistence colonnaire – équiaxe. D'une part on peut supposer que des grains équiaxes germent devant le front colonnaire dans la zone de surfusion devant les pointes colonnaires, d'autre part, suivant les indications de Jackson [2] on peut s'attendre dans certaines conditions, notamment lors d'une évolution non-stationnaire du front colonnaire, à ce que les grains colonnaires puissent subir des phénomènes de fragmentation. Cette fragmentation doublée d'une convection au niveau du macrofront colonnaire peut transporter les fragments solides devant le front colonnaire en les transformant ainsi en germes équiaxes. Dans ce contexte il est inévitable qu'une zone de coexistence entre les grains équiaxes et colonnaires apparaîtra dans le lingot. Cette zone de coexistence colonnaire-équiaxe suppose aussi l'existence d'interactions complexes entre les deux structures. En effet, dans certaines conditions la zone équiaxe se trouvant devant le front colonnaire peut arrêter l'avancement des pointes colonnaires déclanchant la transition colonnaire-équiaxe (CET). Ce phénomène a été étudié dans les dernières années en essayant de quantifier le mieux possible les interactions entre la zone équiaxe et colonnaire. Deux types d'interactions ont été identifiés. Le premier type, les interactions « mécaniques », a été quantifié d'abord par Hunt [3]. En effet, en quantifiant la zone équiaxe devant les pointes colonnaires par une fraction granulaire, Hunt a pu déterminer les conditions d'apparition de la CET en supposant l'existence d'une fraction granulaire équiaxe critique au dessus de la quelle le front colonnaire était stoppé dans son avancement. Hunt [3] a aussi identifié les conditions pour lesquelles une zone quasi-stationnaire mixte (colonnaire+équiaxe) pouvait être identifiée dans le lingot. Toutefois, le grand désavantage de l'approche de Hunt réside dans le choix quasi-empirique des seuils de la fraction granulaire équiaxe. De plus l'approche de Hunt [3] ne prend pas en compte les interactions solutales entre les grains équiaxes. Le deuxième mode d'interaction colonnaire-équiaxe de type solutale, a été quantifié pour la première fois par Martorano et al. [4]. En effet à cause des interactions solutales entre les grains équiaxes le liquide qui se trouve entre les grains équiaxe subit un enrichissement en soluté. Comme les pointes colonnaires avancent à travers la zone équiaxe l'enrichissement en soluté du liquide inter-granulaire équiaxe aura une très grande influence sur l'avancement des pointes colonnaires. Dans certaines conditions les interactions solutales entre la zone équiaxe devant les pointes colonnaires et la zone colonnaire sont si fortes que la zone colonnaire se voit complètement stoppée. En quantifiant d'une manière rigoureuse les interactions solutales entre les grains équiaxes et l'enrichissement du liquide inter-granulaire équiaxe

Martorano et al. [4] a pu déterminer avec précision les conditions pour lesquelles la transition colonnaire-équiaxe avait lieu. Toutefois le désavantage majeur de ce modèle est l'incapacité de modéliser les interactions mécaniques entre les deux structures ainsi que l'existence d'une éventuelle zone mixte colonnaire+équiaxe.

Dans ce contexte l'existence d'un modèle qui pourrait modéliser rigoureusement les interactions à la fois mécaniques et solutales entre les structures colonnaires et équiaxes serait d'un grand intérêt. Une partie de cette thèse (voir références II et III, Annexe 7.2) sera en effet consacrée à la modélisation de la coexistence des structures colonnaires et équiaxes ainsi qu'à la modélisation de la transition colonnaire-équiaxe. En effet, en utilisant la méthode de la prise de moyenne statistique nous sommes parvenus à modéliser rigoureusement les interactions mécaniques et solutales entre les deux structures et par conséquent à mieux approfondir le phénomène de la transition colonnaire-équiaxe.

2.2 Les macroségrégations

En ce qui concerne la cause des ces défauts, il est déjà bien connu que le mouvement du liquide inter-dendritique pendant la solidification est le principal motif pour les grandes redistributions de soluté dans la zone pâteuse. Dans le cas d'une solidification habituelle sous champ de gravité (sans brassage magnétique) les canaux apparaissent dans la masse solidifiée comme des traits étroits alignés parallèlement à la direction de la gravité $\vec{g}$, les « freckles ». Il existe différentes études expérimentales et numériques sur la formation des « freckles » dans les alliages binaires et les conclusions sont quasi unanimes pour dire que ce sont des phénomènes d'instabilité hydrodynamique du liquide enrichi en soluté se trouvant dans la zone pâteuse supérieure qui mènent à l'apparition des canaux ségrégés.

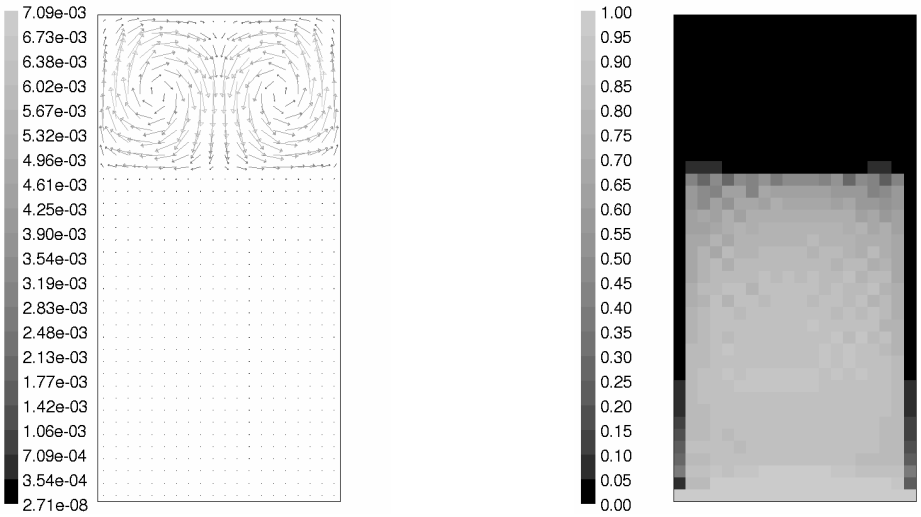

a) b)

Figure 4 : Canaux ségrégés formé dans la zone pâteuse :. a) Le champ des vitesses ; b) La fraction solide (alliage Pb-10% en masse Sn)

Par contre dans le cas d'une solidification faite sous l'influence d'un brassage forcé les macroségrégations sont principalement causées par l'écoulement forcé existant dans la zone pâteuse. En effet, comme on le verra plus loin, le brassage forcé du liquide va significativement influencer l'écoulement dans la zone pâteuse. Ceci va déterminer l'apparition des canaux ségrégés dans la zone pâteuse et par conséquent l'apparition des macroségrégations radiales importantes. Dans la Figure 4 on peut voir la présence de deux canaux ségrégés dans la zone pâteuse colonnaire et l'écoulement correspondant. Les

résultats sont obtenus avec le nouveau modèle mathématique développé et implémenté en Fluent pour un alliage Pb-10% en masse Sn. Le brassage électromagnétique se fait à l'aide d'un champ électromagnétique glissant. En effet, dans ce cas le mouvement forcé dans le bain liquide influence fortement la solidification dans la zone pâteuse et redistribue spatialement le soluté (Cu) en déterminant l'apparition des macroségrégations radiales. Comme phénomène de transport, les canaux sont donc un résultat de la convection dans la zone pâteuse (« the mushy zone »).

2.3 L'approche mathématique utilisée

Notre but est donc d'essayer de modéliser l'évolution hydrodynamique, thermique, et chimique d'un mélange binaire fondu, pendant sa solidification. Le système à traiter (le creuset) est composé à la fois du liquide et du solide. On a alors à faire à un milieu diphasique.

Il serait nécessaire dans l'absolu de résoudre directement le système d'équations locales décrivant le phénomène de solidification : conservation locale de masse de QDM ; d'énergie, de soluté. Malheureusement une telle résolution n'est pas envisageable en raison de la présence des interfaces solide - liquide très complexes, aussi bien dans la zone pâteuse où la croissance colonnaire a lieu mais également dans le bain liquide où de nombreux grains équiaxes existent (voir Figure 1).

Une solution avantageuse consiste donc à appliquer une procédure de prise de moyenne au système d'équations locales. De cette façon, on obtient un système d'équations moyennées, dont la résolution fournit des champs physiques moyens dépourvus des informations sur les fluctuations. Par contre, les fluctuations seront prises en compte par un modèle de fermeture en vue de modéliser leur influence sur les champs moyens (par exemple l'effet du tenseur de Reynolds sur le mouvement moyen).

Mais quelle prise de moyenne doit-on utiliser ? Parmi les méthodes les plus utilisées dans la modélisation macroscopique de la solidification nous trouvons : la prise de moyenne volumique, les méthodes variationnelles, les méthodes spectrales et la prise de moyenne statistique d'ensemble. Toutefois la méthode utilisée presque exclusivement dans les processus de solidification est de loin celle de la prise de moyenne volumique. La méthode de prise de moyenne d'ensemble gagne de plus en plus de terrain, notamment par rapport à ces avantages et possibilités de généralisation.

La méthode de prise de moyenne volumique est basée sur le concept d'un volume élémentaire représentatif (VER). Ainsi toutes les grandeurs physiques dépendantes du temps et de l'espace résultant de l'application de cette méthode sont des valeurs intégrées spatialement dans ce VER. Il est important de noter que la prise de moyenne spatiale ne peut être envisagée que s'il y a une séparation d'échelles entre l'échelle microscopique et celle correspondante au VER. En pratique, cette condition n'est pas toujours vérifiée. Dans le cas de la solidification colonnaire, par exemple, la condition est fortement mise en défaut à cause de la présence des structures ségrégées très allongées (les canaux) dans la zone pâteuse. En effet ces structures ont une dimension caractéristique longitudinale de l'ordre de celle du lingot.

Lors de cette étude nous avons employé la méthode de la prise de moyenne statistique d'ensemble en raison de ses nombreux avantages. Celle-ci a été utilisée dans le développement d'un modèle eulérien multiphasique. Suivant Drew et Passman [5] on peut définir la moyenne d'ensemble comme étant la moyenne qui permet l'interprétation des phénomènes en termes de répétitivité des systèmes multiphasiques. Il faut noter que chaque expérience (réalisation) d'un certain processus physique ne peut être répété parce que les conditions initiales et limites diffèrent d'une expérience à l'autre. En effet, le

concept de la moyenne d'ensemble qu'on considèrera par la suite consiste à dire que l'évolution du système est déterministe, mais que la caractéristique aléatoire du mouvement provient de l'incertitude des conditions initiales. Alors chaque nouvelle expérience donne naissance à un nouveau membre de l'ensemble de toutes les réalisations possibles du phénomène physique en question. Dans le cas des écoulements multiphasiques, cet ensemble est constitué par un nombre quasiment infini des réalisations d'une même expérience.

Prenons à présent le cas de la solidification d'un alliage binaire dans un lingot rectangulaire. La solidification d'un tel lingot fait intervenir de nombreux facteurs. Si l'on regarde de façon plus précise les processus physiques qui gèrent la solidification d'un tel lingot on s'aperçoit de la complexité du phénomène. Premièrement, comme nous l'avons déjà évoqué au début de ce travail, il faut noter la présence de plusieurs phénomènes de transport : de la QDM, de masse, d'énergie et du soluté. De plus tous ces phénomènes sont très fortement couplés, aspect qui rend encore plus difficile le problème. Deuxièmement, il faut aussi prendre en compte les phénomènes de changements de phase qui compliquent encore le processus et qui font apparaître de nouveaux termes dans les équations de transport de l'énergie et de soluté : ce sont les rejets de chaleur latente et de soluté à l'interface solide - liquide. Enfin, pour compliquer encore plus la résolution du problème, on est confronté à un système diphasique liquide - solide qui présente d'innombrables interfaces liquide - solide d'une très grande complexité, voir les dendrites colonnaires et équiaxes. Il faut aussi noter que le milieu diphasique qu'on veut traiter, présente plusieurs échelles spatiales. En conséquence la multiplicité des échelles spatiales dans la zone « pâteuse » rend inenvisageable une modélisation supposant la séparation d'échelles.

La moyenne d'ensemble présente des avantages très intéressants qui recommandent vivement son utilisation dans l'étude des écoulements multi-constituants :

- la moyenne d'ensemble reste très proche physiquement des aspects aléatoires des phénomènes physiques décrits. De plus elle représente le point de départ mathématique du concept de moyennage. Les autres types de prise de moyenne, comme par exemple la prise de moyenne volumique ou celle temporelle, ne sont, en fait, que des solutions approchées de la moyenne d'ensemble obtenues sous la condition de la validité des hypothèses d'ergodicité des phénomènes. Ces hypothèses d'ergodicité nous permettent de faire le passage de la moyenne d'ensemble aux moyennes volumiques et temporelles. Ceci peut se faire, si et seulement si, pour les champs étudiés, les hypothèses d'homogénéité d'une part et de stationnarité d'autre part, restent valides (hypothèses qui ne sont pas toujours acceptables) ;
- la définition de la moyenne d'ensemble ne suppose pas la définition d'un volume élémentaire caractéristique (VER). Par contre pour que la prise de volume ait un sens il faut que le VER contienne un grand nombre de particules c'est-à-dire qu'il y ait une séparation d'échelle entre l'échelle du VER et l'échelle de la plus petite particule. Ainsi, la moyenne d'ensemble n'est pas conditionnée par l'existence d'une hypothèse de séparation d'échelle quelle qu'elle soit : spatiale ou temporelle ;
- le concept de moyennage d'ensemble est très simple. La moyenne statistique d'un champ physique ψ en $\mathbf{x}$ et au temps t n'est plus que la moyenne des valeurs $\psi(\mathbf{x},t;\mu)$ obtenues pour chaque réalisation μ du phénomène physique en question. La loi des grands nombres suggère que si l'on utilise un nombre suffisamment grand d'expériences indépendantes d'un même phénomène on tend vers la moyenne d'ensemble qui a une limite réelle.

3 Objectifs

Les objectifs principaux fixés en début de thèse se sont affinés au fur et à mesure que le travail a progressé.

3.1.1 L'élaboration d'un modèle mathématique pour les phénomènes de solidification

Notre premier objectif consiste à créer un nouveau modèle diphasique eulerien. En effet, l'ancien travail numérique élaboré par Ghislain Quillet [6] et par moi-même [7] dans le cadre de la première étape MICAST a à sa base un modèle diphasique simplifié, développé par Felicelli, Heinrich et Poirier [8]. Celui-ci a quelques limitations extrêmement pénalisantes. Premièrement, ce modèle ne peut prendre en compte que la solidification du type colonnaire, celle dans laquelle le solide reste stationnaire. Le solide en mouvement, spécifique à la solidification équiaxe ne peut pas être traité avec ce modèle. Deuxièmement ce modèle considère que le liquide dans la zone pâteuse est dans un état de mélange parfait ce qui implique que ce liquide se trouve à une concentration en soluté égale avec la concentration du liquide à l'interface solide-liquide, qui s'exprime explicitement en fonction de la température locale par l'intermédiaire de la courbe du liquidus. Cette caractéristique ne permet pas la modélisation des phénomènes de non-équilibre solutal entre les interfaces et le liquide dendritique, phénomènes présents dans les parties supérieures de la zone colonnaire ou dans les zones équiaxes. Enfin il faut ajouter les approximations faites au niveau des termes d'advection dans l'équation de conservation de mouvement pour le liquide ainsi que l'inexistence dans le modèle d'un traitement de la germination et de la réaction eutectique.

Dans ce contexte nous avons voulu développer un modèle mathématique plus complexe qui pallie tous ces inconvénients. Ainsi, on établit que le nouveau modèle doit avoir les caractéristiques suivantes :

i. La formulation mathématique doit prendre la forme d'un modèle diphasique du type eulerien avec des équations de conservation écrites pour chaque phase et comprenant des lois d'échange entre les phases.
ii. L'obtention du modèle mathématique macroscopique doit être faite par une prise de moyenne statistique d'ensemble en évitant ainsi les incertitudes liées à l'hypothèse de la séparation d'échelles micro-macro.
iii. Le système d'équations doit être valable aussi bien pour la solidification colonnaire que pour celle équiaxe. Les différences entre les deux traitements se manifestent seulement par une particularisation des coefficients d'échanges entre les phases ; par contre les équations garderont la même forme. Cette caractéristique est très importante car elle nous permettra d'aborder dans le même domaine physique et avec les mêmes méthodes numériques les deux types de solidification, équiaxe et colonnaire, rendant envisageable un traitement numérique de la transition colonnaire-équiaxe (CET).
iv. Le modèle prend en compte le non équilibre solutal entre l'interface solide-liquide et le liquide dendritique.
v. Le modèle prend en compte la séparation d'échelle entre le liquide inter-dendritique et le liquide extra-dendritique.
vi. L'existence d'un modèle de germination, rendant possible le traitement des zones équiaxes.

Les objectifs que l'on s'est fixés au début de cette thèse se sont au fur et à mesure affinés. Ces modifications se réfèrent principalement à l'idée de l'utilisation du modèle

numérique colonnaire/équiaxe dans le but de prédire les phénomènes de transition colonnaire-équiaxe. En effet, sa formulation statistique en fait un candidat bien placé pour un tel objectif, mais il y a toutefois des obstacles à surmonter. Les difficultés majeures sont liées principalement au fait que la prédiction de la transition colonnaire-équiaxe nécessite une détermination précise de l'évolution de l'interface entre les zones colonnaire et équiaxe. Ceci nécessiterait l'utilisation d'une technique de suivi de front très coûteuse en temps de calcul. En essayant de contourner ce problème on a commencé à travailler sur un modèle multiphasique qui suppose l'existence dans un même endroit des structures équiaxes et colonnaires. Ce concept part du concept statistique de l'existence d'un ensemble contenant toutes les réalisations possibles d'un même processus de solidification. En effet il ne peut y avoir que pour un point *P* du domaine une partie des réalisations du processus telle que le point *P* se trouve au sein d'une structure colonnaire. L'autre partie des réalisations possibles du processus est telle que le point *P* se trouve au sein d'une structure équiaxe. Ainsi, on écrit des équations moyennes (dans le sens statistique d'ensemble) qui prennent en compte ce phénomène de coexistence des structures colonnaires et équiaxes.

3.1.2 L'implémentation du modèle mathématique dans le moteur de calcul CFD « Fluent © »

« Fluent © » est un logiciel commercial spécialisé dans la modélisation numérique en mécanique des fluides. Il a à sa base une méthode à volumes finis, méthode qui fait de celui-ci un très bon et robuste outil pour la prédiction des écoulements bi et tridimensionnels que ce soit en régime laminaire ou turbulent.

Il dispose en même temps d'un nombre considérable de modèles pour la turbulence, mais également de modèles pour la combustion, pour les écoulements diphasiques et même d'un modèle pour la solidification des corps purs. En outre, ce logiciel comprend trois modules de résolution numérique spécialisés dans le domaine des écoulements multi-phasiques : un modèle « volume du fluide », VOF ; un modèle diphasique de « mélange » et enfin, le modèle le plus complet, le modèle diphasique eulérien. En considérant ses possibilités à la fois de généralisation et de particularisation on a décidé d'implémenter le modèle mathématique dans ce dernier module.

Un des autres points forts de « Fluent » est la présence d'un logiciel auxiliaire – « Gambit » - qui nous aide à définir la géométrie du problème et facilite le maillage de ce domaine. On peut également mailler des couches limites et définir des maillages structurés ou non-structurés.

3.1.3 Validation du modèle

Tout modèle numérique doit être vérifié en comparant ses résultats avec les résultats expérimentaux. Dans cette direction nous avons envisagé dans un premier temps une comparaison avec les résultats obtenus par Ghislain Quillet [6]. Ainsi, nous avons pu vérifier le modèle dans ces aptitudes à modéliser la solidification colonnaire.

Dans le cadre du même projet MICAST il y aura une continuation et une amélioration de l'expérience benchmark initialement développée par Ghislain Quillet [6]. En effet le travail expérimental est déjà commencé au sein du laboratoire EPM et il aboutira au début de 2006 à une manipulation plus complexe que la précédente. Elle sera plus complète sous l'aspect thermique mais elle comprendra aussi un brasseur électromagnétique linéaire. On pense ainsi pouvoir obtenir des régimes de solidification équiaxes et des zones de transition colonnaire – équiaxe. Malheureusement le manque de résultats ne nous a pas encore permis de faire une comparaison directe entre cette

expérience et le modèle numérique. Toutefois nous avons pu comparer le modèle numérique avec une autre expérience de solidification, celle développée par l'équipe ACCESS à Aachen, Allemagne. La comparaison avec les résultats expérimentaux sera présentée plus tard dans ce manuscrit.

4 Résultats

Nous présentons maintenant les résultats actuels. Dans un premier temps je présenterai le résumé des quatre publications en anglais élaborées tout au long de la thèse. Ces publications se trouvent attachées à ce document et portent sur :

- la morphologie dendritique (espacement dendritique secondaire et primaire) vue dans la perspective de la théorie constructale ;
- l'élaboration du nouveau modèle mathématique capable de modéliser la coexistence des structures équiaxes et colonnaires dans un cas purement diffusif ;
- la modélisation unidimensionnelle de la transition colonaire-équiaxe et la validation du modèle mathématique précédent ;
- l'élaboration du modèle mathématique capable de modéliser la coexistence des structures équiaxes et colonnaires dans un cas où la convection est prise en compte.

Dans un deuxième temps je présenterai les résultats numériques obtenus avec le modèle purement colonnaire et la validation de celui-ci avec des résultats expérimentaux.

4.1 La morphologie dendritique regardé dans la perspective de la théorie constructale

Dans ce premier papier (référence I, Annexe 7.2) on se concentre sur l'application de la théorie constructale dans la prédiction de la structure dendritique solide. Premièrement on analyse le critère de stabilité marginale vu dans la perspective de la théorie constructale. En ayant comme principe de base la loi constructale on conclu que la forme de la dendrite s'adapte de telle manière que la vitesse de croissance de la pointe dendritique soit maximale. Dans ce contexte on a montré que, parmi le domaine des rayons possibles de la pointe dendritique prédit par l'analyse de stabilité, la pointe dendritique va choisir le plus petit rayon ça veut dire un rayon égal avec la plus petite longueur d'onde des perturbations donnant naissance à des instabilités. On identifie aussi l'existence d'une compétition entre la croissance contrôlée par la diffusion moléculaire et la croissance dendritique. En analysant cette compétition on a été capable de déterminer le temps critique et le rayon critique pour lesquels la déstabilisation de l'interface solide-liquide se déclanche. Dans un deuxième temps on développe un modèle pour l'espacement dendritique secondaire. En analysant la croissance d'une seule pointe dendritique on conclu que la croissance latérale de la pointe dendritique est proche d'une croissance contrôlée par la diffusion moléculaire et par conséquent est caractérisé par une vitesse de croissance qui diminue dans le temps. Dans ce contexte la théorie constructale prédit une optimisation de la croissance latérale de la dendrite. En faite on identifie encore une fois une compétition entre la croissance latérale contrôlée par la diffusion moléculaire et la croissance dendritique. En analysant cette compétition on a été capable de caractérisé le mécanisme de la croissance latérale des branches dendritiques secondaires et de calculer finalement l'espacement dendritique secondaire. Le résultat est en bon accord avec le modèle de J.S. Langer and H. Muler-Krumbhaar, Acta Metallurgica **26**, 1681 (1978) mais aussi avec des différents résultats expérimentaux. Finalement, l'espacement dendritique primaire est analysé dans la perspective de la loi constructale. Quand on l'applique à un front colonnaire la loi constructale prédit que le seul moyen dont le pointes dendritique dispose pour l'optimisation du processus de solidification est la minimisation de l'espace entre deux pointes adjacentes, c'est-à-dire la minimisation du λ_1. Le mécanisme responsable pour la diminution du λ_1 a été identifié dans le mécanisme de division dendritique. Toutefois, à

cause des interactions solutales entre les pointes adjacentes il a été trouvé qu'il existe un espacement critique λ_{cr} en dessous duquel la division des pointes colonnaire ne peut plus se faire. Dans ce sens la loi constructale prédit que l'espacement primaire caractérisant l'état quasi-stationnaire du front colonnaire sera proche de l'espacement stable minimum λ_{cr}. En quantifiant la division dendritique et les interactions solutales entre les pointes colonnaire on a finalement été capable d'obtenir un modèle pour l'espacement dendritique primaire. En effet, on obtient que λ_1 est de même ordre de grandeur avec λ_{cr} et plus précisément que $\lambda_1 \approx 1.5\lambda_{cr}$. Le résultat est par la suite validé avec plusieurs donnés expérimentales et on obtient que le nouvel modèle est en très bon accord avec les expériences.

4.2 Modèle à prise de moyenne statistique pour la solidification colonnaire/equiaxe des alliages binaires.

Au cours de la deuxième publication (référence II, Annexe 7.2) nous avons développé un nouveau modèle diphasique eulérien valide pour la solidification colonnaire et équiaxe et pour un cas purement diffusif (sans convection). Les équations moyennes ont été obtenues à l'aide d'un moyennage statistique de phase et la formulation finale du modèle est valable aussi bien pour une structure équiaxe que colonnaire. L'utilisation d'une telle prise de moyenne a plusieurs avantages devant la prise de moyenne volumique, largement utilisée durant les vingt dernières années. Premièrement l'approche statistique n'a pas besoin de la définition d'un volume élémentaire représentatif (VER). Deuxièmement, cette approche est cohérente avec l'aspect aléatoire de la germination des grains équiaxes et avec l'existence possible d'un régime turbulent de l'écoulement fluide. Le facteur le plus important est que nous sommes finalement capable, grâce à la nature statistique du modèle, de traiter rigoureusement la coexistence des grains équiaxes et colonnaires et par conséquent la transition colonnaire-équiaxe.

Nous nous proposons tout d'abord d'analyser le cas d'une structure colonnaire pure ou équiaxe pure. A l'aide des fonctions de densité de probabilité des particules les plus proches, $\widetilde{f}^{(1)}\left(t,\mathbf{x};\tilde{\mathbf{z}}_1\right)$, on est capable de calculer rigoureusement les termes et les tenseurs inconnus existant dans les équations de conservation moyennes non-fermées. En effet, en utilisant « l'approximation de la cellule » [5] pour ces fonctions de densité de probabilité, les champs moyens peuvent être facilement calculés à l'aide de simples intégrations volumiques dans une cellule sphérique caractéristique. La principale hypothèse physique du modèle se réfère à la séparation d'échelle entre le liquide inter- et extra-dendritique. Dans une approche similaire avec celui de Rappaz et Thévoz [9] et Wang et Beckermann [10] le modèle de l'enveloppe dendritique est utilisé pour paramétrer les échelles de longueur plus petites que la dimension de la dendrite, c'est-à-dire l'espacement inter-dendritique. L'enveloppe dendritique est définie comme la surface virtuelle enveloppant la dendrite qui connecte toutes les pointes dendritiques de la dendrite. Ce procédé nous conduit à distinguer deux types de liquide, le liquide inter-dendritique et le liquide extra-dendritique. Le liquide inter-dendritique est supposé à l'état d'équilibre avec l'interface, sa concentration étant uniquement déterminée par la température locale et le diagramme de phase. Par contre le liquide extra-dendritique peut avoir une concentration différente de celle à l'équilibre. Le modèle de la maille couplé avec les hypothèses valides à la échelle du grain nous permet de fermer le système des équations de conservation moyennes. Le modèle final valide soit pour une structure colonnaire soit pour une structure équiaxe est similaire à celui obtenu par Wang et Beckermann [10]. L'équivalence entre les deux

modèles est une conséquence directe de l'utilisation de l'hypothèse de l'équilibre thermique local. En effet, si l'hypothèse d'homogénéité thermique locale est prise en compte alors la moyenne statistique d'ensemble reproduit l'approche de la prise de moyenne volumique. Toutefois le moyennage statistique est fondamentalement différent du moyennage volumique. En effet, si l'hypothèse d'homogénéité thermique locale n'est plus valide, l'utilisation de la prise de moyenne statistique donne naissance à des expressions de fermetures différentes de celles obtenues par l'application du moyennage volumique. De plus, les résultats obtenus avec le moyennage volumique ne sont pas physiquement corrects. Dans ce contexte il est montré en référence II (Annexe 7.2) que l'utilisation de la prise de moyenne statistique couplé avec le modèle de la cellule permet avec succès l'intégration des effets des inhomogénéités locales (gradients locaux des champs physiques) sur les expressions de fermeture.

Deuxièmement, le cas de la coexistence entre les structures colonnaires et équiaxes (c/e) est analysé du point de vue du moyennage statistique. Plus précisément, le cas de la pénétration du front colonnaire dans une zone équiaxe développée est analysé. Ce type de couplage peut être fréquemment rencontré pendant les phénomènes de solidification et spécialement dans le cas des phénomènes de transition colonnaire-équiaxe (CET). Le principal avantage de la prise de moyenne statistique réside dans le fait qu'à l'aide des distributions de probabilité des particules les plus proches, $\widetilde{f}_{c/e}\left(t,\mathbf{x};\tilde{\mathbf{z}}_1\right)$, on peut quantifier d'une manière rigoureuse les influences des particules colonnaires/équiaxes (c/e) en **x**. En utilisant l'approximation de la cellule pour $\widetilde{f}_{c/e}$ deux cellules sphériques centrées en **x** et de rayon R_{1c}^* et R_{1e}^* ont été identifiées. Chacune de ces cellules caractérise d'une manière simple la statistique des deux structures (c/e) en **x**. En utilisant ces deux cellules il est possible de séparer l'influence des structures c/e dans le point **x** en définissant des moyennes d'ensemble correspondantes à chaque structure. Ces moyennes vont ainsi quantifier les effets moyens en **x** produit par chaque structure. De plus, toute valeur moyenne (ex. fractions c/e, fractions solide/liquide, moyennes de la concentration, moyennes interfaciales, etc.) peut être facilement calculée à l'aide des simples intégrations sur les positions possibles des grains c/e dans les cellules c/e. Ainsi, suivant le cas où la particule la plus proche de **x** est colonnaire ou équiaxe, le modèle nous conduit à différentier deux types principaux de valeurs moyennes : respectivement colonnaires et équiaxes. Dans ce contexte deux fractions importantes sont identifiées : la fraction colonnaire et celle équiaxe, ε_c et ε_e. Ces deux fractions quantifient la manière dont les deux structures partagent l'espace en **x**. Comme les grains colonnaires et équiaxes partagent le même espace en **x** la somme des ces deux fractions fait 1, $\varepsilon_c+\varepsilon_e=1$. On note aussi que chaque structure sera caractérisée par sa propre fraction solide et liquide et par conséquent la fraction c/e sera une somme entre les fractions solides et liquides correspondantes, $\varepsilon_{c/e}=\varepsilon_{se/c}+\varepsilon_{fe/c}$. Une autre caractéristique importante de la moyenne statistique réside dans le fait qu'elle nous permet de quantifier le blocage mécanique produit par la structure équiaxe sur les pointes colonnaires. On a démontré que les structures équiaxes et colonnaires interagissent suivant un double mécanisme. Le premier effet de blocage mécanique déterminera une raréfaction de la zone colonnaire au moment où cette dernière pénètre dans la zone équiaxe. En effet, à cause de la dimension finie des grains équiaxes les pointes colonnaires disposent seulement d'un espace limité $(1-\varepsilon_{ge})$ dans lequel elles peuvent germer. Ainsi seulement une fraction, $1-\varepsilon_{ge}$, du nombre initial des colonnes, n_c^0, est capable de pénétrer dans la zone équiaxe. Le deuxième effet de blocage mécanique reflète le fait que pour une zone mixte (colonnaire+équiaxe), les deux

structures sont forcées de partager localement un même espace. Par conséquent, l'espace disponible pour chaque structure sera différent et plus petit par rapport à l'espace correspondant disponible juste avant l'état de coexistence. En fait, le deuxième blocage mécanique dit que les rayons des cellules des deux structures, $R^*_{1c/e}$, caractérisant l'état de coexistence sont plus petits que les rayons correspondants caractérisant les structures c/e juste avant leur coexistence, $R_{1c/e}$. Cet effet est d'une très grande importance parce que les rayons $R^*_{1c/e}$ peuvent être très différents des rayons originaux $R_{1c/e}$ et par conséquent l'évolution de la zone colonnaire+équiaxe sera très différente de celle caractérisant une zone purement colonnaire ou purement équiaxe.

Finalement, en utilisant le modèle de la cellule couplé avec les hypothèses physiques valides à l'échelle du grain on a été capable de fermer rigoureusement le système des équations moyennes. Un modèle complet décrivant la coexistence des grains colonnaires et équiaxes est finalement obtenu.

4.3 Validation du modèle statistique d'ensemble.

Dans la troisième publication (référence III, Annexe 7.2) le nouveau modèle mathématique qui a été développé au cours de la référence II (Annexe 7.2) est validé contre plusieurs expériences de solidification dirigés. En effet, en raison de la nature statistique de la prise de moyenne, le nouveau modèle est capable de modéliser rigoureusement la coexistence des structures équiaxes et colonnaire et par conséquent de mieux approcher le phénomène de la transition colonnaire-équiaxe (CET). Dans cette troisième publication on se concentre premièrement sur la simulation numérique des solidifications quasi-stationnaires dans le but d'obtenir les cartes de la CET. On a trouvé qu'en fonction du choix de la vitesse de tirage par rapport à deux vitesses critiques caractérisant le zone équiaxe devant les pointes colonnaires on peut identifier sur la carte CET trois zones : une zone purement colonnaire, une zone purement équiaxe et finalement une zone mixte colonnaire+équiaxe. En quantifiant le mécanisme de division des dendrites colonnaires on a pu déterminer si la zone mixte colonnaire+équiaxe correspondait à un état quasi-stationnaire aux pointes colonnaires. Ce mécanisme de division des colonnes (mécanisme de redensification de la zone colonnaire) a été quantifié à l'aide du modèle de l'espacement dendritique primaire (voir référence I, Annexe 7.2). La zone mixte colonnaire+équiaxe a été quantifiée à l'aide de la fraction colonnaire ε_c, qui à son tour quantifie rigoureusement l'état de coexistence des deux structures. Le nouveau modèle nous permet aussi de quantifier aussi bien le blocage mécanique que celui solutal produit par la zone équiaxe devant les pointes colonnaires. En fait, parce que les effets de blocage solutal et mécanique sont intrinsèquement inclus, le nouveau modèle unifie l'approche semi-empirique de Hunt [3] (le blocage purement mécanique) et celui de Martorano et al. [4] (le blocage purement solutal).

Dans un deuxième partie de la publication, le nouveau modèle est utilisé pour la simulation des expériences unidirectionnelles de solidification en [11, 12]. On a ainsi analysé le couplage complexe entre la zone colonnaire et la zone équiaxe devant les pointes colonnaires. La stationnarité du front colonnaire par rapport aux conditions locales de refroidissement a aussi été analysée. Cette analyse a montré que le front colonnaire évolue dans un état de quasi-stationnarité jusqu'à très proche du moment de la transition colonnaire-équiaxe. Elle a également montré que la surfusion de nucléation des grains équiaxes est très proche de la surfusion maximale des pointes colonnaires et qu'ainsi la CET est virtuellement indépendante de la zone équiaxe devant le front colonnaire. Ceci est en concordance avec les résultats de Martorano et al. [4] et vient appuyer l'idée que la CET

est principalement causée par la fragmentation des dendrites colonnaires. Si la zone équiaxe n'est pas prise en compte par le modèle on observe que la vitesse du front colonnaire subit une croissance brusque au début de la solidification suivi par un quasi-plateau correspondant à l'état quasi-stationnaire aux pointes colonnaires et finalement, après un temps critique, une évolution oscillatoire. Il est important de noter le fait que le début de l'évolution oscillatoire du front colonnaire a pu être corrélé avec la position de la CET mesurée dans les expériences. L'évolution oscillatoire du front colonnaire correspond en fait à un état non stationnaire de pointes colonnaires par rapport aux conditions locales de refroidissement. Cette évolution oscillatoire du front colonnaire pourrait aussi être très favorable à la fragmentation des dendrites colonnaires et par conséquent très favorable à la CET. On conclut que le régime non stationnaire du front colonnaire par rapport aux conditions locales de refroidissement représente la cause principale de la CET, au moins pour les alliages non raffinés.

4.4 Extension du modèle statistique pour le cas convectif

Le modèle à prise de moyenne statistique développé dans la deuxième publication (référence II, Annexe 7.2) est, dans la quatrième publication (référence IV, Annexe 7.2), étendu pour prendre en compte les effets de la convection du fluide. Comme pour le modèle initial le nouveau modèle approche la moyenne d'ensemble à l'aide des fonctions de probabilité les plus proches, $\widetilde{f}_{c/e}\left(t,\mathbf{x};\tilde{\mathbf{z}}_1\right)$. De cette manière les interactions solutales et mécaniques entre les deux structures (c/e) sont bien prises en compte par le nouveau modèle. Toutefois, les hypothèses physiques valides à l'échelle du grain sont réévaluées par rapport à celles initialement décrites en référence II, Annexe 7.2. Tour à tour on analyse l'écoulement fluide autour des grains perméables colonnaires et équiaxes puis la croissance du grain en présence de la convection et enfin le transfert de soluté autour des grains c/e en tenant compte de la convection. On trouve ainsi que le transfert de masse à l'interface du grain c/e en présence de la convection est plus intense par rapport au cas sans convection. On propose des corrélations pour le calcul du coefficient de transfert de masse global dans la limite des très petites et de très grandes fractions granulaires. Les hypothèses physiques valides à l'échelle micro couplées avec le modèle de la cellule nous permettent de fermer le système complexe formé par les équations de conservation. Tout d'abord les équations de conservation des grains sont dérivées. La nucléation équiaxe est modélisée comme un événement instantané tandis que la nucléation colonnaire (l'apparition soudaine des pointes colonnaires dans un point **x**) est modélisé à l'aide d'un algorithme de suivi du front. On propose ainsi une technique simple de suivi du front ayant à la base le modèle du volume fluide (volume of fluid (VOF) model). De plus, le modèle de coexistence proposé en référence II (Annexe 7.2) est ici étendu pour prendre en compte la convection des grains équiaxes. En effet, les dimensions des cellules R_{1c}^{*}, R_{1e}^{*} et le calcul des fractions colonnaires et équiaxes (ε_c et ε_e) sont ici déterminées à l'aide d'un nouveau modèle de coexistence. Les équations de conservation de masse, de quantité de mouvement et de l'énergie sont dérivées par la suite. Il faut remarquer que, pour des raisons de simplicité, l'équation de conservation de quantité de mouvement pour le liquide est écrite pour le fluide total et non pas séparément pour le fluide colonnaire et équiaxe. Pour l'équation de l'énergie une seule équation de mélange est écrite. Finalement, les équations de conservation de soluté sont dérivées. Ainsi deux équations pour le solide colonnaire et équiaxe ainsi qu'une équation pour la conservation de soluté dans le fluide total sont prises en compte. De plus, les deux équations de conservation de soluté dans le liquide inter-dendritique sont utilisées pour le calcul du transfert de masse liquide-solide. On a aussi

proposé un algorithme pour le traitement implicite du calcul de la concentration dans le liquide extra-dendritique. Ceci est fait par le couplage à chaque pas de temps de l'équation de conservation de soluté dans le liquide extra-dendritique avec l'équation de conservation de soluté dans le fluide total. Finalement un modèle complet à prise de moyenne statistique d'ensemble est proposé, celui-ci étant capable de modéliser le couplage complexe entre la structure colonnaire et équiaxe en présence de la convection.

4.5 Implémentation du modèle mathématique dans Fluent. Validation.

Dans un but de validation, le nouveau modèle (référence IV, Annexe 7.2) doit d'abord être implémenté dans un code de résolution spécialisé dans le calcul des écoulements et transferts de chaleur et de masse en milieux multiphasiques. Le logiciel FLUENT a été choisi car il a déjà été utilisé avec succès dans la résolution du modèle diphasique de Felliceli [6]. FLUENT est un logiciel commercial spécialisé dans la modélisation des écoulements fluides et de transfert de chaleur. Il utilise comme méthode de discrétisation la méthode des volumes finis. Les avantages de ce code sont nombreux :

- Il est associé à un logiciel très performant de maillage (Gambit) permettant ainsi de varier facilement la géométrie étudiée ;
- Le passage de 2D à un problème, 2D axisymétrique ou 3D se fait automatiquement : il faut juste adapter le maillage ;
- La robustesse et la fiabilité du solveur ont déjà été confirmées dans la littérature ;
- Très important, FLUENT propose un module multiphasique qui utilise une formulation eulérienne, donc très proche de la formulation du modèle développé en référence IV (Annexe 7.2).

4.5.1 Modèle mathématique

Il est important de noter que pour l'instant seulement le modèle colonnaire pur a été complètement implémenté et testé en Fluent. Une version du modèle équiaxe pur est en phase de développement mais les résultats actuels ne permettent pas encore une validation judicieuse de celui-ci. Il reste que dans la suite de ce travail, une fois que le modèle équiaxe pur est testé, le modèle complet de la référence IV, permettant la simulation avec couplage équiaxe/colonnaire, sera implémenté dans Fluent. Ceci se fera relativement facilement dans le sens ou il faudra juste coupler les deux modèles colonnaires purs et équiaxes purs, en tenant compte de la formulation déjà établie dans la référence IV.

Donc, par la suite, seuls les résultats obtenus avec le modèle colonnaire seront présentés. Ce modèle mathématique s'obtient facilement à partir du modèle complet présenté en référence IV en considérant uniquement l'existence d'une structure colonnaire dans le lingot. Les équations formant ce modèle colonnaire sont résumées dans le Tableau 1.

Tableau 1: Équations constitutives du modèle purement colonnaire

Equations de conservation :	**Solide:**	**Liquide:**
Grain	$\frac{\partial n}{\partial t} = n_c^0 \, \delta\left(T - T_{liq}\right)$,	$n_c^0 = \left[\frac{4}{3}\pi\left(\lambda_1 / 2\right)^3\right]^{-1}$
Masse	$\frac{\partial\left(\rho_s \varepsilon_s\right)}{\partial t} = \Gamma_s$	$\frac{\partial\left(\rho_f \varepsilon_f\right)}{\partial t} + div\left(\rho_f \varepsilon_f \mathbf{v}_f\right) = -\Gamma_s$

QDM	$\frac{\partial\left(\varepsilon_f\rho_f\mathbf{v}_f\right)}{\partial t}+\nabla\left(\varepsilon_f\rho_f\mathbf{v}_f\mathbf{v}_f\right)=-\varepsilon_f\nabla p+\nabla\left[\varepsilon_f\mu_f\left(\nabla\mathbf{v}_f+\left(\nabla\mathbf{v}_f\right)^{\mathrm{T}}\right)\right]+$ $+\varepsilon_f\rho_f\,\mathbf{g}-K_f\varepsilon_f\mathbf{v}_f+\varepsilon_f F_{é.m.}$
Energie	$\frac{\partial\left[\left(\varepsilon_s\rho_s c_s+\varepsilon_f\rho_f c_f\right)T\right]}{\partial t}+div\left(\varepsilon_f\rho_f c_f\mathbf{v}_f\right)=$ $=div\left[\left(\varepsilon_s\lambda_s+\varepsilon_f\lambda_f\right)\nabla T\right]+\Gamma_s L$
Soluté	$\frac{\partial\left(\varepsilon_s\rho_s C_s\right)}{\partial t}=div\left(\varepsilon_s\rho_s D_s\nabla C_s\right)+$ $+C_s^*\Gamma_s$ | $\frac{\partial\left(\varepsilon_f\rho_f C_f\right)}{\partial t}+div\left(\varepsilon_f\rho_f\mathbf{v}_f C_f\right)=$ $=div\left(\varepsilon_f\rho_f D_f\nabla C_f\right)-C_s^*\Gamma_s$
Equations de conservation auxiliaires :.	
C. masse dans le liquide inter-dendritique	$\frac{\partial\left(\rho_f\varepsilon_d\right)}{\partial t}=-\Gamma_s+\Gamma_g\ ,\qquad \Gamma_g=\rho_f S_g\overline{w}_g$
C. soluté dans le liquide extra-dendritique	$\varepsilon_l\rho_f\frac{\partial C_l}{\partial t}+\varepsilon_l\rho_f\mathbf{v}_f\nabla C_l=\nabla\cdot\left(\varepsilon_l\rho_f D_f\nabla C_l\right)+\left(\frac{\rho_f S_g D_l}{\delta_{l-d}}-\Gamma_g\right)\left(C_l^*-C_l\right)$
C. soluté dans le liquide inter-dendritique	$\Gamma_s\left(C_l^*-C_s^*\right)=\varepsilon_d\rho_f\frac{\partial C_l^*}{\partial t}+\frac{\rho_f S_g D_l}{\delta_{l-d}}\left(C_l^*-C_l\right)+\varepsilon_d\rho_f\mathbf{v}_f\nabla C_l^*$
Expressions auxiliaires :	
Contraintes:	$\varepsilon_l+\varepsilon_d+\varepsilon_s=1\,,\qquad \varepsilon_d+\varepsilon_s=\varepsilon_g\,,\qquad \varepsilon_d+\varepsilon_l=\varepsilon_f$
Concentrations interfaciales:	$C_s^*=\begin{cases}kC_l^* & if\quad \Gamma_s\geq 0\\ C_s & if\quad \Gamma_s<0\end{cases}$ | $C_l^*=\frac{T-T_f}{m}$
Rayon de la cellule :	$R_1=\left(4/3\pi n\right)^{-1/3}$
Rayon du grain :	$a=R_1\varepsilon_g^{\,1/3}$
Densité d'air de l'enveloppe du grain :	$S_g=4\pi a^2 n$
Longueur de diffusion :	$\delta_{l-d}=\delta\left[1-\frac{10a^2\delta+10a\delta^2+4\delta^3}{5\left(R_1{}^3-a^3\right)}\right]$ où $\delta=\begin{cases}D_l/\overline{w}_g & si\quad \left(R_1-a\right)\geq 2\left(D_l/\overline{w}_g\right)\\ \left(R_1-a\right)/2 & si\quad \left(R_1-a\right)<2\left(D_l/\overline{w}_g\right)\end{cases}$
La croissance du grain :	$\Gamma_g=\rho_f S_g\overline{w}_g\ ,\qquad \overline{w}_g=\frac{D_l m\left(k-1\right)C_l^*}{\pi^2\Gamma}\left(Pe_t\right)^2$

Toutefois quelques simplifications ont été apportées par rapport à la formulation de la référence IV, à savoir :

- Le coefficient de transfert e QDM à l'interface, K_f, n'est pas calculé avec la formule énoncée en référence IV. Ici une expression simplifiée pour K_f est utilisée qui fait intervenir la perméabilité au fluide isotrope de type Carman-Kozeny [13], K_f^* :

$$K_f = \frac{\mu \varepsilon_f}{K_f^*} \ , \qquad K_f^* = \frac{{\lambda_1}^2 {\varepsilon_f}^3}{\pi^2 K_c t^2 (1-\varepsilon_f)^2} \tag{1}$$

où $K_c = 5$ et $t = 2$ sont deux paramètres adimensionnels, λ_1 est l'espacement primaire de la structure colonnaire et ε_f la fraction fluide. Cette loi a déjà été utilisée par Ghislain Quillet [6] et a été choisie par la suite pour avoir une même base de comparaison avec les résultats obtenus déjà en [6].

- Comme dans l'approche de Ghislain Quillet [6], la surfusion de la pointe colonnaire est considérée comme étant négligeable. Ainsi, on contourne le problème de suivi du front colonnaire car la nucléation colonnaire est de cette façon approchée par un événement local dépendant seulement des paramètres locaux comme la température et la concentration fluide locale. En effet, la nucléation colonnaire se déclenche instantanément dès que la température T est inférieure à la température liquidus locale, $T_{liq} \left(= T_{fusion} + mC_f\right)$. Comme les cas de solidification analysés par la suite sont caractérisés par des forts gradients thermiques (G>1000K/m), la zone de surfusion devant les pointes colonnaires peut être supposée négligeable.
- L'effet de convection solutale et thermique est prise en compte par la suite par l'approximation de Boussinesq : seule la densité qui apparaît dans la force volumique d'origine gravitaire dépend linéairement de la température locale et de la concentration locale :

$$\rho_f = \rho_f^0 \left[1 + \beta_T \left(T - T_0\right) + \beta_C \left(C_f - C_0\right)\right] \tag{2}$$

où β_T et β_C sont respectivement les coefficients d'expansion thermique et solutale.

Il faut noter que l'équation de conservation de soluté dans le liquide extra-dendritique est utilisée en couplage avec l'équation de conservation de soluté dans le fluide total. Comme nous l'avons expliqué dans la référence IV (Annexe 7.2), ceci est nécessaire pour pouvoir traiter d'une manière implicite le rejet de soluté dans le liquide extra-dendritique en obtenant ainsi un algorithme de résolution plus robuste. L'équation de conservation de soluté dans le liquide extra-dendritique est discrétisée de la manière suivante (référence IV) :

$$\begin{aligned} V_{cell}\left(\varepsilon_l \rho_f\right)_i^n \frac{\left(C_l\right)_i^n - \left(C_l\right)^{n-1}}{\Delta t} + \left(\varepsilon_l \rho_f \mathbf{v}_f\right)_i^n \sum_\sigma \left(C_l\right)_\sigma^n \mathbf{n}_\sigma S_\sigma = \sum_\sigma \left(\varepsilon_l \rho_f D_f \nabla C_l\right)_\sigma^n \cdot \mathbf{n}_\sigma S_\sigma + \\ + V_{cell}\left(\frac{\rho_f S_g D_l}{\delta_{l-d}} - \Gamma_g\right)_i^n \left[\left(C_l^*\right)_i^n - \left(C_l\right)_i^n\right] \end{aligned} \tag{3}$$

où V_{cell} est le volume de la maille de discrétisation, σ la $\sigma^{ème}$ face la maille, $\mathbf{n}_\sigma$ la normale extérieure à la $\sigma^{ème}$ face, S_σ la surface de la $\sigma^{ème}$ face, n la $n^{ème}$ itération temporelle et i la $i^{ème}$ itération de convergence. On met facilement en évidence le traitement implicite du rejet de soluté dans le liquide extra-dendritique, c'est-à-dire le dernier terme du membre de droite de l'équation (3). Comme nous l'avons expliqué dans la référence IV le couplage avec l'équation de conservation de soluté dans le fluide se fait à chaque pas de temps par l'intermédiaire de $\left(C_l\right)^{n-1}$:

$$\left(C_l\right)^{n-1} = \left(\frac{\varepsilon_f C_f - \varepsilon_d C_l^*}{\varepsilon_l}\right)^{n-1} \tag{4}$$

Ainsi le taux de solidification Γ_s se calculera de la manière suivante :

$$\begin{aligned}\left(\Gamma_s\right)_i^n \left(C_l^* - C_s^*\right)_i^n V_{cell} = \left(\varepsilon_d \rho_f \frac{\partial C_l^*}{\partial t}\right)_i^n V_{cell} + \left(\frac{\rho_f S_g D_l}{\delta_{l-d}}\right)_i^n \left[\left(C_l^*\right)_i^n - \left(C_l\right)_i^n\right] V_{cell} + \\ + \varepsilon_d \rho_f \mathbf{v}_f \sum_\sigma \left(C_l^*\right)_i^n \mathbf{n}_\sigma S_\sigma\end{aligned} \tag{5}$$

où $\left(C_l\right)_i^n$ est calculé à l'aide de l'équation (3).

4.5.2 L'implémentation des équations dans Fluent

La formulation des équations diphasiques proposée par Fluent est très semblable à la formulation des équations du Tableau 1. Ainsi, les équations de conservation de masse et de QDM pour la phase solide et fluide peuvent être rentrées directement dans Fluent telles quelles sont décrites en Tableau 1. Par contre il faut spécifier dans le logiciel Fluent, par l'intermédiaire des fonctions utilisatrices (« User Defined Functions »), les sources et les coefficients de transfert correspondants : la source de masse Γ_s, les coefficients de transfert de QDM à l'interface K_f et les forces volumiques électromagnétiques ($F_{é.m.}$) ou de gravité. En ce qui concerne les équations de conservation de l'énergie et de soluté, celles-ci sont introduites dans Fluent à l'aide des équations de transport scalaires. En effet, dans Fluent on a la possibilité de définir en dehors des équations de transport classiques (masse, QDM) des équations de transport scalaires supplémentaires (les « User Defined Scalars »). La forme générale d'une équation scalaire est la suivante :

$$\frac{\partial\left(m\psi\right)}{\partial t} + div\left(\boldsymbol{\varphi}\,\psi\right) = div\left(D^*\nabla\psi\right) + S \tag{6}$$

où ψ représente le champ physique transporté, m le terme de l'accumulation, $\boldsymbol{\varphi}$ le flux massique, D^* la diffusivité et S les éventuelles sources. On note que m, $\boldsymbol{\varphi}$, D^* et S sont des paramètres à définir par l'utilisateur. Ceux-ci peuvent être facilement particularisés à l'aide des fonctions utilisatrices (« User Defined Functions »). Ainsi l'équation de

l'énergie peut être facilement implémentée dans Fluent en particularisant ψ, m, $\boldsymbol{\varphi}$, D_k^* et S_k comme suit :

$$\begin{aligned} \psi &= T \\ m &= \rho_s \varepsilon_s c_s + \rho_f \varepsilon_f c_f \\ \boldsymbol{\varphi} &= \cancel{\rho_s \varepsilon_s c_s \mathbf{v}_s} + \rho_f \varepsilon_f c_f \mathbf{v}_f \\ D^* &= \varepsilon_s \lambda_s + \varepsilon_f \lambda_f \\ S &= L \Gamma_s \end{aligned} \tag{7}$$

L'équation de conservation de soluté en solide est introduite dans Fluent en prenant :

$$\begin{aligned} \psi &= C_s \\ m &= \rho_s \varepsilon_s \\ \boldsymbol{\varphi} &= 0 \\ D^* &= \varepsilon_s \rho_s D_s \\ S &= C_s^* \Gamma_s \end{aligned} \tag{8}$$

Finalement l'équation de conservation de soluté dans le fluide est implémentée en Fluent en considérant:

$$\begin{aligned} \psi &= C_f \\ m &= \rho_f \varepsilon_f \\ \boldsymbol{\varphi} &= \rho_f \varepsilon_f \mathbf{v}_f \\ D^* &= \varepsilon_f \rho_f D_f \\ S &= -C_s^* \Gamma_s \end{aligned} \tag{9}$$

4.5.3 L'algorithme de résolution

On rappelle que la méthode de discrétisation est celle des volumes finis. Ainsi toutes les équations aux dérivées partielles du modèle sont résolues en les intégrant sur les cellules du domaine de discrétisation. La méthode de discrétisation spatiale utilisée est celle UPWIND du 2ème ordre avec un traitement intégralement implicite. La discrétisation temporelle est celle d'Euler de premier ordre, implicite. Le système d'équations du Tableau 1 est résolu selon un algorithme ségrégé ce qui signifie que toutes les équations sont résolues d'une manière séquentielle et itérative. L'algorithme de résolution peut être synthétisé de la manière suivante :

- Etape I : Toutes les valeurs au pas de temps t^n sont supposées connues ;
- Etape II : L'incrémentation du pas de temps : $t^{n+1} = t^n + \Delta t$;

- Etape III : Entrée dans la boucle d'itération : $i=0$; $\left(\varepsilon_s\right)_i^{n+1}=\left(\varepsilon_s\right)^n$, $\left(\varepsilon_f\right)_i^{n+1}=\left(\varepsilon_f\right)^n$, $p_i^{n+1}=p^n$, $\mathbf{v}_i^{n+1}=\mathbf{v}^n$, $T_i^{n+1}=T^n$, $\left(C_s\right)_i^{n+1}=\left(C_s\right)^n$, $\left(C_f\right)_i^{n+1}=\left(C_f\right)^n$, $\left(\varepsilon_g\right)_i^{n+1}=\left(\varepsilon_g\right)^n$, $\left(\Gamma_s\right)_i^{n+1}=\left(\Gamma_s\right)^n$;

- Etape IV : Itération $i+1$:

  - Calcul en utilisant la méthode de couplage pression-vitesses SIMPLEC de $\left(\varepsilon_s\right)_{i+1}^{n+1}$, $\left(\varepsilon_f\right)_{i+1}^{n+1}$, p_{i+1}^{n+1} et $\mathbf{v}_{i+1}^{n+1}$;
  - Résolution de l'équation scalaire UDS_0 représentant l'équation de l'énergie. Ainsi on obtient : T_{i+1}^{n+1} ;
  - Résolution de l'équation scalaire UDS_1 représentant l'équation de conservation de soluté dans le fluide. Ainsi on obtient : $\left(C_f\right)_{i+1}^{n+1}$;
  - Résolution de l'équation scalaire UDS_2 représentant l'équation de conservation de soluté dans le solide. Ainsi on obtient : $\left(C_s\right)_{i+1}^{n+1}$;
  - Calcul de la croissance du grain : $\left(\Gamma_g\right)_{i+1}^{n+1}$, $\left(\varepsilon_g\right)_{i+1}^{n+1}$;
  - Calcul de la nouvelle concentration dans le liquide extradendritique $\left(C_l\right)_{i+1}^{n+1}$ en utilisant l'équation (3). On note le traitement implicite du rejet de soluté dans l'équation (3) ;
  - **Calcul de la rate de solidification $\left(\Gamma_s\right)_{i+1}^{n+1}$ en utilisant l'équation (5) ;

- Etape V : On vérifie si les valeurs $\left(\varepsilon_s\right)_{i+1}^{n+1}$, $\left(\varepsilon_f\right)_{i+1}^{n+1}$, p_{i+1}^{n+1}, $\mathbf{v}_{i+1}^{n+1}$, T_{i+1}^{n+1}, $\left(C_f\right)_{i+1}^{n+1}$, **$\left(C_s\right)_{i+1}^{n+1}$, $\left(\Gamma_g\right)_{i+1}^{n+1}$, $\left(\varepsilon_g\right)_{i+1}^{n+1}$ et $\left(\Gamma_s\right)_{i+1}^{n+1}$ sont convergées. Si oui, on passe au pas de temps suivant donc à l'étape II. Si non on continue les itérations en revenant à l'étape IV.

4.5.4 Convection naturelle vs. convection forcée

Dans la suite du mémoire nous analyserons l'influence de la convection naturelle et forcée sur la solidification des alliages binaires sera analysée. Le modèle mathématique présenté ci-dessus sera résolu à l'aide du logiciel Fluent pour les différents cas 2D et 3D de solidification colonnaire dirigée effectués sous l'influence de la convection naturelle et/ou forcée. La convection forcée est le résultat des forces électromagnétiques produites par l'application d'un champ électromagnétique alternatif. Les champs électromagnétiques tournants et glissants seront analysés par la suite. Même si les cas traités par la suite ne permettent pas une comparaison directe avec des expériences réelles, les résultats obtenus permettront une validation partielle du modèle par une comparaison directe avec d' autres codes numériques mais aussi avec des ordres de grandeur théoriques. L'ensemble des expériences numériques suivantes prend en compte un alliage binaire Pb-10% en masse Sn.

4.5.4.1 Convection naturelle – cas 2D

Le cas analysé

Dans un souci de validation du code, le cas bidimensionnel analysé sera identique à celui utilisé lors de plusieurs expériences numériques effectuées par Ghislain Quillet [6] et

Mabel Medina [14] en ayant à la base des modèles numériques différents du présent modèle. On considérera par la suite un lingot bidimensionnel rectangulaire ayant 5 mm de largeur et 10 mm de hauteur (voir Figure 5). En essayant d'approcher le plus possible le cas d'une solidification dirigée, les conditions limites sont les suivantes :

- Les parois latérales sont adiabatiques ;
- Une température linéairement décroissante est imposée sur la paroi inférieure :

$$T_{\inf}(t) = T_0 - CR \cdot t \tag{10}$$

où CR est la vitesse de refroidissement [K/s] ;

- Un flux entrant est imposé sur la paroi supérieure, flux correspondant au gradient de température vertical initial, G_0 :

$$\varphi_{\sup} = \lambda_{liq} G_0 \quad \left[W.m^{-2}\right] \tag{11}$$

- Le flux de masse à travers les parois est nul, ainsi que les flux de soluté.

Les conditions initiales quant à elles peuvent être résumées comme suit :

- La température initiale sur la paroi inférieure, T_0, est égale à la température de liquidus correspondante à la concentration initiale C_0 ;
- Le gradient de température initial est fixé à la valeur G_0 ;
- Vitesses nulles dans le liquide ;
- La concentration de l'étain initiale dans le liquide est considérée comme étant très proche de $C_0 = 10\%$, mais légèrement et aléatoirement perturbé par rapport à C_0 :

$$C_0 = C_0 \pm 0.005 C_0 \tag{12}$$

On note que la configuration étudiée est thermiquement stable. Par contre, la distribution de soluté dans la zone pâteuse est fortement instable à cause de la différence de masse volumique entre étain et plomb. Ainsi, la distribution aléatoire de soluté autour de la valeur C_0 aura comme effet la génération d'un léger mouvement aléatoire dans le ligot qui permettra la déstabilisation du macrofront et la création des éventuels canaux ségrégés.

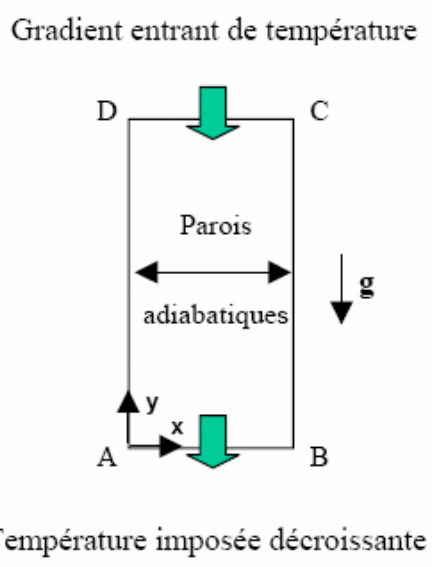

Figure 5: Géométrie du cas 2D et conditions aux limites

Les conditions de solidification sont résumées dans le Tableau 2. Ces conditions de solidification ont été choisies pour avoir une base cohérente de comparaison avec les calculs de Ghislain Quillet [6]. D'ailleurs les paramètres numériques utilisés par la suite (voir Tableau 3) sont eux aussi quasi-identiques à ceux utilisés en [6].

Tableau 2: Conditions de solidification - cas 2D

$C_0 = 10$ wt% Sn
$G = 1000\,K/m$
$CR = 1\,K/\min$
$\lambda_1 = 300\ \mu m$

Tableau 3: Paramètres numériques - cas 2D

Maillage :	20 x 40
Pas de temps :	0,02 s
Schéma temporel :	1er ordre Euler
Couplage pression –vitesse :	SIMPLE C
Schéma spatial :	2ème ordre UPWIND
Durée de simulation :	20 minutes

On remarque encore une fois que la configuration étudiée est thermiquement stable et solutalement instable au regard de la distribution de soluté dans la zone pâteuse. En effet, la zone pâteuse est enrichie en soluté par le rejet de soluté à l'interface solide-liquide tel que rapidement derrière les pointes colonnaires, le liquide est proche du mélange parfait, c'est-à-dire à une concentration très voisine de la concentration à l'équilibre C_l^*. Ainsi le gradient de soluté dans la zone pâteuse est négatif. Ceci ajouté au fait que l'étain est plus léger que le plomb fait que la configuration est fortement instable. Toutefois pour qu'une déstabilisation du macrofront plan apparaisse et s'amplifie il faut induire dans le système une faible perturbation solutale qui, par la suite, sera amplifiée et donnera

naissance à un canal ségrégé. Cette perturbation n'est plus que la distribution initiale aléatoire de soluté (équation (12)). Il faut remarquer aussi que la convection naturelle dans le cas analysé est essentiellement de nature solutale et non thermique. Pour quantifier ceci on peut déjà regarder le rapport des forces d'Archimède d'origine solutale et thermique :

$$\begin{aligned} N &= \frac{\Delta\rho_C}{\Delta\rho_T} = \frac{\beta_C \Delta C}{\beta_T \Delta T} \\ &= \frac{\beta_C}{\beta_T m} = 19.5 \end{aligned} \tag{13}$$

en tenant compte des paramètres physiques de l'alliage Pb-Sn, voir Annexe 7.1. Le nombre N s'appelle aussi le nombre de flottaison. On remarque ainsi l'importance des forces d'Archimède de nature solutale face à celles d'origine thermique.

A présent si l'on admet l'existence d'un canal ségrégé dans la zone pâteuse on peut aussi comparer les nombres de Rayleigh thermique et solutal. En sachant que dans le canal la concentration est proche de celle de l'équilibre on peut écrire :

$$\begin{aligned} \frac{Ra_C}{Ra_T} &= \left(\frac{g\beta_C \Delta C\, l^3}{\rho_0 \nu D} \right) \Bigg/ \left(\frac{g\beta_T \Delta T\, l^3}{\rho_0 \nu \alpha} \right) \\ &= \frac{\beta_C}{\beta_T m} \times \frac{\alpha}{D} = 3.4 \times 10^5 \end{aligned} \tag{14}$$

au regard des paramètres physiques de l'alliage Pb-Sn, voir Annexe 7.1. On remarque donc une nouvelle fois une prépondérance de la convection solutale dans les éventuelles poches liquides dans la zone pâteuse. Ce résultat a une conséquence très importante, car si une déstabilisation du macrofront apparaît, créant une poche liquide dans la zone pâteuse, celle-ci sera encore amplifiée par la forte convection solutale qui se forme. Dans ces conditions, le canal ségrégé, une fois formé, s'auto entretient dans le temps par l'intermédiaire de la convection naturelle qui lui est associée. Une nouvelle question se pose alors : est-ce que la déstabilisation du macrofront colonnaire peut apparaître ou non ? Pour répondre à cette question une analyse de l'écoulement d'origine solutale et dans le voisinage du macrofront doit être faite. Ici, évidemment entre en jeu la perméabilité au fluide de la zone pâteuse derrière les pointes colonnaires. L'analyse de Ghislain Quillet [6] basée sur le modèle de Worster [15] a pu confirmer le fait que pour le cas analysé par la suite il existe les conditions étaient remplies pour que l'écoulement au niveau du macrofront devienne instable.

Résultats numériques

En regardant les résultats obtenus au niveau de la distribution de concentration dans le liquide et de la carte de fraction solide (Figure 6a,b) à t=50s du début de la solidification, on peut déjà observer deux instabilités au niveau du macrofront. Le mouvement ascendant correspondant, les panaches de liquide enrichi, (Figure 6c) apporte du liquide riche en soluté de la zone pâteuse au niveau du macrofront et y retarde la solidification formant deux poches liquides (Figure 6b).

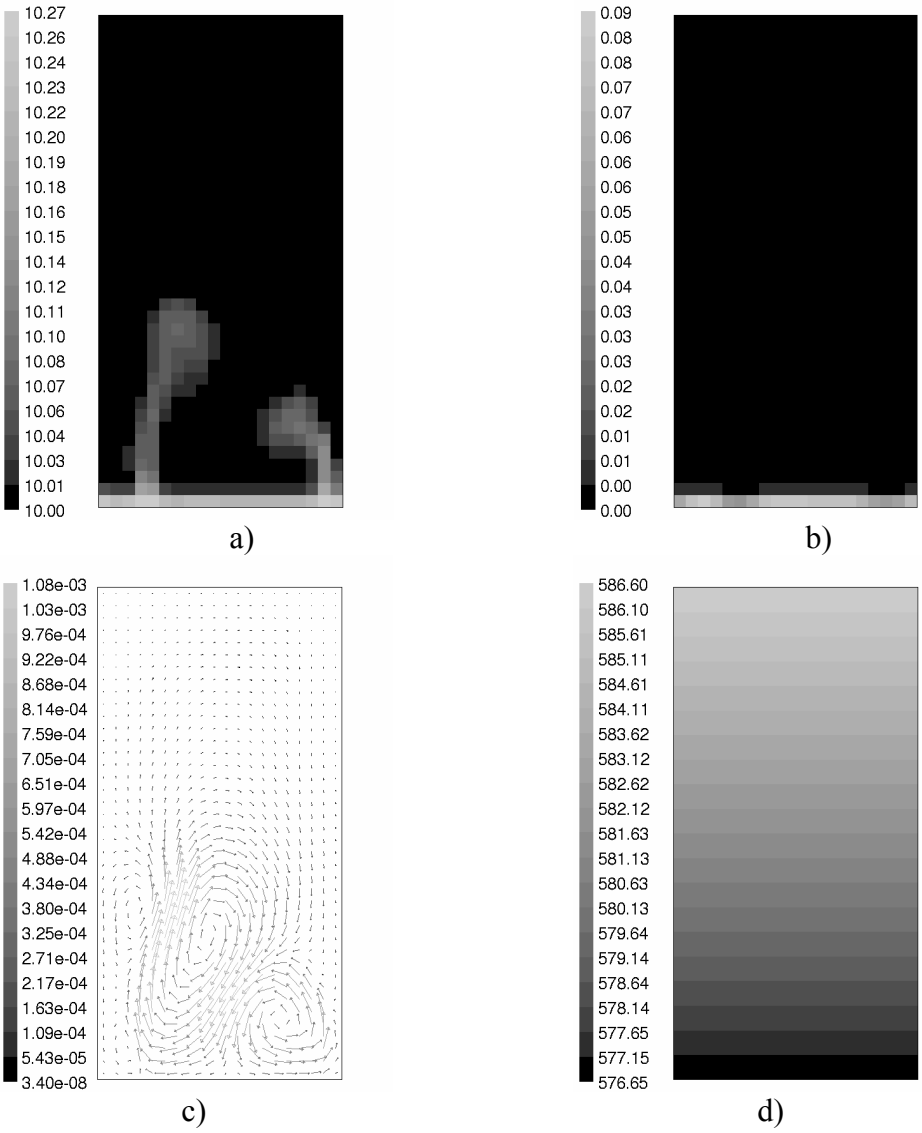

Figure 6: La distribution a) de la concentration dans le fluide, C_f ; b) de la fraction solide, ε_s ; c) de la vitesse ; d) de la température, à $t = 50\,s$ du début de la solidification.

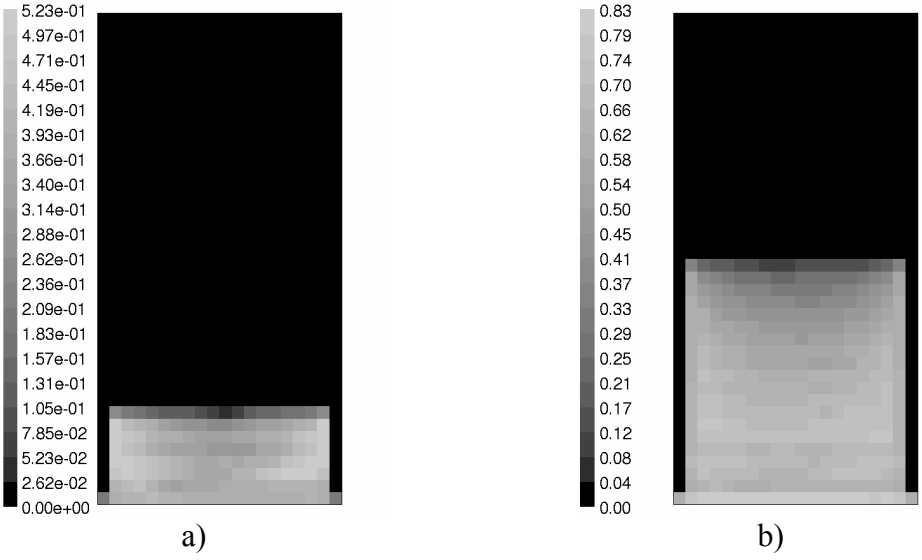

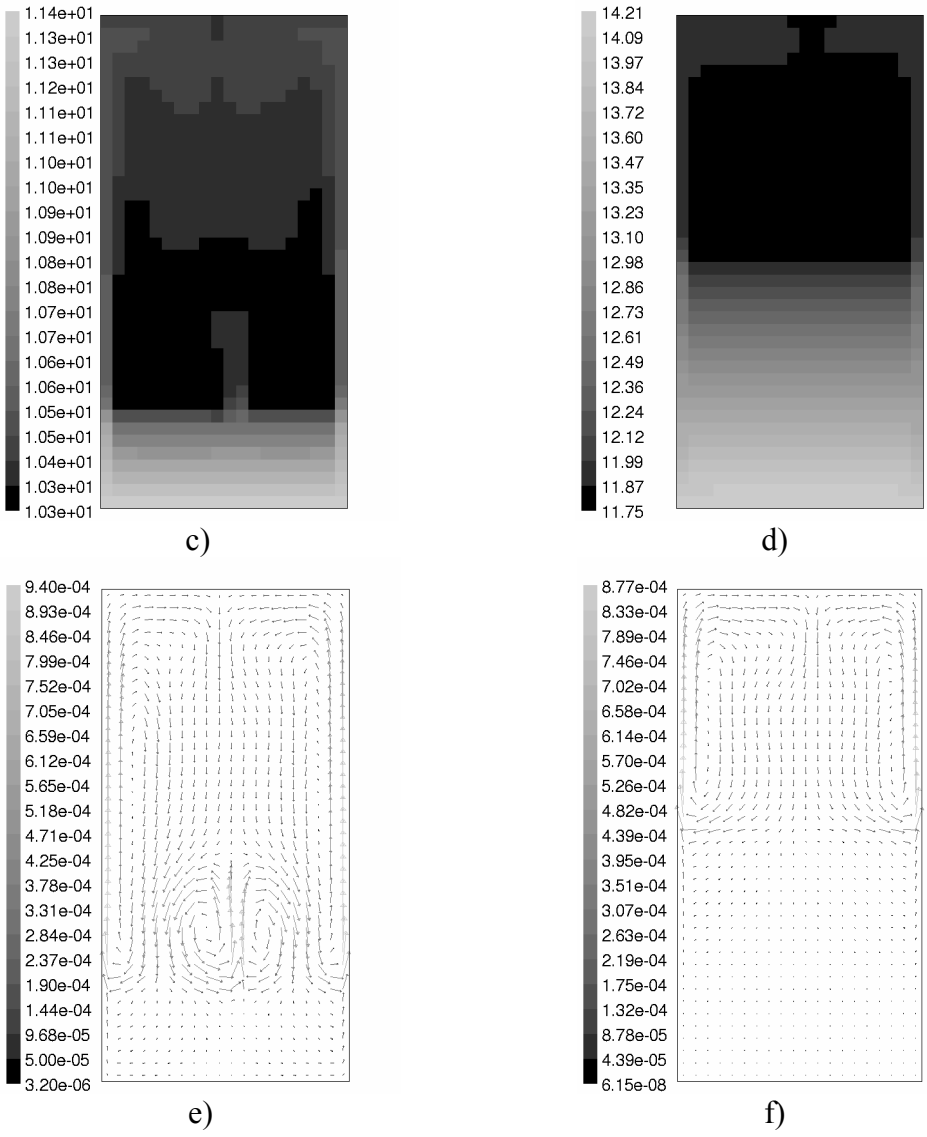

Figure 7: La fraction liquide (a, b), la distribution de la concentration dans le fluide (c, d) et la vitesse du liquide (e, f)) à $t = 200s$ (a, c, e) et $t = 600s$ (b, d, f).

Au fur et à mesure que le macrofront avance, les zones correspondantes aux panaches enrichies en soluté restent liquides et les poches liquides se transforment progressivement en canaux ségrégés (Figure 7a, b). Il est donc important de remarquer que le mouvement solutal ascendant est assez intense ($v \simeq 9 \times 10^{-4}\, m/s$) et ne fait qu' auto-entretenir le canal ségrégé car il apporte du liquide riche en soluté de la zone pâteuse inférieure vers les zones supérieures plus chaudes en empêchant ainsi la solidification dans le canal. En effet le mouvement solutal dans le canal prélève du liquide à l'équilibre de la zone pâteuse environnante et la concentre dans le canal. Ainsi le canal se retrouvera toujours à une concentration proche de celle de l'équilibre, mais légèrement plus grande (Figure 7c, d). Ceci est possible justement à cause de l'écoulement ascendant dans le canal qui, même s'il est caractérisé par des vitesses faibles, est bien capable de déformer localement les lignes iso-concentrations (Figure 7c, d). En effet, le nombre de Péclet chimique dans le canal pour une vitesse moyenne dans le canal de l'ordre de $10^{-4}\, m/s$ soit :

$$Pe_c = \frac{V_c h}{D_l} = \frac{10^{-4} \times 0.005}{1.8 \times 10^{-9}} = 270 \tag{15}$$

est grand. Donc, la convection dans le canal reste prédominante face à la diffusion moléculaire. On peut ainsi assimiler le canal ségrégé à une pompe de soluté qui draine en soluté la zone pâteuse environnante en l'appauvrissant. L'énergie motrice de cette pompe est évidemment la convection naturelle d'origine solutale dans le canal même. Effectivement cet effet de pompage de soluté a comme principale conséquence la déplétion en soluté de la zone pâteuse environnante. En regardant la concentration moyenne à deux instants de temps $t = 600\,s$ et $t = 1200\,s$ (Figure 8) on peut observer l'appauvrissement important en soluté de la zone pâteuse adjacente au canal et l'enrichissement de ce dernier.

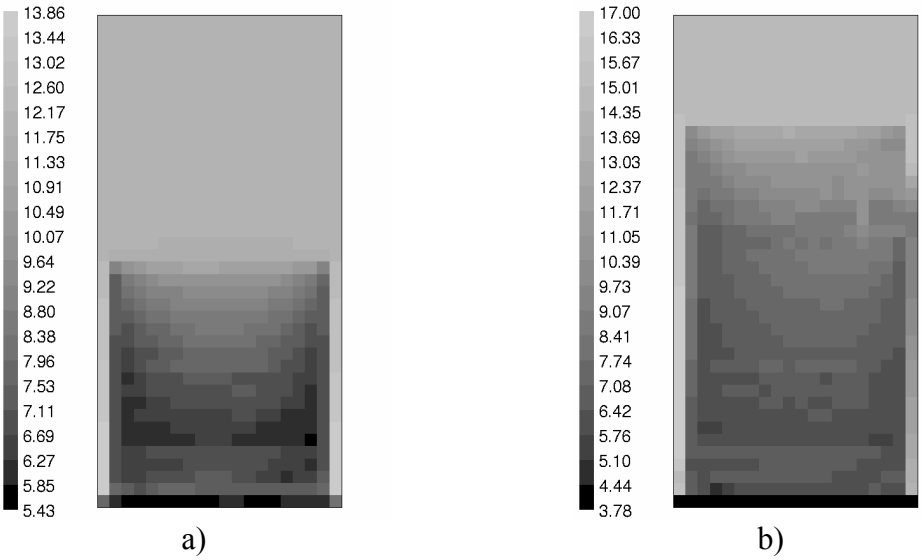

a) b)

Figure 8: La concentration moyenne à $t = 600\,s$ (a) et $t = 1200\,s$ (b)

Il serait intéressant d'essayer d'expliquer et de quantifier ce phénomène. En effet, la déplétion en soluté de la zone pâteuse s'explique par le fait que le soluté apporté dans le canal par le mouvement inter-dendritique à partir de la zone pâteuse adjacente n'est pas compensé par la quantité de soluté qui entre dans la zone pâteuse par la partie supérieure. Pour mieux comprendre ce phénomène il suffit de regarder le bilan de soluté d'une tranche de zone pâteuse situé entre deux canaux adjacents et ayant une profondeur *H* assez grande pour que l'écoulement inter-dendritique au niveau *H* soit négligeable (Figure 9). L'équation de conservation de la concentration moyenne $\overline{C} = \varepsilon_s C_s + \varepsilon_f C_f$ est :

$$\frac{\partial \rho \overline{C}}{\partial t} + div\left(\rho \varepsilon_f C_f \mathbf{v}_f\right) = div\left(\rho \varepsilon_f D_l \nabla C_f\right) \tag{16}$$

En tenant compte de la très faible diffusivité chimique D_l et des vitesses liquides relativement importantes dans la zone pâteuse derrière le macrofront ($v \simeq 10^{-4}\,m/s$) on

pourra négliger le terme de diffusion macroscopique de soluté par rapport aux effets convectifs (*Pe* grand).

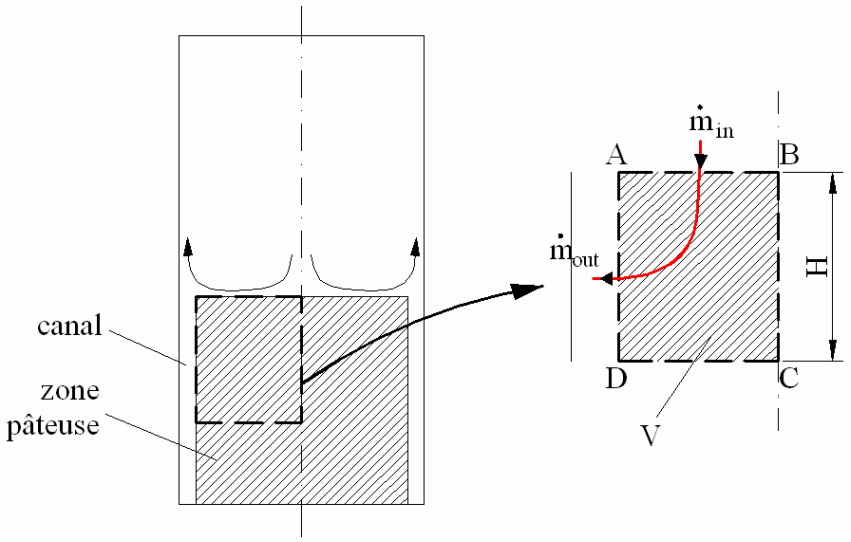

Figure 9: Schéma de l'écoulement dans la zone pâteuse environnant le canal ségrégé

Le bilan total de soluté dans le volume de contrôle considéré dans la Figure 9 peut s'obtenir par une intégration de l'équation ci-dessus dans le volume de contrôle V (voir Figure 9). Avant même de passer à l'intégration proprement dite, identifions d'abord les flux de soluté entrant et sortant du volume de contrôle V :

- Le flux liquide entrant dans le volume au niveau du macrofront (surface $S_1 = AB$) :

$$\dot{m}_{in} = \int_{S_1} \varepsilon_f \mathbf{v}_f dS \tag{17}$$

En tenant compte du fait qu'au niveau du macrofront la fraction liquide est proche de l'unité on obtient:

$$\dot{m}_{in} = \rho S_1 \overline{\mathbf{v}}_{f1} \tag{18}$$

où S_1 est la surface du macrofront entre deux canaux adjacents (AB) et $\overline{\mathbf{v}}_{f1}$ la vitesse moyenne du flux de masse pénétrant dans la zone pâteuse. Il est important de noter que ce flux de masse dépend principalement de la distribution de pression au niveau du macrofront. En effet, en raison de sa très faible perméabilité au fluide les effets inertiels dans la zone pâteuse sont négligeables par rapport au gradient local de pression. Ainsi l'équation de conservation de QDM dans la zone pâteuse peut être approchée par la loi de Darcy caractérisant les écoulements dans les milieux poreux à faible perméabilité. Ainsi l'écoulement dans cette zone pâteuse sera dicté principalement par le gradient de pression local et la perméabilité locale. Cette distribution particulière de pression au niveau du macrofront créé par l'écoulement ascendant associé à chaque canal (basses pressions au niveau du canal et hautes pressions entres les deux canaux) fait qu'une partie du flux de masse venant impacter le macrofront pénétrera également dans la zone pâteuse, c'est le flux $\dot{m}_{in}$.

Il est aussi important de remarquer que la concentration caractérisant le flux entrant $\dot{m}_{in}$ est très proche de celle du bain liquide C_0.

- Le flux de liquide latéral sortant du volume V et débouchant dans le canal :

$$\dot{m}_{out} = \int_{S_2} \varepsilon_f \mathbf{v}_f dS \tag{19}$$

où $S_2 \left(= AD\right)$ est la surface latérale du canal. A la différence du flux entrant, le liquide débouchant dans le canal est proche de la concentration d'équilibre C_l^* puisqu'il vient de sortir de la zone pâteuse.

Comme le volume V est lié au macrofront, pour faire l'intégration sur V il faut aussi tenir compte de la vitesse d'avancement du macrofront V_{mf}. Dans le cas ou le bain liquide n'est pas encore enrichi en soluté celle-ci est proche de la vitesse des isothermes dans le lingot, c'est-à-dire de la vitesse de tirage V_t. En appliquant la règle d'intégration de Leibnitz on obtient :

$$\frac{\partial}{\partial t}\int_V \overline{C} dV - C_0 V_t S_1 + \overline{C}_H V_t S_1 - \underbrace{\int_{S_1} \varepsilon_f \mathbf{v}_f C_0 \, \mathbf{n} dS}_{\dot{m}_{in} C_0} + \underbrace{\int_{S_2} \varepsilon_f \mathbf{v}_f C_l^* \, \mathbf{n} dS}_{\dot{m}_{out} \overline{C}_l^*} = 0 \tag{20}$$

où $\overline{C}_l^* = \dfrac{1}{\dot{m}_{out}} \int_{S_2} \varepsilon_f \mathbf{v}_f C_l^* \, \mathbf{n} dS$ et la concentration moyenne du liquide débouchant dans le canal et $\overline{C}_H = \dfrac{1}{S_1} \int_{S_1} \overline{C} \, dS$ la concentration moyenne dans la zone pâteuse au niveau $y = -H$. Le problème peut être sensiblement simplifié si l'on considère l'évolution du processus de solidification comme étant quasi-stationnaire. En effet, à l'exception du début de la solidification quand les panaches solutaux sont instationnaires (essentiellement dans les premières minutes) l'évolution des deux canaux ségrégés latéraux et le champ de vitesse associé sont proches d'une évolution quasi-stationnaire par rapport à l'évolution du macrofront. L'hypothèse de quasi-stationnarité nous permet de faire les simplifications suivantes :

- la variation de soluté dans le volume V, le premier terme de l'équation (20), peut être négligé ;
- l'équation de conservation de masse pour le liquide écrite sous l'hypothèse de quasi-stationnarité devient :

$$\dot{m}_{in} = \dot{m}_{out} = \dot{m} \tag{21}$$

Dans ces conditions on obtient aisément que :

$$\overline{C}_H = C_0 - \frac{\dot{m}\left(\overline{C}_l^* - C_0\right)}{S_1 V_t} \tag{22}$$

C'est-à-dire que la concentration moyenne au niveau $y=-H$, $\overline{C}_H$, est toujours plus petite que la concentration nominale de l'alliage C_0. Le canal agit donc comme une pompe de soluté, en appauvrit toujours la zone pâteuse.

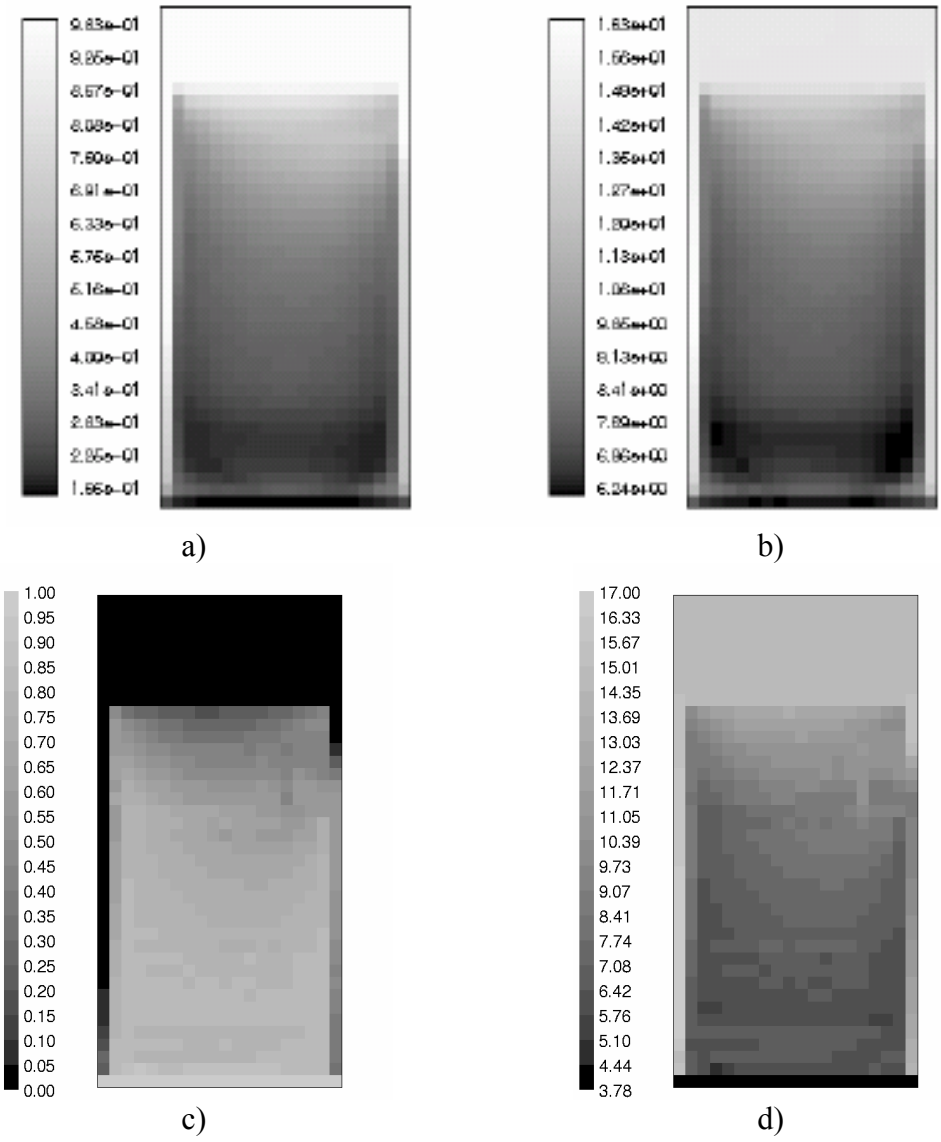

Figure 10: La fraction solide (a) et la concentration moyenne (b) ($\overline{C}_{\max}=16.3\%$) obtenues avec le modèle en [6] et la fraction solide (c) et la concentration moyenne (d) ($\overline{C}_{\max}=17\%$) obtenues avec le modèle présent ; $t=1200s$

Il faut aussi remarquer que, à terme, le liquide dans le bain liquide s'enrichit en soluté. Ce phénomène est évidemment un effet direct de l'apport net de liquide enrichi dans le bain liquide dû aux panaches de liquide enrichi correspondants aux canaux ségrégés. L'effet de l'enrichissement du bain liquide est bien prononcé dans ce cas particulier (à *t=20 min*, $C_{bain}\approx 15\%$, Figure 8b) et il est dû aux petites dimensions du lingot. Ceci implique aussi un important ralentissement de l'avancement du macrofront. Aussi l'enrichissement du bain liquide détermine d'importantes ségrégations normales dans la zone pâteuse (voir Figure 8). A ce stade il serait intéressant de comparer les résultats présents avec les résultats obtenus par Ghislain Quillet [6] en utilisant le modèle

mathématique simplifié de Felliceli [8]. En Figure 10 illustre la comparaison entre la distribution de la concentration moyenne et de la fraction liquide au temps $t = 1200s$. On peut observer un bon accord entre les deux modèles tant au niveau des macroségrégations que de la structure de la zone pâteuse (les présences des deux canaux latéraux). On s'attendait à ce que le nouveau modèle donne des résultats semblables à ceux en [6] car d'un côté les paramètres numériques sont similaires et de l'autre côté la distance entre les bras primaires choisie est petite ($\lambda_1 = 300\,\mu m$). En effet, pour cette valeur de λ_1 il correspond une grande densité volumique des grains colonnaires (n_c^0). Ceci fait que l'enrichissement du liquide extra-dendritique caractérisant les zones derrière les pointes colonnaires se fait très rapidement. Ainsi, la zone pâteuse sera, à l'exception d'une très mince zone proche de T_{liq}, proche de la concentration de l'équilibre C_l^*. Le chemin de solidification d'un point dans le lingot sera par conséquent très proche de celui obtenu en référence [6] où l'équilibre thermodynamique est considéré dans toute la zone pâteuse. Le bon accord entre les deux codes dans la limite où λ_1 petit ne peut donc que renforcer la confiance dans les calculs présents. Toutefois l'utilisation du présent modèle comporte par rapport au modèle décrit en [6] certains avantages :

- une approche rigoureuse de l'équation du bilan de QDM (en [6] la l'équation de conservation de QDM provient d'une approche simplifiée).
- la prise en compte des situations de non-équilibre local (C_l peut être en déséquilibre avec l'interface) ;
- la prise en compte de la cinétique de croissance des grains ;
- la modélisation de la réaction eutectique.

4.5.4.2 L'influence de la convection forcée sur la solidification – cas 2D

Le cas analysé

On s'attachera par la suite à analyser l'influence de la convection forcée produite par le brassage électromagnétique glissant sur la solidification. Les cas analysés par la suite sont identiques au cas précédant c'est-à-dire au cas de la solidification dirigée d'un alliage Pb-10wt% Sn dans un lingot bidimensionnel de dimensions $5 \times 10\,mm$. Les conditions de refroidissement restent elles aussi les mêmes : $G = 10\,K/cm$, $CR = 1\,K/\min$. La différence réside dans la prise en compte cette fois d'une force électromagnétique non-nulle sera considérée.

En effet, l'application d'un champ électromagnétique dans le lingot génère une force électromagnétique qui à son tour modifie significativement l'écoulement dans le bain liquide et la distribution de soluté dans la zone pâteuse. Par la suite on appliquera un champ magnétique $\mathbf{B}$ alternatif de module $|\mathbf{B}| = B_0$, glissant dont le déplacement est parallèle à l'axe vertical du lingot. Ce champ peut être engendré par un inducteur linéaire dont l'axe est parallèle à l'axe vertical du lingot (Figure 11). Celui-ci donne naissance à une force électromagnétique :

$$\mathbf{F} = \frac{1}{\mu_0}\mathbf{B} \times \left(\nabla \times \mathbf{B}\right) \tag{23}$$

où μ_0 représente la perméabilité magnétique du milieu.

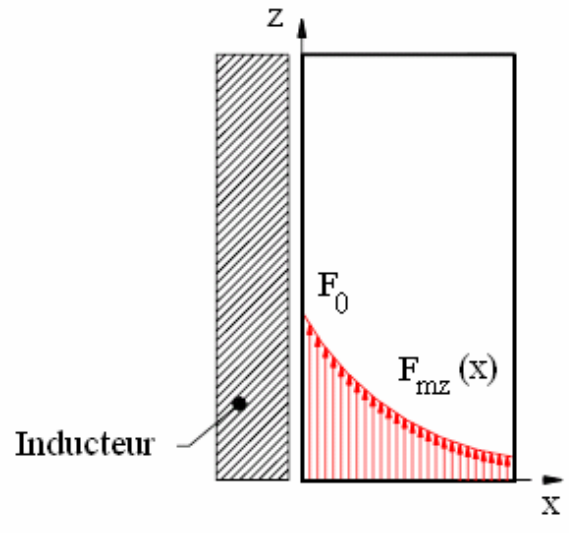

Figure 11: La force électromagnétique produite par un inducteur linéaire

Si l'on admet l'existence d'un inducteur parfait et très long par rapport à la hauteur du lingot on peut supposer que la force motrice n'a qu'une composante verticale. On peut alors calculer la force électromagnétique moyenne agissant sur le métal liquide :

$$F_{mz} = F_0 e^{-\frac{2x}{\delta}}; \qquad F_0 = \frac{\sigma\omega\lambda_m}{2\pi} B_0{}^2 \tag{24}$$

où ω est la pulsation du champ magnétique, σ la conductivité électrique du milieu, λ_m le pas polaire et δ est l'épaisseur de peau magnétique :

$$\delta = \mathrm{Re}\left\{\left(i\mu_0\sigma\omega + k^2\right)^2\right\} \tag{25}$$

Deux configurations de brassage électromagnétique seront étudiées par la suite :

- brassage électromagnétique engendrant une convection forcée à double vortex, ascendant sur les côtés. Cette configuration est susceptible d'être créée par deux brasseurs linéaires latéraux produisant une force verticale résultante dirigée vers le haut :

$$F_{mz} = F_0\left(e^{-\frac{2x}{\delta}} + e^{-\frac{2(l-x)}{\delta}}\right) \tag{26}$$

  où l est la largeur du creuset.
- brassage à double vortex, ascendant au milieu produit par deux brasseurs latéraux à polarité inversée. La force moyenne résultante sera dirigée vers le bas et aura la forme suivante :

$$F_{mz} = -F_0\left(e^{-\frac{2x}{\delta}} + e^{-\frac{2(l-x)}{\delta}}\right) \tag{27}$$

Pour les deux configurations ci-dessus présentées on prendra $F_0 = 1000\,N/m^3$ et $\delta = 0.01m$ en analogie avec les cas traités en [6]. Cette force reste suffisamment faible pour que l'écoulement soit laminaire mais suffisamment grande pour que l'influence du brassage électromagnétique soit supérieure à celle induite par la convection naturelle dans le bain liquide. Pour confirmer cela il suffit d'estimer la vitesse maximale dans le bain liquide produite par la force électromagnétique En admettant que l'équilibre entre les forces inertielles et les forces magnétiques s'établisse et en faisant une simple analyse d'échelles de l'équation de mouvement dans le bain liquide on peut écrire :

$$\begin{aligned} \rho V \frac{\partial V}{\partial y} &= F_{mz} \\ &\approx \\ \rho \frac{V^2}{H} &\approx F_{mz} \end{aligned} \tag{28}$$

On peut facilement obtenir que:

$$V \approx \sqrt{\frac{F_{mz} H}{\rho}} \quad \left(= 2.7 \times 10^{-2} \frac{m}{s} \right) \tag{29}$$

Dans ces conditions la vitesse maximale dans le bain liquide est d'un ordre de grandeur plus grand que la vitesse engendrée par la convection naturelle seule ($v \simeq 10^{-3}\,m/s$, voir sous paragraphe précédent). L'effet prépondérant du brassage électromagnétique permettra comme on va le voir le contrôle de l'écoulement dans le bain liquide et par conséquent dans la zone pâteuse.

Résultats numériques

La force électromagnétique de l'équation (27), engendre un écoulement forcé à double vortex ascendant au milieu (voir Figure 12c). On observe que l'amplitude de la vitesse se situe autour du *1.4 cm/s*, donc du même ordre de grandeur que la valeur estimée en (29).

Dans la Figure 12 les cartes de la fraction solide et de la concentration liquide sont présentées à $t = 200s$ après le début de la solidification. On distingue déjà le début d'un canal central ségrégé et le panache de liquide enrichi qui lui est associé. Ce canal est la conséquence directe de l'écoulement dans le bain liquide. En effet, l'écoulement à double vortex engendre une distribution particulière de pression au niveau du macrofront : des hautes pressions là où le liquide impacte le macrofront (sur les parois latérales) et des basses pressions au centre où le liquide remonte (Figure 13). Comme l'écoulement dans la zone pâteuse est déterminé principalement par les gradients de pression locaux, la distribution de pression au niveau du macrofront détermine un écoulement en zone pâteuse qui se fera de l'extérieur vers l'axe du lingot (voir Figure 13). Celui-ci apportera du liquide enrichi dans l'axe du lingot et y retardera la solidification. Ainsi une poche liquide commence à se former qui à terme se transformera en un canal ségrége (voir Figure 12b).

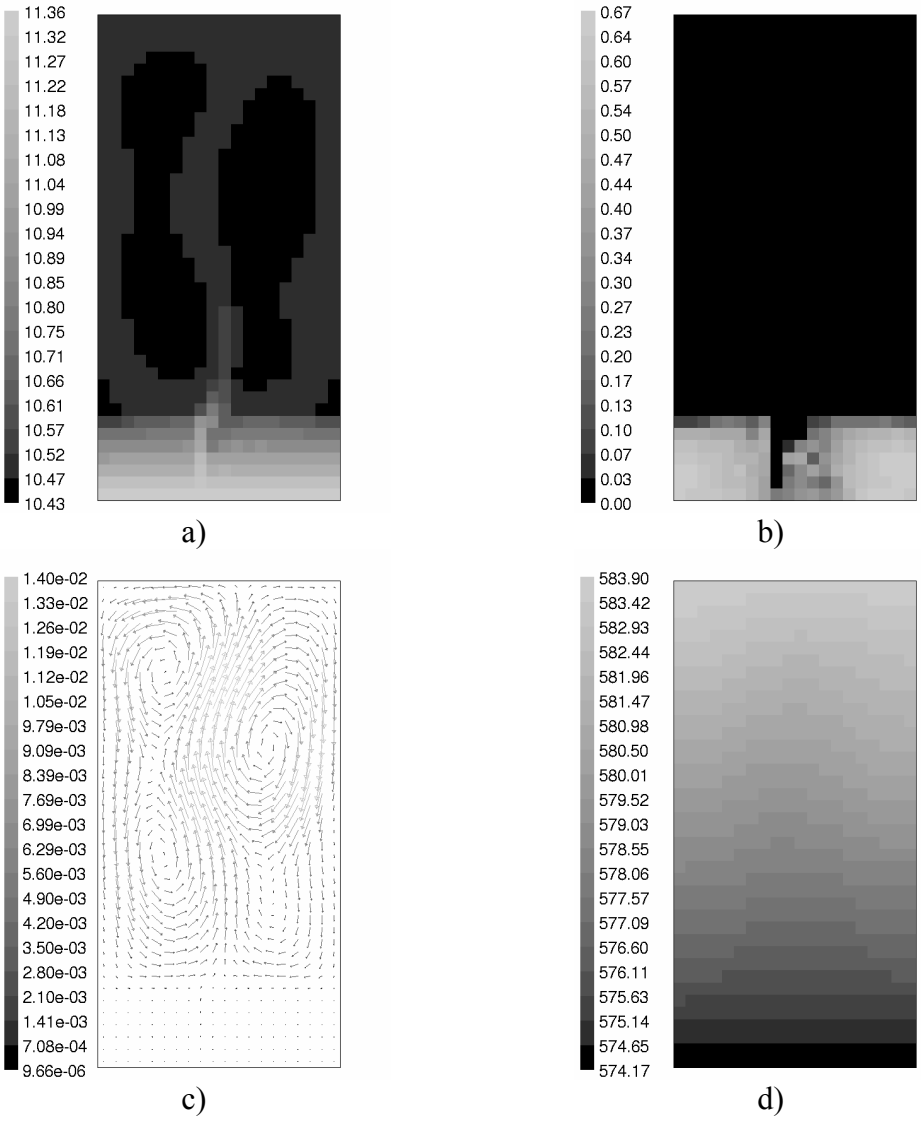

Figure 12: La a) concentration de soluté dans le liquide; b) fraction solide; c) vitesse; d) température, à $t = 200s$ du début de la solidification.

Il est donc intéressant de remarquer que l'écoulement dans le bain liquide influence l'écoulement dans la zone pâteuse par l'intermédiaire de la distribution de pression au niveau du macrofront. Toutefois il faut remarquer que l'écoulement dans le bain liquide détermine l'apparition d'un canal ségrégé seulement si l'écoulement pâteux généré reste suffisamment fort par rapport aux conditions particulières de solidification. Une analyse relativement simple de l'écoulement nous permet de quantifier la capacité de celui-ci de créer un canal ségrégé ou non. Considérons par exemple une tranche élémentaire de zone pâteuse ayant une fraction solide ε_s et la température T. Supposons qu'un flux de liquide le traverse (voir Figure 14), ce flux ayant une vitesse moyenne $\mathbf{v}_f$.

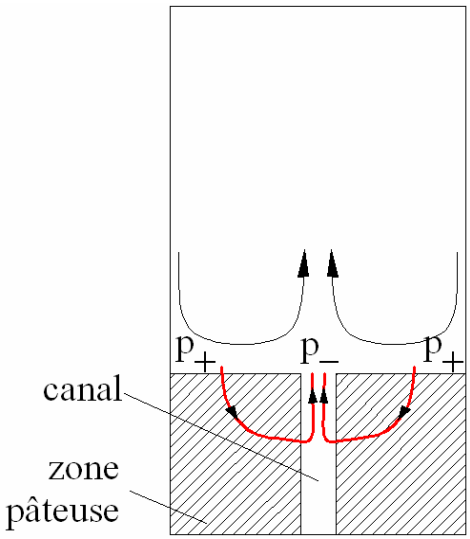

Figure 13: L'écoulement pâteux suit la distribution de pression au niveau du macrofront

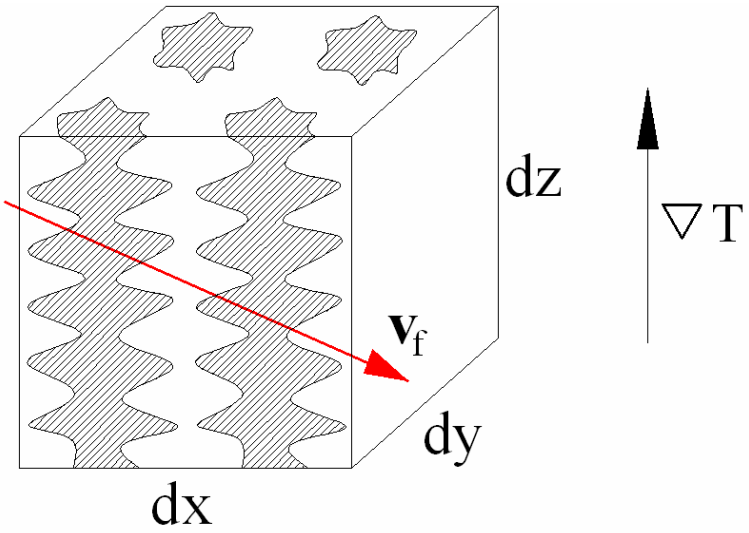

Figure 14: Une tranche élémentaire de zone pâteuse et l'écoulement inter-dendritique correspondant

Admettons aussi que le liquide est dans un état de mélange parfait ayant donc la concentration à l'équilibre C_l^*. Ceci est généralement valable pour la zone pâteuse à l'exception d'une zone très mince située proche des pointes colonnaires. L'équation caractérisant le transport de soluté dans cette tranche de zone pâteuse n'est plus que l'équation moyenne de conservation de soluté dans le liquide :

$$\frac{\partial\left(\varepsilon_f \rho_f C_l^*\right)}{\partial t} + div\left(\varepsilon_f \rho_f C_l^* \mathbf{v}_f\right) = div\left(\varepsilon_f \rho_f D_f \nabla C_l^*\right) - C_s^* \Gamma_s \qquad (30)$$

En négligeant la diffusion macroscopique de soluté (le premier terme de la partie droite) et en tenant compte de la conservation de masse du liquide l'équation ci-dessus devient :

$$\varepsilon_f \rho_f \frac{\partial C_l^*}{\partial t} + \varepsilon_f \rho_f \mathbf{v}_f \nabla C_l^* = \left(C_l^* - C_s^* \right) \Gamma_s \tag{31}$$

Cette équation nous permet d'exprimer le transfert de masse Γ_s et l'on observe aisément que s'il n'y a pas de convection dans la zone pâteuse ($\mathbf{v}_f = 0$) l'équation (31) ne représente plus que la loi de Scheil. Par contre si l'écoulement pâteux est non nul celui-ci va significativement influencer le processus de solidification par l'intermédiaire du terme $\varepsilon_f \rho_f \mathbf{v}_f \nabla C_l^*$. Il est intéressant d'analyser le signe de ce terme. Pour ceci il est utile de l'écrire sous la forme :

$$\varepsilon_f \rho_f \mathbf{v}_f \frac{|\nabla T|}{m} \mathbf{n}_G = \varepsilon_f \rho_f v_{fG} \frac{|\nabla T|}{m} \tag{32}$$

où $\mathbf{n}_G$ désigne un vecteur unitaire porté par le vecteur gradient thermique ∇T et v_{fG} la composante de la vitesse $\mathbf{v}_f$ le long du vecteur gradient thermique. Ainsi on observe facilement que si la vitesse v_{fG} est positive le terme convectif $\varepsilon_f \rho_f \mathbf{v}_f \nabla C_l^*$ devient négatif et l'inverse. C'est-à-dire, si le flux de masse est localement orienté dans le même sens que le gradient local de température la solidification diminue en intensité par rapport à un cas purement diffusif et si le flux de masse est orienté dans le sens contraire avec le gradient local de température la solidification est intensifiée. Pour le cas 2D analysé dans la Figure 12 il est maintenant facile de voir qu'aux endroits où le fluide remonte la zone pâteuse (dans l'axe) la solidification diminue en intensité et aux endroits où le flux de masse descend (sur les latérales) la solidification est accélérée. Il est intéressant maintenant d'analyser les conditions critiques pour lesquelles la solidification est complètement annulée. On obtient que la vitesse critique correspondante est telle que :

$$\varepsilon_f \rho_f \frac{\partial C_l^*}{\partial t} + \varepsilon_f \rho_f v_{fG} \frac{|\nabla T|}{m} = 0 \tag{33}$$

où:

$$\begin{aligned} v_{fG}^{crit} &= -|\nabla T| \left(\frac{\partial T}{\partial t} \right)^{-1} \\ &= V_{isoth} \end{aligned} \tag{34}$$

c'est-à-dire la vitesse critique est égale à la vitesse locale des isothermes. Dans le cas où dans la zone pâteuse la vitesse locale $\mathbf{v}_f$ est dirigée dans le même sens que le gradient local de température et que sa composante le long du même gradient est égale à la vitesse locale des isothermes alors le taux local de solidification s'annule. Si

$$v_{fG} > V_{isoth} \tag{35}$$

alors $\Gamma_s < 0$ et des phénomènes locaux de refusion ont lieu.

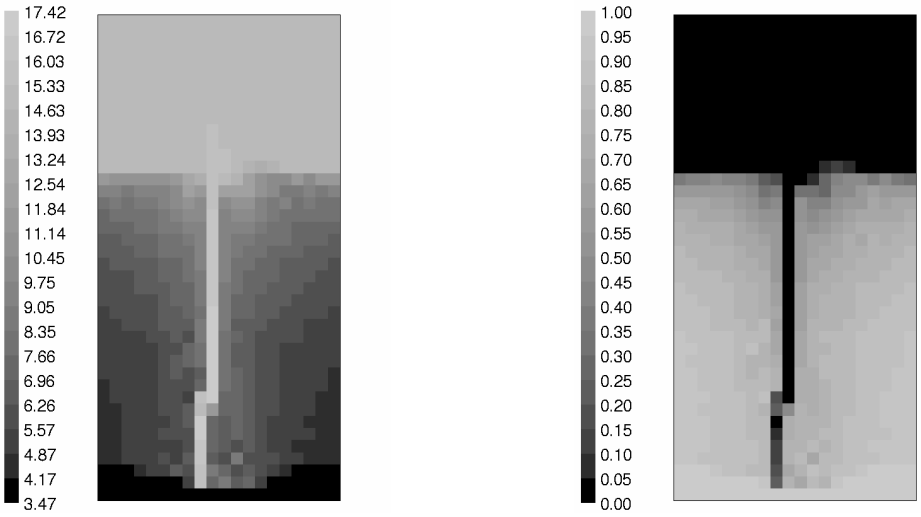

a) b)

Figure 15: La concentration moyenne (a) et la fraction solide (b) à $t = 1200s$

En revenant sur les résultats numériques on observe que l'écoulement pâteux pour le cas analysé est assez fort pour que la zone centrale reste non-solidifiée. Ceci indique que l'écoulement dans le canal est assez fort pour que la solidification n'ait pas lieu dans le canal. On remarque aussi le fort enrichissement du bain liquide dans le temps (voir Figure 15a, $C_{bain} \simeq 15\%$). Ceci est évidemment l'effet direct du liquide enrichi en soluté qui sort du canal central et débouche dans le bain liquide. En regardant la carte de la concentration moyenne à $t = 1200s$ (Figure 15a) on remarque clairement le fort enrichissement de la zone centrale ainsi que la déplétion en soluté de la zone pâteuse entourant le canal, conséquence de la présence du canal central (Figure 15b). On remarque aussi une importante ségrégation normale, conséquence de l'enrichissement continu du bain liquide.

En analysant maintenant la deuxième configuration de la force électromagnétique, équation (26), on observe que celle-ci produit dans le bain liquide un écoulement à double vortex ascendant sur les côtés (Figure 16c). Si on regarde la carte de la fraction liquide et de la concentration liquide à $t = 1200s$ (Figure 16a, b) on observe la présence des deux canaux latéraux et des panaches de liquide enrichi correspondants. En effet, l'écoulement dans le bain liquide influence de telle manière celui dans la zone pâteuse que cette fois deux canaux latéraux apparaissent. En fait les zones où le liquide vient impacter le macrofront (zone centrale) sont caractérisées par des pressions plus grandes que les pressions caractérisant les zones où le liquide remonte (zone latérales). Ainsi un mouvement dans la zone pâteuse apparaît se produisant de l'axe du lingot vers les zones latérales. Celui-ci apporte du liquide enrichi en soluté vers les zones latérales ce qui y retarde la solidification. Ainsi des poches de liquide se forment initialement proche des parois latérales qui à terme évoluent vers des canaux ségrégés (Figure 16b). En regardant la carte de concentration moyenne (Figure 16d) on observe le fort enrichissement des canaux et la déplétion en soluté de la zone pâteuse centrale. On remarque aussi un fort enrichissement du bain liquide ($C_{bain} \simeq 15\%$ à $t = 1200s$) ceci étant la conséquence de la petite dimension du domaine liquide analysé. En comparant la carte de la fraction solide à $t = 1200s$ (Figure 16b) avec la carte correspondant au cas de la convection naturelle pure (Figure 10c) on observe que la zone centrale du lingot pour le cas de la convection forcée est caractérisée par une plus grande fraction solide par rapport au cas de la convection

naturelle. Ceci peut être expliqué par le fait que pour le cas de la convection forcée le brassage de la zone pâteuse est plus intense que pour le cas de la convection naturelle. Ceci est principalement du au fort brassage du bain liquide qui à son tour va influencer la distribution de pression au niveau du macrofront de telle manière que le gradient de pression au niveau du macrofront sera plus fort par rapport au cas de la convection naturelle. Un brassage plus fort de la zone pâteuse signifie des vitesses plus grandes. Comme nous l'avons déjà montré, un écoulement plus intense dirigé dans le sens contraire au gradient local de température déterminera une solidification plus intense. Ainsi pour le cas de la convection forcée la zone centrale subira une solidification plus intense par rapport au cas de la convection naturelle.

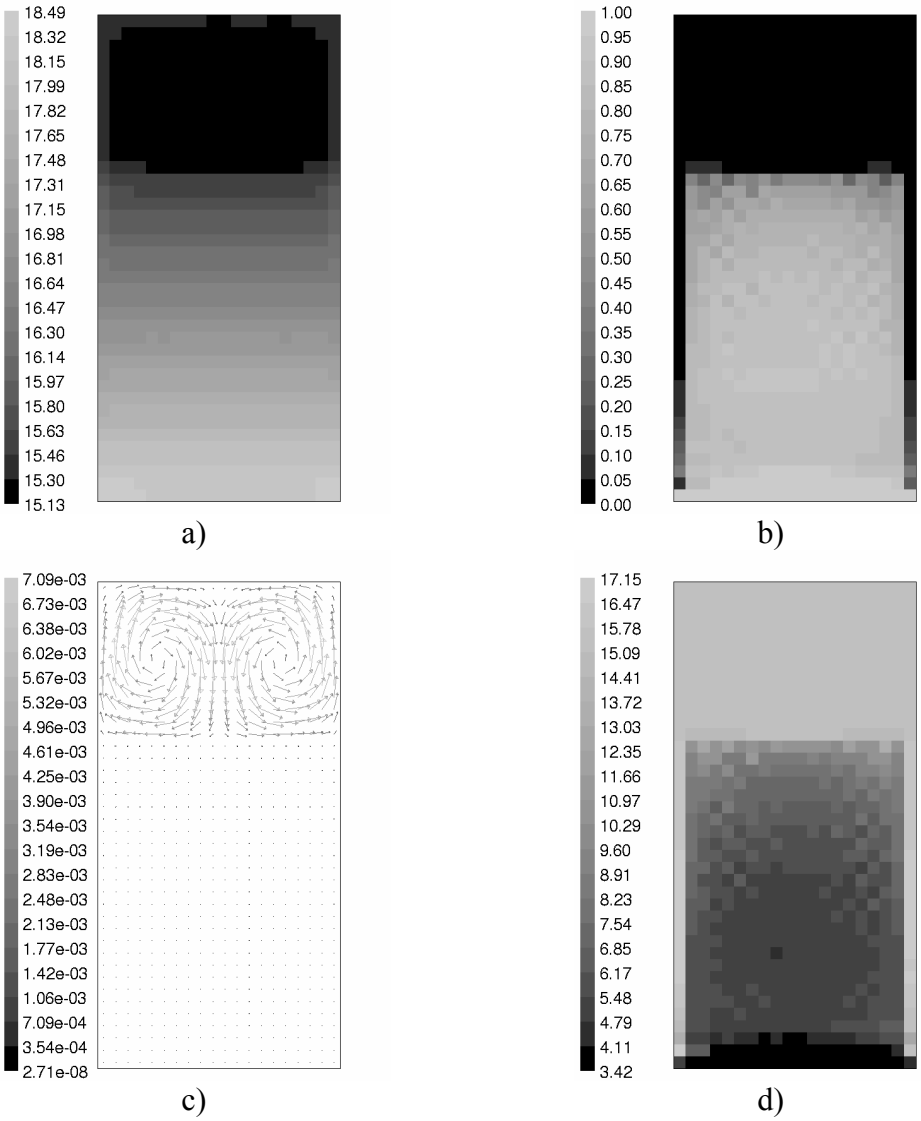

Figure 16: La concentration dans le liquide (a), la fraction solide (b), la vitesse (c) et la concentration moyenne (d) à $t = 1200s$ depuis le début de la solidification.

4.5.4.3 L'influence de la convection forcée sur la solidification – cas 3D

Le cas analysé

On a pu analyser et comparer avec les résultats de référence [6] plusieurs cas 2D de solidification dirigée tout en mettant en évidence l'influence de la convection naturelle/forcée sur le processus de solidification et les macroségrégations. Toutefois on note que notamment dans le cas d'une solidification dirigée sous l'influence de la convection naturelle, les effets tridimensionnels ne peuvent pas être négligés. En effet les canaux ségrégés ont une structure essentiellement tridimensionnelle. De plus leur position dans le lingot n'est pas toujours déterministe. Aussi on se propose par la suite d'analyser une configuration de solidification tridimensionnelle : une solidification dirigée dans un barreau cylindrique de 12 mm de diamètre et 30 mm de hauteur (voir Figure 17).

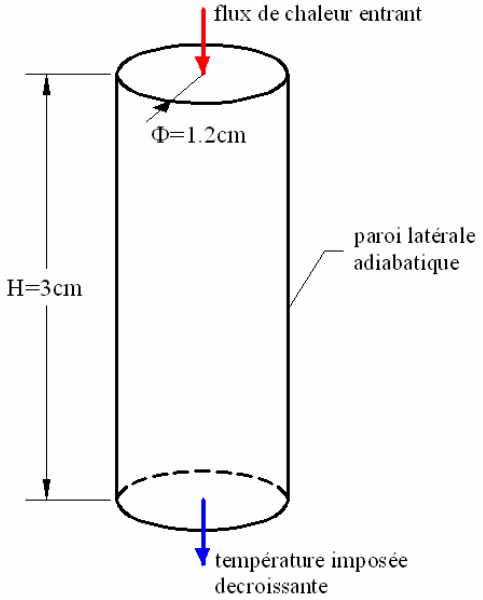

Figure 17: Géométrie du cas 3D et conditions limites correspondantes

En sachant que les conditions expérimentales des solidifications dirigées de type Bridgman supposent des échantillons très allongés on a choisi un facteur de forme $H/\Phi \simeq 3$ en essayant de minimiser l'influence de la paroi supérieure imperméable et de maintenir en même temps un temps de calcul acceptable. Les conditions limites sont semblables à celles déjà utilisées pour les cas 2D, c'est-à-dire :

- paroi inférieure imperméable ayant une température imposée et décroissante en temps, équation (10) ;
- paroi supérieure imperméable sur laquelle un flux de chaleur entrant est imposé, équation (11) ;

Les conditions initiales sont elles aussi similaires avec les cas 2D :

- un gradient vertical initial constant, G ;
- un champ de concentration initial proche de C_0 mais légèrement et aléatoirement perturbé (équation (12)). Comme nous l'avons expliqué antérieurement cette perturbation initiale est introduite dans le système pour initier la déstabilisation de l'écoulement proche du macrofront et donc pour initier la formation des canaux ségrégés.

Tableau 4: Paramètres numériques pour le cas 3D

Alliage :	Pb-10wt%Sn
Diamètre :	12 mm
Hauteur :	30 mm
No. de cellules :	20000
Schéma temporel :	1er ordre Euler
Schéma spatial :	2ème ordre UPWIND
Couplage pression-vitesse :	SIMPLEC
Pas de temps :	0.02s
Temps de simulation :	1000s

Les paramètres numériques utilisés sont réunis dans le Tableau 4. Il faut noter que les conditions de solidification (gradient thermique, vitesse de solidification) ont été choisies similaires avec le cas 3D déjà analysé en [6]. Même si la géométrie est légèrement différente (diamètre et hauteur du barreau plus grandes pour le cas présent) la densité du maillage a été gardé constante. Ceci permettra une comparaison qualitative avec les résultats de Ghislain Quillet [6].

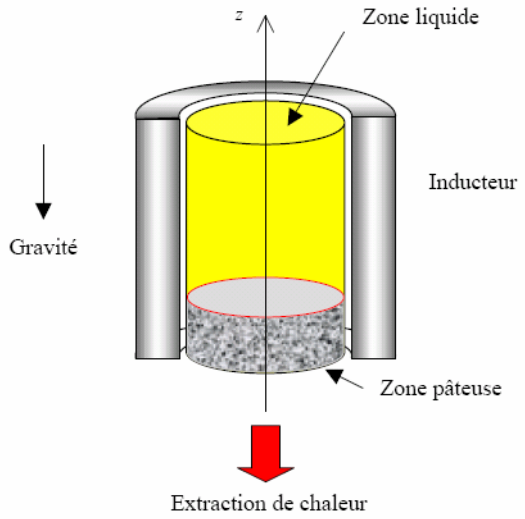

Figure 18: La configuration de l'inducteur rotatif

En essayant de mettre en évidence l'effet de la convection naturelle et du brassage électromagnétique à l'aide d'une seule expérimentation numérique on a choisi la configuration temporelle suivante :

- on commence l'expérience sans champ magnétique pour une période de *800 s* ;
- à partir de $t = 800\,s$ on applique un champ magnétique rotatif produisant une force électromagnétique située dans le plan transversal au barreau cylindrique (xOy) suivant la direction θ et ayant la variation radiale suivante :

$$F_\theta = F_0 \frac{r}{R} \tag{36}$$

où R est le rayon du cylindre. En effet, en considérant l'inducteur autour du lingot suffisamment long (voir Figure 18), on peut approcher la force motrice agissant sur le liquide avec la distribution décrite dans l'équation ci-dessus. Comme intensité maximale pour F_θ on a choisi $F_0 = 50\,N/m^3$, valeur similaire au cas analysé en [6].

Résultats numériques en convection naturelle

On observe très tôt après le début de la solidification l'apparition des instabilités de l'écoulement au niveau du macrofront (voir Figure 19, 20). Celles-ci, par un mécanisme similaire à celui déjà expliqué auparavant va engendrer l'apparition des poches liquides au niveau du macrofront et à terme le développement des canaux ségrégés, les « freckles » (Figure 21). On note que ces structures ont été fréquemment observées expérimentalement [1] mais aussi numériquement [6, 8]. En effet on peut observer dans la Figure 2 la présence de plusieurs canaux sur une métallographie obtenue après la solidification d'un alliage Pb - Sn dans une géométrie cylindrique.

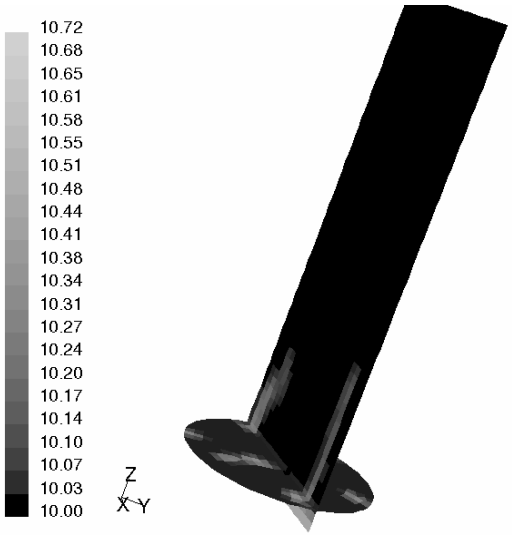

Figure 19: La concentration dans le liquide pour une coupe verticale à $t = 120s$ du début de la solidification

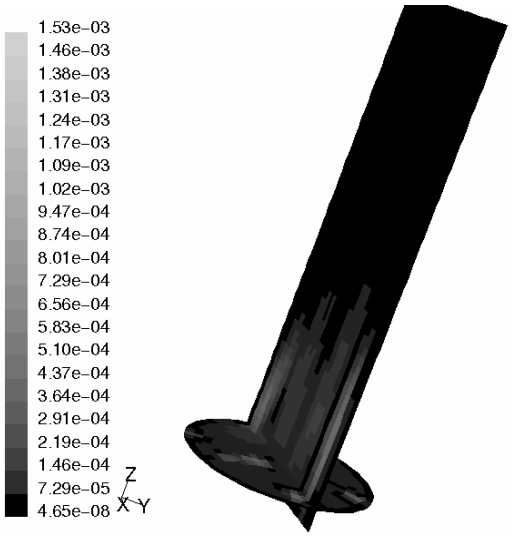

Figure 20: Le module de la vitesse pour une coupe verticale à $t = 120s$ du début de la solidification

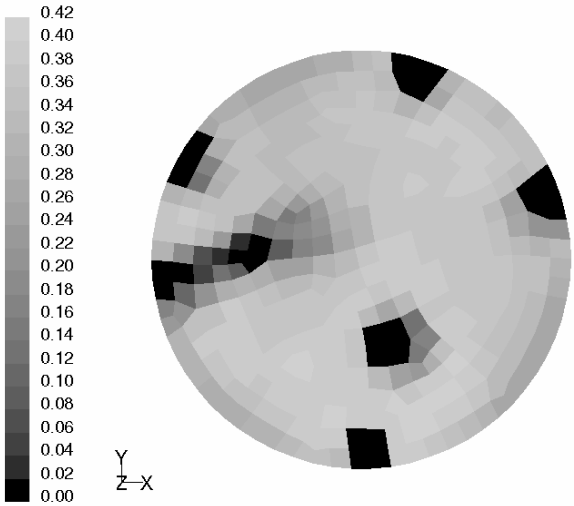

Figure 21: La fraction solide dans une coupe transversale ($h = 1.5mm$ de la base du creuset) à $t = 200s$ du début de la solidification

On remarque la présence des panaches de liquide enrichi en soluté qui sortent de chaque canal et débouchent dans le bain liquide en l'enrichissant (Figure 19). Les vitesses maximales au niveau de ces panaches sont de l'ordre de *1.5 mm/s* (Figure 20). Dans la Figure 21 on peut voir la présence de plusieurs canaux ségrégés dans la zone pâteuse. Il faut remarquer la prédominance des canaux près de la paroi latérale ceci corroborant les résultats obtenus en [6]. Toutefois, par opposition au cas 2D des canaux centraux subsistent aussi. Ceci peut être expliqué par le fait que le domaine choisi pour ce cas 3D ($\Phi = 12mm$) est plus grand par rapport au cas 2D ($L = 5mm$). En fait pour le cas 2D, même si au début de la solidification des poches liquides se développent à l'intérieur du lingot (Figure 6a), seuls les deux canaux latéraux subsistent. En effet il pourrait exister un espacement minimal entre deux canaux latéraux. Ceci a déjà été observé numériquement par Ghislain Quillet [6]. Il semble qu'en dessous d'un certain seuil (si les canaux sont trop proches) les interactions solutales et hydrodynamiques trop fortes entre deux canaux adjacents vont engendrer la disparition de l'un d'entre eux au profit de l'autre. Ainsi, la survie de deux canaux latéraux pour le cas 2D peut s'expliquer par la dimension trop petite du lingot par rapport à l'espacement minimal entre deux canaux adjacents. En choisissant un domaine 3D plus grand des canaux centraux subsistent aussi à côté des canaux latéraux.

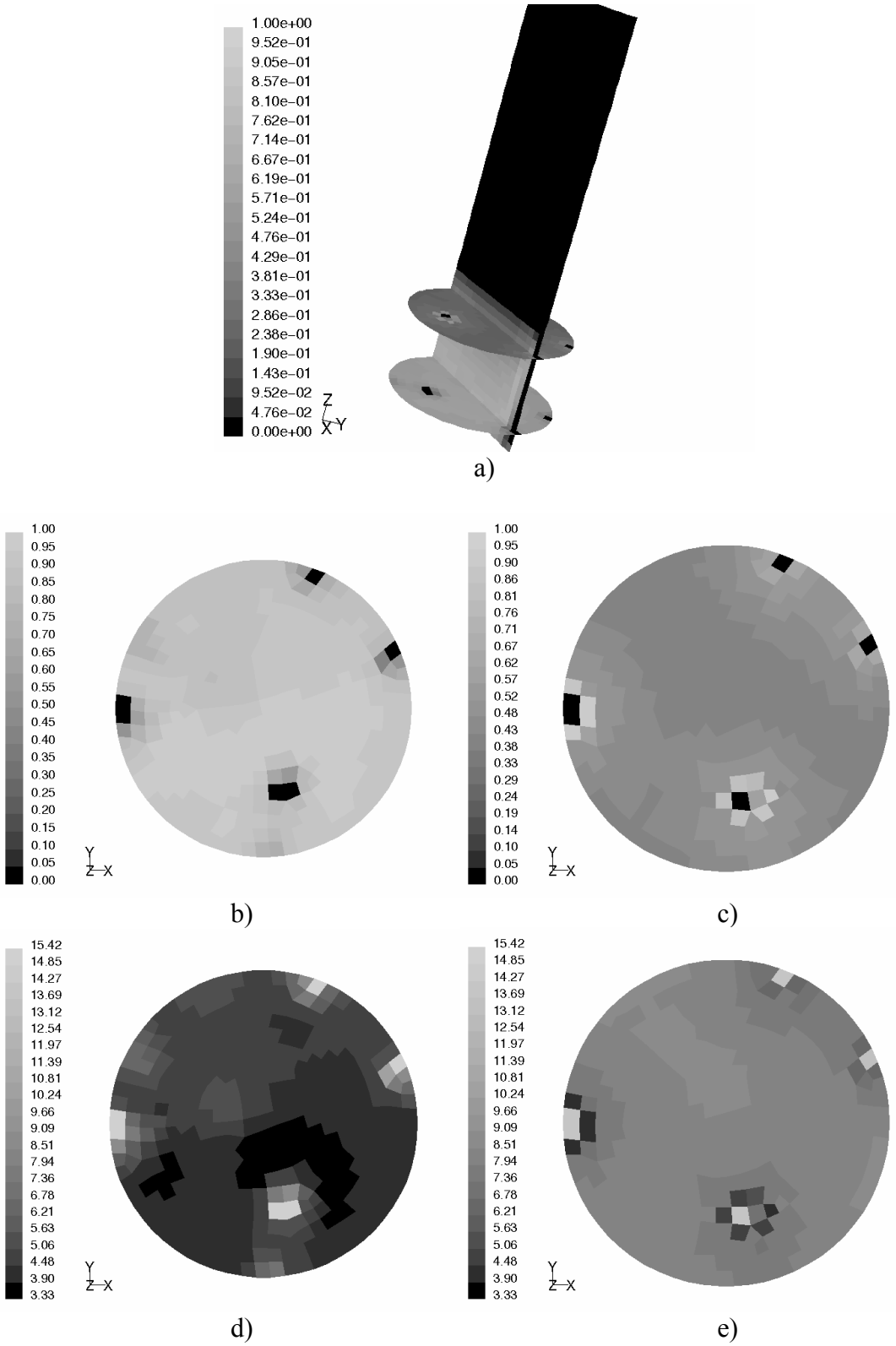

Figure 22: a) Fraction solide dans une section verticale ; b), c) Fraction solide et d), e) concentration moyenne dans deux sections transversales (situées à $h = 1.5mm$ respectivement $h = 7mm$ de la base du creuset), à $t = 800s$ du début de la solidification.

Comme pour les observations de Quillet [6] on remarque nous aussi une évolution de la configuration des canaux dans le temps. Ainsi au temps *t=800 s* on ne retrouve que

quatre canaux (Figure 22b, c) sur les 7 canaux ségrégés observés au début de la solidification dans la zone pâteuse (Figure 21). Il est intéressant d'observer que les canaux qui ont disparu ont laissé place à une configuration plus homogène dans le sens où les quatre canaux finaux sont plus uniformément distribués dans l'espace. Ce phénomène peut s'expliquer par le fait que la configuration initiale contenait des canaux qui étaient trop proches l'un de l'autre par rapport à l'espacement minimal ci-dessus défini. Ceci a engendré la disparition de certains d'entre eux, laissant place à une configuration comprenant des canaux plus distants l'un de l'autre et aussi répartis dans l'espace de manière plus homogène. Il serait intéressant dans la suite de cette thèse de se pencher davantage sur cet aspect d'espace minimal en essayant de le quantifier. Une approche intéressante serait celle de la théorie constructale [16] que nous avons déjà appliquée pour calculer l'espacement primaire (référence I, Annexe 7.2). Toutefois on s'attend ici à une analyse plus complexe car il semble que l'espace optimal entre deux canaux ségrégés soit dépendant des interactions à la fois hydrodynamiques et solutales entre les canaux adjacents.

On remarque aussi la forte ségrégation radiale produite par la présence des canaux (Figure 22d, e) : le fort enrichissement des canaux et l'appauvrissement en soluté de la zone pâteuse environnant les freckles.

Résultats numériques en brassage rotatif

On a vu qu'à partir de $t = 800s$ un brassage rotatif est pris en compte. Ce brassage engendre évidemment un mouvement principal de rotation du liquide autour de l'axe du cylindre (Figure 23). Toutefois à cause de la présence des parois supérieures et du macrofront, l'écoulement ne peut pas rester uniquement dans le plan xOy car la conservation de quantité de mouvement ne serait pas satisfaite. En effet un mouvement secondaire prendra place dans le lingot cylindrique. Ceci correspond à un mouvement toroïdal qui va brasser le liquide axialement. La cause de cet écoulement secondaire n'est que la conséquence de la distribution de pression créée par le mouvement rotatif principal. En effet la force centrifuge créée par le mouvement rotatif principal engendre une pression plus élevée proche des parois latérales et plus basse dans l'axe du cylindre (voir Figure 24a). Ainsi un écoulement secondaire se forme en déplaçant du fluide des zones de haute pression (latérales du cylindre) vers les zones de basse pression (l'axe du cylindre). Si l'influence des gradients de soluté dans le bain liquide n'est pas prise en compte, deux écoulements toroïdaux de sens contraire : un supérieur et un inférieur prendront naissance dans le bain liquide (voir Figure 24a). En regardant maintenant la distribution réelle de vitesse (voir la distribution de la composante verticale de vitesse, Figure 25) on observe que les écoulements secondaires ont une configuration un peu plus compliquée dans le sens où deux écoulements toroïdaux et non pas un existent dans la partie supérieure du lingot. Ceci peut toutefois s'expliquer lorsque l'on tient compte de la distribution de soluté dans le bain liquide. En effet, le mouvement toroïdal inférieur (Figure 24a) va apporter du liquide pauvre en soluté près des parois latérales, ce qui va finalement accélérer la solidification dans ces zones. Ainsi les canaux ségrégés latéraux vont être finalement bouchés. En même temps la distribution particulière de pression au niveau du macrofront, hautes pressions sur les latérales et basses pressions dans l'axe du lingot, va générer un mouvement correspondant dans la zone pâteuse. En effet, comme l'écoulement dans la zone pâteuse est principalement créé par la distribution locale de pression, un écoulement prendra naissance dans la zone pâteuse de la paroi latérale vers le centre. Ainsi du liquide enrichi est apporté dans l'axe du lingot et par un mécanisme identique à celui déjà rencontré au cas 2D cet écoulement va engendrer la formation d'un canal ségrégé central. On peut remarquer en effet dans la Figure 26 la configuration de la zone pâteuse engendrée

par le brassage électromagnétique glissant. On observe très bien la disparition des canaux latéraux et l'apparition d'un gros canal central. Maintenant le canal central va déterminer à son tour l'apparition d'un panache central de liquide enrichi. L'étain étant plus léger que le plomb, le panache aura la tendance naturelle à monter. L'effet de poussée produit par ce panache de liquide enrichi aura comme conséquence la modification sensible des écoulements secondaires dans la partie supérieure du bain liquide de telle manière que le liquide monte aussi dans la partie centrale du creuset (voir Figure 25).

On note aussi que la présence du canal central engendre de fortes ségrégations radiales (Figure 27), phénomène auquel nous nous attendions puisque le canal central se comporte comme une pompe de soluté drainant la zone pâteuse environnante.

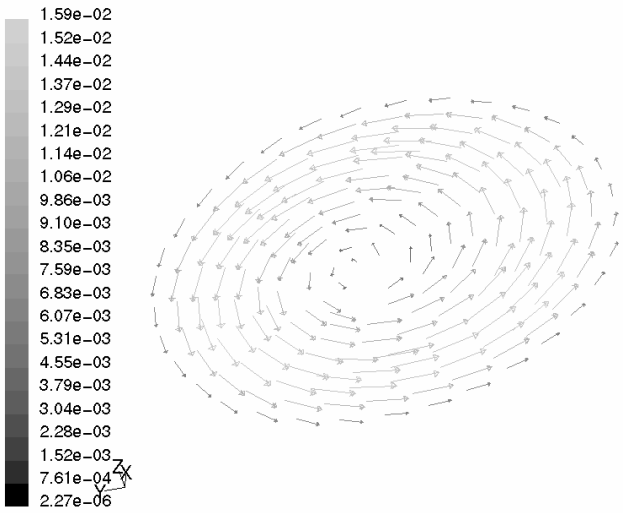

Figure 23: Vecteurs vitesses dans la section transversale situé à $h = 15\,mm$ de la base du creuset, à $t = 1000s$ du début de la solidification

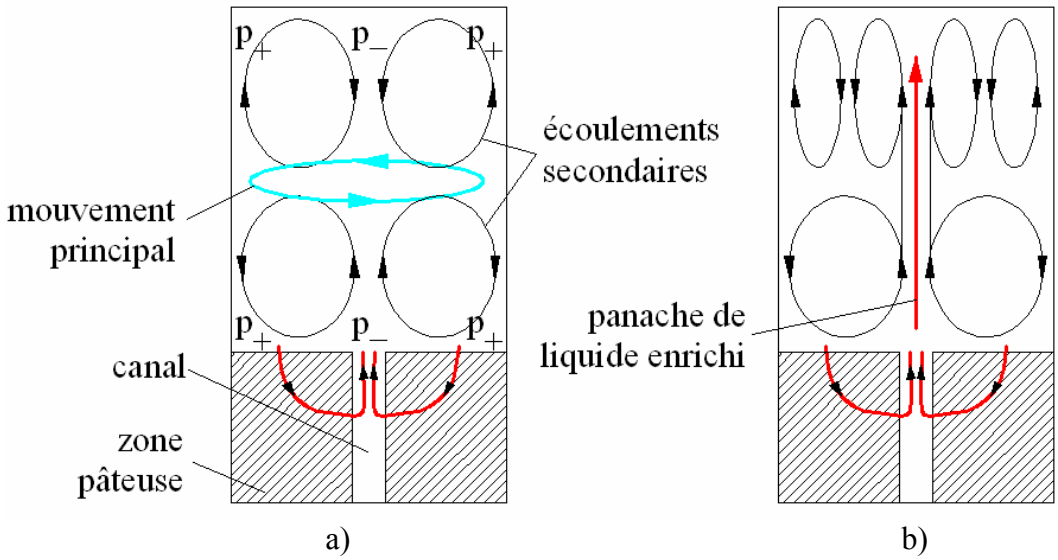

Figure 24: a) La configuration des écoulements secondaires si le mouvement d'origine solutale n'est pas prise en compte ; b) La configuration réelle des écoulements secondaires quand l'influence du panache de liquide enrichi est prise en compte.

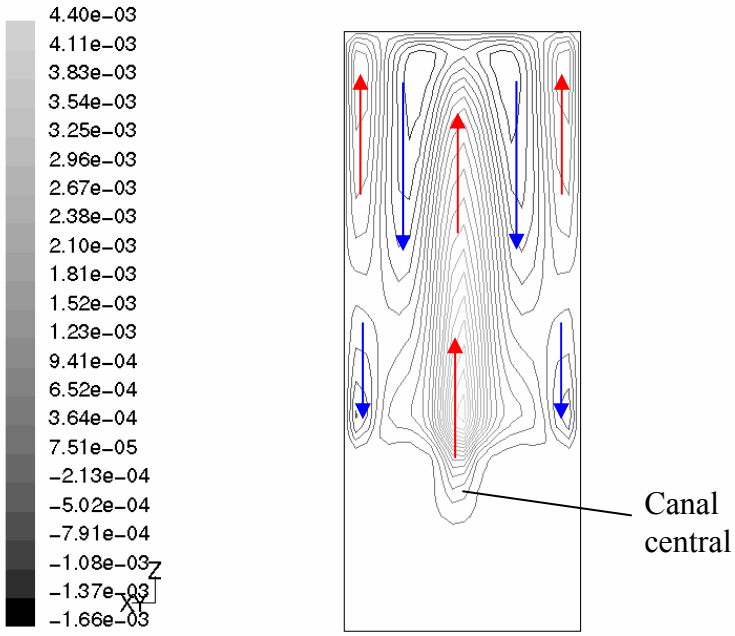

Figure 25: La magnitude de la composante verticale de la vitesse v_z dans une section verticale à $t = 1000s$ du début de la solidification

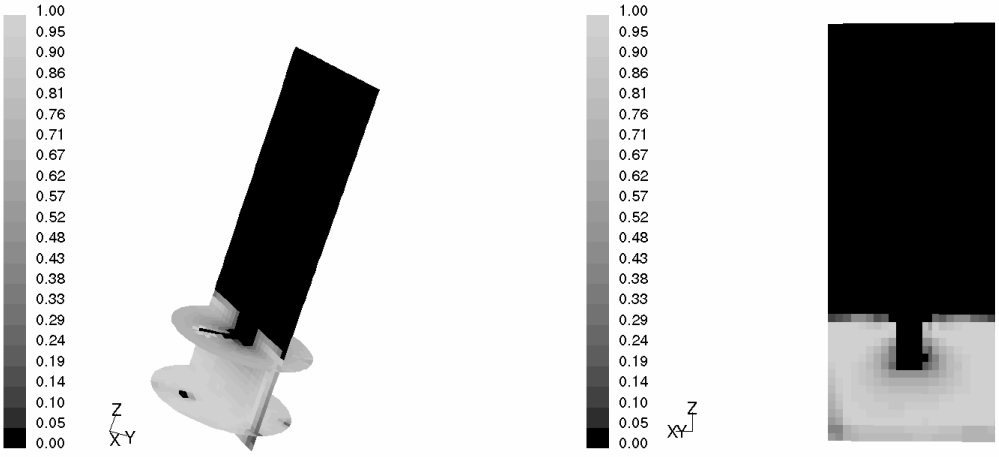

a) b)

Figure 26: a) La fraction solide à $t = 840\,s$ (40s après le début du brassage électromagnétique) ; b) La fraction solide dans une section verticale à $t = 1000\,s$.

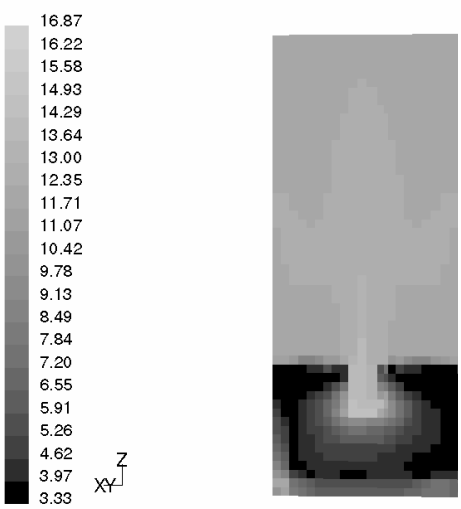

Figure 27: La concentration moyenne dans une section verticale à $t = 1000\,s$.

4.5.4.4 Conclusions partielles

En analysant plusieurs cas de solidification dirigée sous l'influence de la convection naturelle et/ou forcée on a observé que la structure de l'écoulement à proximité du macrofront a une très grande influence sur le développement des éventuels canaux ségrégés. Le passage du cas sans brassage électromagnétique au cas où l'écoulement dans le bain liquide est contrôlé est très bien reflété par la structure de la zone pâteuse. Dans le cas de la convection naturelle plusieurs canaux ségrégés isolés sont présents dans la zone pâteuse. Par contre l'écoulement forcé dans le bain liquide imposé par le brassage électromagnétique modifie complètement la configuration des canaux. En effet, en contrôlant l'écoulement dans le bain liquide, on peut aussi contrôler la distribution de pression au niveau du macrofront. Principalement contrôlé par la distribution de pression locale, l'écoulement dans la zone pâteuse va à son tour contrôler la distribution des canaux ségrégés dans la zone pâteuse. Effectivement, un brassage important prend naissance dans la zone pâteuse celui-ci étant dirigé des zones de basse pression vers les zones de haute pression. Ce brassage amène du liquide enrichi en soluté vers les zones de basse pression en y empêchant la solidification. Ainsi des canaux ségrégés sont donc susceptibles de se développer aux endroits où l'écoulement pâteux débouche dans le bain liquide. Toutefois les canaux ne peuvent exister seulement si l'écoulement dans la zone pâteuse est suffisamment fort par rapport aux conditions locales de solidification. En effet on a montré que les zones pâteuses où l'écoulement est dirigé dans le même sens que la vitesse locale des isothermes V_{is} subiront un processus de solidification intensifié. Ces zones correspondent aux zones de haute pression où l'écoulement pénètre dans la zone pâteuse. Au contraire, aux endroits où l'écoulement pâteux se fait dans le sens contraire de la vitesse locale des isothermes, le processus de solidification est diminué en intensité par rapport à un cas purement diffusif. Si l'écoulement dépasse en intensité la vitesse des isothermes, la solidification est annulée et un processus de refusion prend naissance localement. Ainsi, un canal ségrégé peut naître et subsister dans le temps si seulement l'écoulement pâteux local est suffisamment fort pour que la condition (35) soit respectée.

La présence d'un canal détermine aussi de fortes ségrégations dans la zone pâteuse : le canal agit comme une pompe de soluté drainant la zone pâteuse. On a montré aussi que le fort appauvrissement de la zone pâteuse autour d'un canal est du au fait que la

concentration moyenne caractérisant le flux de masse entrant dans la zone pâteuse est plus petit par rapport à la concentration moyenne caractérisant le flux de liquide sortant de la zone pâteuse et débouchant dans le canal.

On conclut ainsi que l'utilisation d'un brassage électromagnétique glissant ou rotatif ne permet pas d'annuler les macroségrégations dues aux canaux ségrégés. Par contre l'avantage de l'utilisation du brassage électromagnétique est le contrôle de la position des canaux et donc la localisation précise des macroségrégations positives correspondantes en opposition avec le cas de convection naturelle où la distribution des canaux était aléatoire.

4.5.5 Comparaison avec l'expérience ACCESS

Nous allons à présent exposer un essai de validation du modèle colonnaire à l'aide de l'expérience de solidification sous l'influence d'un champ magnétique rotatif effectué au laboratoire ACCESS, Aachen, Allemagne. Cette expérience a porté sur la solidification dirigée d'un alliage binaire Al-7wt% Si.

4.5.5.1 Dispositif expérimental

L'expérience ACCESS est une expérience de solidification dirigée de type Bridgman où un gradient thermique vertical $G = 10\,K/mm$ est imposé dans le four. L'échantillon est tiré dans ce gradient thermique avec une vitesse de tirage constante $V_t = 4.2\,\mu m/s$. Le schéma de l'expérience est présenté dans la Figure 28.

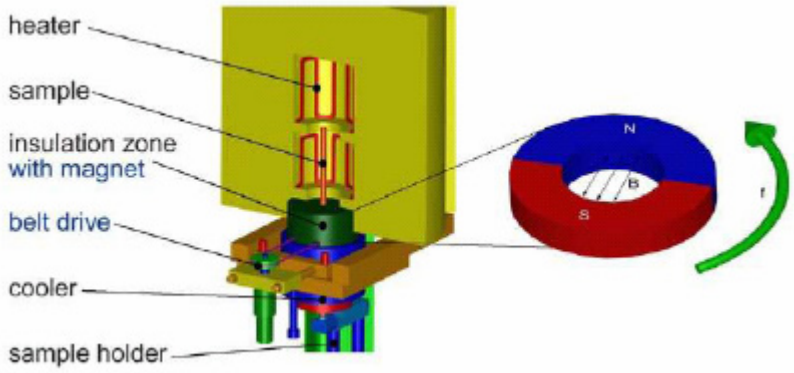

Figure 28: Le schéma de l'expérience de solidification dirigée ACCESS

Pour analyser l'influence du brassage électromagnétique sur la solidification, un aimant permanent (voir Figure 28) est utilisé pour générer un champ magnétique rotatif dans la section transversale du lingot. Les caractéristiques principales de cette expérience sont résumées dans le Tableau 5. Une particularité intéressante de cette expérience est la possibilité de décantation soudaine du liquide. Ce processus est réalisé par un basculement rapide de l'échantillon qui en vertu de la force centrifuge importante expulse le liquide de l'échantillon en exposant l'interface solide-liquide à un certain moment. Ceci permet de quantifier l'interface solide-liquide au niveau du macrofront : rayon des pointes colonnaires, espacement primaire, présence des éventuels canaux ségrégés dans la zone pâteuse.

Tableau 5: Les caractéristiques principales de l'expérience ACCESS

Alliage utilisé :	Al-7wt%Si-0.6wt%Mg
Gradient thermique vertical :	10000 *K/m*
Vitesse de tirage :	$4.2\,\mu m/s$
Le type d'aimant :	permanent
Intensité maximale du champ magnétique :	$B_0 = 2.5\times10^{-2}\,T$
Fréquence de rotation de l'aimant :	50 *Hz*
Diamètre de l'échantillon :	8 *mm*

4.5.5.2 Paramètres numériques

Une première approximation est faite au niveau de l'alliage. Nous serons en effet contraints par le code est développé uniquement pour des alliages binaires de considérer dans la suite la solidification d'un alliage binaire Al-7wt%Si même si l'alliage réel est Al-7wt%Si-0.6wt%Mg. Toutefois en raison du faible pourcentage de Mg (0.6%) on s'attend à ce que cette approximation n'introduise pas d'erreurs significatives.

Une deuxième approximation porte sur la distribution radiale de la force électromagnétique. On considère que cette force agit uniquement dans le plan transversal à l'échantillon, même si la force magnétique réelle n'est pas uniquement dans un plan horizontal. Un champ uniforme d'intensité $B_0 = 25\,mT$ a été mesuré dans l'axe de l'aimant. La force électromagnétique qui agit dans un plan horizontal et suivant la direction θ a l'expression générale suivante:

$$F_\theta(r,z) = F_0(z)\frac{r}{R} \tag{37}$$

Toutefois il faut remarquer qu'en raison de la hauteur finie de l'aimant (h = 8*mm*) le champ magnétique B_0 subira une variation décroissante en fonction de la distance par rapport à l'axe de l'aimant. En utilisant les mesures expérimentales mises à notre disposition par ACCESS on a calculé la force électromagnétique résultante qui par la suite a été approchée par la loi empirique suivante :

$$F_\theta(r,z) = F_0 \exp\left[-\frac{|z-z_a|^2}{\left(1.18\times10^{-2}\right)^2}\right]\frac{r}{R} \tag{38}$$

où $F_0 = 500\,N/m^3$ et z_a est la coordonnée verticale de l'axe de l'aimant. On note aussi que la position de l'aimant est légèrement décalée par rapport à l'isotherme T_{liq} correspondante à la concentration C_0. En effet, le plan axial de l'aimant est positionné en arrière de 16 mm par rapport à la position de T_{liq}. Ceci implique que l'intensité du champ magnétique au niveau du macrofront n'est pas de 25 *mT* mais plus faible, d'environ 10 *mT*. En tenant compte des conditions initiales choisies on considère qu'à $t = 0$ la température sur la paroi inférieure est T_{liq}. Ainsi, la variation de la position de l'aimant peut être aisément calculée comme étant :

$$z_a(t) = V_t\, t - \Delta z_0 \tag{39}$$

où Δz_0 est le décalage de l'aimant par rapport à T_{liq}, $\Delta z_0 = 16mm$.

La hauteur de l'échantillon considérée dans les calculs est de 7cm plus petite que celle réelle ($\approx 12cm$). Toutefois comme on va pouvoir le constater, en raison du domaine limité d'action de la force magnétique, le choix d'une hauteur de l'échantillon plus grande que 7 *cm* ne change en rien les résultats finaux.

Comme la force électromagnétique est axisymétrique le problème réel 3D peut être analysé avec succès avec un modèle axisymétrique de type swirl. En effet, même si il y a un mouvement dans la direction azimutale θ, le problème peut être analysé dans un domaine 2D car les dérivées $\partial / \partial\theta$ de tous les champs physiques sont nulles. Toutefois pour quantifier le transport convectif le long de la direction θ une équation de conservation de QDM suivant θ doit être considérée. Au niveau de l'implémentation du modèle en Fluent rien ne change par rapport à ce qui a été déjà dit auparavant (paragraphe 4.5.2) parce que le passage d'un modèle 3D à un modèle 2D axisymétrique se fait automatiquement en Fluent. Il faut juste adapter le maillage au problème axisymétrique. Les paramètres numériques utilisés dans la résolution numérique du cas de solidification sont réunis dans le Tableau 6.

Tableau 6: Paramètres numériques du cas ACCESS

Alliage :	Pb-10wt%Sn
Diamètre :	8 mm
Hauteur :	70 mm
Maillage :	20 X 350
Schéma temporel :	1er ordre Euler
Schéma spatial :	2ème ordre UPWIND
Couplage pression-vitesse :	SIMPLEC
Pas de temps :	0.02s
Temps de simulation :	8000s

4.5.5.3 Résultats numériques et comparaison

A cause du brassage électromagnétique rotatif un écoulement de rotation s'établit principalement dans le plan xOy (voir Figure 29a). Les vitesses maximales sont de l'ordre de $1.1cm/s$. Il faut aussi remarquer que l'écoulement engendré par le brassage électromagnétique reste non-négligeable sur une hauteur finie au-dessus du macrofront. Ceci est logique car l'aimant d'épaisseur fini crée un champ magnétique qui diminue en intensité dès que l'on s'éloigne de l'axe de l'aimant, équation (38). Il faut remarquer toutefois que l'écoulement ne reste pas uniquement dans le plan xOy. En effet un mouvement secondaire toroïdal naît au dessus du macrofront comme le montre la Figure 29b. Celui-ci est du principalement à la distribution particulière de pression créée par l'écoulement rotatif principal. Comme nous l'avons déjà expliqué auparavant, les forces centrifuges qui agissent sur le liquide vont engendrer des pressions plus grandes proches de la paroi latérale et plus basses dans l'axe du lingot (voir Figure 24a). Cependant, à cause de la couche limite hydrodynamique au niveau du macrofront le maximum de pression se trouvera non pas au niveau du macrofront mais à une certaine distance au-dessus de celui-ci (voir Figure 30). En même temps l'écoulement diminue en intensité en s'éloignant du

macrofront. Alors les forces centrifuges et les pressions induites par celles-ci vont diminuer aussi. Ainsi, l'existence de pressions plus basses caractérisera la zone éloignée du macrofront (voir Figure 30). Cette distribution particulière de pression va engendrer deux mouvements secondaires toroïdaux qui vont se diriger des zones de hautes pressions vers les zones de basses pressions (voir Figure 29b et Figure 30).

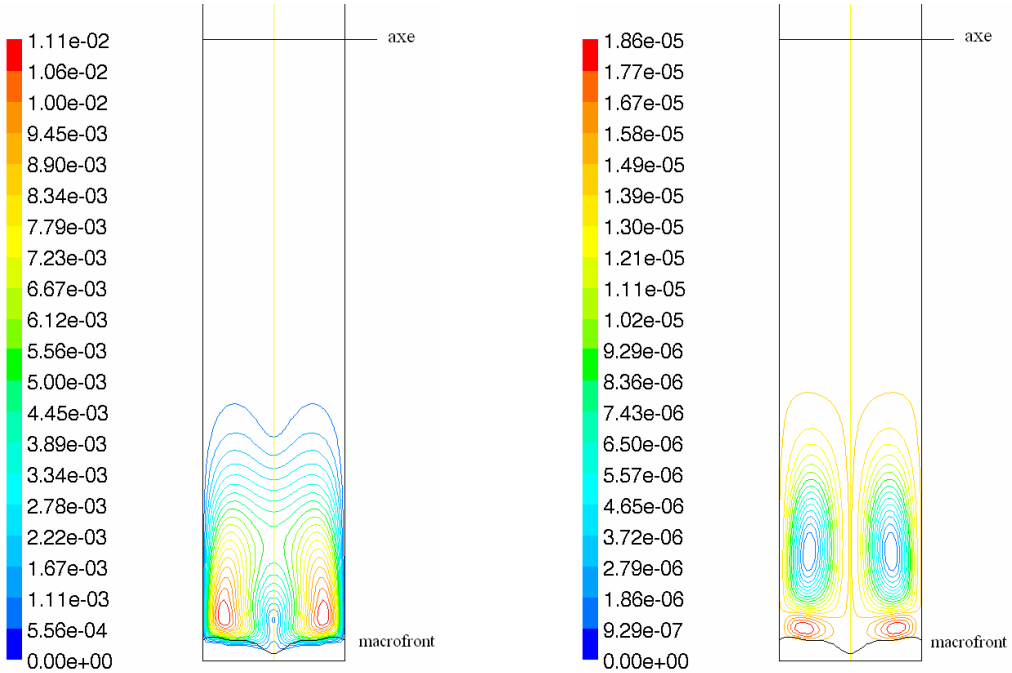

Figure 29: a) La magnitude de la vitesse et b) les lignes de courant dans le creuset à $t = 400\,s$ du début de la solidification

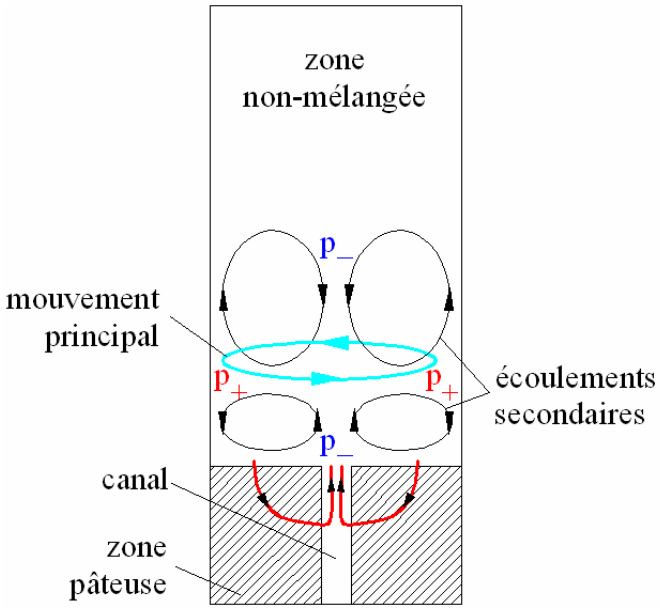

Figure 30: Mécanisme d'apparition des écoulements secondaires

De plus la distribution de pression au niveau du macrofront, les hautes pressions proche de la paroi latérale et les basses pressions dans l'axe du barreau génèrent un brassage de la zone pâteuse (Figure 30) qui apporte du liquide riche en soluté dans l'axe du lingot. Ceci ajouté au mouvement toroïdal de même sens dans le bain liquide juste au-dessus du macrofront donne naissance à un gros canal ségrégé central (Figure 31a) similaire à celui déjà obtenu dans le cas 3D précédemment analysé. L'écoulement dans la zone pâteuse aura comme effet l'enrichissement du canal et l'appauvrissement de la zone pâteuse environnante par le mécanisme de pompage de soluté déjà identifié au paragraphe 4.5.4.1 (Figure 31b). Il est important de noter qu'expérimentalement un gros canal central similaire à celui obtenu numériquement a été observé. On peut observer dans la Figure 32 l'interface solide-liquide au niveau du macrofront découverte par la technique de décantation du liquide. On peut donc facilement observer un gros canal central. Sa dimension est tout à fait comparable à celle du canal obtenu dans la simulation numérique. Il est aussi important de noter qu'expérimentalement il a été observé que la zone centrale du lingot était remplie par des grains équiaxes en opposition avec la zone extérieure du lingot qui restait colonnaire. On observe très bien dans la Figure 33 la structure des grains équiaxes qui caractérise la zone centrale du lingot. La corrélation entre le canal central et la zone équiaxe centrale met en évidence le fait que des germes naissent dans le liquide enrichi du canal probablement par nucléation homogène et/ou fragmentation des grains colonnaires. En effet des phénomènes de refusion ont lieu dans le canal dus à l'écoulement du liquide dans le sens contraire à la vitesse locale des isothermes. Ceci peut amplifier les phénomènes de fragmentation des colonnes. Les fragments ainsi obtenus vont ensuite se sédimenter au fond du canal donnant naissance à cette structure centrale équiaxe.

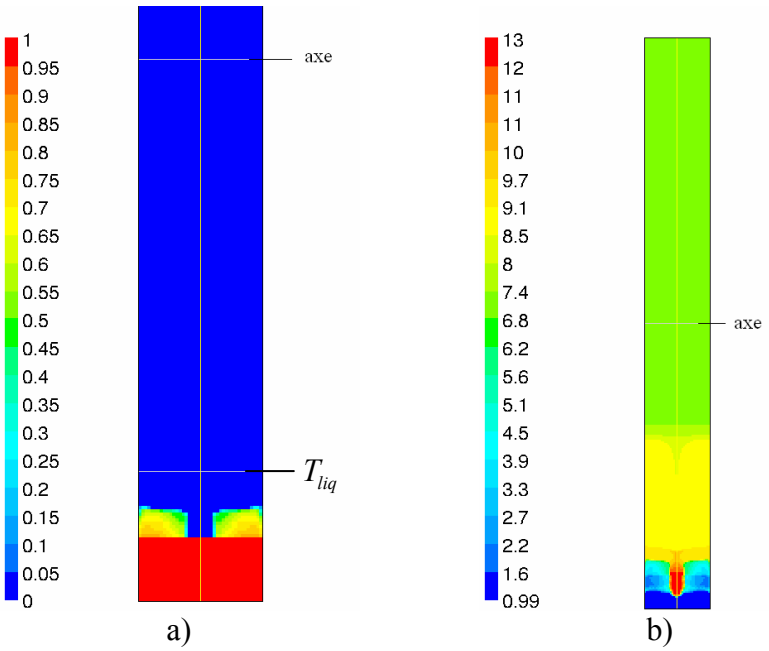

Figure 31: a) La fraction solide et b) la concentration moyenne dans le creuset à $t = 2000\,s$ du début de la solidification

Les cartes de la microstructure suivant une section transversale et longitudinale sont présentées dans la Figure 34. On observe une fois de plus la structure colonnaire extérieure et une structure centrale équiaxe enrichie en Si. En effet on remarque l'existence d'une fraction eutectique (zone en gris foncé) beaucoup plus importante dans la zone centrale par rapport aux zones périphériques. Ceci confirme l'effet prononcé

d'enrichissement du canal central et l'appauvrissement de la zone colonnaire environnant le canal. Un autre phénomène intéressant est l'augmentation du diamètre de la zone centrale le long du lingot. Pour le moment on ne peut pas avancer une explication raisonnable de ce phénomène, mais comme on va le découvrir dans la suite, la modélisation numérique semble fournir une réponse pertinente à cette question.

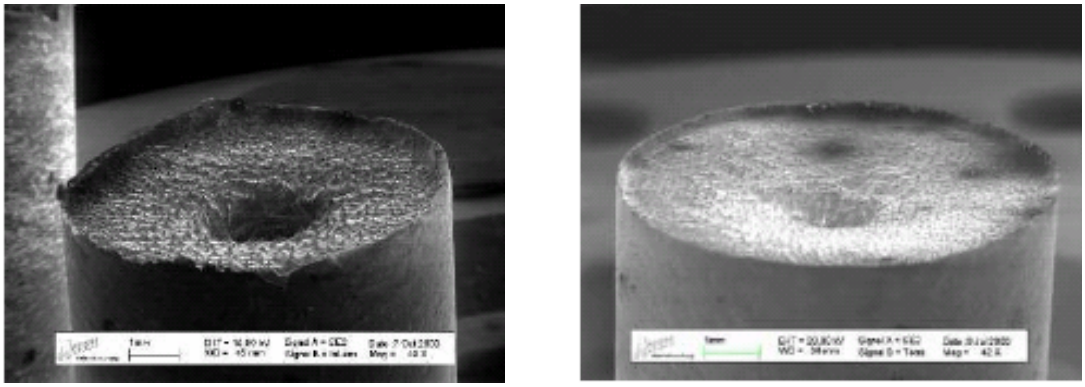

Figure 32: Vue macroscopique des deux interfaces solide-liquide obtenues par la technique de décantation du liquide. On remarque la présence d'un canal central (Weiss et al.)

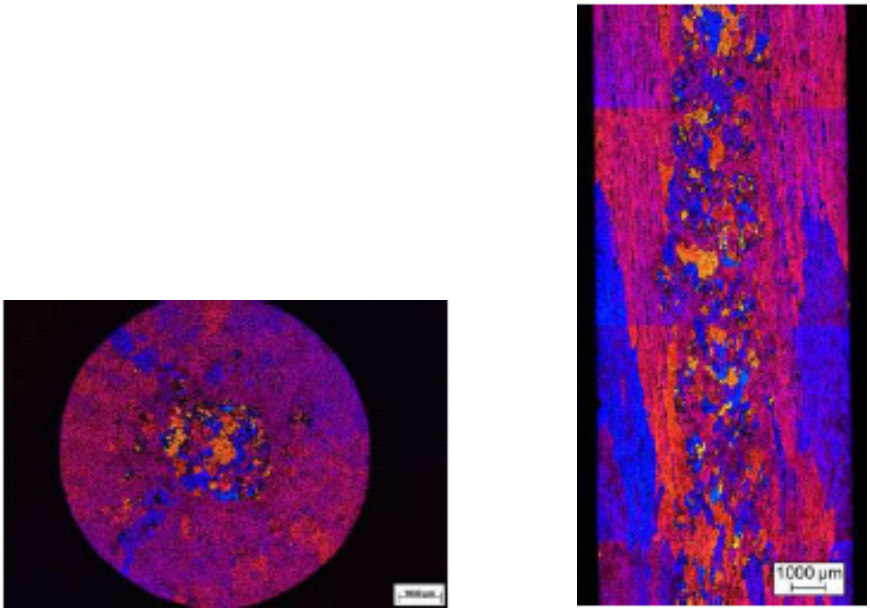

a) b)

Figure 33: La structure des grains dans une section transversale (a) et une section longitudinale (b). On observe la présence des grains équiaxes dans la partie centrale du lingot (Weiss et al.).

En revenant maintenant aux résultats numériques on observe des phénomènes très semblables. Premièrement on note le fort enrichissement du canal ségrégé central (Figure 31b, Figure 35b,d). Celui-ci reste liquide jusqu'à pratiquement la température eutectique au fond du canal. En dessus de cette température la réaction eutectique se déclenche. Ainsi au fur et à mesure que le front de solidification avance, une phase eutectique importante occupera la partie centrale en concordance avec les résultats expérimentaux. Deuxièmement à cause de l'existence du canal central le bain liquide s'enrichit en soluté

au fur et à mesure que le front de solidification avance. Ceci est évidemment la conséquence du flux de liquide enrichi sortant du canal et débouchant dans le bain liquide.

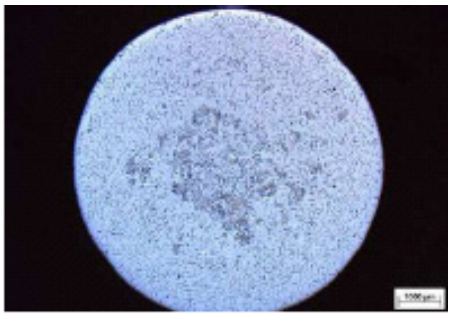

a)

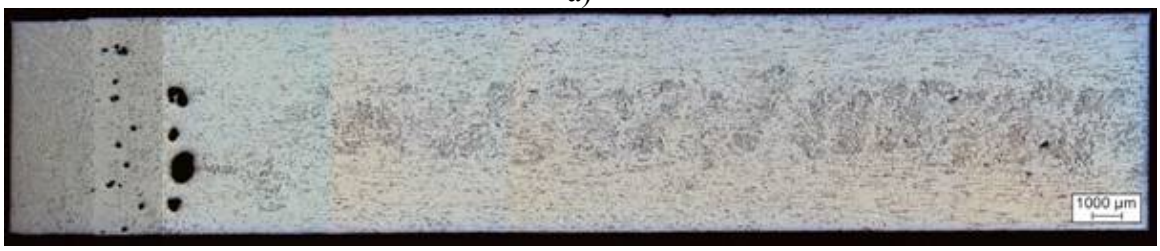

b)

Figure 34: La microstructure dans une section transversale (a) et une section longitudinale (b). Les deux sections polies montrent la microstructure dendritique avec l'enrichissement de la phase eutectique dans la partie centrale. Expériences réalisées par ACCESS (Weiss et al.).

Toutefois il est intéressant d'observer qu'à cause de la limitation spatiale de l'écoulement forcé dans le bain liquide, l'enrichissement du bain liquide n'est que partiel. En effet, seule la zone où l'effet de mélange produit par la convection forcée est non-négligeable s'enrichit en soluté (voir Figure 31b, Figure 35b,d). Ce phénomène a une conséquence très importante sur l'évolution de la solidification. En effet, en raison de la présence de la zone de mélange limité, le liquide au-dessus du macrofront s'enrichit rapidement par rapport à un cas de brassage glissant où l'effet de mélange serait étendu à la totalité du bain liquide. Ceci a plusieurs conséquences importantes :

- d'une part cet enrichissement est tellement rapide que le macrofront se voit vite ralenti par rapport à sa vitesse initiale de $4.2\,\mu m/s$. Ceci entraîne le rapprochement de l'axe de l'aimant par rapport au macrofront. On peut aisément remarquer ce phénomène dans la Figure 31a et la Figure 35a,c où la position de l'isotherme T_{liq} est montrée. On observe que le macrofront est de plus en plus en arrière par rapport à l'isotherme T_{liq}, ce qui signifie que l'axe de l'aimant s'approche de plus en plus du macrofront.
- D'autre part à cause du rapprochement de l'aimant du macrofront, le liquide au dessus du macrofront est plus fortement brassé. On peut remarquer qu'à t=8000 *s* la vitesse est augmentée jusqu'à 2.8 *cm/s* (Figure 36c) par rapport à une vitesse proche de 1 *cm/s* à t=400 *s* (Figure 29b). Ceci a une influence importante sur la distribution de pressions proche du macrofront. En effet, la configuration de la couche limite hydrodynamique au-dessus du macrofront dépend fortement du nombre de Reynolds local. La théorie de Prandtl prédit une modification de l'épaisseur de la couche limite en fonction du *Re* local comme suit : $\delta / R \sim 1/\sqrt{\mathrm{Re}}$. Ainsi pour un brassage plus fort ($\mathrm{Re}\nearrow$) l'épaisseur de la couche limite hydrodynamique diminue. Ceci déplacera le maximum de pression

plus proche du macrofront et aura comme conséquence une modification sensible de la structure de l'écoulement secondaire au dessus du macrofront. On observe clairement cette modification dans la Figure 29b et Figure 36b, d. En regardant l'évolution de la convection au dessus du macrofront on observe qu'avec le temps les deux boucles de convection au dessus du macrofront deviennent de plus en plus aplaties et inclinées vers les parois latérales. Ceci aura une influence significative sur la configuration du canal central. En effet on observe (Figure 35b, d) une augmentation de la largeur du canal dans le temps due à la modification de l'écoulement au-dessus du macrofront. Il est important de noter que ce phénomène correspond qualitativement aux résultats expérimentaux. Ainsi les résultats numériques semblent éclairer ce point qui était jusqu'à maintenant non résolu.

- L'enrichissement rapide du bain liquide a une conséquence directe sur la hauteur de la zone pâteuse. En effet cette dernière diminue dans le temps en raison de la diminution de l'intervalle de solidification $\Delta T_0 = T_{liq}(C_{bain}) - T_{eut}$. En effet de t=0s à t=4000s la concentration au-dessus du macrofront augmente de 7% à 10% (voir Figure 35b). L'intervalle de solidification diminue par conséquent et, pour un gradient thermique donné, l'épaisseur de la zone pâteuse diminue aussi. Ceci est facilement observable en comparant la Figure 31a avec les Figure 35a, c.
- Finalement l'augmentation de la concentration du liquide au dessus du bain liquide déterminera l'apparition, en dehors des ségrégations radiales créées par le canal central, d'une macroségrégation longitudinale (normale) importante (voir Figure 35b, d).

Tableau 7: Résultats expérimentaux sur les macro ségrégations

Distance à partir du bas de l'échantillon	Diamètre de la région centrale	Concentration moyenne du Si dans la région centrale	Concentration moyenne du Si dans la région périphérique
9 mm	2,0 mm	10.8 wt%	3.8 wt%
17 mm	3,2 mm	10.2 wt%	4.1 wt%
27 mm	3,5 mm	11,0 wt%	5.9 wt%

A ce stade il est intéressant de faire une comparaison directe entre les résultats numériques et expérimentaux obtenus au niveau des macroségrégations. Les auteurs de l'expérience nous fournissent la variation radiale de la concentration moyenne pour trois sections transversales différentes. Ces résultats sont résumés dans le Tableau 7. Il faut noter que ces profils sont obtenus après une procédure de prise de moyenne sur la partie centrale et périphérique du lingot et ne représentent pas la variation radiale exacte de la concentration moyenne locale. En Figure 37 les résultats numériques et expérimentaux sont superposés. On observe que le modèle reproduit bien le niveau de la concentration dans la partie centrale qui est proche de la concentration eutectique. On observe un bon accord avec l'expérience en ce qui concerne le niveau de concentration dans les zones périphériques. On remarque notamment la ségrégation normale positive importante : l'augmentation de la concentration périphérique avec la hauteur des sections dans le lingot. Malgré l'accord général satisfaisant avec l'expérience on remarque un désaccord quantitatif au niveau de la concentration dans la zone centrale et ceci pour les trois sections analysées. Une explication pour ce désaccord pourrait provenir du fait que la solidification équiaxe n'est pas prise en compte par le modèle actuel. En effet, on a observé expérimentalement que la zone centrale était toujours occupée par des grains équiaxes qui très probablement se sédimentent au fond du canal central. La présence du solide dans le canal ainsi que leur effet de sédimentation aura comme effet une diminution de la concentration moyenne du

canal par rapport à un cas où le canal resterait liquide jusqu'à un régime très proche de l'eutectique. En fait c'est précisément ce qu'on obtient : la concentration de la zone centrale est surestimée par rapport aux résultats expérimentaux.

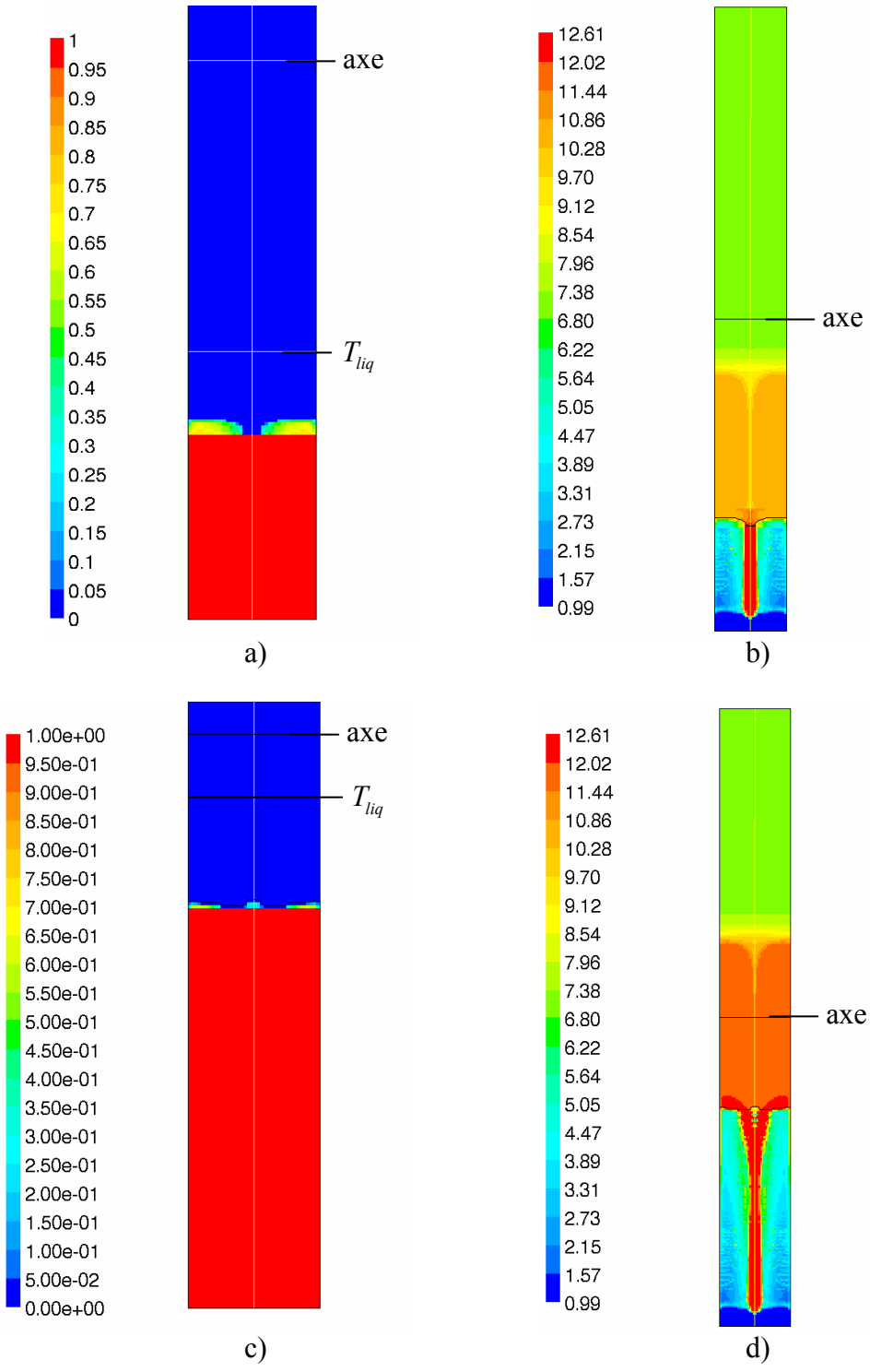

Figure 35: Résultats du modèle. La fraction solide (a) et la concentration moyenne (b) à $t = 4000s$ et la fraction solide (c) et la concentration moyenne (d) à $t = 7400s$.

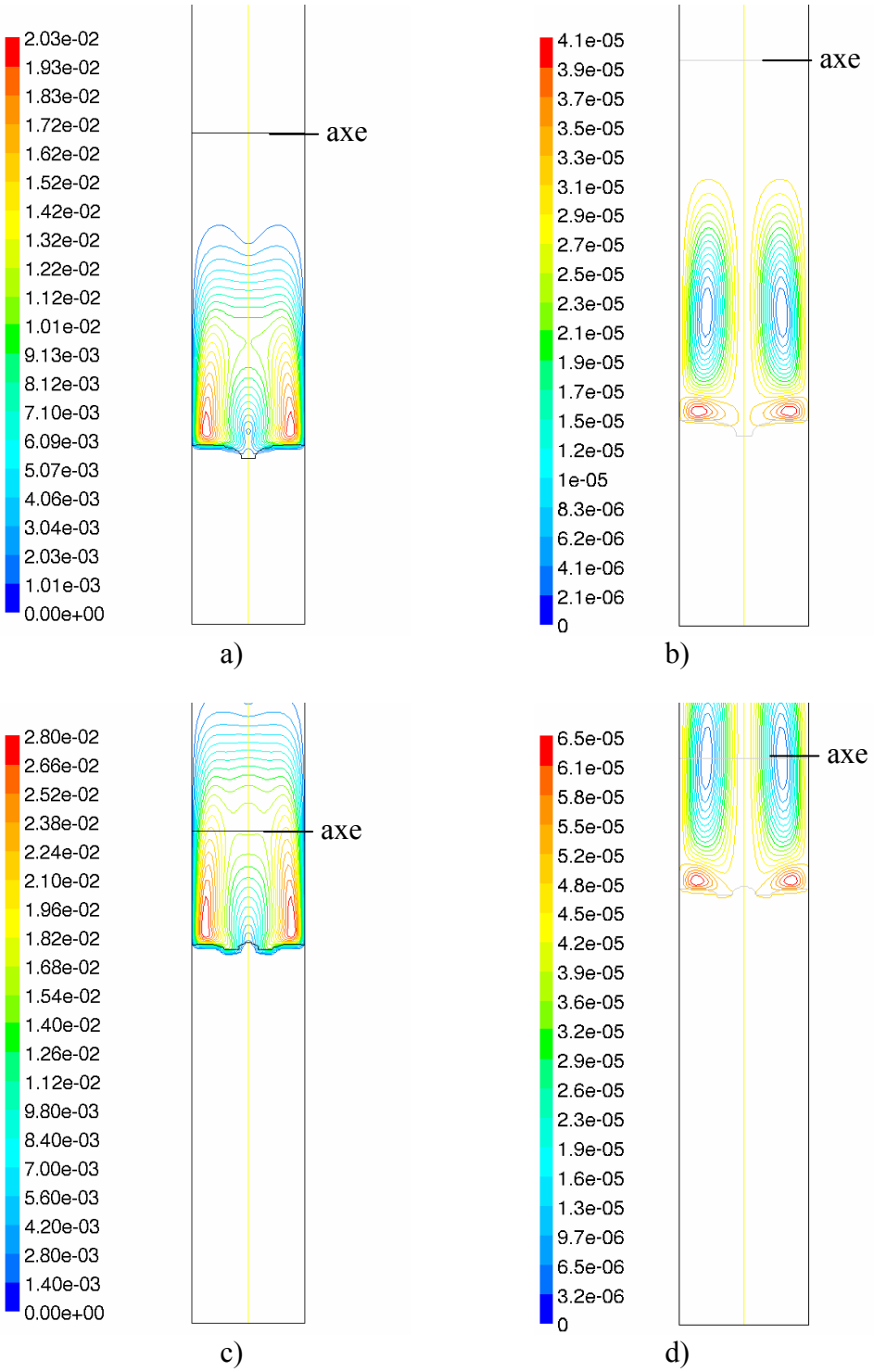

Figure 36: La magnitude de la vitesse (a) et les lignes de courant (b) à $t = 4000s$ et la vitesse (c) et les lignes de courant (d) à $t = 8000s$.

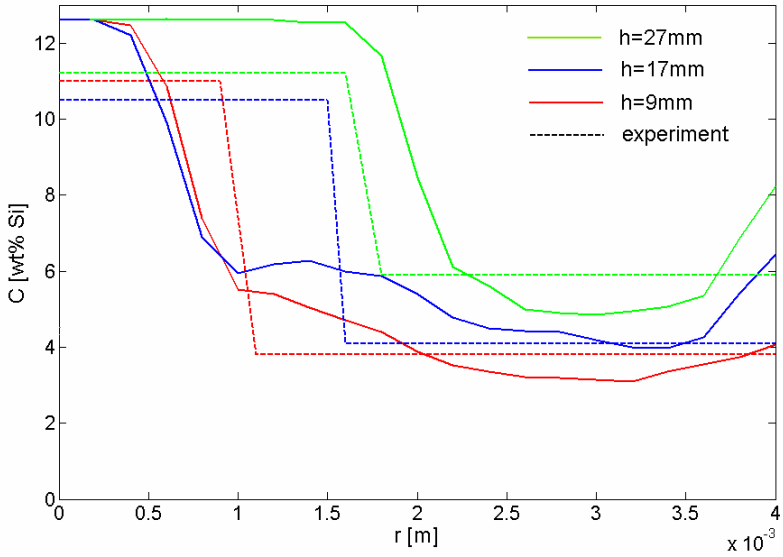

Figure 37: Comparaison entre les résultats du modèle et les résultats expérimentaux de la variation radiale de la concentration moyenne pour trois sections transversales différentes. Expériences réalisées par ACCESS.

4.5.5.4 Conclusions partielles

On a essayé de modéliser l'expérience de solidification dirigée sous l'influence du brassage électromagnétique rotatif, expérience réalisée au laboratoire ACCESS. L'accord des résultats numériques avec ceux expérimentaux est aussi bon sous l'aspect qualitatif que quantitatif. Plus précisément :

- Le modèle reproduit le gros canal central produit par la convection forcée dans le bain liquide. Les dimensions du canal central sont très proches des dimensions obtenues expérimentalement.
- Les ségrégations radiales et longitudinales sont en bon accord avec les résultats expérimentaux à l'exception de la zone centrale qui est légèrement surestimée. La cause de ce désaccord semble être la non-prise en compte de la zone équiaxe.
- L'élargissement du canal dans le temps est aussi qualitativement reproduit par le modèle. La cause de cet élargissement réside dans la modification des recirculations secondaires au niveau du macrofront. Ces dernières sont à leur tour dues au ralentissement du macrofront et au rapprochement du plan axial de l'aimant du macrofront.
- A cause de la présence du canal central, le bain liquide au dessus du macrofront s'enrichit en soluté. A cause du brassage limité en extension dans le bain liquide, cet enrichissement se fait très rapidement. En même temps l'enrichissement du liquide au dessus du macrofront a comme conséquence directe la diminution sensible de l'épaisseur de la zone pâteuse.

5 Conclusions finales

Dans une première partie de la thèse (référence I, Annexe 7.2) on se concentre sur l'application de la théorie constructale dans la prédiction de la structure dendritique solide. Premièrement on analyse le critère de stabilité marginale vu dans la perspective de la théorie constructale. En ayant comme principe de base la loi constructale on conclu que la forme de la dendrite s'adapte de telle manière que la vitesse de croissance de la pointe dendritique soit maximale. Dans ce contexte on a montré que, parmi le domaine des rayons possibles de la pointe dendritique prédit par l'analyse de stabilité, la pointe dendritique va choisir le plus petit rayon ça veut dire un rayon égal avec la plus petite longueur d'onde des perturbations donnant naissance à des instabilités. On identifie aussi l'existence d'une compétition entre la croissance contrôlée par la diffusion moléculaire et la croissance dendritique. En analysant cette compétition on a été capable de déterminer le temps critique et le rayon critique pour lesquels la déstabilisation de l'interface solide-liquide se déclanche. Dans un deuxième temps on développe un modèle pour l'espacement dendritique secondaire. En analysant la croissance d'une seule pointe dendritique on conclu que la croissance latérale de la pointe dendritique est proche d'une croissance contrôlée par la diffusion moléculaire et par conséquent est caractérisé par une vitesse de croissance qui diminue dans le temps. Dans ce contexte la théorie constructale prédit une optimisation de la croissance latérale de la dendrite. En faite on identifie encore une fois une compétition entre la croissance latérale contrôlée par la diffusion moléculaire et la croissance dendritique. En analysant cette compétition on a été capable de caractérisé le mécanisme de la croissance latérale des branches dendritiques secondaires et de calculer finalement l'espacement dendritique secondaire. Le résultat est en bon accord avec le modèle de J.S. Langer and H. Muler-Krumbhaar, Acta Metallurgica **26**, 1681 (1978) mais aussi avec des différents résultats expérimentaux. Finalement, l'espacement dendritique primaire est analysé dans la perspective de la loi constructale. Quand on l'applique à un front colonnaire la loi constructale prédit que le seul moyen dont le pointes dendritique dispose pour l'optimisation du processus de solidification est la minimisation de l'espace entre deux pointes adjacentes, c'est-à-dire la minimisation du λ_1. Le mécanisme responsable pour la diminution du λ_1 a été identifié dans le mécanisme de division dendritique. Toutefois, à cause des interactions solutales entre les pointes adjacentes il a été trouvé qu'il existe un espacement critique λ_{cr} en dessous duquel la division des pointes colonnaire ne peut plus se faire. Dans ce sens la loi constructale prédit que l'espacement primaire caractérisant l'état quasi-stationnaire du front colonnaire sera proche de l'espacement stable minimum λ_{cr}. En quantifiant la division dendritique et les interactions solutales entre les pointes colonnaire on a finalement été capable d'obtenir un modèle pour l'espacement dendritique primaire. En effet, on obtient que λ_1 est de même ordre de grandeur avec λ_{cr} et plus précisément que $\lambda_1 \approx 1.5\lambda_{cr}$. Le résultat est par la suite validé avec plusieurs donnés expérimentales et on obtient que le nouvel modèle est en très bon accord avec les expériences.

Dans une deuxième partie de la thèse (référence II, Annexe 7.2) on a développé un nouveau modèle multiphasique eulérien valide pour la solidification colonnaire et équiaxe et pour un cas purement diffusif (sans convection). Les équations moyennes ont été obtenues à l'aide d'un moyennage statistique de phase et la formulation finale du modèle est valable aussi bien pour une structure équiaxe que colonnaire. Premièrement le cas d'une structure colonnaire pure ou équiaxe pure est analysé. A l'aide de la densité de

probabilité des particules les plus proches, $\widetilde{f}^{(1)}\left(t,\mathbf{x};\tilde{\mathbf{z}}_1\right)$, on a pu calculer rigoureusement les termes et les tenseurs inconnus existant dans les équations de conservation moyennes non-fermées. En effet, en utilisant « l'approximation de la cellule » [5] pour cette fonction de densité de probabilité, les champs moyens peuvent être facilement calculés à l'aide de simples intégrations volumiques dans une cellule sphérique caractéristique de rayon R_1. Le modèle final valide soit pour une structure colonnaire soit pour une structure équiaxe est similaire à celui obtenu par Wang et Beckermann [10]. On note que l'équivalence entre les deux modèles est une conséquence directe de l'utilisation de l'hypothèse de l'équilibre thermique local. En effet, si l'hypothèse d'homogénéité thermique locale est considérée alors la moyenne statistique d'ensemble reproduit l'approche de la prise de moyenne volumique. Toutefois le moyennage statistique est fondamentalement différent du moyennage volumique. En effet, si l'hypothèse d'homogénéité thermique locale n'est plus valide, l'utilisation de la prise de moyenne statistique donne naissance à des expressions de fermetures différentes de celles obtenues par l'application du moyennage volumique. En plus, les résultats obtenus avec le moyennage volumique ne sont pas physiquement corrects. Dans ce contexte il est montré en référence II (Annexe 7.2) que l'utilisation de la prise de moyenne statistique couplée avec le modèle de la cellule permet avec succès l'intégration des effets des inhomogénéités locales (gradients locaux des champs physiques) sur les expressions de fermeture. Deuxièmement, le cas de la coexistence entre les structures colonnaires et équiaxes (c/e) est analysé du point de vue du moyennage statistique. Plus précisément, le cas de la pénétration du front colonnaire dans une zone équiaxe développée est analysé. Ce type de couplage peut être fréquemment rencontré pendant les phénomènes de solidification et spécialement dans le cas des phénomènes de transition colonnaire-équiaxe (CET). Le principal avantage de la prise de moyenne statistique réside dans le fait qu'à l'aide des distributions de probabilité des particules les plus proches, $\widetilde{f}_{c/e}\left(t,\mathbf{x};\tilde{\mathbf{z}}_1\right)$, on peut quantifier d'une manière rigoureuse les influences des particules colonnaires/équiaxes (c/e) en **x**. En utilisant l'approximation de la cellule pour $\widetilde{f}_{c/e}$ deux cellules sphériques centrées en **x** et de rayon R_{1c}^* et R_{1e}^* ont été identifiées. En utilisant ces deux cellules il est possible de séparer l'influence des structures c/e dans le point **x** en définissant des moyennes d'ensemble correspondantes à chaque structure. Ces moyennes vont quantifier les effets moyens en **x** produit par chaque structure. Ainsi, suivant le cas où la particule la plus proche de **x** est colonnaire ou équiaxe, le modèle nous conduit à différentier deux types principaux de valeurs moyennes : respectivement colonnaires et équiaxes. Dans ce contexte deux fractions importantes sont identifiées : la fraction colonnaire et celle équiaxe, ε_c et ε_e. Ces deux fractions quantifient la manière dont les deux structures partagent l'espace en **x**. Une autre caractéristique importante de la moyenne statistique est le fait qu'elle nous permet de quantifier le blocage mécanique produit par la structure équiaxe sur les pointes colonnaires. On a démontré que les structures équiaxes et colonnaires interagissent suivant un double mécanisme de blocage. Le premier effet de blocage mécanique déterminera une raréfaction de la zone colonnaire au moment où cette dernière pénètre dans la zone équiaxe. En effet, à cause de la dimension finie des grains équiaxes les pointes colonnaires disposent seulement d'un espace limité $(1-\varepsilon_{ge})$ dans lequel elles peuvent germer. Ainsi seulement une fraction, $1-\varepsilon_{ge}$, du nombre initial des colonnes, n_c^0, va être capable de pénétrer à travers la zone équiaxe. Le deuxième effet de blocage mécanique reflète le fait que pour une zone mixte (colonnaire+équiaxe), les deux structures sont forcées de partager localement un même espace. Par conséquent, l'espace disponible pour chaque structure sera différent et plus

petit par rapport à l'espace correspondant disponible juste avant l'état de coexistence. Ainsi l'évolution de la zone colonnaire+équiaxe sera très différente de celle caractérisant une zone purement colonnaire ou purement équiaxe. Finalement, en utilisant l'approximation de la cellule pour $\widetilde{f}_{c/e}$ et les hypothèses physiques valides à l'échelle du grain nous avons pu fermer rigoureusement le système des équations moyennes. Un modèle complet décrivant la coexistence des grains colonnaires et équiaxes a été finalement obtenu.

Dans une troisième partie de la thèse (référence III, Annexe 7.2) nous nous sommes concentré sur l'utilisation du nouveau modèle mathématique pour la simulation de la transition colonnaire-équiaxe. Premièrement nous avons effectué la simulation numérique des solidifications quasi-stationnaires dans le but d'obtenir les cartes de la CET. Nous avons trouvé qu'en fonction du choix de la vitesse de tirage par rapport à deux vitesses critiques caractérisant le zone équiaxe devant les pointes colonnaires on pouvait identifier sur la carte CET trois zones : une zone purement colonnaire, une zone purement équiaxe et finalement une zone mixte colonnaire+équiaxe. En quantifiant le mécanisme de division des dendrites colonnaires on a pu déterminer si la zone mixte colonnaire+équiaxe correspondait à un état quasi-stationnaire aux pointes colonnaires. Le mécanisme de division des colonnes (mécanisme de redensification de la zone colonnaire) a été quantifié à l'aide d'un nouveau modèle pour l'espacement dendritique primaire. Ce modèle a à sa base une analyse de la stabilité des pointes colonnaires par rapport aux conditions locales de solidification (gradient thermique, vitesse des isothermes). Il a été aussi validé par plusieurs données expérimentales. Finalement, la zone mixte colonnaire+équiaxe a été quantifiée à l'aide de la fraction colonnaire ε_c, qui à son tour quantifie rigoureusement l'état de coexistence des deux structures. Il est important de noter que les effets de blocage solutal et mécanique produits par la zone équiaxe sur les pointes colonnaires sont intrinsèquement inclus dans le nouveau modèle. Ainsi ce modèle réussit à unifier l'approche semi-empirique de Hunt [3] (le blocage purement mécanique) et celui de Martorano et al. [4] (le blocage purement solutal). Dans une deuxième partie de ce travail on s'est concentré sur l'utilisation du nouveau modèle pour la simulation des expériences unidirectionnelles de solidification en [11, 12]. On a tout d'abord mis en évidence le couplage complexe entre la zone colonnaire et la zone équiaxe devant les pointes colonnaires. Ensuite la stationnarité du front colonnaire par rapport aux conditions locales de refroidissement a été analysée. Nous avons ainsi pu mettre en évidence que le front colonnaire évoluait dans un état quasi-stationnaire par rapport aux conditions locales de refroidissement jusqu'à des moments très proche de la transition colonnaire-équiaxe. Nous avons également trouvé que la surfusion de nucléation des grains équiaxes était très proche de la surfusion maximale des pointes colonnaires et qu'ainsi la CET était virtuellement indépendante de la zone équiaxe devant le front colonnaire. Ceci est en concordance avec les résultats de Martorano et al. [4] et vient appuyer l'idée que la CET est principalement causée par la fragmentation des dendrites colonnaires. Si la zone équiaxe n'est pas prise en compte par le modèle on observe que la vitesse du front colonnaire subit une croissance brusque au début de la solidification suivi par un quasi-plateau correspondant à un état quasi-stationnaire aux pointes colonnaires et finalement, après un temps critique, suivi par une évolution oscillatoire. Il est très intéressant de noter que le début de l'évolution oscillatoire du front colonnaire a pu être corrélé avec la position de la CET mesurée dans les expériences. On a montré aussi que l'évolution oscillatoire du front colonnaire correspondait en fait à un état non stationnaire des pointes colonnaires par rapport aux conditions locales de refroidissement. On a trouvé aussi que cette évolution oscillatoire du front colonnaire était très favorable à la fragmentation des dendrites colonnaires et par

conséquent très favorable à la CET. Finalement, on a conclu que le régime non stationnaire du front colonnaire par rapport aux conditions locales de refroidissement représentait la cause principale de la CET, au moins pour les alliages non raffinés.

Dans une quatrième partie de la thèse (référence IV, Annexe 7.2) le modèle à prise de moyenne statistique développé dans la deuxième publication (référence II, Annexe 7.2) est étendu pour prendre en compte les effets de la convection du fluide. En similitude avec le modèle initial, le nouveau modèle approche la moyenne d'ensemble à l'aide des densités de probabilité des particules les plus proches, $\widetilde{f}_{c/e}\left(t,\mathbf{x};\tilde{\mathbf{z}}_{\mathrm{l}}\right)$. De cette manière les interactions solutales et mécaniques entre les deux structures colonnaire et équiaxe (c/e) mises en évidence par le modèle initial sont aussi prises en compte par le nouveau modèle. Toutefois, à cause de la prise en compte de l'écoulement fluide les hypothèses physiques valides à l'échelle du grain sont réévaluées par rapport à celles initialement décrites en référence II. Premièrement, l'écoulement fluide autour des grains perméables colonnaires et équiaxes est analysé. Deuxièmement, la croissance du grain en présence de la convection est décrite. Finalement, on fait une analyse du transfert de soluté autour des grains c/e en tenant compte de la convection. On trouve ainsi que le transfert de masse à l'interface du grain c/e en présence de la convection est plus intense par rapport au cas sans convection. On propose des corrélations pour le calcul du coefficient de transfert de masse global dans la limite de très petites et de grandes fractions granulaires. Ces hypothèses physiques valides à l'échelle du grain couplées avec le modèle de la cellule nous permettent de fermer le système complexe formé par les équations de conservation. Premièrement les équations de conservation des grains sont dérivées. La nucléation équiaxe est modélisée comme un événement instantané tandis que la nucléation colonnaire (l'apparition soudaine des pointes colonnaires dans un point **x**) est modélisée à l'aide d'un algorithme de suivi du front. On propose ainsi une technique simple de suivi du front ayant à la base le modèle du volume fluide (« volume of fluid model »). De plus, les dimensions des cellules $R_{\mathrm{l}c}^{*}$, $R_{\mathrm{l}e}^{*}$ et le calcul des fractions colonnaires et équiaxes (ε_c et ε_e) sont ici déterminés à l'aide d'un nouveau modèle de coexistence qui prend en compte la convection des grains équiaxes. Les équations de conservation de masse, de la quantité de mouvement et de l'énergie sont dérivées par la suite. Il faut remarquer que pour des raisons de simplicité l'équation de conservation de quantité de mouvement pour le liquide est écrite pour le fluide total et non pas séparément pour le fluide colonnaire et équiaxe. Pour l'équation de l'énergie une seule équation de mélange est écrite. Finalement, les équations de conservation de soluté sont dérivées. Ainsi deux équations pour le solide colonnaire et équiaxe ainsi qu'une équation pour la conservation de soluté dans le fluide total sont considérées. De plus, les deux équations de conservation de soluté dans le liquide inter-dendritique sont utilisées pour le calcul du transfert de masse liquide-solide. On propose aussi un algorithme pour le traitement implicite du calcul de la concentration dans le liquide extra-dendritique. Ceci est fait par le couplage à chaque pas de temps de l'équation de conservation de soluté dans le liquide extra-dendritique avec l'équation de conservation de soluté dans le fluide total. Enfin un modèle complet à prise de moyenne statistique d'ensemble est proposé, celui-ci étant capable de modéliser le couplage complexe entre les structures colonnaire et équiaxe en présence de la convection.

Finalement, dans un but de validation, le modèle mathématique développé dans la référence IV (Annexe 7.2) a été implémenté dans le logiciel FLUENT. Toutefois, il est important de noter que pour l'instant seulement le modèle colonnaire pur a été complètement implémenté et testé en Fluent. Dans un premier temps, à l'aide du modèle numérique plusieurs cas de solidification dirigée sous l'influence de la convection naturelle et/ou forcée ont été analysés. On a observé que la structure de l'écoulement à proximité du

macrofront a une très grande influence sur le développement des éventuels canaux ségrégés. Le passage du cas sans brassage électromagnétique au un cas où l'écoulement dans le bain liquide est contrôlé est très bien reflété par la structure de la zone pâteuse. Dans le cas de la convection naturelle plusieurs canaux ségrégés isolés sont présents dans la zone pâteuse. Par contre l'écoulement forcé dans le bain liquide imposé par le brassage électromagnétique modifie complètement la configuration des canaux. En effet, en contrôlant l'écoulement dans le bain liquide la distribution de pression au niveau du macrofront est également contrôlée. Principalement contrôlé par la distribution de pression locale, l'écoulement dans la zone pâteuse va à son tour contrôler la distribution des canaux ségrégés dans la zone pâteuse. Effectivement, un brassage important prend naissance dans la zone pâteuse celui-ci étant dirigé des zones de basse pression vers les zones de haute pression. Ce brassage amène du liquide enrichi en soluté vers les zones de basse pression en y empêchant la solidification. Ainsi des canaux ségrégés sont donc susceptibles de se développer aux endroits où l'écoulement pâteux débouche dans le bain liquide. Toutefois les canaux peuvent exister seulement si l'écoulement dans la zone pâteuse est suffisamment fort par rapport aux conditions locales de solidification. Nous avons en effet montré que les zones pâteuses subissait un processus de solidification intensifié, là où l'écoulement est dirigé dans le même sens avec la vitesse locale des isothermes V_{is}. Ces zones correspondent aux zones de haute pression où l'écoulement pénètre dans la zone pâteuse. Au contraire aux endroits où l'écoulement pâteux se fait dans le sens contraire à la vitesse locale des isothermes, le processus de solidification est diminué en intensité par rapport à un cas purement diffusif. Si l'écoulement dépasse en intensité la vitesse des isothermes, la solidification est stoppée et un processus de refusion prend naissance localement. Ainsi, un canal ségrégé peut naître et subsister dans le temps seulement si l'écoulement pâteux local est suffisamment fort pour que la vitesse locale du liquide soit plus grande ou égale à la vitesse locale de l'isotherme. La présence d'un canal détermine aussi de fortes ségrégations dans la zone pâteuse : le canal agit comme une pompe de soluté drainant la zone pâteuse. On a montré aussi que le fort appauvrissement de la zone pâteuse autour d'un canal provenait du fait que la concentration moyenne caractérisant le flux de masse entrant dans la zone pâteuse était plus petite par rapport à la concentration moyenne caractérisant le flux de liquide sortant de la zone pâteuse et débouchant dans le canal. On conclut ainsi que l'utilisation d'un brassage électromagnétique glissant ou rotatif ne permet pas d'annuler les macroségrégations dues aux canaux ségrégés. Par contre l'avantage de l'utilisation du brassage électromagnétique réside dans le contrôle de la position des canaux et donc la localisation précise des macroségrégations positives correspondantes, en opposition donc avec le cas sans brassage où la distribution des canaux était aléatoire (les freckles).

Ensuite, dans un but de validation, le modèle numérique a été utilisé dans la modélisation de l'expérience de solidification dirigée sous l'influence du brassage électromagnétique rotatif, expérience réalisée au laboratoire ACCESS. L'accord entre les résultats numériques et les résultats expérimentaux est aussi bon tant sur le plan qualitatif que quantitatif. D'une part le modèle reproduit le large canal central induit par la convection forcée dans le bain liquide : les dimensions du canal central sont très proches des dimensions obtenues expérimentalement. D'autre part les ségrégations radiales et longitudinales sont en bon accord avec les résultats expérimentaux à l'exception de la zone centrale qui est légèrement surestimée. La cause de ce désaccord semble être la non-modélisation de la zone équiaxe. Finalement l'élargissement du canal dans le temps est aussi qualitativement reproduit par le modèle. La cause de cet élargissement réside dans la modification des recirculations secondaires au niveau du macrofront. Ces dernières sont à

leur tour dues au ralentissement du macrofront et au rapprochement du plan axial de l'aimant du macrofront.

En conclusion, les objectifs principaux de cette thèse, à savoir :

- Le développement d'un modèle mathématique eulérien à prise de moyenne statistique capable de modéliser le couplage complexe entre les structures colonnaire et équiaxe,
- La validation de ce modèle avec des résultats expérimentaux et notamment avec des expériences de solidification dirigée faisant intervenir le phénomène de transition colonnaire-équiaxe,
- L'implémentation du modèle dans le logiciel FLUENT et la validation de celui-ci avec des expériences,

ont été atteints. Toutefois, il est important de noter que pour l'instant seul le modèle colonnaire pur a été complètement implémenté et testé dans Fluent. Une version du modèle équiaxe pur est en phase de développement mais les résultats actuels n'ont pas permis une validation approfondie de celui-ci. Comme perspectives de continuation de ce travail on note :

- L'implémentation dans Fluent du modèle mathématique permettant la modélisation de la structure équiaxe pure et la validation de celui-ci,
- L'implémentation dans Fluent et la validation du modèle mathématique complet développé en référence IV (Annexe 7.2) permettant la simulation du couplage équiaxe/colonnaire en présence de la convection.

6 Références

1. Sarazin, J.R., and A. Hellawell: "Channel Formation in Pb-Sn, Pb-Sb and Pd-Sn-Pb Alloy Ingots and Comparison With the System.", *Metallurgical Transactions A*, 1988, vol. 19A, pp. 1861-1871.

2. Jackson, K.A., et al.: "On the Origin of the Equiaxed Zone in Castings.", *Transactions of the metallurgical society of AIME*, 1966, vol. 236, pp. 149-158.

3. Hunt, J.D.: "Steady State Columnar and Equiaxed Growth of Dendrites and Eutectic.", *Materials Science and Engineering*, 1984, vol. 65, pp. 75-83.

4. Martorano, M. A., C. Beckermann, and Ch.-A. Gandin: "A Solutal Interaction Mechanism for the Columnar-To-Equiaxed Transition in Alloy Solidification.", *Metallurgical and Materials Transactions A*, 2003, vol. 34A, pp. 1657-1674.

5. Drew, D.A., and S.L. Passman. Theory of Multicomponent Fluids. . New York: Springer-Verlag, 1999.

6. Quillet, G. "Influence de la Convection, Naturelle ou Forcée, sur l'apparition des Mésoségrégations lors de la Solidification des Alliages Métalliques.", Thèse de doctorat, INPG-ENSHMG, Grenoble, 2003.

7. Ciobanas, A.I. "Modélisation numérique de la solidification interdendritique. Influence du brassage électromagnétique sur les macroségrégations. ", DEA de l'INPG, 2002

8. Felicelli, S.D., J.C. Heinrich, and D.R. Poirier: "Simulation of Freckels During Vertical Solidification of Binary Alloys.", *Metallurgical Transactions B*, 1991, vol. 22B, pp. 847-859.

9. Rappaz, M., and Ph. Thévoz: "Solute Diffusion Model for the Equiaxed Dendritic Growth.", *Acta Metallurgica*, 1987, vol. 35.7, pp. 1487-1497.

10. Wang, C.Y, and C. Beckermann: "A Multiphase Solute Diffusion Model for Dendritic Alloy Solidification.", *Metallurgical and Materials Transactions A*, 1993, vol. 24A, pp. 2787-2802.

11. Mahapatra, R.B., and F. Weinberg: "The Columnar to Equiaxed Transition in Tin-Lead Alloys.", *Metallurgical Transactions B*, 1987, vol. 18B, pp. 425-432.

12. Ziv, I., and F. Weinberg: "The Columnar-To-Equiaxed Transition in Al 3 Pct Cu.", *Metallurgical Transactions B*, 1989, vol. 20B, pp. 731-734.

13. Carman, P.C. Flow of Gases Through Porous Media. . London: Butterworth Scientific, 1956.

14. Medina M. "Ségrégation en solidification en présence de convection forcée ", Thèse de doctorat, INPG – ENSHMG, Grenoble, 2000.

15. Worster, M.G.: "Convection in Mushy Layers.", *Ann. Rev. Fluid Mech.*, 1997, vol. 29, pp. 91-122.

16. Bejan, A. Shape and Structure, From Engineering to Nature. . New York: Cambridge University Press, 2000.

7 Annexes

7.1 Les propriétés physiques des alliages utilisés

Tableau 8: Propriétés de l'alliage Pb – 10wt% Sn

Coefficient de conduction thermique du solide, λ_s	$W.m^{-1}.K^{-1}$	24,65
Coefficient de conduction thermique du fluide, λ_s	$W.m^{-1}.K^{-1}$	24,65
Chaleur latente de solidification, L	$J.kg^{-1}$	40000
Chaleur spécifique du solide, c_s	$J.kg^{-1}.K^{-1}$	145
Chaleur spécifique du fluide, c_f	$J.kg^{-1}.K^{-1}$	145
Coefficient d'expansion thermique, β_T	K^{-1}	$-1,2\times10^{-4}$
Coefficient d'expansion solutale, β_C	$(wt\%)^{-1}$	$-5,15\times10^{-3}$
Coefficient de diffusion solutale dans le solide, D_s	$m^2.s^{-1}$	0
Coefficient de diffusion solutale dans le liquide, D_f	$m^2.s^{-1}$	3×10^{-9}
Viscosité dynamique, μ	$kg.m^{-1}.s^{-1}$	$1,8\times10^{-3}$
Mass volumique du solide, ρ_s	$kg.m^{-3}$	10000
Mass volumique du liquide, ρ_l	$kg.m^{-3}$	10000
Coefficient de partage, k	--	0,31
Pente du liquidus, m	$K.(wt\%)^{-1}$	$-2,32$
Température de fusion du Pb pur, T_f	K	600,65
Température du liquidus à C_0, T_{liq}	K	577,4
Concentration eutectique, C_E	$wt\%$	61,9
Température eutectique, T_E	K	456,42

Tableau 9: Propriétés de l'alliage Al –7wt% Si

Coefficient de conduction thermique du solide, λ_s	$W.m^{-1}.K^{-1}$	100
Coefficient de conduction thermique du fluide, λ_s	$W.m^{-1}.K^{-1}$	100
Chaleur latente de solidification, L	$J.kg^{-1}$	400000
Chaleur spécifique du solide, c_s	$J.kg^{-1}.K^{-1}$	1140
Chaleur spécifique du fluide, c_f	$J.kg^{-1}.K^{-1}$	1140
Coefficient d'expansion thermique, β_T	K^{-1}	$1,2\times10^{-3}$
Coefficient d'expansion solutale, β_C	$(wt\%)^{-1}$	$-2,5\times10^{-4}$
Coefficient de diffusion solutale dans le solide, D_s	$m^2.s^{-1}$	$\cong 0$
Coefficient de diffusion solutale dans le liquide, D_f	$m^2.s^{-1}$	3×10^{-9}
Viscosité dynamique, μ	$kg.m^{-1}.s^{-1}$	$2,52\times10^{-3}$

Mass volumique du solide, ρ_s	$kg.m^{-3}$	2452
Mass volumique du liquide, ρ_l	$kg.m^{-3}$	2452
Coefficient de partage, k	--	0,13
Pente du liquidus, m	$K.(wt\%)^{-1}$	$-6,62$
Température de fusion de l'Al pur, T_f	K	933,45
Température du liquidus à C_0, T_{liq}	K	887,11
Concentration eutectique, C_E	$wt\%$	12,6
Température eutectique, T_E	K	850

7.2 Les références en anglais

Référence I

INSTITUTE OF PHYSICS PUBLISHING JOURNAL OF PHYSICS D: APPLIED PHYSICS
J. Phys. D: Appl. Phys. **39** (2006) 5252–5266 doi:10.1088/0022-3727/39/24/023

Dendritic solidification morphology viewed from the perspective of constructal theory

A I Ciobanas[1], A Bejan[2] and Y Fautrelle[1]

[1] EPM/CNRS Laboratory, ENSHMG, BP 95, 38402 Saint Martin d'Hères cedex, France
[2] Duke University, Department of Mechanical Engineering and Materials Science, Durham, NC 27708-0300, USA

E-mail: aciobanas@yahoo.com

Received 16 July 2006, in final form 23 October 2006
Published 1 December 2006
Online at stacks.iop.org/JPhysD/39/5252

Abstract
In this paper we focus on the application of the constructal theory in predicting the dendritic solid structure. First we analyse the marginal stability criterion from the perspective of the constructal principle. Having as a guiding principle the constructal law we have shown that among the whole range of possible dendrite tip radiuses predicted by the stability analysis the dendrite tip will choose the smallest one, that is a radius equal with the smallest perturbation wavelength leading to instabilities. We identify as well the existence of a competition between the diffusion controlled growth and the dendritic growth. Second, we develop a model for the secondary arm spacing. We identify a competition between the lateral diffusion controlled growth of a needle and the dendritic growth of lateral secondary arms. By analysing this competition we are able to characterize the sidebranching mechanism and to finally compute the secondary arm spacing. The result is in good agreement with the experimental results. Finally, the primary arm spacing is analysed from the perspective of the constructal law. The constructal law predicts that the only way the columnar tips can optimize the solidification process is to minimize the spacing between two adjacent tips, namely λ_1. By quantifying the two mechanisms responsible for the selection of λ_1, the dendrite division and the dendrite overgrown mechanisms, we were finally able to obtain a model for the primary arm spacing. This model is also validated against various experimental data.

Nomenclature

Symbol	Meaning	Unit
C	Solute concentration field	(wt%)
C_s^*	Interfacial concentration at the solid interface	(wt%)
C_l^*	Interfacial concentration at the liquid interface	(wt%)
T	Temperature field	(K)
T_{liq}	Liquidus temperature corresponding to the initial concentration C_0	(K)
T_f	Fusion temperature of the pure solvent	(K)
T_{ts}	Isotherm corresponding to the quasi-steady columnar tips	(K)
x_{st}	Position of the quasi-steady columnar tips	(m)
G	Thermal gradient	(K m^{-1})
G_c	Solutal gradient at the solid–liquid interface	(wt% m^{-1})
λ_1	Primary arm spacing	(m)
λ_2	Secondary arm spacing	(m)
λ_{min}	Minimum perturbation wavelength leading to instabilities	(m)
α	Thermal diffusivity	(m^2 s^{-1})
D_s	Chemical diffusivity of the solute in the solid	(m^2 s^{-1})

D_l	Chemical diffusivity of the solute in the liquid	($m^2\ s^{-1}$)
m	Slope of the liquidus line	($K\ wt\%^{-1}$)
k	Partition coefficient	
t_{rs}	Return time to the steady state of a tip perturbed from its initial quasi-steady position	(s)
t_{dw}	Time scale characterizing the strength of the solutal interactions between two adjacent columnar tips	(s)
R_t	Dendrite tip radius	(m)
V_t	Dendrite tip velocity	($m\ s^{-1}$)
V_{is}	Isotherm velocity	($m\ s^{-1}$)
Pe	Tip Peclet number ($= R_t V_t / 2D_l$)	
Ω	Dimensionless undercooling	

1. Introduction

It is well known that a columnar dendritic structure can be characterized with a precise length scale named the primary arm spacing. In fact the primary arm spacing is a measure of the average spacing between two adjacent columnar tips. This length scale defines a quasi-steady state columnar structure and hence was directly linked to the thermal gradient and the isotherm velocity defining the local cooling conditions. Moreover, both the columnar and the equiaxed dendritic structures can be characterized with a smaller length scale, the secondary arm spacing. The secondary arm spacing is a measure of the length scale between two adjacent secondary dendrite arms and it is usually an order of magnitude smaller than the primary arm spacing. The presence of primary and secondary dendrite arms within an equiaxed or columnar zone thus contributes to the complexity of the dendritic solid structure. Hence, the existence of a model which could predict these two important lengths scales would be of great interest. In fact various models were developed in the past decades aiming to predict both the primary and secondary arm spacing. Concerning the secondary arm spacing, Lager and Muller-Krumbhaar (L–M) [1] developed a theoretical model to predict the stability of dendrite tips and the inherent instability that gives rise to sidebranches (secondary arms). Their model predicts that the secondary arm spacing (λ_2) is almost equal to the double of the primary arm dendrite tip radius, R_t. One should note that this result was subsequently validated experimentally [2] and it was observed that the L–M model fits very well with the experimental data. One should however note the high complexity of the stability analysis which stands behind this relatively simple result. In this respect we will present in the following study a more original (and simpler) approach to the secondary arm spacing. In fact we will propose a model for the secondary arm spacing developed from the perspective of the constructal law [3–5]. Basically the constructal law states that the geometric form of a freely changing flow system[3] develops in such a way that the currents find the path of maximal access. In this context one should see the dendritic structure as an optimal solid structure that forms for the most rapid solidification given certain physical constraints (i.e. given undercooling, isotherm velocity or thermal gradient). As we will point out, when seen from the perspective of the constructal law, the sidebranching mechanism appears as a needed mechanism in order to counter the slower lateral growth (diffusion controlled growth) of the primary arm. By quantifying the competition between the diffusion controlled growth and the dendritic growth we are able to predict the secondary arm spacing.

Concerning the primary arm spacing, various models exist in the literature [6–12]. We will depart once more from the classical approach to the prediction of primary arm spacing by forcing ourselves to look at the columnar structure from the perspective of the constructal law. We conclude that the natural tendency of the columnar tips is to minimize the average spacing between them. In fact, by minimizing the primary arm spacing (λ_1) the columnar structure is optimizing the solidification process behind the columnar tips. By identifying and quantifying the two mechanisms responsible for the selection of a unique primary arm spacing (the dendrite division mechanism and the overgrown mechanism) we are finally able to obtain a model for λ_1. This model is subsequently validated against various experimental data [2, 13–15].

The paper comprises four sections. In section 2, the marginal stability criterion is analysed from the perspective of the constructal theory. As well, we introduce the concept of 'competition' between the diffusion controlled growth and the dendritic growth. Using this concept we are able to predict the moment corresponding to the solid–liquid destabilization. In section 3 the secondary arm spacing is also analysed from the perspective of the constructal theory. The proposed model is in very good agreement with the model of L–M [1] and with different experimental data [2, 16]. Finally throughout section 4 a model for the primary arm spacing is developed. Again the concept of the selection of the primary arm spacing is analysed from the perspective of the constructal theory. The model is also tested against different experimental data.

2. The stability criterion

One should note that the theoretical findings in the two following sections are entirely based on the findings of Bejan *et al* [4,5]. However we introduce here two original approaches regarding the stability criterion and the computation of the secondary arm spacing.

In [5], in order to quantify the evolution of a solid region in space and time Bejan relied entirely on the constructal law [4]. Basically the constructal law states that the geometric form of a freely changing flow system develops in time in such a way that the currents find the path of maximal access. Applied to a solutal controlled solidification the constructal law means that [5]:

1. the heat currents generated on the solidification fronts will shape their fronts such that they flow with least resistance;
2. the solid region grows as fast as possible;
3. equilibrium is reached in minimal time because of the generation of geometric structure.

[3] Flow does not refer to fluid flow only but has a more general meaning in the sense of energy flows (heat, mass, etc).

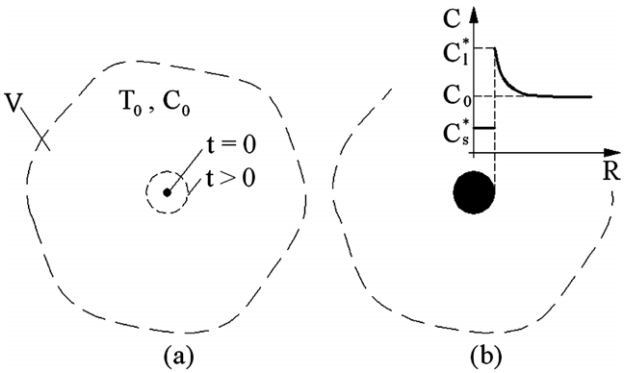

Figure 1. (*a*) The isothermal solidification of a solid nuclei; (*b*) the concentration distribution around the solid grain.

Even if the study in [5] focuses on the solidification of a pure substance we will in the following consider the case of a binary alloy. Let us consider a volume V (see figure 1(*a*)) filled with a liquid binary alloy, having a uniform solute concentration C_0 and a uniform temperature T_0. We will consider as well that the liquid is undercooled, meaning that its temperature is lower than the liquidus temperature, T_{liq}, corresponding to C_0. One has

$$T_0 = T_{\mathrm{liq}} - \Delta T_0. \tag{1}$$

We will also consider that the volume V is maintained at a constant temperature T_0. Let us suppose now that at $t = 0\,\mathrm{s}$ a solid germ nucleates within the liquid phase. Due to the undercooled state of the liquid phase the solid germ will start to grow for $t > 0$. Moreover, due to the relative high thermal diffusivity of the liquid metals the latent heat will be rapidly diffused away from the solid–liquid interface. In this respect, one can consider that a thermal equilibrium exists at the scale of the solid grain and that the solidification process is very close to an isothermal one ($T = T_0 = ct$). One should also note that for liquid metals the Lewis number,

$$Le = \frac{\alpha}{D_{\mathrm{l}}}, \tag{2}$$

is very large. Hence, the thermal diffusion process at the solid–liquid interface will be much faster than the solutal diffusion process. Therefore unlike for pure substances where the solid growth is controlled by the thermal diffusion process of the latent heat away from the moving solid–liquid interface, for binary alloys the solid growth is mainly driven by the solute diffusion process at the solid–liquid interface.

One interesting aspect of the binary alloy solidification is that usually the solubility of the solute in the solid is lower than the solubility in the liquid phase. As a consequence, as the solidification process evolves, the growing solid phase accepts less solute than the liquid is actually able to offer. Basically the concentration at the solid interface is smaller than the one at the liquid interface (see figure 1(*b*)). One has

$$C_{\mathrm{s}}^* = kC_{\mathrm{l}}^*, \tag{3}$$

where $k < 1$ is called the partition coefficient and C_{l}^* is the solute concentration at the liquid interface. The latter is linked to the phase diagram (the liquidus line) and can be computed with respect to the local temperature. Usually one has

$$C_{\mathrm{l}}^* = \frac{T - T_{\mathrm{f}}}{m}, \tag{4}$$

where m is the liquidus line slope and T_{f} the fusion temperature of the pure solvent. The main consequence of this particular solid behaviour is the continuous enriching of the liquid phase due to the inherent solute rejection at the solid–liquid interface. The rejected solute will diffuse away from the interface as the solid–liquid interface is advancing (see figure 1(*b*)). In fact for binary alloys the solid growth is mainly controlled by this solute diffusion process at the solid–liquid interface. Moreover, the solute conservation written at the solid–liquid interface enables one to link the solid growth rate and the solute fluxes at the solid–liquid interface. One has

$$(C_{\mathrm{l}}^* - C_{\mathrm{s}}^*)\, V = -D_{\mathrm{l}} \frac{\partial C_{\mathrm{l}}}{\partial n_{\mathrm{l}}} + D_{\mathrm{s}} \frac{\partial C_{\mathrm{s}}}{\partial n_{\mathrm{s}}}, \tag{5}$$

where V is the normal velocity of the solid–liquid interface. Since usually $D_{\mathrm{s}} \ll D_{\mathrm{l}}$ the solute flux in the solid can be neglected.

Due to the liquid undercooling, subsequent to the solid nucleation, the concentration at the solid–liquid interface will jump to $C_{\mathrm{l}}^* (> C_0)$. Hence the solid nucleation will trigger a spherical solute diffusion wave around the nucleation site. The distance travelled by this diffusion wave can be expressed as a function of time as follows:

$$x = (D_{\mathrm{l}} t)^{1/2}. \tag{6}$$

A solutal boundary layer will develop around the solid grain triggering a non-zero solute flux at the solid–liquid interface. In fact, it is precisely this solute flux which also drives the grain growth. This particular free boundary diffusion problem is no more than the Stefan free boundary problem. Written for plane solid interface (see figure 2) the Stefan problem writes as follows:

$$\begin{aligned} &\frac{\partial C}{\partial t} = D \frac{\partial^2 C}{\partial x^2}, \\ &C\,(x = \infty, t) = C_0, \\ &C\,(x = x_{\mathrm{sf}}, t) = C_{\mathrm{l}}^*, \\ &C_{\mathrm{l}}^*\,(1 - k)\,\frac{\mathrm{d}x_{\mathrm{sf}}}{\mathrm{d}t} = -D \left(\frac{\partial C}{\partial x} \right)_{x_{\mathrm{sf}}}. \end{aligned} \tag{7}$$

The solution to the Stefan problem can be easily found in the literature [17]. The main result concerns the time evolution of the planar solid front. Indeed, for the case of small St numbers, one obtains that the position of the solid front as a function of time is

$$x_{\mathrm{sf}} \cong (2St\, D_{\mathrm{l}} t)^{1/2}, \tag{8}$$

where St is the dimensionless Stefan number. For the particular case of a binary alloy St number is no more than the dimensionless undercooling:

$$St\ (= \Omega) = \frac{C_{\mathrm{l}}^* - C_0}{C_{\mathrm{l}}^* - C_{\mathrm{s}}^*}. \tag{9}$$

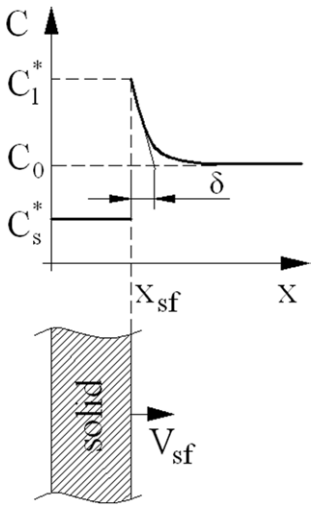

Figure 2. The uni-dimensional Stefan problem.

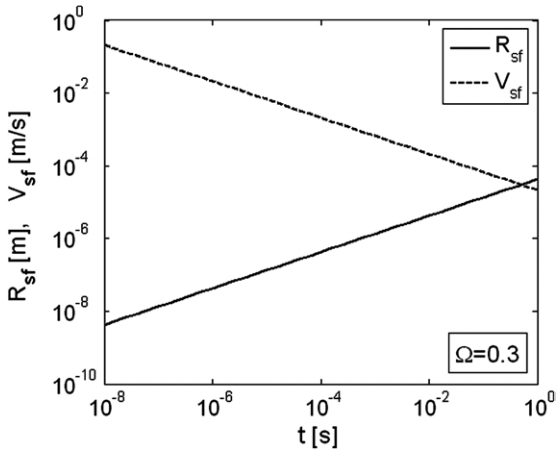

Figure 3. The solid grain radius R_{sf} and the solid growth rate V_{sf} as a function of time for an Al–3wt%Cu alloy ($\Omega = 0.3$).

Even if the problem analysed above is valid for a planar solid front, one can assume that the central result in (8) applies as well for the case of growing sphere but only as an order of magnitude estimate; that is,

$$R_{sf} \sim (2\,\Omega\,D_l\,t,)^{1/2}, \tag{10}$$

where R_{sf} is the solid grain radius. An interesting aspect of the diffusion controlled growth in (10) is that the solid growth rate

$$V_{sf} \sim \frac{dR_{sf}}{dt} \sim \frac{1}{2}\,(2\,\Omega\,D_l)^{1/2}\,t^{-1/2} \tag{11}$$

is continuously decreasing in time. In fact at the very beginning of the solidification, due to the infinite propagation speed of the diffusion wave, the solid growth rate is also infinite, equation (11). However, soon after the nucleation, the solid growth rate decreases rapidly ($V_{sf} \propto t^{-1/2}$). This is mainly due to the rapid increase in the solute boundary layer (δ) around the spherical solid grain. This boundary layer can be easily estimated from the solute conservation at the solid–liquid interface:

$$C_l^*\,(1-k)\,V_{sf} = -D\left(\frac{\partial C}{\partial r}\right)_{R_{sf}} = D\frac{C_l^* - C_0}{\delta}. \tag{12}$$

Using the result in (11) one can easily obtain that

$$\delta \sim (2\,\Omega\,D_l)^{1/2}\,t^{1/2} \sim R_{sf}. \tag{13}$$

This means that the solutal boundary layer around the grain is of the same order of magnitude as the radius of the solid grain. In figure 3 the representation of the grain radius and of the grain growth rate as a function of time is presented for an Al–3wt%Cu alloy and an undercooling of $\Omega = 0.3$. The Al–3wt%Cu alloy physical properties can be found in table 1. We can thus state that the diffusion controlled growth is very effective at the very beginning of the solidification and rapidly decreases in efficiency after the nucleation. From the point of view of the constructal law the natural tendency in the evolution of the solid structure will be the maximization of the radius R_{sf} through the *generation* of the solid geometry. Since the maintenance of a spherical geometry means a continuous decreasing growth rate, see equation (11), in respect with the constructal law, the solid will be forced to select a different geometry, a more effective one. As pointed out by Bejan *et al* [5] the geometric alternative for the solid is to invade the liquid in the form of needles.

The needles which are at the base of the dendritic form of the solid are a direct consequence of the solid–liquid interface instabilities. Indeed, given some particular solidification conditions (thermal gradient G and solutal gradient G_c at the interface) the solid–liquid interface becomes instable to small perturbation of its shape. The Mullins–Sekerka [18] linear stability analysis provided, for the case of a planar front, the conditions under which the planar solid–liquid interface becomes instable. Indeed, using the Mullins–Sekerka results, Kurtz and Fisher [7] computed the perturbation wavelengths range leading to instabilities. Their central result states that for a perturbation wavelength λ,

$$\lambda > 2\pi\left(\frac{\Gamma}{mG_c - G}\right)^{1/2}, \tag{14}$$

the solid–liquid interface becomes instable. In (14) G_c is the solutal gradient and G is the thermal gradient at the solid–liquid interface. As Kurtz and Fisher pointed out, one expects the dendrite point radius (the needle radius) to be equal to the perturbation wavelength λ, namely that

$$R_t = \lambda. \tag{15}$$

This result coupled with equation (14), would mean that for a given directional solidification experiment one should observe various dendrite tip radii corresponding to different perturbations wavelengths within the range determined in (14). However in reality, one observes a unique radius for the dendrites tip. The solution to this problem was given by Langer and Muler-Krumbhaar [19]. Indeed, they proposed a selection criterion (the marginal stability criterion) for the dendrite tip, namely that the radius of the dendrite tip is equal to the minimum Mullins–Sekerka wavelength leading to instabilities. That is,

$$R_t = \lambda_{min} = 2\pi\left(\frac{\Gamma}{mG_c - G}\right)^{1/2}. \tag{16}$$

We note that this result was extensively validated with the experiments. In this context, an interesting question would be why the solid selects a precise geometry among its infinite possibilities, equation (14). Even if L–M answered this question by means of a complex stability analysis we will hereafter propose a simple explanation by citing the constructal principle. Indeed, the geometric form of the solid will develop in such a way that the solidification process will be the most effective one. As already pointed out, applied to the solidification of a binary alloy, the constructal law predicts that the shape of the solid shape will adapt in order to grow as fast as possible. Let us consider the case of an isothermal solidification ($G = 0$) of a binary alloy. Putting $G = 0$ in (14) and using equation (15) we can state that the range of possible radiuses of the dendrite tip (needle) is

$$R_t > 2\pi \left(\frac{\Gamma}{mG_c}\right)^{1/2}. \tag{17}$$

Using now the solute balance at the solid–liquid interface, $C_l^*(1-k)V = -D_l G_c$, the above inequality can be rewritten as follows:

$$\left(\frac{R_t V}{2D_l}\right)^2 > \pi^2 \frac{\Gamma V}{m(k-1)C_l^* D_l}, \tag{18}$$

where V is the growth velocity of the solid needle. We recognize in the LHS of the above equation the tip Peclet number $Pe = R_t V/2D_l$. If we approach the needle tip with a hemisphere we can further link the Pe number to the tip dimensionless undercooling Ω [7]:

$$Pe = \Omega. \tag{19}$$

Now one can easily obtain

$$V < \frac{m(k-1)C_l^* D_l}{\pi^2 \Gamma}\Omega^2 \tag{20}$$

meaning that the growth velocity of the solid needle will be always smaller than a maximum velocity. One can easily recognize that the RHS of (20) is no more than the dendrite tip velocity obtained if the marginal stability criterion of L–M is used [19]; that is,

$$R_t\,(=\lambda_{\min}) = 2\pi \left(\frac{\Gamma}{mG_c}\right)^{1/2} = 2\pi \left[\frac{\Gamma D_l}{m\,(k-1)\,C_l^* V}\right]^{1/2}. \tag{21}$$

The constructal principle enunciated above says that the needle shape will adapt in such a way as to grow with a maximum velocity. Looking at (20) it is now easy to see that a maximum dendrite tip velocity can be achieved only if among the whole range of possible radii, equation (17), the dendrite tip chooses the smallest one, equation (21). We can thus see how the constructal law manages to explain in a simple way the difficult concept of the marginal stability criterion. It is interesting to note that the choice of the minimum stable tip radius is somewhat similar to the phenomenon of laminar–turbulent transition. Bejan [20] showed that the choice between the viscous diffusion and the 'needles' of eddy flow is also made at the smallest (neutral) wavelength of instability. Moreover Bejan [4] used this particular observation to predict the laminar–turbulent transition and the obtained results are very convincing. In this context it appears that the turbulent structure and dendrites in solidification are analogous manifestations of the constructal phenomenon of generation of flow configuration. In fact, in an isolated system the generation of configuration brings the nonequilibrium system to equilibrium the fastest.

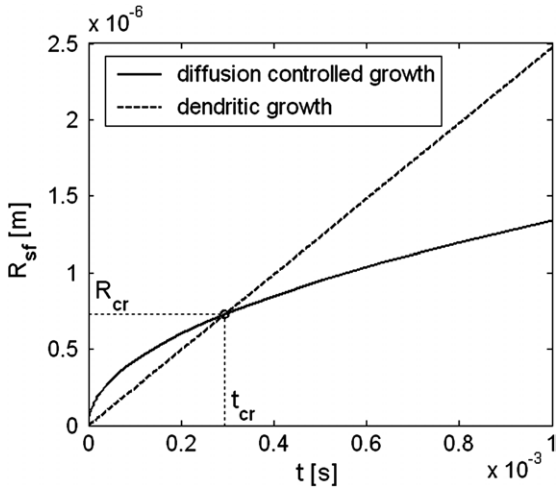

Figure 4. Diffusion controlled growth versus dendritic growth (Al–3wt%Cu alloy, $\Omega = 0.3$).

Returning now to the evolution of the solid nuclei we are able to state that due to the continuous decrease in the solid growth rate (figure 3) the solid is forced to select a different more effective geometry. We concluded that a valid alternative for the solid shape is the needle (the dendrite tip). Indeed, the most interesting feature of the needle is that due to its slender shape the dendrite tip is able to advance in the undercooled liquid with a constant velocity:

$$V_t = \frac{m(k-1)C_l^* D_l}{\pi^2 \Gamma}\Omega^2. \tag{22}$$

Note again that the above equation is valid if we assume a spherical shaped dendrite tip. Given a needle shape for the solid one can easily see that the radius of the solid region would increase linearly with time:

$$R_{sf} = V_t\, t. \tag{23}$$

If the above equation is plotted against the diffusion controlled growth in equation (10) one can easily see (figure 4) that at the beginning of the solidification the diffusion controlled growth is more effective than the dendritic solidification (the needle geometry). However soon after nucleation, the needle geometry wins over the diffusion controlled growth. With respect to the constructal principle this would also mean that at about t_{cr} (see figure 4) from the start of the solidification the solid interface will select a more effective shape, that is the needle geometry. These findings are very interesting since they are evidence of a competition between the diffusion controlled growth and the dendritic solidification. It is worthwhile to note that the competition between these two solidification regimes has been observed numerically by means of phase

field simulations of solid nuclei growth [21]. Note as well that figure 4 is the same as the figure for eddy formation in turbulence presented in [4]. This emphasizes once more the similarity between the turbulent structure and the formation of dendrites in solidification. It would be interesting to compute the critical time t_{cr}. This can be easily achieved by equalling (10) and (23). One can easily obtain

$$t_{cr} = \frac{2\Omega D_l}{V_t^2}. \tag{24}$$

The critical radius at which the shifting of the geometry occurs therefore becomes

$$R_{cr} = \frac{2\Omega D_l}{V_t}. \tag{25}$$

Using now the result in equation (19) one can easily see that

$$R_{cr} = R_t. \tag{26}$$

The above result is remarkable since it states that the critical radius of the solid nuclei which marks the shift between the two growth regimes, the diffusion controlled and the dendritic regime, is no more than the stable dendrite tip radius. As Bejan *et al* [5] observed, t_{cr} and R_{cr} represent no more than the smallest time and length scales of the dendritic structure, the 'heartbeat and capillarity of the much more complex dendritic structure that develops as time progresses'.

One may say that the concept of competition between diffusion controlled growth and dendritic growth does not have a rigorous physical explanation. However as we will show in the following, one can easily explain this particular phenomenon using a more rigorous stability analysis. Indeed we have shown that just after the solid nucleation a solute diffusion wave starts to propagate around the solid grain. This will determine the creation of a solutal boundary layer around the grain having a thickness of the same order of magnitude as the grain radius, equation (13). By knowing the solutal gradient at the solid–liquid interface one can easily compute the minimum perturbation wavelength leading to instabilities using the equation (14). One can easily obtain

$$\lambda_{min} = 2\pi\left[\frac{\Gamma}{-m\left(C_l^* - C_0\right)/\delta}\right]^{1/2} = 2\pi\left[\frac{\Gamma}{mC_l^*(k-1)}\right]^{1/2}\left(\frac{2D_l}{\Omega}\right)^{1/4} t^{1/4}. \tag{27}$$

It would be interesting to compare now the minimum perturbation wavelength λ_{min} with the radius of the grain R_{sf}, equation (10) (see figure 5). One can see that at the very beginning of the solidification the minimum wavelength leading to instabilities is larger than the actual radius of the grain. One should also note that a real interface perturbation cannot have a wavelength larger than the actual radius of the grain. In fact one expects the perturbation wavelengths to be of the same order of magnitude as the grain radius. Hence, during this first stage of the grain solidification ($\lambda_{min} > R_{sf}$) the solid grain will be stable to perturbations of its solid–liquid interface. However soon after the solid nucleation (at t^*, see figure 5) the minimum perturbation wavelength leading to instabilities (λ_{min}) equals the grain radius R_{sf}. Since the interface perturbations are of the same order of magnitude as

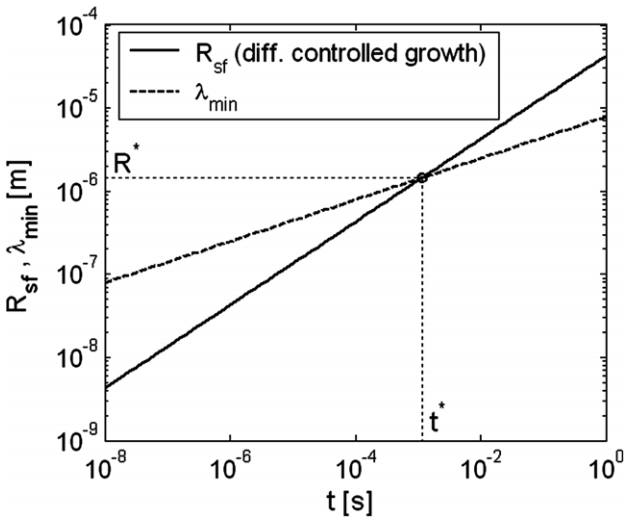

Figure 5. The grain radius (R_{sf}) and the minimum perturbation wavelength leading to instabilities (λ_{min}) as a function of time (Al–3wt%Cu alloy, $\Omega = 0.3$).

R_{sf}, it is easy to see that the grain interface becomes unstable for $t > t^*$. In this context t^* will be a measure of the time at which the destabilization of the interface will take place. Furthermore, t^* will quantify the time at which the grain growth commutes from a diffusion controlled regime to a dendritic regime. It would be interesting to compute this critical time. Putting $\lambda_{min} = R_{sf}$ one can easily obtain

$$t^* = \left[\frac{\pi^2\Gamma}{m(k-1)C_l^* D_l \Omega^2}\right]^2 8\Omega D_l = \frac{8\Omega D_l}{V_t^2}. \tag{28}$$

It is easy to see now that,

$$t^* = 4t_{cr}, \tag{29}$$

obtaining thus that the destabilization time t^* computed rigorously from a stability analysis is of the same order of magnitude as the critical time t_{cr} predicted based on the constructal principle. Moreover one obtains that the critical radius at which the interface destabilization takes place is

$$R^* = \frac{4\Omega D_l}{V_t} = 2R_{cr}. \tag{30}$$

We thus conclude that the results obtained by applying the constructal principle are of the same order of magnitude as the ones obtained by means of a more complex stability analysis. Hence, the idea of a competition between the diffusion controlled growth and the dendritic growth and consequently between two solid geometries (the sphere and the dendrite tip) has a secure physical basis. In this context the constructal principles do not appear as a collection of ad hoc established statements but as a physical reality having a rigorous explanation.

3. The secondary arm spacing

We have therefore shown that in view of the constructal law the solid grain will choose the most effective geometry (either a sphere or a dendrite tip) with respect to the local

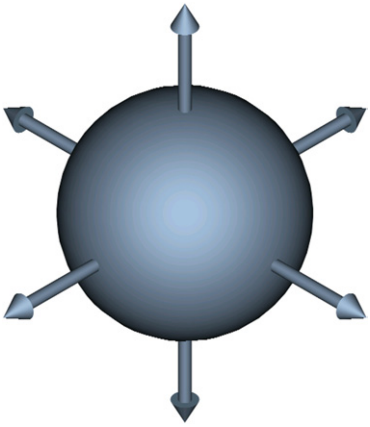

Figure 6. The growth of the dendrite tips from the initial spherical solid grain.

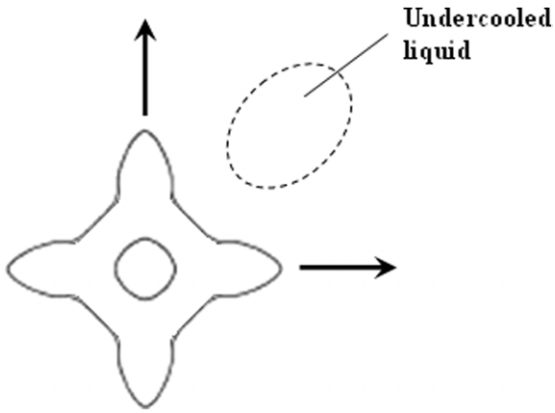

Figure 7. The evolution of the initial solid nuclei into a dendritic equiaxed grain. One can observe the increasing undercooled region that forms between the primary dendrite arms.

conditions at the solid–liquid interface (i.e. the local solute gradient). However one should note that when the solid–liquid destabilization triggers, the dendrite tip will not develop randomly around the initial spherical grain. In fact, and as Bejan [4,5] pointed out, the needles cannot form at every point on the surface of the solid sphere because each needle needs space to breathe. In order to survive each needle needs a certain amount of undercooled liquid region around it. Hence needles can only grow from a few discrete points on the surface of the initial solid sphere. Indeed, the angles between the needles are controlled by the inner molecular structure of the substance. For instance, for metallic alloys which form a body-centred cubic crystal the dendrite tips will grow at an angle of 90°. Hence a total of six dendrite tips will develop from the initial solid sphere (see figure 6). Note that the dendrite tips will grow provided that they advance into a reservoir of undercooled liquid.

At this point it would be interesting to focus on the third identified constructal principle. This one states that the geometric structure of the solid adapts in such a way that the solutal equilibrium is reached in minimal time. If one carefully analyses the solid structure of the four dendrite points in figure 7 one can easily observe that as the tips grow and advance into the undercooled melt an increasing amount of undercooled liquid is left between the tips. The increasing undercooled space between the dendrite tips therefore calls for an optimization of the solid structure.

To be able to predict the optimal geometric structure one should first analyse in more detail a single dendrite tip. As Bejan *et al* [5] pointed out the needle could be seen as a straight line string of discs that are growing following a diffusion controlled regime, thus obeying equation (10). Hence the tip arriving at point x_0 at time t_0 (figure 8) will trigger the growth of a disc of radius R:

$$R \sim [2\,\Omega\,D_{\mathrm{l}}\;(t - t_0)]^{1/2}\,. \tag{31}$$

Points where solidification has been triggered earlier are situated near the 'root' of the needle and more recent points are positioned near the tip (see figure 8). In sum, at a fixed time t the transversal radius of the dendrite trunk is

$$R \sim \left[\frac{2\,\Omega\,D_{\mathrm{l}}}{V_{\mathrm{t}}}\;(x - x_0)\right]^{1/2}, \tag{32}$$

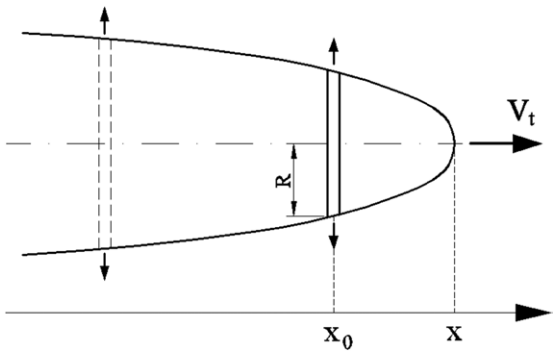

Figure 8. The dendrite arm viewed as a string of discs growing following a diffusion controlled regime.

where $x - x_0$ is the distance measured from the dendrite tip and V_{t} is the tip velocity (see figure 8). It is obtained therefore that the dendrite tip has a parabolic shape. Or it is well known that in reality the tip does not have a hemispheric shape but a parabolic one. For a parabolic shaped tip the tip Peclet number would no longer be equal to the dimensionless undercooling Ω as for the spherical tip. In reality one has

$$Pe = Iv^{-1}(\Omega), \tag{33}$$

where Iv^{-1} represents the inverse Ivantsov function [22] (a complex integral function). However even though the dendrite tip has a parabolic shape the tip Peclet number $Pe = R_{\mathrm{t}}V_{\mathrm{t}}/2D_{\mathrm{l}}$ will still be of the same order of magnitude as the local dimensionless undercooling. Putting thus $Pe \sim \Omega$ in (32) one finally obtains

$$R \sim [R_{\mathrm{t}}\;(x - x_0)]^{1/2}\,. \tag{34}$$

We have thus obtained that the dendrite tip radius is of the same order of magnitude as the minimum Mullins–Sekerka wavelength leading to instabilities, equation (21). In fact, from equation (34) one has that the dendrite tip radius is $R_{\mathrm{t}}/2$. Or the marginal stability criterion states that the dendrite tip radius is precisely equal to the minimum Mullins–Sekerka wavelength leading to instabilities. Hence the real dendrite shape is described by the following law:

$$R = [2R_{\mathrm{t}}\;(x - x_0)]^{1/2}\,, \tag{35}$$

where R is the transversal radius of the dendrite at a coordinate x_0 behind the dendrite tip and R_t is the dendrite tip radius verifying equation (21). However, using equation (21) solely does not permit the computation of the tip radius and the tip velocity. Therefore one needs one more equation linking R_t and V_t. This one is obtained from the solution of the stationary solute transport at the parabolic tip. A solution to this problem has been found by Ivantsov [22]. Ivantsov was able to link the tip Peclet number $Pe = R_t V_t/2D_l$ to the dimensionless undercooling Ω by means of equation (33). By coupling now equation (33) with the marginal stability criterion, equation (21), the tip velocity and the tip radius can be computed analytically. An interesting particularity of the parabolic shape of the dendrite is that behind the dendrite tip the solid spreads laterally as

$$R = (2R_t V_t)^{1/2} (t - t_0)^{1/2}, \tag{36}$$

meaning that the lateral solid growth rate

$$\frac{dR}{dt} = \frac{1}{2} (2R_t V_t)^{1/2} (t - t_0)^{-1/2} \tag{37}$$

is continuously decreasing in time. This property is responsible for the slenderness of the dendrite and, at the same time, for the increasing amount of undercooled liquid between the primary dendrite tips (see figure 7). In this context the third constructal principle calls for an optimization of the solid structure in order to minimize the time during which solutal equilibrium is reached between the primary dendrite arms. Since the maximum solid velocity is the dendrite tip velocity, the fastest way to invade the undercooled liquid between the primary dendrite arms would be if secondary dendrites arms would grow in a direction perpendicular to the primary arms (see figure 10). Indeed, since the liquid concentration between the primary arms remain close to C_0, the local undercooling could finally trigger the growth of secondary dendrite arms perpendicular to the primary ones. It would be interesting to analyse from the perspective of the constructal law the conditions for the growth of lateral dendrites arms. In fact, somewhat similar to the preceding case, one should analyse the competition between the lateral diffusion controlled growth of the primary arm, equation (36), and the dendritic growth of the lateral secondary arms. Given a dendritic growth regime, the solid region would spread laterally as

$$R = V_t\ (t - t_0), \tag{38}$$

where V_t is the tip velocity given the local undercooling Ω. Plotting now the above equation versus the diffusion controlled growth, equation (36), one can easily observe (figure 9) the following: at the beginning of solidification, that is just behind the dendrite tip, the diffusion controlled growth is more effective than the dendritic growth. However, soon after the start of the solidification (that is at a small distance behind the dendrite tip) the dendritic growth regime becomes more effective than the diffusion controlled growth. The constructal principle calls for the choice of the optimal solid shape. Hence at $\Delta t_{cr} = t_{cr} - t_0$ from the start of the solidification at x_0 (that is at a distance $x_{cr} = V_t(t_{cr} - t_0)$ behind the dendrite tip) a dendrite arm will start to grow laterally (see figure 10(*a*)). The critical time can be easily estimated as

$$\Delta t_{cr} = t_{cr} - t_0 = \frac{2R_t}{V_t}, \tag{39}$$

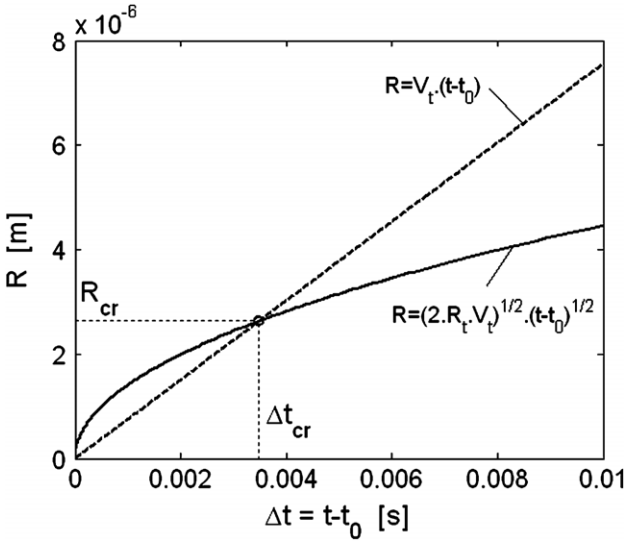

Figure 9. The lateral growth of the dendrite at a fixed position x_0: the full line represents the diffusion controlled growth and the dashed line the dendritic growth of lateral secondary arms.

meaning that

$$x_{cr} = 2R_t. \tag{40}$$

The distance x_{cr} has a very important meaning. In fact, as the primary dendrite trunk is advancing into the undercooled melt, secondary arms will always develop at a distance x_{cr} behind the primary dendrite tip (see figure 10). In this respect, as the primary arm is advancing, an array of secondary dendrite arms will develop laterally behind the primary dendrite tip (figure 10). One can easily observe that at $2\Delta t_{cr}$, $3\Delta t_{cr}$, etc from the moment corresponding to the destabilization of the initial spherical nucleus new secondary dendrite arms will start to grow laterally. Hence a network of orthogonal secondary dendrite arms develops between the primary dendrite arms. The distance between two adjacent lateral arms will be no more than x_{cr}. Hence x_{cr} will also be a measure of the secondary arm spacing λ_2. One has thus

$$\lambda_2 = x_{cr} = 2R_t. \tag{41}$$

It is important to note the equivalence between the result in (41) and the result of the stability analysis made by L–M [1]. Moreover, the last result can be easily validated with experiments. In [2] and [16] for instance the authors measured the secondary arm spacing and their conclusion was unanimous: λ_2 is almost equal to the double of the primary arm tip radius

$$\lambda_2 \cong 2R_t. \tag{42}$$

The agreement between the present theory, the model in [1] and the experiments is remarkable. This good agreement emphasizes once more the physical correctness of the constructal principle when applied to predict the solid geometry of a dendritic structure.

4. The primary arm spacing

Many studies dealing with the modelling of the primary arm spacing have been conducted in the past 20 years [6–12].

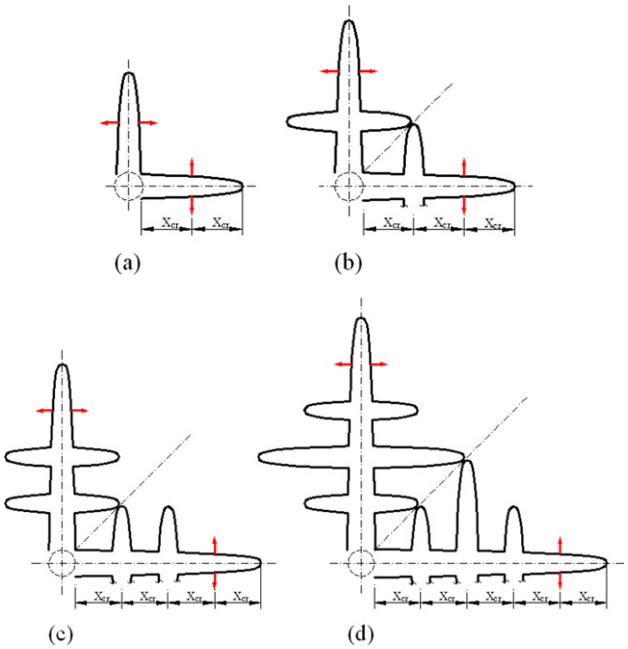

Figure 10. The evolution of the dendrite structure at four different moments: (*a*) at $2\Delta t_{cr}$; (*b*) at $3\Delta t_{cr}$; (*c*) at $4\Delta t_{cr}$ and (*d*) at $5\Delta t_{cr}$ from the moment corresponding to the destabilization of the initial spherical solid nuclei. The lateral arrows point to the positions on the primary arm where new (lateral) secondary arms start to grow.

The majority of primary arm models [6, 7, 9, 10] manage to obtain an analytical expression for λ_1 by fixing in an *ad hoc* manner the solid (or the grain fraction [9, 10]) at the eutectic temperature behind the columnar dendrite points. Even if the results obtained for λ_1 reproduce well enough the experimental data the approach chosen in these models hides partially the fact that λ_1 is mainly controlled by the columnar tip kinetics, hence by what happens at the tip and not at a certain distance behind the tip. A completely different approach is used in [11, 12]. Here the primary arm spacing is regarded from the perspective of the stability of a dendrite array advancing within an imposed thermal gradient and isotherm velocity. Besides the complex mathematical derivation, these models fail to fit accurately the experimental data. However the major trends in the variation of λ_1 with respect to the thermal gradient and isotherm velocity are well reproduced. Finally Lu [8] manages by using a complex numerical model of the dendrite tips to closely predict the variation of the primary arm spacing as well as the cellular spacing. An important feature of the Lu [8] model is that the cell/primary arm spacing is obtained from a stability criterion. Indeed, the authors emphasized the idea based upon which the observed cell/primary arm spacing defines a stable cell/dendrite configuration. In [8] two mechanisms determining the existence of a stable configuration are identified. First in the lower cell/dendrite spacing range there is the mechanism of overgrowth which limits from below the stable cell dendrite spacing. Indeed if the spacing between the dendrites array is low enough, due to strong solutal interactions between adjacent dendrite tips, some of the dendrites are overgrown by the surrounding members of the array. Hence the natural tendency of a highly dense dendrite array is to increase its average dendrite spacing by means of the overgrowth mechanism.

Second, in the upper cell/dendrite spacing range the mechanism of dendrite division is identified. Indeed, for a large average spacing between dendrites, the solutal interactions between adjacent dendrites are weak and the liquid behind the dendrite points will remain close to the initial concentration C_0 due to the thin solutal boundary layers around the columnar tips (see figure 12). Therefore this solutally untouched space leaves an undercooled liquid melt between the columnar grains. Secondary or even tertiary arms developed behind the columnar tips may evolve into vertical primary arms thus reducing the primary arm spacing. In this respect one expects to find at the intersection of these two unstable regimes a stable dendrite array configuration defined by the primary arm spacing λ_1 (see figure 11). Lu [8] managed to quantify the stable regime of the dendrite array by using their full numerical model describing the growth of a dendrite tip. Despite the accuracy of the Lu model the primary arm spacing can only be obtained by solving the complex numerical dendrite model. Therefore, an important limitation of the model is that no general analytical expression for λ_1 can be obtained.

In this context the existence of a simple and reliable solution for the primary arm spacing would be of great interest. Let us first analyse the columnar dendrite array from the perspective of the constructal theory. We have already identified in section 2 three constructal principles which define an optimal solidification process. When applied to a columnar front forced to advance into an undercooled melt with a constant velocity (V_{is}) and within a given constant gradient G, the three constructal principles predict that the only way the columnar tips can optimize the solidification process is to minimize the spacing between two adjacent tips, namely λ_1. Indeed, since the tip velocity is fixed at the level of the isotherm velocity, V_{is}, the only way the columnar tips can optimize the solidification process is by decreasing the dendrite array spacing, λ_1. By reducing λ_1, the time during which the solutal equilibrium is reached behind the columnar tips will also be reduced since the lateral diffusion process around the dendrite tips is characterized by a diffusion time scale depending directly on $\lambda_1(\tau_{dw} \cong \lambda_1^2/4/D_l)$. At the same time, a smaller λ_1 will also mean that the solid is more effectively invading the undercooled liquid. As already pointed out, the mechanism responsible for the decrease in λ_1 was identified as the 'dendrite division mechanism'. However, the division of columnar grains cannot reduce λ_1 indefinitely due to stability reasons. Indeed, one expects that due to strong solutal interactions between adjacent dendrite tips, there is a critical λ_{cr} below which the division of the columnar tips cannot take place. As we will see in the following, below λ_{cr} the mechanism of overgrowth becomes non-negligible and the dendrite array becomes unstable to small perturbation of the dendrite tips. Therefore, with respect to the constructal law the primary arm spacing characterizing the quasi-steady columnar tips will be close to the minimum stable spacing, λ_{cr}.

In the following we will quantify analytically the two mechanisms described above (the dendrite division and the dendrite overgrowth mechanism), to obtain a simple analytical expression for the primary arm spacing λ_1 defining the stable dendrite array configuration.

Let us consider a columnar directional solidification experiment involving a constant vertical thermal gradient G

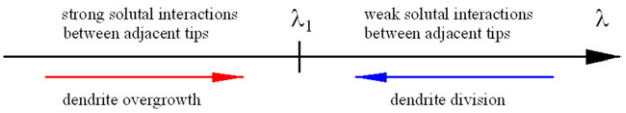

Figure 11. The two mechanisms responsible for the selection of the primary arm spacing.

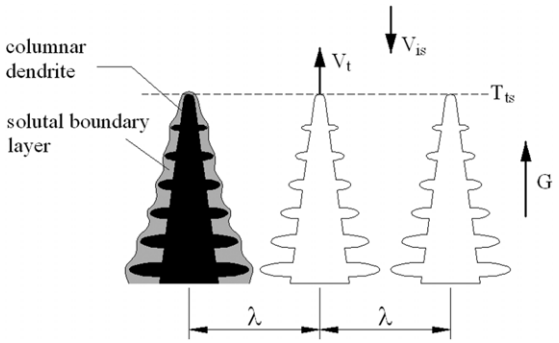

Figure 12. A quasi-steady state columnar dendrite array.

and a constant isotherm velocity V_{is} (figure 12). The columnar dendrite tips will be forced to advance within an undercooled melt of initial composition C_0 with a growth velocity equal to the isotherm velocity. After an initial transition time the columnar dendrites, growing opposite to the heat flux direction, will finally reach a quasi-steady state when their tip velocity V_t will equal V_{is}. The quasi-steady state is defined with respect to the dendrite tips only. Since the dendrites always grow opposite to the isotherm velocity (see figure 12) the tip temperature (and consequently the local tip undercooling) will remain constant in time when the condition $V_t = V_{is}$ is verified. Hence, if no perturbation of the tip is considered, the dendrite tip velocity will remain constant in time as well, defining thus the quasi-steady state at the tip. Note that we are interested in the primary arm spacing defining a quasi-steady state and not a transition stage in the evolution of dendrite tips. Therefore we will focus in the following on the stability of the dendrite array, given the hypothesis of a quasi-steady state at the columnar tips.

Let us consider a directional solidification experiment (fixed G and V_{is}) in which the columnar dendrite array is advancing with the velocity $V_t = V_{is}$, that is in a quasi-steady state. Let us denote with λ the average spacing between two adjacent dendrites of the dendrite array (figure 12). Let us denote as well with T_{ts} the columnar tip temperature corresponding to this quasi-stationary state. This temperature can be easily computed since the columnar tip velocity V_t ($= V_{is}$) can be directly linked to the local tip undercooling $\Omega_s = \frac{C_l^* - C_0}{C_l^*(1-k)}$ by means of a tip kinetics law. Indeed, by assuming a parabolic tip shape one can write

$$V_t = \frac{D_l m\,(k-1)\,C_l^*}{\pi^2 \Gamma}\left[Iv^{-1}\left(\Omega_s\right)\right]^2, \tag{43}$$

where $C_l^* = (T_{ts} - T_f)/m$ is the equilibrium concentration corresponding to the tip temperature T_{ts} and Iv^{-1} represents the inverse Ivantsov function. Since this function has no simple analytical solution, we will use in the following the fit computed by Wang and Beckermann [23]:

$$Iv^{-1}\left(\Omega\right) = a\left[\Omega/\left(1-\Omega\right)\right]^b, \tag{44}$$

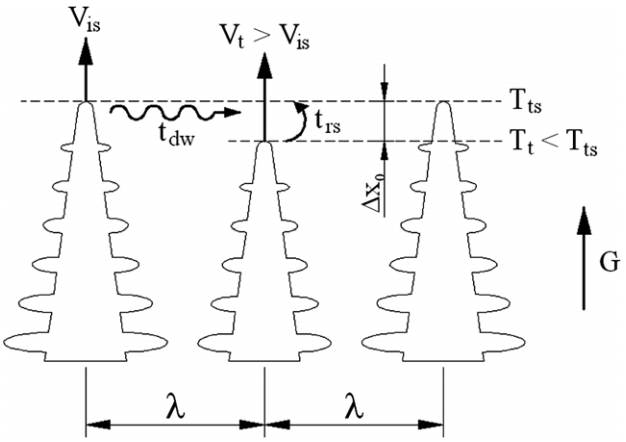

Figure 13. The perturbed columnar dendrite array.

where $a = 0.4567$ and $b = 1.195$. One can see now that T_{ts} can be computed from (43).

To analyse whether or not the configuration in figure 12 is stable one should first consider the existence of a small perturbation at the dendrite tips. Let us consider that one dendrite is slightly perturbed from its initial quasi-steady position defined by the isotherm T_{ts}. In figure 13 it was considered that the dendrite tip is perturbed such that the tip found itself behind the quasi-steady position. As we will see in the following, considering the reverse would not change anything in the conclusions that we draw. It is now important to notice that the natural tendency of the perturbed tip would be to reach back its quasi-steady position. Indeed, since the new dendrite tip temperature T_t is lower than T_{ts}, the local undercooling Ω will be higher than Ω_s. Hence one expects the perturbed tip to have a higher velocity than V_{is}. Since $V_t > V_{is}$ one expects that in time the perturbed tip will get closer to the quasi-steady position defined by the isotherm T_{ts}. The same can be stated for the case where the perturbed tip found itself ahead of the isotherm T_{ts}. In this case the tip temperature will be greater than T_{ts} and the tip velocity will be lower than the isotherm velocity. Consequently the tip temperature will decrease in time, the perturbed tip getting closer and closer to the quasi-steady state position. In this context one important aspect of the dendrite tip behaviour is revealed: subject to perturbations from their steady state position the dendrite tips will tend to reach back their initial quasi-steady position. However this process will not be instantaneous but will follow a certain dynamics. We propose in the following to determine the characteristic time within which the perturbed dendrite tips reach back the quasi-steady position. Let us denote this time with t_{rs} (see figure 13). Let us consider too that the perturbed dendrite tip is deviated at a distance Δx_0 from its initial quasi-steady position (figure 13). To determine t_{rs} one should therefore resolve the kinetic equation of the dendrite tip

$$\frac{\mathrm{d}x}{\mathrm{d}t} = V_t, \tag{45}$$

where x is the position of the dendrite tip. One question remains, however: what is the relevant tip velocity V_t? We can assume that the tip velocity can be linked at any moment to the local tip undercooling using a standard tip kinetic theory,

equation (43). The latter hypothesis is not straightforward since equation (43) is valid for a steady state dendrite tip. It is worthwhile to note that experimental evidence exists to support the steady state approximation to the tip velocity V_t. Indeed, Liu [16] showed that the measured instantaneous tip velocity of a decelerating columnar dendrite array (linear decrease of the isotherm velocity) could be almost exactly correlated with the steady state velocity computed with the help of local undercooling conditions at the tip.

In fact, the use of a stationary solution for the tip velocity V_t in a case where the local tip undercooling is unstationary were to be valid only if the velocity response time of the tip to changes in local conditions at the tip were to be much smaller than the time scale characterizing the same changes in the local conditions. For rapid solidification cases involving fast advancing columnar dendrites, the dendrite tip R_t is very small ($\cong 10^{-6}$ m). Since the solutal boundary layer at the tip is of the order of R_t the time scale characterizing the solute transport at the tip would be of the order of $\tau_t \cong {R_t}^2/4D_l$, thus small too ($D_l \cong 10^{-9} \mathrm{m}^2\,\mathrm{s}^{-1}$). Because the tip velocity is intrinsically linked to the solute transport at the tip the velocity response time of the tip to changes in local undercooling conditions will be of the order of τ_t as well. Now, the time scale characterizing the variations in local undercooling conditions will be no more than t_{rs}, which is the tip return time to the quasi-steady position. Hence, the tip velocity V_t can be approximated with the steady state solution only if $\tau_t \ll t_{rs}$. For the moment we consider this as a valid hypothesis. The inequality $\tau_t \ll t_{rs}$ will be verified *a posteriori* once the time scale t_{rs} is determined.

As pointed out, to compute the return time t_{rs} one should resolve equation (45) where V_t is expressed with the help of (43). However, the use of (43) for the tip velocity would render very difficult, if not impossible, the analytical solving of the differential equation (45). In this respect one should look for a simple approximation of the kinetic law. Remember that we need to analyse the dynamics of the tip subject to small perturbation from the steady state. Hence equation (45) must be solved for very small deviations Δx_0 from the steady position. In this context a reasonable approximation for the V_t variation about the quasi-steady position would be its linear approximation (the first order Taylor expansion):

$$V_t \cong V_{is} + \left(\frac{\partial V_t}{\partial x}\right)_{x=x_{st}} (x - x_{st}), \tag{46}$$

where x_{st} is the position of the isotherm T_{ts} corresponding to the quasi-steady state of the tip. Notice that x_{st} is not a static coordinate since the isotherm T_{ts} is moving with the imposed isotherm velocity V_{is}. Indeed the temperature field in the vertical ingot is

$$T(x) = T_0 + Gx - GV_{is}t, \tag{47}$$

where T_0 is the temperature at the bottom of the ingot at $t = 0$. Since considering an initial overheating at the bottom of the ingot would not change anything in the problem we will hereafter consider that T_0 is the liquidus temperature corresponding to the initial concentration C_0, that is $T_0 = T_f + mC_0$. In this respect one can identify the quasi-steady state position of the tip, x_{st}, knowing the corresponding temperature at the tip T_{ts}. Indeed, from (47) one obtains

$$x_{st} = \frac{T_{ts} - T_0}{G} + V_{is}t. \tag{48}$$

The differential equation to be solved becomes

$$\frac{\mathrm{d}x}{\mathrm{d}t} = V_{is} + \left(\frac{\partial V_t}{\partial x}\right)_{x=x_{st}} \left[x - \frac{T_{ts} - T_0}{G} - V_{is}t\right], \tag{49}$$

where for $t = 0$, $x(0) = x_{st} - \Delta x_0$. The ordinary differential equation can be solved, and one obtains

$$x - x_{st} = -\Delta x_0 \exp\left[\left(\frac{\partial V_t}{\partial x}\right)_{x=x_{st}} t\right]. \tag{50}$$

Notice that $(\partial V_t/\partial x)_{x=x_{st}} < 0$. Hence, it is easy to observe that the initial tip deviation (Δx_0) from its quasi-steady position is constantly reducing in time. Looking at the particular exponential variation in (50) one can identify a characteristic time scale, $-(\partial V_t/\partial x)^{-1}_{x_{st}}$, within which the perturbed tip almost reaches back the quasi-steady position x_{st}. It is important to note that this time scale is independent of the initial perturbation Δx_0. This is a very important remark because the determined time scale will characterize in a unique way the dynamics of the perturbed tip. In fact $-(\partial V_t/\partial x)^{-1}_{x_{st}}$ is only dependent on parameters external to the tip perturbation such as the thermal gradient, isotherm velocity, initial alloy composition and tip kinetics law. Since the initial deviation is almost entirely reduced during a time equal to the double of $-(\partial V_t/\partial x)^{-1}_{x_{st}}$ one can state that the return time to the quasi-stationary state, t_{rs}, is of the order of

$$t_{rs} \cong -2\left(\frac{\partial V_t}{\partial x}\right)^{-1}_{x_{st}}. \tag{51}$$

Hence a unique time scale characterizing the dynamics of the dendrite array has been determined. It is somewhat evident that this time would be a key parameter in determining the stable regime of the dendrite array. In addition to quantifying the return time to the stationary state of a perturbed tip, t_{rs} will also quantify the time during which a dendrite tip issued from a dendrite division mechanism (like the tertiary arm evolving into a primary arm) will reach back the isotherm T_{ts} corresponding to the quasi-stationary state. Hence, t_{rs} will also be a measure of the dendrite division mechanism. In order to determine whether or not the division mechanism can take place one should try to quantify as well the mechanism opposing the natural tendency of dendrite tips to reach back the steady state position. This mechanism can be found in the existing solutal interactions between two adjacent tips. A dendrite tip that falls behind the quasi-steady position will be solutally influenced by the adjacent tips. A question remains to be answered however: how can one quantify these solutal interactions? To answer this question one should take into account the existence of the solutal boundary layers around the tips. An advancing dendrite tip will always leave behind it a solutal diffusion wave which spreads laterally at the speed $w_{dw}(x) \sim 2D^{1/2}(t^*)^{-1/2}$, where $t^* = t - t_p$ is the time computed from the time t_p at which the dendrite tip reached a certain coordinate x. Looking in the frame of reference linked to the isotherm T_{ts} one can see the perturbed tip trying to reach back the steady state position but always positioned behind the two adjacent tips (figure 13). Since the two adjacent tips are located ahead of the perturbed one they can solutally influence it by means of lateral diffusion waves. The travel

time of a diffusion wave from one tip to another can be easily estimated [4] as

$$t_{dw} \cong \frac{\lambda^2}{4D_l}. \tag{52}$$

In conclusion, with the help of t_{dw} we have managed to quantify the strength of the solutal interaction between adjacent tips. In this context it would be interesting to compare the two mechanisms: the dendrite division mechanism (t_{rs}) and the solutal interactions between adjacent tips (t_{dw}). If $t_{rs} \gg t_{dw}$, then the solutal diffusion wave has the time to capture the perturbed tip before the latter reaches back the quasi-steady position. Therefore it is likely that the adjacent tips solutally overgrow the perturbed one. Hence, the dendrite array is not stable to small perturbation of the dendrite tips. On the contrary if $t_{rs} \ll t_{dw}$ then the perturbed tip has the time to reach back the quasi-steady position before any lateral solutal wave captures it. Hence, the dendrite array is stable to small perturbations of the dendrite tips. However, one expects for this configuration the dendrite division mechanism to be active. Indeed, perturbed tertiary arms can easily transform into a primary arm since they have the ability (the time) to reach back the isotherm T_{ts} (the steady state position) before any lateral diffusion wave stops them. This configuration will not be stable with respect to the dendrite division mechanism.

In the lower range of the dendrite array spacing ($\lambda \ll (4D_l t_{rs})^{1/2}$) the dendrite array is unstable to small perturbations of the dendrite tips whereas in the upper dendrite spacing range ($\lambda \gg (4D_l t_{rs})^{1/2}$) the dendrite array is stable to small perturbation of the dendrite tips but unstable with respect to the dendrite division mechanism (figure 11). One should look therefore for the stable dendrite spacing somewhere at the intersection of these two domains, that is somewhere around the critical spacing defined by $t_{rs} = t_{dw}$:

$$\lambda_{cr} = (4D_l t_{rs})^{1/2}. \tag{53}$$

However, since λ_{cr} represents the upper limit of the unstable regime to small perturbation of the dendrite tips one expects the real primary arm spacing to be somewhat larger than λ_{cr}. Similarly to the Lu [8] hypothesis, we suppose that the dendrite division mechanism becomes active for a local spacing greater than two times the critical spacing λ_{cr}. In this respect one expects the real primary spacing to be somewhat between λ_{cr} and $2\lambda_{cr}$. Hence, we will consider that the primary arm spacing will be of the order of

$$\lambda_1 \cong 1.5\lambda_{cr} \cong \sqrt{18D_l\left[-\left(\frac{\partial V_t}{\partial x}\right)^{-1}_{x_{st}}\right]}. \tag{54}$$

We have thus obtained a simple analytical expression for the primary arm spacing. At this moment it would be interesting to validate the hypothesis we made regarding the tip response time to changes in local conditions, $\tau_t \ll t_{rs}$. Since it was proven that $\tau_t \cong (R_t)^2/4/D_l$ and $t_{rs} \cong (\lambda_1/1.5)^2/4/D_l$ it is now easy to see that the $\tau_{tip} \ll t_{rs}$ inequality would be equivalent to

$$R_t \ll \lambda_1/1.5. \tag{55}$$

The above equality is obviously true since it was proven [7] that $R_t \ll \lambda_1$.

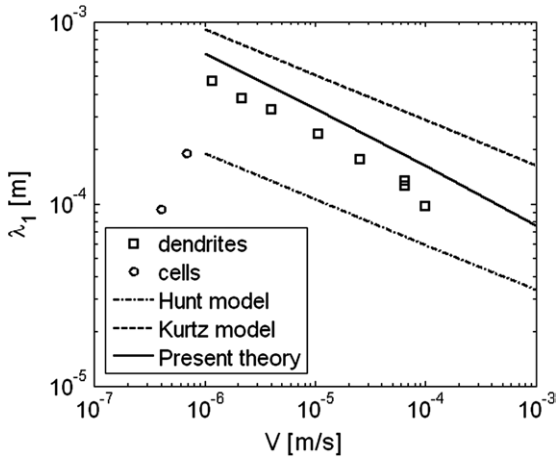

Figure 14. Comparison of the present theory and the Hunt [6] and Kurtz [7] models with the experimental results in [2]: succinonitrile–5.5 mol% acetone system, $G = 67\,\mathrm{K\,cm^{-1}}$.

At this moment it is interesting to note that the analysis of the dendrite array from the perspective of constructal theory helped us to conclude that the primary arm spacing characterizing a columnar dendrite array should be close to the critical spacing, λ_{cr}. And we have indeed identified the real primary arm spacing as being of the order of $1.5\lambda_{cr}$, equation (54). Basically the dendrite array is always searching for an optimum configuration given some external constraints (G, V_{is}). The constructal theory helps us to define these optimal conditions (in our case a minimum dendrite spacing) and to identify the mechanism pointing to the optimal configuration (in our case the dendrite division and the dendrite overgrown mechanisms).

At this moment it would be interesting to compare the main result in equation (54) with different experimental data. First the present model is compared with the experimental data provided by Somboonsuk *et al* [2]. The directional experiments in [2] have been carried out on a succinonitrile–5.5 mol% acetone system at a constant thermal gradient of $G = 67\,\mathrm{K\,cm^{-1}}$. The properties used in the present calculation are summarized in table 1. In figure 14 the comparison of the experimental data with the present model as well as with the well-known Hunt [6] and Kurtz [7] models is presented. As one can see, despite the relative simplicity of the model, the agreement of the present model with the experimental data is very good. Equation (54) does much better than the Hunt [6] and Kurtz [7] models. Moreover, it better predicts the slope of the real primary arm variation with respect to the pulling velocity.

Next a comparison with the experimental data of McCartney and Hunt [13] obtained for an Al–0.34 wt % Si–0.14 wt% Mg system is presented in figure 15. We note again a very satisfactory agreement of the present theory with the experimental data. Notice that in table 1 we have approximated the real ternary alloy with an effective binary Al–0.34 wt % Si alloy.

In figure 16 a comparison with the experimental data provided by Young and Kirkwood [14] on three different Al–Cu alloys is presented. One can observe the good agreement of the present theory with the experimental data. Notice again

Table 1. The physical properties used for the comparison of the present theory with experiments.

Alloy system	Properties and units					
	C_0 (wt %)	T_f (K)	m (K wt%$^{-1}$)	k	D_l (m^{2}s^{-1})	Γ (mK)
Scn – 0.35 wt % acetone	0.35	331.08	−2.8	0.1	1.3×10^{-9}	0.64×10^{-7}
Scn–5.5 mol% acetone	5.5 (mol %)	331.08	−2.2 (K mol%$^{-1}$)	0.1	1.27×10^{-9}	0.64×10^{-7}
Al–0.34 wt % Si–0.14 wt % Mg	0.34	933.4	−5.5	0.18	3.5×10^{-9}	2.4×10^{-7}
Al–2.4 (4.4; 10.1) wt % Cu	2.4 (4.4; 10.1)	934.2	−2.6	0.14	3×10^{-9}	1×10^{-7}
Pivalic acid–0.076 wt % ethanol	0.076	308.9	−2.94	0.16	0.6×10^{-9}	4.34×10^{-8}

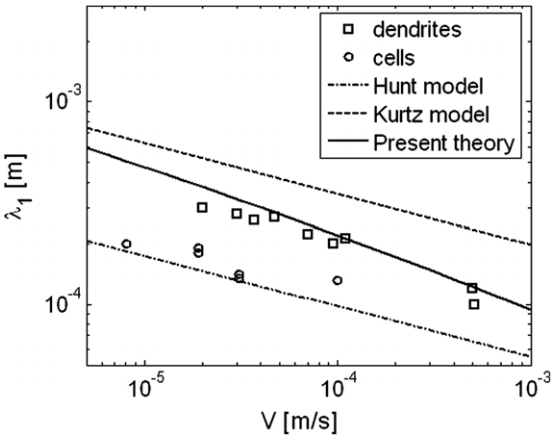

Figure 15. Comparison of the present theory and the Hunt [6] and Kurtz [7] models with the experimental results in [13]:Al–0.34 wt % Si–0.14 wt% Mg system, $G = 30\,\mathrm{K\,cm^{-1}}$.

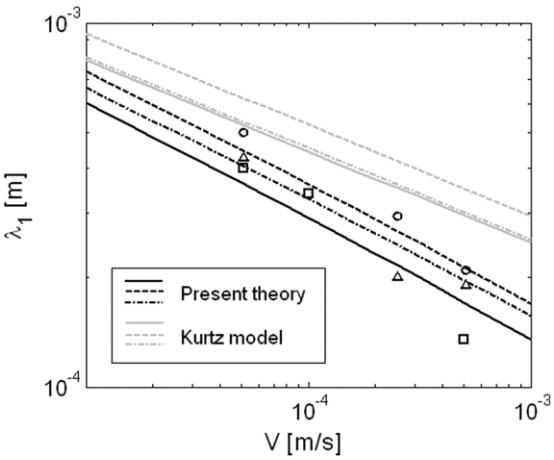

Figure 16. Comparison of the present theory and the Kurtz [7] model with the experiments in [14]: full lines, dashed lines and dashed-dot lines are theory and squares, circles and triangles are experiment for Al–2.4 ($G = 27$), Al–4.4 ($G = 26$) and Al–10.1 wt% Cu ($G = 53\,\mathrm{K\,cm^{-1}}$), respectively.

that equation (54) better predicts the trend in the real primary arm spacing variation with respect to the pulling velocity when compared with the Kurtz [7] model.

Next a comparison with the Eshelman [15] experiments made on succinonitrile–0.35 wt% acetone system at $G = 37.6\,\mathrm{K\,cm^{-1}}$ is assessed in figure 17. As one can see, the agreement with the model in the velocity range corresponding to the dendrite structures is excellent. In fact, in [15] the authors provided spacing data for the dendrite domain as well as for the cell domain. It is interesting to observe that both

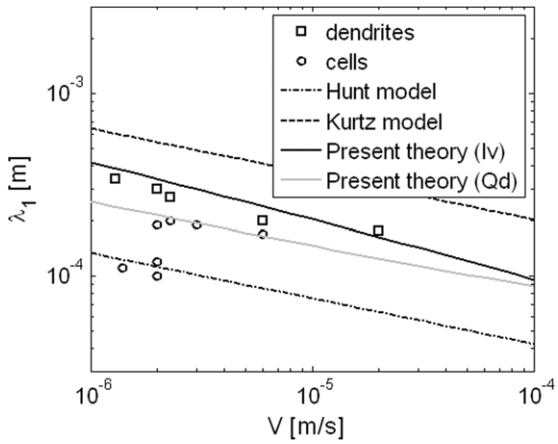

Figure 17. Comparison of the present theory and the Hunt [6] and Kurtz [7] models with the experimental results in [15]: succinonitrile–0.35 wt% acetone system, $G = 37.6\,\mathrm{K\,cm^{-1}}$.

cellular and dendritic structure coexist within a finite band of pulling velocities. In fact, when the experiment was repeated several times, the authors observed cells in some experiments and dendrite in others. In this respect it would be interesting to modify the present model in order to compare it with the cellular spacing within this finite band of velocities. Until now, in order to obtain relevant data for the full dendritic regime we have used for the computation of the tip velocity gradient, $-(\partial V/\partial x)_{x_{st}}^{-1}$, the Ivantsov solution for the dendrite tip kinetics. However, since a parabolic shape approximation to the dendrite shape can no more be used for the cellular arrays, one should look for a more appropriate approximation. Since the tip of the cells obtained within this finite velocity band is close to a spherical shape [15] an interesting approximation for the dendrite tip shape would be the spherical approximation. In this respect, the tip Peclet number, Pe, becomes equal to the dimensionless tip undercooling, Ω. Hence, the tip velocity would become

$$V_t = \frac{D_l m(k-1)\,C_l^*}{\pi^2 \Gamma}\Omega^2. \tag{56}$$

By using the above law for the computation of the velocity gradient, $-(\partial V/\partial x)_{x_{st}}^{-1}$ and time scale t_{rs} one can approach now the cellular spacing. The comparison between the quadratic approach to λ_1 and the experimental data is presented in figure 17. One can notice the excellent agreement with the real cellular spacing. The agreement of the present model with both the dendrite and cellular spacing emphasizes once more the fact that the primary arm spacing λ_1 is mainly controlled by the tip kinetics, hence by what happens at the dendrite tips and not at a certain distance behind the tips.

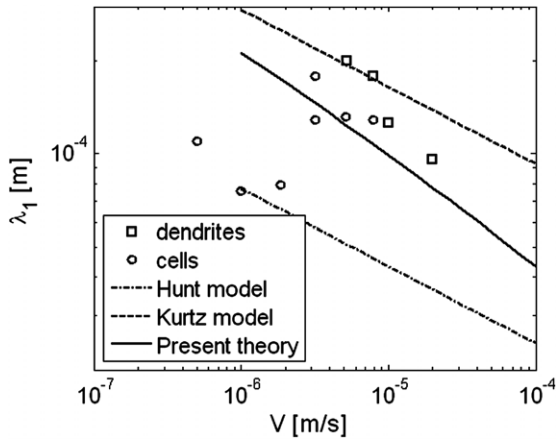

Figure 18. Comparison of the present theory and the Hunt [6] and Kurtz [7] models with the experimental results in [15]: pivalic acid–0.076 wt% ethanol system, $G = 29.8\,\mathrm{K\,cm^{-1}}$.

Finally a comparison with the experiments in [15] on pivalic acid–0.076 wt% ethanol is presented in figure 18. Here again the agreement is very satisfactory.

We finally conclude that, in spite of its relative simplicity, the present theory correctly predicts the primary arm spacing. Even more, by means of the two time scales t_{rs} and t_{dw}, we have managed to quantify in a simple way the two mechanisms responsible for the selection of the primary arm spacing: the dendrite division mechanism and the solutal interactions between two adjacent tips, the latter also being responsible for the dendrite overgrown phenomena.

5. Conclusions

In this paper we have focused on the application of the constructal theory to predicting the dendritic solid structure. First we have analysed the marginal stability criterion from the perspective of the constructal principle. Having as guiding principle the constructal law we have concluded that the dendrite shape will adapt in such a way as to grow with a maximum velocity. In this context we have shown that among the whole range of possible dendrite tip radii predicted by the stability analysis the dendrite tip will choose the smallest one, that is a radius equal to the smallest perturbation wavelength leading to instabilities. This is somewhat similar to the phenomenon of laminar–turbulent transition where the choice between the viscous diffusion and the 'needles' of eddy flow is also made at the smallest (neutral) wavelength of instability. In this context it appears that the turbulent structure and dendrites in solidification are analogous manifestations of the constructal phenomenon of generation of flow configuration.

We have also shown that the initial diffusion controlled growth regime of the solid grain is characterized by a continuously decreasing growth rate. By applying again the constructal principle we obtain that solid is forced to select a different more effective geometry: the dendrite tip. In this respect we identify the existence of a competition between the diffusion controlled growth and the dendritic growth. By analysing this competition we were able to determine the critical moment and the critical radius of the solid grain at which the destabilization of the solid–liquid interface takes place. Moreover, these two critical time and length scales are computed by means of a more rigorous stability analysis. We conclude thus that the results obtained by applying the constructal principle are of the same order of magnitude as the ones obtained by means of the more complex stability analysis. Hence, the idea of a competition between the diffusion controlled growth and the dendritic growth and consequently between two solid geometries (the sphere and the dendrite tip) has a secure physical basis. The constructal principles do not appear as *ad hoc* established statements but as a physical reality having a rigorous explanation.

Second, we developed a model for the secondary arm spacing having as the basis the same concept of the constructal theory. We analysed first the growth of a single dendrite tip and concluded that the lateral growth of a needle is close to a diffusion controlled growth, therefore being characterized by a continuously decreasing growth rate. In this respect the constructal theory calls for an optimization of the lateral growth. This can be achieved if secondary dendrite arms start to grow laterally. In fact, we identify once more a competition between the lateral diffusion controlled growth and the dendritic growth. By analysing this competition we are finally able to compute the secondary arm spacing. It appears that the secondary arm spacing is equal to the double of the primary arm dendrite tip radius. This result is in good agreement with the model of L–M [1] as well as with different experimental results [2, 16].

Finally, the primary arm spacing is analysed from the perspective of the constructal law. When applied to a columnar front forced to advance into an undercooled melt with a constant velocity (V_{is}) and within a given constant gradient G, the constructal law predicts that the only way that the columnar tips can optimize the solidification process is by minimizing the spacing between two adjacent tips, namely λ_1. By minimizing the primary arm spacing the columnar structure is also optimizing the solidification process behind the columnar tips. The mechanism responsible for the decrease in λ_1 was identified as the dendrite division mechanism. However, the division of columnar grains cannot reduce λ_1 indefinitely due to stability reasons. Due to strong solutal interactions between adjacent dendrite tips, there is a critical λ_{cr} below which the division of the columnar tips cannot take place. We have shown that below λ_{cr} the mechanism of dendrite overgrowth becomes non-negligible and the dendrite array becomes unstable to small perturbation of the dendrite tips from their quasi-steady position. Therefore, with respect to the constructal law the primary arm spacing characterizing the quasi-steady columnar tips will be close to the minimum stable spacing, λ_{cr}. By quantifying the two mechanisms, the dendrite division and the dendrite overgrowth mechanisms, we were finally able to obtain a model for the primary arm spacing. We found that λ_1 is of the same order of magnitude as λ_{cr}, and more precisely that $\lambda_1 \cong 1.5\lambda_{cr}$. This result is validated subsequently against various experimental data. We showed that this new theory is in very good agreement with the experiments.

We conclude that the constructal theory can be successfully used in predicting the dendritic solid structure. A complete review of the progress on the constructal theory of generation of configuration in nature can also be found in [24, 25].

References

[1] Langer J S and Muler-Krumbhaar H 1978 Theory of dendritic growth:I. Elements of a stability analysis *Acta Metall.* **26** 1681–7

[2] Somboonsuk K, Mason J T and Trivedi R 1984 Interdendritic Spacing: I. Experimental Studies *Metall. Trans.* A **15** 967–75

[3] Bejan A 1997 *Advanced Engineering Thermodynamics* 2nd edn (New York: Wiley) pp 794–804

[4] Bejan A 2000 *Shape and Structure, From Engineering to Nature* (Cambridge: Cambridge University Press) pp 175–8

[5] Bejan A, Fautrelle Y and da Silva A K 2002 Dendritic solidification structures deduced from constructal theory (unpublished work)

[6] Hunt J D 1979 Cellular and primary dendrite spacings *Solidification and Casting of Metals* (London: Metals Society) pp 3–9

[7] Kurtz W and Fisher D J 1981 Dendrite growth at the limit of stability: tip radius and spacing *Acta Metall.* **29** 11–20

[8] Lu S-Z and Hunt J D 1992 A numerical analysis of dendritic and cellular array growth: the spacing adjustement mechanism *J. Cryst. Growth* **123** 17–34

[9] Ma D and Sahm P R 1998 Primary spacing in directional solidification *Metall. Mater. Trans.* A **29** 1113–9

[10] Ma D 2002 Modeling of primary spacing in dendrite arrays during directional solidification *Metall. Mater. Trans.* B **33** 223–33

[11] Warren J A and Langer J S 1990 Stability of dendritic arrays *Phys. Rev.* A **42** 3518–25

[12] Warren J A and Langer J S 1993 Prediction of dendritic spacing in a directional-solidification experiment *Phys. Rev.* E **47** 2702–12

[13] McCartney D G and Hunt J D 1981 Measurements of cell and primary dendrite arm spacings in directionally solidified aluminium alloys *Acta Metall.* **29** 1851–63

[14] Young K P and Kirkwood D H 1975 The dendrite arm spacings of aluminium–copper alloys solidified under steady state conditions *Metall. Trans.* A **6** 197–205

[15] Eshelman M A, Seetharman V and Trivedi R 1988 Cellular spacing: I. steady state growth *Acta Metall.* **36** 1165–74

[16] Liu S, Lu S-Z and Hellawell A 2002 Dendritic array growth in the systems NH_4Cl–H_2O and $[CH_2CN]2$–H_2O: the detachement of dendrite side arms induced by deceleration *J. Cryst. Growth* **234** 740–50

[17] Bianchi A M, Fautrelle Y and Etay J 2004 *Transferts Thermiques* (Lausanne: Presses Polytechniques et Universitaires Romandes) pp 339–44

[18] Mullins W W and Sekerka R F 1964 Stability of a planar interface during solidification of a dilute binary alloy *J. Appl. Phys.* **35** 444–51

[19] Langer J S and Muler–Krumbhaar H 1977 Stability effects in dendritic crystal growth *J. Cryst. Growth* **42** 11–14

[20] Bejan A 1984 *Convection Heat Transfer* (New York: Wiley) pp 215–19

[21] Boettinger W J, Warren J A, Beckermann C and Karma A 2002 Phase-field simulation of solidification *Annu. Rev. Mater. Res.* **32** 163–94

[22] Ivantsov G P 1947 Temperature field around spherical, cylindrical and needle-shaped crystals which grow in supercooled melt *Dokl. Akad. Nauk SSSR* **58** 567–9

[23] Wang C Y and Beckermann C 1996 Equiaxed dendritic solidification with convection: I Multiscale/multiphase *Modelling Metall. Mater. Trans.* A **27** 2754–64

[24] Bejan A 2006 *Advanced Engineering Thermodynamics* 3rd edn (Hoboken, NJ: Wiley) chapter 13

[25] Bejan A and Lorente S 2006 Constructal theory of generation of configuration in nature and engineering *J. Appl. Phys.* **100** 041301

Référence II

Ensemble averaged multi-phase eulerian model for columnar/equiaxed solidification of a binary alloy Part I. The mathematical model

A I Ciobanas[1] and Y Fautrelle[1]

[1] EPM/CNRS Laboratory, ENSHMG, BP 95, 38402 Saint Martin d'Hères cedex, France

E-mail: aciobanas@yahoo.com

Abstract
A new multi-phase Eulerian model for the columnar and equiaxed dendritic solidification has been developed. The mean conservation equations are derived by means of a statistical phase averaging technique, and the mathematical formulation of the model can be used for both columnar and equiaxed solidification. The model uses three different phases respectively the columnar and equiaxed solid and the liquid. The new set of equations enables us to simulate the CET during the directional solidification of a binary alloy. Owing to the statistical nature of the model, we are able to treat rigorously the coexistence of equiaxed and columnar structures and consequently the CET phenomena. The averaged equations are closed by means of the cell model approximation. This technique can be successfully used to model the various interactions between the liquid and the solid. It may also incorporate the effects of the inhomogeneities of the various scalar fields, e.g., the solute and temperature gradients. An envelope model is used to parameterize the small scales, i.e., the dendrite scale. This leads us to distinguish two types of liquid, namely the extra-dendritic and inter-dendritic liquid. In part I the equations are rigorously derived in the purely diffusive case, whilst in part II we present one-dimensional simulations of Sn-Pb and Al-Cu directional solidification experiments involving CET phenomena. Quasi-steady state CET maps are as well computed.

PACS: 81.30.Fb Solidification, 82.20.Wt Computational modeling; simulation

1. Introduction

Modeling of the solidification at the scale of the process remains a challenging issue. The reason is obviously linked to the complexity of the phenomena occurring in real practical situations. The first difficulty rests in the existence of many length scales, from the dimension of the ingot (a few 10cm) to the chemical diffusion microscale (a few microns). Another major problem lies in the nature of the solidification process. The growth of the solid may be columnar or equiaxed, and a competition between the two types often occurs during the solidification process: the so-called columnar-to-equiaxed transition (CET).

Concerning the prediction of solidification, numerical models have been developed in the past twenty years [1-7], in which equations for heat transfer, fluid flow, solidification and solute transfer are solved in a coupled way. The objective of such models is to simulate how operation parameters (alloy composition, thermal and hydrodynamical conditions) can influence some characteristics of the defects (composition difference, position in the product). So far most of the models are based on continuum models [1] or space-averaged equations [2-7]. In the latter case, the local equations are integrated in an elementary representative volume (REV) whose size is greater than the dendrite scale [2]. Such an averaging procedure has proved its efficiency. However, the method itself may be questionable. Firstly, the spatial averaging procedure is based on a scale separation between the micro and macro-scales. This is not true in practice, and the existence of mesoscale phenomena; e.g., the freckles, contradicts the separation hypothesis. Secondly, the extension of the models based on spatial averaging method to situations where the flow is turbulent, especially when an electromagnetic stirring is applied, is generally rigorously impossible. The statistical approach avoids those objections. Furthermore, it is consistent with the random nature of the germination process as well as the behavior of the equiaxed grains.

The aim of the present work is to transpose the statistical phase averaging procedure, used in two-phase flows [8, 9], to the modeling of the solidification. Such an approach has been suggested first by Furmanski [10]. A first preliminary set of equations has been proposed by Fautrelle et al. [11] and Ciobanas et al. [12] using the statistical phase averaging approach. In the present paper, we extend the idea proposed by Fautrelle et al. [11] to propose a complete set of equations which describe both the columnar and the equiaxed solidification. Moreover, combined with the so-called cell model [9] the averaging procedure can take into account the effects of inhomogeneous nature of the solute and temperature fields.

2. Ensemble averaging

To approach numerically a solidification process one has to solve a set of balance equations, characterizing the balance of mass, energy, momentum and solute in the ingot. At the smallest scale one can easily write down the local form of these equations but the resolution of the system at the smallest length scale present in the ingot will be a virtual impossible task for real solidification problems usually involving ingots larger than 10^{-1} m. On the other hand one is not always interested on variations of parameters at the smallest scale but instead on average parameters like velocity, solute concentration characterizing large vortices or mesosegregation. Moreover the latter phenomena are also more easily captured experimentally. In this respect we are interested in a set of average equations which could reproduce the evolutions in time of different averaged parameters, like velocity, temperature, solute concentration, etc. These average equations can be obtained by applying an average operator to each of the local balance equation (Kataoka [13]).

2.1. Ensemble operator

To be able to apply a statistical averaging operator to a physical process, the latter must be a repeatable one. To be more precise the process must not be very sensitive to small changes of initial and boundary conditions. If it is not, from one experiment to another, one will obtain incompatible results which cannot be validated by different experimentalists. The first hypotheses of our analytical study will refer thus to property of repeatability of the process.

Under this condition we can define the ensemble average [9] as the average which allows the interpretation of physical phenomena in terms of the repeatability of the multiphase phenomenon. However, it is worthwhile to notice that since the initial and boundary conditions will be slightly different from one experience to another, each new experiment (realization) of a multiphase process will be unique. Following Drew [9] by assuming the flow as deterministic, the randomness of the multiphase flow arises from the uncertainty in the initial conditions. Thus, each experiment will give birth to a new element of the ensemble that contains all the possible realizations of the experiment. In the case of multiphase flows this ensemble contains a virtual infinite number of realizations. This ensemble is of great importance since the averaging operator will act on it. Note that, the physical parameter to be averaged is completely at the choice of the researcher: it can be the pressure, velocity, temperature or solute concentration field or the positions of the interface between the solid and the liquid.

Thus, if we denote with μ the realization and with $\psi(t,\mathbf{x})$ the physical field we are interested in, then $\psi(t,\mathbf{x};\mu)$ will denote the dependence of the field ψ with respect to the realization ensemble μ. Let now θ be the ensemble made of all possible realizations of the multiphase system. Note that each subset of θ is an ensemble too Drew [9]. However this ensemble has to posseses a particular feature in order to be useful in the statistical description of the system. One should be able to assign probabilities for any subset of θ, or in mathematical language, that θ be a Borel set. Given this proprety, one could define a measure (the probability) on the set of all possible realizations θ. In this context the ensemble average of ψ can be defined as follows [9]:

$$\overline{\psi}(t,\mathbf{x}) = \int_{\theta} \psi(t,\mathbf{x};\mu)\, dm(\mu) \tag{1}$$

with $dm(\mu)$ the probability density on the Borel set θ.

2.2. Ensemble averaged equations

The first step in obtaining of the macroscopic equations is the writing of the local conservation equations of a generic field $\psi(\mathbf{x},t)$ [9, 13]:

$$\frac{\partial(\rho\psi)}{\partial t} + div(\rho\mathbf{v}\psi) = div\left(\mathbf{j}^{\psi}\right) + \rho b^{\psi}, \tag{2}$$

along with the jump conditions (the conservation of ψ) at the solid-liquid interface:

$$\left[\rho\psi(\mathbf{v}-\mathbf{v}_i) + \mathbf{j}^{\psi}\right]\cdot\mathbf{n} = m^{\psi}, \tag{3}$$

where ρ represents the density, $\mathbf{v}$ the velocity, $\mathbf{v}_i$ the solid-liquid interface velocity, $\mathbf{j}^{\psi}$ the molecular diffusion flux of ψ, b^{ψ} the body source of ψ, $\mathbf{n}$ the unit normal at the solid-liquid interface and m^{ψ} is the interfacial source of ψ. In (2) ψ is a generic physical field and can be replaced with 1, the velocity, the specific enthalpy or the solute concentration, obtaining respectively the local mass, momentum, energy and solute conservation equations. These local balance equations (2) and (3) are valid in each point of the two-phase system, but, as already pointed out, their numerical resolution at the smallest length scale would be a virtual impossible task. Moreover, these equations states for the conservation of ψ inside the whole multiphase system. As one would desire to track the average evolution for each phase separately, the effect of each phase on the total balance of ψ has to be identified first. This is done by multiplying the local conservation equations with the characteristic phase function:

$$X_k(t,\mathbf{x}) = \begin{cases} 1 & if \quad (t,\mathbf{x}) \text{ is within the } k \text{ phase} \\ 0 & if \quad (t,\mathbf{x}) \text{ is not within the } k \text{ phase} \end{cases} \tag{4}$$

Then, in order to have an insight on average quantities, one has to further apply the ensemble average operator defined in (1). Using then the topological relations characterizing X_k [9], one can easily obtain the average conservation equations for ψ in each phase k as well as the corresponding jump equations:

$$\frac{\partial\left(\overline{X_k\rho\psi}\right)}{\partial t} + div\left(\overline{X_k\rho\mathbf{v}\psi}\right) = div\left(\overline{X_k\mathbf{j}^{\psi}}\right) + \overline{X_k\rho b^{\psi}} + \overline{\rho\psi(\mathbf{v}-\mathbf{v}_i)\cdot\nabla X_k} - \overline{\mathbf{j}^{\psi}\cdot\nabla X_k} \tag{5}$$

$$\sum_k\left[\overline{\rho\psi(\mathbf{v}-\mathbf{v}_i)\cdot\nabla X_k} - \overline{\mathbf{j}^{\psi}\cdot\nabla X_k}\right] = \overline{m} \tag{6}$$

Equation (5) states for the average balance of ψ inside each phase k in the multiphase system and equation (6) for the conservation of ψ across the phase interfaces. The term ∇X_k has to be understood in the sense of distributions (see Drew [8]) and therefore the two terms in (5) and (6) containing ∇X_k are intrinsically linked to the interface and have a meaning only on the solid-liquid interface. Indeed, ∇X_k can be also written as [9]:

$$\nabla X_k = -\mathbf{n}_k\delta\left(\mathbf{x}-\mathbf{x}_i(t)\right) \tag{7}$$

where $\mathbf{n}_k$ is the unit normal to the interface of phase k, pointing out of the phase interface and $\delta\left(\mathbf{x}-\mathbf{x}_i(t)\right)$ represents the Dirac delta function at the interface.

To be useful in a numerical model, the formulation of (5) and (6) has to be structured by defining adequate average variables. These average variables can be of different types following the choice of the weighted function: average variables weighted with the characteristic function X_k, mass weighted averages (Favré weighted) with $X_k\rho$ and finally, interfacial averages weighted with ∇X_k, having a meaning at the interface only. Definition of all these variables is synthesized in Table 1.

Table 1: Average variable definition

Definition	Variable description
$\varepsilon_k = \overline{X_k}$	The "volume" fraction of phase *k*
$S_k = -\overline{\mathbf{n}_k \cdot \nabla X_k}$	The interfacial area density of phase *k*
$\overline{\rho}_k = \dfrac{\overline{X_k \rho}}{\varepsilon_k}$	The average density within phase *k*
$\overline{\psi}_k = \dfrac{\overline{X_k \rho \psi}}{\varepsilon_k \overline{\rho}_k}$	The mass-weighted average of ψ within phase *k*
$\overline{\mathbf{j}^{\psi}}_k = \dfrac{\overline{X_k \mathbf{j}^{\psi}}}{\varepsilon_k}$	The average molecular flux of ψ within phase *k*
$\overline{\mathbf{j}^{'\psi}}_k = -\dfrac{\overline{X_k \mathbf{v}_k^{'} \psi_k^{'}}}{\varepsilon_k}$	The fluctuation (Reynolds) flux within phase *k*
$\overline{b^{\psi}}_k = \dfrac{\overline{X_k \rho b^{\psi}}}{\varepsilon_k \overline{\rho}_k}$	The mass-weighted average body souces of ψ within phase *k*
$\overline{\Phi^{\psi}}_k = -\overline{\mathbf{j}^{\psi} \cdot \nabla X_k}$	The average molecular flux of ψ at the interface of phase *k*
$\overline{\Gamma^{\psi}}_k = \overline{\rho\psi\left(\mathbf{v}-\mathbf{v}_i\right)\cdot\nabla X_k}$	The average source of ψ at the interface of phase *k*, due to the exchange between phases

With the help of definitions in Table 1 one is able now to write down the ensemble averaged conservation equation for the general physical field ψ and the corresponding jump conditions:

$$\frac{\partial\left(\varepsilon_k \overline{\rho}_k \overline{\psi}_k\right)}{\partial t} + div\left(\varepsilon_k \overline{\rho}_k \overline{\mathbf{v}}_k \overline{\psi}_k\right) = div\left[\varepsilon_k\left(\overline{\mathbf{j}^{\psi}}_k + \overline{\mathbf{j}^{'\psi}}_k\right)\right] + \varepsilon_k \overline{\rho}_k \overline{b^{\psi}}_k + \overline{\Phi^{\psi}}_k + \overline{\Gamma^{\psi}}_k \quad ; \quad k = \{s,l\} \tag{8}$$

$$\sum_k \left(\overline{\Phi^{\psi}}_k + \overline{\Gamma^{\psi}}_k\right) = \overline{m} \quad ; \quad k = \{s,l\} \tag{9}$$

The final system of averaged equations describing the solidification process will consist of mass, momentum, energy and solute balance written for each phase in the multiphase system. This is done by particularizing the general field ψ, the corresponding molecular flux $\mathbf{j}^{\psi}$ and the volumetric source b^{ψ} with the appropriated expressions for each balance equation. Table 2 synthesizes all of this parameters. Note that the molecular fluxes for the to momentum, energy and solute balance correspond respectively to the classical stress tensor of a newtonian fluid, the

Fourier heat flux, and the Fick solute flux as follows:

$$\begin{aligned} \mathbf{T} &= -p\mathbf{I} + \mu\left[\nabla\mathbf{v} + (\nabla\mathbf{v})^T\right] + \lambda_v \nabla\cdot\mathbf{v}\mathbf{I} \\ \mathbf{q} &= -\lambda\nabla T \\ \mathbf{j}_c &= -\rho D\nabla C \end{aligned} \tag{10}$$

where p is the local pressure, μ is the dynamical fluid viscosity, λ_v is the bulk viscosity, λ represents the thermal conductivity and D is the solute diffusivity.

Table 2: Particularization of the general averaged equations

Balance equations:	ψ	Molecular flux $\mathbf{j}^{\psi}$	Body sources b^{ψ}
Mass	1	0	0
Momentum	velocity $\mathbf{v}\left[m.s^{-1}\right]$	stress tensor $\mathbf{T}\left[kg.m^{-1}.s^{-2}\right]$	gravity or magnetic force $\mathbf{g}$ or $\mathbf{F}_m/\rho\ \left[m.s^{-2}\right]$
Energy	enthalpie $h\left[J.kg^{-1}\right]$	molecular heat flux: $-\mathbf{q}\left[J.s^{-1}.m^{-2}\right]$	body heat source $Q\left[J.s^{-1}.m^{-3}\right]$
Solute	solute conc. $C\left[wt\%\right]$	molecular mass flux: $-\mathbf{j}_c\left[kg.s^{-1}.m^{-2}\right]$	(no chemical reactions) 0

3. The pure columnar or equiaxed solidification

The concept of ensemble averaging as defined in equation (1) is rather abstract. Consequently the unknown terms arising from the averaging procedure will be difficult to model. In order to better understand the nature of this average technique one should approach the ensemble average through the distributions functions attached to the macroscopic process to be studied.

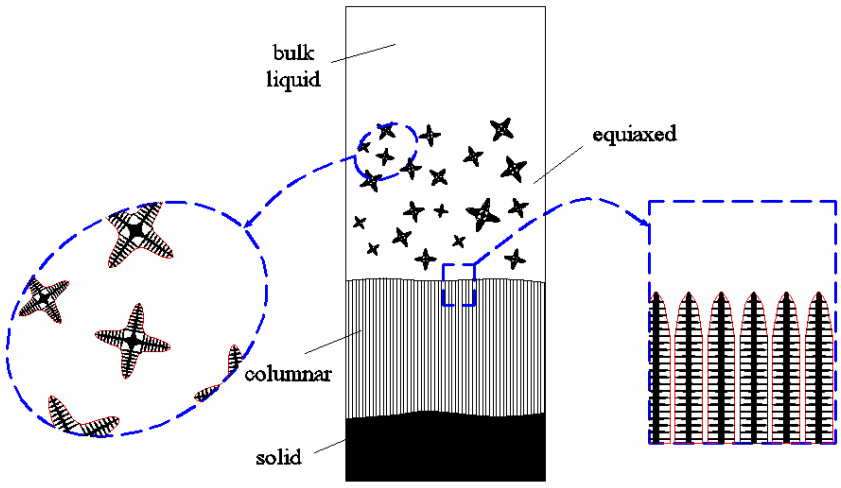

Figure 1: A typical directional solidification distinguishing the full solid, the columnar, the equiaxed and the bulk liquid zone.

Let us consider a solidification process taking place in an ingot filled initially with a liquid metallic alloy. During the solidification process solid phase is forming and, since we are placing ourselves in the case of quite rapid solidification, the solid growth will give birth to columnar or/and equiaxed structures. We are dealing thus with a two-phase system having an extremely complex liquid-solid interface and more, its evolution in time may imply sudden changes of the solid structure (e.g. columnar-to-equiaxe transition). During the solidification one can identify in

the ingot a very large number of columnar and equiaxe grains. Let us denote by N this number. Note however that this number N is extremely variable in time due to various phenomena like nucleation of equiaxed grains within an undercooled liquid, fusion of equiaxed grains convected into overheated liquid and changes in column number due to changes in local cooling conditions (cooling rate and thermal gradient). Moreover the grains in the ingot may have very different dimensions since each columnar or equiaxed grain has a unique growth history.

In fact after nucleation, the solid nuclei will grow with respect to local undercooling conditions. For a quite rapid solidification case the liquid-solid interface will destabilize soon after nucleation giving birth to highly dendritic grains (Figure 1). For the equiaxed grains, due to specific interfacial anisotropies, a precise number of primary arms are developing forming the 3D structure. These primary arms are advancing in the undercooled melt with a velocity depending on the local undercooling conditions at their tips. During their growth the primary arms develop laterally a network of secondary arms and in some cases even tertiary ones. Thus, soon after nucleation the solid-liquid interface becomes quickly highly complex. For the columnar grains the situation is somehow different in the sense that each columnar grain evolves around a main primary arm oriented along the heat flux direction, giving birth to the well known quasi-parallel columnar structure (Figure 1). However during its growth the primary arm develops lateral secondary or tertiary arms, similar to the equiaxed case. In this light, the main difference between the two structures lies in the fact that columnar grains evolve along a preferred direction (opposite to the heat flux lines) and have no growth constraints far from the primary arm tips. In contrast equiaxed grains have no preferred growth direction, and their growth is constrained by the presence of other equiaxe grains uniformly distributed around it. As a consequence of these constraints, in contrast with the relative isotropic equiaxed grains, the columnar grains are highly anisotropic ones due to their preffered growth direction (Figure 1). Hence one deals with a very complex two-phase system since to describe it one should have information on various parameters describing each of the columnar or equiaxed grains: their position, dimensions, volume grain density as well as their orientation. In this context a simplified appoach in describing the grains will be addopted.

First, due to their quasi-isotropic arrangement in space, the equiaxed grain distribution will be in the following approximated with a local homogenoeus distribution of spherical dendritic grains. Their local grain density will be denoted with $n\left[m^{-3}\right]$ and their radius with $a[m]$. Note as well that one can easily identify the length scale $R_1 = \left(4/3\pi n\right)^{-1/3}$ defining locally the average spacing between two neighbour particles. However, that the equiaxed grains can be highly dendritic. In this context the radius a must be seen as a measure of the extension in space of the whole grain solid matrix and not of the smallest solid scale (inter-dendritic spacing). This apprach is similar with the envelope model introduced by Rappaz and Thévoz [14] who introduced a virtual surface envelopping the solid matrix and separating thus the inter-dendritic liquid from the extra-dendritc liquid. The same apprach has been succesfully used by Wang and Beckermann [6] within their volume averaged model.

Secondly, due to their highly anisotropic shape, the columnar grains could be locally approximated with a cylindrical shape oriented along their prefered growth direction. However, besides from being more complex this approach would also mean that one would have to use two different models for the equiaxed and the columnar zone respectively. In an attempt to obtain a average model that uses the same mathematical formulation for both equiaxed and columnar grains we will try to adopt in the following a simplified approach for the columnar grains. In fact we will approximate locally the columnar grains as beeing quasi-isotropic. Given this hypothesis one can approach locally the columnar grains with a spherical model.

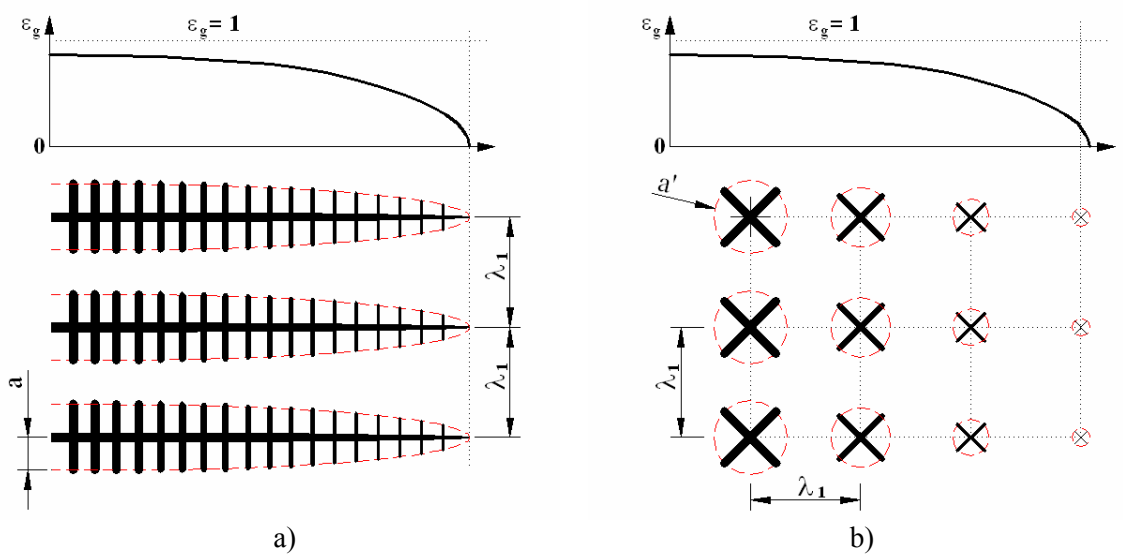

Figure 2: a) The columnar structure and the corresponding grain fraction variation along their preferred growth direction; b) The equivalent columnar structure formed by spherical grains.

Let us consider a columnar structure (Figure 2a) being characterized with a primay arm spacing, λ_1. Using the cylindrical approximation to the columnar grain enveloppe, one can easily compute the grain fraction variation along their preferred growth direction:

$$\varepsilon_g^{cyl} = \frac{a^2}{\lambda_1^2} \tag{11}$$

Approximating locally the columnar grains with an isotropic model would mean to replace the original columnar zone with an equivalent columnar structure (Figure 2b) formed by spherical grains. However, one should use for the spherical structure the same main parameters - the average spacing between grains (λ_1) and the grain volume fraction (ε_g^{cyl}) – as those defining the original columnar structure:

$$R_1 = \lambda_1 , \qquad \varepsilon_g^{sph} = \varepsilon_g^{cyl} \tag{12}$$

Hence, to a first approximation, we have approached the columnar zone with an equivalent spherical model for which the two main geometrical characteristics, the average spacing between the particles and the grain fraction were inherited from the real columnar zone, (λ_1 and ε_g^{cyl}). Thus, the columnar zone is *locally* approximated with a homogeneous spherical grain distribution, having a grain density determined from the primary arm spacing as follows:

$$n_c = \left[\frac{4}{3} \pi \left(\lambda_1 / 2 \right)^3 \right]^{-1} \tag{13}$$

This is somewhat equivalent with transforming the columnar zone into an equivalent equiaxed one. However this is a particular "equiaxed" zone since one must have in mind the fact that there is a strong statistical correlation between these spherical particles: first no mobility of the grains is allowed and secondly an axial gradient of the local grain fraction ε_g would be equivalent with a local variation of the columnar grain diameter along their preferred growth direction. It is worthwhile to notice that this approximation was already used by Martorano *et al.* [15]. This hypothesis was also supported by numerical results [15]. Indeed, the computation of the solute

diffusion process in the extra-dendritic liquid for the cylindrical and spherical approach respectively showed that a negligeble difference exists between the two approaches. Since the molecular diffusion processes (e.g. of solute or momentum) around the grains depend strongly on the length scale of the extra-dendritic liquid, $l_l = \lambda_1 - a$, it would be interesting to evaluate the error introduced by the spherical approximation of the columnar zone when computing l_l. One has:

$$\frac{l_l^{cyl}}{l_l^{sph}} = \frac{1-\varepsilon_g^{1/2}}{1-\varepsilon_g^{1/3}} \tag{14}$$

As one can easily observe, in the range $\varepsilon_g \in [0,1]$, the difference between l_l^{cyl} and l_l^{sph} does not exceed 50%, and the two length scales remain thus of the same order of magnitude. Therefore the corresponding diffusion processes in the extra-dendritic liquid would remain of the same order of magnitude as well, supporting thus the numerical findings of Martorano *et al.* [15].

In this context, in the following we shall treat both the equiaxed grains and the column in the same way, that is using a spherical approximation.

3.1. Probability distribution functions

A detailed derivation of the probability distribution for a case of a simple two-phase system can be found in Drew [9]. However the two-phase environment considered in that study was a simple one: the number of solid particles in the system was constant (*N*), the spherical particle were identical and had a known dimension (*a*). This is completely different from the two-phase system one could encounter during a solidification process (variable number of solid particles having variable dimension as well).

In this light, the new probability distribution functions must be computed taking into account the complexities of a solidification problem. The main difficulty in deriving these distributions resides in the fact that the number of particles in the ingot is varying with time. Indeed, considering the multiphase system as a repeatable one, Drew [9] supposed the existence of a master function $f^{(N)}\left(t,\mathbf{z}_1,\mathbf{v}_1,a_1,\ldots,\mathbf{z}_N,\mathbf{v}_N,a_N\right)$ able to describe the randomness of the system such as:

$$f^{(N)}\left(t,\mathbf{z}_1,\mathbf{v}_1,a_1,\ldots,\mathbf{z}_N,\mathbf{v}_N,a_N\right)d\mathbf{z}_1 d\mathbf{v}_1 da_1 \ldots d\mathbf{z}_N d\mathbf{v}_N da_N \tag{15}$$

is the probability of finding at time *t* a particle within $d\mathbf{z}_1$ of $\mathbf{z}_1$, having the velocity within $d\mathbf{v}_1$ of $\mathbf{v}_1$, the diameter within da_1 of a_1 and finding a particle within $d\mathbf{z}_2$ of $\mathbf{z}_2$, having the velocity within $d\mathbf{v}_2$ of $\mathbf{v}_2$ and the diameter within da_2 of a_2, etc.

For a case in which *N* is variable in time the existence of a single master function has no more meaning. In turn, one can define a family of master functions each corresponding to a certain grain number *N* in the ingot, that is:

$$f\left(N,t,\mathbf{z}_1,\mathbf{v}_1,a_1,\ldots,\mathbf{z}_N,\mathbf{v}_N,a_N\right), \quad N \in \mathbb{N}^+ \tag{16}$$

The distribution function above has the meaning that:

$$f\left(N,t,\mathbf{z}_1,\mathbf{v}_1,a_1,\ldots,\mathbf{z}_N,\mathbf{v}_N,a_N\right)d\mathbf{z}_1 d\mathbf{v}_1 da_1 \ldots d\mathbf{z}_N d\mathbf{v}_N da_N \tag{17}$$

is the probability that at the moment t we found N particles in the ingot (columnar or equiaxed grains), each particle i ($=\overline{1,N}$) being centered within $d\mathbf{z}_i$ of $\mathbf{z}_i$, having the velocity within $d\mathbf{v}_i$ of $\mathbf{v}_i$ and the diameter within da_i of a_i. It is interesting to note that with the help of these distributions one can easily compute the probability of finding in the ingot, at time *t*, *N* particles:

$$P_N = \iint \cdots \int f\left(N,t,\mathbf{z}_1,\mathbf{v}_1,a_1,\ldots,\mathbf{z}_N,\mathbf{v}_N,a_N\right) d\mathbf{z}_1 d\mathbf{v}_1 da_1 \ldots d\mathbf{z}_N d\mathbf{v}_N da_N \tag{18}$$

Obviously the probabilities P_N verify:

$$\sum_{i=1}^{\infty} P_i = 1 \tag{19}$$

To simplify the mathematical formulation from now on we will use the following master distribution function which integrates only the position of particles:

$$f\left(N,t,\mathbf{z}_1,\ldots,\mathbf{z}_N\right) = \iint \cdots \int f\left(N,t,\mathbf{z}_1,\mathbf{v}_1,a_1,\ldots,\mathbf{z}_N,\mathbf{v}_N,a_N\right) d\mathbf{v}_1 da_1 \ldots d\mathbf{v}_N da_N \tag{20}$$

where $f\left(N,t,\mathbf{z}_1,\ldots,\mathbf{z}_N\right) d\mathbf{z}_1 \ldots d\mathbf{z}_N$ is the probability of finding at time *t* in the ingot *N* particles, centered within $d\mathbf{z}_i$ of $\mathbf{z}_i$. It is important to notice that the use of the particle distribution *f* in (20) does not imply a loss in generality since all information related to particle velocity or dimension are included in f by means of integrations in (20).

With the help of (20) we can define an important density function which will be extensively and this is the unconditional density function for any sphere center being at $\mathbf{z}_1$:

$$f^{(1)}\left(t,\mathbf{z}_1\right) = f\left(1,t,\mathbf{z}_1\right) + \sum_{i=2}^{\infty} \left[\iint \cdots \int f\left(i,t,\mathbf{z}_1,\ldots,\mathbf{z}_i\right) d\mathbf{z}_2 \ldots d\mathbf{z}_i \right] \tag{21}$$

having the property that $f^{(1)}\left(t,\mathbf{z}_1\right) d\mathbf{z}_1$ is the unconditional probability that at time *t* in the ingot one can find a particle centered within $d\mathbf{z}_1$ of $\mathbf{z}_1$. Note that $f^{(1)}$ verifies as well:

$$\int f^{(1)}\left(t,\mathbf{z}_1\right) d\mathbf{z}_1 = 1 \tag{22}$$

This distribution is a very important one since it can be linked to the bulk particle density *n*, a key parameter defining the nucleation phenomena. Indeed, if we admit at $\tilde{\mathbf{z}}_1$ a local homogeneous grain density $n\left(t,\tilde{\mathbf{z}}_1\right)$ we have:

$$f^{(1)}\left(t,\mathbf{z}_1\right) = n\left(t,\mathbf{z}_1\right) \tag{23}$$

Note however that all distributions defined until now refer only to the position of particles at the time *t*. In turn we would like to compute the ensemble average of a certain field ψ at $\mathbf{x}$ and at time *t*. Thus, to describe statistically a physical field $\psi\left(\mathbf{x},t\right)$ one should define a distribution function which includes the position of particles with respect to a certain point $P\left(\mathbf{x},t\right)$. Following Drew [9] a simple way to do this would be to order the *N* particles in the ingot following their distance from the reference point $\mathbf{x}$. Let us consider the following rearrangement of the particles:

$$\mathbf{z}_{i_1}, \mathbf{z}_{i_2}, \ldots, \mathbf{z}_{i_N} \tag{24}$$

such as the particles $i_1, i_2, \ldots, i_N$ be ordered in order of closeness to the point $\mathbf{x}$, that is:

$$\left|\mathbf{x} - \mathbf{z}_{i_1}\right| \le \left|\mathbf{x} - \mathbf{z}_{i_2}\right| \le \ldots \le \left|\mathbf{x} - \mathbf{z}_{i_N}\right| \tag{25}$$

Since (24) is only a rearrangement of the original series of particles $\mathbf{z}_1,\ldots,\mathbf{z}_N$ it is obvious that

$$f\left(N,t,\mathbf{z}_{i_1},\mathbf{z}_{i_2},\ldots,\mathbf{z}_{i_N}\right)=f\left(N,t,\mathbf{z}_1,\ldots,\mathbf{z}_N\right) \tag{26}$$

By denoting the positions of the rearranged particles as follows:

$$\tilde{\mathbf{z}}1=\mathbf{z}_{i_1};\tilde{\mathbf{z}}2=\mathbf{z}_{i_2};\ldots;\tilde{\mathbf{z}}N=\mathbf{z}_{i_N} \tag{27}$$

one can define a new family of distribution function: the nearest-neighbor distribution functions $\widetilde{f}\left(N,t,\mathbf{x};\tilde{\mathbf{z}}_1,\tilde{\mathbf{z}}_2,\ldots,\tilde{\mathbf{z}}_N\right)$. As noted the new distribution function is no more that a transformation of (20):

$$\widetilde{f}\left(N,t,\mathbf{x};\tilde{\mathbf{z}}_1,\tilde{\mathbf{z}}_2,\ldots,\tilde{\mathbf{z}}_N\right)=f\left(N,t,\mathbf{z}_1,\ldots,\mathbf{z}_N\right) \tag{28}$$

Roughly the distribution $\widetilde{f}$ has the interpretation that:

$$\widetilde{f}\left(N,t,\mathbf{x};\tilde{\mathbf{z}}_1,\tilde{\mathbf{z}}_2,\ldots,\tilde{\mathbf{z}}_N\right)d\tilde{\mathbf{z}}_1d\tilde{\mathbf{z}}_2\ldots d\tilde{\mathbf{z}}_N \tag{29}$$

is the probability that one find in the ingot, at time *t*, *N* particles and that the closest particle to the point $\mathbf{x}$ is centered within $d\mathbf{z}_1$ of $\mathbf{z}_1$, that the next closest particle is centered within $d\mathbf{z}_2$ of $\mathbf{z}_2$, etc.

The nearest-neighbor distribution in (28) is of extreme importance since it involves a reference point $\mathbf{x}$ in space. This eneables ones to easily analyse statistically any physical field ψ at $\mathbf{x}$ and *t*.. Moreover the distribution $\widetilde{f}$ include valuable information on the position of particles in order of closeness to point $\mathbf{x}$. Indeed knowing that the closest particles influence to a greater extend the field ψ at $\mathbf{x}$ than the farthest ones do, we can think to limit our interest to the closest particles to the point $\mathbf{x}$. Doing this we could simplify extensively the closure problem inherent to any average approach. In this respect the computing of the unconditional distribution function that the closest particle to the point $\mathbf{x}$ is centered within $d\tilde{\mathbf{z}}_1$ of $\tilde{\mathbf{z}}_1$, would be of great interest:

$$\widetilde{f}^{(1)}\left(t,\mathbf{x},\tilde{\mathbf{z}}_1\right)=\widetilde{f}\left(1,t,\mathbf{x},\tilde{\mathbf{z}}_1\right)+\sum_{i=2}^{\infty}\left[\int\int\cdots\int\widetilde{f}\left(i,t,\tilde{\mathbf{z}}_1,\ldots,\tilde{\mathbf{z}}_i\right)d\tilde{\mathbf{z}}_2\ldots d\tilde{\mathbf{z}}_i\right] \tag{30}$$

The interpretation of $\widetilde{f}^{(1)}$ is that $\widetilde{f}^{(1)}\left(t,\mathbf{x},\tilde{\mathbf{z}}_1\right)d\tilde{\mathbf{z}}_1$ represents the unconditional probability that the closest particle to the point $\mathbf{x}$ is centered within $d\tilde{\mathbf{z}}_1$ of $\tilde{\mathbf{z}}_1$.

3.2. The ensemble average

The derivation of probability distribution functions enables us now to approach annalytically the abstract ensemble average formulation defined in (1). Let us denote by $\psi\left(t,\mathbf{x}\right)$ a generic physical field. The value of ψ at *t* and at $\mathbf{x}$ will vary naturally with respect to each realization of the process and consequently with the corresponding configuration of the two-phase system (number of particles in the ingot, their position, velocity, dimensions, etc.)

$$\psi\left(t,\mathbf{x}\right)\equiv\psi\left(t,\mathbf{x};N,\mathbf{z}_1,\mathbf{v}_1,a_1,\ldots,\mathbf{z}_N,\mathbf{v}_N,a_N\right) \tag{31}$$

Since the ensemble average $\overline{\psi}(t,\mathbf{x})$ is the average of $\psi(t,\mathbf{x})$ on the ensemble of all possible realizations of the two-phase process, $\overline{\psi}(t,\mathbf{x})$ can be expressed as the integration of $\psi(t,\mathbf{x})$ over all possible configuration of the multiphase system, integration weighted with the corresponding configuration probability, that is $f(i,t,\mathbf{z}_1,\mathbf{v}_1,a_1,\ldots,\mathbf{z}_N,\mathbf{v}_N,a_N)$:

$$\overline{\psi}(t,\mathbf{x})=\sum_{i=1}^{\infty}\left[\iint\cdots\int f(i,t,\mathbf{z}_1,\mathbf{v}_1,a_1,\ldots,\mathbf{z}_i,\mathbf{v}_i,a_i)\psi(t,\mathbf{x})d\mathbf{z}_1d\mathbf{v}_1da_1\ldots d\mathbf{z}_id\mathbf{v}_ida_i\right] \tag{32}$$

To simplify the mathematical formalism on one hand and to concentrate only on the position of the particles on the other hand we will introduce from now on conditional averages of ψ. Indeed it is easy to observe that (32) can be rewritten as follows:

$$\overline{\psi}(t,\mathbf{x})=\sum_{i=1}^{\infty}\left[\iint\cdots\int f(i,t,\mathbf{z}_1,\ldots,\mathbf{z}_i)\psi(t,\mathbf{x}|i,\mathbf{z}_1,\ldots,\mathbf{z}_i)d\mathbf{z}_1\ldots d\mathbf{z}_i\right] \tag{33}$$

in which:

$$\begin{aligned}\psi(t,\mathbf{x}|i,\mathbf{z}_1,\ldots,\mathbf{z}_i)=&\frac{1}{f(i,t,\mathbf{z}_1,\ldots,\mathbf{z}_i)}\iint\cdots\int f(i,t,\mathbf{z}_1,\mathbf{v}_1,a_1,\ldots,\mathbf{z}_i,\mathbf{v}_i,a_i)\\&\times\psi(t,\mathbf{x})d\mathbf{v}_1da_1\ldots d\mathbf{v}_ida_i\end{aligned} \tag{34}$$

is the conditionally averaged field ψ, averaged on the condition that in the ingot are *i* particles, each of them centered in $\mathbf{z}_i,\ldots,\mathbf{z}_i$. We have thus restricted ourselves to the position of the particles in the ingot solely, the information regarding the particle velocity and their dimension being now included in $f(i,t,\mathbf{z}_1,\ldots,\mathbf{z}_i)$ and $\psi(t,\mathbf{x}|i,\mathbf{z}_1,\ldots,\mathbf{z}_i)$ expressions respectively. However, the computation of $\overline{\psi}(\mathbf{x},t)$ with the help of equation (33) still remains a challenging issue and this, of course, to the large number of particles in the ingot. Therefore we will restrict even more our interest to a single particle, the one centered in $\mathbf{z}_1$. Using again the conditional averages we can write:

$$\overline{\psi}(t,\mathbf{x})=\int f^{(1)}(t,\mathbf{z}_1)\psi^{(1)}(t,\mathbf{x}|\mathbf{z}_1)d\mathbf{z}_1 \tag{35}$$

where:

$$\begin{aligned}\psi^{(1)}(t,\mathbf{x}|\mathbf{z}_1)=&\frac{1}{f^{(1)}(t,\mathbf{z}_1)}\\\times&\left\{f(1,t,\mathbf{z}_1)\psi(t,\mathbf{x}|1,\mathbf{z}_1)+\sum_{i=2}^{\infty}\left[\begin{array}{l}\iint\cdots\int f(i,t,\mathbf{z}_1,\ldots,\mathbf{z}_i)\\\times\psi(t,\mathbf{x}|i,\mathbf{z}_1,\ldots,\mathbf{z}_i)d\mathbf{z}_2\ldots d\mathbf{z}_i\end{array}\right]\right\}\end{aligned} \tag{36}$$

is the conditionally averaged field ψ, averaged on the condition that there is a particle centered within $d\mathbf{z}_1$ of $\mathbf{z}_1$.The distribution $f^{(1)}(t,\mathbf{z}_1)$ is no more than the unconditional density function for any sphere center being at $\mathbf{z}_1$ already defined in (21) and (23).

In a similar way, using this time the nearest-neighbor distribution functions, we can define the ensemble average of ψ as follows:

$$\overline{\psi}(\mathbf{x},t)=\int\widetilde{f}^{(1)}(t,\mathbf{x},\tilde{\mathbf{z}}_1)\widetilde{\psi}^{(1)}(t,\mathbf{x}|\tilde{\mathbf{z}}_1)d\tilde{\mathbf{z}}_1 \tag{37}$$

in which $\widetilde{f}^{(1)}\left(t,\mathbf{x},\tilde{\mathbf{z}}_1\right)$ is the unconditional probability already defined in (30) and:

$$\widetilde{\psi}^{(1)}\left(t,\mathbf{x}\middle|\tilde{\mathbf{z}}_1\right)=\frac{1}{\widetilde{f}^{(1)}\left(t,\mathbf{x},\tilde{\mathbf{z}}_1\right)} \times\left[\widetilde{f}\left(1,t,\mathbf{x},\tilde{\mathbf{z}}_1\right)\psi\left(t,\mathbf{x}\right)+\sum_{i=2}^{\infty}\left[\iint\cdots\int\widetilde{f}\left(i,t,\mathbf{x},\tilde{\mathbf{z}}_1,\ldots,\tilde{\mathbf{z}}_i\right)\psi\left(t,\mathbf{x}\right)d\tilde{\mathbf{z}}_2\ldots d\tilde{\mathbf{z}}_i\right]\right] \tag{38}$$

represents the conditionally averaged field ψ, averaged on the condition that the closest particle to the point $\mathbf{x}$ is centered within $d\tilde{\mathbf{z}}_1$ of $\tilde{\mathbf{z}}_1$. The ensemble average of ψ expressed as in equation (37) is of extreme importance because, given certain assumptions, one is able to express analytically the distribution $\widetilde{f}^{(1)}\left(t,\mathbf{x},\tilde{\mathbf{z}}_1\right)$ and the conditional average $\widetilde{\psi}^{(1)}\left(t,\mathbf{x}\middle|\tilde{\mathbf{z}}_1\right)$.

Indeed, we have seen that if we consider locally at $\tilde{\mathbf{z}}_1$ and t an uniform grain density $n\left(t,\tilde{\mathbf{z}}_1\right)$ then the unconditional distribution function $f^{(1)}\left(t,\tilde{\mathbf{z}}_1\right)$ for any sphere being at $\tilde{\mathbf{z}}_1$ equals n, equation (23). Using this result, Drew [9] proved that the nearest-neighbor distribution $\widetilde{f}^{(1)}\left(t,\mathbf{x},\tilde{\mathbf{z}}_1\right)$ has the following analytic expression:

$$\widetilde{f}^{(1)}\left(t,\mathbf{x},\tilde{\mathbf{z}}_1\right)=n\cdot\exp\left[-\frac{4}{3}\pi n\left(\left|\mathbf{x}-\tilde{\mathbf{z}}_1\right|\right)^3\right] \tag{39}$$

As we will see in more detail later, the conditionally averaged field $\widetilde{\psi}^{(1)}\left(t,\mathbf{x}\middle|\tilde{\mathbf{z}}_1\right)$ can be approached analytically if one assumes that that the field $\psi\left(t,\mathbf{x}\right)$ is mainly influenced by the closest grain to $\mathbf{x}$ and that the influence of distant grains is negligible. This would be equivalent to what Drew [9] pointed out, namely "to assume that each grain is isolated in the sense that it only interacts with its neighbors through the average fields".

3.3. The cell model

The use of the exact distribution function in (39) to compute the ensemble average in (37) will increase excessively the complexity of the closure problem. Thus, a simpler approximation for $\widetilde{f}^{(1)}\left(t,\mathbf{x},\tilde{\mathbf{z}}_1\right)$ would be of great interest. Looking at the exact distribution (Figure 3) one can see that the probability to find the closest grain at the distance $r=\left|\mathbf{x}-\tilde{\mathbf{z}}_1\right|$ from the point $\mathbf{x}$ decreases exponentially with the increase of r. Indeed $\widetilde{f}^{(1)}\left(t,\mathbf{x},\tilde{\mathbf{z}}_1\right)$ remains of order of n for exponential arguments $4/3\pi nr^3$ of order of one and decreases dramatically with further increase of $4/3\pi nr^3$.

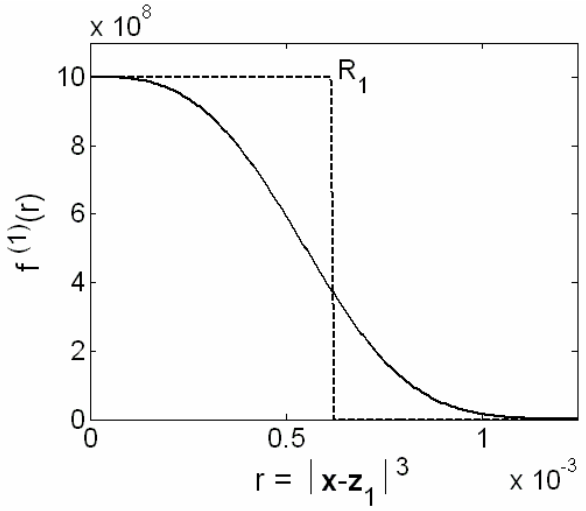

Figure 3: The exact form (continuous line) and the cell model approximation (dashed line) of the probability distribution $\tilde{f}^{(1)}\left(t,\mathbf{x},\tilde{\mathbf{z}}_1\right)$ for $n=10^9\ m^{-3}$

This variation for $\tilde{f}^{(1)}$ clearly evidence the existence of a characteristic distance R_1 from $\mathbf{x}$ above which the probability to find the closest particle to $\mathbf{x}$ becomes negligible. In this light, an interesting approximation for $\tilde{f}^{(1)}$ would be the following "top-hat" distribution:

$$\tilde{f}^{(1)}\left(t,\mathbf{x},\tilde{\mathbf{z}}_1\right)=\begin{cases} n & for \quad \left|\mathbf{x}-\tilde{\mathbf{z}}_1\right|\le R_1 \\ 0 & for \quad \left|\mathbf{x}-\tilde{\mathbf{z}}_1\right|> R_1 \end{cases} \tag{40}$$

This approximation is called *the "cell model" approximation to the one particle distribution* [9]. The characteristic length R_1 can be analytically computed since we know that the probability of finding the center of the closest particle to $\mathbf{x}$ between $\mathbf{x}$ and ∞ is *1*, that is:

$$\lim_{R\to\infty}\left(\int_{\left|\mathbf{x}-\tilde{\mathbf{z}}_1\right|\le R}\tilde{f}^{(1)}\left(t,\mathbf{x},\tilde{\mathbf{z}}_1\right)d\tilde{\mathbf{z}}_1\right)=1 \tag{41}$$

Using (40) together with (41) one can easily obtain:

$$R_1=\left(\frac{4}{3}\pi n\right)^{-\frac{1}{3}} \tag{42}$$

This is a very important result since it evidences the existence at each point $\mathbf{x}$ of a sphere of radius R_1 within which we can find one and only one particle. So, using the probability distribution functions we were able to retrieve a local characteristic length which quantifies in a certain point of the two-phase system the amount of space within which one can find one and only one particle. For this reason a cell of radius R_1 enveloping a particle will also enclose the space proper to that particle, the "zone of influence" characterizing that particle (Figure 4). Outside this cell one will found itself under the influence of a neighbor particle. In other words, the characteristic length R_1 represents half of the average distance between two adjacent grains. Notice however that all the above conclusions are based on the assumption of a local homogeneous grain distribution n at **x**.

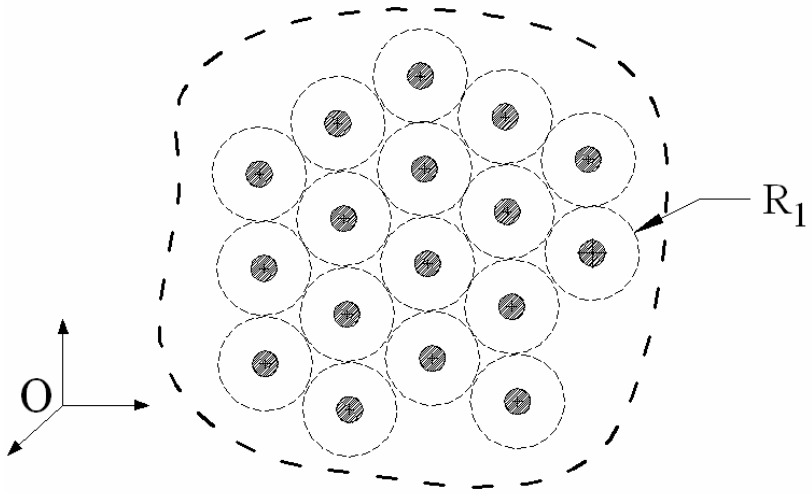

Figure 4: The average distance between two adjacent grains

Using the cell approximation to $\widetilde{f}^{(1)}\left(t,\mathbf{x},\tilde{\mathbf{z}}_1\right)$, the ensemble average $\overline{\psi}(t,\mathbf{x})$ defined in (37) becomes:

$$\begin{aligned}\overline{\psi}(\mathbf{x},t) &= \int \widetilde{f}^{(1)}\left(t,\mathbf{x},\tilde{\mathbf{z}}_1\right)\widetilde{\psi}^{(1)}\left(t,\mathbf{x}\middle|\tilde{\mathbf{z}}_1\right)d\tilde{\mathbf{z}}_1 \\ &= n \int\limits_{\left|\mathbf{x}-\tilde{\mathbf{z}}_1\right|\le R_1} \widetilde{\psi}^{(1)}\left(t,\mathbf{x}\middle|\tilde{\mathbf{z}}_1\right)d\tilde{\mathbf{z}}_1\end{aligned} \tag{43}$$

Notice that the use of the cell approximation for $\widetilde{f}^{(1)}$ transforms the improper integral in (37) into a definite volume integral over the sphere of radius R_1 and centered at $\mathbf{x}$. Notice as well that the integration in (43) is made with respect to $\tilde{\mathbf{z}}_1$, meaning that we integrate over all position of the grain in the cell. This result is of great importance because, one one hand it simplifies the ensemble average formulation and on the other hand, and most importantly, it quantifies the ensemble θ of all possible realisations of the multiphase flow, so abstactly used in (1). Indeed the ensemble θ indentifies now with the ensemble of flows for which the nearest particle to $\mathbf{x}$ is centered anywhere within the sphere ("cell") of radius R_1 and centered at $\mathbf{x}$ (Figure 5a). Hence, the integration in (43) is made over all positions of the grain in the cell that is over the ensemble of all possible realisation of the multiphase system. The equation (43) represents no more than the "*cell approximation to the ensemble average*".

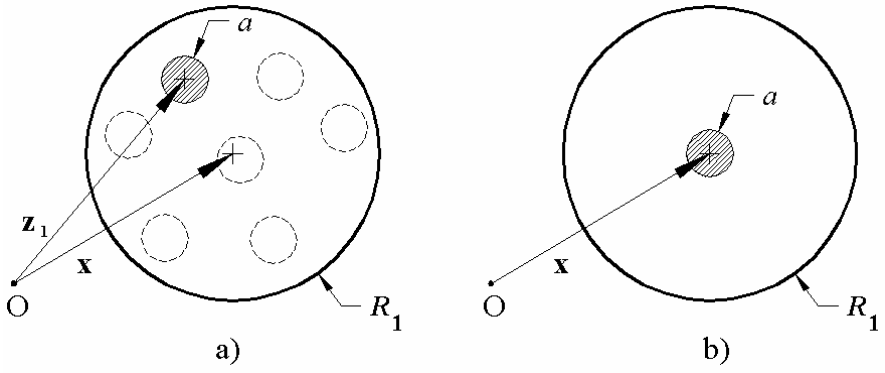

Figure 5: a) The cell approximation to the ensemble average; b) The cell approximation to the volume average

However, to be able to compute $\overline{\psi}(\mathbf{x},t)$ one has to approach analytically $\widetilde{\psi}^{(1)}\left(t,\mathbf{x}\middle|\tilde{\mathbf{z}}_1\right)$. As already anticipated one can assume that the field $\psi(\mathbf{x},t)$ is mainly influenced by the closest grain to $\mathbf{x}$. In this respect, by negleting the influence at $\mathbf{x}$ of all grains except the closest one to $\mathbf{x}$, the conditionnaly averaged field $\widetilde{\psi}^{(1)}$ can be approximated with the exact solution of $\psi(\mathbf{x},t)$ given a single grain at $\tilde{\mathbf{z}}_1$. Hence $\widetilde{\psi}^{(1)}\left(t,\mathbf{x}\middle|\tilde{\mathbf{z}}_1\right)\cong\psi\left(t,\mathbf{x};\tilde{\mathbf{z}}_1\right)$. Equation (43) becomes:

$$\overline{\psi}(t,\mathbf{x})=n\int\limits_{\left|\mathbf{x}-\tilde{\mathbf{z}}_1\right|\le R_1}\psi\left(t,\mathbf{x};\tilde{\mathbf{z}}_1\right)d\tilde{\mathbf{z}}_1 \tag{44}$$

One important consequence of (44) is that, in order to compute $\overline{\psi}$, one has to evaluate the exact field $\psi\left(t,\mathbf{x};\tilde{\mathbf{z}}_1\right)$ around a particle only to maximum distance R_1 from its center $\tilde{\mathbf{z}}_1$. As already explained, above this limit the field would not be anymore "proper" to the particle centered in $\tilde{\mathbf{z}}_1$, but to its neighbours. Using equation (44) let us compute now some of the average quantites defined in Table 1 for a simple two-phase particulate system (spherical particles of radius a, uniformely distributed in space and having a known particle density n_p).

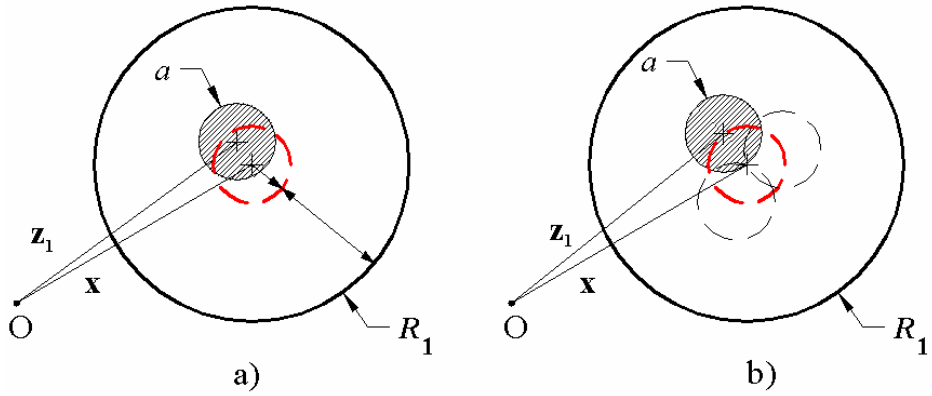

Figure 6: Computation of a solid (a) and of an interfacial (b) ensemble average

The solid fraction becomes:

$$\begin{aligned}\varepsilon_s(t,\mathbf{x})&=\int\limits_{\left|\mathbf{x}-\tilde{\mathbf{z}}_1\right|\le R_1}\widetilde{f}^{(1)}\left(t,\mathbf{x};\tilde{\mathbf{z}}_1\right)X_s(t,\mathbf{x})\,d\tilde{\mathbf{z}}_1\\&=n_p\int\limits_{\left|\mathbf{x}-\tilde{\mathbf{z}}_1\right|\le R_1}X_s(t,\mathbf{x})\,d\tilde{\mathbf{z}}_1\end{aligned} \tag{45}$$

Taking into account the definition of the characteristic function X_s the last integral transforms in an integral over the positions of the particle within the cell such as the point $\mathbf{x}$ is within the solid phase. This is equivalent with an integral of the particle position over the spherical domain $\left|\mathbf{x}-\tilde{\mathbf{z}}_1\right|\le a$ (Figure 6a):

$$\begin{aligned}\varepsilon_s(t,\mathbf{x}) &= n_p \int_{|\mathbf{x}-\tilde{\mathbf{z}}_1|\le a} d\tilde{\mathbf{z}}_1 \\ &= n_p \frac{4}{3}\pi a^3 \qquad \left(=\frac{a^3}{R_1{}^3}\right)\end{aligned} \tag{46}$$

Using a similar reasoning the liquid fraction $\varepsilon_l(t,\mathbf{x})$ becomes:

$$\begin{aligned}\varepsilon_l(t,\mathbf{x}) &= n_p \int_{a\le|\mathbf{x}-\tilde{\mathbf{z}}_1|\le R_1} d\tilde{\mathbf{z}}_1 \\ &= n_p \frac{4}{3}\pi\left(R_1^3 - a^3\right) \qquad \left(=1-\frac{a^3}{R_1{}^3}\right)\end{aligned} \tag{47}$$

In the latter case the integration is made over the positions of the particle within the cell such as the point $\mathbf{x}$ is within the liquid phase, that is over the sperical domain $a \le \left|\mathbf{x}-\tilde{\mathbf{z}}_1\right| \le R_1$ (Figure 6a). It is worthwhile to notice that the results for the solid/liquid fraction are identical with the ones obtained by Wang and Beckermann [6] using the volume average technique and *the cell approximation to the volume average*. However (46) and (47) result from a closure technique fundamentally different from the one used in [6]. Indeed, the equations (45) and (47) engage integrations over the position of the closest particle to $\mathbf{x}$, $\tilde{\mathbf{z}}_1$, such as the point $\mathbf{x}$ be always in the solid or in the liquid phase, respectively. Therefore, during the average process the field to average is always evaluated in the phase for which one computes the average. Note that this seemingly minor feature is one of the key advantages of the cell approximation to the ensemble average.

The approach used by Wang and Beckermann [6], the cell approximation to the volume average, considers an equivalent cell of radius R_1 (Figure 5b). However, during the average process the particle is fixed and centered at $\mathbf{x}$. All fields are averaged in this cell and the average results (including the liquid and interfacial averages) are artificially attached to the point $\mathbf{x}$, a point that it is always in the solid. As we will see later on this incoherence may produce wrong results, especially at the evaluation of interfacial averaged fields.

For a generic field $\psi(t,\mathbf{x})$ the solid and liquid ensemble average becomes respectively:

$$\begin{aligned}\overline{\psi}_s(t,\mathbf{x}) &= \frac{1}{\varepsilon_s}\int_{|\mathbf{x}-\tilde{\mathbf{z}}_1|\le R_1} \tilde{f}^{(1)}\left(t,\mathbf{x},\tilde{\mathbf{z}}_1\right) X_s(t,\mathbf{x})\psi\left(t,\mathbf{x};\tilde{\mathbf{z}}_1\right) d\tilde{\mathbf{z}}_1 \\ &= \frac{n_p}{\varepsilon_s}\int_{|\mathbf{x}-\tilde{\mathbf{z}}_1|\le a} \psi\left(t,\mathbf{x};\tilde{\mathbf{z}}_1\right) d\tilde{\mathbf{z}}_1 \qquad \left(=\frac{1}{4/3\pi a^3}\int_{|\mathbf{x}-\tilde{\mathbf{z}}_1|\le a} \psi\left(t,\mathbf{x};\tilde{\mathbf{z}}_1\right) d\tilde{\mathbf{z}}_1\right)\end{aligned} \tag{48}$$

and:

$$\begin{aligned}\overline{\psi}_l(t,\mathbf{x}) &= \frac{n_p}{\varepsilon_l}\int_{a\le|\mathbf{x}-\tilde{\mathbf{z}}_1|\le R_1} \psi\left(t,\mathbf{x};\tilde{\mathbf{z}}_1\right) d\tilde{\mathbf{z}}_1 \\ &= \frac{1}{4/3\pi\left(R_1{}^3 - a^3\right)}\int_{a\le|\mathbf{x}-\tilde{\mathbf{z}}_1|\le R_1} \psi\left(t,\mathbf{x};\tilde{\mathbf{z}}_1\right) d\tilde{\mathbf{z}}_1\end{aligned} \tag{49}$$

Notice again that the integrations in (48) and (49) are made over the position of the particle such as the point $\mathbf{x}$ is respectively in the solid or the liquid phase.

Let us compute now the interfacial average S_s (the area density, see Table 1):

$$\begin{aligned} S_s &= n_p \int_{\left|\mathbf{x}-\tilde{\mathbf{z}}_1\right|\le R_1} \mathbf{n}_s \cdot \mathbf{n}_s \delta\left(\mathbf{x}-\mathbf{x}_i(t)\right) d\tilde{\mathbf{z}}_1 \\ &= n_p \int_{\Omega(a)} d\Omega \qquad \left(= n_p 4\pi a^2\right) \end{aligned} \tag{50}$$

Because ∇X_k has a meaning at the solid-liquid interface only, the volume integral in (50) transforms into an integral over the positions of the particle such as the point $\mathbf{x}$ is on the interface, namely into a surface integral over the spherical envelope of radius a, centered at $\mathbf{x}$ (Figure 6b). Notice that, since the liquid and the solid share the same interface, $S_s = S_l$.

Let us compute now the two averaged interfacial sources $\overline{\Phi^{\psi}}_k$ and $\overline{\Gamma^{\psi}}_k$ which quantifies the two types of interactions between the solid and the liquid (see Table 1). Since we are dealing with solid rigid particles, the relative velocity $\mathbf{w}_k = \left(\mathbf{v}_i - \mathbf{v}\right)_k$ and the molecular flux $\mathbf{j}_k^{\psi}$ at the phase *k* interface have only normal components:

$$\begin{aligned} \mathbf{w}_k &= w_k \mathbf{n}_k \\ \mathbf{j}^{\psi} &= j_k^{\psi} \mathbf{n}_k \end{aligned} \tag{51}$$

Having this in mind $\overline{\Phi^{\psi}}_k$ and $\overline{\Gamma^{\psi}}_k$ become:

$$\begin{aligned} \overline{\Phi^{\psi}}_k &= n_p \int_{\left|\mathbf{x}-\tilde{\mathbf{z}}_1\right|\le R_1} \left(-j_k^{\psi}\mathbf{n}_k\right) \cdot \left[-\mathbf{n}_k \delta\left(\mathbf{x}-\mathbf{x}_i(t)\right)\right] d\tilde{\mathbf{z}}_1 \\ &= n_p \int_{\Omega(a)} j_k^{\psi} d\Omega \end{aligned} \tag{52}$$

and:

$$\begin{aligned} \overline{\Gamma^{\psi}}_k &= n_p \int_{\left|\mathbf{x}-\tilde{\mathbf{z}}_1\right|\le R_1} \rho\psi\left(-w_k\mathbf{n}_k\right) \cdot \left[-\mathbf{n}_k \delta\left(\mathbf{x}-\mathbf{x}_i(t)\right)\right] d\tilde{\mathbf{z}}_1 \\ &= n_p \int_{\Omega(a)} \rho\psi w_k d\Omega \end{aligned} \tag{53}$$

where again the integration is made over the positions of the particle such as the point $\mathbf{x}$ is on the interface. It is customary to rewrite the flux $\overline{\Phi^{\psi}}_k$ as follows:

$$\overline{\Phi^{\psi}}_k = S_k \overline{j_k^{\psi}}^{*}, \qquad \overline{j_k^{\psi}}^{*} = \frac{1}{A_k} \int_{\Omega(a)} j_k^{\psi} d\Omega \tag{54}$$

where S_k is the area density of *k* phase interface, $\overline{j_k^{\psi}}^{*}$ is the interfacial average flux of ψ at the *k* phase interface. The latter equation evidence the interfacial diffusion process caused by the molecular diffusion of ψ at the interface.

Likewise, $\overline{\Gamma^{\psi}}_k$ can be rewritten as follows:

$$\overline{\Gamma^{\psi}}_k = \Gamma_k \overline{\psi_k}^{*} \tag{55}$$

where:

$$\Gamma_k \left(\equiv \overline{\Gamma^{1}}_k\right) = \int_{\Omega(a)} \rho w_k d\Omega \qquad \textit{and} \qquad \overline{\psi_k}^{*} = \frac{1}{\Gamma_k} \int_{\Omega(a)} \rho\psi w_k d\Omega \tag{56}$$

are respectively the mass transfer rate at the k interface (the solid/liquid mass transfer rate in our case) and the average interfacial field at the k interface, averaged with respect to the mass transfer rate. This latter formulation evidence clearly the physical meaning of $\overline{\Gamma^{\psi}}_k$, namely the interfacial transfer of ψ due to the mass exchange between phases.

3.4. Model closure

Let us now particularize these results with a real binary alloy solidification case. The processes taking place within an ingot during a rapid solidification are very complex to model since various coupled phenomena like nucleation, grain growth, coarsening need to be accounted. In view of this complexity one should first propose physical models at the micro-scale for all these processes and only then try to compute closure expressions for the unknown terms in the ensembled averaged equations like (8). Hence, first one has to write down the physical assumptions valid at the micro-scale.

3.4.1. Micro-scale physical assumtions.

A pure diffusion case. The first assumption we made refers to the fluid flow regime. In the folowing we will neglet the existence of any flow in the system. So $\mathbf{v}_s$ and $\mathbf{v}_l$ will be zero and the balance equation for momentum will become identical zero. Therefore, the final model will include only balance equations for mass, energy and solute.

Phase diagram aspects.

During the binary alloy solidification the solute concentration field has a discontinuity at the solid-liquid interface. Indeed the solute concentration at the liquid interface C_l^* is linked directly to the interface temperature through the liquidus curve in the phase diagram. In contrast, due to a lower solubility of the solute in the solid, the solute concentration at the solid interface C_s^* is usually lower than C_l^* (for the case of ususal metal alloys). C_s^* can be also linked directly to the interface temperature through the solidus curve this time. One can approximate the liquidus and the solidus curves with a linear law and therefore express the two interfacial concentrations as follows:

$$C_l^* = \frac{T - T_f}{m} \quad , \quad C_s^* = kC_l^* \tag{57}$$

where m is the liquidus line slope, T_f is the fusion temperature of the pure solvant and k is the partition coefficient (<1).

Solute diffusion controlled solidification

Due to a high value of the Lewis number, i.e., the ratio between the thermal and the solute diffusivity in the liquid Le $= \alpha / D_l$, the solidification of a binary metallic alloy is mainly controlled by the solute diffusion. In this respect the solute conservation at the solid-liquid interface:

$$C_l^* (1-k) w_n = -D_l \frac{\partial C_l}{\partial n_l} + D_s \frac{\partial C_s}{\partial n_s} \tag{58}$$

is sufficient for the computation of the solid liquid interface velocity, w_n. It is worthwhile to notice that the solid interface evolution is intrinsically linked to the solute diffusion at the solid/liquid interface. Therefore, great attention must be paid to the modeling of the solute flux at the solid-liquid interface. Notice as well that for binary metallic alloys the solute diffusivity in the solid, D_s, has a very small value compared with D_l, and it is usually neglected except for some alloys like steel.

Local thermal equilibrium

The hypothesis of a local thermal equilibrium was constantly employed in different average solidification models [6, 7, 14, 15]. In brief, the local thermal equilibrium states that, due to the high thermal diffusivity characterizing the metallic alloys, one can assume that locally, at the scale of the grain, the temperature field is uniform: $T_s = T_l$. The use of such an approximation is based on the assumption that due to the high alloy diffusivity the diffusion time at length scales of the grain is small enough to consider a local uniform temperature. Indeed, if l_g denotes the length scale of a dendrite grain (usually $\sim 10^{-4} - 10^{-3} m$) and α the thermal diffusivity ($\sim 10^{-5} m^2/s$), the thermal diffusion time at the scale of l_g becomes $t_d \simeq \left(l_g\right)^2/\alpha = 10^{-1} - 10^{-3} s$, thus a quite small one. However, for average or high local cooling rates $\partial T/\partial t > 1 - 10^2 K/s$ the order of magnitude of the temperature differences at the scale of the grain $\left(\Delta T_g \simeq \left(\partial T/\partial t\right) t_d\right)$ becomes non-negligible $\left(> 0.1K\right)$. Even more, for solidification processes that imply high thermal gradients $G > 10^3 - 10^4$, the order of magnitude for temperature differences at the scale of the grain $\left(\Delta T_g \simeq G l_g\right)$ may be high enough $> 1K$ as to invalidate the hypothesis of local thermal equilibrium.

This hypothesis is of primary importance since, as we will see, it greatly simplifies the closure expressions. Moreover, as one will notice, the closure expressions obtained given this hypothesis are very similar with those obtained by Wang and Beckermann in their volume averaged model [6]. To anticipate, notice that if one does not consider anymore a local thermal equilibrium at the scale of the grain, the results obtained using the statistical approach are completely different from those obtained using a volume average model. Even more, the volume averaged approach gives birth to non-physical closure expressions.

Equiaxed nucleation

The nucleation phenomena are intrinsically linked to the equiaxed grain nucleation within an undercooled melt. For a pure equiaxed case (no columnar grains) we will approach the nucleation with an instantaneous phenomena triggering at a temperature T_{Ne}. The latter one is usually lower that liquidus temperature corresponding to the local liquid concentration: $T_{Ne} = T_{liquidus} - \Delta T_{nucl}$, where ΔT_{nucl} represents the nucleation undercooling. The instantaneous germination model has been proposed by Stefanescu et al. [16] and was extensively used in average models [6, 7] due to its simplicity. In this respect, when the local liquid temperature reach the critical temperature T_{Ne}, solid nuclei appear instantaneously in the undercooled melt with a density equal to n_e^0. The value of n_e^0 is a input parameter of the model difficult to predict. One could have an insight on this parameter by means of post-mortem microstructure analysis or, for the case of refined alloys, by estimating the number of refining particles introduced in the ingot. However, n_e^0 along with the nucleation undercooling ΔT_{nucl} still remains the parameters with the highest degree of incertitude among all input parameters used in the solidification model.

Another parameter linked to the nucleation process is the radius of the initial nuclei a_0. We have considered $a_0 = 10^{-6} m$, similar to the value used in [7]. Numerical test were done with radius a_0 smaller than $10^{-6} m$ and no significant influence was observed.

Columnar "nucleation"

As mentioned the nucleation phenomena is linked to the equiaxed solidification only. However, for an average model describing the columnar solidification as well one will have to model the sudden appearance of a columnar dendrite tip in a certain point of the ingot. We will denote this particular

phenomenon with the "*columnar nucleation*". Describing the "columnar nucleation" phenomena will involve, just as for equiaxed nucleation, the definition of the local undercooling conditions at which the columns tips are supposed to appear in one point and on the other hand of the density of columns grains n_c^0.

As already mentioned, the columnar structure is approximated with an isotropic model (a spherical model). In this context, the density of columns n_c^0 is quantified by the average spacing between two dendrite tips, namely the primary dendrite spacing λ_1, e.g. equation (13). In turn, λ_1 can be easily related to local conditions like the local thermal gradient and local isotherms velocity by means of various models existing in the literature [17, 18].

Defining the undercooling conditions for the "columnar nucleation" would mean, just as for the case of equiaxe nucleation undercooling, defining the critical parameters at $\mathbf{x}$ corresponding to the sudden appearance of the columnar tips at $\mathbf{x}$. However, this approach would consider the sudden appearance of a columnar tip at $\mathbf{x}$ as a local event, depending on local parameters only (like temperature, solute concentration, nucleation undercooling). This is not physically valid since the columnar front position is a function not only of local parameters at the tip but of the whole history of the tip evolution. In this light and in contrast with the equiaxed nucleation the "columnar nucleation" can not be treated as a local event.

Thus, to determine the precise moment at which the dendrite tip appears at $\mathbf{x}$ one would need to track at each moment the position of a dendrite tip in the ingot. This could be done with the help of a front tracking technique which demands in turn the evaluation of the instantaneous velocity of the columnar tip V_{tip} with respect to the local undercooling conditions. One can assume that the tip velocity can be linked at any moment to the local tip undercooling using a standard tip kinetic theory [19]. The latter hypothesis is not straightforward since the existing kinetic theories of a dendrite tip are valid for stationary state at the dendrite tip. Therefore, the use of a stationary solution for V_{tip} for a case where the local tip undercooling conditions are nonstationary would not be valid. However if the velocity response time to changes in local undercooling conditions is much smaller that time scale characterizing the variations of local conditions, the dendrite tip velocity can be approximated with the steady state solution. Indeed, for rapid solidification processes involving fast advancing columnar dendrites, the dendrite tip radius r_{tip} is very small ($\sim 10^{-6} - 10^{-5} m$). Knowing that the solute boundary layer at the tip is of the same order as r_{tip} the time scale characterizing the solute transport at the tip would be of order of $\tau_{tip} \sim \left(r_{tip}\right)^2 / D_l$, thus small too $\left(\sim 10^{-1} - 10^{-3} s\right)$ for a typical $D_l \sim 10^{-9} m^2 / s$. Because the instant tip velocity is intrinsically linked to the solute transport at the tip, equation (58), the velocity response time of the tip subject to changes in local undercooling conditions will be of order of τ_{tip}. On the other hand the local undercooling conditions are subject to changes as well. These changes are produced mainly by macroscopic processes (fluid flow and heat transfer at the scale of the ingot) and their characteristic time scale is usually much larger than τ_{tip}. In this respect, one can approach the tip velocity with the results from a steady state tip kinetic theory like the one proposed by Lipton et al. [19].

If the implementation of a front tracking technique for a 1D domain is quite simple, the columnar front tracking for a 2D or 3D case can be extremely difficult and highly time consuming. Even more, the columnar front tracking technique represents a discrete approach and its use within an average model whose main advantage is precisely to avoid any interface tracking would not be consistent. In this context, the "columnar nucleation" represents one of the major problems in columnar modeling and in modeling the coupling between columnar and equiaxe structures (e.g. CET). The existence of a model which would help avoiding any front tracking would be of great interest. As already discussed, one would have to model the "columnar nucleation" as a local event depending on local parameters only. However for reasons of clarity, we will consider in the following that the the exact position of the columnar front within the ingot, $\mathbf{x}_{cf}$, is a known

parameter (e.g. obtained from a front tracking algorithm). In this respect, the columnar nucleation can be approached as an instantaneous phenomena somewhat similar with the equiaxed case.

Grain growth. Envelope model.

For rapid solidification processes the solid-liquid interface quickly destabilizes after the nucleation and gives birth to highly complex dendritic grains. To be able to model the precise evolution of the dendritic interface one should precisely model the solute fluxes within the complex interdendritic network. Obviously this would be a very difficult task. However, the problem of modeling the grain evolution can be simplified if one compares the length scales characterizing the interdendritic and the extradendritic zone (Figure 7). Indeed, the interdendritic spacing λ_2 is of order of the primary arm tip radius and measures typically $10^{-5} m$ (in some cases even smaller), whereas the length scale of the extradendritic zone is of order of the average spacing between equiaxe grains or, for columnar grains, of the order of λ_1. In both cases this length scale is at least one order of magnitude larger than the interdendritic spacing, λ_2. This particular feature of the dendritic grain has enabled Rappaz and Thévoz [14] to admit a scale separation hypothesis between the inter- and extra-dendritic liquid. A similar hypothesis was used by Wang and Beckermann in their volume average model [6, 7]. The most important consequence of this hypothesis is that due to extremely small inter-dendritic spacings the liquid between secondary and/or tertiary arms can be considered at equilibrium with the liquid interface meaning that its concentration would be equal to the liquid interface concentration C_l^*. This hypothesis is valid since the solute diffusion time at the scale of the inter-dendritic liquid $\tau_d^{inter} \sim (\lambda_2)^2 / D_l$ is usually much smaller that the time scale characterizing the variations of local temperature (and consequently of C_l^*). In this context one can separate the inter-dendritic zone and the extra-dendritic one with a virtual surface, enveloping the external dendrite tips of the grain (Figure 7a). In the following we will denote this surface as the *grain envelope*. This envelope separates the liquid phase in two sub-liquid phases: an inter-dednritc liquid phase in equilibrium with the interface and an extra-dendritic liquid phase which can be in a non-equilibrium state with respect to the interface. As we will see in more detail this approach is extremely useful since it encompasses the need of modeling the evolution of the complex inter-dendritic solid-liquid interface. To compute the solidification rate, one will only have to model the grain envelope evolution and the solute field in the extra-dendritical zone.

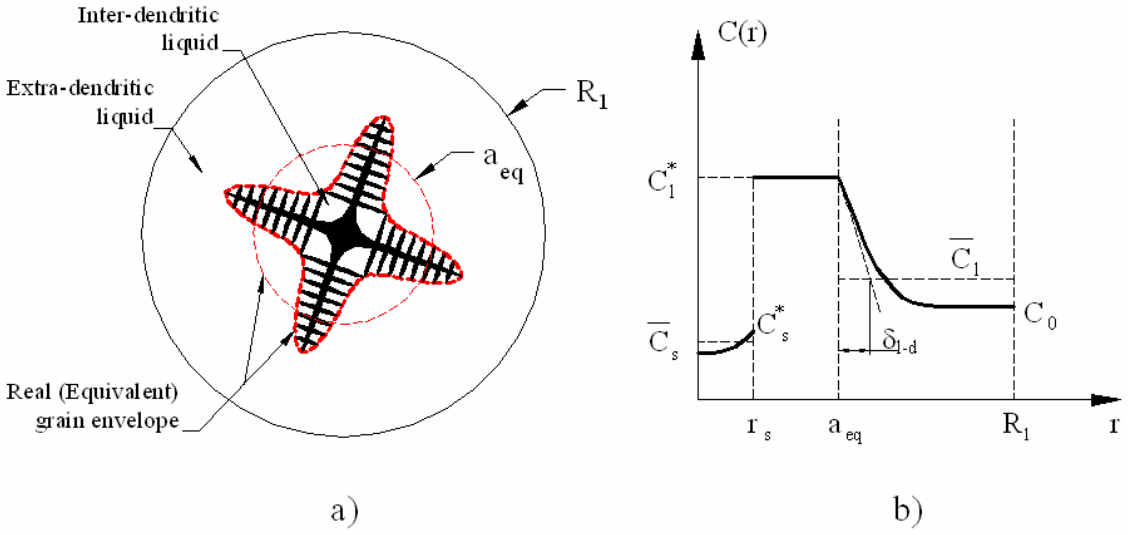

Figure 7: The envelope model (a) and the coresponding solute field distribution (b)

The complex quasi-symmetrical shape of the grain envelope (Figure 7a) is simplified with an equivalent spherical envelope as in Rappaz and Thévoz [14] and Wang and Beckermann [6].

Notice that the envelope deviation from a spherical shape can be partially encompassed by means of a shape correction factor [7]. However, for clarity reasons we will not use in the following this correction.

Because the envelope joins all the dendrite tips of the grain, the envelope evolution will be controlled by the dendrite tips local velocity V_{tip}. As already discussed, one can link the tip velocity V_{tip} to local undercooling conditions (T, C_l^* and C_∞) by using a standard tip kinetic theory. Using the marginal stability criterion and assuming no back diffusion in the solid Lipton et al. [19] has shown that:

$$V_{tip} = \frac{D_l m (k-1) C_l^*}{\pi^2 \Gamma} (Pe_t)^2 \tag{59}$$

Admitting a certain shape for the dendrite tip the Peclet tip number Pe_t can be linked to the dimensionless solutal undercooling $\Omega = \left(C_l^* - C_\infty\right) / C_l^* / (1-k)$. For a spherical dendrite tip one obtains:

$$Pe_t = \Omega \tag{60}$$

whereas for a parabolic shape a more complex function is found: $Pe_t = Iv^{-1}(\Omega)$, where Iv^{-1} represents the inverse Ivantsov function. This function has no simple analytical solution and therefore, we will use in the following the fit computed by Wang and Beckermann [7]:

$$Pe_t = a\left[\Omega / (1-\Omega)\right]^b \tag{61}$$

where $a = 0.4567$ and $b = 1.195$.

Note that equation (59) provides the velocity of a steady-state tip advancing in a semi-infinite liquid domain with the concentration far away from the tip, C_∞. In reality the grain growth does not take place within an infinite liquid domain but is constrained by the presence of neighbor grains. As we have seen, for a local grain distribution having the grain density *n* the sphere of influence proper to each grain is equivalent to the cell of radius R_1 enveloping the respective grain (Figure 4). Outside this cell one enters in the sphere of influence of a neighbor particle. One important remark is that for given the hypothesis of local homogeneity the spherical shell of radius R_1 will play as well the role of a periodic boundary. Moreover, for a pure diffusion case and a local thermal equilibrium at the scale of the grain, the solute field in the extradendritic liquid will be a function of *r* only and the boundary condition at $r = R_1$ will write as follows:

$$\left(\frac{\partial C_l}{\partial r}\right)_{R_1} = 0 \tag{62}$$

meaning that *locally*, the solute flux between two adjacent grains is zero.

In view of these results a physically plausible choice for C_∞ would be $\overline{C}_l$, having in mind however that equation (59) in which $C_\infty = \overline{C}_l$ would represent only a first approximation of the real tip velocity advancing in an finite undercooled liquid domain.

Considering a quasi-stationary solute profile in the extra-dendritic liquid and using an integral approach, Wang and Beckermann [6] found an analytic expression for $C_l(r)$ which unfortunately has no explicit form and requires a numerical evaluation. More recently, Martorano *et al.* [15] proposed an complex explicit analytical approximation to $C_l(r)$. It is important to

notice that both these solutions do not verify the zero flux condition in (62) and that their deviation from (62) is not negligible, especially for cases involving small Pe_t. In this context we propose in Appendix A an approximate solution for $C_l(r)$ which encompasses both these problems: the obtained result, equation (A.16), has a simple analytical form and verifies the zero flux condition in (62).

3.4.2. The final averaged equations. For a pure diffusion case the model will contain the mass, energy and the solute average equations only. The use of the scale separation hypothesis between the inter- and extra-dendritic liquid divides the liquid in two sub-phases. In the following we will denote with d and l subscripts respectively the inter- and the extra- dendritic liquid. For a simpler notation we will introduce the subscript g for the "grain phase"; this is no more than the inter-dendritic phase plus the solid phase (Figure 7a). The separation of the total liquid (f) in two sub-phases transforms the two-phase problem into a three phase one: two liquid phases d and l, and one solid phase s. Notice however that the liquid division is a virtual one and in reality the problem still remains a two-phase problem: $f+s$. In fact, the three phase approach is interesting mainly from the point of view of the solute diffusion phenomena.

Let us now compute the closure expressions for each balance equation. We consider at $\mathbf{x}$ a local homogeneous grain distibution (columnar or equiaxed) with a known density n and a known grain dimension a. We will also consider the solid and liquid densities (ρ_s and ρ_f) as being uniform at the scale of the grain and within each phase, namely that: $\overline{\rho}_s = \rho_s$ and $\overline{\rho}_l = \overline{\rho}_d = \rho_f$. Moreover for simplicity reasons, we will drop the average sign of all variables defined in Table 1. Note however that in the following all variables are averaged ones.

The grain balance

The general grain density balance can be written (Drew [9]) as follows:

$$\frac{\partial n}{\partial t} + \cancel{div\left(\mathbf{v}_s n\right)} = \dot{n}_{c/e} \tag{63}$$

where $\mathbf{v}_s$ is the ensemble averaged solid particle velocity (0 in the present case) and $\dot{n}_{c/e}$ the colunar/equiaxed grain nucleation rate $\left[m^{-3}s^{-1}\right]$. Using, as already discussed, the hypothesis of instantaneous nucleation the equiaxed grains source $\dot{n}_e$ can be written as follows:

$$\dot{n}_e = n_e^0 \delta\left(T - T_{Ne}\right) \tag{64}$$

where $\delta\left(T - T_N\right)$ is the Dirac delta function, T is the local temperature, T_{Ne} the nucleation temperature and n_e^0 is the equiaxed nucleation grain density. On the other hand for the columnar grains the nucleation phenomena can be treated as being instantaneous if one considers a columnar front tracking algorithm. In this case the columnar grain source in equation (63) can be written as follows:

$$\dot{n}_c = n_c^0 \delta\left(\mathbf{x} - \mathbf{x}_{cf}\right) \tag{65}$$

where again $\delta\left(T - T_N\right)$ is the Dirac delta function, $\mathbf{x}$ is the local coordinate within the ingot, $\mathbf{x}_{cf}$ is the exact columnar front position (determined for exemple from a front tracking algorithm) and n_c^0 is the columnar nucleation grain density determined from the primary arm spacing λ_1 (see equation (13)).

The mass balance

Particularizing the generic variable ψ (see Table 2) one can easily obtain the solid and liquid mass balance:

$$\frac{\partial\left(\varepsilon_s\rho_s\right)}{\partial t}=\Gamma_s \quad , \qquad \frac{\partial\left(\varepsilon_f\rho_f\right)}{\partial t}=-\Gamma_s \tag{66}$$

where Γ_s represents the mass exchange rate between the liquid and the solid ($\Gamma_s>0$ and $\Gamma_s<0$ means respectively solidification and fusion at $\mathbf{x}$). Γ_s represents an interfacial averaged variable and can be expressed analytically using the cell model approximation in equation (53):

$$\Gamma_s=\rho_s n_p \int_{\Omega_s} w_s d\Omega \tag{67}$$

Notice again that in (67) the integration is made over all possible positions of the grain such as the point $\mathbf{x}$ is on the solid-liquid interface. This is equivalent to the integration over a surface Ω_s constructed with all possible positions of the grain in the cell such $\mathbf{x}$ is on the solid-liquid interface. Notice as well that:

$$A_s=\int_{\Omega_s} d\Omega \tag{68}$$

is equal to the area of the dendritical grain interface since Ω_s is only a transformation of the real dendritic interface of a grain centered at $\mathbf{x}$. It is customary to rewrite (67) as follows:

$$\Gamma_s=\rho_s S_s \overline{w}_s \tag{69}$$

where:

$$S_s=n_p A_s \qquad \textit{and} \qquad \overline{w}_s=\frac{1}{A_s}\int_{\Omega_s} w_s d\Omega \tag{70}$$

represent respectively the solid-liquid interfacial area, as defined in Table 1 and (50), and the mean solid-liquid interface velocity. Both of these are very difficult to model due to the complexity of the dendrite shape. However, as we will see, using the scale separation hypothesis between the inter- and extra-dedritic liquid the mass exchange rate Γ_s can be determined from the solute mass balance in the inter-dendritic liquid.

Since one will need to the track the evolution of the inter-dendritical liquid fraction a mass balance equation must be written for the d phase:

$$\frac{\partial\left(\varepsilon_d\rho_f\right)}{\partial t}=\Gamma_d \tag{71}$$

where:

$$\Gamma_d=n_p \int_{\left|\mathbf{x}-\tilde{\mathbf{z}}_1\right|\le R_1} \rho\left(-w_d\mathbf{n}_d\right)\cdot\left[-\mathbf{n}_d\delta\left(\mathbf{x}-\mathbf{x}_i\left(t\right)\right)\right]d\tilde{\mathbf{z}}_1 \tag{72}$$

Due to the particular three-phase approach, the inter-dendritic liquid interacts with two phases in the same time. Indeed, the inter-dendritic liquid is bounded by both the solid and the extra-dendritic liquid. In contrast, the solid and the extra-dendritic liquid have an interface with the inter-dendritic liquid only. This comes from the particular choice of the grain boundary which

envelops the dendrite tips and has no finite interface with the solid [6]. Therefore, the integration in (72) can be divided in two, one over the positions of the grain ($\tilde{\mathbf{z}}_1$) such as the point $\mathbf{x}$ is on the $d-s$ interface and one over the positions of the grain such as $\mathbf{x}$ is on the $d-l$ inteface

$$\Gamma_d = \rho_f n_p \left(\int_{\Omega_{d-s}} w_{d-s} d\Omega + \int_{\Omega_{d-l}} w_{d-l} d\Omega \right) \tag{73}$$

Notice that $\Omega_{d-s} \equiv \Omega_s$ and $w_{d-s} \equiv -w_s$, whereas Ω_{d-l} is no more than the spherical grain envelope of radius a and centered in $\mathbf{x}$ (Figure 6b). Finally w_{d-l} is the local velocity of the grain dendrite tips and can be computed with the help of (59). Due to a uniform temperature distribution within the cell (local thermal equilibrium) and to the spherical symmetry of the solute distribution around the grain envelope the interface velocity w_{d-l} will be constant with respect to the integration in (73). One obtains finally:

$$\Gamma_d = -\Gamma_s + \Gamma_g \tag{74}$$

where:

$$\Gamma_g = \rho_f S_g \overline{w_g} \tag{75}$$

is the mass exchange between d and l phase due to grain growth, $S_g = n_p \left(4\pi a^2 \right)$ represents the grain interfacial area and:

$$\overline{w_g} = \frac{1}{4\pi a^2} \int_{\Omega_{d-l}} w_{d-l} d\Omega \quad \left(= \frac{D_l m (k-1) C_l^*}{\pi^2 \Gamma} (Pe_t)^2 \right) \tag{76}$$

is the mean velocity of the grain envelope (see as well equations (59), (61)).

The energy equation

To derive the energy balance equations for each phase one has to explicit first the solid and liquid specific enthalpies h_s and h_f (Table 2). These will depend on the local temperature as follows:

$$h_f = c_f T_f + L \; ; \qquad h_s = c_s T_s \tag{77}$$

where c_f and c_s are respectively the solid and liquid specific heats and L the latent heat of fusion. However, using the local thermal equilibrium hypothesis, the solid and liquid temperatures are locally equal. In this respect, a two-phase approach to the energy equation is no more suited and a simpler mixture approach is sufficient. The mixture energy equation is obtained by summing the solid and the liquid energy equations. With $T_s = T_f = T$ the mixture energy equation writes as follows:

$$\frac{\partial \left[\left(\varepsilon_s \rho_s c_s + \varepsilon_f \rho_f c_f \right) T \right]}{\partial t} = div \left[\left(\varepsilon_s \lambda_s + \varepsilon_f \lambda_f \right) \nabla T \right] + \Gamma_s L \tag{78}$$

Notice the presence in the final equation of the heat source $\Gamma_s L$. This is no more than the latent heat release due to solidification.

The solute balance

As already discussed for the solute balance we are using a three phase approach: $s+d+l$. Using the data in Table 2 the corresponding three solute balance equations can be written as follows:

$$\frac{\partial\left(\varepsilon_s\rho_s C_s\right)}{\partial t} = div\left(\varepsilon_s\rho_s D_s \nabla C_s\right) + \Phi_s^C + \Gamma_s^C \tag{79}$$

$$\frac{\partial\left(\varepsilon_d\rho_f C_d\right)}{\partial t} = div\left(\varepsilon_d\rho_f D_f \nabla C_d\right) + \Phi_d^C + \Gamma_d^C \tag{80}$$

$$\frac{\partial\left(\varepsilon_l\rho_f C_l\right)}{\partial t} = div\left(\varepsilon_l\rho_f D_f \nabla C_l\right) + \Phi_l^C + \Gamma_l^C \tag{81}$$

To close this system one has to propose closure expressions for each of the two exchange terms Φ_k^C and Γ_k^C responsible of the solute interactions between phases due to molecular fluxes at the interface and to the solute exchange at the interface due to phase change respectively. Their general expression is detailed in Table 1 and their ensemble average formulation can be found respectively in (52) and (53).

Notice that, using the hypotheses of chemical equilibrium in the inter-dendritic liquid and of local thermal equilibrium at the scale of the grain, the ensemble average of the inter-dendritic liquid concentration is obviously equal to the local interface concentration, $C_d = C_l^*$.

Let us compute the exchange terms for the solute balance equation in the solid. First, the term Φ_s^C is zero since we neglect the solute diffusivity in the solid ($D_s = 0$). Secondly, since the temperature is uniform within the grain, the solid interface concentration C_s^* is uniform too at the scale of the grain. Using (53) one can easily show that:

$$\Gamma_s^C = C_s^* \Gamma_s \tag{82}$$

Now, for the extra-dendritic liquid the term Γ_l^C becomes:

$$\begin{aligned}\Gamma_l^C &= \rho_f n_p \int_{\Omega_{l-d}} w_{l-d} C_{l-d}\, d\Omega \\ &= -C_l^* \Gamma_g\end{aligned} \tag{83}$$

where C_{l-d} was computed using the continuity of the solute field at the $l-d$ interface: $C_{l-d} = C_{d-l}\left(= C_l^*\right)$.

Using (54) the mean solute flux Φ_l^C can be written as $\Phi_l^C = S_g \overline{j_l^C}^*$. With the help of analytic results giving the solute field in the extra-dendritic liquid (see Appendix A), one easily obtains:

$$\Phi_l^C = \frac{\rho_l S_g D_l}{\delta_{l-d}}\left(C_l^* - C_l\right) \tag{84}$$

where δ_{l-d} is the diffusion length characterizing the solute transfer in the extra-dendritic liquid at the grain interface (see equation (A.18)). With (83) and (84) the solute balance equation in the extra-dendritic liquid is now completely determined. However the conservative formulation in (81) does not evidence the continuous enriching of the extra-dendritic liquid during the solidification

process. In turn, using the mass balance in the extra-dendritic liquid, $\partial\left(\varepsilon_l\rho_f\right)\big/\partial t=-\Gamma_g$ one can easily rewrite (81) as follows:

$$\varepsilon_l\rho_f\frac{\partial C_l}{\partial t}=div\left(\varepsilon_l\rho_f D_f\nabla C_l\right)+\left(\frac{\rho_f S_g D_l}{\delta_{l-d}}-\Gamma_g\right)\left(C_l^*-C_l\right), \tag{85}$$

Since $\delta_{l-d}\le D_l\big/\overline{w}_g$ (Appendix A) and $\Gamma_g=\rho_f S_g\overline{w}_g$ it is easy to notice that the last term on the RHS of (85) is always positive. Since the macroscopic diffusion $div\left(\varepsilon_l\rho_f D_f\nabla C_l\right)$ only redistributes the solute in the ingot it now evident from (85) that the extra-dendritic liquid is always enriching during the solidification process.

Let us compute now the exchange terms related to the inter-dendritic liquid. In computing Φ_d^C and Γ_d^C one has to take into account the fact that phase d interacts with both s and l phase. Indeed, each of the two exchange terms can be expressed as a sum of two terms corresponding to interactions with s and l phase. Given the local thermal equilibrium and using (55) one can easily obtain:

$$\Gamma_d^C=\Gamma_{d-s}^C+\Gamma_{d-l}^C\qquad\left(=-C_l^*\Gamma_s+C_l^*\Gamma_g\right) \tag{86}$$

Similarly, the mean flux Φ_d^C becomes:

$$\Phi_d^C=\Phi_{d-s}^C+\Phi_{d-l}^C \tag{87}$$

The second tem in RHS is no more than $-\Phi_l^C$ since $j_{d-l}^C=-j_{l-d}^C$. In turn, the exchange term Φ_{d-s}^C, is difficult to model directly due to the complex $d-s$ interface. However, one can express Φ_{l-s}^C from the solute balance at the $d-s$ interface:

$$\left(\Gamma_s^C+\Phi_s^C\right)+\left(\Gamma_{d-s}^C+\Phi_{d-s}^C\right)=0 \tag{88}$$

Indeed, using (82) and (86) one easily obtains:

$$\Phi_{d-s}^C=\left(C_l^*-C_s^*\right)\Gamma_s \tag{89}$$

We have managed therefore to close the solute balance equations (79)-(81). Notice that the unknowns in these three equations are respectively C_s, Γ_s and C_l. Thus, by fixing the concentration in the inter-dendritic liquid one encompasses the need to model C_d obtainig in turn an equation for the solidification rate Γ_s. Indeed the inter-dendritic solute balance equation becomes an equation for the solidification rate Γ_s:

$$\begin{aligned}\frac{\partial\left(\varepsilon_d\rho_f C_l^*\right)}{\partial t}=&\,div\left(\varepsilon_d\rho_f D_f\nabla C_l^*\right)+\left(C_l^*-C_s^*\right)\Gamma_s-\frac{\rho_f S_g D_f}{\delta_{l-d}}\left(C_l^*-C_l\right)\\&-C_l^*\Gamma_s+C_l^*\Gamma_g\end{aligned} \tag{90}$$

Using the mass balance in the inter-dendritic liquid, equation (71), one can simplify further the above equation:

$$\left(C_l^* - C_s^*\right)\Gamma_s = \varepsilon_d \rho_f \frac{\partial C_l^*}{\partial t} + \frac{\rho_f S_g D_f}{\delta_{l-d}}\left(C_l^* - C_l\right) - div\left(\varepsilon_d \rho_f D_f \nabla C_l^*\right) \tag{91}$$

The latter equation expresses as pointed out the solute balance in the inter-dendritic liquid. Since the last term on the RHS of (91) can be usually neglected due to the large length scale involved in the macroscopical diffusion process, the above balance equation can be understood as follows: the solute rejection at the solid - inter-dendritic liquid interface (LHS) balance the solute accumulation in the inter-dendritic liquid and the solute flux in the extra-dendritic liquid. It is important to notice that equation (91) reduces to the well-known Scheil law when the extra-dendritic liquid reaches a state of perfect solutal mixing, that is when $C_l = C_l^*$. Indeed, using the solid mass balance equation (66) equation (91)becomes:

$$\left(C_l^* - C_s^*\right)\frac{\partial \varepsilon_s}{\partial t} = \varepsilon_d \frac{\partial C_l^*}{\partial t} \tag{92}$$

that is equivalent to the Scheil solidification law. It is worthwhile to notice as well the important role played by the solute flux in the extra-dendritic liquid: the positive solute flux at the grain boundary intensifies the solidification process ($\Gamma_s \nearrow$). Hence to a non-equilibrium state of the extra-dendritic liquid corresponds a more intense solidification process compared with a state of state of perfect solutal mixing. Even more the solute flux at the grain boundary is strongly influenced by the grain growth. Basically, a rapid grain growth will intensify the solute transfer at the grain boundary and therefore the solidification process.

3.4.3. Summary of the model. In the following table a summary of all equations derived until now is presented. Notice again the three phase approach of the solute balance: three solute balance equations are written in order to account for the solid, extra- and inter-dendritic liquid. The later equation is no more than the supplementary equation expressing the solidification rate.

It is worthwhile to notice as well the similarity between the present model formulation and the volume averaged model of Wang and Beckermann [6]. The equivalence between the two models is a direct consequence of the use of the local thermal equilibrium hypothesis. Indeed if the local homogeneity hypothesis is considered, meaning that no local gradients of physical fields (temperature, solute, grain fraction) are taken into account, then the ensemble average reproduces the volume average technique [9]. This gives confidence in the present model formulation. However the ensemble average technique and the cell model approximation to the ensemble average are fundamentally different from the volume average approach. As we will notice in the following if the local homogeneity hypothesis is no more valid, the use of the ensemble average results into closure expression different from the ones obtained with the help of the volume average technique. Moreover the volume average results will not be physically correct.

Table 3: The summary of the model

Main balance equations	**Solid:**	**Liquid:**
Mass	$\partial\left(\varepsilon_s \rho_s\right)/\partial t = \Gamma_s$	$\partial\left(\varepsilon_f \rho_f\right)/\partial t = -\Gamma_s$
Energy	$\partial\left[\left(\varepsilon_s \rho_s c_s + \varepsilon_f \rho_f c_f\right)T\right]/\partial t = div\left[\left(\varepsilon_s \lambda_s + \varepsilon_f \lambda_f\right)\nabla T\right] + \Gamma_s L$	
Solute	$\partial\left(\varepsilon_s \rho_s C_s\right)/\partial t = \nabla\cdot\left(\varepsilon_s \rho_s D_s \nabla C_s\right) + C_s^* \Gamma_s$	$\varepsilon_l \rho_f \frac{\partial C_l}{\partial t} = \nabla\cdot\left(\varepsilon_l \rho_f D_f \nabla C_l\right) + \left(\rho_f S_g D_l / \delta_{l-d} - \Gamma_g\right)\left(C_l^* - C_l\right)$
Supplementary		

balance eq.	
Inter-dendritic mass balance	$\partial\left(\varepsilon_d \rho_f\right)/\partial t = \Gamma_g - \Gamma_s$
Grain balance	$\partial n/\partial t = n_e^0 \delta\left(T - T_{Ne}\right)$ or $\partial n/\partial t = n_c^0 \delta\left(\mathbf{x} - \mathbf{x}_{cf}\right)$
Solidification rate	$\left(C_l^* - C_s^*\right)\Gamma_s = \varepsilon_d \rho_f \left(\partial C_l^*/\partial t\right) + \rho_f S_g D_f \left(C_l^* - C_l\right)/\delta_{l-d}$ $-div\left(\varepsilon_d \rho_f D_f \nabla C_l^*\right)$
Auxiliary expressions	
Constraints:	$\varepsilon_l + \varepsilon_d + \varepsilon_s = 1$, $\varepsilon_d + \varepsilon_s = \varepsilon_g$
Interfacial concentrations:	$C_s^* = \begin{cases} kC_l^* & if \quad \Gamma_s \geq 0 \\ C_s & if \quad \Gamma_s < 0 \end{cases}$ $C_l^* = \left(T - T_f\right)/m$
Cell radius	$R_1 = \left(4/3\pi n\right)^{-1/3}$
Grain radius	$a = R_1 \varepsilon_g^{1/3}$
Grain envelope interfacial area	$S_g = 4\pi a^2 n$
Diffusion length	see equation (A.18)
Grain growth rate	$\Gamma_g = \rho_f S_g \overline{w}_g$, $\overline{w}_g = \frac{D_l m\left(k-1\right)C_l^*}{\pi^2 \Gamma}\left(Pe_t\right)^2$

4. The coexistence of columnar and equiaxed structures

We will focus in the following paragraph on the possible coexistence from a statistical point of view between the equiaxed and the columnar grains. Let us consider an ingot containing at **x** both columnar and equiaxed grains each of them having different grain densities (Figure 8). To model the columnar/equiaxed coexistence one should be able to separate the influence of each structure at $\mathbf{x}$ and at time t. Of course, what happens at $(\mathbf{x},t)$ (i.e. the solute field) will be a sum of the influence of all grains in the ingot, starting with the closest one to $\mathbf{x}$ and ending with farthest grain. However, quantifying the influence at $\mathbf{x}$ of all grains in the ingot would be a very difficult task, increasingly difficult with the increase of the accounted number of grains. Denoting with ψ the physical field to be studied, we can suppose as a first approximation that only the closest grains to $\mathbf{x}$ would influence significantly $\psi(\mathbf{x},t)$. Notice that this hypothesis is similar with the one considered for the single grain distribution. Based on this assumption it would be interesting to focus on the closest grain to $\mathbf{x}$ only. Consequently, for a case where both equiaxed and columnar grains coexist in the ingot one should have an insight on the conditions that the closest grain to **x** is a columnar or, on the contrary, an equiaxed grain. Indeed, since equiaxed and columnar structures can have very different grain densities one expects that the influences of each of the two structures at $\mathbf{x}$ be different as well.

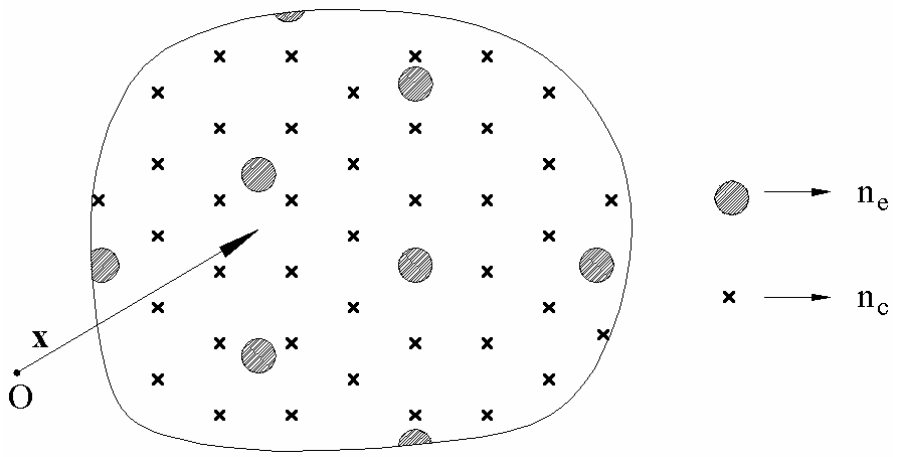

Figure 8: Coexistence between two different grain distributions ($n_e < n_c$)

Let us now consider n_c and n_e the two corresponding grain densities for the columnar and equiaxed structures. Similar to the previous case one can assume the existence of a "master" distribution function family (Equation (15)) which completely describes statistically the multiphase process. The only difference with the single grain distribution is that among the N particles in the ingot one can find this time both columnar and equiaxed grains ($N = N_c + N_e$). Notice again that locally, the columnar structures are approached with a spherical model. In this view the modeling of coexistence between the columnar and equiaxed structures reduces to the coexistence between two populations of spherical grains having different grain densities.

4.1. Probability distribution functions. The ensemble average

Making for the moment no distinction between columnar and equiaxed grains one can define the unconditional density function for any sphere center being at $\mathbf{z}_1$, namely $f^{(1)}(t,\mathbf{z}_1)$. If we suppose that the grains are uniformly distributed in space the unconditional probability $f^{(1)}(t,\mathbf{z}_1)d\mathbf{z}_1$ will represent the probability that at time t we find in the ingot one particle (regardless of its nature) within $d\mathbf{z}_1$ of $\mathbf{z}_1$. Moreover $f^{(1)}(t,\mathbf{z}_1)$ is equal to:

$$f^{(1)}(t,\mathbf{z}_1) = n_c + n_e \tag{93}$$

where n_c and n_e are the corresponding grain densities. These latter values represent as well the unconditional density functions for any columnar/equiaxed grain center being within $d\mathbf{z}_1$ of $\mathbf{z}_1$, that is
:

$$\begin{aligned} f_c^{(1)}(t,\mathbf{z}_1) &= n_c \\ f_e^{(1)}(t,\mathbf{z}_1) &= n_e \end{aligned} \tag{94}$$

Using a similar reasoning as in paragraph 3.1., the nearest-neighbor distribution function family $\tilde{f}\left(N,t,\mathbf{x};\tilde{\mathbf{z}}_1,\tilde{\mathbf{z}}_2,\ldots,\tilde{\mathbf{z}}_N\right)$ can also be defined (see equation (29)). As already discussed, we will focus in the following on the closest particle to $\mathbf{x}$ only. Thus it is useful to define the unconditional density function for any sphere, *regardless of its nature*, being closest to $\mathbf{x}$ and centered within $d\tilde{\mathbf{z}}_1$ of $\tilde{\mathbf{z}}_1$. This is no more than $\tilde{f}^{(1)}\left(t,\mathbf{x};\tilde{\mathbf{z}}_1\right)$ defined already in equation (30). Therefore, the ensemble average of a generic field $\psi(\mathbf{x},t)$ can be written as follows:

$$\overline{\psi}(\mathbf{x},t)=\int\widetilde{f}^{(1)}\left(t,\mathbf{x};\tilde{\mathbf{z}}_1\right)\widetilde{\psi}^{(1)}\left(t,\mathbf{x};\tilde{\mathbf{z}}_1\right)d\tilde{\mathbf{z}}_1 \tag{95}$$

where $\widetilde{\psi}^{(1)}\left(t,\mathbf{x};\tilde{\mathbf{z}}_1\right)$ is the conditional average of ψ, averaged on the condition that the closest grain to $\mathbf{x}$, regardless of its nature, is centered within $d\tilde{\mathbf{z}}_1$ of $\tilde{\mathbf{z}}_1$. Notice that until now we didn't make a difference between the two coexisting structures. We have treated the grains regardless of their type. To separate the effects of columnar or equiaxed structures at $\mathbf{x}$ it would be extremely useful to know whether or not the closest particle to $\mathbf{x}$ is a columnar or an equiaxed particle. This requires an detailed insight on the distribution function $\widetilde{f}^{(1)}\left(t,\mathbf{x};\tilde{\mathbf{z}}_1\right)$.

Let us consider the two following events: E_c the event that the closest particle to $\mathbf{x}$ is columnar and is centered within $d\tilde{\mathbf{z}}_1$ of $\tilde{\mathbf{z}}_1$ and E_e the event that the closest particle to $\mathbf{x}$ is equiaxed and is centered within $d\tilde{\mathbf{z}}_1$ of $\tilde{\mathbf{z}}_1$. Obviously $P\left(E_c\cap E_e\right)=\varnothing$ and

$$\begin{aligned}\widetilde{f}^{(1)}\left(t,\mathbf{x};\tilde{\mathbf{z}}_1\right)d\tilde{\mathbf{z}}_1 &= P\left(E_c\cup E_e\right)\\ &= P\left(E_c\right)+P\left(E_e\right)\end{aligned} \tag{96}$$

Thus the probability of having the closest particle to $\mathbf{x}$ centered within $d\tilde{\mathbf{z}}_1$ of $\tilde{\mathbf{z}}_1$ is the probability of having either a columnar or an equiaxed particle closest to $\mathbf{x}$ and centered within $d\tilde{\mathbf{z}}_1$ of $\tilde{\mathbf{z}}_1$. The two probabilities in the RHS of (96) can be computed with the help of the two corresponding density functions $\widetilde{f}^{(1)}_{c,e}\left(t,\mathbf{x};\tilde{\mathbf{z}}_1\right)$ that the closest particle to $\mathbf{x}$ is columnar/equiaxed and is centered within $d\tilde{\mathbf{z}}_1$ of $\tilde{\mathbf{z}}_1$. One has therefore:

$$\widetilde{f}^{(1)}\left(t,\mathbf{x};\tilde{\mathbf{z}}_1\right)d\tilde{\mathbf{z}}_1=\widetilde{f}_{\,c}^{\,(1)}\left(t,\mathbf{x};\tilde{\mathbf{z}}_1\right)d\tilde{\mathbf{z}}_1+\widetilde{f}_{\,e}^{\,(1)}\left(t,\mathbf{x};\tilde{\mathbf{z}}_1\right)d\tilde{\mathbf{z}}_1 \tag{97}$$

In this context, the ensemble average written in (95), transforms into:

$$\overline{\psi}(\mathbf{x},t)=\int\widetilde{f}_c^{(1)}\left(t,\mathbf{x};\tilde{\mathbf{z}}_1\right)\widetilde{\psi}^{(1)}\left(t,\mathbf{x};\tilde{\mathbf{z}}_1\right)d\tilde{\mathbf{z}}_1+\int\widetilde{f}_e^{(1)}\left(t,\mathbf{x};\tilde{\mathbf{z}}_1\right)\widetilde{\psi}^{(1)}\left(t,\mathbf{x};\tilde{\mathbf{z}}_1\right)d\tilde{\mathbf{z}}_1 \tag{98}$$

This result is very important since it states for the fact that the ensemble θ of all possible realizations of the multiphase flow (see equation (1)) can be approached as the union of two sub-ensembles: the sub-ensemble θ_c which corresponds to the ensemble of realizations such as the closest particle to $\mathbf{x}$, at time *t*, is a columnar one and the sub-ensemble θ_e of realizations such as the closest particle to $\mathbf{x}$, at time *t*, is an equiaxed one. Thus:

$$\theta=\theta_c\cup\theta_e \tag{99}$$

Notice that integration in (98) is made with respect to the variable $\tilde{\mathbf{z}}_1$, that is over the possible positions of the closest grain to $\mathbf{x}$. Thus, equation (98) express the ensemble average of ψ as a sum of two averages corresponding to situations where the closest particle to $\mathbf{x}$ is respectively columnar and equiaxed. To separate the effects of columnar and equiaxed structures at $\mathbf{x}$, it is now useful to introduce the following two discrete functions (phase functions):

$$X_k(t,\mathbf{x})=\begin{cases}1 & \textit{if} \quad \text{the nearest particle to } \mathbf{x} \text{ is a } k \text{ type}\\ 0 & \textit{if} \quad \text{the nearest particle to } \mathbf{x} \text{ is a } k \text{ type}\end{cases} \qquad k=\{c,e\} \tag{100}$$

With the help of these two functions two new phases are defined: the columnar (*c*) and the equiaxed (*e*) phase. Hence, corresponding average variables just as those defined in Table 1 can be attached to the newly defined phases. For example, using (98), the columnar fraction becomes

$$\varepsilon_c = \int X_c(t,\mathbf{x}) \widetilde{f}_c^{(1)}\left(t,\mathbf{x};\tilde{\mathbf{z}}_1\right) d\tilde{\mathbf{z}}_1 + \int X_c(t,\mathbf{x}) \widetilde{f}_e^{(1)}\left(t,\mathbf{x};\tilde{\mathbf{z}}_1\right) d\tilde{\mathbf{z}}_1 \tag{101}$$

Notice that the second term in the RHS of (101) is identically zero since it expresses an integral over the ensemble of realizations θ_e such as the closest particle to $\mathbf{x}$ is equiaxed. The phase field $X_c(t,\mathbf{x})$ is 0 in this case and ε_c finally becomes

$$\varepsilon_c = \int \widetilde{f}_c^{(1)}\left(t,\mathbf{x};\tilde{\mathbf{z}}_1\right) d\tilde{\mathbf{z}}_1 \tag{102}$$

Likewise, the equiaxed fraction can be expressed as:

$$\varepsilon_e = \int \widetilde{f}_e^{(1)}\left(t,\mathbf{x};\tilde{\mathbf{z}}_1\right) d\tilde{\mathbf{z}}_1 \tag{103}$$

and the columnar/equiaxed ensemble average of a generic field $\psi(\mathbf{x},t)$ becomes:

$$\begin{aligned} \overline{\psi}_{c,e}(\mathbf{x},t) &= \frac{1}{\varepsilon_{c,e}} \int X_{c,e} \left[\widetilde{f}_c^{(1)}\left(t,\mathbf{x};\tilde{\mathbf{z}}_1\right) + \widetilde{f}_e^{(1)}\left(t,\mathbf{x};\tilde{\mathbf{z}}_1\right) \right] \widetilde{\psi}^{(1)}\left(t,\mathbf{x};\tilde{\mathbf{z}}_1\right) d\tilde{\mathbf{z}}_1 \\ &= \frac{1}{\varepsilon_{c,e}} \int \widetilde{f}_{c,e}^{(1)}\left(t,\mathbf{x};\tilde{\mathbf{z}}_1\right) \widetilde{\psi}^{(1)}\left(t,\mathbf{x};\tilde{\mathbf{z}}_1\right) d\tilde{\mathbf{z}}_1 \end{aligned} \tag{104}$$

Notice that in order to compute any average field the two nearest distributions $\widetilde{f}_{c,e}^{(1)}\left(t,\tilde{\mathbf{z}}_1\right)$ and the conditional average $\widetilde{\psi}^{(1)}\left(t,\mathbf{x};\tilde{\mathbf{z}}_1\right)$ have to be approached. Analytic expressions for $\widetilde{f}_{c,e}^{(1)}\left(t,\tilde{\mathbf{z}}_1\right)$ are proposed in the following paragraph. Then, similar to the closure approach used for the case involving a single grain distribution (see paragraph 3), the conditional average $\widetilde{\psi}^{(1)}$ will be resolved analytically using the hypotheses that a field $\psi(\mathbf{x},t)$ is solely influenced by the closest grain to $\mathbf{x}$.

4.2. The equiaxed/columnar nearest neighbor distribution functions

In the following the coexistence between two grain populations is analyzed. More precisely, the coupling between a grain population having a finite grain diameter and a second grain population having infinitely small dimension. This type of coupling can be frequently encountered during solidification problems especially in processes involving the so-called columnar-to-equiaxed transition (CET) phenomena. Indeed, CET phenomena are a direct consequence of the coupling between an advancing columnar front and a developed equiaxed structure, thus between an infinitely small grain distribution (columnar dendrite tips) and a finite sized grain distribution (the equiaxed structure).

In this light, the case of a columnar front "*penetration*" into a developed equiaxed zone will be analyzed next. Note that the developped theory will not be limited to this particular phenomenon. Indeed, the results can be straightforward applied to different phenomena involving the coexistence between two grain distributions, i.e. equiaxed nucleation within a columnar zone or equiaxed grain advection into an already existing columnar zone.

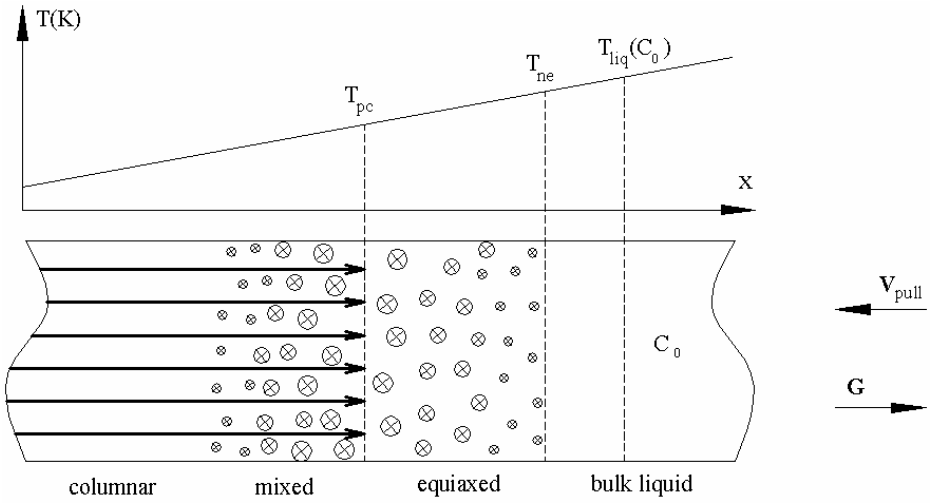

Figure 9: A typical directional solidification and the subsequent columnar-equiaxed interaction

Consider the classical case of a directional solidification involving an axial thermal gradient G and puling a velocity V_p (Figure 9). It can be assumed that equiaxed grains nucleate at the nucleation temperature T_{ne} within the undercooled zone existing ahead of the advancing columnar tips (between $T_{liq}(C_0)$ and the columnar front temperature T_{pc}). Therefore under certain conditions it is likely that columnar tips would encounter in their way a developed equiaxed zone.

Let us consider at $\mathbf{x}$ an homogeneous equiaxed grain distribution having a grain density n_e. Let us consider as well that the equiaxed grain are spherical, have a finite diameter a_e and that at moment t the columnar front arrives at $\mathbf{x}$ (the exact evolution of the columnar front is assumed to be known). Note that columnar grains are approached with a spherical model too and their equivalent grain density n_c^0 can be directly related to the primary arm spacing λ_1 (equation (13)). Obviously one expects that the statistics characterizing the coexistence state (Figure 10) will be fundamentally different from the one characterizing separately each structure at $\mathbf{x}$ prior to the columnar "penetration" into the equiaxed zone.

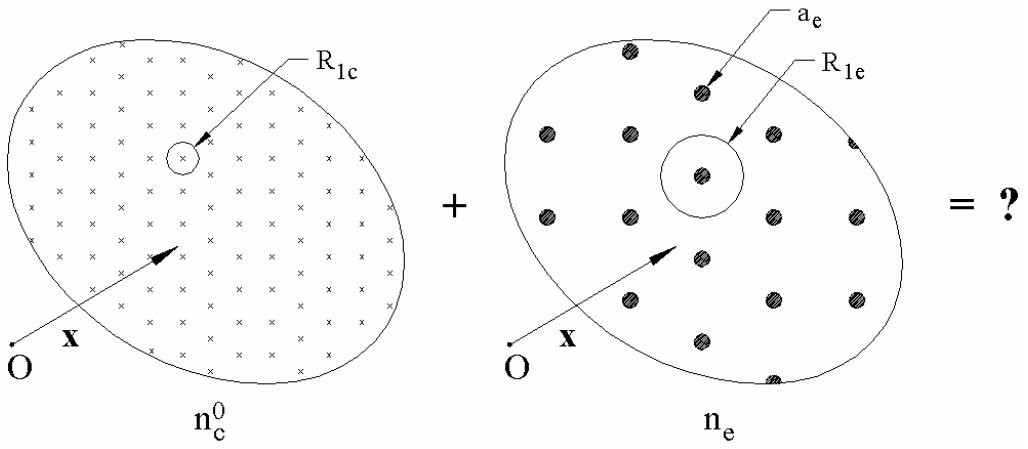

Figure 10: The two grain distributions just before the coexistence state

As pointed out in the preceding section, following the case where the closest particle to $\mathbf{x}$ is either columnar or equiaxed, the ensemble average $\overline{\psi}(\mathbf{x},t)$ can be written, equation (98), as a sum of the columnar and the equiaxed average. The two averages will measure the contribution of

each of the two structures to the "total" ensemble average $\overline{\psi}(\mathbf{x},t)$. To be able to compute these two averages the distributions $\tilde{f}_{c/e}^{(1)}\left(t,\mathbf{x};\tilde{\mathbf{z}}_1\right)$, that a c/e grain is centered within $d\tilde{\mathbf{z}}_1$ of $\tilde{\mathbf{z}}_1$ and is the closest to $\mathbf{x}$ *among all particles in the ingot*, needs to be determined.

4.2.1. Equiaxed nearest neighbor distribution function. To compute $\tilde{f}_e^{(1)}\left(t,\mathbf{x};\tilde{\mathbf{z}}_1\right)$ it is useful to consider first the A_e event that the closest equiaxed grain to **x,** *among the equiaxed grains,* is centered within $d\tilde{\mathbf{z}}_1$ of $\tilde{\mathbf{z}}_1$. The probability of A_e event can be derived from the distribution probability function $\hat{f}_e^{(1)}\left(t,\mathbf{x};\tilde{\mathbf{z}}_1\right)$ that the closest equiaxed particle to $\mathbf{x}$ *among the equiaxed particles* is centered within $d\tilde{\mathbf{z}}_1$ of $\tilde{\mathbf{z}}_1$. It can be proved (see Appendix B) that:

$$\hat{f}_e^{(1)}\left(t,\mathbf{x};\tilde{\mathbf{z}}_1\right)=n_e\cdot\exp\left[-\frac{4}{3}\pi n_e\left(\left|\mathbf{x}-\tilde{\mathbf{z}}_1\right|\right)^3\right] \tag{105}$$

However, after the columnar "penetration" into the equiaxed zone, besides the closest equiaxed grain at $\tilde{\mathbf{z}}_1$, one may find as well newly "germinated" columnar tips between $\mathbf{x}$ and $\tilde{\mathbf{z}}_1$ (see Figure 11a).

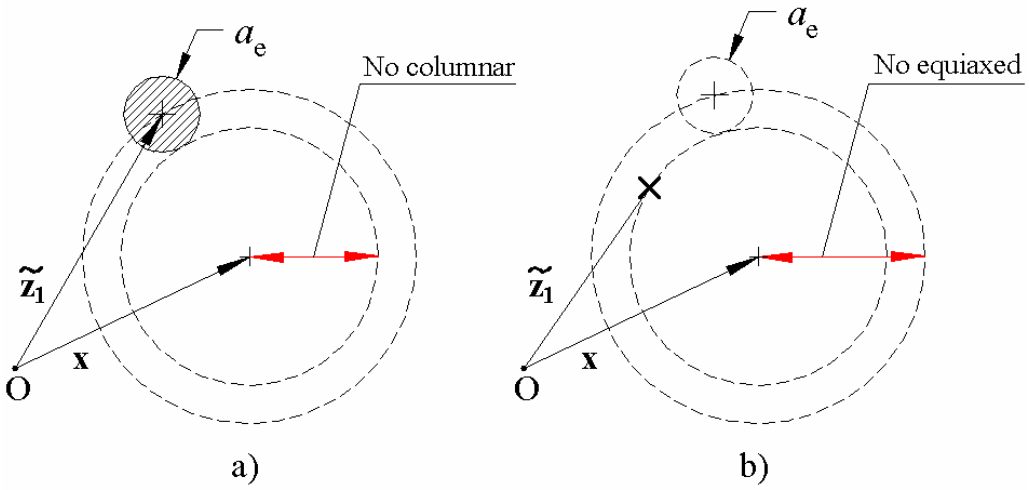

Figure 11: Computing the nearest neighbor distribution for the equiaxed (a) and columnar (b) distributions

Hence, to compute $\tilde{f}_e^{(1)}$, one has to quantify as well the probability that a columnar tip centered between $\mathbf{x}$ and $\tilde{\mathbf{z}}_1$ is closer to $\mathbf{x}$ than the existing equiaxed grain at $\tilde{\mathbf{z}}_1$. Due to the finite dimension of the equiaxed grains ($a_e>0$) two cases have to be analyzed. First, if $\left|\mathbf{x}-\tilde{\mathbf{z}}_1\right|\le a_e$ the equiaxed grain centered at $\tilde{\mathbf{z}}_1$ "touches" the point $\mathbf{x}$. Since the columnar tips penetrate into an developed equiaxed grain and can only "nucleate" within the liquid space between the equiaxed grains (i.e. the equiaxed extra-dendritic liquid) it is obvious that there is no possibility that a columnar grain centered between $\mathbf{x}$ and $\tilde{\mathbf{z}}_1$ be closer that the equiaxed grain at $\tilde{\mathbf{z}}_1$. Hence, the probability that an equiaxed grain centered at $\tilde{\mathbf{z}}_1$ is the closest to $\mathbf{x}$ among all particles in the ingot can be identified in this particular case ($\left|\mathbf{x}-\tilde{\mathbf{z}}_1\right|\le a_e$) to $P\left(A_e\right)$. One has:

$$\widetilde{f}_e^{(1)}\left(t,\mathbf{x};\tilde{\mathbf{z}}_1\right)d\tilde{\mathbf{z}}_1=\widehat{f}_e^{(1)}\left(t,\mathbf{x};\tilde{\mathbf{z}}_1\right)\tilde{\mathbf{z}}_1\ ,\qquad \left|\mathbf{x}-\tilde{\mathbf{z}}_1\right|\le a_e \tag{106}$$

In contrast, if $\left|\mathbf{x}-\tilde{\mathbf{z}}_1\right|>a_e$ any columnar tips centered at $\tilde{\mathbf{z}}_1^*$ such as $\left|\mathbf{x}-\tilde{\mathbf{z}}_1^*\right|<\left|\mathbf{x}-\tilde{\mathbf{z}}_1\right|-a_e$ (see Figure Figure 11a) will be obviously closer to $\mathbf{x}$ than the equiaxed grain at $\tilde{\mathbf{z}}_1$. It is important to notice that columnar grains centered at $\tilde{\mathbf{z}}_1^*$ such as $\left|\mathbf{x}-\tilde{\mathbf{z}}_1\right|-a_e\le\left|\mathbf{x}-\tilde{\mathbf{z}}_1^*\right|\le\left|\mathbf{x}-\tilde{\mathbf{z}}_1\right|$ are not considered to be closer to $\mathbf{x}$ than the equiaxed grain at $\tilde{\mathbf{z}}_1$. Indeed, due to its finite dimension, the equiaxed grain at $\tilde{\mathbf{z}}_1$ will influence preponderantly the field $\psi\left(\mathbf{x},t\right)$ (i.e. solutal field, velocity, pressure, etc.) and not the columnar tip at $\tilde{\mathbf{z}}_1^*$. Denoting now with B_c the event that there is no columnar tip centered within the spherical cell of radius $\left|\mathbf{x}-\tilde{\mathbf{z}}_1\right|-a_e$ and centered at $\mathbf{x}$, $\widetilde{f}_e^{(1)}\left(t,\mathbf{x};\tilde{\mathbf{z}}_1\right)$ becomes

$$\begin{aligned}\widetilde{f}_e^{(1)}\left(t,\mathbf{x};\tilde{\mathbf{z}}_1\right)d\tilde{\mathbf{z}}_1&=P\left(A_e\cap B_c\right)\\&=P\left(B_c\middle|A_e\right)P\left(A_e\right)\end{aligned} \tag{107}$$

The conditional probability $P\left(B_c\middle|A_e\right)$ can be computed with the help of the conditional probability $\widehat{f}_e^{(1)}\left(t,\mathbf{x};\tilde{\mathbf{z}}_1^*\middle|A_e\right)d\tilde{\mathbf{z}}_1^*$ that a columnar tip centered at $\tilde{\mathbf{z}}_1^*$ is the closest to $\mathbf{x}$ among the columnar particles, given the event A_e that the closest equiaxed grain to $\mathbf{x}$ is at $\tilde{\mathbf{z}}_1$. It is shown in the Appendix B that:

$$\widehat{f}_c^{(1)}\left(t,\mathbf{x};\tilde{\mathbf{z}}_1^*\middle|A_e\right)=n_c^0\cdot\exp\left[-\frac{4}{3}\pi n_c^0\left(\left|\mathbf{x}-\tilde{\mathbf{z}}_1^*\right|\right)^3\right]\ ,\ \left|\mathbf{x}-\tilde{\mathbf{z}}_1^*\right|<\left|\mathbf{x}-\tilde{\mathbf{z}}_1\right|-a_e \tag{108}$$

Now, it is easy to see that

$$\begin{aligned}P\left(B_c\middle|A_e\right)&=1-\int\limits_{\left|\mathbf{x}-\tilde{\mathbf{z}}_1^*\right|<\left|\mathbf{x}-\tilde{\mathbf{z}}_1\right|-a_e}\widehat{f}_c^{(1)}\left(t,\mathbf{x};\tilde{\mathbf{z}}_1^*\middle|A_e\right)d\tilde{\mathbf{z}}_1^*\\&=\exp\left[-\frac{4}{3}\pi n_c^0\left(\left|\mathbf{x}-\tilde{\mathbf{z}}_1\right|-a_e\right)^3\right]\end{aligned} \tag{109}$$

Thus, the distribution function $\widetilde{f}_e^{(1)}$ becomes

$$\widetilde{f}_e^{(1)}\left(t,\mathbf{x};\tilde{\mathbf{z}}_1\right)=\begin{cases}n_e e^{-\frac{4}{3}\pi n_e\left(\left|\mathbf{x}-\tilde{\mathbf{z}}_1\right|\right)^3} & if\quad \left|\mathbf{x}-\tilde{\mathbf{z}}_1\right|\le a_e\\ n_e e^{-\frac{4}{3}\pi n_c^0\left(\left|\mathbf{x}-\tilde{\mathbf{z}}_1\right|-a_e\right)^3}e^{-\frac{4}{3}\pi n_e\left(\left|\mathbf{x}-\tilde{\mathbf{z}}_1\right|\right)^3} & if\quad \left|\mathbf{x}-\tilde{\mathbf{z}}_1\right|>a_e\end{cases} \tag{110}$$

4.2.2. Columnar nearest neighbor distribution function. Notice again that due to the finite dimension of the equiaxed particles a columnar particle positioned at $\tilde{\mathbf{z}}_1$ can be the closest particle

to **x** only if there is no equiaxed particle within a range $\left|\mathbf{x}-\tilde{\mathbf{z}}_1\right|+a_e$ around the point **x** (Figure 11b). By considering the two following events, A_c the event that a columnar tip positioned at $\tilde{\mathbf{z}}_1$ is the closest columnar particle to **x** and B_e the event that there is no equiaxed particle within a range $\left|\mathbf{x}-\tilde{\mathbf{z}}_1\right|+a_e$ around the point **x**, one has

$$\begin{aligned}\tilde{f}_c^{(1)}\left(t,\mathbf{x};\tilde{\mathbf{z}}_1\right)d\tilde{\mathbf{z}}_1 &= P\left(A_c\cap B_e\right)\\ &= P\left(A_c\middle|B_e\right)P\left(B_e\right)\end{aligned} \tag{111}$$

The B_e probability can be easily computed with the help of the $\hat{f}_e^{(1)}\left(t,\mathbf{x};\tilde{\mathbf{z}}_1\right)$ distribution that there the closest equiaxed particle to **x** is centered within $d\tilde{\mathbf{z}}_1$ of $\tilde{\mathbf{z}}_1$. Indeed, it is clear that

$$\begin{aligned}P\left(B_e\right) &= 1-\int\limits_{\left|\mathbf{x}-\tilde{\mathbf{z}}_1'\right|<\left|\mathbf{x}-\tilde{\mathbf{z}}_1\right|+a_e}\hat{f}_e^{(1)}\left(t,\mathbf{x};\tilde{\mathbf{z}}_1'\right)d\tilde{\mathbf{z}}_1'\\ &= \exp\left[-\frac{4}{3}\pi n_e\left(\left|\mathbf{x}-\tilde{\mathbf{z}}_1\right|+a_e\right)^3\right]\end{aligned} \tag{112}$$

In turn the probability $P\left(A_c\middle|B_e\right)$ can be derived from the conditional probability $\hat{f}_c^{(1)}\left(t,\mathbf{x};\tilde{\mathbf{z}}_1\middle|B_e\right)$ that the closest columnar particle to **x** is at $\tilde{\mathbf{z}}_1$, given no equiaxed particle within a range $\left|\mathbf{x}-\tilde{\mathbf{z}}_1\right|+a_e$ around the point **x** (see Figure 11b). Similar to the second case analysed in the Appendix B one can obtain

$$\hat{f}_c^{(1)}\left(t,\mathbf{x};\tilde{\mathbf{z}}_1\middle|B_e\right) = n_c^0\cdot\exp\left[-\frac{4}{3}\pi n_c^0\left(\left|\mathbf{x}-\tilde{\mathbf{z}}_1\right|\right)^3\right] \tag{113}$$

Hence, the columnar nearest neighbor distribution becomes

$$\tilde{f}_c^{(1)}\left(t,\mathbf{x};\tilde{\mathbf{z}}_1\right) = n_c^0\exp\left(-\frac{4}{3}\pi n_e\left(\left|\mathbf{x}-\tilde{\mathbf{z}}_1\right|+a_e\right)^3\right)\exp\left(-\frac{4}{3}\pi n_c^0\left(\left|\mathbf{x}-\tilde{\mathbf{z}}_1\right|\right)^3\right) \tag{114}$$

4.2.3. The double mechanical blockage effect. In Figure 12 the two nearest distributions $\tilde{f}_{c,e}^{(1)}\left(t,\mathbf{x};\tilde{\mathbf{z}}_1\right)$, characterizing the coexistence state along with the $\hat{f}_c^{(1)}\left(t,\mathbf{x};\tilde{\mathbf{z}}_1\middle|B_e\right)$ and $\hat{f}_e^{(1)}\left(t,\mathbf{x};\tilde{\mathbf{z}}_1\right)$ distributions characterizing the equiaxed and columnar structures just before their coexistence (Figure 10) are presented for $a_e=810\,\mu m$, $n_e=10^8\,grains/m^3$ and $n_c^0=10^{10}\,grains/m^3$. As a general trend the coexistence state is characterized by a decrease in the probabilities $\tilde{f}_{c,e}^{(1)}\left(t,\mathbf{x};\tilde{\mathbf{z}}_1\right)d\tilde{\mathbf{z}}_1$ that the closest grain to **x** is columnar/equiaxed and is centered at $\tilde{\mathbf{z}}_1$.

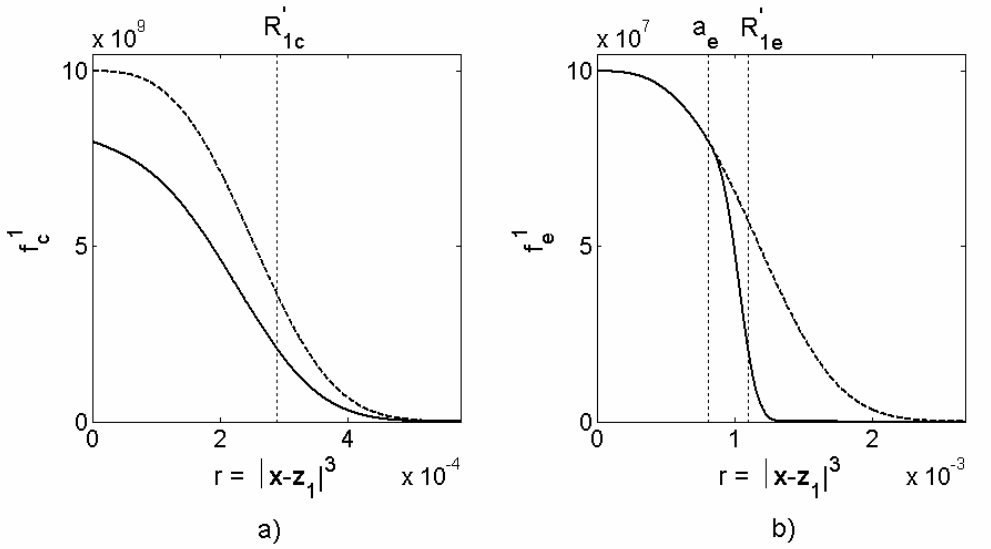

Figure 12: The nearest columnar (a) and equiaxed (b) neighbor distribution before (dashed line) and after (full line) the c/e coexistence ($a_e = 810\,\mu m$, $n_e = 10^8$ *grains/m*^{3} and $n_c = 10^{10}$ *grains/m*^{3})

Using the two analytical distributions in (110) and (114) the two columnar and equiaxed fractions as defined in (102) and (103) can now be computed

$$\begin{aligned} \varepsilon_c &= \exp\left(-\frac{4}{3}\pi n_e a_e^{\,3}\right) - I \\ \varepsilon_e &= 1 - \exp\left(-\frac{4}{3}\pi n_e a_e^{\,3}\right) + I \end{aligned} \tag{115}$$

where $r = \left|\mathbf{x} - \tilde{\mathbf{z}}_1\right|$ and

$$I = \int_0^\infty n_e \exp\left[-\frac{4}{3}\pi n_e \left(r + a_e\right)^3\right] \exp\left(-\frac{4}{3}\pi n_c^0 r^3\right) 4\pi \left(r + a_e\right)^2 dr \tag{116}$$

is a positive infinite integral having no explicit expression. As expected ε_e and ε_c sum to one validating a physically important constraint. Indeed, the probability to find the closest grain to **x** (regardless of its nature) centered between **x** and ∞ must be 1. Note that $\left[1 - \exp\left(-4/3\pi n_e a_e^{\,3}\right)\right]$ is no more than the equiaxed grain fraction ε_{ge} (0.2 for the case in Figure 12). By defining the characteristic function X_{ge} (equal to 1 if the point **x** is within an equiaxed grain and 0 otherwise) and using (98) the equiaxed grain fraction becomes indeed

$$\begin{aligned} \varepsilon_{ge}\left(\equiv \overline{X_{ge}}\right) &= \int_{\left|\mathbf{x} - \tilde{\mathbf{z}}_1\right| \le a_e} \tilde{f}_e^{(1)}\left(t, \mathbf{x}; \tilde{\mathbf{z}}_1\right) d\tilde{\mathbf{z}}_1 \\ &= 1 - \exp\left(-4/3\pi n_e a_e^{\,3}\right) \end{aligned} \tag{117}$$

Since $I > 0$ one has thus $\varepsilon_e > \varepsilon_{ge}$ and $\varepsilon_c < 1 - \varepsilon_{ge}$. These two inequalities express another important constraint of the coexistence state: the newly germinated columnar phase cannot occupy a space larger than the available space for its germination existing prior to columnar "nucleation", namely the equiaxed extra-dendritic liquid $1 - \varepsilon_{ge}$. Indeed, due to the finite dimension of the

equiaxed grains, the columnar tips can only "nucleate" within the equiaxed extra-dendritic liquid (see Figure 10) and the subsequent columnar fraction will be therefore always smaller than $1-\varepsilon_{ge}$. This particular constraint has another important consequence on the columnar structure. Note first that $\tilde{f}_c^{(1)}(t,\mathbf{x};\mathbf{x})$ is equal as well to the unconditional density function for any columnar tip being at $\mathbf{x}$, $f_c^{(1)}(t,\mathbf{x})$. Remember that, given the hypothesis of a local homogeneous grain distribution, $f_c^{(1)}(t,\mathbf{x})$ equals as well the local columnar grain density n_c, equation (23). Hence, one has

$$\begin{aligned} f_c^{(1)}(t,\mathbf{x})\ (\equiv n_c) &= \tilde{f}_c^{(1)}(t,\mathbf{x};\mathbf{x}) \\ &= n_c^0\left(1-\varepsilon_{ge}\right) \end{aligned} \tag{118}$$

that is, the columnar grain density characterizing the coexistence (n_c) will be lower than n_c^0, the columnar grain density valid just before the columnar "penetration" into the equiaxed zone. Indeed, due to the finite dimension of equiaxed grains the advancing column tips (Figure 13a) would be partially stopped by the equiaxed particles. Therefore, only a fraction $(1-\varepsilon_{ge})$ of the total number of columnar tips per unit volume would be able to "penetrate" the equiaxed zone. The presence of developed equiaxed grains at $\mathbf{x}$ will determine thus *a rarefaction of columnar tips* and equation (118) mathematically expresses this blocking effect. We will hereafter refer to this effect as to the *first mechanical blockage effect* of the coexistence.

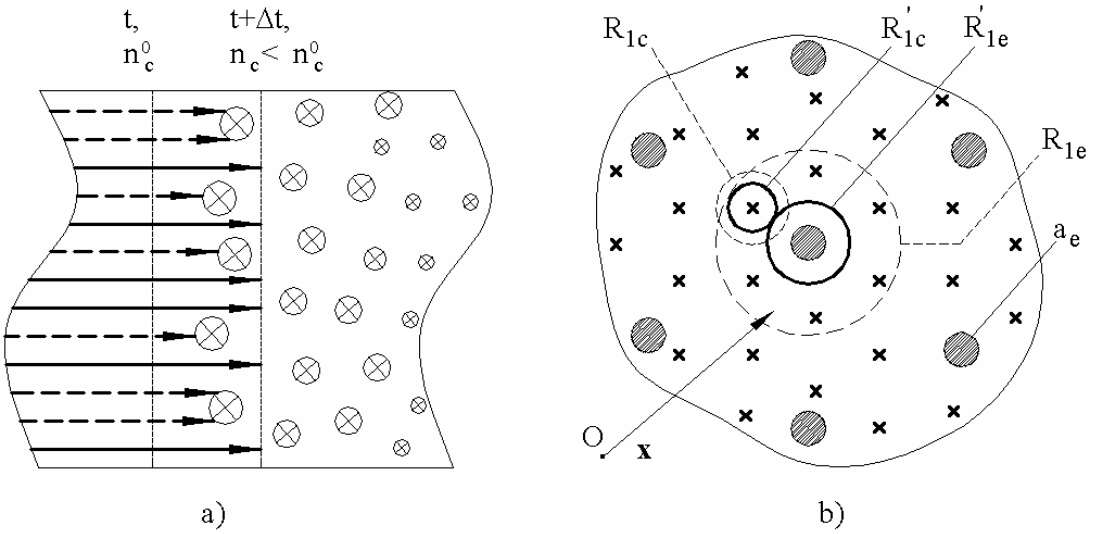

Figure 13: The first (a) and the second (b) mechanical blockage: the full line circles represent the two cells characterizing the mixed c/e zone and the dashed line circles are the cells characterizing the two structures (c/e) separately, that is just before the coexistence state

Apart from the decrease of the columnar grain density (Equation (118)), one can see from Figure 12 that both $\tilde{f}_{c/e}^{(1)}$ distributions become negligible for a smaller $r=\left|\mathbf{x}-\tilde{\mathbf{z}}_1\right|$ than their correspondant single grain distributions. Indeed, looking closely to their particular exponential variation (cf. equations (110) and (114)), one can easily identify a characteristic distance from **x**, above which the two distributions decrease rapidly towards 0. Each exponential term of type $\exp\left(-4/3\pi n r^3\right)$ remains of order of 1 for $r\le\left(4/3\pi n\right)^{-1/3}$ and decrease rapidly towards *0* for $r>\left(4/3\pi n\right)^{-1/3}$. Therefore one can easily identify the two characteristic distances from **x** as

$$R_{1c}^{'} = \min\left(R_{1c},\, R_{1e} - a_e\right)$$
$$R_{1e}^{'} = \min\left(R_{1c} + a_e,\, R_{1e}\right) \tag{119}$$

where

$$R_{1c} = \left(4/3\pi n_c^0\right)^{-1/3}, \qquad R_{1e} = \left(4/3\pi n_e\right)^{-1/3} \tag{120}$$

Remember that $R_{1c/e}$ represents half of the average distance between two adjacent c/e grains before their coexistence (Figure 10) and quantify as well the cell dimension used in the modeling of the ensemble average for a single grain distribution, e.g., equation (42). Likewise, the distance $R_{1c/e}^{'}$ would represent the average distance between two adjacent c/e particles characterizing the coexistence state. In addition $R_{1c}^{'} + R_{1e}^{'}$ would be the average distance between two different adjacent grains (a columnar and an equiaxed grain, see Figure 13b). Moreover, from the equation (119), one has

$$R_{1c}^{'} < R_{1c} \ , \qquad R_{1e}^{'} < R_{1e} \tag{121}$$

meaning that the coexistence state is characterized by smaller average distances between particles compared with the single grain distribution state valid just before the coexistence. Consequently, the two spherical cells describing at **x** the statistics of the two c/e distributions will be smaller than the ones valid just before the coexistence (Figure 13b). This trend is physically plausible since subsequent to the columnar "nucleation an increase number of particles will have to share the same space. We will hereafter refer to this effect as to *the second mechanical blockage* effect of the coexistence. Notice that this effect is of primary importance for the evolution of the coexisting c/e grains since it's directly linked to the diffusion lengths characterizing the solute fluxes in the c/e extra-dendritic liquid. Indeed the two diffusion lengths depend strongly on $R_{1e}^{'} - a_e$ and $R_{1c}^{'}$, respectively. Note as well that

$$R_{1e}^{'} - a_e = R_{1c}^{'} \tag{122}$$

meaning that the length scales of the coexisting columnar/equiaxed extra-dendritic liquid are equal. Therefore, the initial equiaxed extra-dendritic liquid, $1 - \varepsilon_{ge}$, is shared by the two structures such as the length scales characterizing the two coexisting extra-dendritic liquids have the same order of magnitude (Figure 13b).

An interesting limit case is the coexistence between two infinite small grain distributions, that is $a_e \to 0$. For this particular case, one obtains

$$\varepsilon_{c/e} = n_{c/e}/\left(n_c + n_e\right) \ , \qquad R_{1c}^{'}\left(= R_{1e}^{'}\right) = \left[\frac{4}{3}\pi\left(n_c + n_e\right)\right]^{-1/3} \tag{123}$$

Note that $R_{1c}^{'} = R_{1e}^{'}$, meaning that the average distance between two adjacent grains (equiaxed and/or columnar) is equal. Indeed, due to the infinite small dimension of the two structures and due to their homogeneous distribution in space, the mixing between columnar and equiaxed grains would be equivalent from a statistical point of view to a homogenous grain distribution having the density $\left(n_c + n_e\right)$ for which no distinction is made between equiaxed and columnar nuclei. Note however that the equality in (123) does not mean an equal filling of space with columnar and equiaxed nuclei. The average distance between two particles is the same but each type of grain will fill a given volume according to its grain density $n_{c/e}$. If, for example, $n_c \gg n_e$ one will find in the ingot many more columnar nuclei than equiaxed ones. This unbalance is well reflected by the

fractions (probabilities) $\varepsilon_{c/e}$; one has $\varepsilon_c \gg \varepsilon_e$ in this case, meaning that it is much more likely that the closest particle to **x** be a columnar particle than an equiaxed one.

4.2.4. The cell model. The use of the exact formulations (110) and (114) to compute an ensemble averages, equation (98), would be extremely complex. Moreover, the c/e fractions ε_c and ε_e, key parameters within an average model, have no explicit form for $a_e > 0$. Therefore, a simpler form for $\tilde{f}_{c/e}^{(1)}$, resulting in an explicit formulation for $\varepsilon_{c/e}$, would be of great interest.

Note first that a coexistence state between equiaxed and columnar grains is always succeeding a state where equiaxed and columnar structures grains evolve separately. Thus, one can logically assume that this previous state is modeled using the cell model approach developed for a single grain distribution , throughout paragraph 3 In this respect, the exact forms for $\hat{f}_e^{(1)}\left(t,\mathbf{x};\tilde{\mathbf{z}}_1\right)$, $\hat{f}_c^{(1)}\left(t,\mathbf{x};\tilde{\mathbf{z}}_1^*\middle|A_e\right)$ and $\hat{f}_c^{(1)}\left(t,\mathbf{x};\tilde{\mathbf{z}}_1\middle|B_e\right)$, equations (105), (108) and (113), could be replaced with their corresponding cell model approximations

$$\hat{f}_e^{(1)}\left(t,\mathbf{x};\tilde{\mathbf{z}}_1\right)=\begin{cases} n_e & if \quad \left|\mathbf{x}-\tilde{\mathbf{z}}_1\right|\le R_{1e} \\ 0 & if \quad \left|\mathbf{x}-\tilde{\mathbf{z}}_1\right|> R_{1e} \end{cases} \tag{124}$$

and

$$\hat{f}_c^{(1)}\left(t,\mathbf{x};\tilde{\mathbf{z}}_1\middle|A_e\right)\left(=\hat{f}_c^{(1)}\left(t,\mathbf{x};\tilde{\mathbf{z}}_1\middle|B_e\right)\right)=\begin{cases} n_c^0 & if \quad \left|\mathbf{x}-\tilde{\mathbf{z}}_1\right|\le R_{1c} \\ 0 & if \quad \left|\mathbf{x}-\tilde{\mathbf{z}}_1\right|> R_{1c} \end{cases} \tag{125}$$

where R_{1c} and R_{1e} are already defined in (120). Using now these approximations in (106), (109) and (113) the approximate nearest-neighbor distributions, characterizing the coexistence state, become respectively

$$\tilde{f}_e^{(1)}\left(t,\mathbf{x};\tilde{\mathbf{z}}_1\right)=\begin{cases} n_e & if \quad \left|\tilde{\mathbf{z}}_1-\mathbf{x}\right|\le a_e \\ n_e\left[1-\frac{4}{3}\pi\left(\left|\tilde{\mathbf{z}}_1-\mathbf{x}\right|-a_e\right)^3 n_c^0\right] & if \quad \left|\tilde{\mathbf{z}}_1-\mathbf{x}\right|\in\left(a_e;R_{1e}^{'}\right] \\ 0 & if \quad \left|\tilde{\mathbf{z}}_1-\mathbf{x}\right|> R_{1e}^{'} \end{cases} \tag{126}$$

and

$$\tilde{f}_c^{(1)}\left(t,\mathbf{x};\tilde{\mathbf{z}}_1\right)=\begin{cases} n_c^0\left[1-\frac{4}{3}\pi\left(\left|\tilde{\mathbf{z}}_1-\mathbf{x}\right|+a_e\right)^3 n_e\right] & if \quad \left|\tilde{\mathbf{z}}_1-\mathbf{x}\right|\le R_{1c}^{'} \\ 0 & if \quad \left|\tilde{\mathbf{z}}_1-\mathbf{x}\right|> R_{1c}^{'} \end{cases} \tag{127}$$

where $R_{1c}^{'}$ and $R_{1e}^{'}$ are already defined in (119). A graphic comparison between the exact distributions and their corresponding approximation is given in Figure 14 for $a_e = 810\,\mu m$, $n_e = 10^8$ grain/m^3 and $n_c = 10^{10}$ grain/m^3. As one can see, (126) and (127) approximate reasonably well the exact distributions in (110) and (114). Notice the difference between the exact and the approximate columnar distributions at $r = 0$, that is $\tilde{f}_c^{(1)}\left(t,\mathbf{x};\mathbf{x}\right)\left(\equiv n_c\right)$. This is a normal consequence of the difference between the exact and the approximate equiaxed grain fraction ε_{ge}. Indeed, in contrast with the exact approach, equation (117), the cell approximation to ε_{ge} is

$$\varepsilon_{ge} = 4/3\pi n_e a_e^{\,3} \tag{128}$$

Note as well that the approximate distributions integrate the same lengths scales $R_{1c}^{'}$ and $R_{1e}^{'}$ which characterized the exact distributions.

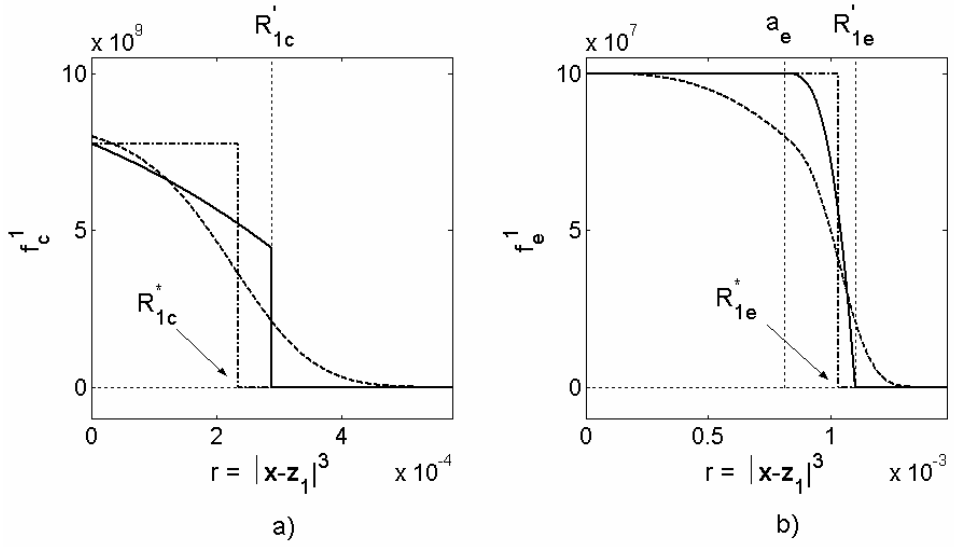

Figure 14: The exact (dash), the approximate (full) and the cell model approximation form (dash-dot) for $\widetilde{f}_c^{(1)}$ (a) and $\widetilde{f}_e^{(1)}$ (b) distributions, ($a_e = 810\,\mu m$,$n_e = 10^8$ grain/m^3 and $n_c = 10^{10}$ grain/m^3)

Using (131) the c/e fraction can be now computed explicitly. One obtains

$$\frac{\varepsilon_c}{(1-\varepsilon_e)} = \begin{cases} 1-\varepsilon_{ge} - \dfrac{1}{20n_c^0}\left[\begin{array}{l} 10n_e + 36(n_e)^{\frac{2}{3}}\left(n_c^0\varepsilon_{ge}\right)^{\frac{1}{3}} \\ +45(n_e)^{\frac{1}{3}}\left(n_c^0\varepsilon_{ge}\right)^{\frac{2}{3}} \end{array}\right] & if \quad R_{1c} \le R_{1e}\left(1-\varepsilon_{ge}^{\,1/3}\right) \\ \dfrac{n_c^0}{20n_e}\left[\begin{array}{l} \left(\varepsilon_{ge}\right)^2 - 20\varepsilon_{ge} + 45\left(\varepsilon_{ge}\right)^{\frac{2}{3}} \\ -36\left(\varepsilon_{ge}\right)^{\frac{1}{3}} + 10 \end{array}\right] & if \quad R_{1c} > R_{1e}\left(1-\varepsilon_{ge}^{\,1/3}\right) \end{cases} \tag{129}$$

where ε_{ge} is the equiaxed grain fraction computed with the cell model approximation, equation (128). A plot of (129) is given in Figure 15. Note that, in contrast with the discrete distributions in (126) and (127), the resulting c/e fraction is a continuous function. Notice as well that the constraint $\varepsilon_c < 1-\varepsilon_{ge}$ is verified too.

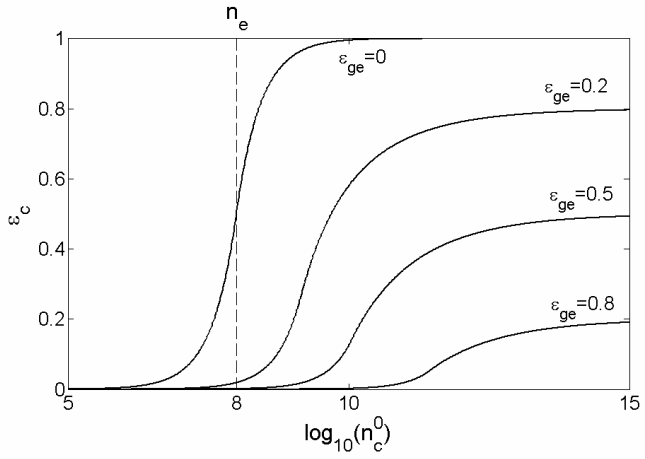

Figure 15: The columnar fraction ε_c with respect to n_c^0 and ε_{ge}, given $n_e = 10^8$ grain/m^3

However, we are looking for an even more simpler form for $\widetilde{f}_{c,e}^{(1)}$, that is for their "top hat" approximation (cell approximation)

$$\widetilde{f}_{c/e}^{(1)}\left(t,\mathbf{x};\tilde{\mathbf{z}}_1\right)=\begin{cases} n_{c/e} & if \quad \left|\mathbf{x}-\tilde{\mathbf{z}}_1\right| \le R_{1c/e}^{*} \\ 0 & if \quad \left|\mathbf{x}-\tilde{\mathbf{z}}_1\right| > R_{1c/e}^{*} \end{cases}, \tag{130}$$

where $n_c = n_c^0\left(1-\varepsilon_{ge}\right)$. The two length scales $R_{1c/e}^{*}$ can be determined by ensuring that

$$\int \widetilde{f}_{c,e}^{(1)}\left(t,\mathbf{x};\tilde{\mathbf{z}}_1\right)d\tilde{\mathbf{z}}_1 = \varepsilon_{c,e}\,, \tag{131}$$

One easily obtains for $R_{1c,e}^{*}$

$$R_{1c,e}^{*}=\left(\frac{4}{3}\pi n_{c,e}\right)^{-1/3}\varepsilon_{c,e}{}^{1/3} \tag{132}$$

The cell approximations to $\widetilde{f}_c^{(1)}$ and $\widetilde{f}_e^{(1)}$ are now fully determined from (130) and (132). A plot of these two "top-hat" distributions is shown in Figure 14 along with their exact and approximated forms. It is important to see that, even if equations in (130) represent a double approximation for the exact distributions (110) and (114), they integrate in a much simpler form all the constraints and features characterizing the exact distributions. First, $\varepsilon_c + \varepsilon_e = 1$. Then the inequality $\varepsilon_c < 1-\varepsilon_{ge}$ is verified as well. Moreover, the length scales, $R_{1c,e}^{*}$, characterizing the c/e cells are of the same order of magnitude with $R_{1c,e}^{'}$, previously determined for the exact distributions. Indeed it can be verified that

$$\begin{aligned} 0.63 < R_{1c}^{*}/R_{1c}^{'} < 1 \\ 0.79 < R_{1e}^{*}/R_{1e}^{'} < 1 \end{aligned} \tag{133}$$

Finally, the length scales of the c/e extradendritic liquid characterizing the coexistence are of the same order of magnitude. It can be verified that

$$0.63 < R_{1c}^{*} / \left(R_{1e}^{*} - a_e \right) < 1.34 \tag{134}$$

With the help of the cell approximations to $\tilde{f}_{c,e}^{(1)}$ one is now able to easily compute c/e averages using the general equation (98). For a generic field ψ one obtains

$$\begin{aligned} \overline{\psi}_{c,e}\left(\mathbf{x},t\right) &= \frac{1}{\varepsilon_{c,e}} \int \tilde{f}_{c,e}^{(1)}\left(t,\mathbf{x};\tilde{\mathbf{z}}_1\right) \tilde{\psi}^{(1)}\left(t,\mathbf{x};\tilde{\mathbf{z}}_1\right) d\tilde{\mathbf{z}}_1 \\ &= \frac{n_{c,e}}{\varepsilon_{c,e}} \int\limits_{\left|\mathbf{x}-\tilde{\mathbf{z}}_1\right| \le R_{1c,e}^{*}} \tilde{\psi}^{(1)}\left(t,\mathbf{x};\tilde{\mathbf{z}}_1\right) d\tilde{\mathbf{z}}_1 \end{aligned} \tag{135}$$

It is worthwhile to notice that the use of the cell model transforms the infinite integrals in (98) into definite ones. The equiaxed and columnar averages reduce to an integral over all possibile positions ($\tilde{\mathbf{z}}_1$) of the closest columnar/equiaxed grain to **x** within the two spherical cells of radius $R_{1c,e}^{*}$ and centered at **x** (Figure 16). This result is of great importance since it quantifies the two sub-ensembles $\theta_{c,e}$, defined in (99) (ensembles of realizations such as the closest particle to **x**, at time *t*, be a columnar/equiaxed one). Indeed, in the light of the cell model θ_c become the ensemble of realizations such as the closest particle to **x** is columnar and is centered within the cell of radius R_{1c}^{*} centered at **x**. Likewise, θ_e is the ensemble of realizations such as the closest particle to **x** is equiaxed and is centered within the sphere of radius R_{1e}^{*} centered at **x**.

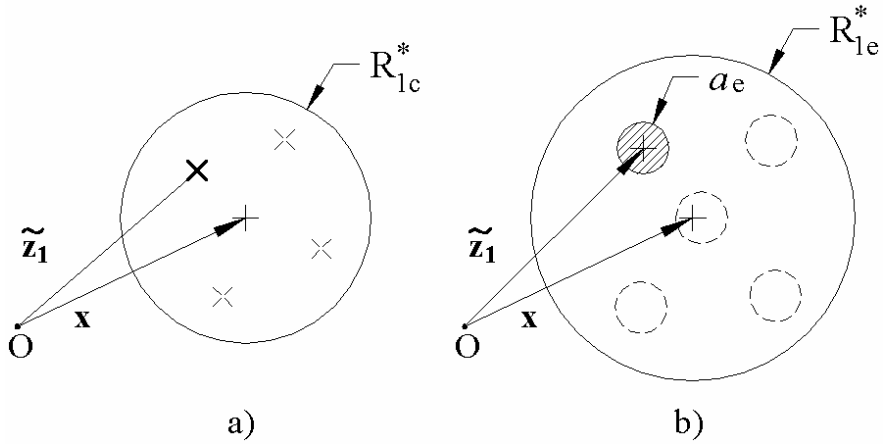

Figure 16: The cell model approximation to the columnar (a) and the equiaxed (b) ensemble average

Using the cell model, one can easily express as well *e/c* interfacial averages like $S_{ke/c}$, $\overline{\Phi^{\psi}}_{ke/c}$ or $\overline{\Gamma^{\psi}}_{ke/c}$. Their mathematical formulation will be very similar to the one used for the case of single grain distribution, equations (52) and (53), with the difference that all integrations are made over all possible positions of the equiaxed/columnar particle within the cell of radius $R_{1e/c}^{*}$ such as the point **x** is on the *e/c* solid interface. For exemple, the generic exchange term $\overline{\Phi^{\psi}}_{k}$ written for the equiaxed strucure would write as follows

$$\begin{aligned}\overline{\Phi^{\psi}}_{ke} &= n_e \int_{\left|\mathbf{x}-\tilde{\mathbf{z}}_1\right|\le R_{1e}^*} \left(-j_{ke}^{\psi}\mathbf{n}_{ke}\right)\cdot\left[-\mathbf{n}_{ke}\delta\left(\mathbf{x}-\mathbf{x}_i\left(t\right)\right)\right] d\tilde{\mathbf{z}}_1 \\ &= n_e \int_{\Omega(a_e)} j_{ke}^{\psi} d\Omega \qquad \left(= S_{ke}\overline{j_{ke}^{\psi}}^{*}\right)\end{aligned} \tag{136}$$

that is, an integral over all posible positions ($\tilde{\mathbf{z}}_1$) of the equiaxed grain within the equiaxed cell of radius R_{1e}^* and such as the point **x** is on the *k* phase interface. Hence, using the two nearest-neighbor distributions two spherical cells have been delimited around **x**, characterizing the statistics of the coexisting c/e structures. Moreover the cell of radius $R_{1c,e}^*$ enveloping a c/e grain will delimit locally the "zone of influence" of that grain. Any point outside this sphere will be under the influence of a neighbor particle.

4.3. Model closure

The physical assumptions valid at the micro-scale remain exactly the same as those defined for a single grain distribution. Note however that the scale separation between the inter- and the extra-dendritic liquid divide now the total liquid into four sub-phases: the equiaxed inter- (*de*) and extra- (*le*) dendritic liquid and the columnar inter- (*dc*) and extra- (*lc*) dendritic liquid. Therefore, the solute field around an equiaxed or a columnar grain has to be reviewed since one has to take into account the fact that the solute diffusion in the *e/c* extra-dendritic liquid is limited within the cell of radius $R_{1e/c}^*$ enveloping each *e/c* grain. However using the hypotheses of the local thermal equilibrium at the scale of the grain the solute field in the *e/c* extra-dendritic liquid will be a function of *r* only. Moreover since

$$R_{1c}^* \simeq R_{1e}^* - a_e \tag{137}$$

the *e/c* cell boundary will play the role of a symmetry surface between two adjacent grains. Hence, locally, the solute flux between two adjacent grains is zero, namely

$$\left(\frac{\partial C_{le/c}}{\partial r}\right)_{R_{1e/c}^*} = 0 \tag{138}$$

In this respect the solute diffusion field already determined for the case of a single grain distribution (Appendix A) can be used for the two coexisting structures too. In (A.18) one needs only to replace R_1 with $R_{1e/c}^*$ and a with $a_{e,c}$ in order to obtain the corresponding *e/c* solute fields.

4.3.1. Final averaged equations. Given the separation between the inter- and extra-dendritic liquid, for the case of equiaxe/columnar coexistence six distinct phases can be identified: the c/e (columnar/equiaxed) solid (*sc*, *se*), the c/e inter-dendritic liquid (*dc*, *de*) and finally the c/e extra-dendritic liquid (*lc*, *le*). Basically the problem is a three-phase one: *se* + *sc* + total liquid (*f*). However, the present model needs to quantify for the solute balance within the c/e extra-dendritic liquid and therefore one has to account as well for the virtual separation of the total liquid in four sub-phases ($f = de + le + dc + lc$).

Before writing the final averaged equation first one has to define the characteristic functions X_k, equation (4), for each of the six phases, $k \in \{se, de, le, sc, dc, lc\}$. Then using the averaged variables defined in Table 1 the generic balance equation, (8) can be particularized to obtain respectively the mass, energy and solute balance for each phase.

Grain balance equations

The equiaxed grain balance remains unchanged with the one determined for the single grain distribution case

$$\partial n_e / \partial t + \cancel{div\left(\mathbf{w}_{se} n_e\right)} = n_e^0 \delta\left(T - T_{Ne}\right) \tag{139}$$

where δ is the Dirac delta function, T the local temperature, T_{Ne} the equiaxed nucleation temperature and n_e^0 is the germination nuclei density.

As pointed out, in contrast with the equiaxed germination, the "columnar nucleation" can not be treated as a local event since the positions of the columnar front at a precise moment cannot be linked to local parameters only. In the absence of a precise local criterion defining the columnar front, one has to track exactly the position of the columnar front at each moment. In this light, the columnar nucleation can be approached with a local instantaneous germination

$$\partial n_c / \partial t = n_c^{'} \delta\left[\mathbf{x} - \mathbf{x}_{cf}(t)\right] \tag{140}$$

where again δ is the Dirac delta function, $\mathbf{x}_{cf}(t)$ the known columnar front position at time *t* and $n_c^{'}$ the columnar germination nuclei density. It was proven that the columnar tips penetrating into a developed equiaxed structure will be partially blocked by the equiaxed grains (first mechanical blockage), equation (118). Hence, $n_c^{'} = n_c^0\left(1 - \varepsilon_{ge}\right)$ where ε_{ge} is the local equiaxed grain fraction ($\varepsilon_{se} + \varepsilon_{de}$) and n_c^0 is the local columnar grain density valid just before the columnar "nucleation" within the equiaxed zone. In turn, n_c^0 is linked, equation (13), to the local primary arm spacing λ_1. Note that with the help of n_c^0, n_e, ε_{ge}, the columnar and equiaxed fractions as defined in (129) and the two cell radii R_{1c}^*, R_{1e}^* can now be computed. The cell model to the ensemble average can therefore be applied as detailed in the precedent section, equations (135), (136).

Mass balance

The mass balance for the two solid phases (*sc* and *se*) and for the total liquid (*f*) become respectively

$$\begin{aligned} &\partial\left(\varepsilon_{se}\rho_s\right)/\partial t = \Gamma_{se}\ , \qquad \partial\left(\varepsilon_{sc}\rho_s\right)/\partial t = \Gamma_{sc} \\ &\partial\left(\varepsilon_f\rho_f\right)/\partial t = -\left(\Gamma_{se} + \Gamma_{sc}\right) \end{aligned} \tag{141}$$

where Γ_{se} and Γ_{sc} are the mass exchange rates between the total liquid and the equiaxed and columnar solid respectively. Both Γ_{se} and Γ_{sc} can be computed from the solute balance in the *e/c* inter-dendritic liquid. To account for the inter/extra- dendritic separation, the mass balances for the *e/c* inter-dendritic liquid have to be considered too

$$\partial\left(\varepsilon_{dk}\rho_f\right)/\partial t = \Gamma_{gk} - \Gamma_{sk}\ , \qquad k = \{e,c\} \tag{142}$$

where Γ_{gk} is the mass exchange rate at the $dk - lk$ interface as a result of the e/*c* grain growth. Using the cell model approximation to the ensemble average one easily obtains

$$\Gamma_{gk} = \rho_f S_{gk} \overline{w}_{gk}\ , \qquad k = \{e,c\} \tag{143}$$

where $S_{gk} = n_k\left(4\pi a_k{}^2\right)$ is the grain interfacial area of the *e/c* grain envelope, a_k is the radius of the *e/c* grains and $\overline{w}_{gk}$ is the mean velocity of the *e/c* grain envelope. Similar to the single grain distribution case, $\overline{w}_{gk}$ can be computed using a standard tip kinetic law, equation (59), by replacing Ω with the corresponding local *e/c* undercooling

$$\Omega_{e/c} = \left(C_l^* - C_{le/c}\right) / C_l^* / \left(1-k\right) \tag{144}$$

Energy equation

Similar to the single grain distribution and given the local thermal equilibrium, the energy balance can be approached with a unique mixture equation. Since the density and the thermal conductivities are common to both equiaxed/columnar liquid and solid phases, the energy balance equation is identical with the one obtained for the precedent case, equation (78) in which one has evidently

$$\varepsilon_s = \varepsilon_{se} + \varepsilon_{sc}\ , \quad \varepsilon_f = 1 - \varepsilon_s\ , \quad \Gamma_s = \Gamma_{se} + \Gamma_{sc} \tag{145}$$

Solute balance

A total of six balance equations have to be written. Indeed, for each of the two structures (*e/c*) one has three corresponding solute balance equations: for the solid and for the inter- and extra-dendritic liquid

$$\begin{aligned}
&\frac{\partial\left(\varepsilon_{sk}\rho_s C_{sk}\right)}{\partial t} = div\left(\varepsilon_{sk}\rho_s D_s \nabla C_{sk}\right) + \Phi_{sk}^C + \Gamma_{sk}^C \\
&\frac{\partial\left(\varepsilon_{dk}\rho_f C_{dk}\right)}{\partial t} = div\left(\varepsilon_{dk}\rho_f D_f \nabla C_{dk}\right) + \Phi_{dk}^C + \Gamma_{dk}^C \qquad k \in \{c,e\} \\
&\frac{\partial\left(\varepsilon_{lk}\rho_f C_{lk}\right)}{\partial t} = div\left(\varepsilon_{lk}\rho_f D_f \nabla C_{lk}\right) + \Phi_{lk}^C + \Gamma_{lk}^C
\end{aligned} \tag{146}$$

Using the cell approximation to the *c/e* ensemble average, the above equations can be closed using a similar procedure as for the single grain distribution, see paragraph 3.4.2. The main difference lays in the choice of the integration cell with respect to the columnar/ equiaxed structure. Indeed, each one of the exchange terms in (146) is determined as an integral over all posible positions of the c/e grain within the cell of radius $R_{1c/e}^*$ centered at **x**, i.e. equation (136). Thus, it is easy to verify that

$$\begin{aligned}
&\Phi_{sk}^C = 0 && \Gamma_{sk}^C = C_s^* \Gamma_{sk} \\
&\Phi_{lk}^C = \frac{\rho_f S_{gk} D_l}{\delta_{lk-dk}}\left(C_l^* - C_{lk}\right) && \Gamma_{lk}^C = -C_l^* \Gamma_{gk}
\end{aligned}\ , \qquad k = \{e,c\} \tag{147}$$

and finally

$$\Phi_{dk}^C + \Gamma_{dk}^C = C_l^* \Gamma_{gk} - C_s^* \Gamma_{sk} - \frac{\rho_f S_{gk} D_l}{\delta_{lk-dk}}\left(C_l^* - C_{lk}\right)\ , \qquad k = \{e,c\} \tag{148}$$

where δ_{lk-dk} is the diffusion length characterizing the solute transfer at the *e/c* grain interface. As pointed out, this diffusion length can be computed from equation (A.18) by replacing R_l with $R_{le/c}^*$ and a with $a_{e,c}$.

Using the e/c solid mass balance equation, the solute balance in the e/c extra-dendritic liquid can be written as follows:

$$\varepsilon_{lk}\rho_f \frac{\partial C_{lk}}{\partial t} = \nabla\cdot\left(\varepsilon_{lk}\rho_f D_f \nabla C_{lk}\right) + \left(\frac{\rho_f S_{gk} D_l}{\delta_{lk-dk}} - \Gamma_{gk}\right)\left(C_l^* - C_{lk}\right),\ k=\{e,c\} \qquad (149)$$

Using the special property of δ_{lk-dk}, equation (A.19), it is easy to see that the last term of the RHS of (149) is always positive. Since the macroscopic diffusion process is only redistributing solute in the ingot, $\partial C_{lk}/\partial t \geq 0$ and therefore the extra-dendritic liquid is always enriching. Notice that the solute diffusion around an e/c grain is spatially limited to a maximum distance $R^*_{le/c}$ around each grain. This together with zero solute flux condition at the cell boundary, equation (138) will determine a continuous enriching of the extra-dendritic liquid which will finally arrive at a state of complete solute mixing. This would be equivalent with a complete stop of the grain growth. For this reason the grain growth stop will always take place for an e/c grain fraction lower than the corresponding e/c fraction one. Hence, the maximum *e/c* grain fraction will always be smaller than $\varepsilon_{e/c}$, verifying thus an important physical constraint.

4.3.2. Summary of the model. In the following table the equations of the model are sumarized. It is important to notice that it involves a six-phase approach to the solute balance. Indeed one can identify two solute balance equation in the e/c solid, two solute balances in the e/c extra-dendritic liquid and finally two equations stating for the solute balance in the e/c inter-dendritic liquid. The last two equations are presented as auxiliary equations since they are used to compute the e/c solid mass transfers, Γ_{se} and Γ_{sc}. Indeed, by fixing the concentration in the inter-dendritic liquid one encompasses the need to model C_d obtaining in turn an equation for the solidification rate $\Gamma_{se/c}$.

Table 4: Summary of the model

Main balance equations	**Solid:** $k=\{e,c\}$	**Liquid:** $k=\{e,c\}$
Mass	$\partial\left(\varepsilon_{sk}\rho_s\right)/\partial t = \Gamma_{sk}$	$\partial\left(\varepsilon_f\rho_f\right)/\partial t = -\Gamma_{se} - \Gamma_{sc}$
Energy	$\partial\left[\left(\varepsilon_s\rho_s c_s + \varepsilon_f\rho_f c_f\right)T\right]/\partial t = div\left[\left(\varepsilon_s\lambda_s + \varepsilon_f\lambda_f\right)\nabla T\right] + \left(\Gamma_{se}+\Gamma_{sc}\right)L$, $\left(\varepsilon_s = \varepsilon_{se} + \varepsilon_{sc}\right)$	
Solute	$\partial\left(\varepsilon_{sk}\rho_s C_{sk}\right)/\partial t = \nabla\cdot\left(\varepsilon_{sk}\rho_s D_s \nabla C_{sk}\right) + C_s^*\Gamma_{sk}$	$\varepsilon_{lk}\rho_f \frac{\partial C_{lk}}{\partial t} = \nabla\cdot\left(\varepsilon_{lk}\rho_f D_f \nabla C_{lk}\right) + \left(\rho_f S_{gk} D_l/\delta_{lk-dk} - \Gamma_{gk}\right)\left(C_l^* - C_{lk}\right)$
Supplementary balance eq.		
Inter-dendritic mass balance	$\partial\left(\varepsilon_{dk}\rho_f\right)/\partial t = \Gamma_{gk} - \Gamma_{sk}$	
Grain balance	$\partial n_e/\partial t = n_e^0\delta\left(T - T_{Ne}\right)$ $\partial n_c/\partial t = n_c^0\left(1-\varepsilon_{ge}\right)\delta\left[\mathbf{x} - \mathbf{x}_{cf}(t)\right]$	
Solidification rate	$\left(C_l^* - C_s^*\right)\Gamma_{sk} = \varepsilon_{dk}\rho_f\left(\partial C_l^*/\partial t\right) + \rho_f S_{gk} D_f\left(C_l^* - C_{lk}\right)/\delta_{lk-dk} - div\left(\varepsilon_{dk}\rho_f D_f \nabla C_l^*\right)$	
Auxiliary expressions		
Constraints:	$\varepsilon_{le} + \varepsilon_{de} + \varepsilon_{se} = \varepsilon_e$ $\varepsilon_{lc} + \varepsilon_{dc} + \varepsilon_{sc} = \varepsilon_c$, $\varepsilon_c + \varepsilon_e = 1$,	$\varepsilon_{de} + \varepsilon_{se} = \varepsilon_{ge}$ $\varepsilon_{dc} + \varepsilon_{sc} = \varepsilon_{gc}$

Interfacial concentrations:	$C_s^* = \begin{cases} kC_l^* & if \quad \Gamma_s \geq 0 \\ C_s & if \quad \Gamma_s < 0 \end{cases}$	$C_l^* = \left(T - T_f\right)/m$
Equiaxed/columnar fractions	$\varepsilon_e, \varepsilon_c = f\left(n_e, n_c^0, \varepsilon_{ge}\right)$, see equation (129)	
Cell radius	$R_{1k}^* = \left(4/3\pi n_k\right)^{-1/3} \varepsilon_k^{1/3}$	
Grain radius	$a_k = R_{1k} \varepsilon_{gk}^{1/3}$	
Grain envelope interfacial area	$S_{gk} = 4\pi a_k^2 n_k$	
Diffusion length	δ_{lk-dk}, see equation (A.18)	
Grain growth rate	$\Gamma_{gk} = \rho_f S_{gk} \overline{w}_{gk}$, $\quad \overline{w}_{gk} = \frac{D_l m (k-1) C_l^*}{\pi^2 \Gamma} \left[Pe_t\left(\Omega_k\right)\right]^2$	

5. Differences between the volume average and the ensemble average approach

As already anticipated one can expect to observe significant differences between the results provided by the ensemble average approach on one hand and the volume average on the other hand. In paragraph 3.4.3. the similarity between the present approach and the volume average model of Wang and Beckermann [6] was remarked. However the similarities between the two models are a direct consequence of the local homogeneity hypothesis of all fields, meaning that no local gradients at the scale of the grain are considered. In the following we will show that given the hypothesis of local non-homogeneity the ensemble and the volume average closure techniques give birth to very different results especially when the computation of the closure expressions for interfacial averaged fields are considered.

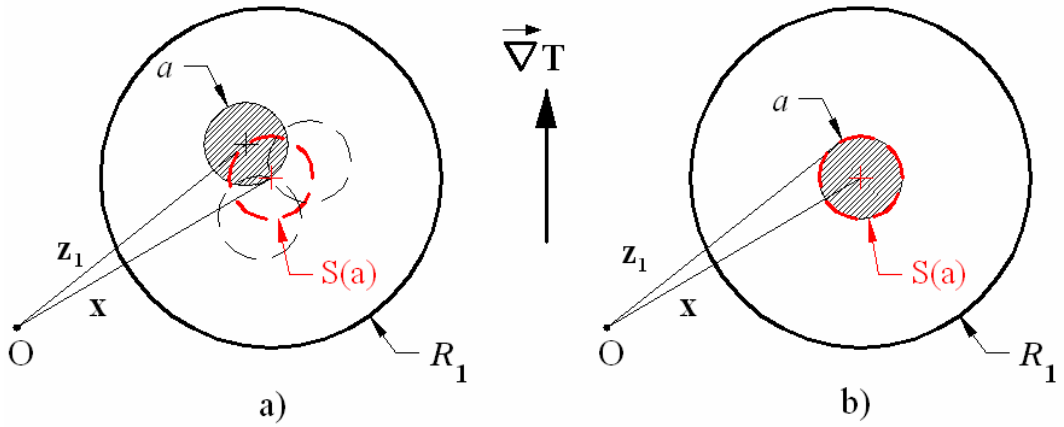

Figure 17: a) The cell approximation to the ensemble average; b) The cell approximation to the volume average.

Let us consider that no local thermal equilibrium can be considered at **x**. Hence a non-negligible thermal gradient exist at the scale of the grain. Let us denote it with ∇T (see Figure 17). Let us consider as well that the far concentration from the grain interface is constant, C_0. In this respect, let us compute for example the interfacial average Γ_g (the grain growth) using both ensemble and volume approach. The use of the ensemble average and more precisely of the cell approximation to the ensemble average, equation (53), would give the following results:

$$\begin{aligned}\Gamma_g &= n \int_{|\mathbf{x}-\tilde{\mathbf{z}}_1|\le R_1} \rho\left(-w_g \mathbf{n}_g\right)\cdot\left[-\mathbf{n}_g \delta\left(\mathbf{x}-\mathbf{x}_i(t)\right)\right] d\tilde{\mathbf{z}}_1 \\ &= n\rho_l \int_{\tilde{\mathbf{z}}_1 \in S(a)} w_g(\mathbf{x})\, dS \\ &= n 4\pi a^2 \rho_l\, w_g(\mathbf{x})\end{aligned} \tag{150}$$

where the velocity $w_k = \dfrac{D_l m(k-1) C_l^*}{\pi^2 \Gamma}\left[Pe_t(\Omega)\right]^2$ is always evaluated at **x** since the above integration is the made over the position of the grain in the cell such as the point **x** is always on the grain interface, that is over the spherical shell $S(a)$ of radius *a* and centered at **x**. Hence the local undercooling is evaluated at **x** too, $\Omega = \dfrac{C_l^*(\mathbf{x}) - C_0}{C_l^*(\mathbf{x}) - kC_l^*(\mathbf{x})}$.

On the other hand the use of the cell approximation to the volume average to compute Γ_g would mean an integration of w_g over the grain interface $S(a)$, given a fixed grain centered at x (see Figure 17b). Hence one obtains:

$$\begin{aligned}\Gamma_g &= n \int_{\tilde{\mathbf{z}}_1 \in S(a)} \rho\, w_g\left(\tilde{\mathbf{z}}_1\right) dS \\ &= n 4\pi a^2 \rho_l \overline{w}_g\end{aligned} \tag{151}$$

where

$$\overline{w}_k = \frac{1}{4\pi a^2} \int_{\tilde{\mathbf{z}}_1 \in S(a)} w_g\left(\tilde{\mathbf{z}}_1\right) dS \tag{152}$$

is the mean growth velocity of the grain. It is important to notice that due to the non-linearity of w_g with respect to C_l^* and consequently with respect to *T*, the mean velocity $\overline{w}_g$ will be different from the velocity $w_g(\mathbf{x})$ in (150). Hence, different closure expressions are obtained using the ensemble and the volume average respectively. Moreover the result in (151) is incorrect because the mean interfacial velocity $\overline{w}_g$ at **x** should be an average of the velocity w_g evaluated at **x** and not on the grain interface $S(a)$ as in Figure 17b. The error comes from the fact that the cell approximation to the volume average considers a fixed grain centered at **x**. Therefore the average fields computed in the cell (including the liquid and the interfacial fields) are attached to the point **x**, a point that is always located in the solid.

Similar findings are obtained by Drew [9] when he compared the volume and the ensemble average of the interfacial pressure force acting on the grain interface. Indeed if a pressure gradient ∇p is to be considered at the scale of the grain the ensemble average of the interfacial pressure force would be zero since:

$$\begin{aligned}\overline{\mathbf{F}}_p &= n \int_{\tilde{\mathbf{z}}_1 \in S(a)} p(\mathbf{x})\mathbf{n}_g\, dS \\ &= 0\end{aligned} \tag{153}$$

On the other hand the volume average approach would give:

$$\overline{\mathbf{F}}_p = n \int_{\tilde{\mathbf{z}}_1 \in S(a)} p\left(\tilde{\mathbf{z}}_1\right)\mathbf{n}_g dS \neq 0 \tag{154}$$

that is a non-zero buoyancy force because the pressure force is integrated over the grain interface $S(a)$, given the grain centered at **x**. The result in (154) is physically incorrect since the buoyancy force would appear in the momentum equation twice, along with the already existing force due to the fluid pressure gradient. This emphasizes the difficulties inherent to the volume average approach.

6. Conclusions

In the present paper a new multi-phase Eulerian model valid for both columnar and equiaxed dendritic solidification has been developed in the purely diffusive case. The mean conservation equations are derived by means of a statistical phase averaging technique, and the mathematical formulation of the model can be used for both columnar and equiaxed solidification. The use of such an averaging procedure has several advantages compared with the volume averaging technique which has been widely used during the last decade. Firstly, the statistical approach does not need the definition of a representative elementary volume. Secondly, it is consistent with the random aspect of the equiaxed grain germination and motion as well as the possible turbulent behavior of the fluid flow. Finally, and the most important, owing to the statistical nature of the model, we are able to treat rigorously the coexistence of equiaxed and columnar structures and consequently the CET phenomena.

First the pure columar/equiaxed case is analyzed. With the help of the nearest neighbor probability distribution functions one is able to rigorously compute the unknown terms and tensors existing in the unclosed averaged balance equations. Indeed, using the cell approximation to the nearest neighbor distribution, $\widetilde{f}^{(1)}\left(t,\mathbf{x};\tilde{\mathbf{z}}_1\right)$, the average fields can be easily computed by means of simple integration within a characteristic spherical cell. The main physical hypothesis refers to the scale separation between the inter- and the extra-dendritic liquid. In a similar way as Rappaz and Thévoz [14] and Wang and Beckermann [6], an envelope model is used to parameterize the length scale smaller than the size of the dendrite, that is the interdendritic spacing. The dendrite envelope is defined as the virtual surface surrounding the c/e dendrite grain and connecting all c/e dendrite tips. This leads us to distinguish two types of liquid, the inter- and the extra- dendritic one, and this for each one of the two grain structures. The inter-dendritic liquid is supposed to be in a state of perfect solutal mixing, its solute concentration, C_l^*, being uniquely determined from the local temperature and the phase diagram. The cell model together with the physical meaningful hypotheses valid at the micro-scale enables one to completely close the complex system of averaged balanced equations. The final model valid either for the pure columnar or equiaxed case is similar with the one obtained by Wang and Beckermann [6]. The equivalence between the two models is a direct consequence of the use of the local thermal equilibrium hypothesis. Indeed if the local homogeneity hypothesis is considered, meaning that no local gradients of physical fields (temperature, solute, grain fraction) are taken into account at the scale of the grain, then the ensemble average reproduces the volume average technique. However the ensemble average technique and the cell model approximation to the ensemble average are fundamentally different from the volume average approach. Indeed, if the local homogeneity hypothesis is no more valid, the use of the ensemble average results into closure expression different from the ones obtained with the help of the volume average technique. Moreover the volume average results are not physically sound. In this respect it is shown that the use of the cell appoxmation to the ensemble average can be successfully used to incorporate the effects of the inhomogeneities of the various scalar fields, e.g., the solute and temperature gradients on the closure expressions.

Secondly the case of the coexistence between the columnar and equiaxed grains is analyzed from the perspective of the ensemble average technique. More precisely the case of a columnar front "*penetration*" into a developed equiaxed zone is analyzed. This type of coupling can be frequently encountered during solidification problems especially in processes involving the so-

called columnar-to-equiaxed transition (CET) phenomena. The main advantage of the ensemble averaging is that, with the help of the nearest neighbor distributions $\widetilde{f}_{c/e}\left(t,\mathbf{x};\tilde{\mathbf{z}}_1\right)$, one can quantify in a rigorous way the c/e influence at **x**. Using the cell approximation to $\widetilde{f}_{c/e}$, two spherical cells centered at **x** and of radius R_{1c}^* and R_{1e}^* were identified, each of them characterizing in a simple way the statistics of the c/e grain distributions (see Figure 16). Using the two spherical cells it is possible to separate the influence at **x** of the c/e grains by defining corresponding c/e ensemble averages which will quantify the average effects of the two structures at **x**. Moreover, any ensemble average (i.e. c/e fractions, solid/liquid fractions, average solute fields, interfacial averages, etc.) can be easily computed by means of relative simple integrations over all possible positions of the c/e grain within the respective c/e cell. Thus, following the case where the closest grain to **x** is columnar or equiaxed, the model leads us to distinguish two main types of ensemble averages, columnar and equiaxed ensemble averages respectively. In this respect, two important fractions are identified, the columnar and equiaxed fraction, ε_c and ε_e respectively. These two averages quantify the way how the two structures share the space at **x**. Since the columnar and equiaxed grains share a same space at **x** their corresponding fractions will obviously sum to one, i.e., $\varepsilon_c+\varepsilon_e=1$. Moreover each structure will be characterized by its proper solid (s) and liquid (f) phase and therefore the c/e fraction will be a sum of their corresponding c/e solid and liquid fractions, $\varepsilon_{c/e}=\varepsilon_{se/c}+\varepsilon_{fe/c}$. Another important feature of the ensemble average is that it enables one to quantify the mechanical blockage of the equiaxed grains on the columnar tips. It was proven that the columnar and the equiaxed grain distributions interact "mechanically" following a two-fold mechanism. The first mechanical blockage effect of the equiaxed grains will determine a rarefaction of the columnar zone when entering ("nucleating") into a developed equiaxed zone. Indeed, due to the finite equiaxed grain fraction the columnar tips have only a limited space $(1-\varepsilon_{ge})$ within which they "nucleate". Hence only a fraction, $1-\varepsilon_{ge}$, of the total number of columns, n_c^0, will be able to enter (to nucleate within) the equiaxed zone. The second mechanical blockage effect of the coexistence reflects the fact that for a mixed zone (i.e. columnar + equiaxed), the two coexisting structures are forced to share a same space. Consequently, the space available for each structure will be different and smaller with respect to the corresponding space available just before the coexistence state. Basically the second mechanical blockage states that the cell radii $R_{1c/e}^*$ characterizing the coexistence statistics are smaller than the corresponding length scales characterizing the c/e state separately just before their coexistence, $R_{1c/e}$. This effect is of primary importance because $R_{1c/e}^*$ can be very different form the original length scales $R_{1c/e}$ and consequently the evolution of the mixed zone can be significantly different from that of the pure columnar or equiaxed zone. Using the cell model together with the physical assumptions valid at the micro-scale we are able to close rigorously the whole system of balance equations. Finally, a complete model describing the coexistence of equiaxed and columnar case grains is obtained.

Appendix A: *Solute diffusion field in the extradendritical liquid*

As pointed out in section 3.4.1., by assuming a spherical shape for the dendrite grain, a thermal equilibrium at the scale of the grain and the local homogeneity hypothesis, the solute field around the grain will be a function of *r* only. As well, the solute flux at the cell boundary ($r=R_1$) is zero, meaning that $\left(\partial C_l/\partial r\right)_{r=R_1}=0$. In this respect the solute diffusion process within the extra-dendritic liquid will be controlled by the following boundary moving equation:

$$\frac{\partial C_l}{\partial t} = \frac{D_l}{r^2}\frac{\partial}{\partial r}\left(r^2 \frac{\partial C_l}{\partial r}\right)$$
$$C_l\left(t, r = a\right) = C_l^* \ , \qquad \left(\partial C_l / \partial r\right)_{r=R_1} = 0 \tag{A.1}$$
$$\frac{da}{dt} = \overline{w}_{ge}$$

where $\overline{w}_{ge}$ is the growth velocity of the grain envelope, computed from (59) where C_∞ would be equal to the mean extra-dendritic concentration $\overline{C}_l$:

$$\overline{C}_l = \frac{1}{4/3\pi\left(R_1^{\,3} - a^3\right)} \int_a^{R_1} C_l 4\pi r^2 dr \tag{A.2}$$

.

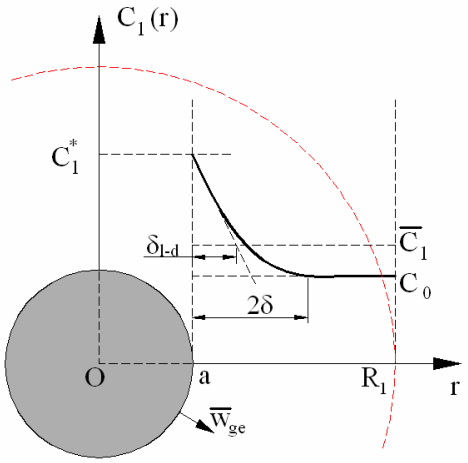

Figure A1: The solute field in the extra-dendritic liquid

By integrating the diffusion equation in equation (A.1) on the extra-dendritic liquid domain and using the well known Leibnitz integral rule one can easily obtain the solute balance equation in the extra-dendritic liquid:

$$\frac{\partial}{\partial t}\int_a^{R_1} C_l 4\pi r^2 dr + C_l^*\left(4\pi a^2\right)\overline{w}_{ge} = -\left(4\pi a^2\right) D_l \left(\frac{\partial C_l}{\partial t}\right)_{r=a} \tag{A.3}$$

By denoting with 2δ the solutal boundary layer existing around the spherical grain (Figure A1) one can rewrite the above solute balance as follows

$$\frac{\partial}{\partial t}\int_{R_g}^{R_g+2\delta} C_l 4\pi r^2 dr + \frac{\partial}{\partial t}\int_{a+2\delta}^{R_1} C_0 4\pi r^2 dr + C_l^*\left(4\pi a^2\right)\overline{w}_{ge} = \left(4\pi a^2\right) D_l \frac{C_l^* - C_0}{\delta} \tag{A.4}$$

The first term in the RHS of the above equation is no more than the solute variation of the solute within the solutal boundary. This can be rewritten as:

$$\frac{\partial}{\partial t}\int_a^{a+2\delta} C_l 4\pi r^2 dr = \frac{\partial}{\partial t}\left(V_{sb}\overline{C}_{sb}\right) \tag{A.5}$$

where V_{sb} is the volume of the boundary layer and $\overline{C}_{sb}$ the average concentration within the same boundary layer. The second term in the RHS of (A.4) represent the variation of the solute within the space outside the solutal boundary untouched by the solute diffusion wave. One has therefore:

$$\frac{\partial}{\partial t}\int_{a+2\delta}^{R_l} C_0 4\pi r^2 dr = \frac{\partial}{\partial t}\left[\left(V_l - V_{sb}\right)C_0\right] \tag{A.6}$$

where V_l is the volume of the extra-dendritic liquid and C_0 the uniform concentration of the liquid untouched by the diffusion wave. By assuming now a solute profile within the boundary layer one can obtain from (A.4) an ordinary differential equation controlling the evolution of δ. This technique is no more than the integral approach to a boundary layer problem as detailed in Burmeister [20]. Note that this approximate integral approach in (A.4) is simpler than the one used by Rappaz and Thévoz [14] since it requires the solution of a relative simple ODE in order to obtain the δ evolution. In contrast in [14] the full solution of the PDE equation in (A.1) is computed. However, solving an additional ODE for each cell of the spatial mesh would increase greatly the computational time of the already complex problem. To simplify and similar with the approach adopted by Wang and Beckermann [6] we will consider that the solute diffusion problem within the extra-dendrite liquid is quasi-stationary. This hypothesis would be valid only if the solute boundary layer around the grain readapts more rapidly to the external conditions (a, C_l^*) than the later ones are actually changing. In this respect one expects that the variation of the parameters characterizing the solutal boundary layer (both V_{sb} and $\overline{C}_{sb}$) with respect to time is negligible. It is worthwhile to notice that Rappaz and Thévoz [21] made a similar assumption in his approximate approach of the solute diffusion problem in the extra-dendritic liquid. Given this hypothesis, from (A.4) one finally obtains:

$$-C_0\left(4\pi a^2\right)\overline{w}_{ge} + C_l^*\left(4\pi a^2\right)\overline{w}_{ge} = \left(4\pi a^2\right)D_l\frac{C_l^* - C_0}{\delta} \tag{A.7}$$

The solute boundary layer characterizing the quasi-steady state becomes:

$$\delta_{st} = \frac{D_l}{\overline{w}_{ge}} \tag{A.8}$$

Notice that the same result was obtained by Rappaz and Thévoz in [21]. It would be however interesting to analyze the validity domain of the quasi-steady hypothesis. To do this let us quantify first the transition time from an initial solutal state characterized by the following initial and boundary conditions:

$$\left.\begin{aligned} &C_l^* = ct\left(T = ct\right)\\ &C_l^* > C_0\\ &a(t=0) > 0 \end{aligned}\right\} \Rightarrow \overline{w}_{ge} = ct \tag{A.9}$$

to a quasi-stationary state . This transition time would be of order of the time scale t_{st} during which the solute boundary around the grain extends to a dimension corresponding to the quasi-steady state already detailed above. Knowing the travel time of a diffusion wave is $t_{diff} = l^2/4/D_l$ [22] one easily obtains for t_{st} :

$$t_{st} = \frac{\left(2\delta_{st}\right)^2}{4D_l} = \frac{D_l}{\overline{w}_{ge}^{\,2}} \tag{A.10}$$

So, one can approximate the solute diffusion problem with a quasi-steady state if the readaption time of the solutal boundary to the new condition is smaller than the time scale characterizing the changes of external parameters like $a, \overline{w}_{ge}, T$. For the case of a grain distribution characterized by an average spacing between particles $2R_1$ the time scale characterizing the change of external conditions could be approximated with the total growth time of the grain:

$$t^* \simeq \frac{R_1 - a}{\overline{w}_{ge}} \tag{A.11}$$

In this respect the quasi-steady approximation would be valid if

$$t_{st} << t^* \Leftrightarrow \qquad \delta_{st} << \left(R_1 - a\right) \tag{A.12}$$

It is interesting to note that the above condition is also coherent with the result in (A.8). Indeed, due to the spatially limited diffusion around the grain, the stationary boundary layer δ_{st} have a meaning only if $2\delta_{st} << \left(R_1 - a\right)$ (see Figure A1) or:

$$Pe_g = \frac{\overline{w}_{ge}\left(R_1 - a\right)}{D_l} >> 2 \tag{A.13}$$

If on the contrary $Pe_g << 2$ a quasi-steady state cannot be considered. In fact, $Pe_g = 2$ would correspond to a case where the solute boundary layer around the grain have already reached the cell boundary. Above this limit, due to the zero flux condition at $r = R_1$, the enriching of the extra-dendritic liquid becomes non-negligible and the far concentration C_0 starts to increase. For this non-stationary regime, the solute distribution in the extra-dendritic liquid becomes highly time dependent and the precise modeling of the solute transfer at the grain boundary would require a more complex model for δ. However, as a first approximation, one could consider that for $Pe_g < 2$ a pertinent solutal boundary layer would be $2\delta = R_1 - a$. One would have therefore:

$$\delta = \begin{cases} D_l / \overline{w}_{ge} & if \quad Pe_g \geq 2 \\ \left(R_1 - a\right)/2 & if \quad Pe_g < 2 \end{cases} \tag{A.14}$$

It is importnant to notice that the above solutal boundary layer model enable one to express the interfacial solute transfer in the extra-dendritic liquid Φ_l^C, equation (81). However, in an average model one knows a priori the mean concentration in the extra-dendritic liquid, $\overline{C}_l$, and not the far concentration C_0. Hence one should express the solute flux at the grain interface with respect to $\overline{C}_l$ and not C_0:

$$\begin{aligned} \varphi_g &= D_l \frac{C_l^* - C_0}{\delta} \\ &= D_l \frac{C_l^* - \overline{C}_l}{\delta_{l-d}} \end{aligned} \tag{A.15}$$

One must therefore compute an analytical expression for δ_{l-d} (Figure A1). This can be done if one assumes a solute profile within the solute boundary layer. A straightforward profile would be the second order approximation:

$$C_l(r) = br^2 + cr + d \ , \qquad r \in (a, a+2\delta) \tag{A.16}$$

The three constants *b*, *c*, *d* can be easily found by imposing that:

$$C_l(a) = C_l^* \ ; \qquad C_l(a+2\delta) = C_0 \ ; \qquad \left(\frac{\partial C_l}{\partial r}\right)_{a+2\delta} = 0 \tag{A.17}$$

It is worthwhile to notice that equation verifies as well the constraint: $(\partial C_l / \partial r)_{a+2\delta} = \delta$. Using (A.2), (A.15) and (A.16) one finally obtains:

$$\varphi_g = D_l \frac{C_l^* - \overline{C}_l}{\delta_{l-d}} \quad \text{where} \quad \delta_{l-d} = \delta\left[1 - \frac{10a^2\delta + 10a\delta^2 + 4\delta^3}{5\left(R_1{}^3 - a^3\right)}\right] \tag{A.18}$$

Coupled with the equation (A.14) the above expression form a complete analytical model describing the solute flux at the grain interface. Note as well that δ_{l-d} verifies an important constraint relative to the solute diffusion process in the extra-dendritic liquid, namely that:

$$\delta_{l-d} < \frac{D_l}{w_{ge}} \tag{A.19}$$

Indeed, as noticed by Wang and Beckermann [6], due to the continuous enriching process of the extra-dendritic liquid δ_{l-d} has to verify (A.19) as to be physical meaningful.

Appendix B: *Probability distribution functions. The coexistence case.*

The distribution function $\hat{f}_e^{(1)}\left(t, \mathbf{x}; \tilde{\mathbf{z}}_1\right)$

In order to find an expression for $\hat{f}_e^{(1)}\left(t, \mathbf{x}; \tilde{\mathbf{z}}_1\right)$ one must see that $\hat{f}_e^{(1)}\left(t, \mathbf{x}; \tilde{\mathbf{z}}_1\right) d\tilde{\mathbf{z}}_1$ is the probability that there is no sphere within $r = \left|\mathbf{x} - \tilde{\mathbf{z}}_1\right|$ of $\mathbf{x}$ and there is one sphere within $d\tilde{\mathbf{z}}_1$ of $\tilde{\mathbf{z}}_1$. Note as well that the probability that there is no sphere within *r* of $\mathbf{x}$ and the probability that the nearest sphere is within *r* of $\mathbf{x}$ sum to one. Hence one has:

$$\hat{f}_e^{(1)}\left(t, \mathbf{x}; \tilde{\mathbf{z}}_1\right) d\tilde{\mathbf{z}}_1 = \left(1 - \int\limits_{\left|\mathbf{x} - \tilde{\mathbf{z}}_1'\right| < \left|\mathbf{x} - \tilde{\mathbf{z}}_1\right|} \hat{f}_e^{(1)}\left(t, \mathbf{x}; \tilde{\mathbf{z}}_1'\right) d\tilde{\mathbf{z}}_1'\right) f_e^{(1)}\left(\tilde{\mathbf{z}}_1\right) d\tilde{\mathbf{z}}_1 \tag{B.1}$$

where $f_e^{(1)}\left(\tilde{\mathbf{z}}_1\right)$ is the unconditional density functions for any equiaxed grain center being within $d\tilde{\mathbf{z}}_1$ of $\tilde{\mathbf{z}}_1$, that is equal with equiaxed grain desnity n_e. Hence, one can notice from (B.1) that $\hat{f}_e^{(1)}\left(t, \mathbf{x}; \tilde{\mathbf{z}}_1\right)$ is a function of $r = \left|\mathbf{x} - \tilde{\mathbf{z}}_1\right|$ only. By replacing $d\tilde{\mathbf{z}}_1$ with $4\pi r^2 dr$ one can observe that the left side of (B.1) is the differential of the integral on the right. One has therefore:

$$\frac{d}{dr}\ln\left(1-4\pi\int_0^r \hat{f}_e^{(1)}\left(t,r'\right)\left(r'\right)^2\,dr'\right)=-4\pi n_e r^2 \tag{B.2}$$

Integrating,

$$\hat{f}_e^{(1)}\left(t,\mathbf{x};\tilde{\mathbf{z}}_1\right)=C_1\exp\left(-\frac{4}{3}\pi n_e\left|\mathbf{x}-\tilde{\mathbf{z}}_1\right|^3\right) \tag{B.3}$$

where C_1 is a constant which is evaluating by requiring that

$$\int \hat{f}_e^{(1)}\left(t,\mathbf{x};\tilde{\mathbf{z}}_1\right)d\tilde{\mathbf{z}}_1=1 \tag{B.4}$$

Hence one obtains:

$$\hat{f}_e^{(1)}\left(t,\mathbf{x};\tilde{\mathbf{z}}_1\right)=n_e\exp\left(-\frac{4}{3}\pi n_e\left|\mathbf{x}-\tilde{\mathbf{z}}_1\right|^3\right) \tag{B.5}$$

The distribution function $\hat{f}_c^{(1)}\left(t,\mathbf{x};\tilde{\mathbf{z}}_1^*\middle|A_e\right)$

Similar with the previous case one can state that:

$$\hat{f}_c^{(1)}\left(t,\mathbf{x};\tilde{\mathbf{z}}_1^*\middle|A_e\right)d\tilde{\mathbf{z}}_1^*=\left(1-\int_{\left|\mathbf{x}-\tilde{\mathbf{z}}_1'\right|<\left|\mathbf{x}-\tilde{\mathbf{z}}_1^*\right|}\hat{f}_c^{(1)}\left(t,\mathbf{x};\tilde{\mathbf{z}}_1'\middle|A_e\right)d\tilde{\mathbf{z}}_1'\right)f_c^{(1)}\left(\tilde{\mathbf{z}}_1^*\middle|A_e\right)d\tilde{\mathbf{z}}_1^* \tag{B.6}$$

where $f_c^{(1)}\left(\tilde{\mathbf{z}}_1^*\middle|A_e\right)$ is the conditional density functions for any columnar grain center being within $d\tilde{\mathbf{z}}_1^*$ of $\tilde{\mathbf{z}}_1^*$, given the event A_e that the the closest equiaxed grain to $\mathbf{x}$ is centered at $\tilde{\mathbf{z}}_1$ where $\left|\mathbf{x}-\tilde{\mathbf{z}}_1^*\right|<\left|\mathbf{x}-\tilde{\mathbf{z}}_1\right|$. It is important to notice that $f_c^{(1)}\left(\tilde{\mathbf{z}}_1^*\middle|A_e\right)$ is equal with the columnar nucleation grain density n_c^0. Similar with the previous case one finally obtains

$$\hat{f}_c^{(1)}\left(t,\mathbf{x};\tilde{\mathbf{z}}_1^*\middle|A_e\right)=C_1\exp\left(-\frac{4}{3}\pi n_c^0\left|\mathbf{x}-\tilde{\mathbf{z}}_1^*\right|^3\right) \tag{B.7}$$

Requiring that $\int \hat{f}_c^{(1)}\left(t,\mathbf{x};\tilde{\mathbf{z}}_1^*\middle|A_e\right)d\tilde{\mathbf{z}}_1=1$ one has

$$\hat{f}_c^{(1)}\left(t,\mathbf{x};\tilde{\mathbf{z}}_1^*\middle|A_e\right)=n_c^0\exp\left(-\frac{4}{3}\pi n_c^0\left|\mathbf{x}-\tilde{\mathbf{z}}_1^*\right|^3\right) \tag{B.8}$$

Nomenclature

Symbol	Meaning	Unit
$\mathbf{v}$	velocity field	$[m/s]$
C	solute concentration field	$[wt.\ \%]$
T	temperature field	$[K]$
n	grain density	$[\,m^{-3}\,]$
ρ	density field	$[\,kg.m^{-3}\,]$
ψ	the generic physical field	---
ε_k	the "volume" fraction of phase k	---
w_k	the interface velocity of the k phase interface	$[m/s]$
C_k^*	the interfacial concentration at the k phase interface	$[wt.\ \%]$
X_k	the k phase characteristic phase function	---
$n_{c/e}^0$	the columnar/equiaxed nucleation grain density	$[\,m^{-3}\,]$
λ_1	columnar primary arm spacing	$[m]$
S_k	the interfacial area density of phase k	$[\,m^{-1}\,]$
δ_{k-p}	the solute diffusion length at the k-p interface	$[m]$
$\mathbf{x}_{cf}$	position of the columnar front	$[m]$
T_{ne}	the equiaxed nucleation temperature	$[K]$
T_f	the fusion temperature of the pure solvent	$[K]$
m	the slope of the liquidus line	$[\,K.(wt\%)^{-1}\,]$
k	the partition coefficient	---
c_k	heat capacity for the k-phase	$[\,J.kg^{-1}.K^{-1}\,]$
λ_k	the phase k thermal conductivity	$[\,W.m^{-1}.K^{-1}\,]$
L	the latent heat	$[\,J.kg^{-1}\,]$
Ω	the dimensionless local undercooling	---
Pe_t	the dendrite tip Peclet number	---
D_k	the solute diffusivity within the phase k	$[\,m^2.s^{-1}\,]$
$a_{c/e}$	the local columnar/equiaxed grain radius	$[m]$
$R_{1c/e}$	the cell radius corresponding to the single columnar/equiaxed grain distributions	$[m]$
$R_{1c/e}^*$	the cell radius corresponding to the coexisting columnar/equiaxed grain distribution	$[m]$
$\mathbf{z}_i$	the position in the ingot of the ith grain	$[m]$
$f^{(1)}(t,\mathbf{z}_1)$	the unconditional density function that at time t in the ingot one can find a particle centered within $d\mathbf{z}_1$ of $\mathbf{z}_1$	$[\,m^{-3}\,]$
$\tilde{\mathbf{z}}_i$	the position in the ingot of the ith closest grain to $\mathbf{x}$	$[m]$
$\tilde{f}_{c/e}^{(1)}(t,\mathbf{x};\tilde{\mathbf{z}}_1)$	the unconditional density function that the closest grain to the point $\mathbf{x}$ is centered within $d\tilde{\mathbf{z}}_1$ of $\tilde{\mathbf{z}}_1$ and is a columnar/equiaxed grain	$[\,m^{-3}\,]$
Γ_k	the k phase mass transfer rate	$[\,kg.m^{-3}.s^{-1}\,]$
Over lines		
$\bar{}$	ensemble average	

~	relative to the nearest neighbor distributions	
Subscripts		
c	columnar phase	
e	equiaxed phase	
c/e	columnar / equiaxed phase	
s	solid phase	
l	extra-dendritic liquid phase	
d	inter-dendritic liquid phase	
f	total fluid phase ($= l + d$)	
g	grain phase ($= d + s$)	
kc	columnar *k* phase	
ke	equiaxed *k* phase	

References

1. Bennon W D and Incropera F P 1987 *Int. J. Heat Mass Transfer* **30** 2161
2. Ganesan S and Poirier D R 1990 *Metallurgical Transactions B* **21B** 173
3. Poirier D R, Nadapurkar P J and Ganesan S 1991 *Metallurgical Transactions B* **22B** 889
4. Ni J and Beckermann C 1991 *Metallurgical Transactions B* **22B** 349
5. Felicelli S D, Heinrich J C and Poirier D R 1991 *Metallurgical Transactions B* **22B** 847
6. Wang C Y and Beckermann C 1993 *Metallurgical and Materials Transactions A* **24A** 2787
7. Wang C Y and Beckermann C 1996 *Metallurgical and Materials Transactions A* **27A** 2754
8. Drew D A 1983 *Ann. Rev. Fluid Mech.* **15** 261
9. Drew D A and S L Passman 1999 *Theory of Multicomponent Fluids* (New York: Springer-Verlag)
10. Furmanski P 2000 *Computer assisted mechanics and engineering sciences* **7** 402
11. Fautrelle Y, Lehmann P, Quillet G, Medina M, Durand F and Du Terrail Y 2000 *Proc. EUROMECH Colloquium 408 "Interactive dynamics of convection and solidification"* ed. By Kluwer Pub 87
12. Ciobanas A I, Baltaretu F and Fautrelle Y 2004 *Proc. of Solidification and Gravity, Miskolc*
13. Kataoka I, 1986 *Int. J. Multiphase Flow* **12.5** 745
14. Rappaz M and Thévoz Ph 1987 *Acta Metallurgica* **35.7** 1487
15. Martorano M A, Beckermann C and Gandin Ch-A 2003 *Metallurgical and Materials Transactions A* **34A** 1657
16. Stefanescu D M, Upadhya G and Bandyopahyoy D 1990 *Metallurgical Transactions A* **21A** 997
17. Hunt J D 1979 *Solidification and casting of metals – Metals Society, London* 3

18. Kurz W and Fisher D J 1981 *Acta Metallurgica* **29** 11

19. Lipton J, Glicksman M E and Kurz W 1984 *Materials Science and Engineering* **65** 57

20. Burmeister L C 1993 *Convective Heat Transfer* (New York: Wiley)

21. Rappaz M and Thévoz Ph 1987 *Acta Metallurgica* **35.12** 2929

22. Bejan A 2000 *Shape and Structure, From Engineering to Nature* (New York: Cambridge University Press)

Référence III

Ensemble averaged multi-phase eulerian model for columnar/equiaxed solidification of a binary alloy Part II. Simulation of the columnar-to-equiaxed transition

A. I. Ciobanas[1], Y. Fautrelle[1]

[1] EPM/CNRS laboratory, ENSHMG, BP 95, 38402 Saint Martin d'Hères Cedex, France

E-mail: aciobanas@yahoo.com

Abstract

A new multi-phase Eulerian model for the columnar and equiaxed dendritic solidification has been developed. In this paper we first focus on the numerical simulation of quasi-steady solidification experiments in order to obtain corresponding CET maps. We have identified three main zones on the CET map: the pure columnar, the pure equiaxed zone and finally the mixed columnar+equiaxed zone. The mixed c/e zone was further quantified by means of a columnar fraction ε_c which quantifies in a rigorous the way the two coexisting structures. Since it intrinsically includes the solutal and the mechanical blocking effects, the new ensemble model unifies the semi-empirical Hunt's approach (pure mechanical blocking mechanism) and the Martorano *et al.* approach (pure solutal blocking mechanism). Secondly the present model was used to simulate unidirectional solidification experiments. It was found that the columnar front evolved in a quasi-steady state until a time very close to the critical CET moment. It is also found that the equiaxed nucleation undercooling is close to the maximum columnar dendrite tip undercooling and that the CET is virtually independent of the equiaxed zone ahead of the *CF*. If the equiaxed zone is not taken into account it is observed that the *CF* velocity exhibits a sudden increase at the beginning of the solidification followed by a quasi-plateau corresponding to a quasi-state at the columnar tips and finally, above a critical time, an oscillatory evolution. The beginning of the oscillatory evolution of the *CF* was well correlated with the CET position measured in the experiments. We find as well that this oscillatory evolution of the *CF* is very favorable for the fragmentation of the columnar dendrites and thus for the CET. In this respect, it seems that the unsteady regime of the *CF* with respect to the local cooling conditions represent the main cause for the CET phenomena, at least for the non-refined alloys.

PACS: 81.30.Fb Solidification, 82.20.Wt Computational modeling; simulation

1 Introduction

The present paper is devoted to the application of a model derived in a previous publication [1]. That model is aimed at predicting the macroscale solidification of a binary alloy. It is based on the ensemble averaging technique, which allows the treatment of various types of solidification, i.e., columnar or/and equiaxed. The use of an ensemble averaging technique for deriving a micro-macro scale model has some important advantages compared with the volume averaging technique which has been widely used during the last decade (see for example [2, 3]) . Firstly, the statistical approach does not need the definition of a representative elementary volume. Secondly, it is consistent with the random aspect of the equiaxed grain germination and motion as well as the possible turbulent behavior of the fluid flow. Finally, and the most important, owing to the statistical nature of the model, one is able to treat rigorously the coexistence of equiaxed and columnar structures and consequently the CET phenomena. Knowing that the CET phenomena are direct consequence of complex mechanical and solutal interactions between an advancing columnar front and an equiaxed zone ahead of the columnar dendrite tips, the existence of a model that could integrate mathematically these interactions would be of great interest.

The paper comprises four sections. In Section 2, the mathematical is briefly described, and the overall equations are summarized. Section 3 is devoted to the analysis of the ability of the model to predict the CET mechanism in a simple 1D directional solidification situation. In the

fourth section the model is tested on previous basic CET experiments [4, 5] devoted to the study of the CET.

2 Mathematical model

2.1 The ensemble averaged model

The model is based on the ensemble averaging procedure coupled with the so-called cell model. The model is described in detail in a first part [1]. We only summarize here the main features of the model. Given two coexisting grain populations (i.e. columnar and an equiaxed) characterized by two different grain densities, $n_{c/e}$ (c/e stands for either the columnar or the equiaxed structure), their influence at a certain point $\mathbf{x}$ may be different as well. The main advantage of the ensemble averaging is that, with the help of the nearest neighbor distributions $\tilde{f}_{c/e}\left(t,\mathbf{x};\tilde{\mathbf{z}}_1\right)$, one can quantify in a rigorous way the c/e influence at $\mathbf{x}$. Indeed, $\tilde{f}_{c/e}\left(t,\mathbf{x};\tilde{\mathbf{z}}_1\right)$ measures the density of probability that one c/e grain centered at $\tilde{\mathbf{z}}_1$ is the closest grain to $\mathbf{x}$ among all the grains existing in the ingot. These two distributions play a vital role in determining the influence of c/e grains at $\mathbf{x}$ since one expects that what happens at $\mathbf{x}$ would be mainly influenced by the closest grain to $\mathbf{x}$. Using the cell approximation to $\tilde{f}_{c/e}$, two spherical cells centered at $\mathbf{x}$ and of radius R^*_{1c} and R^*_{1e} can be identified, each of them characterizing in a simple way the statistics of the c/e grain distributions (see Figure 1).

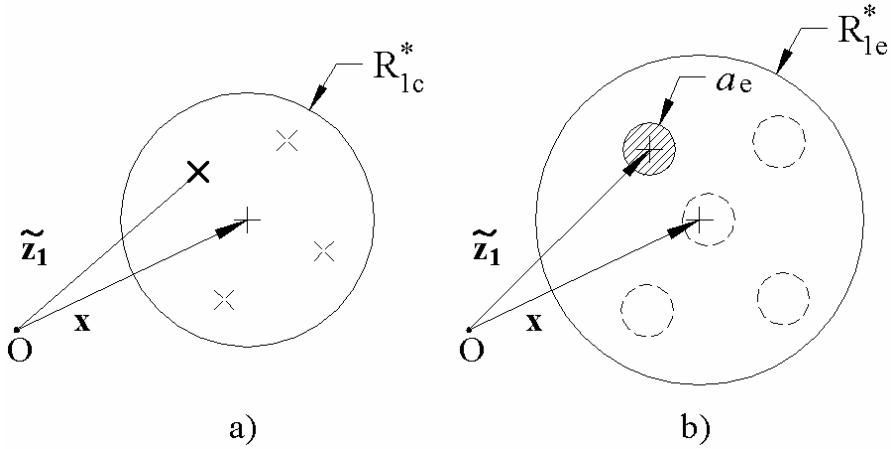

Figure 1: The cell model approximation to the columnar (a) and the equiaxed (b) ensemble average

Indeed, in the light of the cell model the ensemble $\theta_{c/e}$ of realizations such as the closest particle to $\mathbf{x}$ be a columnar/equiaxed one is equivalent with the ensemble of realizations such as the closest particle to $\mathbf{x}$ is c/e and is centered within the cell of radius $R^*_{1c/e}$ centered at $\mathbf{x}$. Using the two spherical cells it is possible to separate the influence at $\mathbf{x}$ of the c/e grains by defining c/e ensemble averages which will quantify the average effects of the two structures at $\mathbf{x}$. Moreover, any ensemble average (i.e. e/c fractions, solid/liquid fractions, average solute fields, interfacial averages, etc.) can be easily computed by means of relative simple integrations over all possible positions of the c/e grain within the respective c/e cell. Hence, following the case where the closest grain to $\mathbf{x}$ is columnar or equiaxed, the model leads us to distinguish two main types of ensemble averages, the columnar and equiaxed ensemble averages respectively. Accordingly, two important fractions are identified, the columnar and equiaxed fraction, ε_c and ε_e respectively. These two averages quantify the way the two structures share the space at $\mathbf{x}$. Since the columnar and equiaxed grains share a same space at $\mathbf{x}$ their corresponding fractions will obviously sum to one, $\varepsilon_c + \varepsilon_e = 1$. Moreover each structure will be characterized by its proper solid (s) and liquid (f) phase therefore

the c/e fraction will be a sum of their corresponding c/e solid and liquid fractions, $\varepsilon_{c/e} = \varepsilon_{sc/e} + \varepsilon_{fc/e}$.

In a similar way as Rappaz and Thévoz [6] and Wang and Beckermann [2], an envelope model is used to parameterize the smallest scale of the dendrite, that is the interdendritic spacing. The dendrite envelope is defined as the virtual surface surrounding the dendrite grain and connecting all dendrite tips. This leads us to distinguish two types of liquid, the inter- and the extra-dendritic one, and this for each of the two grain structures. The inter-dendritic liquid is supposed to be in a state of perfect solutal mixing, its solute concentration, C_l^*, being uniquely determined from the local temperature and the phase diagram. On the other hand, due mainly to its relative large diffusion length scale, the extra-dendritic liquid may be in a non-equilibrium state with respect to the local solid-liquid interface, meaning that its average concentration $C_{lc/e}$ can be different from C_l^*. The consequent local undercooling $C_l^* - C_{lc/e}$ will drive the c/e grain growth which in turn will strongly influence the solute transfer in the extra-dendritic liquid. This complex coupled solute transfer behavior is taken into account by the present model by introducing the diffusion length scale $\delta_{lc/e-dc/e}$ which quantifies the solute flux at the grain – extra-dendritic liquid interface. This is a key parameter in modeling the c/e grain evolution since it controls the solute rejection in the limited extra-dendritic liquid enveloping each c/e grain. The extra-dendritic liquid will undergo a solutal enriching process reducing the local undercooling $C_l^* - C_{lc/e}$, to finally arrive at a state of complete solute mixing and consequently to a complete stop of the grain growth. In this light, the correct modeling of the diffusion length is of great importance for the correct simulation of the c/e grain evolution and of the solidification process as a whole.

It is important to notice that the length scale $\delta_{lc/e-dc/e}$ is strongly influenced by the length scale of the c/e extra-dendritic liquid, that is $R_{1c/e}^* - a_{c/e}$. So special care has to be taken in modeling the c/e cell dimensions $R_{1c/e}^*$. It is noticeable that the present ensemble average model gives a pertinent answer, allowing a rigorous approach to the mixed columnar/equiaxed zone. In contrast with the present model, the Martorano et al. model [7] can deal with the columnar and the equiaxed zone in a separate way only. The mixed zone which can eventually develop behind the advancing columnar front is artificially approximated with a pure columnar zone. This implies as well that the resulting mixed zone is resolved using the length scales characterizing uniquely the columnar structure. This approximation leads to discontinuities regarding the variations of the grain dimensions at the columnar front and, as one will see next, produce non-negligible underestimations in the evaluation of the CET position.

Let us consider a simple directional solidification involving a constant thermal gradient *G* and a constant pulling velocity V_p (see Figure 2). Admitting for the moment that the columnar front has reached a quasi-steady state, its velocity, V_{cf} would be therefore equal to V_p. The local undercooling at the columnar tip $\Delta T_c = T_{liq} - T_{cf}$ will result in an undercooled liquid melt ahead of the columnar front (Figure 2), zone which is favorable to an eventual equiaxed nucleation. In this respect, the columnar front will be forced to advance through a developed equiaxed zone, leaving behind a mixed columnar/equiaxed zone. Let us consider for example that the grain density of the equiaxed zone is n_e and that of the columnar zone is $n_c^0 > n_e$.

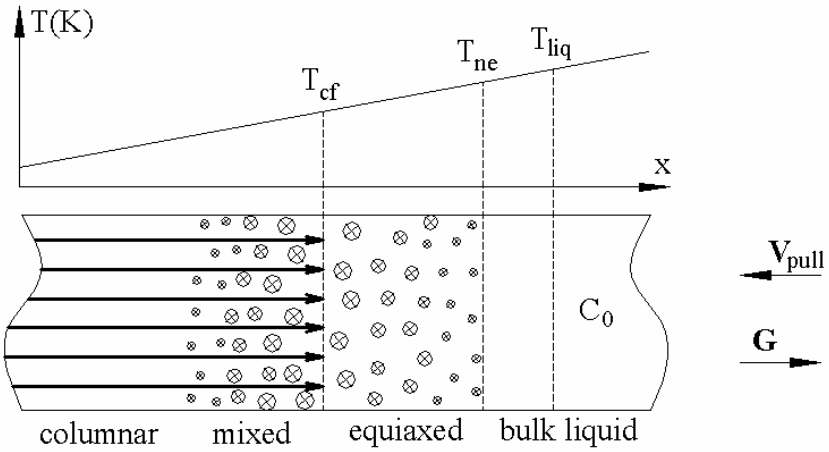

Figure 2: A typical directional solidification and the subsequent columnar-equiaxed interaction

Using the Martorano *et al.* model [7] the mixed zone behind the *CF* is approached with an equivalent pure columnar zone. In their model the position of the *CF* is solely needed in order to decide what grain density to use in modeling the two zones. Hence, the columnar front will play the role of a discontinuity surface for the variation of the grain density n, separating the pure equiaxed zone ahead from the pure columnar zone behind. On the other hand all other average variables (i.e. solid and grain fractions) are considered to be continuous. Since all length scales (i.e. grain diameter *a*, interfacial area S_g) involved in the modeling of the solidification depend on the grain density n, at the *CF* the variation of all these length scales will be discontinuous too. As we will see further on, beside from being physically non-realistic, this approximation can lead to important errors in the modeling of the mixed zone behind the CET.

In contrast with this approximate approach the present model takes into account the fact that within this mixed zone columnar and equiaxed grains coexist sharing a same space. As pointed out previously, the coexistence state is quantified by means of two length scales, R_{1c}^* and R_{1e}^*, each of them characterizing at **x** the amount of space available for a columnar or an equiaxed grain respectively. The c/e grains evolution can be accounted separately and average variables can be attached to each one of the two structures. Using this new approach, the columnar front is not viewed anymore as a discrete separation between two different grain distributions because the mathematical formulation of the model is valid for the pure equiaxed zone ahead of the *CF* as well as for the mixed zone behind it. Indeed, the position of the columnar tips is only needed in order to trigger the columnar "nucleation" within the equiaxed zone, this in turn being intrinsically accounted by the model. Hence, no particular condition has to be used to commute from a single grain distribution zone to a mixed one. It is important to notice that, since the equiaxed grain density n_e is conserved at the columnar front, the equiaxed grain diameter a_e and the interfacial area S_{ge} will be conserved too. As one will note next, the use of ensemble model enables one to quantify in a more precise way the limited solute diffusion processes in the c/e extra-dendritic liquid. Finally it provides the user with accurate results on the mixed c/e zone behind the columnar front.

2.2 The mathematical formulation

The mathematical model used in the following study is based entirely on the ensemble averaged model thoroughly detailed in [1]. However, a simpler mathematical formulation is retained here (see Table 1) due to several simplifying assumptions.

Table 1: Equation summary

Main balance equations	**Solid:**	**Liquid:**

	$k=\{e,c\}$	$k=\{e,c\}$
Mass	$\partial\left(\varepsilon_{sk}\rho_s\right)/\partial t=\Gamma_{sk}$	$\partial\left(\varepsilon_f\rho_f\right)/\partial t=-\Gamma_{se}-\Gamma_{sc}$
Energy	$\dfrac{\partial\left[\left(\varepsilon_s\rho_s c_s+\varepsilon_f\rho_f c_f\right)T\right]}{\partial t}=\dfrac{\partial\left[\left(\varepsilon_s\lambda_s+\varepsilon_f\lambda_f\right)\partial T/\partial x\right]}{\partial x}+\left(\Gamma_{se}+\Gamma_{sc}\right)L$	
Solute	$\dfrac{\partial\left(\varepsilon_{sk}\rho_s C_{sk}\right)}{\partial t}=C_s^*\Gamma_{sk}$	$\varepsilon_{lk}\rho_f\dfrac{\partial C_{lk}}{\partial t}=\left(\dfrac{\rho_f S_{gk}D_l}{\delta_{lk-dk}}-\Gamma_{gk}\right)\left(C_l^*-C_{lk}\right)$
Supplementary balance eq.		
Inter-dendritic mass balance	$\partial\left(\varepsilon_{dk}\rho_f\right)/\partial t=\Gamma_{gk}-\Gamma_{sk}$	
Grain balance	$\partial n_e/\partial t=n_e^0\delta\left(T_{liq}-T-\Delta T_{ne}\right)$ $\partial n_c/\partial t=n_c^0\left(1-\varepsilon_{ge}\right)\delta\left[\mathbf{x}-\mathbf{x}_{cf}(t)\right]$	
Inter-dendritic solute balance	$\left(C_l^*-C_s^*\right)\Gamma_{sk}=\varepsilon_{dk}\rho_f\left(\partial C_l^*/\partial t\right)+\rho_f S_{gk}D_f\left(C_l^*-C_{lk}\right)/\delta_{lk-dk}$	
Auxiliary expressions		
Statistical constraints:	$\begin{matrix}\varepsilon_{le}+\varepsilon_{de}+\varepsilon_{se}=\varepsilon_e\\ \varepsilon_{lc}+\varepsilon_{dc}+\varepsilon_{sc}=\varepsilon_c\end{matrix}$, $\varepsilon_c+\varepsilon_e=1$, $\begin{matrix}\varepsilon_{de}+\varepsilon_{se}=\varepsilon_{ge}\\ \varepsilon_{dc}+\varepsilon_{sc}=\varepsilon_{gc}\end{matrix}$	
Interfacial concentrations:	$C_s^*=\begin{cases}kC_l^* & if\quad \Gamma_s\geq 0\\ C_s & if\quad \Gamma_s<0\end{cases}$	$C_l^*=\left(T-T_f\right)/m$
Equiaxed/columnar fractions	$\varepsilon_e,\varepsilon_c=f\left(n_e,n_c^0,\varepsilon_{ge}\right)$, see equation (18)	
Cell radius	$R_{1k}^*=\left(4/3\pi n_k\right)^{-1/3}\varepsilon_k{}^{1/3}$	
Grain radius	$a_k=R_{1k}^*\varepsilon_{gk}{}^{1/3}$	
Grain envelope interfacial area	$S_{gk}=4\pi a_k{}^2 n_k$	
Diffusion length	$\delta_{lk-dk}=\delta_k\left[1-\dfrac{10a_k{}^2\delta_k+10a_k\delta_k{}^2+4\delta_k{}^3}{5\left(R_{1k}^*{}^3-a_k{}^3\right)}\right]$ where $\delta_k=\begin{cases}D_l/\overline{w}_{gk} & if\quad \left(R_{1k}^*-a_k\right)\geq 2\left(D_l/\overline{w}_{gk}\right)\\ \left(R_{1k}^*-a_k\right)/2 & if\quad \left(R_{1k}^*-a_k\right)<2\left(D_l/\overline{w}_{gk}\right)\end{cases}$	
Grain growth rate	$\Gamma_{gk}=\rho_f S_{gk}\overline{w}_{gk}$, $\overline{w}_{gk}=\dfrac{D_l m(k-1)C_l^*}{\pi^2\Gamma}\left[Iv^{-1}\left(\Omega_k\right)\right]^2$	

First, since we will deal with unidirectional solidifications, only the 1D formulation will be used hereafter. Moreover, in the solute balance equations, the macroscopical diffusion terms $\nabla\left(\varepsilon_{pk}D_p\nabla C_{pk}\right)$ will be neglected transforming the solute balance equations from PDE equations into non-linear ODE equations. This can be quite easily justified [2] observing that the length scales involved in the macroscopical diffusion terms are much larger than the ones involved in the corresponding interfacial exchange terms. Moreover, this approximation allows a direct comparison with the results of Martorano *et al.* model [7].

Hence, for the case where no convection is considered, the model will include only mass energy, solute and grain balance equations. Since the model takes into account a mixed zone, separate balance equations are written for the columnar and equiaxed structure. First, concerning the mass balance, two balance equations are written for the c/e solid phase (*sc, se*), two for the c/e inter-dendritic liquid (*dc, de*) and one for the total fluid (*f*). Note that all these five equations are simple ODE equations. Secondly, given the hypothesis of local thermal equilibrium the energy balance can be approached with the help of a single mixture equation. Next the solute balance equations are written for the solid, inter- and extra-dendritic liquid respectively and this for each one of the two structures. Hence, a total of six equations need to be considered. Notice however that all those six equations are ODE ones as well and that the solute balance in the c/e inter-dendritic liquid is used solely for computing the c/e solidification rate, Γ_{sc}, Γ_{se}. Finally two grain balance equations quantifying the equiaxed and columnar grain conservation have to be considered. Notice as well that for the no convection case, these two equations are only quantifying the corresponding c/e nucleation since no grain transport must be accounted. On one hand, the equiaxed nucleation is modeled as a local event: the equiaxed grains are supposed to nucleate instantaneously at a given undercooling ΔT_{ne}. On the other hand and in contrast with the equiaxed nucleation, the columnar "nucleation" (the sudden arrival of the columnar dendrite tips at **x**) cannot be treated as a local event depending solely on local parameters. Indeed, the presence at **x** of the columnar tips will be a function of its evolution history and therefore a front tracking technique must be used in order to determine the precise position of the columnar front (referred hereafter as to *CF*) at **x** and at time *t*. The model has to be completed therefore with the following equation, describing the precise evolution of the *CF*

$$\frac{dx_{cf}}{dt} = V_{cf}\left(x_{cf}\right) \tag{1}$$

where x_{cf} is the columnar dendrite tips position and V_{cf} is their corresponding local velocity. The later is modeled in a similar way as in reference [7] considering that

$$V_{cf} = \overline{w}_{ge} \tag{2}$$

meaning that V_{cf} is equal to the local equiaxed tip velocity. Indeed, the columnar tips "nucleate" within an equiaxed zone and more precisely within the equiaxed extra-dendritic liquid $(1-\varepsilon_{ge})$. Therefore the latter liquid will be shared between the two coexisting grain distributions. One can logically assume that subsequent to the columnar nucleation the newly formed equiaxed and columnar extra-dendritic liquids (*le, lc*) will share as well the same average concentration. Accordingly, at the columnar tips one has

$$C_{lc} = C_{le} \tag{3}$$

the subsequent columnar and equiaxed undercoolings being equal as well. As already noted by Martorano *et al.* [7] this is one of the most important feature of the model since it couples the *CF* evolution with the equiaxed zone ahead of the columnar tips. If the equiaxed zone ahead of the *CF* eventually arrives to a state of complete mixing, the columnar tips will be stopped, triggering the CET. This is no more than the solutal interaction mechanism, as defined in [7].

It is important to notice that the formulation of the model in Table 1 can be used for the pure columnar or equiaxed zone as well as for the possible mixed c/e zone. Moreover, no particular condition has to be used to commute form one zone to another (i.e. from a pure equiaxed formulation to a mixture one). In fact, the pure c/e formulation is only the limit of the model in Table 1 for $n_{c/e} \to 0$ and $\varepsilon_{c/e} \to 0$. The exact position of the *CF*, x_{cf}, is used only to trigger the

columnar "nucleation" within the equiaxed zone. A mixed columnar+equiaxed zone will therefore be implicitly modeled behind the *CF*.

Finally the model has to be completed with several auxiliary relations, expressing statistical and phase diagram constraints as well as with the length scales involved in the cell model approach: c/e cell dimensions $R^*_{lc/e}$, grain diameters $a_{c/e}$, interfacial areas $S_{gc/e}$ and diffusion length scales δ_{lk-dk}. Moreover, the c/e grain growth rates $\Gamma_{gc/e}$ and the local c/e tip velcities need to be considered.

2.3 Numerical procedure

The mathematical model to be solved contains five mass balance equations, one energy equation, six solute balance equations and finally two grain balance equations. Despite the increase number of equations to be solved, one should note however that only the energy equation represents a PDE equation, the rest of them being relative simple ODE equations. To the model in Table 1 one should add the columnar front tracking equation (1), an ODE too. The equations are discretised using a fully implicit control volume method [8]. The implicit first order Euler method is used for the time discretisation. The system of equation in Table 1 together with equation (1) is solved in a segregated manner: first the energy equation is treated and the resulting tri-diagonal system is solved using a direct method by means of a simple LU decomposition. It must be noted that due to the latent heat release, the energy equation has a highly non-linear character and therefore, special care must be paid to the discretisation of the latent heat source. This one is implicitied using a special numerical implicitation algorithm as described in Patankar [8]. Then the conditions for the equiaxed and columnar nucleation are analyzed and the grain balance equations are solved together with the computation of all parameter needed for the modeling of an eventual mixture zone. Next the solute balance equations are solved. Note that the solute diffusion equations in the extra-dendritic c/e liquid have as well a high non-linear character In addition, for problems involving high cooling rates of small grain densities (large $R_{lc/e}$), they become stiff equations too. Hence, special care must be paid to the discretisation of the interfacial sources in the extra-dendritic solute balance equations. On one hand the interfacial sources are always treated in an implicit way. On the other hand the stiff behavior of these two solute balance equations requires very small time steps in order to converge properly. To limit the computational time an adaptive time scheme is used in the following study. First, the time line is discretised uniformly using an initial time step Δt (see Figure 3).

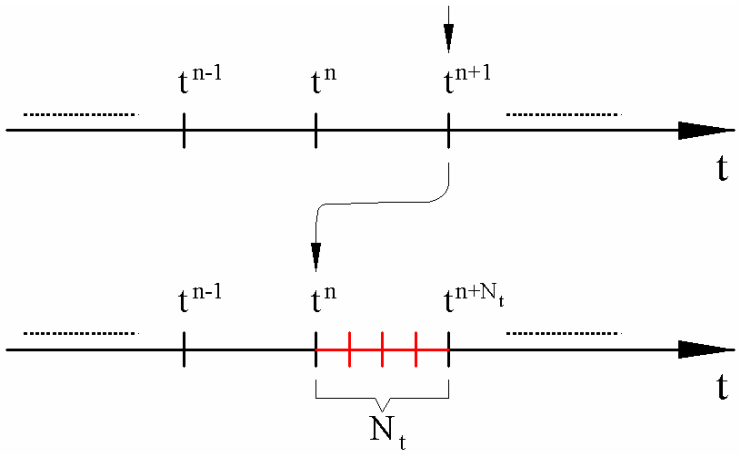

Figure 3: The adaptive time step scheme used in the current study

If the problem does not converge at the n^{th} time iteration, the current time step $\Delta t^n = t^{n+1} - t^n$ is divided into N_t smaller time steps and the simulation is retaken form the last converged time position, that is t^n. Since this algorithm is recursive, meaning that the time refining

procedure can be applied to an already refined time step, a minimum time step $\Delta t_{\min}$ is imposed, below which no time refining is allowed. A typical $N_t = 5$ was found to give satisfactory results for the problems analyzed subsequently.

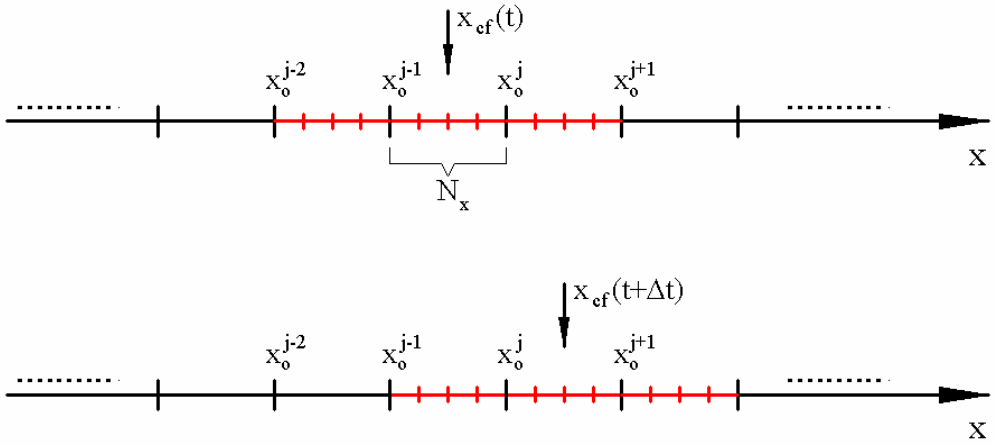

Figure 4: The adaptive mesh scheme used in the current study

As pointed out, a front tracking technique has to be used in order to determine the precise position of the columnar front. The approach used in this study is very similar with the one used by Martorano *et al.* [7]. The equation (1) is discretised as follows

$$\left(x_{cf}\right)_i^n = \left(x_{cf}\right)^{n-1} + \left(V_{cf}\right)_i^n \Delta t \tag{4}$$

where n is the current time step and i the current iteration. Note that, since V_{cf} is strongly depending on local parameter like temperature and solute concentrations, the above equation is solved iteratively together with all other balance equations. In addition a mesh refining technique is used for the control volumes close to the columnar front. This procedure is required due to the fact that the columnar-equiaxed interactions result into high solutal and solid/grain fraction gradients close to the columnar front. The mesh adaptation scheme is identical with the one used in reference [7]: the three closest control volumes to the *CF* are each refined into N_x smaller cells. This is done in a dynamic way (see Figure 4) as the columnar front is moving from one control volume to another.

Finally the whole numerical algorithm is implemented and solved within Matlab® computing environment, taking thus advantage of its powerful matrix computing procedures.

3 The quasi-steady state CET - The CET maps.

Before attempting to fully model the unidirectional solidification experiments [4, 5], the model described in the previous section is used first to analyze the simpler case of a quasi-steady state CET. Hence, a directional solidification, involving a constant vertical gradient (G) and a constant pulling velocity (V_p, equal as well to the isotherm velocity V_{is}) will be studied in the following, in an attempt to compare the new ensemble average model with the Hunt [9] and Martorano *et al.* [7] model.

By imposing a constant thermal gradient and a constant pulling velocity the temperature field in the ingot will be imposed too. Indeed the temperature distribution becomes

$$T\left(x,t\right) = T_0 - G.V_p.t + G.x \tag{5}$$

where T_0 is the initial temperature at the bottom of the ingot, that is $T(0,0)$. Since the ingot cooling starts from a pure liquid state, T_0 must be larger than T_{liq} (the liquidus temperature corresponding to the initial uniform liquid concentration C_0). Since for this particular case an eventual overheating of the liquid would not influence the subsequent solidification process it is customary to consider [7] that $T_0 = T_{liq}$. Knowing a priori the temperature field, the energy equation in Table 1 doesn't need to be considered anymore.

It is assumed as well that the columnar front starts forming at the bottom wall at the liquidus temperature, that is at $t = 0$. Since its velocity V_{cf} is initially close to 0 and logically smaller than the local isotherm velocity $V_{is}\left(\equiv V_p\right)$, the temperature at the columnar front T_{cf} will progressively decrease increasing consequently the local undercooling $\Delta T_{cf} = T_{liq} - T_{cf}$ and the columnar tip velocity V_{cf}. If no equiaxed grains are supposed to nucleate within this increasing undercooled zone ahead of the *CF*, the columnar tips will finally reach a quasi-steady state when their velocity equals the isotherm velocity V_{is}. Indeed, when $V_{cf} = V_{is}$, the temperature at the columnar tips does not change anymore and the corresponding undercooling ΔT_{cf}^{steady} remains constant. Therefore, the columnar front is advancing undisturbed and no CET phenomenon appears. However, when equiaxed grains are allowed to nucleate within the undercooled zone ahead of the *CF*, the interaction between this equiaxed zone and the advancing columnar front needs to be analyzed in order to determine if whether or not CET occurs in the ingot. Let us consider that equiaxed grains nucleate at a given undercooling ΔT_{ne} below the local liquidus temperature. As pointed out, as the cooling of the liquid progresses ($t > 0$), the columnar front velocity and the undercooling at the columnar tips ΔT_{cf} increase as well. If ΔT_{cf} becomes larger that ΔT_{ne} the conditions for the equiaxed nucleation within the undercooled melt ahead of the *CF* are established and the columnar tips will be forced to advance through a developed equiaxed zone. Given some particular conditions the latter will eventually stop the advancing of the *CF* and trigger the CET. One should therefore determine these particular conditions producing the CET phenomena.

In this context, the ensemble model will be used to simulate this particular unidirectional solidification and more precisely the complex solutal and mechanical interactions between the advancing *CF* and the equiaxed zone ahead. Since we are interested in obtaining uniquely CET transition maps specifying whether or not a CET takes place given *G*, V_p and ΔT_{ne}, one does not need to model the whole ingot evolution but only the evolution of the columnar front and of the eventual equiaxed zone ahead. Indeed, by imposing the temperature field and by neglecting the macroscopic solute diffusion terms in the solute balance equations one decouples the equiaxed zone ahead of the *CF* from the columnar/equiaxed mixed zone behind the *CF*. This will greatly simplify the modeling task since by transforming the solute balance equations into ODE ones, the pure equiaxed zone ahead of columnar tips can be uniquely determined from the local temperature. Thus one has to model first the evolution of a pure equiaxed zone for a given ΔT_{ne}, cooling rate CR and grain density n_e. The complete state of the equiaxed zone ($\varepsilon_{ge}, \varepsilon_{se}, C_{le}$) will be therefore known for any temperature T below T_{liq}. Since the local temperature at the *CF*, T_{cf}, is known from the exact position of the columnar front x_{cf}, the equiaxed state at the columnar front can be computed as well, knowing T_{cf}.

Therefore, one has to resolve first the pure equiaxed zone in front of the *CF* knowing that locally the temperature distribution is given by

$$T_{eq}(t) = T_0 + CR.t \tag{6}$$

A complete description of the equiaxed structure is therefore obtained, depending solely on *CR*, ΔT_{ne}, n_e and on the local temperature T_{eq}:

$$\varepsilon_{ge}, \varepsilon_{se}, C_{le}, \overline{w}_{ge} = f\left(T_{eq}, n_e, \Delta T_{ne}, CR\right) \tag{7}$$

To model now the columnar front evolution and an eventual CET, one has only to solve the front tracking equation (1) in which the local columnar tip velocity is linked directly to the local equiaxed tip velocity through the local temperature T_{cf}

$$V_{cf} = \overline{w}_{ge}\left(T_{cf}, n_e, \Delta T_{ne}, CR\right) \tag{8}$$

3.1 The equiaxed zone ahead of the columnar front

Let us first analyze the purely equiaxed case. As already discussed, the pure equiaxed zone ahead of the *CF* is only a limiting case of the complete model in Table 1 for $n_c = 0$ and $\varepsilon_c = 0$. The columnar averaged equations and the energy equations being discarded one will only have to solve the equiaxed solute and mass balance equations where $\varepsilon_e = 1$. As pointed out in [1], this set of equations is equivalent with the Wang and Beckermann model [2] excepting the solute diffusion length δ_{l-d} which in the ensemble averaged model is approached from an approximate model. In this light a validation of the new proposed diffusion length has to be assessed first. For reasons of clarity, the comparison with the Wang and Beckermann model [2] is presented in the Appendix A. It is worthwhile to notice that despite its simplicity, the approximate model gives very accurate results. The agreement with the integral approach in [2] for cases involving high cooling rates or small grain densities is very satisfactory. In contrast with the latter case, for small cooling rates or high n_e, the results deviate considerably from the Wang model [2]. This is due mainly to the fact that the integral approach in [2] does not respect the zero solute flux condition at the cell boundary, and therefore overestimates the enriching process of the extra-dendritic liquid.

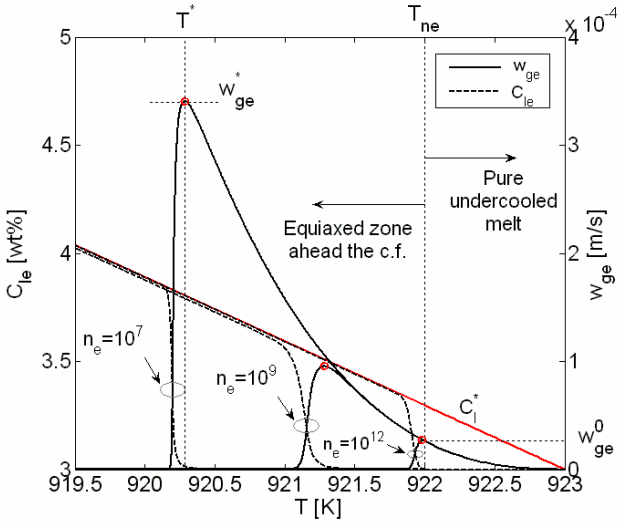

Figure 5: Extra-dendritic liquid solute concentration and tip velocity evolution for the equiaxed grains ahead of the *CF* (Al-3wt%Cu, CR=0.1K/s, $\Delta T_{ne} = 1K$, $n_e = 10^7, 10^9, 10^{12}\ m^{-3}$)

As noted in Appendix A the equiaxed grain density n_e has significant influence on the subsequent equiaxed solidification, given a constant *CR* and ΔT_{ne}. Therefore it is instructive to analyze in more detail the influence of n_e on the pure equiaxed zone evolution and consequently on the CET. The equiaxed solidification of an Al-3wt%Cu alloy is analyzed in the following for a

constant cooling rate of 0.1 *K/s*, a equiaxed undercooling of *1K* and for three different grain densities: $n_e = 10^7, 10^9, 10^{12}\ m^{-3}$. In Figure 5 and Figure 6 the main parameters of the equiaxed grains are plotted against the local temperature of the undercooled zone ahead of the *CF*. Notice that with the use of (6) one can directly obtain their time evolution as well. Two main sub-zones can be identified: a pure undercooled liquid melt between the equiaxed nucleation temperature $T_{ne} = T_{liq} - \Delta T_{ne}$ and T_{liq} within which no equiaxed nucleate and the developed equiaxed zone for $T < T_{ne}$. Note again that for the moment we ignore the columnar zone and we analyze only the equiaxed structure. Hence, when the local temperature reaches T_{ne}, equiaxed nuclei germinate homogeneously with a grain density n_e. As pointed out in [1], this would be also equivalent with an average distance between nuclei of $R_{1e} = \left(4/3\pi n_e\right)^{-1/3}$.

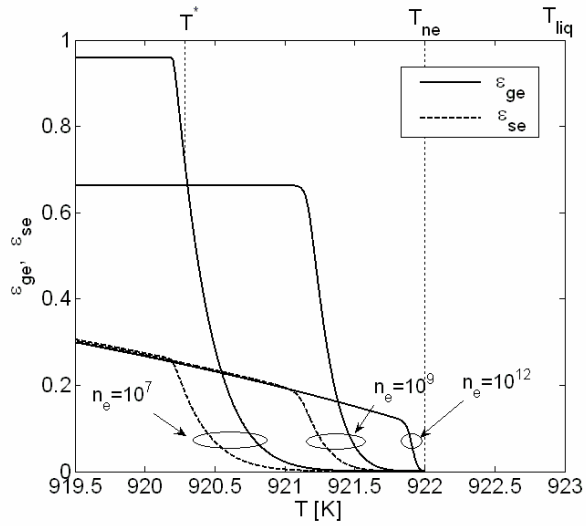

Figure 6: Solid and grain fraction evolution for the equiaxed zone ahead the *CF* (Al-3wt%Cu, CR = 0.1 *K/s*, $\Delta T_{ne} = 1K$, $n_e = 10^7, 10^9, 10^{12}\ m^{-3}$)

Let us focus for the moment on the first case involving the smallest grain density ($n_e = 10^7\ m^{-3}$), and thus the largest distance between adjacent grains, $R_{1e} \simeq 2.9\,mm$. Since the local temperature undergoes a continuous decrease in time, the local solutal undercooling $\Delta C_e = C_l^* - C_l$ will increase as well due to the fact that the mean concentration in the extra-dendritic liquid still remains close to the initial one C_0 (see Figure 5). This in turn is due to the fact that the newly formed nuclei reject only small quantities of solute in the extra-dendritic liquid in view of their small exchange interfacial area ($S_{ge} = n_e 4\pi a_e^{\,2}$). The increasing local undercooling results into increasing local tip velocity (Figure 5) and rapidly, the initial fully solid nuclei evolve into highly dendritic grains for which $\varepsilon_{se} < \varepsilon_{ge}$ (Figure 6). Note however, that for this first case the concentration of the extra-dendritic liquid remains close to C_0 even for high grain fractions and consequently for relative high interfacial exchange areas. This can be explained by the fact that for high dendrite tip velocities, the local Pe_g ($Pe_g = \overline{w}_{ge}\left(R_{1e} - a_e\right)/D_l$) is higher than 1 even for large ε_{ge}. As pointed out in [1] on has

$$\frac{\delta_{l-d}}{R_{1e} - a_e} \simeq \frac{1}{Pe_g} \tag{9}$$

meaning that the solutal boundary layer surrounding the grain envelope is much smaller than the length scale of the extra-dendritic liquid. Basically this means that the solutal interactions between two adjacent grains are negligible. Given these conditions, the liquid will remain close to C_0 as long as $\delta_{l-d} \ll R_{1e} - a_e$. Only when the solutal boundary layer around the grain arrives at the cell boundary, that is when

$$\delta_{l-d} \simeq R_{1e} - a_e \tag{10}$$

the enriching of the equiaxed extra-dendritic liquid becomes non-negligible. Since for high cooling rates $\delta_{l-d} \ll R_{1e} - a_e$ (see equation (9)) one obtain that the enriching process becomes important for grain diameters $a_e \simeq R_{1e}$, that is for equiaxed grain fractions ε_{ge} close to unity. Indeed looking at Figure 6 one can see that the enriching of the extra-dendritic liquid becomes important below a temperature T^* corresponding to a grain fraction ε_{ge}^* of order of 1. Above this limit the extra-dendritic liquid undergoes a rapid enriching process (Figure 5) having as consequence a rapid drop in the local undercooling. The latter will finally vanish ($C_l \simeq C_l^*$) and the grain growth is stopped. Subsequently the solidification will continue within a state of perfect solutal mixing, that is following a Scheil law. It is important to notice as well the particular variation of the local tip velocity which reaches a maximum value, $\overline{w}_{ge}^*$ at the critical temperature T^* (Figure 5). Since the local equiaxed velocity is equal with the columnar tip velocity if a columnar tip would be present there, it is clear that the particular variation of the equiaxed tip velocity would also influence the columnar front evolution and eventually the CET phenomena.

If the second case is analyzed ($n_e = 10^9\, m^{-3}; R_{1e} \simeq 620\,\mu m$) one can observe that due to somewhat larger interfacial areas S_{ge}, the extra-dendritic liquid is enriching faster than the previous case. Basically due to a larger n_e and smaller average distance between grains, R_{1e}, the solutal interactions between adjacent grains are more important. This will determine smaller characteristic Pe_g numbers and consequently a faster solutal enriching process. The latter becomes non negligible for smaller equiaxed grain fractions (ε_{ge}^*) and is characterized by a smaller maximum tip velocity $\overline{w}_{ge}^*$ (Figure 5).

A limit case is the third one ($n_e = 10^{12}\, m^{-3}; R_{1e} = 62\,\mu m$) which corresponds to a highly grain refined alloy. The solutal interactions between two adjacent grains are so strong that the extra-dendritic liquid is enriched from the very beginning of the equiaxed solidification. As seen in Figure 5, C_{le} equals C_l^* soon after the equiaxed nucleation. Moreover, the equiaxed grains solidify in a globulitic manner ($\varepsilon_{ge} = \varepsilon_{se}$) following a Scheil law (Figure 6).

Knowing now the exact evolution of the pure equiaxed zone ahead the columnar front with respect to the CR, n_e and ΔT_{ne} one is able to analyze its influence on the advancing CF and consequently on the CET. As discussed earlier, the equiaxed grains reject solute in their extra-dendritic liquid and decrease consequently the local undercooling at the dendrite tip. This would influence of course the evolution of the columnar tips if they were present within the equiaxed zone. This effect is no more than the solutal blockage mechanism of the equiaxed grains on the columnar tips, just as it was identified in [7].

On the other hand it is expected that due to the finite equiaxed grain dimension, the equiaxed structure would partially obstruct the columnar tips in their advance, producing a kind of "mechanical blockage" effect on the columnar front, somewhat similar with what Hunt [9] predicted. Before presenting the full modeling of the columnar front advance, it would be instructive to analyze in detail the solutal and the mechanical blocking effects.

3.1.1 Solutal blockage effect. Now we consider both types of solidification, e. g., columnar and equiaxed. Basically we are interested on the particular conditions describing the unidirectional solidification $\left(V_p, G, n_e, \Delta T_{ne}\right)$ under which a CET can be triggered. First, we have assumed that the columnar tips and the equiaxed zone at the *CF* share a same undercooling and consequently a same tip velocity $\left(V_{cf} = \overline{w}_{ge}\right)$. Secondly, by neglecting the macro-diffusion terms in the solute balance equations, the pure equiaxed zone ahead of the *CF* is completely decoupled from the evolution of the zone behind the *CF*. Hence, knowing the local temperature at the columnar tips T_{cf}, one can completely describe the equiaxed state at the *CF*. Since the equiaxed zone ahead of the *CF* is completely determined from the CR, n_e and ΔT_{ne}, one has to analyze only the influence of the pulling velocity V_p on the CET phenomenon. In turn, the thermal gradient is directly resolved from the *CR*, $G = CR/V_p$. Let us focus on the second equiaxed case analyzed in the previous section ($n_e = 10^9\ m^{-3}$). It is assumed first that the pulling velocity V_p is smaller than the maximum equiaxed velocity $\overline{w}^*_{ge}$ (Figure 7).

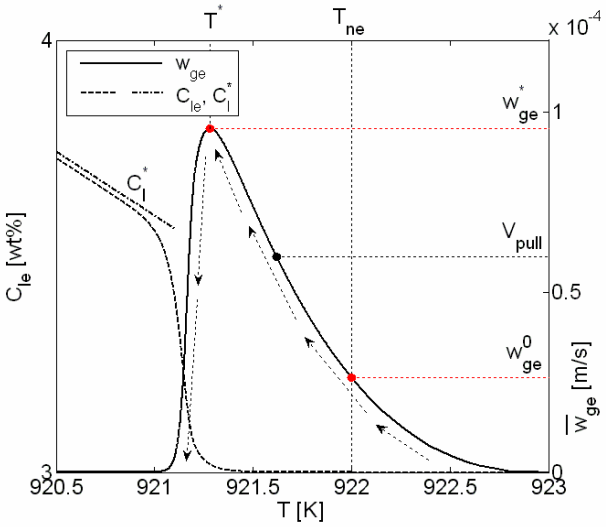

Figure 7: Solutal blockage effect of the equiaxed zone ahead the *CF* (Al-3wt%Cu, CR=0.1 *K/s*, $\Delta T_{ne} = 1K$, $n_e = 10^9\ m^{-3}$)

As pointed out, the columnar grains nucleate at the bottom wall when the local temperature reaches the liquidus one T_{liq}, that is at $t = 0$, given the initial conditions in (5). Initially the *CF* velocity will be close to 0 and obviously smaller that the local isotherm velocity $V_{is}\left(= V_p\right)$. Consequently the columnar tip temperature T_{cf} will decrease and the local undercooling ΔT_{cf} and V_{cf} at the *CF* will increase. At the very beginning the undercooling ΔT_{cf} is lower than the equiaxed nucleation undercooling ΔT_{ne} and no equiaxed grains exist in front of the *CF*. The *CF* is advancing in a pure undercooled melt (Figure 7, see the columnar evolution path coupled with the $\overline{w}_{ge}$ evolution). The *CF* undercooling increases further until it reaches the equiaxed nucleation undercooling ΔT_{ne}. At this precise moment equiaxed grains nucleate instantaneously at the *CF*. Let us denote with $\overline{w}^0_{ge}$ the equiaxed tip velocity corresponding to the nucleation undercooling ΔT_{ne}. Since $V_{cf}\left(= \overline{w}^0_{ge}\right)$ is still smaller than the isotherm velocity, T_{cf} decreases further and the equiaxed zone ahead of the *CF* becomes larger too. The columnar tips will be forced to advance through a

developed equiaxed zone (Figure 2). Notice that for the moment $T_{cf} > T^*$, and therefore to a decrease of the *CF* temperature it corresponds an increase of both the local undercooling ΔT_{cf} and tip velocity V_{cf}. This is due to the fact that equiaxed grains ahead the *CF* don't reject yet enough solute in their extra-dendritic liquid and consequently C_{le} remains close to C_0. In turn, the increase in the *CF* velocity is continuously decreasing the difference between V_{cf} and the local isotherm velocity V_p. When V_{cf} becomes equal to V_p the *CF* reach a quasi-steady state. Indeed following this moment the *CF* temperature does not change anymore and the local undercooling at the tip remains unchanged too. Hence, the *CF* velocity reaches the quasi-steady state.

Therefore for this particular choice of the pulling velocity, the *CF* reaches a quasi-steady state and, neglecting for the moment the mechanical blocking effect of the equiaxed grains, a mixed columnar/equiaxed structure will be identified in the ingot.

Let us analyze now the case $V_p < \overline{w}_{ge}^{0}$. Using a similar reasoning as for the previous case, one can couple the *CF* evolution with the one of the equiaxed tip velocity (Figure 7). Following the *CF* evolution path one can observe that the condition for the existence of a quasi-steady state at the columnar tips, $V_{cf} = V_p$, is reached before the equiaxed grains have the possibility to nucleate within the undercooled melt ahead of the *CF*. In this case the undercooled zone ahead of the *CF* is not sufficiently large to allow for equiaxed nucleation. Thus, the *CF* will advance undisturbed in a pure undercooled melt and no CET can be identified. A fully columnar structure will be identified in the ingot.

Now let us consider a third case for which $V_p > \overline{w}_{ge}^{*}$. Following again the evolution path of the *CF* (Figure 7) it is observed that the *CF* velocity increases until it reaches the maximum equiaxed velocity $\overline{w}_{ge}^{*}$. Since V_{cf} is still smaller than the local isotherm velocity V_p, T_{cf} will continue to decrease. However, at this level the equiaxed grains would have already started to enrich the extra-dendritic liquid and diminish the local undercooling (Figure 7). Therefore, to a decrease in the local *CF* temperature will correspond now a decrease in local tip velocity (Figure 7). The *CF* velocity will therefore decrease below $\overline{w}_{ge}^{*}\left(< V_p\right)$ and the *CF* temperature, T_{cf}, will undergo an even faster decrease. The columnar tips are slowed down by the equiaxed zone ahead and will be finally stopped, $V_{cf} \to 0$. Hence, no quasi-steady state establishes at the *CF* and a CET occurs. Basically, the equiaxed zone is solutally blocking the columnar front due to the important solutal enriching of the extra-dendritic liquid. It is important to notice that this effect is no more than the solutal blockage mechanism as it was identified by Martorano *et al.* [7]. Finally a fully equiaxed zone will be observed in the ingot.

Therefore for a given CR, n_e and ΔT_{ne} the CET is strongly influenced by the choice of the pulling velocity V_p. Three cases were identified:

- a fully columnar structure in the ingot for $V_p < \overline{w}_{ge}^{0}$;
- a mixed c/e structure for $\overline{w}_{ge}^{0} \le V_p \le \overline{w}_{ge}^{*}$;
- a fully equiaxed structure for $V_p > \overline{w}_{ge}^{*}$.

It is important to notice that $\overline{w}_{ge}^{0}$ depends solely on the choice of the equiaxed undecooling ΔT_{ne}, whereas $\overline{w}_{ge}^{*}$ depends strongly on CR and n_e. In Figure 8 the dependence of $\overline{w}_{ge}^{*}$ on the choice of CR is analyzed. Basically, decreasing the *CR* would decrease the $\overline{w}_{ge}^{*}$ too, limiting thus the difference $\overline{w}_{ge}^{*} - \overline{w}_{ge}^{0}$ and conditions for obtaining a quasi-steady mixed zone. This is due mainly to the fact that for small cooling rates the solute diffusion process at the grain envelope has enough

time to enrich the extra-dendritic liquid. Hence, the enriching of the extra-dendritic liquid will become non-negligible for larger local temperature (Figure 8).

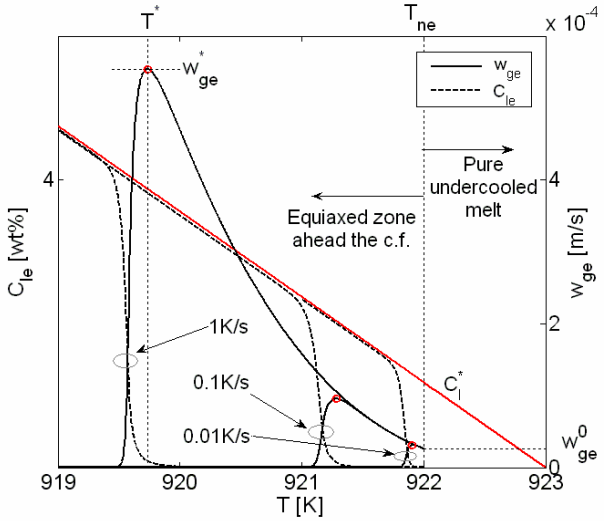

Figure 8: Influence of the cooling rate on the equiaxed zone ahead the *CF* (Al-3wt%Cu, $\Delta T_{ne} = 1K$, $n_e = 10^9\ m^{-3}$)

3.1.2. Mechanical blockage effect. As seen given certain solidification conditions such that $\overline{w}_{ge}^{0} \le V_p \le \overline{w}_{ge}^{*}$, a particular CET can be identified, involving a mixed columnar/equiaxed state at the columnar tips. To characterize more precisely this zone the mechanical blockage effect of the equiaxed zone on the *CF* should be taken into account. Basically, one would have to quantify the mechanical interactions between the advancing *CF* and the developed equiaxed zone ahead. As pointed out in [1], due to its statistical approach, the new ensemble model can take into account these types of interactions and characterizes in a rigorous way the mixed c/e zone behind the *CF*.

Let us consider an advancing columnar front characterized by a grain density n_c^0 (linked to the primary arm spacing) and a developed equiaxed zone ahead having a grain density n_e and a non-zero grain diameter a_e. This would correspond to an equiaxed grain fraction $\varepsilon_{ge} = n_e\left(4/3\pi a_e^{\,3}\right)$. As pointed out in [1] the columnar and the equiaxed grain distributions interact "mechanically" following a two fold mechanism.

First mechanical blockage

The first mechanical blockage effect of the equiaxed grains will determine a rarefaction of the columnar zone when entering ("nucleating") into a developed equiaxed zone. This will decrease the initial columnar grain density n_c^0 with a factor if $(1-\varepsilon_{ge})$, (see as well the columnar grain balance in Table 1). Indeed due to the finite equiaxed grain fraction the columnar tips have only a limited space $(1-\varepsilon_{ge})$ within which they can "nucleate". Hence only a fraction of the total number of columns will be able to enter the equiaxed zone.

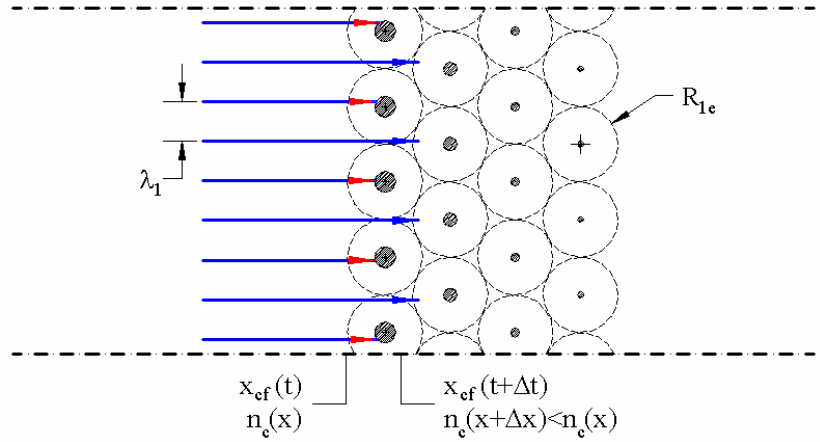

Figure 9: The first mechanical blockage: observe the rarefaction process of the columnar zone.

It is clear now that, *given no redensifying mechanism for the columnar tips*, the advancing columnar front will undergo a continuous rarefying process, its grain density n_c constantly decreasing in time. To quantify this process it would be instructive to consider the simple situation in Figure 9. Since the equiaxed zone ahead of the *CF* has an uniform grain density n_e, the average space between two adjacent equiaxed grains is no more than $R_{1e} = \left(4/3\pi n_e\right)^{-1/3}$. If the *CF* arrives at a point **x** within the equiaxed zone the columnar "nucleation", as defined in [1], triggers within the developed equiaxed zone. A mixture c/e zone is therefore formed. As pointed out the columnar grain density which corresponds to the columnar "nucleation" event can be computed as follows:

$$n_c\left(\mathbf{x}\right) = n_c^0\left(1-\varepsilon_{ge}\right) \tag{11}$$

where n_c^0 is the nucleation grain density of the columnar grains. This is of course valid when it is assumed that a homogeneous spherical grain population nucleate within the equiaxed zone. In reality the columnar grains are not spherical ones but highly anisotropic grains developed along the *x* direction. However, as pointed out in [1] one can approach, to a first approximation, the columnar zone with an equivalent spherical model for which the two main characteristics, the average spacing between the particles λ_1 and the grain fraction ε_{gc} are inherited from the real columnar zone. In this way a pure columnar zone can be *locally* approximated with a homogeneous spherical grain distribution, having a grain density computed from the primary arm spacing

$$n_c^0 = \left(\frac{4}{3}\pi\lambda_1^3\right)^{-1} \tag{12}$$

This is somewhat equivalent with transforming the columnar zone into an equivalent equiaxed one. However this is a particular "equiaxed" zone since one must have in mind the fact that between these columnar spherical particles there is a strong statistical correlation: first no mobility of the grains is allowed and secondly an axial gradient of the local grain fraction ε_{gc} would be equivalent with a local variation of the columnar grain diameter along x direction. Notice that in (12) λ_1 can be expressed with respect to the local thermal gradient G and isotherm velocity V_{is} by means of various models existing in the literature [10, 11].

Returning to the particular case of a columnar front advancing within a developed equiaxed zone, the question to be answered is what the pertinent value for n_c^0 in equation (11) would be. In reference [1] it was proven that, from a statistical point of view, n_c^0 represents the conditional

probability of having a columnar grain nuclei at **x** given no equiaxed grain centered within the sphere centered at **x** and of radius a_e, that is, given no equiaxed grain touching the point **x**. In this light n_c^0 appear to be correlated with the columnar grain density n_c characterizing the columnar zone at a certain distance behind the nucleation site **x** and outside the radius of influence of the closest equiaxed grain to **x**. Knowing the length scale characterizing the equiaxed zone at **x**, i.e. the average distance between equiaxed particles R_{1e}, one expects that n_c^0 to be correlated with the grain density characterizing the columnar zone at its previous position $x - R_{1e}$ (Figure 9), that is just before entering the equiaxed zone at **x**. One expects thus that

$$n_c^0(\mathbf{x}) \simeq n_c(x - R_{1e}) \tag{13}$$

Due to the isotropic approximation used to characterize the columnar zone, the above equation must be seen only as a first approximation to the columnar nucleation grain density n_c^0. A more detailed analysis could be made if we consider the interactions between an advancing anisotropic columnar grains and the developed isotropic equiaxed zone ahead of the columnar front. However, this approach would be more complex since one would have to deal with the statistical coupling between a cylindrical model (2D approach) and a spherical one (3D approach). Note that, despite the simplified approach used above, two important aspects are intrinsically embedded in equations (11) and (13). Firstly, due to the finite dimension of the equiaxed grains the columnar grain density decrease with a factor proportional with the equiaxed grain fraction ε_{ge}. Secondly, the length scale characterizing the distance over which n_c^0 is decreasing with a factor equal to $1-\varepsilon_{ge}$ is no more than the equiaxed length scale R_{1e}. These two information help us to quantify the decrease rate of the columnar grain density, that is to say the rarefaction rate of the columnar zone. Indeed, for a given equiaxed grain fraction ε_{ge} and a constant columnar front velocity V_{cf} advancing through the equiaxed zone the decrease rate of n_c becomes

$$\begin{aligned} \frac{\left[n_c(x) - n_c(x - R_{1e})\right] / n_c(x - R_{1e})}{\left(R_{1e} / V_{cf}\right)} &= -\varepsilon_{ge} \frac{V_{cf}}{R_{1e}} \\ &= -\varepsilon_{ge} V_{cf} \left(4/3\pi n_e\right)^{1/3} \end{aligned} \tag{14}$$

Notice that the decrease rate of n_c is computed with respect to the time scale $\tau = R_{1e} / V_{cf}$. From (14) it is easy to see that the columnar density n_c will decrease more rapidly for a denser equiaxed zone (larger n_e), for a more developed equiaxed zone (larger ε_{ge}) and for a faster advancing *CF* (larger V_{cf}).

Second mechanical blockage effect

As pointed out in reference [1], the second mechanical blockage effect of the coexistence reflects the fact that for a mixed zone (i.e. columnar + equiaxed), the two coexisting structures are forced to share a same space (Figure 10). Consequently, the space available for each structure will be different and smaller too from the corresponding space available just before the coexistence state.

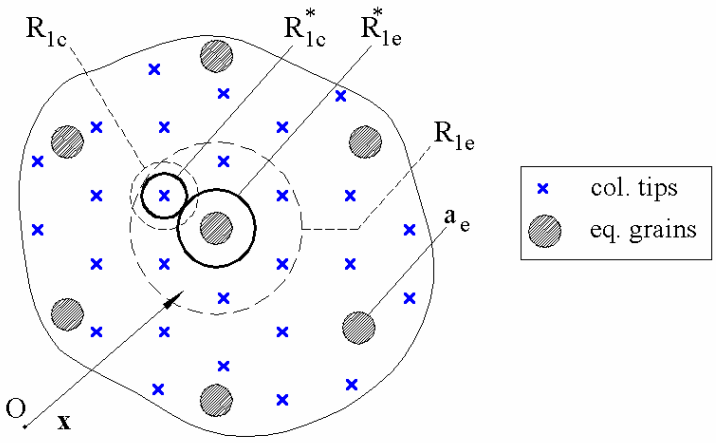

Figure 10: The second mechanical blockage: the full line circles represent the two cells characterizing the mixed c/e zone and the dashed line circles are the cells characterizing the two structures (c/e) separately, that is just before the coexistence state

As discussed already, the space characterizing the mixed c/e structure is quantified in the ensemble model by means of two corresponding spherical cells of radius $R^*_{1c/e}$ (Figure 10). Basically the second mechanical blockage states that the length scales $R^*_{1c/e}$ are smaller than the corresponding length scales characterizing the c/e state separately before their coexistence, namely $R_{1c/e}$. Notice again that $R^*_{1c/e}$ together with their corresponding grain densities $n_{c/e}$ are of primary importance for the modeling of the mixed c/e zone. Indeed these parameters characterize completely the statistics of the coexistence state, enabling one to define average variables (i.e. c/e fractions, average concentrations, etc) for each one of the two structures. Moreover, since $R^*_{1c/e}$ can be very different form the original length scales $R_{1c/e}$ the evolution of the mixed zone can be significantly different from that of an equivalent pure columnar or equiaxed zone.

3.2 Numerical results

Let us now fully resolve the columnar front evolution for an Al-3wt%Cu alloy, a cooling rate of $CR = 0.1 K/s$, an equiaxed grain density $n_e = 10^9\, m^{-3}$ and an equiaxed nucleation undercooling of 1 *K*. As pointed out, the equiaxed zone ahead of the columnar tips is fully determined for a given CR, n_e and ΔT_{ne} (Figure 7). Let us first consider the case where the pulling velocity $V_p = 8 \cdot 10^{-5} m/s$ is smaller than $\overline{w}^*_{ge}$. As pointed out one has only to solve the *CF* tracking equation (1) knowing that the columnar front velocity is equal to the local tip velocity characterizing the equiaxed grains at the *CF*, equation (2). Moreover, the two mechanical blockage effects of the equiaxed grains, as detailed in the previous section need to be considered as well.

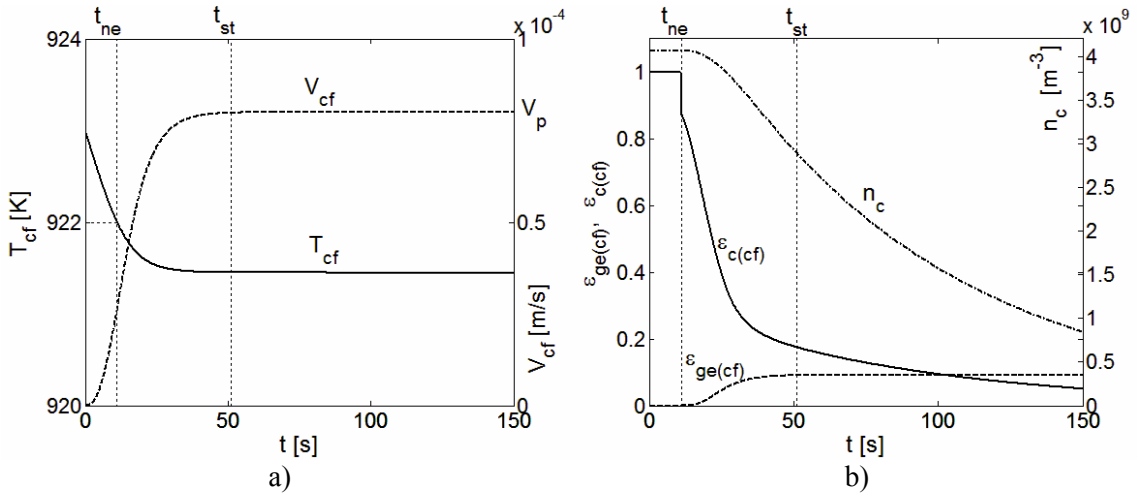

Figure 11: a) The *CF* temperature and the *CF* velocity evolution; b) The evolution of the equiaxed grain fraction, the columnar fraction and the columnar grain density at the *CF* (Al-3wt%Cu, CR = 0.1 *K/s*, $\Delta T_{ne} = 1K$, $n_e = 10^9\ m^{-3}$, $V_p = 8 \cdot 10^{-5} m/s$)

The evolution of several parameters at the *CF* is presented in Figure 11. One can see (Figure 11a) that the *CF* velocity V_{cf} start to increase from the very beginning ($t = 0$). Indeed we supposed that the columnar grains nucleate on the bottom wall when the local temperature reaches T_{liq}, that is at $t = 0$ given the boundary conditions. Due to the fact that its initial velocity is smaller than the local isotherm velocity ($V_{is} = V_p$), T_{cf} decreases and consequently V_{cf} increases. As observed, initially (Figure 11b), the columnar structure conserves its initial grain density n_c^0 (cf. equation (12)), since no equiaxed grains exist ahead of the *CF*. For the same reason, initially (Figure 11b) the columnar fraction ε_c remains equal to unity, meaning that the columnar tips are advancing within a pure undercooled melt; no coexistence with another structure exists. This first stage in the evolution of the *CF* continues until T_{cf} becomes equal to T_{ne}, the equiaxed nucleation temperature. Starting with this moment (t_{ne}) an equiaxed zone develops in front of the *CF* and the columnar tips will be forced to advance within an increasingly developed equiaxed zone. Note again that the *CF* velocity V_{cf} is computed form the local equiaxed tip velocity, equation (2). As expected, since V_{cf} is still smaller than V_{is}, T_{cf} decreases further and V_{cf} increases. This increase is due to the fact that the equiaxed grains have not yet enriched the extra-dendritic liquid ($C_{le} \simeq C_0$). The tip velocity continues to increase until V_{cf} reaches the isotherm velocity V_{is}. Above this moment (t_{st}) the columnar tip velocity and the tip temperature T_{cf} don't change anymore (Figure 11a). Indeed, from the point of view of T_{cf} and V_{cf} the *CF* reaches a quasi-steady state. Note again that this quasi-steady state is possible due to the negligible solutal interaction between the equiaxed zone and the *CF*.

On the other hand the mechanical interactions cannot be neglected. Starting with the moment t_{ne} when $T_{cf} = T_{ne}$ the *CF* will enter into an increasingly developed equiaxed zone. Indeed, the equiaxed grain fraction ε_{ge} at the *CF* (Figure 11b) is continuously increasing obstructing the columnar tips. As discussed earlier two mechanical blockage effects of the equiaxed grains on the *CF* can be identified. Firstly, the finite size equiaxed grains will lead to a rarefaction of the columnar tips, equation (11). As observed (Figure 11b) n_c is continuously decreasing in time for $t > t_{ne}$ and if no other redensifying mechanism is considered, the columnar zone will finally fade away into the equiaxed one.

Secondly, the columnar "nucleation" within an equiaxed zone leads to a sharing of space between the two coexisting structures (columnar and equiaxed). As discussed, the way the two structures share a same space is reflected by the two fractions $\varepsilon_{c/e}$ and the two lengths scales $R^*_{1c/e}$. Basically the coexistence state is characterized by a smaller average distance between particles ($R^*_{1c/e}$) compared with the ones valid if no coexistence between particles would be considered ($R_{1c/e}$). As observed (Figure 11b) at t_{ne}, that is when the columnar tips enters into the newly formed equiaxed zone a drop in the columnar fraction takes place. Indeed, at the t_{ne} freshly new equiaxed nuclei and the columnar tips are forced to share a same space. Consequently the columnar fraction ε_c, a function of n_e, n_c^0 and $\varepsilon_{ge} = 0$ (Table 1), becomes smaller than 1. Since the *CF* is advancing into an increasingly developed equiaxed zone (larger ε_{ge}) ε_c will decrease further. Notice that this effect is amplified by the fact that n_c^0 decreases too due to the first mechanical blockage effect.

The first mechanical blockage effect has another important consequence on the CET. As pointed out due to negligible solutal interaction between the *CF* and the equiaxed zone ahead V_{cf} and T_{cf} reach a quasi-steady state when V_{cf} becomes equal to V_{is}. For $t > t_{st}$ all parameters characterizing the equiaxed state at the *CF* becomes constant with respect to time. Despite this fact, due to the first mechanical blockage effect n_c will continue its decrease even after t_{st}. Hence, given no other redensifying mechanism for the columnar grains, no quasi-steady state at the *CF* can be identified. If the ingot is sufficiently long n_c will become negligible with respect to n_e, ε_c will drop to zero and the columnar zone will finally disappear favoring the pure equiaxed structure. Finally a fully equiaxed structure will be observed in the ingot.

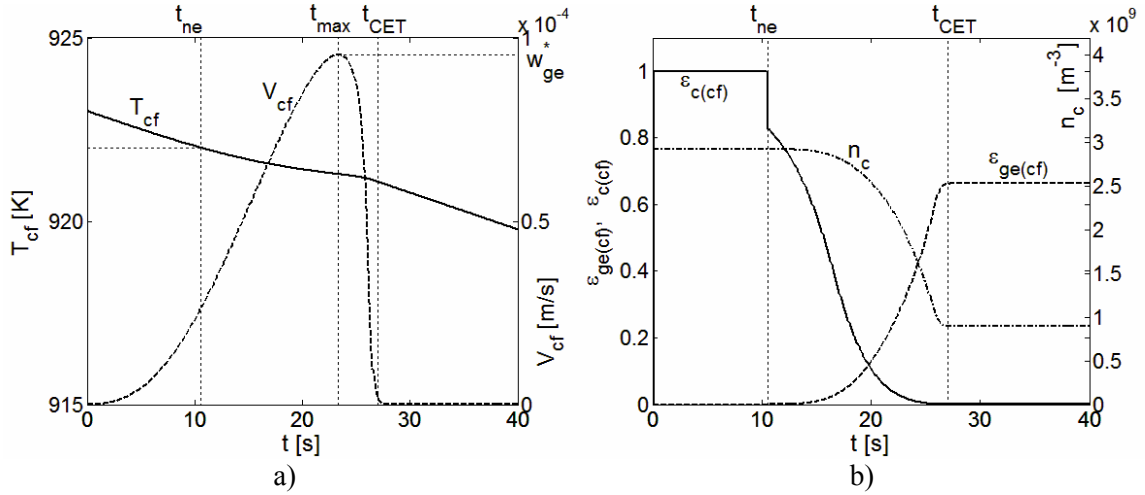

Figure 12: a) The *CF* temperature and the *CF* velocity evolution; b) The evolution of the equiaxed grain fraction, the columnar fraction and the columnar grain density at the *CF* (Al-3wt%Cu, CR = 0.1 *K/s*, $\Delta T_{ne} = 1K$, $n_e = 10^9\ m^{-3}$, $V_p = 1.5 \cdot 10^{-4} m/s$)

Let us now consider a pulling velocity larger than $\overline{w}^*_{ge}$, i.e., $V_p = 1.5 \cdot 10^{-4} m/s$. As noted before, due to initial negligible solutal interactions between equiaxed grains and due to the fact that the local *CF* velcity is initially smaller than V_p, T_{cf} decrease and V_{cf} increases in time (Figure 12a). V_{cf} increases until it reaches the maximum equiaxed velocity $\overline{w}^*_{ge}$, that is at $t = t_{\max}$ (Figure 12a). Since $\overline{w}^*_{ge}$ is still smaller than the local isotherm velocity V_p, T_{cf} will decrease further.

However, at this level, due to the non-negligeble solutal interaction between equiaxed grains, to a decrease in the local *CF* temperature it corresponds a decrease in local tip velocity (Figure 7). The *CF* velocity will therefore decrease below $\overline{w}_{ge}^{*}\left(<V_p\right)$. The columnar tips are slowed down by the equiaxed zone ahead and will be finally stopped ($V_{cf}\rightarrow 0$) at $t=t_{CET}$ (Figure 12a). Thus no quasi-steady state establishes at the *CF*; and a CET occurs. A fully equiaxed zone will further occupy the ingot. Notice that the constant equiaxed grain fraction for $t>t_{CET}$ (Figure 12b) reflects in fact the fully developed equiaxed zone at the *CF*. Since the *CF* is stopped, the columnar grain density at the *CF* remains constant in time as well (Figure 12b).

3.2.1. Redensifying mechanism of the columnar zone. In reality the columnar tip density n_c is not a simple imposed parameter as n_e is, but derives from a complex behavior of the columnar tips advancing into an undercooled melt. As already pointed out the primary arm spacing λ_1 characterizing a quasi-steady columnar front is mainly controlled by the local thermal gradient *G* and the local isotherm velocity V_{is} at the columnar tips. Moreover, if the columnar tips are subject to changes in their local cooling conditions (*G* and V_{is}), λ_1 will readapt to the new conditions. However this readapting process is not at all instantaneous but follows a particular dynamics. This readapting process is analyzed in detail by Ciobanas et al. in [12]. In fact the primary arm spacing is viewed as the spacing characterizing a stable dendrite array configuration. In [12] we have quantified in a simple way the two mechanisms responsible for the selection of the primary arm spacing: the dendrite division mechanism and the dendrite overgrown mechanism. First, in the upper dendrite spacing range the mechanism of dendrite division is identified. Indeed, for a large average spacing between dendrites, the solutal interactions between adjacent dendrites are weak and the liquid behind the dendrite points will remain close to initial concentration C_0 due to the thin solutal boundary layers around the columnar tips. Secondary or even tertiary arms developed behind the columnar tips may evolve into vertical primary arms reducing thus the primary arm spacing. Hence this configuration will not be stable with respect to the dendrite division mechanism. The division of columnar dendrites has been quantified in [12] by means of the characteristic time t_{rs} representing the response time of the columnar tips to a small perturbation from the quasi-steady state. Basically this time quantifies the laps of time during which a tip slightly deviated from the quasi-steady state reach back the isotherm T_{ts} for which $V_t=V_{is}$, that is reach back the quasi-steady state. It was found that

$$t_{rs}\simeq -2\left(\frac{\partial V_t}{\partial x}\right)_{x_{st}}^{-1} \tag{15}$$

where x_{st} is the position of the isotherm T_{ts} corresponding to the quasi-steady state at the tip. Note as well that t_{rs} depends strongly on the thermal gradient *G* at the *CF* and the isotherm velocity V_{is}. Secondly, in the lower dendrite spacing range the mechanism of dendrite overgrown holds. Indeed if the spacing between the dendrites array is small enough, due to strong solutal interactions between adjacent dendrite tips, some of the dendrites are overgrown by the surrounding elements of the array. This configuration will be thus unstable with respect to the dendrite overgrown mechanism. The solutal interactions between adjacent tips has been quantified in [12] with the help of the time scale t_{dw}.

As pointed out in [12] one expects that at the intersection of these two unstable regimes to find a stable dendrite array configuration defined by the primary arm spacing λ_1. It is shown that the stable primary arm spacing can be linked to the characteristic time t_{rs} as follows:

$$\lambda_1=3\left(D_l t_{rs}\right)^{1/2} \tag{16}$$

where D_l is the solute diffusivity in the liquid. A detailed comparison with various directional experiments [12] shows that, despite its simplicity, equation (16) provides results which agree remarkably well with the experimental data.

It is well known that when the dendrite array is subject to changes in local cooling conditions (G and V_{is}) or optimal spacing λ_1 (by means of a blocking mechanism, i.e. the first mechanical blockage effect) the dendrite spacing will always readapt to the new conditions. Notice again that this readapting process is not instantaneous but follows a particular dynamics. An important conclusions of the study in [12] is that the time scale characterizing this dynamics is no more than t_{rs}. Indeed t_{rs}, besides from quantifying the dendrite division mechanism, will also quantify the time during which the dendrite array will reach back the quasi-steady state corresponding to the new conditions at the tip. This time scale is of great interest in determining if whether or not the columnar tips can be considered as evolving in a quasi-steady state with respect to the non-stationary local conditions at the tip (G, V_{is} and λ_1). Indeed, if the time scale characterizing the changes in local conditions at the tip is much larger than t_{rs} that means that the readaptation time of the dendrite array to the new local conditions will be much more rapid than the conditions at the tip are actually changing. Given these conditions, in spite of non-stationary local conditions at the tip, the columnar array evolution should be very close to the quasi-steady state.

As detailed previously (Figure 11) if no redensifying mechanism of the columnar tips is considered, even if V_{cf} and T_{cf} remain constant at the *CF*, no quasi-steady state of the *CF* can be obtained (n_c and ε_c are constantly diminishing for $t > t_{st}$). However, as pointed out earlier, the columnar tips will react to changes in local conditions (i.e. n_c) trying to reach back the quasi-steady state. Indeed, by diminishing the columnar grain density n_c, the effect of the first mechanical blockage is to rarefy the dendrite array. However, the natural tendency of the columnar grains would be to reestablish the optimum primary arm spacing by means of the dendrite division mechanism. Indeed, the decrease of n_c deviates the columnar tips from the optimum state characterized by the primary arm spacing λ_1. Therefore, the columnar division will act to reestablish the optimal primary arm spacing. This mechanism is not instantaneous but have a characterized time scale, namely t_{rs}. In this respect it will be interesting to compare t_{rs} with a time scale characterizing the first mechanical blockage. Let us denote this latter time scale with t_{m1}. For a case where the *CF* advances with a constant velocity through the equiaxed zone $\left(V_{cf} = V_{is}\right)$ (Figure 11a, $t > t_{st}$) the time scale t_{m1} can be easily estimated. Indeed, as pointed out in equation (14), the columnar grain density n_c decrease with a factor ε_{ge} in a distance of order of $R_{1e} = \left(4/3\pi n_e\right)^{-1/3}$. Hence the time scale characterizing the decrease of n_c is simply

$$t_{m1} = R_{1e} / V_{cf} \tag{17}$$

Now, by comparing t_{m1} with t_{rs} one can determine if whether or not the redensifying mechanism of the columnar dendrite tips is rapid enough to neglect the effects of the first mechanical blockage. Indeed, if $t_{rs} \gg t_{m1}$ the first mechanical blockage is acting faster than the rebranching mechanism. As a consequence the columnar zone will be rarefied continuously during the *CF* advancing through the equiaxed zone. The columnar tips will finally disappear leaving place to a fully equiaxed structure.

However, if $t_{rs} \ll t_{m1}$ the rebranching mechanism is much faster than the equiaxed grains are actually blocking the columnar tips. Hence, one can approximate the columnar nucleation density as being constant and equal to the value n_c^0 computed from the optimum primary arm spacing, equation (16).

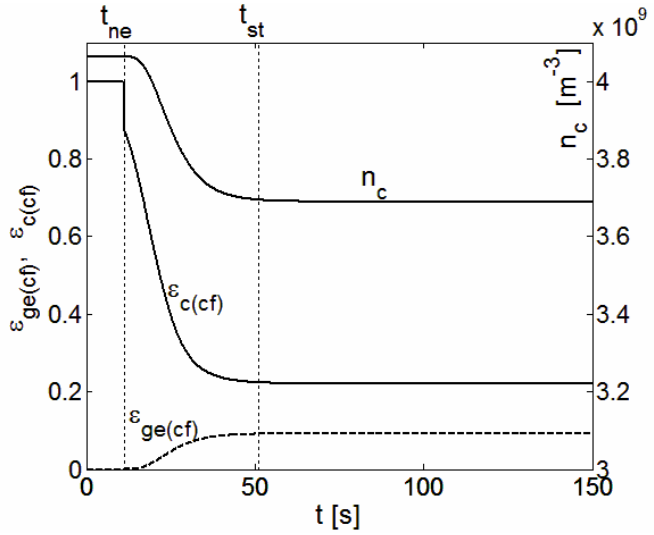

Figure 13: The evolution of the equiaxed grain fraction, the columnar fraction and the columnar grain density at the *CF* (Al-3wt%Cu, CR = 0.1 *K/s*, $\Delta T_{ne} = 1K$, $n_e = 10^9\ m^{-3}$, $V_p = 8 \cdot 10^{-5} m/s$, no first mechanical blockage effect)

Let us for example reanalyze the case shown in Figure 11. If one neglects the first mechanical blockage effect (admit that $t_{rs} \ll t_{m1}$), the columnar grain density n_c and the columnar fraction ε_c at the *CF* for $t > t_{st}$ will remain constant (Figure 13). Hence, all parameters characterizing the state at the *CF* are stationary. A quasi-steady state condition at the *CF* can be obtained and a mixed c/e zone will further occupy the ingot.

3.2.2 CET maps. The CET maps represents in the $(G - V_{is})$-space the different possible quasi-steady CET, i.e. pure equiaxed, pure columnar or mixed columnar-equiaxed. To built a CET diagram one should model the *CF* evolution for different $G - V_{is}$ pairs and see if whether or not a pure columnar, equiaxed or mixed CET is obtained. However this direct approach would be very tedious since many $G - V_{is}$ pairs must be considered to cover a typical $(G - V_{is})$-space. Fortunately, the problem can be greatly simplified by considering the following hypothesis:

i) the equiaxed zone ahead of the *CF* is decoupled from the zone behind the *CF*;
ii) for a given *CR*, ΔT_{ne} and n_e the equiaxed zone ahead of the *CF* can be fully determined from the local temperature;
iii) as pointed out in the previous section, the pure columnar, pure equiaxed or mixed CET depends solely on the pulling velocity $V_p \left(= V_{is}\right)$.

Therefore, to realize a CET map one has to fix first the equiaxed nucleation undercooling ΔT_{ne} and the equiaxed grain density n_e. If the *CR* is further fixed, the equiaxed state ahead of the *CF* can be fully determined. By varying the *CR* the pure equiaxed state ahead of the *CF* is fully determined for the whole range $G - V_{is}$. Finally for a given *CR*, one has only to vary the pulling velocity V_p in order to identify the CET type. In fact for a given *CR*, ΔT_{ne} and n_e the variation of the equiaxed tip velocity can be directly linked to the local temperature (see Figure 7). As discussed, two characteristic velocity have been determined, $\overline{w}_{ge}^{0}$ and $\overline{w}_{ge}^{*}$ (Figure 7). The first one is linked to the equiaxed undercooling ΔT_{ne} and fixes the limit between the pure columnar solidification and the mixed one. The second velocity marks the limit above which the *CF* will be solutally blocked by the equiaxed zone ahead, that is the limit between the mixed and pure equiaxed solidification. Basically one has a pure columnar solidification for $V_p < \overline{w}_{ge}^{0}$, a pure equiaxed solidification for

$V_p < \overline{w}^{*}_{ge}$ and a possible mixed solidification for $\overline{w}^{0}_{ge} \le V_p \le \overline{w}^{*}_{ge}$. We say "possible" mixed solidification because a quasi-steady state can be obtained at the *CF* only if the redensifying mechanism is more effective than the first mechanical blockage effect ($t_{rs} \ll t_{m1}$). Otherwise, a pure equiaxed regime must be considered since the columnar zone will finally vanish into the equiaxed one leaving place to a fully equiaxed structure.

Let us neglect for the moment the first mechanical blockage. In this respect, for a pulling velocity between $\overline{w}^{0}_{ge}$ and $\overline{w}^{*}_{ge}$, a quasi-steady mixed solidification will be obtained. In turn this state can be characterized with a column fraction ε_c which can be expressed as follows:

$$\frac{\varepsilon_c}{(1-\varepsilon_e)} = \begin{cases} 1-\varepsilon_{ge} - \dfrac{1}{20n_c^0}\left[\begin{array}{l} 10n_e + 36(n_e)^{\frac{2}{3}}\left(n_c^0\varepsilon_{ge}\right)^{\frac{1}{3}} \\ +45(n_e)^{\frac{1}{3}}\left(n_c^0\varepsilon_{ge}\right)^{\frac{2}{3}} \end{array}\right] & if \quad R_{1c} \le R_{1e}\left(1-\varepsilon_{ge}{}^{1/3}\right) \\ \dfrac{n_c^0}{20n_e}\left[\begin{array}{l} \left(\varepsilon_{ge}\right)^2 - 20\varepsilon_{ge} + 45\left(\varepsilon_{ge}\right)^{\frac{2}{3}} \\ -36\left(\varepsilon_{ge}\right)^{\frac{1}{3}} + 10 \end{array}\right] & if \quad R_{1c} > R_{1e}\left(1-\varepsilon_{ge}{}^{1/3}\right) \end{cases} \tag{18}$$

where ε_{ge} is the equiaxed grain fraction at the *CF* corresponding to the quasi-steady state (see Figure 13 $t > t_{st}$), n_c^0 is the columnar nucleation grain density which depends on the local primary arm spacing λ_1 and finally $R_{1c} = \left(4/3\pi n_c^0\right)^{-1/3}$, $R_{1e} = \left(4/3\pi n_e\right)^{-1/3}$. Since we neglect for the moment the first mechanical blockage effect, λ_1 can be approached with the quasi-steady solution of Equation (16).

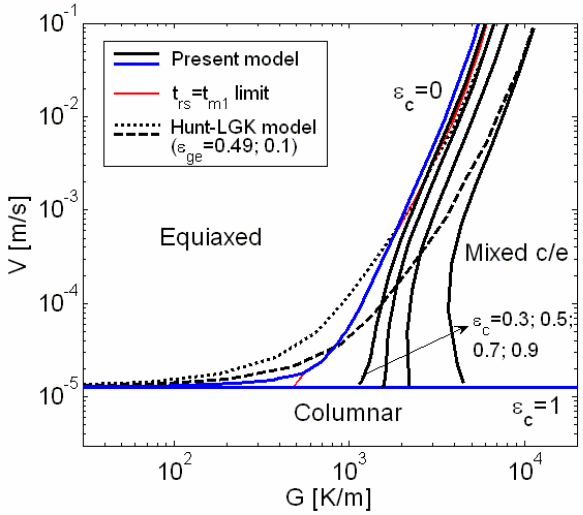

Figure 14: CET map for the Al-3wt%Cu alloy ($\Delta T_{ne} = 0.75K$ and $n_e = 10^9\, m^{-3}$)

By varying now the *CR* and resolving for each CR the equiaxed zone, the two corresponding critical velocities $\overline{w}^{0}_{ge}$ and $\overline{w}^{*}_{ge}$, can be determined. Hence, the CET map can be quite easily built, by marking the two limits between the pure columnar and mixed solidification and between the mixed and pure equiaxed regimes. Moreover, the mixed zone can be further characterized by specifying the iso-columnar fraction curves. In this way the mixed zone predicted semi-empirically by Hunt [9] can now be rigorously characterized.

Two typical CET maps for the Al-3wt%Cu alloy, a constant ΔT_{ne} of 0.75K and two different equiaxed grain density ($n_e = 10^9\, m^{-3}$ and respectively $n_e = 10^5\, m^{-3}$) are presented in Figure 14, Figure 15. One can observe the two important limits corresponding to the two critical velocities $\overline{w}_{ge}^{0}$ and $\overline{w}_{ge}^{*}$ (blue lines). The first one (the horizontal line) marks the limit between the pure columnar and the mixed regime. Indeed, if the pulling velocity is below $\overline{w}_{ge}^{0}$ the maximum undercooled zone ahead of the *CF* will be always smaller than ΔT_{ne}. Hence, no equiaxed grains can nucleate in the pure undercooled melt ahead the *CF*. Finally a fully columnar structure is identified in the ingot.

The second limit separates the mixed from the pure equiaxed regime. Above this limit the solutal blockage mechanism as defined by Martorano *et al.* [7] becomes non-negligible and the equiaxed grains will finally stop the *CF*. As pointed out, for a given CR this limit correspond to a pulling velocity equal to $\overline{w}_{ge}^{*}$, i.e., the maximum equiaxed velocity (Figure 7). Any V_p above this limit corresponds to a sufficiently large undercooled melt ahead the *CF* in such a way as the equiaxed grains have the time to enrich the extra-dendritic liquid and to finally block the columnar tips. For $V_p > \overline{w}_{ge}^{*}$, a pure equiaxed structure will be finally obtained in the ingot. Notice again that this solutal blocking limit is the same as the CET limit identified by Martorano *et al.* in [7].Notice however that due to the different approach regarding the estimate of the diffusion length δ_{l-d} characterizing the solute flux at the grain interface, the Martorano *et al.* model underestimates the solutal limit with respect to the present model. This is a consequence of the fact that for average *CR* Martorano *et al.* approach predicts a faster enriching process of the extra-dendritic liquid than the present model does (see Appendix A). Note as well the important effect of n_e on the solutal blocking limit. The decrease in n_e is significantly shifting this limit towards the low-G regime (Figure 15), increasing therefore the mixed c/e zone. This can be expected since smaller n_e means weaker solutal interactions between equiaxed grains delaying the solutal enriching process of the extra-dendritic liquid. Indeed, for a given *CR* a smaller n_e will determine an increase of $\overline{w}_{ge}^{*}$ (Figure 5). Hence, the solutal blocking effect becomes non-negligible at smaller thermal gradients.

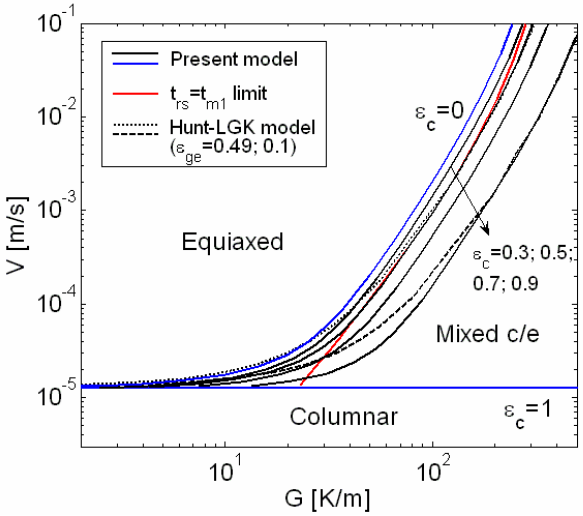

Figure 15: CET map for the Al-3wt%Cu alloy ($\Delta T_{ne} = 0.75K$ and $n_e = 10^5\, m^{-3}$)

As pointed out, between these two limits, a quasi-steady mixed solidification regime is obtained if the first mechanical blockage is neglected. This is quantified by means of the columnar fraction at the *CF* ε_c computed with (18). Consequently iso-columnar fractions can be plotted to better describe the mixed CET zone (Figure 14, Figure 15). An important remark is that by

decreasing the *CR* the mixed zone is shrinking as well. This is a normal consequence of the fact that to a smaller *CR* it corresponds a smaller interval $\overline{w}_{ge}^{0} - \overline{w}_{ge}^{*}$ (Figure 8). As observed (Figure 14, Figure 15, low-G regime), there is a limit value of the *CR* below which $\overline{w}_{ge}^{*} - \overline{w}_{ge}^{0} = 0$. Indeed, below a critical *CR* the equiaxed extra-dendritic liquid remains in a state of perfect solutal mixing from the beginning of the solidification. No mixed zone exists in that case, and the solutal limit can be identified with the horizontal line corresponding to $\overline{w}_{ge}^{0}$.

It is of interest to compare now these CET maps with the simplified Hunt's model [9] for which a LGK approach is used to determine the dendrite tip kinetics (Hunt-LGK model). By imposing empirically two limits on the equiaxed grain fraction at the *CF*, $\left(\varepsilon_{ge}\right)_{cf}$, Hunt's model manages to delimit as well three zones on the CET map: a pure columnar zone if $\left(\varepsilon_{ge}\right)_{cf} < 0.1$, a pure equiaxed zone if $\left(\varepsilon_{ge}\right)_{cf} > 0.49$ and a mixed one if $0.1 \le \left(\varepsilon_{ge}\right)_{cf} \le 0.49$. The two limits corresponding to $\left(\varepsilon_{ge}\right)_{cf} = 0.1$ and respectively $\left(\varepsilon_{ge}\right)_{cf} = 0.49$ are superimposed on the two CET maps. One observes that in the high-*CR* regime these two limits converge almost perfectly with the iso-columnar fractions of *0.9* and *0.5* respectively. This result has a two-fold explanation. On one hand for the high-G regime, due to very small solutal interactions between equiaxed grains the extra-dendritic remains close to C_0 until very close to the moment when the equiaxed grain fraction reaches the unity. Given these conditions, the Hunt's model which neglects completely the solutal interactions between grains would predict a similar equiaxed grain evolution as the present model. On the other hand the equivalence between the two equiaxed grain limits fixed by Hunt (0.1 and 0.49) and the iso-columnar fractions (0.9 and 0.5) can be explained by the fact that for high *CR,* and basically for relatively high *G* and V_{is}, the primary arm spacing λ_1 becomes very small in comparison with the average distance between equiaxed grains, meaning that $n_c^0 \gg n_e$. As a consequence when the columnar tips enters within equiaxed zone, the sharing of space between the equiaxed and the columnar structures will be highly unbalanced. Indeed for $n_c^0 \gg n_e$, the columnar tips will occupy much more effectively the available equiaxed extra-dendritic liquid $(1-\varepsilon_{ge})$ compared with the equiaxed grains. This is well reflected by equation (18) in which for $n_c^0 \gg n_e$ one obtains a columnar fraction $\varepsilon_c \to \left(1-\varepsilon_{ge}\right)$. However, in the middle range of *CR* regime, the Hunt's model deviates sensibly from the present predictions, overestimating the $\left(\varepsilon_{ge}\right)_{cf} = 0.49$ limit. The same has been identified by Martorano *et al.* [7] when comparing the solutal limit and the $\left(\varepsilon_{ge}\right)_{cf} = 0.49$ limit. This non-agreement is a consequence of the fact that for middle range values of CR, the solutal interactions between grains becomes non-negligible. Therefore, by neglecting the solutal enriching process of the equiaxed extra-dendritic liquid, the Hunt's model will overestimate the moment when the equiaxed grain fraction reaches the 0.49 value. This disagreement is somewhat less important for the case involving small equiaxed grain density ($n_e = 10^5\ m^{-3}$). This is due to the fact that for large average distances between equiaxed grains, even for relatively small CR the solutal interactions between grains is negligible. The enriching of the extra-dendritic liquid takes place suddenly when the equiaxed grain fraction approaches unity. Finally, in the low-*CR* regime the two Hunt's limits [9] converge to a same horizontal line as the present model does. As pointed in [7] this should be expected since in the low-G regime the CET should be independent on n_e and depends solely on the isotherm velocity. The good agreement between the Hunt and the present model in the low and high-CR regime is further establishing confidence in the present numerical calculations.

Remember that in characterizing the mixed CET zone we have neglected so far the first mechanical blockage, that is we have supposed that $t_{rs} \ll t_{m1}$. It would be instructive now to superimpose on the two CET maps the limit $t_{rs} = t_{m1}$ (Figure 14, Figure 15, red line). In this way we will divide the mixed CET zone in two sub-domains. For the one corresponding to $t_{rs} < t_{m1}$ (between the red line and the horizontal blue line) one can expect to obtain a quasi-steady mixed zone since the redensifying mechanism of the columnar tips is rapid enough to counter the first mechanical blockage effect. On the other hand for the sub-domain corresponding to $t_{rs} > t_{m1}$ (between the red line and the solutal blocking limit), the columnar structure will finally vanish into the equiaxed zone leaving place to a fully equiaxed zone. It is also interesting to notice that for high cooling rates the limit $t_{rs} = t_{m1}$ almost converge with the solutal blocking limit. Finally three distinct zones have been identified in the CET maps: the pure columnar CET, the quasi-steady mixed c/e CET and the pure equiaxed zone.

The use of the new ensemble averaged model enabled us to quantify rigorously both the solutal and the mechanical blockage mechanism producing the CET phenomena. Basically, since it intrinsically includes the solutal and the mechanical blocking effects, the new ensemble model unifies the semi-empirical Hunt approach [9] (pure mechanical blocking mechanism) and the Martonero approach [7] (pure solutal blocking mechanism).

4 Simulation of unidirectional solidification experiments

In the following section the present model is used to simulate various unidirectional solidification experiments in an attempt to validate the new ensemble averaged model. The series of directional experiments are taken from the studies of Mahpatra and Weinberg [4] and Ziv and Weinberg [5]. Notice as well that the same set of experiments has been used by Wang and Beckermann [13] to validate their CET volume averaged model. Hence a comparison with this model will be assessed too.

4.1 Experimental conditions

For the first experimental study [4], a Sn-Pb alloy is poured into a 100 mm long cylindrical mold which is solidified vertically from the bottom by means of a water-cooled cooper chill (Figure 16). Various experiments (Table 2) are carried out covering a wide range of chill heat transfer coefficients (h_{ext}), pouring superheats (ΔT_0) and lead concentrations (5, 10, 15 wt%). Unidirectional solidification conditions are achieved by minimizing the upper and lateral heat losses.

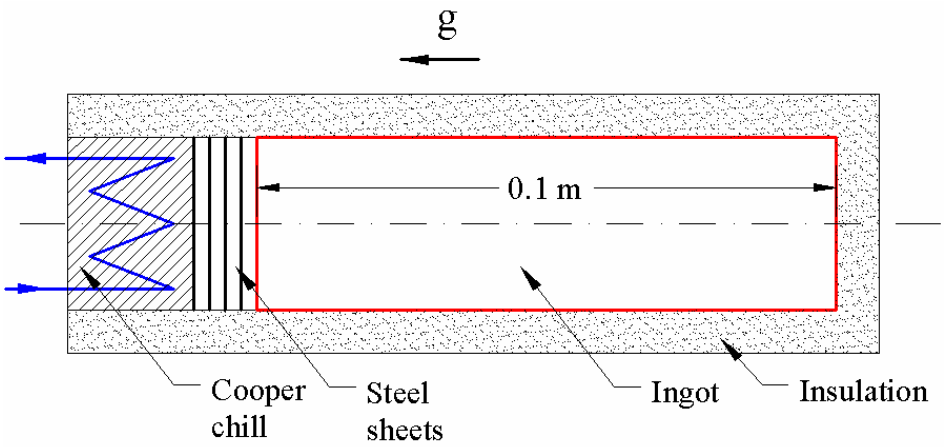

Figure 16: The solidification configuration used in [4] and [5]

The heat transfer coefficients, h_{ext}, are determined by the authors by fitting the numerical results obtained with an approximate heat transfer model with the experimental temperature measurements. Note however that the 1D heat transfer model used in [4] is an approximate one and

therefore the fitted values for h_{ext} may have a relative high degree of uncertainty. Unfortunately the temperature measurements are not provided by the authors and a direct comparison with the simulation results is not possible. However CET positions are observed and measured by sectioning the ingots longitudinally and by polishing and etching the obtained sections. Note however that values for grain size are not provided as well. As one can see in the following, by supposing that fragmentation of columnar grains is the main cause for the CET phenomena, the grain size measurements will not be needed anymore.

The second study [5] uses the same solidification configuration as the previous one. However the solidified alloy is Al-3wt%Cu this time. Again various chill heat-transfer coefficients are covered and the CET positions is measured for each experiment. Note that the authors have carried out as well experiments with grain refined alloy (TiB2 additions) obtaining in some cases a mixed equiaxed-columnar zone behind the CET frontier, confirming therefore the existence of mixed c/e zone behind the *CF*. In contrast with the Sn-Pb experiments, detailed grain size measurements are provided. For the non-refined experiments the equiaxed grain size varied slightly with the heat transfer, between *5.4-6.2 mm*, corresponding thus to an equiaxed grain density equal to $n_e \approx 5\times10^6\ m^{-3}$. An important missing parameter for this set of experiments is the pouring superheat ΔT_0. In the absence of a value for ΔT_0 we used the same approach as Wang and Beckermann [13], by considering that a reasonable approximation for ΔT_0 would be $20^o C$.

A summary of experiments results obtained in [4, 5] is presented in Table 2. A detailed comparison of these data with the model results is assessed in the following.

4.2 Numerical results and discussion

Since the temperature field is not anymore imposed as for the quasi-steady solidifications in the previous section, the fully transient formulation for the energy equation has to be used. Basically, this would be equivalent with solving the full transient 1D model detailed in Table 1.

Table 2: Summary of the unidirectional experiments in [4] and [5]

Exp. No.	**Superheat** [K]	h_{ext} $\left[\frac{W}{m^2.K}\right]$	**Measured CET position** [m]	x_{cf}^{cr} [m]	t_{rs}^{cr} [s]	t_{th}^{cr} [s]	G^{cr} [K/m]
Sn – 10 wt pct Pb							
1	11.5	63	0.038	0.0508	882.1	1549.1	9.16
2	11.5	113	0.060	0.0591	626.3	1003.9	10.91
3	11.5	134	0.065	0.0606	466.9	868.2	14.14
4	19	63	0.040	0.0511	804.7	1558.2	10.09
5	19	84	0.045	0.0535	656.8	1222.6	11.81
6	19	134	0.065	0.0599	344.8	858.5	18.95
7	31	63	0.035	0.0545	841.4	1661.3	9.30
8	31	96	0.050	0.0590	597.9	1179.1	11.84
9	31	113	0.057	0.0587	526.4	997.4	13.20
10	31	134	0.065	0.0617	476.8	883.5	13.72
11	36	96	0.050	0.0585	623.5	1170.7	11.45
12	36	134	0.065	0.0614	380.6	879.8	17.46
13	36	209	0.080	0.0677	280.2	621.7	21.04
Sn – 10 wt pct Pb							
14	7.5	71	0.052	0.0460	686.7	1244.8	8.33
15	12	92	0.060	0.0520	599.7	1086.2	8.86
16	22	113	0.070	0.0556	452.4	944.4	10.86
Sn – 15 wt pct Pb							
17	21.5	151	0.048	0.0630	443.4	800.6	17.89
18	21.5	167	0.055	0.0647	418.5	744.3	18.55

19	21.5	272	0.070	0.0709	282.0	500.6	23.49
20	36	105	0.040	0.0613	550.1	1120.8	15.46
21	41	146	0.050	0.0638	405.5	839.3	19.69
Al – 3 wt pct Cu							
22	20	95	0.072	0.0469	883.1	1678.0	6.66
23	20	65	0.053	0.0421	1103.6	2201.3	6.15
24	20	63	0.048	0.0397	1143.6	2139.6	5.93
25	20	53	0.045	0.0375	1273.2	2406.7	5.69
26	20	50	0.037	0.0368	1219.2	2500.3	6.01
27	20	37	0.034	0.0342	1563.9	3144.3	4.85

The 1D simulations are carried out on a $N = 200$ cells grid. As pointed out the three cells near the columnar front are always refined into N_{ref} smaller cells. Several test were realized and a typical value of $N_{ref} = 41$ was found to be highly sufficient for the typical solidification conditions in Table 2. The CET, cooling curves, and the other average parameters converge in a satisfactory way for $N > 100$ and $N_{ref} > 21$. A time step of $\Delta t = 0.05\ s$ was found to capture well enough the kinetics of the solidification experiments in Table 2. In addition the use of the adaptive time scheme was found to reduce considerably the influence of Δt on the final results. The upper thermal boundary condition is considered adiabatic and at the lower boundary a heat flux is imposed:

$$\phi_{bot} = h_{ext}\left(T_{bot} - T_{ext}\right) \quad \left[W/m^2\right] \tag{19}$$

where $T_{ext} = 293\,K$ is the ambient temperature, T_{bot} the bottom wall temperature and h_{ext} the heat transfer coefficient. The typical CPU time for *1000s* of real solidification was of order of 45 minutes on a AMD Athlon 2000+ standard PC.

It is worthwhile to notice that in the following the columnar nucleation grain density n_c^0 is directly linked to the local cooling conditions G and V_{is} using Equation (16). Therefore we considered that the first mechanical blockage effect on the columnar tips is negligible, meaning that $t_{rs} \ll t_{m1}$.

4.2.1 Base test case. A first test case is discussed in more detailed in the present paragraph. This is the 22nd case in Table 2 that is an Al-3wt%Cu alloy, poured in a superheated liquid ($\Delta T_0 = 20^o C$) and cooled from the bottom ($h_{ext} = 95\,W.m^{-2}.K^{-1}$). We firstly consider in the following a vanishing equiaxed nucleation undercooling, $\Delta T_{ne} = 0^o C$ and an equiaxed nucleation grain density of $n_e = 10^5\ m^{-3}$. The main numerical results are presented in Figure 17-23. In Figure 17 the cooling curves at five different position along the ingot are presented. As expected, the recalescence phenomena are more pronounced close to the bottom wall due mainly to a high heat extraction rate. Far from the bottom wall, the cooling curves exhibit thermal plateaus. As Wang and Beckermann [13] noticed, by taking into account the mixed columnar and equiaxed solidification the recalescence phenomena reduces in intensity compared with a pure equiaxed solidification.

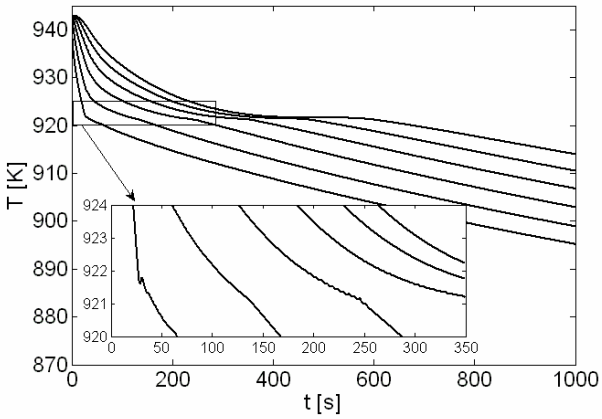

Figure 17: Cooling curves for the Al-3wt%Cu test case experiment ($h_{ext} = 95\, W.m^{-2}.K^{-1}$, $\Delta T_0 = 20^o C$, $\Delta T_{ne} = 0^o C$, $n_e = 10^5\, m^{-3}$) corresponding (from the left to the right) to a distance of $x = 1, 10, 20, 30, 40, 50\ mm$ from the bottom of the ingot

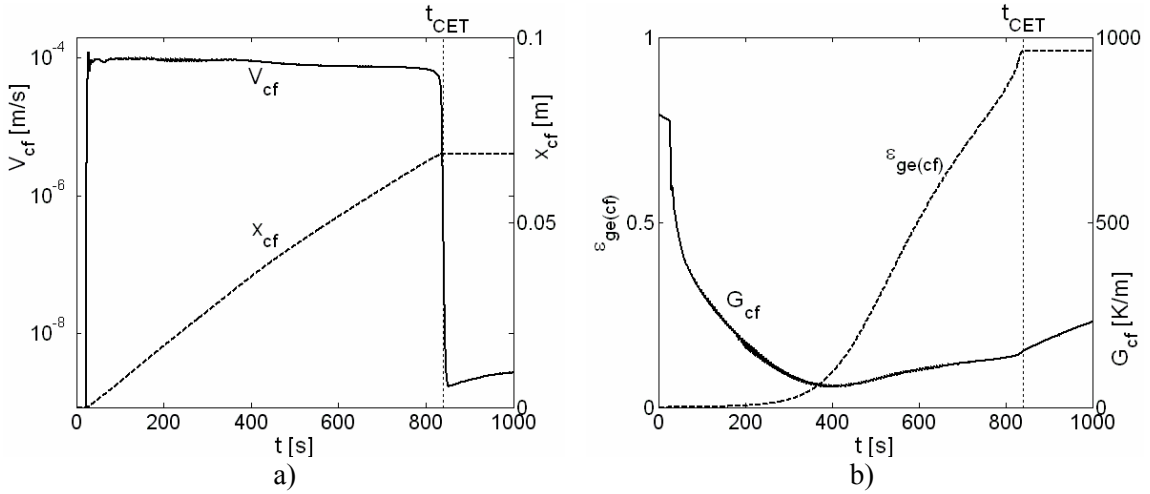

Figure 18: a) the *CF* position and the *CF* velocity and b) the thermal gradient and the equiaxed grain fraction at the *CF* evolution for the Al-3wt%Cu test case experiment ($h_{ext} = 95\, W.m^{-2}.K^{-1}$, $\Delta T_0 = 20^o C$, $\Delta T_{ne} = 0^o C$, $n_e = 10^5\, m^{-3}$)

It is of interest to focus now on the columnar-equiaxed interactions. In Figure 18a the time evolution of the *CF* position with respect to time is presented along with the corresponding *CF* velocity. As it can be observed at $t_{CET} = 840\, s$ the *CF* is stopped, its velocity drops suddenly to 0 and the CET occurs at $x_{CET} = 0.068\, m$. Since no first mechanical blockage effect is considered, the CET is due in this case to the solutal blocking effect of the equiaxed grains ahead the *CF* which reject enough solute in their extra-dendritc liquid to finally block the *CF*. Note as well that the CET occurs very rapidly, similar to what Martorano *et al.* [7] observed. It would be interesting to look in more detail the evolution of the equiaxed grains at the *CF* In Figure 18b, the equiaxed grain and the thermal gradient at the *CF* are plotted against time. As observed the equiaxed grain fraction $\left(\varepsilon_{ge}\right)_{cf}$ is continuously increasing. Indeed since $\Delta T_{ne} = 0^o C$, the equiaxed grains nucleate in front of the *CF* from the very beginning of the solidification. As the *CF* velocity increases in the beginning of the process, the undercooling at the *CF* ΔT_{cf} increases. Hence, the extend of the undercooled zone ahead of the *CF* increases as well and this increase is further amplified by the

decrease of the thermal gradient at the *CF*. The decrease of G_{cf} is a normal consequence of the particular cooling conditions of the ingot. Indeed, the lower wall temperature decreases in time and the flux extracted at the bottom diminishes as well. The decrease of G_{cf} continues until the CET occurs and increases afterwards since, even if the *CF* is stopped, the cooling of the ingot continues. Basically, the increased undercooled region ahead of the *CF* favors the equiaxed growth. The equiaxed grains reject more and more solute in front of the *CF* and will finally solutally block the *CF*. As discussed already, besides the solutal blocking effect, the equiaxed grains ahead the *CF* are also mechanically blocking the columnar grains.

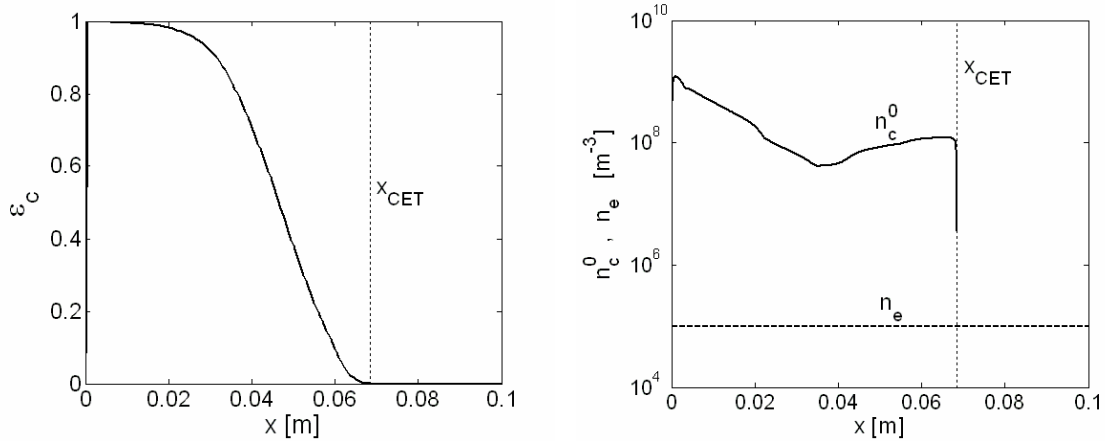

Figure 19: a) the columnar fraction and b) the columnar nucleation grain density ($\propto \lambda_1^{-3}$) variations along the ingot for the Al-3wt%Cu test case experiment ($h_{ext} = 95\, W.m^{-2}.K^{-1}$, $\Delta T_0 = 20^o C$, $\Delta T_{ne} = 0^o C$, $n_e = 10^5\, m^{-3}$)

As seen in Figure 19a the columnar fraction is continuously decreasing along the ingot in favor of the equiaxed structure. This is due to the second mechanical blockage effect as it was detailed in the previous section. Indeed, due to the finite value of $\left(\varepsilon_{ge}\right)_{cf}$ and the differences between n_c^0 and n_e (Figure 19b), the two structures are constrained to share in a different way a same volume. This is quantified in the model by means of the c/e fractions $\varepsilon_{c/e}$. As seen in Figure 19a, at the very beginning of the solidification the columnar structure occupy all the space available ($\varepsilon_c \simeq 1$) despite the presence of equiaxed grains ahead of the *CF*. This is due to a high n_c^0 compared with n_e (Figure 19b) and to the initial small equiaxed grain fraction at the *CF* (Figure 18b). However, as the *CF* advances the equiaxed zone ahead becomes larger, $\left(\varepsilon_{ge}\right)_{cf}$ increases and consequently n_c^0 decreases further. This, of course, is reflected by the rapid drop of the columnar fraction ε_c far from the lower boundary. Finally the ingot will be filled with a relative shallow columnar structure at the bottom of the ingot, followed by a mixed c/e zone which makes the transition to a fully equiaxed structure.

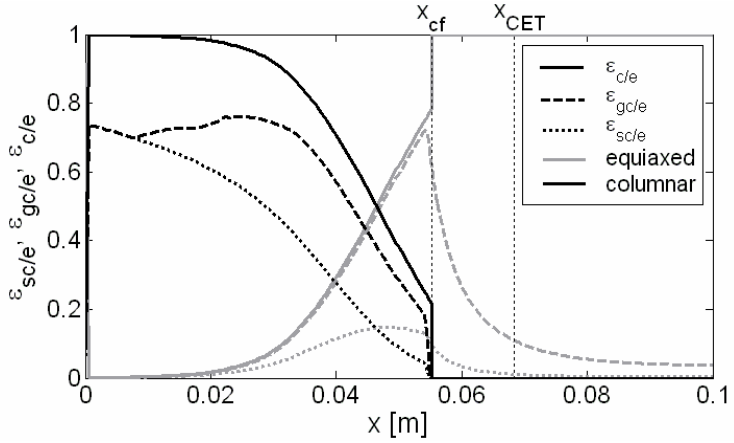

Figure 20: The c/e fraction, the c/e solid fraction and the c/e grain fractions along the ingot at $t = 625\,s$ (Al-3wt%Cu test base case)

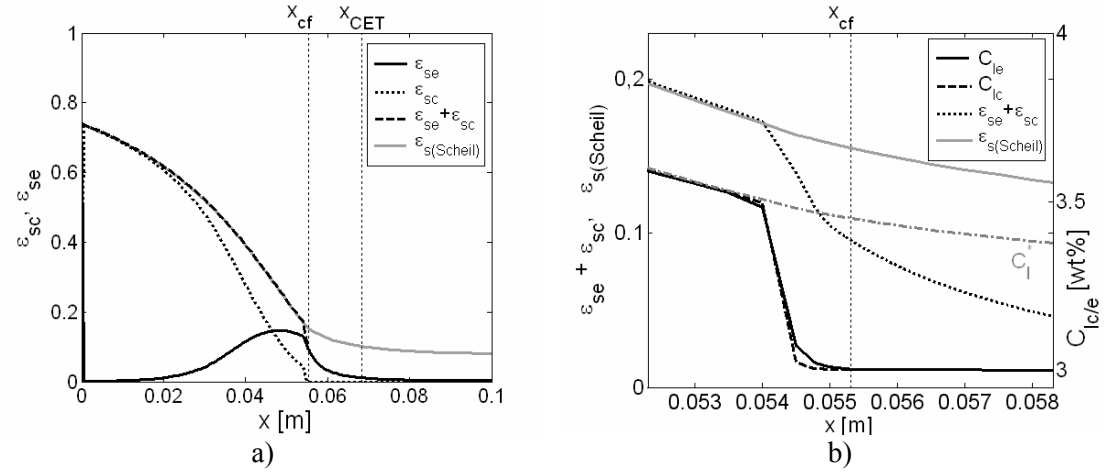

Figure 21: a) The total solid fraction ($\varepsilon_{se} + \varepsilon_{sc}$) evolution along the ingot and b) the c/e extra-dendritic liquid concentration and the total solid fraction near the *CF* at $t = 625\,s$ (Al-3wt%Cu test base case)

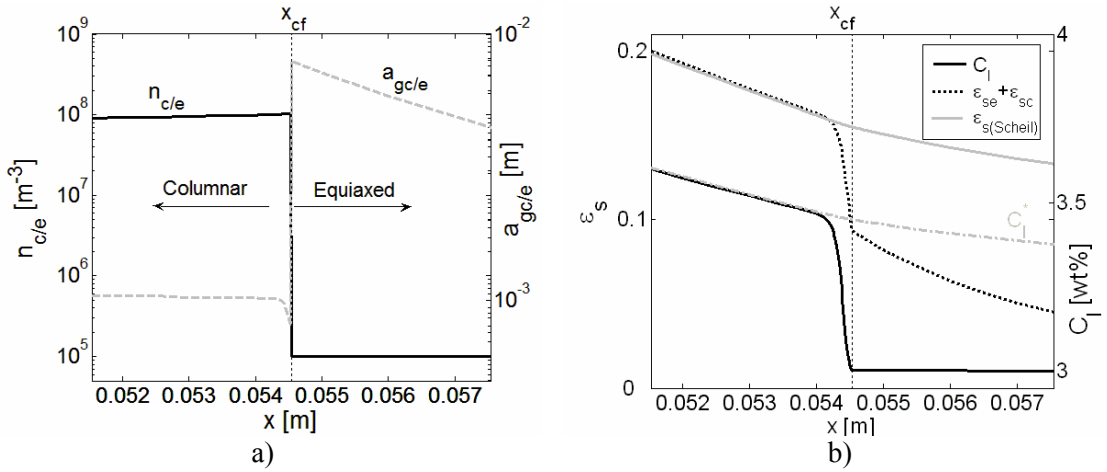

Figure 22: a), the grain density and the grain diameter near the *CF* and b) the solid and extra-dendritic liquid concentration near the *CF* at $t = 625\,s$ ($t = 625\,s$ (Al-3wt%Cu test base case, Martorano *et al.* [7] approach)

The mixed c/e zone which form behind the *CF* will undergo as well a complex evolution. This is well reflected by Figure 20 where the c/e solid and grain variations along the ingot are plotted at $t = 625\,s$, before the CET moment ($t_{CET} \approx 840\,s$). Note the correlation between the decrease of ε_c (increase of ε_e) and the decrease (increase) of the corresponding c/e solid and grain fractions. In addition the constraint $\varepsilon_{c/e} \geq \varepsilon_{gc/e} \geq \varepsilon_{sc/e}$ is verified as well due to the particular mathematical formulation of the model in Table 1 and especially of the length diffusion length δ_{lk-dk}. Indeed, since the solute diffusion process around the c/e equiaxed grain is limited to a distance $R^*_{1c/e}$ around the grain center, the grain growth will be always stopped before it reaches $R^*_{1c/e}$. Since $R^*_{1c/e}$ are no more than the dimensions of the c/e cells characterizing the statistics of the mixture zone, the constraints enounced above are intrinsically verified. In Figure 21b the total solid fraction ($\varepsilon_{se} + \varepsilon_{sc}$) and the c/e extra-dendritic liquid concentration variation near the *CF* are presented at $t = 625\,s$. As seen the solutal blocking effect of the equiaxed zone is still negligible, $\left(C_{le}\right)_{cf} \simeq C_0$. However, just behind the *CF*, the enriching of the liquid becomes important. This is due to the second mechanical blockage which reduces sensibly the characteristic lengths $R^*_{1c/e}$ (n_c^0 is larger than n_e). Note the smooth transition zone (about $1mm$) from the non-enriched state at the *CF* to the perfect mixing state behind. Note as well the small differences between C_{lc} and C_{le}, result which is coherent with the physical fact that both dendrite grains share a same space therefore a same extra-dendritic liquid. The equivalence between C_{lc} and C_{le} is establishing confidence in the model formulation. This is an important aspect of the ensemble averaged model. In fact, even if we have delimited a columnar and an equiaxed extra-dendritic liquid, due to the equivalence between the length scales characterizing each extra-dendritic liquid,

$$R^*_{1c} \simeq R^*_{1e} - a_e \quad \text{(see [1])} \tag{20}$$

the evolution of C_{lc} and C_{le} prior to the coexistence moment will be similar. Note as well the equivalence between the total solid fraction evolution and the Scheil law for points found in state of perfect solutal mixing. Indeed, despite the separate handling of the columnar and equiaxed structures, the c/e solid fraction evolution behind the *CF* is such that when the state of perfect mixing is reached, $\varepsilon_{se} + \varepsilon_{sc}$ evolution identifies with the Scheil regime (Figure 21a). This establishes further confidence in the mathematical formulation of the model since any solid configuration found in a state of perfect mixing should evolve following a Scheil law. By taking into account the coexistence between the two structures one has a more precise approach on the solidification phenomena taken place behind the *CF*. In this respect it would be interesting to compare the above results with the approach used by Martorano *et al.* [7]. In that study, the authors approximate the mixed zone behind the *CF* with an equivalent columnar zone of density n_c^0. The present model was modified to mimic the Martorano *et al.* approach by considering the zone behind the *CF* as pure columnar and enforcing the continuity of average values at the *CF*. For the present base test case, the resulting CET position was found to be $x = 0.064\,m$ that is almost 6% lower than the one obtained with the new model. Even if the difference is not significant it is interesting to look in more detail what could cause this underestimation of the CET position. Since one expects that the two approaches will give similar results for the pure equiaxed zone ahead the *CF* and the perfect solutally mixed zone behind the *CF* (Scheil law), one should focus on the transition zone to the perfect solutally mixed state behind the *CF*. In Figure 22b the solid and the extra-dendritic concentration are presented close to the *CF* at $t = 625\,s$ In contrast with the smooth transition to the perfect solutally mixed state in Figure 21b, Figure 22b shows an extremely rapid increase of C_l to C_l^*. The thickness of the transition zone in this case is not greater than $250\,\mu m$, that is, almost four times smaller than the one obtained with the present model. This is mainly due

to the discontinuity of the grain density n_e at the *CF* (Figure 22a). Indeed, since the continuity of average variables at the *CF* ($\varepsilon_{ge}, \varepsilon_{se}$, etc) is enforced one obtains discontinuities in the evaluation of real dimensional parameters like grain diameter $a = \left(4/3\pi n\right)^{-1/3} \varepsilon_g{}^{1/3}$ or interfacial areas $S_g = 3\varepsilon_g{}^{2/3}\left(4/3\pi n\right)^{1/3}$) (Figure 22a). Since usually $n_c^0 \gg n_e$ the interfacial area will undergo a sudden increase. This in turn will lead to a very rapid enriching process of the extra-dendritic liquid behind the *CF* (Figure 22b) and a significant modification of the solidification rate at the *CF* leading finally to an underestimation of the CET position. The relative small difference between the two approaches is due mainly to the fact that we have neglected the macroscopic solute diffusion terms in the solute balance equations transforming them into local ODE equations. Far from the *CF* the axial gradients of C_l are indeed small. However, behind the *CF* these ones become important and could modify the solute fluxes at the tip, underestimating further the CET. On the other hand for the case analyzed above one had $n_c^0 \gg n_e$. The inclusion of relative dispersed grains into the highly dense columnar structure would not change significantly the solidification conditions behind the *CF* with respect to a pure columnar zone of density n_c^0 . In contrast, for $n_c^0 \ll n_e$ the mixed zone behind would evolve similarly with an equivalent pure equiaxed zone of density n_e and not with a pure columnar zone of density n_c^0 as the Martorano *et al.* [7] approach would have predicted. Even if, given the present solidification conditions, the differences between the CET position predicted by the two approaches is not significant, the use of the present model is of great interest since it gives a rigorous description of the mixed c/e zone behind the *CF*.

Note that so far we have computed the primary arm spacing λ_1 (and n_c^0 consequently) using equation (16). The latter equation is valid for a quasi-steady state *CF*, that is when $V_{is} = V_{cf}$. It should be interesting to investigate if whether or not the *CF* evolves in a quasi-steady state with respect to the local cooling conditions (G , V_{is}). By knowing the precise position of the *CF* one can compute locally the isotherm velocity since $V_{is} = CR/G$. In Figure 23 the columnar tip velocity and the local isotherm velocity at the tip are plotted against time. Basically one can delimit the *CF* evolution in three typical zones. The first one ($t < t_1$), corresponding to the very beginning of the solidification corresponds to a transition stage in the evolution of the *CF*. Indeed the columnar tip velocity V_{cf} increases quite rapidly from 0 to reach finally the local isotherm velocity V_{is} . This stage is similar with the transition zone identified in the previous section for the case involving a fixed G and V_{is} (Figure 11a). The second phase corresponds to a *CF* velocity almost equal with the local V_{is} ($t_1 < t < t_{CET}$), that is to a quasi-steady state at the *CF* In this case the use of the equation (16) to compute λ_1 would be entirely justified. As observed, the isotherm velocity undergoes small oscillations around a mean value. Several tests were carried out to better understand this phenomenon. It was observed that the mesh influenced slightly the nature of these oscillations, and it appears that their origin is mainly a consequence of the particular law used for both columnar and equiaxed instantaneous nucleation. The discrete modeling of the nucleation phenomena generates small thermal perturbations at the *CF* which in turn gives the noisy aspect of the isotherm velocity. This second phase in the evolution of the *CF* ends suddenly close to the critical moment corresponding to the CET. The tip velocity drops suddenly at t_{CET} and the *CF* stops. During the third phase ($t > t_{CET}$) the *CF* velocity is almost zero contrary to the local isotherm velocity at the CET interface.

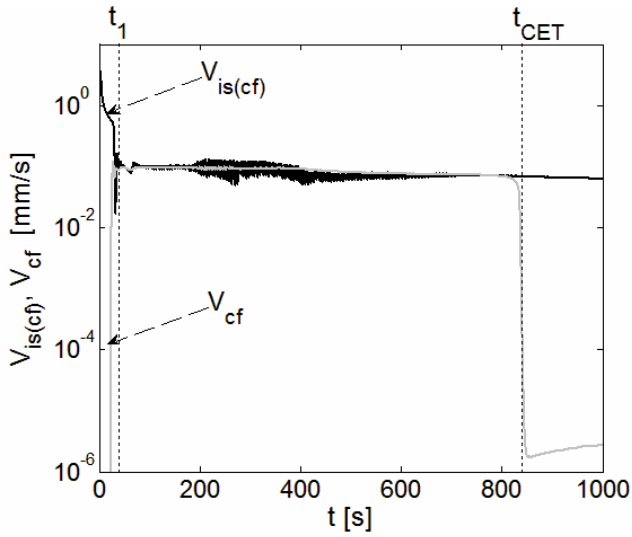

Figure 23: The isotherm velocity at the *CF* and the *CF* velocity with respect to time

In this context one important question is why the tip velocity, during the second phase in Figure 23 evolves in a quasi-steady state with respect to local conditions, despite the continuous changing cooling conditions (V_{is} , G) at the columnar tips (see for example Figure 18). To give a pertinent response to this question it may be interesting to analyze the characteristic times scales of the *CF* dynamics and of the changes in local cooling conditions at the columnar tips. As pointed out previously, the time scale characterizing the *CF* dynamics when perturbed from a quasi-steady state is no more than t_{rs} (cf. Equation (15)). Basically, t_{rs} measures the time during which a columnar tip reach back the quasi-steady state after a small perturbation from an initial quasi-steady state or a sudden change in local cooling conditions at the tip (V_{is} , G). Thus it is interesting now to compare this time scale with the time scale characterizing the changes in local cooling conditions at the columnar tips. Let us denote this latter parameter by t_{th} . This time scale could be approached from a relative simple scale analysis of the energy equation particularized to the given ingot configuration. Let us denote by x_{cf} the distance of the columnar front from the bottom wall at time t and with δ_s the total steel sheet thickness between the cooper chill and the ingot bottom wall. Indeed, the authors vary the heat transfer coefficient h_{ext} by varying the thickness of the steel sheet between the water cooled copper block (maintained at $293\,K$) and the mold bottom wall. The time scale t_{th} characterizing the thermal changes at the *CF* will be no more than the travel time of a thermal diffusion wave from the cooper chill (maintained at T_{ext}) to the *CF* position. One should therefore analyze the following thermal equivalent configuration composed from two inline thermal resistances (Figure 24).

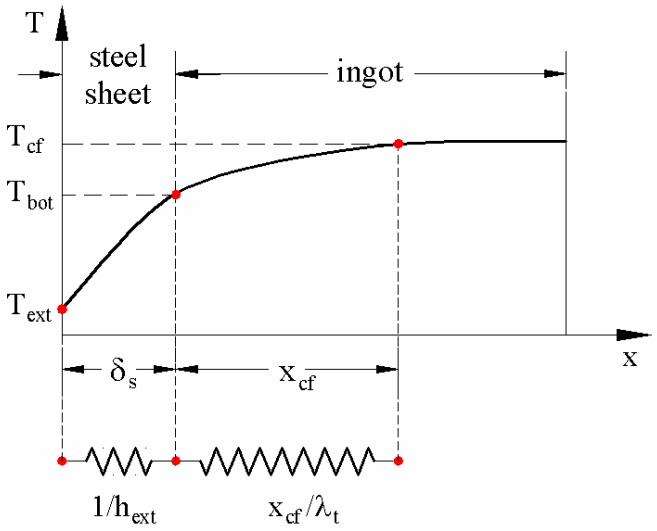

Figure 24: The thermal model used to compute the characteristic thermal time t_{th}

Supposing that the characteristic time related to the latent heat release is larger than the characteristic molecular diffusion time, one could neglect the influence of the latent heat release on t_{th}. This later approximation should be physically reasonable since we are dealing with high conductive materials (liquid metals) and relatively low solidification rates. Hence, from the simplified energy equation (drop of the latent heat release term) one can write approximately

$$\rho c_p \frac{\Delta T}{t_{th}} \approx \frac{1}{x_{cf} + \delta_s} \left(\frac{\Delta T}{1/h_{ext} + x_{cf}/\lambda_t} \right) \tag{21}$$

Noting that $1/h_{ext} >> x_{cf}/\lambda_t$ for the experiments reported in Table 2 ($x_{cf} \approx 0.05\,m$, $\lambda_t \approx 30-100\,W.m^{-1}.K^{-1}$ and $h_{ext} = 50-200\,W.m^{-2}.K^{-1}$) and that δ_s ($< 0.005\,m$ [4]) is typically lower than x_{cf}, one finally obtains the following estimate

$$t_{th} \approx \frac{\rho c_p x_{cf}}{h_{ext}} \tag{22}$$

A comparison between t_{th} and t_{rs} can now be assessed. In Figure 25 the evolution of t_{th} and t_{rs} at the *CF* with respect to time is plotted. One can distinguish three important stages in the evolution of the *CF*, similar with the previous remarks (Figure 23). The first stage ($t < t_1$) represent a transition to a quasi-steady state phase for *CF*. Indeed since $t_{rs} > t_{th}$ the changes in local conditions at the tip are much more rapid than the columnar tips are able to readapt to these new local conditions. The *CF* find it difficult to approach the local V_{is}. In contrast, the second phase ($t_1 < t < t_{CET}$) corresponds to $t_{rs} \ll t_{th}$. Hence, the columnar tip response time to changes in local cooling conditions are much faster than the thermal conditions at the tip are actually changing. Basically, the *CF* is readapting almost instantly to the new thermal conditions and a quasi-stationary state at the *CF* is maintained ($V_{cf} \simeq V_{is}$). Finally, due to the drop in the local thermal gradient and the fast enriching of the liquid at the *CF* by the equiaxed grains ahead, t_{rs} increases rapidly close to the CET and becomes larger than t_{rs}. The *CF* is not readapting anymore to the constantly changing conditions at the tip and the equiaxed zone ahead is extending further favoring the equiaxed grains development. The CET is imminent. Thus it seems that when t_{rs} becomes of

the same order of magnitude with t_{th} the conditions triggering the CET are reached. As we will see next, the relationship between these two time scales is very important since it enables one to quantitatively approach the critical moment corresponding to the CET. The strong correlation between t_{th} and t_{rs} seems indeed to be a relevant indicator regarding the CET phenomena.

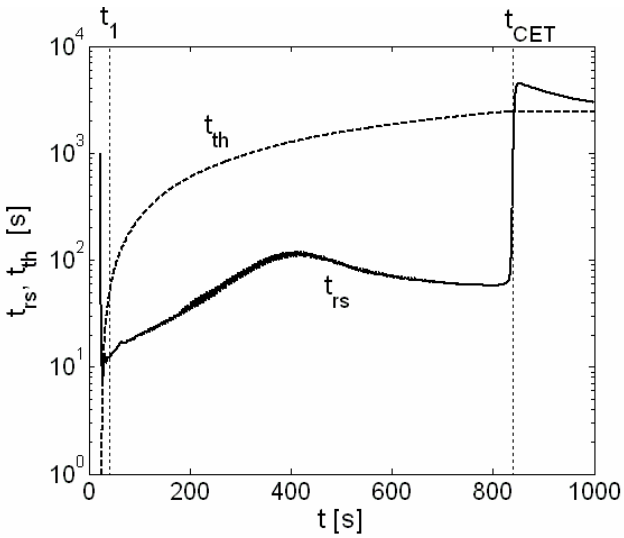

Figure 25: The thermal (t_{th}) and tip response time (t_{rs}) evolution at the *CF* with respect to time

4.2.2 Comparison with the experiments. In the present paragraph a quantitative comparison with the experiments in [4, 5] is attempted. The full transient model summarized in Table 1 is used to simulate the Al-Cu and Sn-Pb unidirectional experiments (Table 2). One expects that the CET position varies strongly with the initial superheat ΔT_0, the heat transfer coefficient h_{ext}, the initial alloy composition C_0 and the equiaxed grain density n_e. A first analysis of the influence of all these parameters on the CET position is very useful for the comprehension of the CET phenomena.

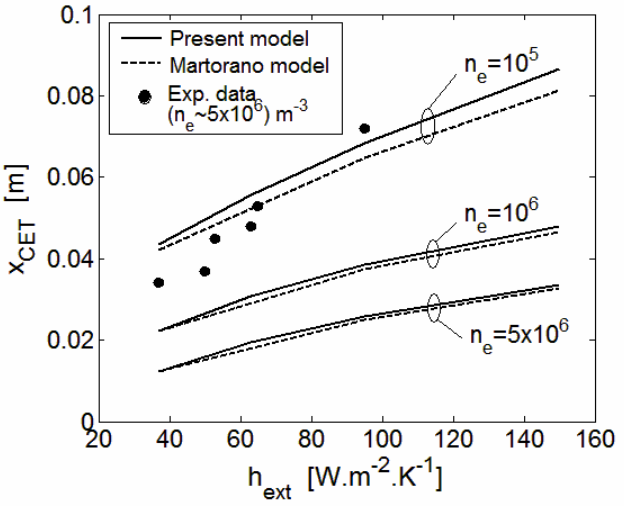

Figure 26: The influence of the heat transfer coefficient and the equiaxed grain density on the CET position for an Al-3wt%Cu alloy ($\Delta T_{ne} = 0$, $\Delta T_0 = 20K$, $C_0 = 3\%$). Comparisons with the experimental data [5] ($n_e \simeq 5 \times 10^6\ m^{-3}$) and with the Martorano *et al.* approach [7].

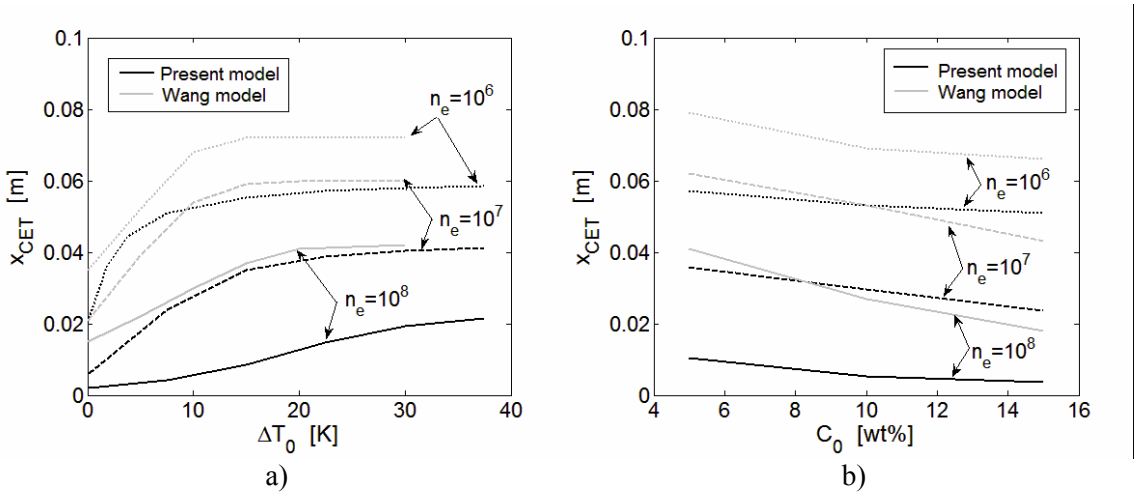

Figure 27: (a) The influence of the initial solute concentration and the equiaxed grain density (Sn-Pb alloy, $\Delta T_{ne} = 0\,K$, $\Delta T_0 = 10\,K$, $h_{ext} = 120\,W/m^2$) and (b) the influence of the pouring superheat and the equiaxed grain density (Sn-10wt%Pb alloy, $\Delta T_{ne} = 0\,K$, $h_{ext} = 120\,W/m^2$) on the CET position. Comparison with Wang and Beckermann model [13].

In Figure 26 the variation of the CET position with respect to the heat transfer coefficient h_{ext} and the equiaxed grain density n_e is presented for an Al-3wt%Cu alloy. As one expected, the increase of n_e will determine a decrease of the CET position. Indeed, since for high equiaxed grain density the solutal enriching process of the extra-dendritic liquid is more effective, the solutal blocking effect is stronger. In contrast, the increase of h_{ext} favors the columnar zone and delays the CET. This can be easily explained by considering the fact that high h_{ext} means higher heat flux at the bottom of the ingot which in turn will lead to higher thermal gradients at *CF*. This narrows the equiaxed zone ahead of the *CF*, favoring the columnar zone. In Figure 27a the influence of the pouring superheat on the CET is analyzed for a Sn-10wt%Pb alloy and for three different n_e values. It can be observed that a higher ΔT_0 favors the columnar zone. This was expected since higher ΔT_0 means as well higher thermal gradients ahead of the *CF* at the beginning of the solidification, delaying further the CET. Again the strong influence of the value of n_e on the CET must be noted. In Figure 27b the sensitivity of the CET to the variation of the initial solute concentration is analyzed for the Sn-Pb alloy. Basically, increasing C_0 leads to a lower CET position. A reasonable explanation for this behavior can be found in the influence of C_0 on the tip kinetics. Indeed, let us consider given cooling condition (V_{iso}, G). If the *CF* arrives to a quasi-steady state ($V_{iso} \simeq V_{cf}$) then the undercooling at the *CF* will be larger for an increase value of C_0. For a given thermal gradient G at the tip this will lead to an extension of the equiaxed zone ahead of the *CF* favoring thus the equiaxed structure.

A comparison with the Martorano *et al.* model [7] can be quantitatively assessed if the present model is modified to mimic the model in [7]. By approximating the mixed zone behind the *CF* with a pure columnar one the Martorano *et al.* model underestimates the CET predictions (Figure 26). Note however that the differences between the present model and the Martorano *et al.* model are not important for the present solidification conditions. As pointed out this is due on one hand to the absence of the macroscopic diffusion terms in the solute equations and on the other hand to the larger columnar density n_c^0 compared to n_e.

The cases analyzed in Figure 27 permit a direct comparison with the Wang and Beckermann model [13]. Significant differences can be observed between the present model and the results provided in [13] (see Figure 27). Considerable higher CET positions are predicted by Wang model. This can be mainly explained by the fact that no solutal coupling between the *CF* and

the equiaxed zone ahead is taken into account in [13].The *CF* velocity is computed by considering that the local extra-dendritic solute concentration is always at C_0, neglecting therefore the solutal blocking effect of the equiaxed grains. Accordingly an over estimation of the CET can be logically expected.

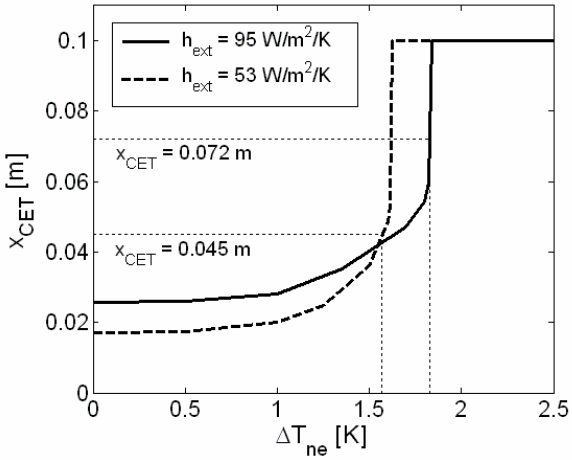

Figure 28: The influence of the equiaxed nucleation undercooling on the CET position for an Al-3wt%Cu alloy: $n_e = 5\times10^6\ m^{-3}$, $\Delta T_0 = 20\,K$.

In the absence of a reliable value for n_e in the case of Sn-Pb experiments, a comparison with the Al-Cu experiments is assessed first, knowing that for these experiments, detailed grain size measurements were carried out. Basically, the equiaxed grain density varies slightly from one experiment to another around the value $n_e \simeq 5\times10^6\ m^{-3}$ [5]. Note however that an important parameter of the model is not known a priori, i.e., the equiaxed nucleation undercooling ΔT_{ne}. In Figure 26 a comparison with the experiments is assessed in the limit of a vanishing equiaxed undercooling, $\Delta T_{ne} = 0\ K$. As one can see no agreement is obtained with the experimental data. Using, $\Delta T_{ne} = 0\ K$, Martorano *et al.* [7] arrived at the same conclusion, that is, a vanishing equiaxed undercooling cannot explain the CET experimental data in [14]. Thus similarly with the Martorano *et al.* approach [7], a parametric study is attempted to determine the value of ΔT_{ne} fitting the experimental results. In Figure 28 the influence of ΔT_{ne} on the CET is analyzed for the experiments 22 and 25 in Table 2. As expected the increase of ΔT_{ne} favors the columnar zone. The influence on the CET position is not important for small values of ΔT_{ne} and increases rapidly when ΔT_{ne} approaches a critical value ΔT_{ne}^{crit}. In fact for $\Delta T_{ne} > \Delta T_{ne}^{crit}$ a fully columnar zone is always obtained ($x_{CET} = 0.1\ m$, see Figure 28). Basically, the same qualitative results are obtained for the four other Al-Cu experiments in Table 2. It is important to notice that similar variations of the CET position with respect to ΔT_{ne} were obtained by Martorano *et al.* in [7]. This particular result can be explained by considering that, for a given solidification condition and in the absence of the equiaxed grains ahead of the *CF*, the local undercooling at the columnar tips, ΔT_{cf} remains always lower than a maximum value ΔT_{ne}^{crit} which depends mainly on the cooling conditions of the ingot and C_0. Basically for a more efficient ingot cooling, the maximum *CF* velocity increases as well and consequently ΔT_{ne}^{crit} increases. It is worthwhile to notice that the real CET position corresponds to a ΔT_{ne} very close to the ΔT_{ne}^{crit}, slightly lower than ΔT_{ne}^{crit} (Figure 28). Essentially, the same result was obtained by Martorano *et al.* [7] when they validated their model with the experiments of Gandin [14]. This interesting remark reveals however some very important issues.

In fact $\Delta T_{ne} \simeq \Delta T_{ne}^{crit}$ means that the equiaxed grains nucleate very close to the *CF* and moreover that their nucleation corresponds more or less to the moment when ΔT_{cf} reaches a maximum. As Martorano *et al.* [7] pointed out, the most reasonable explanation for this phenomenon is that the equiaxed grains are in fact fragments detached form the columnar grains and transported in front of the *CF* by the inherent natural convection acting close to the columnar macro-front. This result was also supported by the findings of Gandin [15] which observed that if no equiaxed zone ahead of the *CF* is assumed, the real CET position corresponds more or less to a local maximum value of the *CF* velocity, that is to a maximum value of the columnar tips undercooling, ΔT_{cf} . This means as well that prior to this moment the *CF* velocity will exhibit a decrease. Since Jackson *et al.* [16] showed that a change in the *CF* velocity may cause dendrite arm remelting and fragmentation it is reasonable to think that the columnar dendrite fragmentation is at the base of the CET phenomena and not the equiaxed nucleation ahead the *CF*. Note that this should be mainly valid for non-refined alloys. For highly refined alloys, the probability of equiaxed nucleation ahead of the *CF* should not be neglected. However important questions remain to be answered: Why the *CF* velocity (in the absence of the equiaxed grains ahead) reaches a local maximum? Why the sudden decrease in the *CF* velocity is susceptible to produce remelting of columnar dendrite? Is there a way to predict the moment corresponding to ΔT_{ne}^{crit} ?

4.2.3 Fragmentation of dendrite columns. A consequence of the CF instability? In the following we will try to give a pertinent response to the questions enounced above. Note first that $\Delta T_{ne} \simeq \Delta T_{ne}^{crit}$ meaning that the equiaxed grains nucleate close to the columar front when the columnar undercooling reach a local maximum, would means as well that the equiaxed zone ahead would not influence the *CF* evolution prior to the critical moment corresponding to the CET since they don't nucleate before the CET moment. In this light by focusing on the *CF* evolution alone and not taking in account the equiaxed zone ahead, one should be able to identify the critical CET moment. The model in Table 1 is used therefore for the modeling of the pure columnar zone, by completely ignoring the equiaxed structure. All solidification experiments in Table 2 are analyzed in the following.

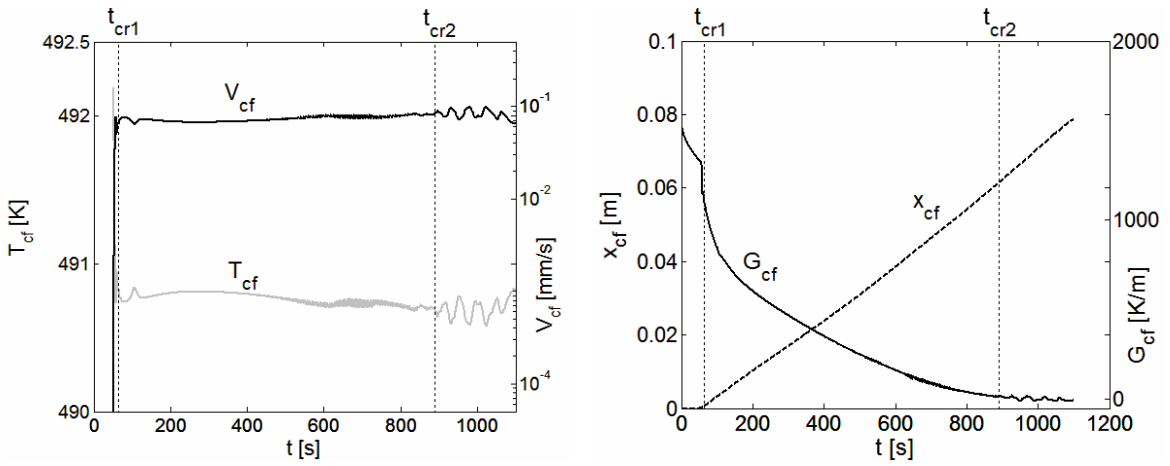

Figure 29: Time evolution of (a) the *CF* velocity and the temperature at the *CF* (b) the *CF* position and the thermal gradient at the *CF* for a Sn-10wt%Pb alloy pure columnar solidification (case no. 12, Table2: $\Delta T_0 = 36 K$, $h_{ext} = 134\ W/m^2$)

In Figure 29a the *CF* velocity and the corresponding temperature at the *CF* are plotted against time for the 12th Sn-Pb experiment in Table 2. The evolution of the *CF* position and the thermal gradient at the *CF* are plotted in Figure 29b. As expected, since no stopping mechanism is accounted for this simulation, the *CF* advances undisturbed in the undercooled melt and the columnar structure will finally occupy the whole ingot. Somewhat similar to the previous base test

case, the *CF* velocity exhibits a sudden increase at the beginning of the solidification ($t < t_{cr1}$) followed by a quasi-plateau corresponding to a quasi-state at the columnar tips and finally, above a critical time (t_{cr2}), a somewhat oscillatory evolution around the mean value characterizing the plateau. Due to the particular cooling conditions at the bottom of the ingot, the gradient at the *CF* decreases as the *CF* distances away from the lower wall. Finally, for $t > t_{cr2}$ G exhibits an oscillatory movement close to the 0 value. To have a more detailed insight on what could determine such a particular evolution at the *CF*, especially for $t > t_{cr2}$, it is instructive to analyze the time scales characterizing the *CF* evolution and the changes in local conditions at the columnar tips. In a similar way as in the previous section, the time scales t_{th} and t_{rs} are plotted together in Figure 30a. As one can observe, the first phase in the *CF* evolution corresponds to $t_{rs} > t_{th}$, that is a transition phase of the *CF* from a non-quasi-steady state to a quasi-steady state. Indeed, even if the *CF* is constantly trying to reach a quasi-steady state with respect to the local conditions (G, V_{is}), due to the fact that the *CF* readapts to the constantly changing conditions at the tip mush more slowly (t_{rs}) than the local conditions are actually changing (t_{th}), the columnar tip velocity does not manage to reach a quasi-steady state. However, for $t > t_{cr1}$, t_{rs} becomes smaller than t_{th} and the columnar tips readapt much more rapidly to the local cooling conditions at the tip. Therefore, V_{cf} will follow closely the local isotherm velocity V_{is} (Figure 30b) and a quasi-steady state at the tip is reached. As long as the gradient at the *CF* remains important, the condition $t_{rs} < t_{th}$ is accomplished. However, due to the constant decrease of *G*, t_{rs} will finally approach t_{th} for $t > t_{cr2}$. Finally for $t_{rs} > t_{th}$ the *CF* will not rapidly readapt itself to the local conditions at the tip. A remarkable fact is that the moment t_{cr2}, corresponding to a slightly smaller t_{rs} than t_{th}, corresponds as well with the beginning of the oscillatory evolution of V_{cf} and *G*. The same conclusion has been obtained for all cases analyzed in Table 2. In Figure 31 two other cases are presented to exemplify the good correlation between the beginning of the oscillatory variation for V_{cf} and the equivalence between the two time scales t_{rs} than t_{th}. In Table 2 the *CF* position x_{cf}^{cr}, t_{th}^{cr}, t_{rs}^{cr} and *G* corresponding to the critical moment $t = t_{cr2}$ are summarized for all experiments. One can observe the good correlation between the beginning of the oscillatory behavior of the *CF* and the two time scales t_{th}^{cr}, t_{rs}^{cr}. Indeed, if t_{rs}^{cr} is plotted against t_{th}^{cr} (Figure 32) one can easily observe that $t_{th}^{cr} \approx 2t_{rs}^{cr}$. To explain this interesting phenomenon first one should remember that since we have not taken into account a blocking mechanism for the *CF* the columnar tips will evolve undisturbed with respect to the constantly changing conditions at the tip (G, V_{is}). Indeed, as pointed out in [12] the *CF* evolution is such that at any moment it tries to reach the isotherm T_{ts} corresponding to a local tip velocity equal to the isotherm velocity V_{is}, that is to reach the quasi-steady state with respect to local cooling conditions. However for $t > t_{cr2}$, one has $t_{rs} > t_{th}$, meaning that the *CF* readapts more slowly to the new conditions at the tip than the later ones are actually changing. In fact in their search of the quasi-steady state, by the time (t_{rs}) the *CF* velocity reaches the local isotherm velocity, the cooling condition at the tip (G, V_{is}) have already changed. The main consequence of this *CF* behavior is the particular oscillatory movement of V_{cf} and *G* for $t > t_{cr2}$. Notice as well that due to the constant decrease of G towards zero, the amplitude of the isotherm velocity at the *CF* greatly increases (Figure 30b) since $V_{is} = CR/G$. Consequently, the oscillatory behavior of the *CF* velocity is further amplified as well. It is important to notice however that the beginning of the oscillatory phase ($t = t_{cr}$) always corresponds to a positive thermal gradient at the *CF* (see Table 2), of order of *10-20 K/m*. Notice that a critical gradient of the same order of magnitude was obtained by Martorano *et al.* [7].

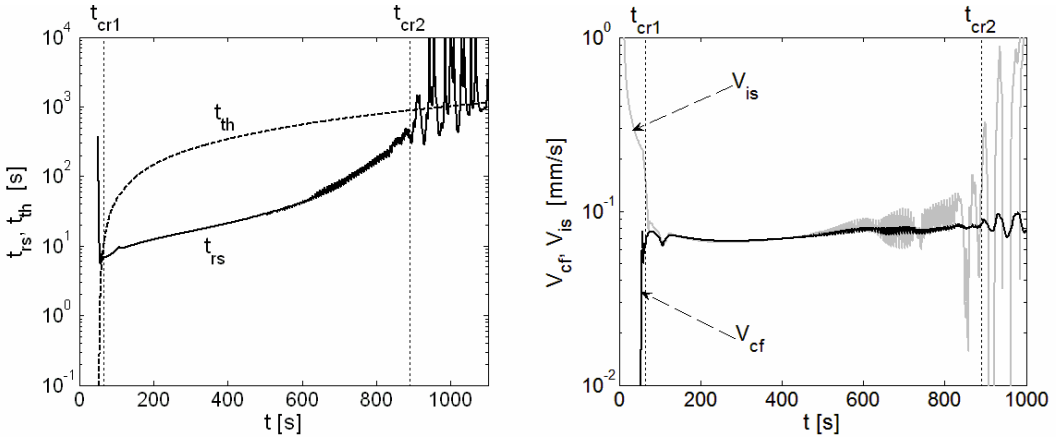

Figure 30: Time evolution of (a) the thermal (t_{th}) and tip response time (t_{rs}) at the *CF* and (b) the isotherm velocity at the *CF* and the *CF* velocity for a Sn-10wt%Pb alloy pure columnar solidification (exp13 in Table2: $\Delta T_0 = 36\,K$, $h_{ext} = 134\,W/m^2$)

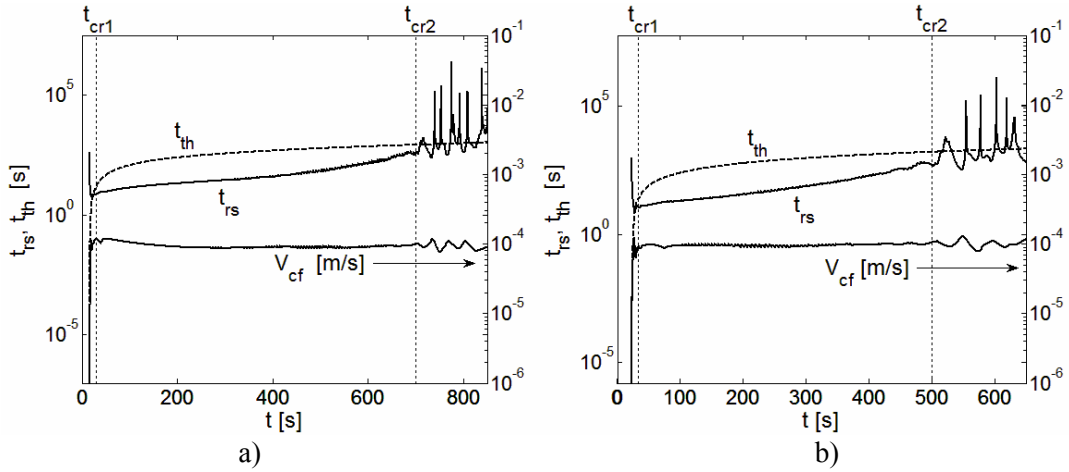

Figure 31: Time evolution of the *CF* velocity, the thermal (t_{th}) and the tip response time (t_{rs}) for a pure columnar solidification: (a) case no. 17, Table 2 and (b) case no. 22, Table 2

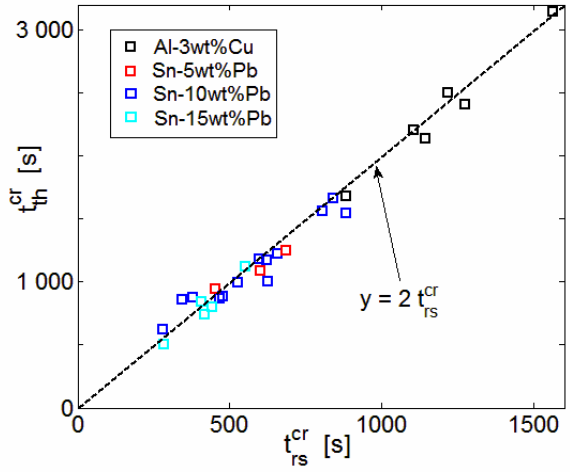

Figure 32: The thermal (t_{th}) and the tip response time (t_{rs}) at the *CF* corresponding to the beginning of the oscillatory evolution of the *CF*

An even more remarkable fact is that the position of the *CF* evolution at $t = t_{cr2}$, x_{cf}^{cr}, corresponds reasonably well with the CET position measured in the experiments. Despite the relative high degree of incertitude on the real cooling conditions for almost all the experiments, the relative error between x_{cf}^{cr} and x_{CET} is lower than 20% (Figure 33). Therefore, it is reasonable to think that the existence of a non-quasi-steady state at the tip with respect to the local cooling conditions ($t_{rs} \geq t_{th}$) is responsible for the CET phenomena. In contrast with Ziv and Weinberg [5], which correlated the gradient ahead of the *CF* with the CET phenomena, in the present study it seems more likely that the CET position is correlated with the two time scales t_{th} and t_{rs}.

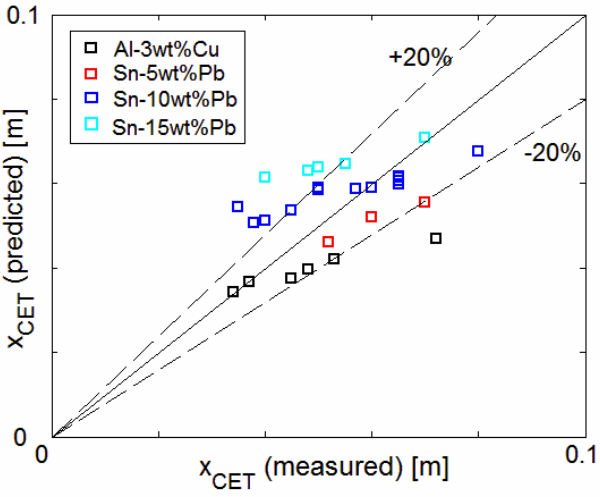

Figure 33: Comparison of the predicted CET position (x_{cf}^{cr}) with all solidification experiments in Table 2

An important question remains however: Why the CET phenomena seems to correlate so well with the equivalence between the two time scales t_{rs}, t_{th} ($t_{th}^{cr} \approx 2t_{rs}^{cr}$)? To answer to this question, one must remember that t_{rs} quantified as well the optimal primary arm spacing of a quasi-steady columnar front λ_1, equation (16). Since the value of time scale t_{rs} strongly oscillates for $t > t_{cr2}$ (Figure 30a, Figure 31) λ_1 will inherit the oscillatory evolution from t_{rs}. As pointed out in [12] the dendrite spacing is always trying to readapt to the new conditions at the tip, that is to the optimum λ_1, by means of two mechanisms. If the dendrite spacing is larger than λ_1, the dendrite division mechanism will determine a decrease in the primary arm spacing. In contrast, if the dendrite spacing is lower than the optimum λ_1 the solutal interactions between two adjacent columnar tips are strong enough in such a way that the dendrite configuration will not be stable to small perturbation at the tip. Hence, some of the columnar tips will be overgrown by the neighbor ones and the dendrite spacing is naturally increased. From this point of view, the oscillatory evolution of the optimal primary arm spacing λ_1 will force the columnar structure to adapt its dendrite spacing very fast. As one can see the typical oscillations frequency of t_{rs} (and λ_1 consequently) is rather small (*~10 s*) and much faster than the time during which the *CF* is actually able to readapt ($t_{rs} \simeq 10^2 - 10^3\ s$). Consequently primary arm spacing will never reach the optimal spacing λ_1 and will therefore be non-adapted to the local cooling conditions at the tip: either the solutal interactions between adjacent grains will be too strong, either too weak, leaving between columnar tips a large undercooled liquid melt. Thus the oscillations of λ_1 for $t > t_{cr2}$ reflects in

fact an instable *CF* state with respect to the local cooling conditions at the tip. The rapid change from a strong solutal interaction state ($\lambda < \lambda_1$) to a weak solutal interaction state ($\lambda > \lambda_1$) will be extremely favorable to dendrite remelting and fragmentation. This, coupled with the inherent natural convection at the macrofront would determine the existence of very favorable CET conditions at the *CF*.

The good agreement between the numerical results and the experimental data support the above findings. It seems that the columnar fragmentation favored by an unstable regime of the *CF* with respect to the local cooling conditions represent the main cause for the CET phenomena, at least for the non-refined alloys. Even more, since the CET seems to be linked to this unsteady regime of the *CF*, the equivalence between the two time scales t_{th} and t_{rs} would further permit to quantitatively approach the critical CET moment.

5 Conclusions

In order to validate the new two-phase Eulerian model developed throughout reference [1], a numerical implementation of the model was developed and applied here to simulate the 1D columnar-to-equiaxed transition. Indeed, owing to the statistical nature of the model, one is able to treat rigorously the coexistence of equiaxed and columnar structures and consequently the CET phenomena. The implemented numerical model is able to rigorously model 1D directional experiments in which both columnar and equiaxed structures may interact. The columnar front evolution is modeled by means of a front tracking technique. Similarly with the Martorano *et al.* model [7] the local columnar tip velocity is directly linked to the local undercooling conditions. Hence the solutal blocking effect of the equiaxed grains ahead of the *CF* is naturally taken into account. Moreover, owing to the statistical nature of the model, the mechanical blockage effect of the developed equiaxed zone ahead of the *CF* on the columnar zone is intrinsically taken into account by means of the two blockage mechanisms already identified in [1].

First we focus on the numerical simulation of quasi-steady solidification experiments in order to obtain corresponding CET maps. Observing the physical decoupling between the evolution of the pure equiaxed zone ahead of the *CF* and the columnar zone evolution behind the *CF* we were able to easily identify three main zones characterizing the CET phenomena. First, two important characteristic equiaxed tip velocities have been identified: $\overline{w}_{ge}^{0}$ and $\overline{w}_{ge}^{*}$. Then, depending on the choice of the pulling velocity with respect to these two characteristic velocities three main zones have been identified on the CET map: the pure columnar, the pure equiaxed zone and finally the mixed columnar+equiaxed zone. The mixed c/e zone was further analyzed to determine if whether or not a quasi-steady state at the tip could be identified. Indeed, due to the first mechanical blockage a continuous rarefying process of the columnar zone can be observed. However, a redensifying mechanism opposing to the first mechanical blockage was identified as well. The redensifying mechanism was quantified by means of the time scale t_{rs} [12]. Finally, by comparing the time scales characterizing the redensifying mechanism and the first mechanical blockage we were able to determine if whether or not a mixed quasi-steady state at the *CF* could be obtained. Two CET maps characterizing an Al-3wt%Cu alloy were built and the three main CET zones were identified. Even more the mixed c/e zone was further quantified by means of a columnar fraction ε_c. The latter one quantifies in a rigorous the way the two coexisting structures share locally a given space. Basically, ε_c will be a measure of the amount of space proper to the columnar structure. Therefore, the present ensemble averaged model was able to reproduce the mixed columnar/equiaxed zones within the CET maps. Moreover, the new model enabled us to quantify rigorously both the solutal and the mechanical blockage mechanism producing the CET phenomena. Basically, since it intrinsically includes the solutal and the mechanical blocking effects, the new ensemble model unifies the semi-empirical Hunt approach (pure mechanical blocking mechanism) and the Martorano *et al.* approach (pure solutal blocking mechanism).

Secondly the present model was used to simulate various unidirectional solidification experiments in an attempt to validate further the new ensemble averaged model. The full transient model in Table 1 was used to simulate different Al-Cu and Sn-Pb unidirectional experiments [4, 5]. The complex coupling between the *CF* and the equiaxed zone ahead as well as the complex

evolution of the mixed c/e zone which forms behind the *CF* were analyzed. We have also compared the present model with the Martorano et al. approach to the mixed zone behind the *CF*. A significant underestimation of the CET position was obtained when the Martorano *et al.* approach [7] was used. This was mainly due to the fact that in [7] the mixed zone behind the *CF* is approximated with an equivalent columnar zone, the interactions between the equiaxed and columnar grains not being taken into account. The steadiness of the *CF* with respect to local cooling conditions was analyzed as well. When the local *CF* velocity was compared with the local isotherm velocity it was observed that the two were almost equal until very close to the CET moment. Hence the columnar front evolved in a quasi-steady state until very close to the critical CET moment. This was possible because the *CF* adapts to the constantly changing conditions at the tip much more rapidly than the latter ones are actually changing. Indeed, when comparing the two time scales characterizing the dynamics of the columnar dendrite tips (t_{rs}) on one hand and the variation in local cooling conditions at the tip (t_{th}), on the other hand it was observed that during the quasi-steady evolution of the *CF* one had always: $t_{rs} \ll t_{th}$. Moreover it was observed that the CET moment corresponds more or less to the equivalence between these two time scales: $t_{rs} \approx t_{th}$. Next a comparison with the Wang and Beckermann model [13] was assessed. Since the latter model neglected the solutal blocking effect of the equiaxed grains the CET position was constantly overestimated with respect to the present model. A comparison of the present model with the Al-Cu alloy experiments is assessed too, in the limit of a vanishing equiaxed undercooling ($\Delta T_{ne} = 0\ K$). It is found that the equiaxed nucleation undercooling is close to the maximum columnar dendrite tip undercooling and that the CET is thus virtually independent of the equiaxed zone ahead of the *CF*. This is in agreement with the Martorano *et al.* findings [7] and supports the idea upon which the CET is mainly caused by the fragmentation of the columnar dendrites, rather than heterogeneous nucleation ahead of the *CF*.

Next, the evolution of the pure columnar structure is analyzed in order to understand the mechanism pointing to the CET. If the equiaxed zone is further ignored it is observed that the evolution of the columnar front follows a three stage evolution. First the *CF* velocity exhibits a sudden increase at the beginning of the solidification followed by a quasi-plateau corresponding to a quasi-state at the columnar tips and finally, above a critical time (t_{cr2}), a somewhat oscillatory evolution around the mean value characterizing the plateau. It is found that the quasi-steady evolution of the *CF* corresponds to the condition at the tip $t_{rs} \ll t_{th}$ hence to a *CF* which adapts much more rapidly to the non-steady conditions at the tip than the latter ones are actually changing. Moreover the critical moment (t_{cr2}) corresponding to the beginning of the oscillatory evolution of the *CF* was well correlated with the equivalence between the two time scales t_{rs}, t_{th} ($t_{th} \simeq 2t_{rs}$).An even more remarkable fact is that the position of the *CF* corresponding to t_{cr2} corresponds reasonably well with the CET position measured in the experiments. Hence, the oscillatory evolution of the *CF* corresponds to a non-quasi-steady state of the columnar tips. It is found as well that the oscillatory evolution of the *CF* determines an oscillatory evolution of the optimal primary arm spacing which in turn creates very favorable conditions for the fragmentation of the columnar dendrites. We conclude that the unstable regime of the *CF* with respect to the local cooling conditions represent the main cause for the CET phenomena, at least for the non-refined alloys. Even more, since the CET could be linked directly to this unsteady regime of the *CF*, the equivalence between the two time scales t_{th} and t_{rs} would further permit a quantitative approach of the critical CET moment.

Appendix A: *The validation of the diffusion length scale* δ_{l-d}

To validate the new diffusion length the present model is first compared with Martorano *et al.* [7] model and more precisely with the numerical results obtained for a uniformly solidified equiaxed morphology. The studied case involves a local cooling rate of *0.005 K/s* and four different grain densities corresponding each to the following four cell dimensions: R_{cell} *(=*R_1*) = 10mm; 3mm; 1mm, 0.1mm* [7]. The alloy considered is an Al 3wt.% Cu metallic alloy. The corresponding

physical properties can be found in [7]. In Figure A1(a) the evolution of the grain fraction is presented for both the present and the Martorano *et al.* [7] model. A very good agreement between the two approaches can be observed for the cases involving the smallest grain densities (R_{cell} = *10mm*). On the contrary for smaller grain densities (R_{cell} = *3mm; 1mm*) differences between the two models can be noticed. First one can observe that the enriching of the liquid and the stop in the grain growth takes place more rapidly with the decrease of R_{cell}. Moreover a decrease of the maximum grain fraction can be observed too with the increase of the grain density. This can be explained by the fact that to a smaller R_{cell} it corresponds smaller Pe_g numbers where $Pe_g = \overline{w}_g \left(R_1 - a_e\right)/D_l$ is the grain Peclet number, already defined in [1]. As pointed out in [1] the solute boundary layer around the grain is of order of $\delta = (R_1 - a)/Pe_g$. Hence for smaller Pe_g numbers (for Pe_g numbers close to unity) the solute boundary layer around the grain becomes of the same order of magnitude as the length scale of the extra-dendritic liquid, $R_1 - a$. This together with the fact that the solute flux at the cell boundary is zero will determine a non-negligible enriching of the extra-dendritic liquid (see Figure A1(b)). Basically, due to a smaller distance between the grains (R_{cell}) the solutal interactions between the grains become more important and the enriching of the extra-dendritic liquid takes place sooner (given the same cooling rate).

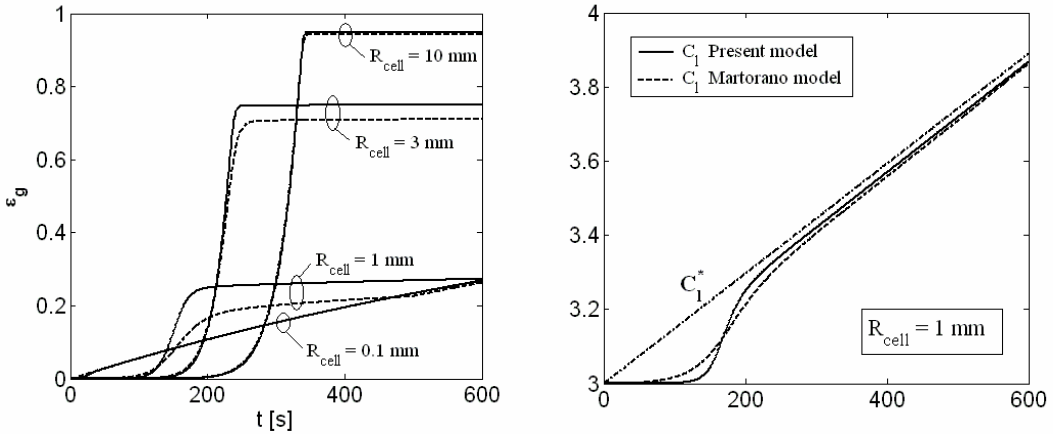

Figure A1: Comparison between Martorano *et al.* [7] model (dashed line) and present model (full line): a) the grain fraction evolution for four different grain densities and b) the average extra-dendritic concentration for R_{cell}=1mm case.

Now, comparing the present and the Martorano *et al.* [7] approach one can observe that for the intermediate cell dimensions the Martorano *et al.* model predicts a smaller maximum grain fractions (Figure A1(a)) and a more rapid solutal enriching of the extra-dendritic liquid (Figure A1(b)). This coupled effect can be explained by the differences in the formulation of the diffusion length scale δ_{l-d}. Indeed, in order to maintain the zero solute flux at the cell boundary, for $Pe_g < 2$ the present model limits the solute boundary layer around the grain at the length scale of the extra-dendritic liquid and more precisely to $\left(R_1 - a\right)$ [1]. In contrast with the present model the Martorano *et al.* model [7] does not impose a zero solute flux condition at the cell boundary. Hence, for cases involving Pe_g smaller than unity the Martorano *et al.* approach would predict a larger solute flux at the grain boundary compared with the present model and a non-negligible solute flux at the cell boundary. Therefore, the Martorano *et al.* model [7] will predict a more effective enriching process of the extra-dendritic liquid compared with the present approach.

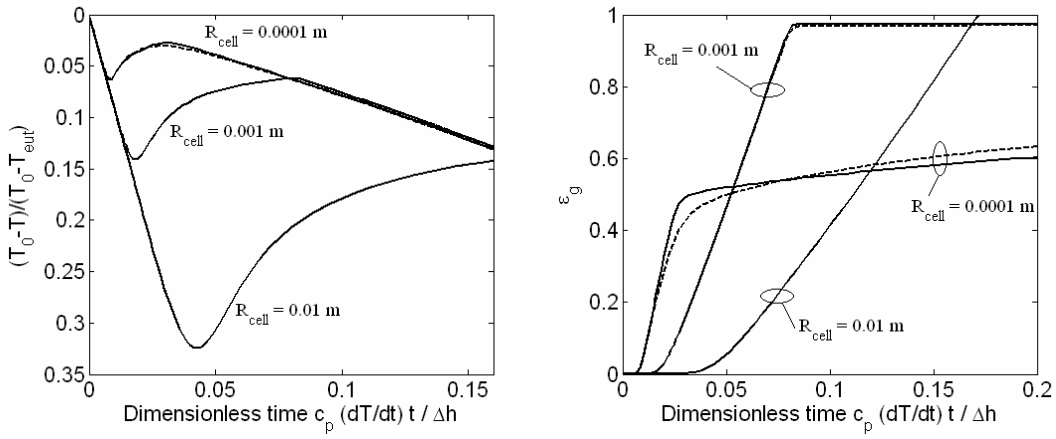

Figure A2: Comparison between Wang and Beckermann [2] model (dashed line) and present model (full line): a) the temperature evolution and b) the grain fraction evolution for three different grain densities

Secondly the present model is compared with the numerical results obtained by Wang and Beckermann [2] for a uniformly solidified system with an equiaxed morphology. Indeed, the system analyzed is identical with the one presented first by Rappaz and Thévoz in [6] in the case of a Al-5wt.%Si. The temperature is assumed to be locally uniform and the local heat extraction corresponds to a local cooling rate of $dT/dt = 45\ K/s$. Finally, results are obtained for three different grain densities corresponding to the following cell dimensions R_{cell} *(=R_1) = 0.01m; 0.001m; 0.0001m* [6]. A detailed comparison of the temperature and the grain fraction evolutions is presented in Figure A2. One can observe that the agreement between the present model and the Wang and Beckermann [2] approach is excellent for the whole range of grain densities. Small differences can be observed for the case involving the smallest grain density (R_{cell} *= 0.0001m*). Indeed, for this case, due to a smaller R_{cell}, the corresponding involved Pe_g numbers will be lower too. As already pointed out this will determine a faster enriching process of the extra-dendritic liquid and a lower maximum grain fraction compared with the other two cases (see Figure A2(b)). Here too a faster enriching process of the extra-dendritic liquid can be observed for the Wang and Beckermann [2] approach compared with the present model. Indeed, due to the particular formulation of δ_{l-d} in [2] and especially due to the non-zero flux at the cell boundary, the flux at the grain boundary is higher than for the present model: consequently the extra-dendritic liquid is more rapidly enriched in solute and the predicted maximum grain fraction will be lower with respect to the present model.

Nomenclature

Symbol	Meaning	Unit
C	solute concentration field	[*wt. %*]
T	temperature field	[K]
N	grain density	[m^{-3}]
ρ	density field	[$kg.m^{-3}$]
ε_k	the "volume" fraction of phase k	---
C_k^*	the interfacial concentration at the k phase interface	[*wt. %*]
$n_{c/e}^0$	the columnar/equiaxed nucleation grain density	[m^{-3}]
λ_1	columnar primary arm spacing	[m]
S_k	the interfacial area density of phase k	[m^{-1}]
δ_{k-p}	the solute diffusion length at the k-p interface	[m]
x_{cf}	position of the columnar front	[m]
x_{st}	the position of the quasi-steady columnar tips	[m]
V_{cf} , V_t	columnar front (tip) velocity	[*m/s*]
V_p	pulling velocity	[*m/s*]
V_{is}	isotherm velocity	[*m/s*]
$\overline{w}_{ge}$	averaged equiaxed tip velocity (average velocity of the equiaxed grain envelope)	[*m/s*]
$\overline{w}_{ge}^*$	maximum equiaxed tip velocity	[*m/s*]
$\overline{w}_{ge}^*$	equiaxed tip velocity corresponding to the equiaxed nucleation undercooling ΔT_{ne}	[*m/s*]
G	thermal gradient	[*K/m*]
CF	columnar front	---
CR	cooling rate	[*K/s*]
T_{liq}	liquidus temperature at the initial concentration C_0	[K]
T_{cf}	temperature at the columnar front	[K]
T_{ne}	the equiaxed nucleation temperature	[K]
T_f	the fusion temperature of the pure solvent	[K]
T_{ts}	the isotherm corresponding to the quasi-steady state of the columnar front	[K]
ΔT_{ne}	equiaxed nucleation undercooling	[K]
ΔT_{cf}	columnar front undercooling	[K]
ΔT_0	initial superheat	[K]
t_{rs}	the return time to the steady state of a perturbed quasi-steady dendrite array	[s]
t_{dw}	the time scale characterizing the solutal interactions by diffusion between two adjacent columnar tips	[s]
t_{th}	the time scale characterizing the non-steadiness of the cooling conditions at the tip	[s]
t_{m1}	the time scale characterizing the first mechanical blockage of the columnar tips	[s]

m	the slope of the liquidus line	$[K.(wt\%)^{-1}]$
k	the partition coefficient	---
c_k	heat capacity for the k-phase	$[J.kg^{-1}.K^{-1}]$
λ_k	the phase k thermal conductivity	$[W.m^{-1}.K^{-1}]$
L	the latent heat	$[J.kg^{-1}]$
Ω	the dimensionless local undercooling	---
Pe_t	the dendrite tip Peclet number	---
D_k	the solute diffusivity within the phase k	$[m^2.s^{-1}]$
$a_{c/e}$	the local columnar/equiaxed grain radius	$[m]$
$R_{1c/e}$	the cell radius corresponding to the single columnar/equiaxed grain distributions	$[m]$
$R^*_{1c/e}$	the cell radius corresponding to the coexisting columnar/equiaxed grain distribution	$[m]$
$\tilde{\mathbf{z}}_i$	the position in the ingot of the ith closest grain to $\mathbf{x}$	$[m]$
$\tilde{f}^{(1)}_{c/e}\left(t,\mathbf{x};\tilde{\mathbf{z}}_1\right)$	the unconditional density function that the closest grain to the point $\mathbf{x}$ is centered within $d\tilde{\mathbf{z}}_1$ of $\tilde{\mathbf{z}}_1$ and is a columnar/equiaxed grain	$[m^{-3}]$
δ_{lk-dk}	diffusion length characterizing the solute transfer at the columnar (equiaxed) grain interface	$[m]$
Γ_k	the k phase mass transfer rate	$[kg.m^{-3}.s^{-1}]$
Over lines		
$\bar{}$	ensemble average	
$\tilde{}$	relative to the nearest neighbor distributions	
Subscripts		
cf	columnar front	
c	columnar phase	
e	equiaxed phase	
c/e	columnar or equiaxed phase	
s	solid phase	
l	extra-dendritic liquid phase	
d	inter-dendritic liquid phase	
f	total fluid phase ($=l+d$)	
g	grain phase ($=d+s$)	
kc	columnar k phase	
ke	equiaxed k phase	

References

1. Ciobanas A I and Fautrelle Y 2006 "Ensemble Averaged Two-Phase Eulerian Model for Columnar/equiaxed Solidification of a Binary Alloy. Part I. The Mathematical Model" *Journal of Physics D: Applied Physics* (Submitted)

2. Wang C Y and Beckermann C 1993 *Metallurgical and Materials Transactions A* **24A** 2787

3. Wang C Y and Beckermann C 1996 *Metallurgical and Materials Transactions A* **27A** 2754

4. Mahapatra R B and Weinberg F 1987 *Metallurgical Transactions B* **18B** 425

5. Ziv I and Weinberg F 1989 *Metallurgical Transactions B* **20B** 731

6. Rappaz M and Thévoz Ph 1987 *Acta Metallurgica* **35.7** 1487

7. Martorano M A, Beckermann C and Gandin Ch-A 2003 *Metallurgical and Materials Transactions A* **34A** 1657

8. Patankar S V 1980 *Numerical Heat Transfer and Fluid Flow* (New York: Hemisphere Publishing Corporation)

9. Hunt J D 1984 *Materials Science and Engineering* **65** 75

10. Hunt J D 1979 *Solidification and casting of metals* (London: Metals Society) 3

11. Kurz W and Fisher D J 1981 *Acta Metallurgica* **29** 11

12. Ciobanas A I, Bejan A and Fautrelle Y 2006 "Dendritic solidification morphology viewed from the perspective of constructal theory" *Journal of Physics D: Applied Physics* (Submitted)

13. Wang C Y and Beckermann C 1994 *Metallurgical and Materials Transactions A* **25A** 1081

14. Gandin Ch-A 2000 *Iron Steel Inst. Jpn.* **40** 971

15. Gandin Ch-A 2000 *Acta Mater.* **48** 2483

16. Jackson K A, Hunt J, Uhlmann D and Seward T 1966 *Transactions of the metallurgical society of AIME* **236** 149

Référence IV

Modeling the mixed columnar/equiaxed solidification of a binary alloy with convection. Mathematical model.

A.I. Ciobanas, Y. Fautrelle

EPM/CNRS Laboratory, ENSHMG, BP 95, 38402 Saint Martin
d'Hères cedex, France

Abstract

The ensemble averaged model derived in reference [1] has been extended here to account for the fluid convection. Owing to the statistical nature of the model, one is able to treat rigorously the coexistence of equiaxed and columnar structures and consequently the CET phenomena. We have approached the ensemble average through the probability distributions functions attached to the macroscopic process to be studied. The new model inherits form the model in [1] which quantified in a rigorous manner the solutal and mechanical (geometrical) interactions between the two coexisting grain distributions. The microscale physical assumptions are reevaluated with respect to the ones in [1]. First, the fluid flow around the columnar/equiaxed (c/e) permeable grains and the grain growth in the presence of fluid convection is analyzed. Finally, an analysis of the solute transfer around the c/e grain in the presence of convection is made. It is concluded that the mass transfer at the grain boundary in the presence of convection is intensified with respect to the pure diffusion case. We propose correlation for the computation of the overall mass transfer coefficient in the limit of small and high c/e grain fractions. Using the microscale physical assumptions the average balance equations are further derived. First the grain balance equations are derived. The equiaxed nucleation is modeled as an instantaneous event whereas the columnar nucleation (the sudden arrival of columnar tips in one point) is modeled by means of a front tracking algorithm. We propose a simple front tracking technique having as basis the volume of fluid model. Moreover the coexistence model developed in [1] is here extended to account for the grain convection. The cell dimensions R_{1c}^* and R_{1e}^* as well as the space partition between the columnar and equiaxed distribution (ε_c and ε_e) is here determined form a new general model describing the coexistence state between two different grain populations. The mass, momentum and energy balance equations are derived next. Notice that for simplicity reasons a total fluid approach is considered for the momentum balance. For the energy equation a single mixture balance equation is derived. Finally the solute balance equations are obtained. Here, a total fluid approach is considered too along with the two solute balance equations in the c/e solid. In addition, the two solute balance equations in the c/e inter-dendritic liquid are used to compute the c/e solidification rates. We have also proposed an algorithm for the implicit computation of the extra-dendritic liquid concentrations. This is done by coupling at each time step the solute balance equations within the c/e extra-dendritic liquids with the solute balance equation in the total fluid (*f* phase). Finally a complete ensemble averaged model is proposed for the modeling of the mixed columnar + equiaxed structures in the presence of convection.

1 Introduction

In reference [1] an ensemble averaged model which can take into account the coexistence between two grain structures (i.e. equiaxed and columnar) was developed. The use of an ensemble averaging technique in deriving a micro-macro scale model has some important advantages compared with the volume averaging technique which has been widely used during the last decade. Firstly, the statistical approach does not need the definition of a representative elementary volume. Secondly, it is consistent with the random aspect of the equiaxed grain germination and motion as well as the possible turbulent behavior of the fluid flow. Finally, and the most important, owing to the statistical nature of the model, one is able to treat rigorously the coexistence of equiaxed and columnar structures and consequently the CET phenomena. Knowing that the CET phenomena are a direct consequence of complex mechanical and solutal interactions between an advancing columnar front and an equiaxed zone ahead of the columnar dendrite tips, a model that could integrate mathematically these interactions would be of great interest. However the final mathematical model proposed in reference [1] is valid for a pure diffusion solidification case only. Hereafter we propose an extension of the model in [1] which takes into account the effect of the fluid convection in the ingot.

2 The ensemble average

As pointed out in [1], in order to obtain an ensemble averaged model describing the solidification process of a binary alloy one has to write first the local conservation equations describing the balance of mass, momentum, energy and solute. These local balance equations are valid in each point of the two-phase system and describe the exact evolution of the two-phase system to the smallest time and length scale. Unfortunately due to the extremely complex solid-liquid interface the numerical resolution of local balance equations will be a virtual impossible task for real solidification problems usually involving ingots larger than 10^{-1} m. On the other hand we are not always interested on variations of parameters at the smallest scale but instead on average parameters like velocity, solute concentration characterizing large vortexes or mesosegregation, that is valid at larger scale (meso or macro scale). Moreover, the local balance equations state for the conservation of ψ inside the whole multiphase system. As one would desire to track the average evolution for each phase separately, the effect of each phase on the total balance of ψ has to be identified first. This is done by multiplying the local conservation equations with the characteristic phase function:

$$X_k(t,\mathbf{x}) = \begin{cases} 1 & if \quad (t,\mathbf{x}) \text{ is within the } k \text{ phase} \\ 0 & if \quad (t,\mathbf{x}) \text{ is not within the } k \text{ phase} \end{cases} \tag{1}$$

Then, in order to have an insight on average quantities, one has to further apply the ensemble average operator defined in [1]. Using then the topological relations characterizing X_k (Drew [2]), one can easily obtain the average conservation equations for ψ in each phase k as well as the corresponding jump equations [1]. However as to be useful these averaged equations has to be structured by defining adequate average variables. These average variables can be of different types following the choice of the weighted function: average variables weighted with the characteristic function X_k, mass weighted averages (Favré) weighted with $X_k\rho$ and finally, interfacial averages weighted with ∇X_k, having a meaning at the interface only. Definition of all these variables is

synthesized in [1]. One is able now to write down the ensemble averaged conservation equation for the general physical field ψ and the corresponding jump conditions:

$$\frac{\partial\left(\varepsilon_k \overline{\rho}_k \overline{\psi}_k\right)}{\partial t} + div\left(\varepsilon_k \overline{\rho}_k \overline{\mathbf{v}}_k \overline{\psi}_k\right) = div\left[\varepsilon_k\left(\overline{\mathbf{j}^{\psi}}_k + \overline{\mathbf{j}'^{\psi}}_k\right)\right] + \varepsilon_k \overline{\rho}_k \overline{b^{\psi}}_k + \overline{\Phi^{\psi}}_k + \overline{\Gamma^{\psi}}_k ; \quad k = \{s,l\} \tag{2}$$

$$\sum_k \left(\overline{\Phi^{\psi}}_k + \overline{\Gamma^{\psi}}_k\right) = \overline{\sigma} \; ; \quad k = \{s,l\} \tag{3}$$

The final system of averaged equations describing the solidification process will consist of mass, momentum, energy and solute balance written for each phase in the multiphase system. This is done by particularizing the general field ψ, the corresponding molecular flux $\mathbf{j}^{\psi}$ and the volumetric source b^{ψ} with the appropriated expressions for each balance equation [1].

The terms encircled in the equation (2) are very important for the correct modeling of the multi-phase system since they express transfer terms (of mass, momentum, etc.) between the phases. We have:

- $\overline{\Phi^{\psi}}_k$, the term responsible of the convecto-diffusive transfer at the phase interface;
- $\overline{\Gamma^{\psi}}_k$, the term responsible of the transfer at the phase interface due to the mass transfer between phases;
- $\overline{\mathbf{j}'^{\psi}}_k$, the dispersive flux due to the ψ fluctuations (also known as the Reynolds stress).

Notice that all these terms are unknown tensors which do not depend on known averaged values. Hence the equations (2) and (3) remains unclosed and one need to find for these terms closure expressions with respect to known average values. This is no more than the model closure procedure and it is here that the modeling effort is concentrated.

2.1 The cell model approximation to the ensemble average

The concept of ensemble averaging as defined in [1] is rather abstract. Consequently the unknown terms arising from the averaging procedure will be difficult to model. In order to better understand the nature of this average technique one should approach the ensemble average through the distributions functions attached to the macroscopic process to be studied.

Given two coexisting grain populations (i.e. columnar and an equiaxed) characterized by different grain densities, $n_{c/e}$, their influence at a certain point $\mathbf{x}$ would be different as well. The main advantage of the ensemble averaging is that, with the help of the nearest neighbor distributions $\tilde{f}_{c/e}\left(t,\mathbf{x};\tilde{\mathbf{z}}_1\right)$ [1], one can quantify in a rigorous way the c/e influence at $\mathbf{x}$. Indeed, $\tilde{f}_{c/e}\left(t,\mathbf{x};\tilde{\mathbf{z}}_1\right)$ measures the density of probability that one c/e grain centered at $\tilde{\mathbf{z}}_1$ is the closest grain to $\mathbf{x}$ among all the grains existing in the ingot. These two distributions play a vital role in determining the influence of c/e grains at $\mathbf{x}$ since one expects that what happens at $\mathbf{x}$ would be mainly influenced by the closest grain to $\mathbf{x}$. Using the cell approximation to $\tilde{f}_{c/e}$, two spherical cells centered at $\mathbf{x}$ and of radius R_{1c}^* and R_{1e}^* can be identified [1], each of them characterizing in a simple way the statistics of the c/e grain distributions (see Figure 1).

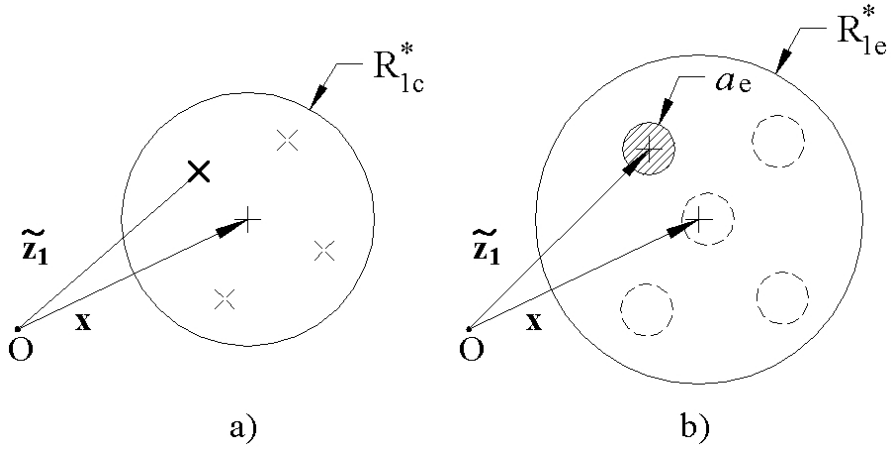

Figure 1: The cell model approximation to the columnar (a) and the equiaxed (b) ensemble average

Indeed, in the light of the cell model the ensemble $\theta_{c/e}$ of realizations such as the closest particle to $\mathbf{x}$ be a columnar/equiaxed one is equivalent with the ensemble of realizations such as the closest particle to **x** is c/e and is centered within the cell of radius $R^*_{1c/e}$ centered at **x**. Using the two spherical cells it is possible to separate the influence at **x** of the c/e grains by defining corresponding c/e ensemble averages which quantify the average effects of the two structures at **x**. Moreover, any ensemble average (i.e. e/c fractions, solid/liquid fractions, average solute fields, interfacial averages, etc.) can be easily computed by means of relative simple integrations over all possible positions of the closest c/e grain to **x**, within the respective c/e cell.

Thus, following the case where the closest grain to **x** is columnar or equiaxed, the model leads us to distinguish two main types of ensemble averages, columnar and equiaxed ensemble averages respectively (i.e. c/e fractions, c/e average concentrations, etc). In this respect, two important fractions are identified, the columnar and equiaxed fraction, ε_c and ε_e respectively. These two averages quantify the way the two structures share the space at **x**. Since the columnar and equiaxed grains share a same space at **x** their corresponding fractions will obviously sum to one, $\varepsilon_c + \varepsilon_e = 1$.

As an example, using the cell approximation, the ensemble average of a generic field ψ, $\overline{\psi}_{c,e}$ becomes [1]:

$$\begin{aligned}\overline{\psi}_{c,e}(\mathbf{x},t) &= \frac{1}{\varepsilon_{c,e}}\int \tilde{f}^{(1)}_{c,e}\left(t,\mathbf{x};\tilde{\mathbf{z}}_1\right)\tilde{\psi}^{(1)}\left(t,\mathbf{x};\tilde{\mathbf{z}}_1\right)d\tilde{\mathbf{z}}_1 \\ &= \frac{n_{c,e}}{\varepsilon_{c,e}}\int\limits_{|\mathbf{x}-\tilde{\mathbf{z}}_1|\le R^*_{1c,e}} \tilde{\psi}^{(1)}\left(t,\mathbf{x};\tilde{\mathbf{z}}_1\right)d\tilde{\mathbf{z}}_1\end{aligned} \tag{4}$$

where $\tilde{\psi}^{(1)}\left(t,\mathbf{x};\tilde{\mathbf{z}}_1\right)$ is the field $\psi(t,\mathbf{x})$ valid at the micro-scale, given that the closest grain to **x** is centered at $\tilde{\mathbf{z}}_1$. This, in turn, can be computed analytically given the micro-scale assumptions and considering that the field $\psi(t,\mathbf{x})$ is uniquely influenced by the closest grain to **x**, therefore neglecting the influence of more distant grains.

Moreover, the use of the probability distributions functions $\widetilde{f}_{c/e}\left(t,\mathbf{x};\tilde{\mathbf{z}}_1\right)$ in approaching the ensemble average reveals as well another important aspect of the coexistence between two grain structures. Indeed, the coexistence between columnar and equiaxed grains implies a sort of geometrical (mechanical) interaction between the two coexisting structures. Using the probability distribution function $\widetilde{f}_{c/e}\left(t,\mathbf{x};\tilde{\mathbf{z}}_1\right)$ one can rigorously characterize and quantify these interactions. As detailed in [1], the columnar and the equiaxed grains interact "mechanically" following a two fold mechanism: the first and the second mechanical blockage effect.

2.1.1 First mechanical blockage

The first mechanical blockage effect of the coexistence will determine a rarefaction of the columnar zone when entering ("nucleating") into a developed equiaxed zone. This will decrease the initial columnar grain density n_c^0 with a factor of $(1-\varepsilon_{ge})$. Indeed due to the finite equiaxed grain fraction the columnar tips have only a limited space $(1-\varepsilon_{ge})$ within which they can "nucleate". Hence only a fraction of the total number of columns will be able to enter the equiaxed zone.

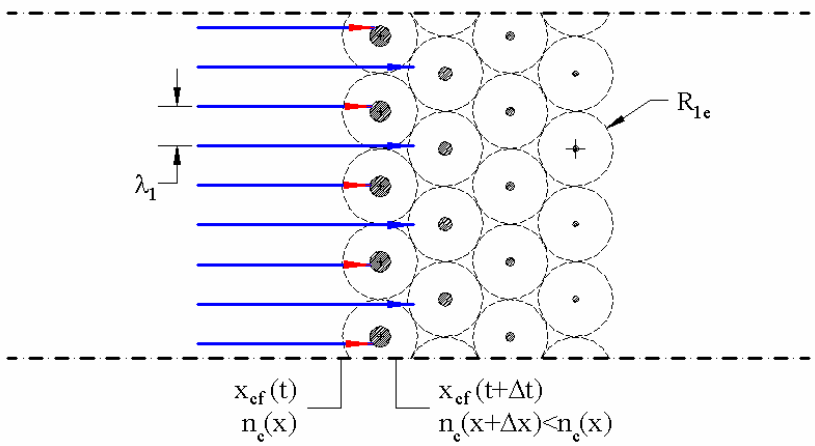

Figure 2: The first mechanical blockage

2.1.2 Second mechanical blockage effect

As pointed out in [1], the second mechanical blockage effect of the coexistence reflects the fact that for a mixed zone (i.e. columnar + equiaxed), the two coexisting structures are forced to share a same space (Figure 3). Consequently, the space available for each structure will be different and smaller too from the corresponding space available just before the coexistence state (the columnar nucleation in this case).

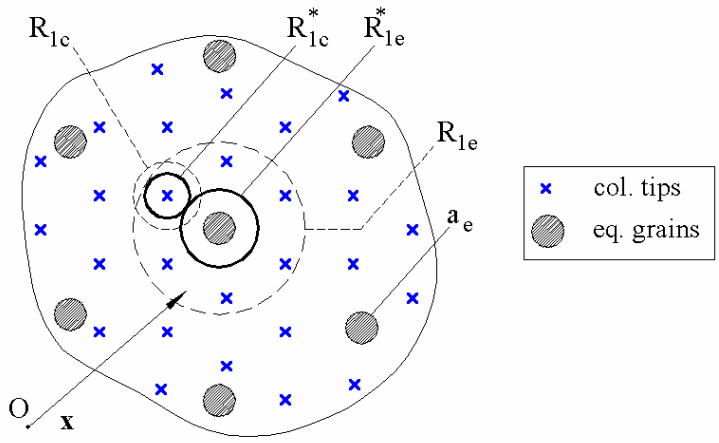

Figure 3: The second mechanical blockage: the full line circles represent the two cells characterizing the mixed c/e zone and the dashed line circles are the cells characterizing the two structures (c/e) separately, that is just before the coexistence state

As discussed already, the space characterizing the c/e structure is quantified by the ensemble model by means of two corresponding spherical cells of radius $R^*_{1c/e}$ (Figure 3). Basically the second mechanical blockage states that the length scales $R^*_{1c/e}$ are smaller than the corresponding length scales characterizing the c/e state separately just before their coexistence, namely $R_{1c/e}$. Notice again that $R^*_{1c/e}$ together with their corresponding grain densities $n_{c/e}$ are of primary importance for the modeling of the mixed c/e zone. Indeed these parameters characterize completely the statistics of the coexistence state, enabling one to define average variables for each one of the two structures. Moreover, since $R^*_{1c/e}$ can be very different form the original length scales $R_{1c/e}$ the evolution of the mixed zone can be significantly different from that of an equivalent pure columnar or equiaxed zone.

3 Model closure

In view of the complexity of the processes involved in a solidification problem one should first propose physical models at the micro-scale for all these processes and only then try to compute closure expressions for the unknown terms in equation (2). Writing down the physical assumptions valid at the micro-scale, would permit to quantify as exactly as possible the velocity, temperature, solute fields around each c/e grain. Then with the use of the cell model approximation to the ensemble average, equation (4), the unknown terms in (2) can be computed rigorously with respect to average variables. The macroscopic system can be in this way closed.

3.1 Micro-scale physical assumptions

Almost all physical assumptions valid at the micro-scale made in [1] for the pure diffusion case remain exactly the same for the case implying convection. The hypothesis linked to the: phase diagrams constraints, the solute diffusion controlled solidification, the local thermal equilibrium, the equiaxed and columnar nucleation remain unchanged. Obviously, the first hypothesis made in [1] concerning the pure diffusion case is no more valid since in the following we would like to account for the fluid flow effects. In fact, it is precisely the fluid convection phenomena that will determine a reevaluation of the final hypothesis made in [1] on the grain growth.

3.1.1 The fluid flow around a c/e dendritic grain

To quantify correctly the fluid flow around an e/c dendritc grain one should quantify the fluid flow across a swarm of permeable particles. Many mathematical models have been used [3-5] to study the fluid flow relative to a swarm of impermeable particles spheres. However the model that seems to give correct results within the entire range of porosity is the well known "free cell model" of Happel [5]. This model was later extended to accommodate the case of permeable spheres by Neal [6] and Davis [7] and their results agree well with experimental data obtained in real solidification problems [8]. In this respect in order to quantify the fluid flow across a mixed c/e zone we will try to adapt the Neal model to the case of a mixed e/c zone.

Basically the free cell model introduced by Happel [5] tries to model the interactions between adjacent particles by resolving a limited fluid flow problem around a single particle of the swarm. Indeed, the velocity field around the permeable particle of radius *a* is accounted to a maximum distance R_1 from the center of the particle such as

$$\left(a / R_1\right)^3 = \varepsilon_p \tag{5}$$

where ε_p is the volume fraction of the particles. Note the resemblance between the cell of radius R_1 around the grain and the columnar or equiaxed cells of radius $R^*_{1c/e}$ (Figure 1) which quantify rigorously the statistics of the columnar/equiaxed coexistence at **x**. As we have pointed out in [1], the two cells enveloping each c/e grain enclose the space uniquely perturbed by the respective c/e grain. Outside this cell one enters into the ray of influence of a neighbor particle. Remember as well that $R^*_{1c/e}$ quantifies as well the average distance between the c/e particles. In this respect in order to describe the fluid flow around a particle it is physically sound to focus mainly on the flow inside the characteristic cell; outside this cell the flow would be characterizing a neighbor cell. This ensemble average interpretation can only enforce the choice made by Happel [5] concerning the dimension of the cell, equation (5).

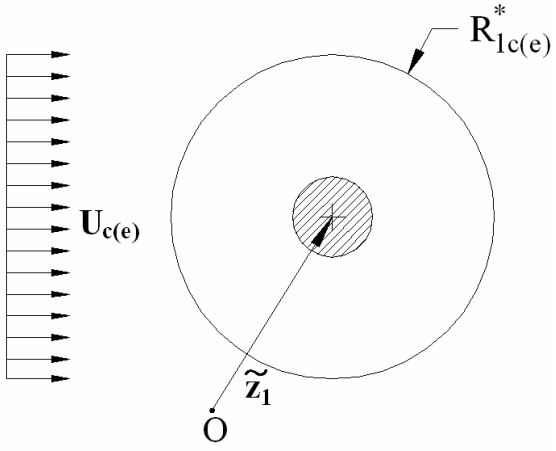

Figure 4: The c/e cell and the corresponding fluid flow

Therefore one should quantify the fluid flow around a dendrite grain to a distance $R^*_{1c/e}$ from the center of the c/e particle (Figure 4). However an important issue must be solved: what are the proper boundary conditions at the cell boundary representative for the

interactions between the adjacent grains? Following Neal [6] it is assumed that the particle is fixed and the cell boundary is traversed by a uniform fluid field of velocity $U_{c/e}$ corresponding to the flow rate per unit area across the c/e structure. For the case of stationary solid, $\mathbf{U}_{c/e}$ is no more than the superficial c/e velocity characterizing c/e fluid (*f*=*d*+*l* phase):

$$\mathbf{U}_{c/e} = \mathbf{v}_{fc/e}.\boldsymbol{\varepsilon}_{fc/e} \tag{6}$$

If the solid has a non-zero velocity, then $\mathbf{U}_{c/e}$ is no more than the relative flow rate per unit rate across the c/e structure:

$$\mathbf{U}_{c/e} = \mathbf{v}_{fc/e}.\boldsymbol{\varepsilon}_{fc/e} - \mathbf{v}_{sc/e} \tag{7}$$

The boundary conditions at the cell boundary are [6, 7]:

- The normal velocity component at the cell boundary matches that of the imposed flow:

$$\left(\mathbf{n}\cdot\mathbf{U} = \mathbf{n}\cdot\mathbf{u}\right)_{r=R_1^*} \tag{8}$$

where $\mathbf{u}$ denotes the velocity field within the characteristic cell of radius R_1^*.

- The tangential stress at the cell boundary is zero:

$$\left(\mathbf{n}\cdot\mathbf{T}\cdot\mathbf{t}\right)_{r=R_1^*} = 0 \tag{9}$$

where **t** is the unit tangent vector to the cell surface. Note that these boundary conditions are not randomly chosen but they are representative of the interactions between neighbor grains. In fact they reflect the hypothesis that the fluid flow to a distance R_1^* from the center of the particle is uniquely influenced by that particle. In this respect, each sphere is isolated in the sense that it only interacts with its neighbors through the average fields. Indeed, the zero tangential stress at the cell boundary means that locally there is no momentum exchange between neighbor particles. Instead the particles interact with their neighbors through the average velocity field $\mathbf{U}_{c/e}$, equation (8).

Assuming low Reynolds numbers, the flow around a particle can be fairly well described with a Stokes approximation. Knowing the internal permeability of the dendrite grain $K_{c/e}^d$, the flow within the permeable particle can be described by the Brinkman equation [6, 7]. Finally by imposing the usual cinematic boundary conditions at the grain boundary [6, 7] one can analytically resolve the fluid flow within the cell of radius $R_{1c/e}^*$ (Figure 4). Consequently one can compute the drag force on the solid particle produced by the fluid flow around it. One obtains a net drag force of [6, 7]:

$$\mathbf{F}_{dk} = 6\pi\mu_f a_k \Omega_k \mathbf{U}_k \ , \quad k = \{c, e\} \tag{10}$$

where μ_f is the dynamic viscosity of the fluid, a_k is the c/e grain diameter and Ω_k is a coefficient depending on the c/e grain diameter a_k, its internal permeability K_k^d and the ratio $\eta = a_k / R_{1k}^*$ [6]:

$$\Omega_k = \frac{2\beta^2 + 4\beta^2\eta^5/3 + 20\eta^5 - \frac{\tanh\beta}{\beta}\left(2\beta^2 + 8\beta^2\eta^5 + 20\eta^5\right)}{\left(\begin{array}{l} 2\beta^2 - 3\beta^2\eta + 3\beta^2\eta^5 - 2\beta^2\eta^6 + 90\beta^{-2}\eta^6 + 42\eta^5 - 30\eta^6 + 3 - \\ -\frac{\tanh\beta}{\beta}\left(-3\beta^2\eta + 15\beta^2\eta^5 - 12\beta^2\eta^6 + 90\beta^{-2}\eta^5 + 72\eta^5 - 30\eta^6 + 3\right) \end{array}\right)} \qquad (11)$$

where $\beta = a_k / \sqrt{K_k^d}$. This coefficient (Ω_k) accounts for both the influence of the internal permeability as well as for the interaction between neighbor particles. In fact, for $K_k^d \to 0$ equation (10) becomes identical with the free cell model proposed by Happel [5] for solid particles. Note as well that for $K_k^d \to 0$ and $\eta_k = 0$, $\Omega_k = 1$. Hence the well known Stokes drag force on a single particle is obtained. It is also important to notice that for the case of a coexistence state between equiaxed and columnar structures, the ratio η_k is no more than:

$$\eta_k = \left(\varepsilon_{gk} / \varepsilon_k\right)^{1/3} , \qquad k = \{c, e\} \qquad (12)$$

Similarly with the Wang approach [8], one can use a Karman-Cozeny model [3] to estimate K_k^d :

$$K_k^d = \frac{(1 - \varepsilon_{sk} / \varepsilon_{gk})^3}{5\left(A_s / V_g\right)^2} \qquad (13)$$

where A_s is the c/e solid/liquid interface area [m^2] and V_g is the grain volume (solid +inter-dendritic liquid). Note that using a simple plat-like model for the dendrite shape Wang and Beckermann [9] quantified the ratio A_s / V_g as:

$$A_s / V_g = 2 / \lambda_2 \qquad (14)$$

where λ_2 is the secondary arm spacing.

3.1.2 The grain growth. The envelope model.

In a similar way as in reference [1], an envelope model [9] is used to parameterize the smallest scale of the dendrite, that is the inter-dendritic spacing. The dendrite envelope is defined as the virtual surface surrounding the c/e dendrite grain and connecting all c/e dendrite tips. This leads us to distinguish two types of liquid, the inter- and the extra-dendritic one, and this for each one of the two grain structures. Therefore one divide the total liquid into four sub-phases: the equiaxed inter- (*de*) and extra- (*le*) dendritic liquid and the columnar inter- (*dc*) and extra- (*lc*) dendritic liquid. The inter-dendritic liquid is supposed to be in a state of perfect solutal mixing, its solute concentration, C_l^*, being uniquely determined from the local temperature and the phase diagram. On the other hand, due mainly to its relative large diffusion length scale, the extra-dendritic liquid may be in a non-equilibrium state with respect to the local solid-liquid interface, meaning that its

average concentration $C_{lc/e}$ can be different from C_l^*. The consequent local undercooling $C_l^* - C_{lc/e}$ will drive the c/e grain growth which in turn strongly influences the solute transfer in the extra-dendritic liquid. Since the solidification process is solutally controlled, special care must be paid to the modeling of the solute transfer at the grain envelope. As pointed out in [1], due to the equivalence between the length scale of the columnar and equiaxed extra-dendritic liquids ($R_{lc}^* \simeq R_{le}^* - a_e$) and the pure diffusion hypothesis, the solute field in the *e/c* extra-dendritic liquid will be a function of *r* only and the *e/c* cell boundary will play the role of a symmetry surface between two adjacent grains. Given this, the solute field in the extra-dendritic liquid was finally approached analytically with a relative simple expression [1].

However, if fluid flow around the grain is considered, the solute field around the grain and the grain growth rate can be significantly changed compared with the pure diffusion case. In the following we will suppose that the fluid flow across the permeable bed is characterized with low *Re* numbers, hypothesis generally valid within the c/e mushy zone. One has to note however that for relative high fluid velocities of the bulk liquid (i.e. high electromagnetic forces) the low Re hypothesis will not be valid for dispersed c/e grains (i.e. zone close to the columnar dendrite tips). Hence, the results provided in the following must be seen as a first order approximation to the grain growth under the influence of the fluid flow.

It was proven [10] that the fluid flow around a dendrite tip can significantly change the operating point of the dendrite. Both the stability criterion and the solute field around the tip are changing. Several studies have been conducted in order to understand the heat transfer around the advancing tip. A summary has been given by Ananth and Gill in [11]. For a Stokes fluid flow regime an analytical solution of the solute field around a parabolic tip has been found by Cantor [12]. However the dimensionless undercooling $\Omega = (C_l^* - C_0)/C_l^*/(1-k)$ and the local tip Peclet number, $Pe_t = V_t r_t / D_l$ are found to be linked by a very complex implicit function. Wang and Beckermann [13] proposed a fitting formula to the complex function in [11] that works reasonably well for *Sc* numbers grater than the 20 (which is the case of metallic alloys):

$$Pe_t = a\left(\frac{\Omega}{1-\Omega}\right)^b \quad , \qquad \begin{array}{l} a = 0.4567 + 0.173 Pe_u^{0.55} \\ b = 1.195 - 0.145 Pe_u^{0.16} \end{array} \tag{15}$$

where

$$Pe_u = \left|\mathbf{v}_l - \mathbf{v}_s\right| r_t / D_l \tag{16}$$

is the ambient Pe number computed with the relative fluid-tip velocity. However with the use of equation (15) the tip velocity cannot be computed explicitly since the tip radius is not known. Equation (15) must be completed with a stability criterion linking r_t and V_t. For fluid convection cases the marginal stability criterion valid for a pure diffusion case would not be anymore valid. Experimental evidence exists to confirm this statement [10]. However for low velocity fields one can assume that the influence of the fluid flow on the stability condition at the tip is not important with respect to the influence on the solute field around the tip. In this respect supposing that the marginal stability criterion remains valid one can write for the tip velocity [14]:

$$V_t = \frac{D_l m(k-1)C_l^*}{\pi^2 \Gamma} Pe_t^{\,2} \tag{17}$$

More recently, Gandin et al [15] found a more reliable correlation between Ω and Pe_t. The approach is less empirical than the one used by Wang and Beckermann [13], equation (15) in the sense that the kinetic boundary layer around the tip, δ (the stagnant layer) is modified accordingly with respect to the local Re and Sc numbers. A correlation of the form

$$\begin{aligned} &\delta = 2r_t / (Sh - 2) \\ &Sh = 2 + A \cdot \mathrm{Re}^B \cdot Sc^C \cdot f(\theta) \\ &\mathrm{Re} = 2r_t |\mathbf{v}_l| / \nu \end{aligned} \tag{18}$$

is proposed by the authors. Moreover, by introducing a correction function $f(\theta)$ their model can be easily modified to account for the influence of the relative angle θ between the dendrite growth direction and the fluid flow direction. By coupling the above equation with the solution of the diffusion field within the stagnant film, Gandin [15] obtained a better agreement with the exact solution in Ananth and Gill [11] than the model of Wang [13] did. The main inconvenient of the Gandin correlation is that no explicit expression of Pe_t is provided with respect to the tip undercooling Ω. Despite the explicit formulation of the stagnant film δ, the inverse function $Pe_t = f^{-1}(\Omega, \delta)$ has not an explicit form. This would require a numerical solution for f^{-1} which could be highly time consuming when coupled with a macroscopical model. Hence, for reasons of simplicity, the Wang and Beckermann [13] correlation, equation (15), will be used in the following.

3.1.3 The mass transfer around a dendrite grain

In [1] it was proved that for a pure diffusion case and a local thermal equilibrium at the scale of the grain, the solute field in the extradendritic liquid will be a function of *r* only. A simple analytical form for the solute field in the extra-dendritic is proposed in [1]. If fluid flow around the grain is accounted, the solute field will not be anymore depending on *r* only. For low *Re* numbers since no hydrodynamic instabilities form behind the spherical grain, the solute field can be at best approximated with an axisymetric field, $C_l(r, \theta)$ (see Figure 5). In the following a scale analysis of the mass transfer around the grain is conducted.

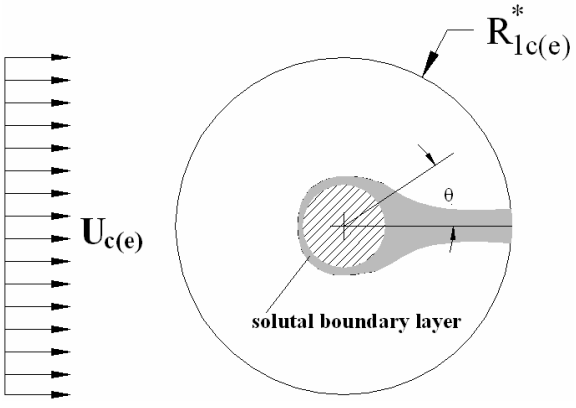

Figure 5: The solute boundary layer around a dendrite grain

The equation controlling the solute transfer within the extra-dendritic liquid is

$$\frac{\partial C_l}{\partial t} + div\left(\mathbf{v}C_l\right) = div\left(D_l \nabla C_l\right) \tag{19}$$

If one integrates the above equation on the extra-dendritic liquid one obtains the solute balance in the extra-dendritic liquid:

$$\begin{aligned} \frac{\partial}{\partial t}\int_{V_{sb}} C_l dV + \frac{\partial}{\partial t}\int_{V_l - V_{sb}} C_l dV + C_l^* A_g \overline{w}_{ge} + \int_{\Sigma_{cell}} \left(\mathbf{v}C_l\right)\mathbf{n}\, d\Sigma = \\ = \int_{\Sigma_{cell}} D_l \nabla C_l \,\mathbf{n}\, d\Sigma + \int_{\Sigma_g} D_l \nabla C_l \,\mathbf{n}\, d\Sigma \end{aligned} \tag{20}$$

where V_{sb} and V_l are the volume of the solutal boundary layer and of the extra-dendritic liquid respectively (Figure 5), Σ_{cell} and Σ_g are the surface boundaries of the cell and the grain respectively, A_g is the area of the grain boundary ($=4\pi a^2$ if the grain is supposed to be spherical) and finally $\overline{w}_{ge}$ is the interfacial average velocity of the grain envelope. One can admit as a first approximation that $\overline{w}_{ge}$ can be computed with the help of equation (17) in which the role for the far concentration C_0 is played by the average extra-dendritic liquid concentration $\overline{C}_l$.

The first two terms on the LHS of the above equation represent the variation of the solute within the boundary layer around the grain and outside the boundary layer respectively. The third term on the LHS is no more than the solute loss of the extra-dendritic liquid due to the grain growth ($\overline{w}_{ge} \neq 0$). Finally the fourth term is no more than the solute flux at the cell boundary due to the liquid advection. This last term is usually positive (a solute loss) because the average concentration characterizing the outflow liquid ($\overline{C}_{out}$) is larger than the mean concentration characterizing the inflow liquid $\overline{C}_{in}$. This is obvious due to the enriching process of the liquid within the wake behind the particle (Figure 5). Hence, one can rewrite the last term on the LHS of as:

$$\int_{\Sigma_{cell}} \left(\mathbf{v}C_l\right)\mathbf{n}\, d\Sigma = U\pi R_1^2 \left(\overline{C}_{out} - \overline{C}_{in}\right) \tag{21}$$

where U is no more than the flow rate per unit area across the permeable bed, equation (7). Now the first term on the RHS of (20) is the molecular solute flux at the cell boundary. This term can be however neglected since one expects however that the gradients at the cell boundary be small compared with the ones at the grain boundary. Finally the last term on the RHS is no more than the total solute flux at the grain interface. Due to convection around the spherical grain, the solute flux at the grain interface will be dependent on the angle θ. Since we are interested for average quantities that could integrate the local effects of the fluid flow one could rewrite the total flux at the grain boundary as:

$$\int_{\Sigma_g} D_l \nabla C_l \,\mathbf{n}\, d\Sigma = D_l A_g \frac{C_l^* - C_0}{\delta_{cv}} \tag{22}$$

where δ_{cv} represent the average diffusion length at the grain boundary and remains to be explicited from the solute balance equation (20). Similar to the analysis made in [1] one can suppose the existence of a quasi-steady solute field around the grain growth. In this respect the parameters characterizing the solute boundary layer remains unchanged with respect to time. Therefore if a quasi-steady state is considered, the time derivates of the mean concentration and of the dimensions characterizing the boundary layer are negligible. Therefore, the solute mass balance in (20) becomes:

$$A_g \overline{w}_{ge} \left(C_l^* - C_0 \right) + U \pi R_1^2 \left(\overline{C}_{out} - \overline{C}_{in} \right) = D_l A_g \frac{C_l^* - C_0}{\delta_{cv}} \tag{23}$$

Hence the mean diffusion length δ_{cv} becomes

$$\delta_{cv} = \frac{D_l}{\overline{w}_{ge} + c} \ , \qquad c = \frac{U \pi R_1^2 \left(\overline{C}_{out} - \overline{C}_{in} \right)}{A_g \left(C_l^* - C_0 \right)} > 0 \tag{24}$$

It is important to notice that since $\overline{C}_{out} > \overline{C}_{in}$ one has always $\delta_{cv} < D_l / \overline{w}_{ge}$, that is smaller than the diffusion length correspondent to the pure diffusion case [1]. This was expected since the effect of the fluid flow can only intensify the solute flux at the grain boundary. The equation (24) can be rewritten as follows:

$$\begin{aligned} Sh \left(= \frac{R_1 - a}{\delta_{cv}} \right) &= \frac{\left(\overline{w}_{ge} + c \right) \left(R_1 - a \right)}{D_l} \\ &= Pe_g + \frac{1}{4} \frac{R_1^2}{a^2} \frac{\left(\overline{C}_{out} - \overline{C}_{in} \right)}{\left(C_l^* - C_0 \right)} Pe_u \end{aligned} \tag{25}$$

where $Pe_g = \overline{w}_{ge} \left(R_1 - a \right) / D_l$ is the Peclet number characterizing the grain growth (see [1]) and $Pe_u = U \left(R_1 - a \right) / D_l$ is the Peclet number relative to the fluid flow around the grain. Note as well that in the above equation one has as well

$$R_1^2 / a^2 = \left(\varepsilon_{gk} / \varepsilon_k \right)^{-2/3} \ , \quad k = \{c, e\} \tag{26}$$

Equation (25) emphasizes the influence of the fluid flow and the grain growth on the global solute transfer around the dendritic grain. It is interesting to note as well that, for a pure diffusion case, one has $Sh_{diff} = Pe_g$, an identical result with the one obtained in [1]. To detail further the result in (25) one should be able to quantify the difference $\overline{C}_{out} - \overline{C}_{in}$. One can expect that $\overline{C}_{in}$ be close to C_0. In contrast, the mean concentration of the outflow $\overline{C}_{out}$ is more difficult to quantify since it directly depends on the flow characterizing the wake behind the grain. This in turn depends strongly on the local Reynolds number ($\mathrm{Re} = U R_g / \nu$) and can be extremely complex for average-high values of *Re*. An interesting limit case can be however treated: for ratios a^2 / R_1^2 close to unity (c/e grain

fractions close to the maximum c/e fractions) one expects that, due to the effective solute flux at the grain boundary, the outflow liquid to be in a state close to the perfect solutal mixing. Hence one has $\overline{C}_{out} \simeq C_l^*$ and the overall solute transfer can be characterized as follows:

$$Sh = Pe_g + \frac{1}{4}\left(\varepsilon_{gk} / \varepsilon_k\right)^{-2/3} Pe_u \ , \qquad k = \{c, e\} \tag{27}$$

Note again that the above correlation would be valid uniquely for $\varepsilon_{gk} / \varepsilon_k$ close to unity. In fact the above equation has a meaning only for non-zero values of the c/e grain fraction ε_{gk}.

In contrast for small values of $\varepsilon_{gk} / \varepsilon_k$, one expects that the solutal interactions between the grains and the extra-dendritic liquid to be small. Hence the overall fluid flow effect on the solute transfer at the grain interface could be approximated as being similar to the case of the mass transfer around a sphere placed in an infinite medium. Several correlations accounting for this case exists in the literature [16]. A typical scaling law describing the mass transfer around a spherical object can be written as follows:

$$Sh_{cv} = A\,\mathrm{Re}^n\, Sc^n \ , \qquad \mathrm{Re} = Ua/\nu \,;\ Sc = \nu / D_l \tag{28}$$

Since the diffusion equation describing the solute transfer in the extra-denditic liquid is linear one can expect that the overall mass transfer around the grain in the limit $\varepsilon_{gk} \to 0$ to be a sum of the effects produced by the grain growth and the fluid flow around the grain respectively. Therefore one has:

$$Sh = Pe_g + Sh_{cv} \tag{29}$$

We have thus tried to approach the analytically the overall mass transfer coefficient at the grain interface in the limit $\varepsilon_{gk} \to 0$ (equation (29)) and $\varepsilon_{gk} \to \varepsilon_k$ respectively (equation (27)). These two scaling laws must be seen only as a first attempt in describing the solute transfer around a dendrite grain in the presence of convection and a future detailed study must be conducted in order to better quantify the solute flux at the grain boundary. Despite the simple approach used before an important conclusion can be drawn: the solute transfer at the grain interface is intensified by the fluid flow compared with the pure diffusion case ($Sh > Pe_g$), meaning that:

$$\delta_{cv} < D_l / \overline{w}_{ge} \tag{30}$$

One should also note that in an average model C_0 is not known a priori. Using however a similar procedure as in reference [1], by assuming a known concentration profile within the solutal boundary layer δ_{cv}, one can express C_0 as a function of $\overline{C}_{lk}$, R_{1k}^* and a_k ($k = \{c, e\}$). In this respect the average solute flux at the grain boundary becomes finally [1]:

$$\overline{\varphi}_{gk} = D_l \frac{C_l^* - \overline{C}_{lk}}{\delta_{lk-dk}}$$
$$\delta_{lk-dk} = \delta\left[1 - \frac{10a_k{}^2\delta + 10a_k\delta^2 + 4\delta^3}{5\left(R_{1k}^{*\,3} - a_k{}^3\right)}\right] \qquad k = \{c, e\} \tag{31}$$

where:

$$\delta = \begin{cases} \delta_{cv} & if \quad 2\delta_{cv} < \left(R_{1k}^* - a_k\right) \\ \left(R_{1k}^* - a_k\right)/2 & if \quad 2\delta_{cv} \geq \left(R_{1k}^* - a_k\right) \end{cases} \tag{32}$$

It is important to notice that, the average diffusion length δ_{lk-dk} verifies always:

$$\delta_{lk-dk} < D_l / \overline{w}_{ge} \tag{33}$$

a necessary condition for δ_{lk-dk} to be physically meaningful [9].

4 The final averaged equations

Using now the cell model approximation to the ensemble average together with the physical hypothesis enounced above one is able to compute the unknown terms and tensors in the averaged equations of mass, momentum, energy and solute, equations.

As pointed out, through the use of the appropriate probability distributions, the new ensemble model enables one to rigorously model the coexistence of equiaxed and columnar grains. However one should not confound the c/e phase with the c/e solid. In fact the c/e phase quantifies the space (liquid + solid) which is under the direct influence of the c/e structure. Based on the hypothesis that at **x** a physical field ψ (velocity, solute conc., etc.) is mainly influenced by the closest c/e particle to **x** one can quantify locally the amount of space corresponding to each of the two structure. By introducing further the grain envelope model, the c/e phase is further divided into three sub-phases: solid (s) , inter-(d) and extra-(l) dendritic liquid. Even if, in reality one deals with a two phase system (solid + liquid), due to the highly complex morphology of the mixed c/e zone (very different c/e grain densities, $n_c \neq n_e$; scale separation between the inter- and the extra-dendritic zone) one needs to consider separately the evolution of the c/e solid, inter- and extra- dendritic liquid, that is a six phase multiphase system. Fortunately, the six phase approach is only needed in describing the solute diffusion problem since this later process is strongly influenced by the length scales present in the system. Moreover, the solute diffusion process needs special attention since it controls directly the solidification process (solid and grain growth).

4.1 The grain balance

As pointed out by Drew [2], the grain balance equation for a given grain distribution can be written as follows:

$$\frac{\partial n}{\partial t} + div\left(n\mathbf{v}_s\right) = \dot{n}_n + \dot{n}_c + \dot{n}_b \tag{34}$$

where $\mathbf{v}_s$ is the grain mean velocity, $\dot{n}_n$ the rate of change of the number of particles per unit volume due to nucleation and $\dot{n}_c$ and $\dot{n}_b$ the rate of change of the number of particles due to aggregation or breakup phenomena. In reality experimental evidence exists [17] to support strong equiaxed grain aggregation, especially at high grain fractions. Moreover, the breakup (fragmentation) of columnar tips has been frequently cited [18, 19] as one of the most important phenomena causing the columnar-to-equiaxed transition. For reasons of simplicity we will only account in the following for the nucleation phenomena. Note however that a future extension of the model in order to account the breakup and aggregation phenomena will be straightforward. One should only propose appropriate models for $\dot{n}_c$ and $\dot{n}_b$. In this respect the c/e grain balance equations becomes:

$$\frac{\partial n_k}{\partial t} + div\left(n_k \mathbf{v}_{sk}\right) = \dot{n}_k \quad , \qquad k = \{c, e\} \tag{35}$$

where the c/e nucleation rate, $\dot{n}_k$, remains to be modeled.

For the equiaxed grains, similar with the approach used in [1], we will adopt in the following the instantaneous nucleation model. This model states that the equiaxed nucleation triggers instantaneously when the local undercooling reaches a certain value, ΔT_{ne}, and is characterized with an homogenous grain density n_e^0. Both the nucleation undercooling ΔT_{ne} and the nucleation grain density n_e^0 represent input parameters which have usually a relative high degree of incertitude. In the frame of the new ensemble model one is able to rigorously account for the nucleation of one structure into another (i.e. equiaxed nucleation within the inter-granular columnar spacing or the columnar "penetration" within an existing equiaxed zone). In this respect, besides the evident equiaxed nucleation within an undercooled pure melt, one is able to account as well for an eventual equiaxed nucleation within an undercooled columnar zone and more precisely within the undercooled columnar extra-dendritic liquid. As pointed out in [1], when a grain structure nucleates within an already existing structure the first one will be partially blocked by the later one. Indeed the newly germinating structure has only a limited space for nucleation, that is, the extra-dendritic liquid of the existing structure. This blocking effect represents no more than the first mechanical blockage (Figure 2) as detailed in [1]. Applied to equiaxed nucleation within the columnar zone, the first mechanical blockage states that the equiaxed grain density prior to the nucleation phenomenon, n_e, will be smaller than its nucleation density n_e^0 with a factor of $(1-\varepsilon_{gc})$:

$$n_e = n_e^0\left(1-\varepsilon_{gc}\right) \tag{36}$$

where ε_{gc} is the columnar grain fraction at the moment of equiaxed nucleation. In this respect the equiaxed nucleation rate becomes

$$\dot{n}_e = n_e^0\left(1-\varepsilon_{gc}\right)\delta\left(T - T_{liq} + \Delta T_{ne}\right) \tag{37}$$

where T_{liq} is the local liquidus temperature.

As pointed out in [1], in contrast with the equiaxed nucleation, the columnar "nucleation" (the sudden arrival of the columnar dendrite tips at **x**) cannot be treated as a

local event depending solely on local parameters. Indeed, the presence at **x** of the columnar tips will be a function of its evolution history and therefore a front tracking technique must be used in order to determine the precise position of the columnar front (c.f.) at **x** and at time *t*. The model has to be completed therefore with a front tracking equation, describing the precise evolution of the c.f position with respect to time, $\mathbf{x}_{cf}(t)$. In this light, the columnar nucleation can be approached with a local instantaneous germination

$$\dot{n}_c = n_c^{'} \delta\left[\mathbf{x} - \mathbf{x}_{cf}(t)\right] \tag{38}$$

where $n_c^{'}$ is the columnar grain density valid after the columnar nucleation within the equiaxed zone and $\delta\left[\mathbf{x} - \mathbf{x}_{cf}(t)\right]$ is the Dirac function pointing to the columnar front surface. Taking into account the first mechanical blockage effect on the columnar tips, produced by an eventual equiaxed zone ahead the columnar front (Figure 2) one has as well:

$$n_c^{'} = n_c^0 \left(1 - \varepsilon_{ge}\right) \tag{39}$$

where ε_{ge} is the local equiaxed grain fraction at the moment of nucleation and n_c^0 is the columnar nucleation density which can be directly related to the primary arm spacing λ_1 and therefore to the local cooling conditions: local gradient *G* and local isotherm velocity V_{is}. One could use for λ_1 the well known laws of Hunt [20] or Kurtz [21] or the new developed scaling law in [22] which relates the primary arm spacing to the local velocity tip gradient at the columnar front,

$$\lambda_1 = \left(16.D_l.t_{rs}\right)^{1/2}, \qquad t_{rs} = -\left(\frac{\partial V_{tip}}{\partial n}\right)_{cf}^{-1} \tag{40}$$

The above scaling law has been derived form the perspective of the constructal theory [23]: the primary arm spacing characterizing the columnar structure is viewed as the optimum arm spacing with respect to the local cooling conditions (G and V_{is}). A detailed comparison with various directional experiments shows that, despite its simplicity, equation (40) provides results which concord remarkable well with various experimental data.

4.1.1 Columnar front tracking algorithm

The most difficult issue to be resolved in the case of the columnar structure is however the need for a columnar front tracking. Indeed the implementation of a front tracking technique would be extremely time consuming. If for one-dimensional case this can be done in a simple way [19, 24], the extension of a direct front tracking technique to 2D and 3D would be extremely tedious. Moreover the discrete approach of the front tracking procedure would not fit in the frame of an averaged multiphase model who's main advantage is precisely to avoid the full modeling of the solid-liquid interface. Attempts in coupling an average model and a discrete columnar front technique were made by Brown [25]. This later model is limited however to bi-dimensional solidifications and to pure diffusion cases (no convection). The extension of this model for convection and three-dimensional cases is

not straightforward. Moreover a discrete approach for the columnar front would be difficult to imagine for the modeling of the complex shapes encountered in the case of solidifications in the presence of convection: freckles and channels characterized by a very anisotropic shape (large length and very small thicknesses).

An alternative to this approach would be a VOF (volume of fluid) model. The VOF model attach to each cell (control volume) of the mesh grid a fraction of fluid, in this case a fraction of the columnar structure, quantifying the fraction of the total control volume occupied by the columnar phase (Figure 6). Thus each control volume in the mesh grid can be characterized with a columnar fraction, f_c such as if

$$f_c(cell_i) = \begin{cases} 1 & then \quad \text{the cell is empty (of the col. structure)} \\ 0 & then \quad \text{the cell is full (of the col. structure)} \\ \in (0,1) & then \quad \text{the cell contains the interface between the col. str. and the bulk liquid (or equiaxed zone) ahead} \end{cases} \tag{41}$$

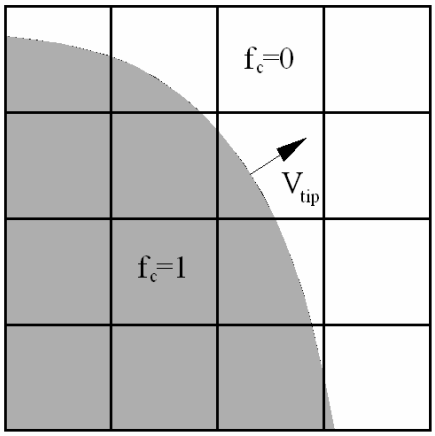

Figure 6: The VOF method

Since the columnar structure is stationary the equation controlling the evolution of f_c becomes:

$$\frac{\partial f_c}{\partial t} = S_c V_{tip} \tag{42}$$

where V_{tip} is the local columnar tip velocity and S_s the columnar interfacial area relative to the control volume ($= A_c / V_{cell}$, the ratio between the interface area within the cell and volume of the cell). Since the mixed columnar and equiaxed grains share the same undercooling, similar with the approach in [19, 24], the local columnar tip V_{tip} can be directly linked to the local tip velocity:

$$V_{tip} = \overline{w}_g \tag{43}$$

As observed (Figure 6) the interfacial area S_c depends both on the columnar structure fraction f_c and the growth direction of the columns. Knowing that columnar dendrites grow opposite to the local heat flux direction, one has $\mathbf{n}_c = \nabla T / |\nabla T|$. Since the shape of the control volume is a priori known the interfacial area can be now computed

$$S_c = funct\left(\mathbf{n}_c,\ \text{shape of the cell},\ f_c\right) \tag{44}$$

Due to the non-regular shape of the cell the above function can be quite complex, therefore a simpler model would be of great interest. The simplest model would be to consider that there is no preferred growth direction for the columnar grains and to assume a simple isotropic shape for the cell: a cube of border *b* aligned with the columnar growth direction. A measure for *b* can be easily obtained from the volume of cell

$$\begin{aligned} b &\simeq V_{cell}^{\ 1/3}\ (3D\,case) \\ &\simeq V_{cell}^{\ 1/2}\ (2D\,case) \end{aligned} \tag{45}$$

Obviously the above scaling law would have a physical meaning only if the real shape of the cell is close to an isotropic one. In this respect and assuming no preferred growth direction for the columnar grains the interfacial area S_c can be easily expressed as:

$$S_c = 1/b \tag{46}$$

Equation (42) and (46) form a complete model for the evolution of the columnar structure fraction f_c. However, equation (42) would predict the evolution of f_c within a control volume containing already a columnar front interface. One needs as well a model for the further expansion of the columnar front from one control volume to another. There are various models to account this issue (the geometric reconstruction scheme, the donor-acceptor scheme). Due to their high complexity we will instead propose here a very simple model describing the progress of the columnar front from one cell to another: when a cell partially filled $0 < f_c < 1$ finally becomes completely filled with the columnar structure (f_c reach 1), only then, the columnar tips are supposed to grow outside the cell and the columnar front progress to the neighbor cells. Notice that Wu and Andreas [26] used a similar columnar front tracking model in their volume averaged model.

The above front tracking model must be seen only as a first order approximation to the real columnar front position. However its main advantage is the fact that one can easily integrate such a front tracking technique within an averaged multiphase model. Indeed, since one has an insight on the moment when the columnar front passes from one cell to another, the columnar nucleation can be easily synchronized with this moment: one can assume that the columnar front nucleation within a cell triggers when the columnar front reaches the respective cell (at time t_{cf}). Hence one has:

$$\dot{n}_c = n_c^0 \left(1 - \varepsilon_{ge}\right) \delta\left(t - t_{cf}\right) \tag{47}$$

The use of such an approach avoids the need of a discrete modeling of the c.f. interface. However, the above VOF approach to the columnar front must be used with care since the method can be extremely dependent on the mesh grid, especially if the controls volume are

highly anisotropic, which can be the case for complex unstructured mesh. Moreover, the accuracy of the prediction of the columnar front position is strongly dependent on the size of the mesh. Knowing that the above VOF approach will converge to the exact discrete front tracking approach for:

$$V_{cell} \to 0 \tag{48}$$

one should use a very fine mesh in order to minimize the errors in the c.f. prediction. In turn this would greatly increase the computation time and would limit the use of such a method to relative small domains. In this respect, the use of an adaptive mesh technique close to the columnar front would be of significant interest.

4.1.2 The second mechanical blockage

Subsequent to the nucleation phenomena of one structure into another one, the two coexisting structure are forced to share a same space and consequently the space available for each structure will be smaller with respect to the space characterizing the two structures separately (i.e. before their coexistence). As already pointed out, this is no more than the second mechanical blockage effect of the coexistence: the length scales $R^*_{1c/e}$, characterizing the coexisting state between the columnar and the equiaxed grains, are smaller than the corresponding length scales characterizing the c/e state separately just before their coexistence, namely $R_{1c/e}$ (see Figure 3). In fact the length scales $R^*_{1c/e}$ together with the two corresponding grain densities $n_{c/e}$ enable one to completely describe the statistics of the coexistence state and consequently to rigorously compute any average field relative to the columnar or the equiaxed structure by means of relative simple integrations within the two corresponding c/e cells (Figure 1). In [1] we have demonstrated that the two length scales characterizing the c/e coexistence state can be written as follows:

$$\begin{aligned} R^*_{1c} &= \left(\frac{4}{3}\pi n_c\right)^{-1/3} \varepsilon_c \\ R^*_{1e} &= \left(\frac{4}{3}\pi n_e\right)^{-1/3} \varepsilon_e \end{aligned} \tag{49}$$

where n_c and n_e represent the columnar and equiaxed grain densities respectively characterizing the two coexisting structures and ε_c and ε_e are the columnar and equiaxed fractions respectively. From a statistical point of view these two fractions quantifies the way the two coexisting structures shares the space at **x**. One has obviously:

$$\varepsilon_c + \varepsilon_e = 1 \tag{50}$$

In [1] a model for $\varepsilon_{c/e}$ was proposed for the case of the columnar nucleation within an already developed equiaxed zone. As detailed in [1], the two fractions depends solely on columnar nucleation grain density n_c^0, equiaxed grain density, n_e and the equiaxed grain fraction valid at the moment of columnar nucleation, ε_{ge}. One has:

$$\frac{\varepsilon_c}{(1-\varepsilon_e)} = \begin{cases} 1-\varepsilon_{ge} - \dfrac{1}{20n_c^0}\begin{bmatrix} 10n_e + 36(n_e)^{\frac{2}{3}}\left(n_c^0\varepsilon_{ge}\right)^{\frac{1}{3}} \\ +45(n_e)^{\frac{1}{3}}\left(n_c^0\varepsilon_{ge}\right)^{\frac{2}{3}} \end{bmatrix} & if \quad R_{1c} \le R_{1e}\left(1-\varepsilon_{ge}^{1/3}\right) \\ \dfrac{n_c^0}{20n_e}\begin{bmatrix} \left(\varepsilon_{ge}\right)^2 - 20\varepsilon_{ge} + 45\left(\varepsilon_{ge}\right)^{\frac{2}{3}} \\ -36\left(\varepsilon_{ge}\right)^{\frac{1}{3}} + 10 \end{bmatrix} & if \quad R_{1c} > R_{1e}\left(1-\varepsilon_{ge}^{1/3}\right) \end{cases} \tag{51}$$

where:

$$R_{1c} = \left(4/3\pi n_c^0\right)^{-1/3}, \quad R_{1e} = \left(4/3\pi n_e\right)^{-1/3} \tag{52}$$

It is important to notice that, since the columnar/equiaxed nucleation phenomena within a developed equiaxed/columnar zone are statistically speaking the same phenomena, the above model can be straightforward extended to account for the equiaxed nucleation within a developed columnar zone as well. One has only to replace in equations (51), (52) n_e with n_c, n_c^0 with n_e^0 and ε_{ge} with ε_{gc}.

Note that besides the constraint in equation(50), the two fractions $\varepsilon_{c/e}$ in (51) verify as well

$$\varepsilon_{e/c} > \varepsilon_{ge/c} \qquad \text{and therefore} \qquad \varepsilon_{c/e} < 1-\varepsilon_{ge/c} \tag{53}$$

These two inequalities express one another important constraint of the coexistence state: the newly germinated c/e phase cannot occupy a space larger than the available space for its germination existing prior to c/e "nucleation", namely the e/c extra-dendritic liquid $1-\varepsilon_{ge/c}$. Indeed, due to the finite dimension of the e/c grains, the columnar tips can "nucleate" only within the e/c extra-dendritic liquid and the subsequent columnar fraction will be therefore always smaller that $1-\varepsilon_{ge/c}$.

Moreover, one more important characteristic of the two fractions $\varepsilon_{c/e}$ was identified in [1]. The statistical analysis of the coexistence between the two grain structures provided us with one important property of the length scales $R^*_{1c/e}$: the two length scales of the c/e structures, $R^*_{1c/e}$, are such that the length scales of the columnar and equiaxed extra-dendritic liquids are of the same order of magnitude:

$$R^*_{1e/c} - a_{e/c} \simeq R^*_{1c/e} \tag{54}$$

Therefore, the initial e/c extra-dendritic liquid, $1-\varepsilon_{ge/c}$, is shared by the two structures such as the length scales characterizing the two coexisting extra-dendritic liquids have the same order of magnitude (Figure 3). In reference [1] the property in equation (54) has been entirely demonstrated analytically but one can provide as well a physical interpretation. In fact, since one assumes a homogenous distribution in space of the two coexisting structures, the columnar and equiaxed solid will also be distributed in space such as the void spaces between the c/e particles are equal. The two grain distributions rearrange in space such as the average distance between two neighbor particle, regardless of their nature (columnar or equiaxed) be equal. There is no reason, given the hypothesis of local homogeneity, to find some particles closer to their neighbors than other particles are. This is one key aspect of the coexistence state between two different grains population because

the length scales characterizing the two extra-dendritic liquids (*le* and *lc* phases) are significantly influencing the solutal evolution of the two liquids and consequently the columnar and equiaxed grain growth ($\overline{w}_{gc/e}$) and solidification rates ($\Gamma_{sc/e}$). Evidence to this statement can be found in evolution of the c/e extra-dendritic concentration $\overline{C}_{lc/e}$ within the mixed columnar + equiaxed zone behind the columnar front as modeled in [24]. Indeed due to the equivalence between the length scales of the *lc* and *le* phases, equation (54), we have obtained that $\overline{C}_{lc} \simeq \overline{C}_{le}$ prior to the "columnar nucleation" into the equiaxed zone.

Note however that the equation (51) expressing the two fractions $\varepsilon_{c/e}$ can be successfully used in the modeling of the coexistence state existing prior to a columnar or equaixed nucleation within an already developed equiaxed or columnar zone. In fact, the two $\varepsilon_{c/e}$ fractions computed by means of equation (51) can be successfully used for the case of pure diffusion case only. Indeed, subsequent to the nucleation of one phase into another the two fractions $\varepsilon_{c/e}$ does not change anymore since the columnar and the equiaxed grains are stationary. However if convection is accounted, the way the two structures are sharing the same space at **x** can be subject to changes. Indeed due to fluid flow the equiaxed grains are free to move through the ingot and therefore the equiaxed grain density in one point will be subject to constant changing. In the case of a mixed c/e zone the change of n_e will determine a redistribution of the space between the columnar and the equiaxed structures and therefore a local change in $\varepsilon_{c/e}$. Since the columnar zone just behind the columnar zone is very permeable (small columnar grain fractions ε_{gc}) one can expect that the fluid flow within the bulk liquid to modify the equiaxed grain density of the mixed c/e zone behind the columnar front. Obviously, since n_c remains constant due to the static columnar grains, a modified n_e would also determine a redistribution of space ($\varepsilon_{c/e}$) between the columnar and equiaxed grains. For example if n_e increases one expects that ε_e increases and ε_c decreases since more equiaxed grains and the same number of columnar grains are forced to share a same volume ($\varepsilon_c + \varepsilon_e = 1$).

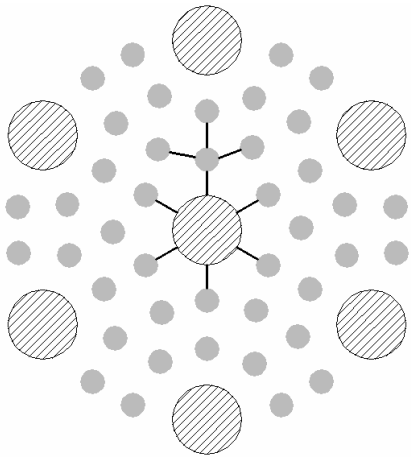

Figure 7: The equiaxed and columnar grains distribute in space such as the average distance between two neighbor grains, regardless of their nature, be equal

In this respect the question to be answered is: how to compute the new c/e fractions $\varepsilon_{c/e}$ and therefore the corresponding length scales $R^*_{1c/e}$ characterizing the statistics of the coexistence, all this with respect to the new conditions at n_e, ε_{ge}, n_c and ε_{gc}? A simple model for $\varepsilon_{c/e}$ is proposed in the flowing.

Note first that a physical meaningful model for $R^*_{1c/e}$ and $\varepsilon_{c/e}$ would have to verify the three constrains expressed in equation (50), (53) and (54) respectively, that is:

1. The columnar and equiaxed grains are sharing at **x** the same space:

$$\varepsilon_c + \varepsilon_e = 1 \tag{55}$$

2. The columnar/equiaxed fractions are always larger than their respective grain fractions:

$$\varepsilon_{c/e} \geq \varepsilon_{gc/e} \tag{56}$$

3. The two grain distributions rearrange in space such as the average distance between two neighbor grains, regardless of their nature be equal. Consequently the length scales of the c/e extra-dendritic liquids are equal (see Figure 7):

$$R^*_{1c} - a_c = R^*_{1e} - a_e = \delta_l \tag{57}$$

In the frame of the cell model approximation to the ensemble average, equation (4), the first two constraints, equations (55) and (56) can be rewritten as follows:

$$n_c \frac{4}{3}\pi R^{*3}_{1c} + n_e \frac{4}{3}\pi R^{*3}_{1e} = 1 \tag{58}$$

and

$$n_{c/e} \frac{4}{3}\pi R^{*3}_{1c/e} \geq n_{c/e} \frac{4}{3}\pi a^3_{c/e} \quad \Leftrightarrow \quad R^*_{1c/e} \geq a_{c/e} \tag{59}$$

respectively. Now from (57) and (58) one can easily compute the two characteristic lengths $R^*_{1c/e}$ and therefore $\varepsilon_{c/e}$. Indeed equation (58) can be rewritten as the sum of the c/e grain and c/e extra-dendritic liquid fractions,

$$n_c \frac{4}{3}\pi \left(R^{*3}_{1c} - a^3_c \right) + n_e \frac{4}{3}\pi \left(R^{*3}_{1e} - a^3_e \right) = 1 - \varepsilon_{gc} - \varepsilon_{ge} \tag{60}$$

Furthermore, using (57), the above equation can be rewritten as a third degree function of δ_l:

$$\frac{4}{3}\pi n_c \delta_l \left[\left(\delta_l^2 + 3a_c\delta_l + 3a_c^2 \right) + \frac{n_e}{n_c}\left(\delta_l^2 + 3a_e\delta_l + 3a_e^2 \right) \right] = 1 - \varepsilon_{gc} - \varepsilon_{ge} \tag{61}$$

where $a_{c/e} = \left(\frac{4}{3}\pi n_{c/e} \right)^{-1/3} \varepsilon^{1/3}_{gc/e}$.

Solving the above third order equation and retaining the positive real root only, one finally obtains:

$$R^*_{1c/e} = a_{c/e} + \delta_l$$
$$\varepsilon_{c/e} = n_{c/e}\frac{4}{3}\pi {R^*_{1c/e}}^3 \tag{62}$$

Equations (62) where δ_l is computed from (61) form a complete model describing the coexistence state between two different grain populations, in occurrence here between the columnar and equiaxed structures. Obviously this model verifies implicitly the three conditions in (55), (56) and (57) respectively.

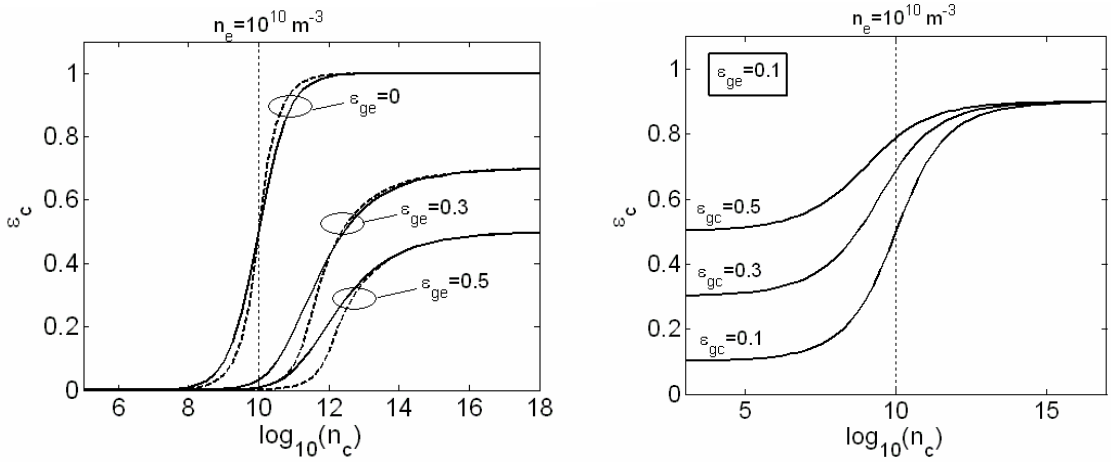

Figure 8: a) the columnar fraction for three different equiaxed fractions: full line, the new model in equation (62); dashed line, the model in equation (51). b) the columnar fraction for three different columnar fractions.

A comparison with the model developed in reference [1], equation (51), is presented in Figure 8a where the columnar fraction, ε_c is plotted against n_c for a given $n_e = 1e10\,m^{-3}$ and three different equiaxed grain fractions ($\varepsilon_{ge} = 0;\ 0.3;\ 0.5$). One can observe the good agreement between the two models. This was somewhat expected since the model in equation (51) verified too the condition (57). In Figure 8b the columnar fraction ε_c computed with the new model in equation (62) is plotted against a variable n_c for a given $n_e = 10^{10}\ m^3$, $\varepsilon_{ge} = 0.1$ and three different columnar fractions $\varepsilon_{gc} = 0.1,\ 0.3,\ 0.5$.

It is important to notice that in the frame of this new model, no special condition need to be imposed in order to commute from a pure e/c zone to a mixed c+e one. Indeed, the nucleation of one structure into another is intrinsically taken into account by the model by means of equations (37) and (38). Hence, by knowing at **x** the c/e grain densites $n_{c/e}$ as well as their grain fractions $\varepsilon_{gc/e}$ one is able to separate the columnar and equiaxed average effects at **x** by means of the two c/e cells of radius $R^*_{1c/e}$ (Figure 1). In turn $R^*_{1c/e}$ can be

locally computed at any moment with respect to $n_{c/e}$ and $\varepsilon_{gc/e}$ respectively with the help of equations (61) and (62).

4.2 The mass balance

Similar with the approach in reference [1], by particularizing the generic average equation (2) with $\psi = 1$ and X_k with X_{se} and X_{sc} respectively one can easily obtain the c/e solid mass balance:

$$\frac{\partial(\rho_s \varepsilon_{sk})}{\partial t} + div(\rho_s \varepsilon_{sk} \mathbf{v}_{sk}) = \Gamma_{sk} \quad , \qquad k = \{c, e\} \tag{63}$$

where $\mathbf{v}_{sk}$ is the average c/e solid velocity. Since the columnar phase is supposed to be stationary one has $\mathbf{v}_{sc} = 0$. Γ_{sk} are the mass exchange rates between the c/e solid and the liquid ($\Gamma_{sk} > 0$ and $\Gamma_{sk} < 0$ means respectively solidification and fusion at $\mathbf{x}$). Γ_{sk} represents an interfacial averaged variable and can be expressed analytically using the cell model approximation similarly with the approach used in [1]. Note again that in view of the ensemble average the two interfacial averages Γ_{sk} can be computed as relative simple integrations over the position of the c/e grain in the c/e cell such as the point **x** is on the c/e solid interface. As detailed in reference [1] one can rewrite Γ_{sk} as follows:

$$\Gamma_{sk} = \rho_s S_{sk} \overline{w}_{sk} \quad , \qquad k = \{c, e\} \tag{64}$$

where S_{sk} and $\overline{w}_{sk}$ are the c/e solid-liquid interfacial area and the mean solid-liquid interface velocity respectively. Both S_{sk} and $\overline{w}_{sk}$ are parameters extremely difficult to model due to the complex solid-liquid interface. As we will see, using the separation between the inter- and the extra-dendritic liquid, one is able to approach analytically the two solidification rates Γ_{sk} form the solute balance in the inter-dendritic liquid.

It is important to notice that form the point of view of the fluid momentum balance, the use of the six phase approach requiring four momentum balance equations would be extremely complex and not practical since the numerical solving of four non-linear equations would also be extremely time consuming. In this respect a simple approach would be of great interest. In the following we will use a single fluid approach meaning that a single fluid momentum balance will be resolved and this for the total fluid phase (*f* phase $= de + dc + le + lc$). The arguments supporting this choice are further detailed in the next two subsections. Hence using now $\psi = 1$ and $X_k = X_f$ in (2) one easily obtains the mass balance of the total fluid phase:

$$\frac{\partial(\rho_f \varepsilon_f)}{\partial t} + div(\rho_f \varepsilon_f \mathbf{v}_f) = -\Gamma_{sc} - \Gamma_{se} \tag{65}$$

where $\mathbf{v}_f$ is the averaged fluid velocity and $\Gamma_{sc/e}$ the c/e solidification rate identified above. By solving the three mass balances in (63) and (65) together with the corresponding momentum balances one obtains the exact evolution of the ε_{sc}, ε_{se}, ε_f fractions. However

as pointed out, one also need to quantify the inter-dendritic spacing as well. Hence a mass balance for the c/e inter-dendritic liquid must be considered too. Using this time, $\psi = 1$ and $X_k = X_{dc/e}$ in (2) one easily obtains

$$\frac{\partial\left(\rho_f \varepsilon_{dk}\right)}{\partial t} + div\left(\rho_f \varepsilon_{dk} \mathbf{v}_{dk}\right) = \Gamma_{dk} \ , \qquad k = \{c, e\} \tag{66}$$

where $\mathbf{v}_{dk}$ is the averaged inter-dendritic velocity and Γ_{dk} the mass exchange rate between the inter-dendritc liquid, the solid and the extra-dendritic liquid. Indeed, the inter-dendritic liquid interacts with two phases in the same time, the solid and the extra-dendritic liquid. This comes from the particular choice of the grain boundary which envelops the dendrite tips and has no finite interface with the solid (Wang and Beckermann [9]). As detailed in reference [1] one can rewrite Γ_{dk} as follows:

$$\Gamma_{dk} = -\Gamma_{sk} + \Gamma_{gk} \ ; \qquad \Gamma_{gk} = \rho_f S_{gk} \overline{w}_{gk} \ , \qquad k = \{c, e\} \tag{67}$$

where Γ_{gk} is the mass exchange between *dk* and *lk* phase due to grain growth, $S_{gk} = n_k\left(4\pi a_k^{\,2}\right)$ represents the grain interfacial area and $\overline{w}_{gk}$ is the mean velocity of the grain envelope, computed from (17). An important question remains however: how to model the c/e inter-dendritic velocities, $\mathbf{v}_{dk}$. One would be tented to use for $\mathbf{v}_{dk}$ the mean velocity characterizing the inter-dendritic flow. This would not be physically sound since the inter-dendritic void is not advected by the inter-dendritic flow but on the contrary by the solid "flow" (movement). Indeed, the inter-dendritic spacing is intrinsically linked to the solid matrix since it quantifies the amount of fluid captured between the secondary and tertiary solid arms. In this respect it is evident that the inter-dendritic phase is advected by the solid flow and not the inter-dendritic fluid flow. One has therefore:

$$\mathbf{v}_{dk} = \mathbf{v}_{sk} \tag{68}$$

This approach is opposite to the one used by Wang and Beckermann model [13]. Indeed, the later consider that $\mathbf{v}_{dk}$ is equal to the average inter-dendritic liquid velocity. We believe that, for the reasons enounced above, this approach is physically unsound and do not reflect the fact that the *dk* phase is moving with the same velocity as the solid (*sk* phase). The most evident counterexample to the approach used in [13] is the case of a columnar mushy zone within which the fluid velocity is non zero. This case is frequently encountered during directional solidifications process where the fluid flow in the bulk liquid determine, through the pressure distribution at the columnar macro-front, the existence of a non-negligible creeping flow within the mushy zone. Following the Wang and Beckermann approach [13], since $\mathbf{v}_{dk}$ will be non-zero the inter-dendritic spacing (ε_{dc}) will be advected with the non zero fluid flow within the mushy zone. This is obviously untrue since the columnar solid and consequently the inter-dendritic voids are stationary.

4.3 The momentum balance

As pointed out before in order to simplify the overall formulation of the model we will consider in the following only the solid and the total fluid momentum balance equations. Using in equation (2) $\psi = \mathbf{v}$ and $X_k = X_{sc},\ X_{se},\ X_f$ one finally obtains after some tedious manipulations [27] the general averaged momentum balance equation for the columnar solid, equiaxed solid and the total fluid respectively:

$$\begin{aligned}\frac{\partial\left(\varepsilon_k\rho_k\mathbf{v}_k\right)}{\partial t}+\nabla\left(\varepsilon_k\rho_k\mathbf{v}_k\mathbf{v}_k\right)=-\varepsilon_k\nabla p_k+\nabla\cdot\varepsilon_k\left(\tau_k+\tau_k^{'}\right)+\varepsilon_k\rho_k\, b^{v}{}_k+\\ +\left(p_{k,i}-p_k\right)\nabla\varepsilon_k+\Gamma_k\mathbf{v}_{k,i}+\mathbf{M}_k\ ,\qquad k=\{sc,se,f\}\end{aligned} \tag{69}$$

Neglecting the surface tension effects the jump equation becomes:

$$\sum_{k=s,f}\left(\Gamma_k\mathbf{v}_{k,i}+p_{k,i}\nabla\varepsilon_k+\mathbf{M}_k\right)=0 \tag{70}$$

where $\mathbf{v}_k$ is the average velocity, τ_k the average stress, $\tau_k^{'}$ the fluctuating average stress, $\Gamma_k\mathbf{v}_{k,i}$ is no more than the momentum exchange rate due to the mass transfer between the two phases ($\overline{\Gamma^{v}}_k$ in equation (2)), $\mathbf{v}_{k,i}$ is the interfacial velocity of the *k* th phase [27], $p_{k,i}$ is the interfacial pressure of the phase *k* and finally $\mathbf{M}_k$ is no more than the interfacial force density $\Phi^{v}{}_k$ in equation (2) from which the effect of the average interfacial pressure was substracted.

As one can easily observe the balance equations in (69) are not closed. One would have to propose closure expression for: τ_k, $\tau_k^{'}$, $\mathbf{v}_{k,i}$, $p_{k,i}$ and $\mathbf{M}_k$ with respect to average variables like $\mathbf{v}_k$, p_k, interfacial areas, etc. It is important to notice that since the columnar solid phase is stationary ($v_{sc}=0$) one does not need to further consider a momentum equation for the columnar solid phase. In fact, solving the columnar solid momentum equation would only reflect the pressure modification inside the columnar solid with respect to the stress imposed by the interfacial drag at the *sc-f* interface.

4.3.1 Interfacial pressure

It is usually assumed [2, 27] that the k^{th} phase pressure p_k, does not differ much from its value on the interface, $p_{k,i}$, thus having $p_k = p_{k,i}$. As Drew pointed out [27] this supposes that there is instantaneous pressure equilibration within the k^{th} phase, which is the case since the speed of sound in each phase is large compared with the local velocities. Moreover neglecting the effect of surface tensions one has as well $p_{s,i} = p_{f,i}$. Using the pressure equilibrium hypothesis above, one finally obtains that:

$$p_s = p_f = p \tag{71}$$

meaning that locally the fluid and the solid share the same pressure.

4.3.2 The interfacial velocity $\mathbf{v}_{k,i}$

The momentum exchange due to phase change can be modeled by introducing an interfacial velocity $\mathbf{v}_{k,i}$ such as $\Gamma^{\mathbf{v}}{}_k$ (equation (2)) equals $\Gamma_k \mathbf{v}_{k,i}$ [27]. Furthermore Ishii [28] showed that the difference $\mathbf{v}_{s,i} - \mathbf{v}_{f,i}$ is proportional with the density difference between the solid and the liquid phase, $\Delta\rho$, and the mass transfer rate Γ_k. For solidification problems, the density difference $\Delta\rho$ is relative small compared, for example, to a liquid-gas two phase flow. Hence, excepting the very rapid solidification processes, the interfacial velocities in the liquid and the solid become equal. Furthermore, for rigid and non rotating particles one has as well $\mathbf{v}_{s,i} = \mathbf{v}_s$. Therefore one finally obtains:

$$\Gamma^{\mathbf{v}}{}_{sc} = 0 \; ; \qquad \Gamma^{\mathbf{v}}{}_{se} = \Gamma_{se}\mathbf{v}_{se} \; ; \qquad \Gamma^{\mathbf{v}}{}_{f} = -\Gamma_{se}\mathbf{v}_{se} \tag{72}$$

4.3.3 The Reynolds stress $\tau_k^{'}$

In a two phase flow there are inherent velocity fluctuations about the mean value $\overline{\mathbf{v}}$. These are due on one hand to the turbulent regime of the liquid flow and on the other hand due to the complex solid-liquid interface morphology. Indeed, the flow around a complex solid-liquid interface will generate spatial fluctuation of $\mathbf{v}$ [2]. These fluctuations coupled with the non-linear character of the advection term in (2) generate a double correlation term which has a similar form with the molecular flux $div\left[\varepsilon_k \overline{\mathbf{j}^{\psi}}_k\right]$. This term is usually called the Reynolds stress and it is customary to add it to the real molecular flux. Traditionally, the Reynolds stress is modeled by means of a turbulent diffusivity which adds to the real molecular diffusivity (viscosity, thermal or mass diffusivity). The inherent velocity fluctuations produced by the complex solid morphology transports momentum in a similar way as the turbulent "eddies" does in turbulent single phase flow. However, since we supposed a laminar flow, one should focus in the following on the velocity fluctuations produced by the complex solid morphology only. Using the cell model approximation to the ensemble average [1] the fluid Reynolds stress can be approached analytically as follows:

$$\begin{aligned} \tau_f^{'} &= -\frac{\overline{X_f \rho \mathbf{v}' \mathbf{v}'}}{\varepsilon_f} \\ &= \frac{1}{\varepsilon_f}\left[n_c \int\limits_{\left|\mathbf{x}-\tilde{\mathbf{z}}_1\right| \le R_{1c}^*} X_f \rho \mathbf{v}' \mathbf{v}' d\tilde{\mathbf{z}}_1 + n_e \int\limits_{\left|\mathbf{x}-\tilde{\mathbf{z}}_1\right| \le R_{1e}^*} X_f \rho \mathbf{v}' \mathbf{v}' d\tilde{\mathbf{z}}_1 \right] \end{aligned} \tag{73}$$

Using now the exact fluid field around the permeable c/e dendrite grain as explained in paragraph 3.1.1, the Reynolds stress can be analytically resolved using the above equation. The result would be however extremely complex. The fact that given a fluid flow model at the grain level one can approach analytically the Reynolds stress using the cell model is however of great interest. For example, by assuming an inviscid flow over a swarm of solid spheres Drew [2] proposed, using the cell model, an expression for the fluid Reynolds stress $\tau_f^{'}$:

$$\tau_f^{'} = -\frac{1}{20\varepsilon_f}\varepsilon_s\rho_f\left[\left(\mathbf{v}_f-\mathbf{v}_s\right)\left(\mathbf{v}_f-\mathbf{v}_s\right)+3\left(\mathbf{v}_f-\mathbf{v}_s\right)\left(\mathbf{v}_f-\mathbf{v}_s\right)\mathbf{I}\right] \tag{74}$$

Note however that the models for $\tau_k^{'}$ are quite complex. This was somewhat expected since the main role for $\tau_k^{'}$ is to recover the relevant information regarding the fluid flow at the micro-scale, lost with the averaging process. The Reynolds stress should be therefore representative for the complex solid morphology of the two phase flow.
In the following we will however neglect the dispersive flux. The arguments for this hypothesis are:

- at small grain fractions (i.e. close to the columnar dendrite tips) the Reynolds stresses is negligible with respect to the advection terms since the influence of the small particles on the fluid flow remains negligible;
- on the other hand, for grain fractions larger than $0.4-0.5$ (i.e. developed equiaxed zone or profound columnar zone) the fluid flow becomes heavily perturbed by the solid particles and the velocity fluctuations becomes important too. Moreover since we have chosen a single fluid formulation (inter- + extra-dendritic liquid) the velocity fluctuations will further be amplified. Indeed, due to the low inter-dendritic permeability to fluid, the inter-dendritic velocity will be usually much lower that the velocity characterizing the extra-dendritic liquid. Hence, the velocity fluctuations around the mean $\overline{\mathbf{v}}_f$ will be important and will in the end reflect a non-negligible Reynolds stress with respect to the non-linear advection term. In fact this is one of the main disadvantages of the unique fluid formulation with respect to a separate description of inter- and extra-dendritic liquid. The Reynolds stress / advection term ratio corresponding to the separate momentum balance in the inter- and extra-dendritic liquid will be much smaller than the same ratio corresponding to the single fluid flow formulation. However, one should also take into account the fact that for relative high grain fractions $\varepsilon_g > 0.4-0.5$ the bed permeability is sufficiently low as the fluid flow to be close to a creeping flow state characterized by very small velocities. Hence, the non-linear advection term in equation (69) and the Reynolds stress become negligible in front of the interfacial stress $\mathbf{M}_k$ and the pressure gradient. In this respect, excepting a small range in the grain fraction $\varepsilon_g = 0.1-0.4$, the Reynolds stress can be negliged since either it is too small in front of the advection term (for small ε_g), either it is negligible compared with the preponderant terms: $\mathbf{M}_k$ and the pressure gradient (for average-high ε_g).
- for typical grain densities $n_{c/e} = 10^6 - 10^9\, m^{-3}$ and cooling rates the grain growth can be very rapid from small values (< 0.1) to relative high ones ($\varepsilon_g > 0.4-0.5$) due to small solutal interactions between the grains [24]. In this respect it is expected that the Reynolds stress to have a negligible influence even at average grain fractions.

All these findings entitles us to neglect the term $\tau_k^{'}$ in the momentum balance equation (69). Notice that Wang and Beckermann [13] proposed a model which takes into account the scale separation between the inter- and the extra-dendritic liquid. By summing the separate momentum balances in the inter- and extra-dendritic liquid Wang and Beckermann [13] obtained the total fluid balance equation. Supposing further a creeping flow across the dendrite bed, the authors managed to obtain a model for the dispersion flux

associated to the differences between the inter- and the extra-dendritic liquid velocities. However, it is important to notice that by assuming creeping flow across the bed, the convective terms and the Reynolds stresses are negligible small with respect to the pressure gradient and interfacial stress. Therefore the development of a Reynolds stress model having at the base the hypothesis of a creeping flow would not be entirely justified physically.

4.3.4 The average viscous stress τ_k

Having as guiding principle "the principle of frame indifference" Drew [2] proposed a general constitutive equation for the average stress τ_k. The principle of frame indifference states that [2] the constitutive equations are invariant under a change of the reference frame since the way in which a two-phase flow distributes forces must be independent of the coordinate system used to express it. Drew [2] identified a list of tensors that are objective regarding the change of coordinate system:

$$\begin{aligned}
&\mathbf{v}_{ki} = \mathbf{v}_k - \mathbf{v}_i \\
&\mathbf{D}_k = \frac{1}{2}\left(\nabla\mathbf{v}_k + \left(\nabla\mathbf{v}_k\right)^{\mathrm{T}}\right) \\
&\mathbf{a}_{ki} = \left(\frac{\partial\mathbf{v}_k}{\partial t} + \mathbf{v}_i\cdot\nabla\mathbf{v}_k\right) - \left(\frac{\partial\mathbf{v}_i}{\partial t} + \mathbf{v}_k\cdot\nabla\mathbf{v}_i\right)
\end{aligned} \tag{75}$$

In this respect one should look for constitutive relations for τ_k on the form [2]:

$$\begin{aligned}
\tau_k = {} & \mu_{kk}\mathbf{D}_k + \mu_{ki}\mathbf{D}_i + E_{k11}\mathbf{v}_{ki}\mathbf{v}_{ki} + E_{k12}\left(\mathbf{v}_{ki}\nabla\varepsilon_k + \nabla\varepsilon_k\mathbf{v}_{ki}\right) \\
& + E_{k13}\left(\mathbf{v}_{ki}\mathbf{a}_{ki} + \mathbf{a}_{ki}\mathbf{v}_{ki}\right)
\end{aligned} \tag{76}$$

where μ_{kk}, μ_{kk}, E_{k11}, E_{k12}, E_{k13} are coefficients to be determined. As one can see a precise closure equation for the average stress would be extremely complex. Drew [2] assumed that in the low velocity regime, when the inertia term are negligible small, one should retain in equation (76) only the linear terms in the velocity obtaining thus:

$$\tau_k = \mu_{kk}\mathbf{D}_k + \mu_{ki}\mathbf{D}_i + E_{k12}\left(\mathbf{v}_{ki}\nabla\varepsilon_k + \nabla\varepsilon_k\mathbf{v}_{ki}\right) \tag{77}$$

It is important to notice that the above constitutive equation has a similar formulation with the result of Ishi [28] or Ni and Beckermann [29]. In the following we will neglect the higher order terms in (77) by assuming that μ_{ki} and E_{k12} are negligible small in front of μ_{kk}. We obtain therefore:

$$\tau_k = \mu_{kk}\frac{1}{2}\left(\nabla\mathbf{v}_k + \left(\nabla\mathbf{v}_k\right)^{\mathrm{T}}\right) \tag{78}$$

For the fluid phase it is customary to consider $\mu_{ff} = 2\mu_f$. In contrast for the solid phase, if the collision between particles is not important then $\mu_{ss} = \beta\mu_f$ where $\beta > 1$ since the solid particles are expected to concentrate the fluid shear stress [2]. In fact their presence results in a larger effective viscosity of the solid-liquid mixture. Indeed, for dilute suspension of

solid particles ($\varepsilon_g \ll 1$) one has the well known Einstein law where $\beta = 7/2$. In contrast, for compacted bed of particles ($\varepsilon_g > 0.65$) the solid phase become a rigid structure and $\mu_{ss} \to \infty$. For the present model we will use the same approach for μ_{ss} as Wang and Beckermann did [13], that is:

$$\mu_{ss} = 2\frac{\mu_f}{\varepsilon_g}\left[\left(1-\frac{\varepsilon_g}{\varepsilon_g^0}\right)^{-2.5\varepsilon_g^0} - \left(1-\varepsilon_g\right)\right] \tag{79}$$

where $\varepsilon_g^0 = 0.637$ and ε_g is the grain fraction of the analyzed solid phase (equiaxed in our case). The above law was proposed initially by Krieger [30] and has the advantage that for $\varepsilon_g \to 0$, $\mu_{ss} = 3.5\mu_f$ and for $\varepsilon_g \to \varepsilon_g^0$, $\mu_{ss} \to \infty$. Note however that, applied to a case where columnar and equiaxed particles coexists, the equiaxed grain fraction in equation (79) should be scaled to the maximum available space for the equiaxed phase, that is ε_e. Indeed, since the equiaxed phase occupy only a fraction of the space at **x** (ε_e) one should consider for the ε_g in (79) not the absolute equiaxed grain fraction ε_{ge} but the internal equiaxed grain fraction:

$$\varepsilon_g \left(= \varepsilon_{gi}\right) = \varepsilon_{ge} / \varepsilon_e \tag{80}$$

since the available space for the equiaxed grains is $\varepsilon_e < 1$ and not 1.

If the transport of particle momentum is dominated by the particle collision the solid viscosity can be related to the particle fluctuating kinetic energy u_s^{Re} [2]. This is somewhat similar with the kinetic theory of gases where the molecular viscosity is related to the mean kinetic energy. Note however that for the case of equiaxed solidification the collisional effect on the momentum transport is not of great importance since the collisions between dendritic particles is far from being elastic (or near elastic). In turn one should expect that phenomena like dendrite breakup or particle aggregation to have a significant effect on the momentum transport.

4.3.5 The interfacial momentum transfer $\mathbf{M}_k$

As pointed in [2] the interfacial momentum transfer $\mathbf{M}_k$ contains the forces on the solid phase due to viscous drag, wake and boundary layer formation, and unbalanced pressure distributions leading to lift or virtual mass effects. For simplicity reasons we will retain hereafter only the contribution of the drag force. In this respect the interfacial force momentum transfer $\mathbf{M}_f$ will a sum of the drag force of the fluid flow on the columnar and equiaxed particles respectively. Note that the fluid flow around a c/e particle and the drag force on the c/e particle are known from the micro-scale assumptions (paragraph 3.1.1). Hence one obtains for $\mathbf{M}_f$:

$$\begin{aligned}\mathbf{M}_f &= \mathbf{M}_{fe} + \mathbf{M}_{fc} \\ &= n_e 6\pi\mu_f a_e \Omega_e \left(\mathbf{v}_{se} - \varepsilon_{fe}\mathbf{v}_{fe}\right) + n_c 6\pi\mu_f a_c \Omega_c \left(-\varepsilon_{fc}\mathbf{v}_{fc}\right)\end{aligned} \tag{81}$$

where $\Omega_{c/e}$ were defined in (11), $\mathbf{v}_{fc}$ and $\mathbf{v}_{fe}$ are the columnar and equiaxed fluid velocities respectively and finally $\varepsilon_{fc/e}$ are the c/e fluid fractions ($=\varepsilon_{dc/e}+\varepsilon_{lc/e}$). Note however that the above equation is defined with respect to the c/e fluid velocities. These two velocities are not known a priori since we have chosen a single fluid approach and only the total fluid velocity, $\mathbf{v}_f$ is known. One could however quantify the c/e fluid velocities if one assumes creeping flow across the mixed c/e zone. Indeed, in the low velocity range the average momentum balance equations within the c/e liquid become:

$$\begin{aligned} -\varepsilon_{fc}\nabla p + n_c 6\pi\mu_f a_c \Omega_c \left(-\varepsilon_{fc}\mathbf{v}_{fc}\right) = 0 \\ \text{and} \\ -\varepsilon_{fe}\nabla p + n_e 6\pi\mu_f a_e \Omega_e \left(\mathbf{v}_{se} - \varepsilon_{fe}\mathbf{v}_{fe}\right) = 0 \end{aligned} \tag{82}$$

The above equations represent no more than the Darcy approximation to the momentum balance. Using equations (82) and knowing that $\varepsilon_f \mathbf{v}_f = \varepsilon_{fc}\mathbf{v}_{fc} + \varepsilon_{fe}\mathbf{v}_{fe}$ one can easily obtain:

$$\mathbf{v}_{fc} = \frac{\varepsilon_f \varepsilon_{fe}\mathbf{v}_f K_c + \varepsilon_{fc}\mathbf{v}_{se}K_e}{\varepsilon_{fe}\left(\varepsilon_{fe}K_c + \varepsilon_{fc}K_e\right)} \tag{83}$$

and

$$\mathbf{v}_{fc} = \frac{K_e\left(\varepsilon_f \mathbf{v}_f - \mathbf{v}_{se}\right)}{\varepsilon_{fe}K_c + \varepsilon_{fc}K_e} \tag{84}$$

where $K_c = n_c 6\pi\mu_f a_c \Omega_c$ and $K_e = n_e 6\pi\mu_f a_e \Omega_e$. Finally the interfacial momentum transfer $\mathbf{M}_f$ becomes:

$$\mathbf{M}_f = \frac{K_c K_e \varepsilon_f \left(\mathbf{v}_{se} - \varepsilon_f \mathbf{v}_f\right)}{\varepsilon_{fe}K_c + \varepsilon_{fc}K_e} \tag{85}$$

As well, the interfacial momentum transfer $\mathbf{M}_{se}$ corresponding to the equiaxed solid becomes:

$$\begin{aligned} \mathbf{M}_{se} &= -\mathbf{M}_{fe} \\ &= -\frac{K_c K_e \varepsilon_{fe}\left(\mathbf{v}_{se} - \varepsilon_f \mathbf{v}_f\right)}{\varepsilon_{fe}K_c + \varepsilon_{fc}K_e} \end{aligned} \tag{86}$$

4.4 The energy equation

Similar to the approach used in reference [1] and given the local thermal equilibrium, the energy balance can be approached with a unique mixture equation. Since the density and the thermal conductivities are common to both equiaxed/columnar liquid and solid phases, the energy balance equation is identical with the one obtained in [1] in which the advection term has to be added. One can easily obtain:

$$\frac{\partial\left[\left(\varepsilon_s\rho_s c_s+\varepsilon_f\rho_f c_f\right)T\right]}{\partial t}+div\left[\varepsilon_{se}\rho_s c_s\mathbf{v}_{se}+\varepsilon_f\rho_f c_f\mathbf{v}_f\right]= \\ =div\left[\left(\varepsilon_s\lambda_s+\varepsilon_f\lambda_f\right)\nabla T\right]+\Gamma_s L \tag{87}$$

where $\varepsilon_s=\varepsilon_{se}+\varepsilon_{sc}$ and $\Gamma_s=\Gamma_{se}+\Gamma_{sc}$.

4.5 The solute balance equations

Using $\psi=C$, $\mathbf{j}_k^C=\rho D\nabla C$ and $X_k=X_{sc},\ X_{se},\ X_f,\ X_{dc},\ X_{de}$ in (2) one obtains:

$$\frac{\partial\left(\varepsilon_k\rho_k C_k\right)}{\partial t}+div\left(\varepsilon_k\rho_k\mathbf{v}_k C_k\right)=div\left[\varepsilon_k\left(\overline{\mathbf{j}^C}_k+\overline{\mathbf{j}'^C}_k\right)\right] \\ +\overline{\mathbf{\Phi}^C}_k+\overline{\Gamma^C}_k\ ;\quad k=\{sc,se,f,dc,de\} \tag{88}$$

that is a total of five equations. Notice that the solute balances in the c/e inter-dendritic liquid are explicit ones since the solute concentration $\overline{C}_{dc/e}$ is fixed at the equilibrium concentration C_l^* computed with respect to the local temperature. Notice as well that one can correctly compute the solute balance within a certain phase only if the corresponding velocity verifies the mass balance within that phase. Since we have chosen a single fluid approach for the momentum balance we are somewhat constrained to consider the solute balance equation within the total fluid and not the two solute balance in the c/e fluid phase (*fc*, *fe*). In fact, even if we have approximated the c/e fluid velocities, equation (83) and (84), these does not verify the mass balance within the c/e fluid phase.

4.5.1 The mean flux $\overline{\mathbf{j}^C}_k$

Since the solute concentration fluctuations within the phase k is

$$C_k'=C-\overline{C}_k \tag{89}$$

one can rewrite the average stress as follows:

$$\varepsilon_k\overline{\mathbf{j}^C}_k=\overline{X_k\rho D\nabla C} \\ =\varepsilon_k\rho D\nabla\overline{C}+\underbrace{\overline{\rho D\nabla\left(X_k C_k'\right)}}_{=0}-\underbrace{\overline{\rho D C_k'\nabla X_k}}_{\approx 0} \tag{90}$$

It is easy to see that the second term on the RHS of the above equation is zero. Noting that $\nabla X_k=-\mathbf{n}_k\delta(\mathbf{x}-\mathbf{x}_i)$ where $\delta(\mathbf{x}-\mathbf{x}_i)$ is the Dirac delta function pointing at the interface, the last term in (90) is no more than the interfacial average of the solute concentration fluctuations, averaged on the phase *k* interface. In turn the solute concentration at the solid-liquid interface is uniquely determined by the temperature, $C_l^*=(T-T_f)/m$. Due to the high thermal diffusivity of the liquid metals one expects to have small thermal perturbations at the grain scale. In this respect this last term can be neglected in front of the first term on the RHS of (90). The average flux becomes:

$$\varepsilon_k \overline{\mathbf{j}^C}_k = \varepsilon_k \rho D \nabla \overline{C}_k \tag{91}$$

Notice that the above average flux is similar with results obtained by various authors [13, 29].

4.5.2 Dispersion flux $\overline{\mathbf{j}'^C}_k$

Since the solute concentration inside the inter-dendritic liquid is equal to C_l^* and the temperature fluctuations at the scale of the grain are negligible one can neglect as well the two inter-dendritic dispersive flux: $\overline{\mathbf{j}'^C}_{dc}$ and $\overline{\mathbf{j}'^C}_{dc}$. As well, due to the extremely low solute diffusivity in the solid the two dispersive fluxes characterizing the c/e solid phase can be neglected too.

In contrast, due to the difference between the concentrations in the inter- and extra-dendritic liquid, the dispersion flux $\overline{\mathbf{j}'^C}_f$ characterizing the total fluid phase may not be negligible. In fact this is the main disadvantage of choosing the total fluid approach. In the flowing however we will neglect this term and the arguments supporting this hypothesis are:

- for high grain densities or low cooling rates due to the strong solutal interactions between grains the extra-dendritic liquid reach a state of perfect solutal mixing ($C_{lc/e} \simeq C_l^*$) very rapidly after the beginning of the solidification (see reference [24]). Hence the total fluid concentration C_f will be equal to C_l^* and consequently the solute fluctuations will be negligible small similar to the case of the inter-dendritic liquid.
- in contrast, for low grain densities or average-high cooling rates the solutal interactions between adjacent grains are negligible small and the extra-dendritic liquid remains at its initial concentration C_0 until the grain fraction ε_g becomes close to unity (in the case of c/e coexistence until $\varepsilon_{gc/e}$ becomes close to $\varepsilon_{c/e}$). Only then the solutal interactions between grains become non-negligible and the extra-dendritic liquid enriches in solute to finally approach C_l^*. In this respect the dispersion solute flux $\overline{\mathbf{j}'^C}_k$ cannot be neglected during this transition stage since the differences between the inter-dendritic concentration (C_l^*) and the extra-dendritic one (C_0) are significant. However one should note that the time scale of this transition phase is small due to the rapid grain growth (see reference [24]). Usually this time scale is smaller than the time scale characterizing the convection within the mushy zone. In this respect neglecting the dispersive flux $\overline{\mathbf{j}'^C}_k$ would not change significantly the solute transport at the scale of the ingot.

4.5.3 The interfacial sources $\overline{\Phi^C}_k$ and $\overline{\Gamma^C}_k$

The interfacial sources $\overline{\Phi^C}_k$ and $\overline{\Gamma^C}_k$ remains practically unchanged with the ones already computed in reference [1]. Note however that in [1] the hypothesis of no convection was assumed. Here the fluid flow is accounted. As already pointed out the fluid flow across a permeable bed is influencing the solute mass transfer at the grain boundary. Basically the overall mass transfer coefficient is increased with respect to the pure diffusion case. It was proven in equation (29) that $Sh > Pe_g$ and that:

$$\delta_{cv} < \delta_{diff}\left(=\frac{D_l}{\overline{w}_{ge}}\right) \tag{92}$$

Hence in the terms $\overline{\Phi^C}_k$ and $\overline{\Gamma^C}_k$ obtained in [1] one should only replace the diffusion length δ_{lk-dk} (k=c,e) with the diffusion length valid for the convection case, equation (31). One obtains:

$$\begin{aligned} &\Phi^C_{sk} = 0 && \Gamma^C_{sk} = C^*_s\Gamma_{sk} \\ &\Phi^C_{lk} = \frac{\rho_f S_{gk} D_l}{\delta_{lk-dk}}\left(C^*_l - C_{lk}\right) && \Gamma^C_{lk} = -C^*_l\Gamma_{gk} \end{aligned} \quad , \quad k = \{e,c\} \tag{93}$$

and finally,

$$\begin{aligned} &\Phi^C_{dk} + \Gamma^C_{dk} = C^*_l\Gamma_{gk} - C^*_s\Gamma_{sk} - \frac{\rho_f S_{gk} D_l}{\delta_{lk-dk}}\left(C^*_l - C_{lk}\right) \ , \qquad k = \{e,c\} \\ &\Phi^C_f + \Gamma^C_f = -C^*_s\left(\Gamma_{sc} + \Gamma_{se}\right) \end{aligned} \tag{94}$$

Notice that since $C_{dc/e} = C^*_l$ the solute balance in the c/e inter-dendritic liquid transform into equations for the solidification rate Γ_{se} and Γ_{sc}. Indeed, one has:

$$\begin{aligned} \frac{\partial\left(\varepsilon_{dk}\rho_f C^*_l\right)}{\partial t} + div\left(\varepsilon_{dk}\rho_f \mathbf{v}_{dk} C^*_l\right) &= div\left(\varepsilon_{dk}\rho_f D_f \nabla C^*_l\right) + C^*_l\Gamma_{gk} \\ &- C^*_s\Gamma_{sk} - \frac{\rho_f S_{gk} D_l}{\delta_{lk-dk}}\left(C^*_l - C_{lk}\right); \qquad k = \{c,e\} \end{aligned} \tag{95}$$

Using the mass balance within the inter-dendritic liquid the above equation become further:

$$\begin{aligned} \Gamma_{sk}\left(C^*_l - C^*_s\right) = \varepsilon_{dk}\rho_f \frac{\partial C^*_l}{\partial t} + \frac{\rho_f S_{gk} D_l}{\delta_{lk-dk}}\left(C^*_l - C_{lk}\right) + \\ + \varepsilon_{dk}\rho_f \mathbf{v}_{dk} div\left(C^*_l\right) - div\left(\varepsilon_{dk}\rho_f D_f \nabla C^*_l\right); \qquad k = \{c,e\} \end{aligned} \tag{96}$$

Usually the macroscopic diffusion flux (the last term on the RHS of the above equation) can be neglected in front of the solute flux at grain boundary. Evidence to this hypothesis can be found in [9]. Notice that the inter-dendritic velocity $\mathbf{v}_{dk}$ is not a priori known. Since the inter-dendritic fluid permeability is known, equation (13), one could approach these velocities from the Darcy approximation of the momentum equation written for the inter-dendritic liquid. For simplicity reasons we will approach the inter-dendritic liquid velocity from the c/e fluid velocities $\mathbf{v}_{fc/e}$. We will suppose in the following that the inter- and extra-dendritic liquids share a same mean velocity:

$$\mathbf{v}_{dk}\left(=\mathbf{v}_{lk}\right) = \mathbf{v}_{fk} \tag{97}$$

where $\mathbf{v}_{fk}$ is computed with the help of equations (83) and (84).

As one can see the solute flux at the c/e grain boundary, $\frac{\rho_f S_{gk} D_l}{\delta_{lk-dk}}\left(C_l^* - C_{lk}\right)$, is expressed with respect to the mean concentration C_{lc} and C_{le}. The later ones are not explicitly known. However, as pointed out in [24], due to the equivalence between the length scales characterizing the c/e extra-dendritic liquid ($R_{le}^* - a_e \simeq R_{lc}^* - a_c$) the two liquids will follow a similar solutal evolution during the c/e coexistence. Therefore one expects to have $C_{lc} \simeq C_{le}$. This is a physical sound hypothesis since the two structures finally share the same liquid around the grains. In this respect, one can now easily compute the two concentrations C_{lc} and C_{le} as follows:

$$C_{lc}\left(=C_{le}\right) = \frac{\varepsilon_f C_f - (\varepsilon_{dc} + \varepsilon_{de}) C_l^*}{\varepsilon_f - (\varepsilon_{dc} + \varepsilon_{de})} \tag{98}$$

At this moment the whole system formed by the balance equations is closed.

4.6 Summary of the model

In the following the summary of the model equations is presented.

4.6.1 The grain balance equations

The equiaxed grain balance is:

$$\frac{\partial n_e}{\partial t} + div\left(n_e \mathbf{v}_{se}\right) = n_e^0 \left(1 - \varepsilon_{gc}\right) \delta\left(T - T_{liq} + \Delta T_{ne}\right) \tag{99}$$

where n_e^0 is the equiaxed nucleation density [m^3], ε_{gc} is the columnar grain fraction at the moment of nucleation, T_{liq} is the local liquidus temperature, ΔT_{ne} the equiaxed nucleation undercooling and $\delta\left(T - T_{liq} + \Delta T_{ne}\right)$ the Dirac function pointing to the equiaxed nucleation temperature.

The columnar grain balance is:

$$\frac{\partial n_c}{\partial t} = n_c^0 \left(1 - \varepsilon_{ge}\right) \delta\left[\mathbf{x} - \mathbf{x}_{cf}(t)\right] \tag{100}$$

where n_c^0 is the columnar nucleation density which can be directly related to the primary arm spacing λ_1 by means of equation (40), ε_{ge} is the local equiaxed grain fraction at the moment of nucleation and $\delta\left[\mathbf{x} - \mathbf{x}_{cf}(t)\right]$ is the Dirac function pointing to the columnar front surface, $\mathbf{x}_{cf}(t)$. This in turn can be computed by means of a front tracking algorithm as detailed in paragraph 4.1.1.

4.6.2 The mass balance

The columnar/equiaxed solid mass balance is:

$$\frac{\partial\left(\rho_s\varepsilon_{se}\right)}{\partial t}+div\left(\rho_s\varepsilon_{se}\mathbf{v}_{se}\right)=\Gamma_{se}\ ;\qquad \frac{\partial\left(\rho_s\varepsilon_{sc}\right)}{\partial t}=\Gamma_{sc} \tag{101}$$

where $\mathbf{v}_{se}$ is the average velocity of the equiaxed solid and Γ_{se} and Γ_{sc} the equiaxed an columnar mass transfer rates respectively. The latter ones will be computed from the solute balance in the e/c inter-dendritic liquid.

The fluid mass balance is:

$$\frac{\partial\left(\rho_f\varepsilon_f\right)}{\partial t}+div\left(\rho_f\varepsilon_f\mathbf{v}_f\right)=-\Gamma_{se}-\Gamma_{sc} \tag{102}$$

where $\mathbf{v}_f$ is the average fluid velocity.

The inter-dendritic mass balance is:

$$\frac{\partial\left(\rho_f\varepsilon_{de}\right)}{\partial t}+div\left(\rho_f\varepsilon_{de}\mathbf{v}_{se}\right)=-\Gamma_{se}+\Gamma_{ge}\ ;\qquad \frac{\partial\left(\rho_f\varepsilon_{dc}\right)}{\partial t}=-\Gamma_{sc}+\Gamma_{gc} \tag{103}$$

where $\mathbf{v}_{se}$ is the average velocity of the equiaxed solid, and Γ_{gk} is the mass exchange between *dk* and *lk* phase due to grain growth:

$$\Gamma_{gk}=\rho_f S_{gk}\overline{w}_{gk}\ ;\qquad k=\{c,e\} \tag{104}$$

where $S_{gk}=n_k\left(4\pi a_k^{\,2}\right)$ represents the grain interfacial area and $\overline{w}_{gk}$ is the mean velocity of the grain envelope, computed from (17).

4.6.3 Momentum balance

The fluid momentum balance is:

$$\begin{aligned}\frac{\partial\left(\varepsilon_f\rho_f\mathbf{v}_f\right)}{\partial t}+\nabla\left(\varepsilon_f\rho_f\mathbf{v}_f\mathbf{v}_f\right)=&-\varepsilon_f\nabla p+\nabla\left[\varepsilon_f\mu_f\left(\nabla\mathbf{v}_f+\left(\nabla\mathbf{v}_f\right)^{\mathrm{T}}\right)\right]\\&+\varepsilon_f\rho_f\,\mathbf{g}-\Gamma_{se}\mathbf{v}_{se}+K_f\left(\mathbf{v}_{se}-\varepsilon_f\mathbf{v}_f\right)\end{aligned} \tag{105}$$

where

$$K_f=\frac{K_cK_e\varepsilon_f}{\varepsilon_{fe}K_c+\varepsilon_{fc}K_e} \tag{106}$$

is the momentum transfer coefficient at the phase *f* interface and $K_{c/e}=n_{c/e}6\pi\mu_f a_{c/e}\Omega_{c/e}$ where $\Omega_{c/e}$ is computed by means of equation (11). The coefficient K_f is no more than a measure of the drag force acting at the c/e solid interface and can be expressed as well as an inverse of an overall permeability to fluid.

The equiaxed solid momentum balance is:

$$\frac{\partial\left(\varepsilon_s\rho_s\mathbf{v}_{se}\right)}{\partial t}+\nabla\left(\varepsilon_s\rho_s\mathbf{v}_{se}\mathbf{v}_{se}\right)=-\varepsilon_s\nabla p+\nabla\left[\varepsilon_s\mu_s\left(\nabla\mathbf{v}_{se}+\left(\nabla\mathbf{v}_{se}\right)^{\mathrm{T}}\right)\right]$$
$$+\varepsilon_s\rho_s\,\mathbf{g}+\Gamma_{se}\mathbf{v}_{se}-K_{se}\left(\mathbf{v}_{se}-\varepsilon_f\mathbf{v}_f\right) \tag{107}$$

where

$$K_{se}=\frac{K_cK_e\varepsilon_{fe}}{\varepsilon_{fe}K_c+\varepsilon_{fc}K_e} \tag{108}$$

and μ_s is the equivalent solid viscosity:

$$\mu_s=\frac{\mu_f}{\varepsilon_{ge}^i}\left[\left(1-\frac{\varepsilon_{ge}^i}{\varepsilon_g^0}\right)^{-2.5\varepsilon_g^0}-\left(1-\varepsilon_{ge}^i\right)\right];\qquad \varepsilon_{ge}^i=\frac{\varepsilon_{ge}}{\varepsilon_e} \tag{109}$$

4.6.4 The energy balance

The energy balance equation is:

$$\frac{\partial\left[\left(\varepsilon_s\rho_sc_s+\varepsilon_f\rho_fc_f\right)T\right]}{\partial t}+div\left[\varepsilon_{se}\rho_sc_s\mathbf{v}_{se}+\varepsilon_f\rho_fc_f\mathbf{v}_f\right]=$$
$$=div\left[\left(\varepsilon_s\lambda_s+\varepsilon_f\lambda_f\right)\nabla T\right]+\Gamma_sL \tag{110}$$

where c_s and c_f are the solid and liquid mass specific heats, L the latent heat, and $\Gamma_s=\Gamma_{se}+\Gamma_{sc}$.

4.6.5 The solute balance

The solute balance in the columnar/equiaxed solid is:

$$\frac{\partial\left(\varepsilon_{se}\rho_sC_{se}\right)}{\partial t}+div\left(\varepsilon_{se}\rho_s\mathbf{v}_{se}C_{se}\right)=div\left(\varepsilon_{se}\rho_sD_s\nabla C_{se}\right)+C_s^*\Gamma_{se}$$
$$\text{and} \tag{111}$$
$$\frac{\partial\left(\varepsilon_{sc}\rho_sC_{sc}\right)}{\partial t}=div\left(\varepsilon_{sc}\rho_sD_s\nabla C_{sc}\right)+C_s^*\Gamma_{sc}$$

The solute balance in the total fluid is:

$$\frac{\partial\left(\varepsilon_f\rho_fC_f\right)}{\partial t}+div\left(\varepsilon_f\rho_f\mathbf{v}_fC_f\right)=div\left(\varepsilon_f\rho_fD_f\nabla C_f\right)-C_s^*\left(\Gamma_{se}+\Gamma_{sc}\right) \tag{112}$$

4.6.6 Supplementary equations

The e/c solid mass transfer rates Γ_{se} and Γ_{sc} are computed from the solute balance equations in the inter-dendritic liquid:

$$\Gamma_{sk}\left(C_l^*-C_s^*\right)=\varepsilon_{dk}\rho_f\frac{\partial C_l^*}{\partial t}+\frac{\rho_f S_{gk}D_l}{\delta_{lk-dk}}\left(C_l^*-C_{lk}\right)+$$
$$+\varepsilon_{dk}\rho_f\mathbf{v}_{fk}\nabla C_l^*\ ;\qquad k=\{c,e\} \tag{113}$$

where $\mathbf{v}_{fk}$ are computed from (83) and (84), $S_{gk}=n_k\left(4\pi a_k^{\,2}\right)$, δ_{lk-dk} is computed with the help of equation (31) and C_{lk} are computed from (98).

4.6.7 Auxiliary expressions

Auxiliary expressions ($k=\{c,e\}$)		
Constraints:	$\varepsilon_{le}+\varepsilon_{de}+\varepsilon_{se}=\varepsilon_e$ $\varepsilon_{lc}+\varepsilon_{dc}+\varepsilon_{sc}=\varepsilon_c$, $\quad\varepsilon_c+\varepsilon_e=1$, $\quad$ $\varepsilon_{de}+\varepsilon_{se}=\varepsilon_{ge}$ $\varepsilon_{dc}+\varepsilon_{sc}=\varepsilon_{gc}$	
Interfacial concentrations:	$C_s^*=\begin{cases}kC_l^* & if\quad \Gamma_s\geq 0\\ C_s & if\quad \Gamma_s<0\end{cases}$	$C_l^*=\left(T-T_f\right)\big/m$
Grain radius	$a_k=\left(4/3\pi n_k\right)^{-1/3}\varepsilon_{gk}^{\,1/3}$	
Equiaxed/columnar fractions	$\varepsilon_e,\varepsilon_c=f\left(n_e,n_c,\varepsilon_{ge},\varepsilon_{gc}\right)$, see equation (62)	
Cell radius	$R_{1k}^*=\left(4/3\pi n_k\right)^{-1/3}\varepsilon_k^{\,1/3}$	
Grain envelope interfacial area	$S_{gk}=4\pi a_k^{\,2}n_k$	
Diffusion length	δ_{lk-dk}, see equation (31)	
Grain growth rate	$\Gamma_{gk}=\rho_f S_{gk}\overline{w}_{gk}$, $\quad\overline{w}_{gk}=\dfrac{D_l m(k-1)C_l^*}{\pi^2\Gamma}\left[Pe_t\left(\Omega_k\right)\right]^2$	

Notice that the cell dimensions R_{1k}^* and the equiaxed and columnar fractions (ε_e and ε_c) are computed locally at each moment with respect to the model presented in paragraph 4.1.2, equation (62).

Observations

As one can see, for reasons of simplicity the total fluid formulation is chosen for both the momentum and the solute balance. Note however that the main disadvantage of this approach is the explicit formulation of the interfacial sources in the fluid solute balance equation as well as the explicit formulation for C_{lc} and C_{le}, equation (98). As already discussed in [24] the solute enriching of the extra-dendritic liquid can be extremely rapid due to the highly stiff character of the solute diffusion problem within the extra-dendritic liquid for high cooling rates and low grain densities. The explicit formulation of the C_{lc} and C_{le} in the inter-dendritic solute balance equations may determine convergence problems especially when the mass transfer rates Γ_{sc} and Γ_{se} are computed, equation (113). One should therefore look for an implicite formulation for C_{lc} and C_{le}. The easiest way to do this is to further consider the solute balance equations in the c/e extra-dendritic liquid. One has:

$$\varepsilon_{lk}\rho_f \frac{\partial C_{lk}}{\partial t} + \varepsilon_{lk}\rho_f \mathbf{v}_{fk}\nabla C_{lk} = \nabla\cdot\left(\varepsilon_{lk}\rho_f D_f \nabla C_{lk}\right) + \\ + \left(\frac{\rho_f S_{gk} D_l}{\delta_{lk-dk}} - \Gamma_{gk}\right)\left(C_l^* - C_{lk}\right), \quad k = c, e \tag{114}$$

As one can notice the above formulation allows one to easily implicite the solute rejection in the extra-dendritic liquid, the last term on the RHS of (114). Moreover since $\delta_{lk-dk} < D_l / \overline{w}_{ge}$ one has as well $\frac{\rho_f S_{gk} D_l}{\delta_{lk-dk}} > \Gamma_{gk}$. Hence, the continuous enriching of the extra-dendritic liquid is ensured. However solving the above equations and the solute balance in the total fluid would be redundant. In fact, one should not try to solve them separately but to couple at each time step equations (114) and the solute balance in the total fluid, equation (112). This can be done quite easily if analyzing the discretized form of (114) with respect to a finite volume method:

$$V_{cell}\left(\varepsilon_{lk}\rho_f\right)_i^n \frac{\left(C_{lk}\right)_i^n - \left(C_{lk}\right)^{n-1}}{\Delta t} + \left(\varepsilon_{lk}\rho_f \mathbf{v}_{fk}\right)_i^n \sum_\sigma \left(C_{lk}\right)_\sigma^n \mathbf{n}_\sigma S_\sigma = \\ = \sum_\sigma \left(\varepsilon_{lk}\rho_f D_f \nabla C_{lk}\right)_\sigma^n \cdot \mathbf{n}_\sigma S_\sigma + V_{cell}\left(\frac{\rho_f S_{gk} D_l}{\delta_{lk-dk}} - \Gamma_{gk}\right)_i^n \left[\left(C_l^*\right)_i^n - \left(C_{lk}\right)_i^n\right], \quad k = c, e \tag{115}$$

where V_{cell} is the volume of the mesh cell, σ the number of the cell face, $\mathbf{n}_\sigma$ the exterior normal to the σ^{th} cell face, S_σ the area of the σ^{th} cell face, n the n^{th} time iteration and i the i^{th} loop iteration. As one can notice, the main advantage of the above formulation is the implicite approach of the last RHS term of (115). Indeed, for high cooling rates or low grain densities, during the rapid growth of the grain, δ_{lk-dk} can become very small. Hence an implicit approach for the solute rejection term in (115) would greatly help to the robustness of the algorithm. Now, to couple at each time step equation (115) with the solute balance equation in the total fluid, equation (112), one has only to express $\left(C_{lk}\right)^{n-1}$ with respect to the last converged value of C_f, that is $\left(C_f\right)^{n-1}$. One obtains:

$$\left(C_{lk}\right)^{n-1} = \left[\frac{\varepsilon_f C_f - (\varepsilon_{dc} + \varepsilon_{de}) C_l^*}{\varepsilon_f - (\varepsilon_{dc} + \varepsilon_{de})}\right]^{n-1} \tag{116}$$

This coupled algorithm would enable the implicit computation of $C_{lc/e}$ and consequently an implicit formulation for $\Gamma_{sc/e}$ in (113).

5 Conclusions

The ensemble averaged model derived in reference [1] has been extended to account for the fluid convection. We have approached the ensemble average through the probability distributions functions attached to the macroscopic process to be studied. Indeed, the main advantage of the ensemble averaging is that, with the help of the nearest neighbor distributions $\tilde{f}_{c/e}\left(t, \mathbf{x}; \tilde{\mathbf{z}}_1\right)$ (see [1]), one can quantify in a rigorous way the c/e influence at

x. Using the cell approximation to $\widetilde{f}_{c/e}$, two spherical cells centered at **x** and of radius R_{lc}^{*} and R_{le}^{*} were identified, each of them characterizing in a simple way the statistics of the c/e grain distributions. The new model inherits form the model in [1] which quantified in a rigorous manner the solutal and mechanical (geometrical) interactions between the two coexisting grain distributions.

The microscale physical assumptions are reevaluated with respect to the ones in [1]. First, the fluid flow around the c/e permeable grains is analyzed. Using the Neal [6] model we managed to quantify the drag force acting on the c/e grain. This in turn is used to compute the interfacial momentum transfer at the solid-liquid interface. Secondly the grain growth in the presence of fluid convection is analyzed. Despite the accuracy of the Gandin model [15], for reasons of simplicity, we use in this study the Wang and Beckermann [13] correlation for the tip kinetics. Finally, the solute transfer around the c/e grain is analyzed. Here a scale analysis of the mass transfer around the grain is conducted. It is concluded that the mass transfer at the grain boundary in the presence of convection is intensified with respect to the pure diffusion case. We propose correlation for the computation of the overall mass transfer coefficient in the limit of small and high c/e grain fractions.

Using the microscale physical assumptions the average balance equations are further derived. First the grain balance equations are derived. If the equiaxed nucleation is modeled as an instantaneous event, the columnar nucleation (the sudden arrival of columnar tips in one point) cannot be approached with a local event. Hence, a columnar front tracking algorithm needs to be considered. We therefore propose a simple front tracking technique having as basis the volume of fluid model. Moreover the coexistence model developed in [1] is here extended to account for the grain convection. Indeed, the cell dimensions R_{lc}^{*} and R_{le}^{*} as well as the space partition between the columnar and equiaxed distribution (ε_c and ε_e) is here determined form a new general model describing the coexistence state between two different grain populations, in occurrence here between the columnar and equiaxed structures. The mass, momentum and energy balance equations are derived next. Notice that for simplicity reasons a total fluid approach is considered for the momentum balance. For the energy equation a single mixture balance equation is derived. Finally the solute balance equations are obtained. Here, a total fluid approach is considered too along with the two solute balance equations in the c/e solid. Moreover the two solute balance equations in the c/e inter-dendritic liquid are used to compute the c/e solidification rates. We have also proposed an algorithm for the implicit computation of the extra-dendritic liquid concentrations. This is done by coupling at each time step the solute balance equations in the c/e extra-dendritic liquids with the solute balance equation in the total fluid (*f* phase). Finally a complete ensemble averaged model is proposed for the modeling of the mixed columnar + equiaxed structures in the presence of convection.

6 Nomenclature

Symbol	Meaning	Unit
$\mathbf{v}$	velocity field	$[m/s]$
C	solute concentration field	$[wt.\ \%]$
T	temperature field	$[K]$
n	grain density	$[\,m^{-3}\,]$
ρ	density field	$[\,kg.m^{-3}\,]$
ψ	the generic physical field	---

ε_k	the "volume" fraction of phase *k*	---
f_c	the columnar fraction attached to the mesh cell	---
$\overline{w}_{gk}$	the interface velocity of the *k* phase interface	$[m/s]$
C_k^*	the interfacial concentration at the *k* phase interface	$[wt.\ \%]$
X_k	the *k* phase characteristic phase function	---
$n_{c/e}^0$	the columnar/equiaxed nucleation grain density	$[\,m^{-3}\,]$
λ_1	columnar primary arm spacing	$[m]$
S_k	the interfacial area density of phase *k*	$[\,m^{-1}\,]$
δ_{k-p}	the solute diffusion length at the *k-p* interface	$[m]$
$\mathbf{x}_{cf}$	position of the columnar front	$[m]$
T_{ne}	the equiaxed nucleation temperature	$[K]$
T_f	the fusion temperature of the pure solvent	$[K]$
m	the slope of the liquidus line	$[\,K.(wt\,\%)^{-1}\,]$
k	the partition coefficient	---
c_k	heat capacity for the *k*-phase	$[\,J.kg^{-1}.K^{-1}\,]$
λ_k	the phase *k* thermal conductivity	$[\,W.m^{-1}.K^{-1}\,]$
L	the latent heat	$[\,J.kg^{-1}\,]$
Ω	the dimensionless local undercooling	---
Pe_t	the dendrite tip Peclet number	---
D_k	the solute diffusivity within the phase *k*	$[\,m^2.s^{-1}\,]$
$a_{c/e}$	the local columnar/equiaxed grain radius	$[m]$
$R_{1c/e}^*$	the cell radius corresponding to the coexisting columnar/equiaxed grain distribution	$[m]$
$\tilde{\mathbf{z}}_i$	the position in the ingot of the ith closest grain to $\mathbf{x}$	$[m]$
$\tilde{f}_{c/e}^{(1)}\left(t,\mathbf{x};\tilde{\mathbf{z}}_1\right)$	the unconditional density function that the closest grain to the point $\mathbf{x}$ is centered within $d\tilde{\mathbf{z}}_1$ of $\tilde{\mathbf{z}}_1$ and is a columnar/equiaxed grain	$[\,m^{-3}\,]$
Γ_k	the *k* phase mass transfer rate	$[\,kg.m^{-3}.s^{-1}\,]$
Over lines		
$\bar{}$	ensemble average	
$\tilde{}$	relative to the nearest neighbor distributions	
Subscripts		
c	columnar phase (*lc*+*dc*+*sc*)	
e	equiaxed phase (*le*+*de*+*se*)	
s	solid phase	
l	extra-dendritic liquid phase	
d	inter-dendritic liquid phase	
f	total fluid phase ($=l+d$)	
g	grain phase ($=d+s$)	
kc	columnar *k* phase	
ke	equiaxed *k* phase	

7 References

1. Ciobanas, A.I., and Y. Fautrelle: "Ensemble Averaged Two-Phase Eulerian Model for Columnar/equiaxed Solidification of a Binary Alloy. Part I. The Mathematical Model.", *Materials Science and Engineering A*, (Submitted 2006).

2. Drew, D.A., and S.L. Passman. Theory of Multicomponent Fluids. . New York: Springer-Verlag, 1999.

3. Carman, P.C. Flow of Gases Through Porous Media. . London: Butterworth Scientific, 1956.

4. Happel, J., and H. Brenner. Low Reynolds Number Hydrodynamics. . Leyden, The Netherlands: Noordhoff International Publishing, 1973.

5. Happel, J.: *AiChE Journal*, 1958, vol. 13, pp. 122-125.

6. Neale, G., N. Epstein, and W. Nader: "Creeping Flow Relative to Permeable Spheres.", *Chemical Engineering Science*, 1973, vol. 28, pp. 1865-1874.

7. Davis, R.H., and H.A. Stone: "Flow Through Beds of Porous Particles.", *Chemical Engineering Science*, 1993, vol. 48.23, pp. 3993-4005.

8. Wang, C.Y, et al.: "Multiparticle Interfacial Drag in Equiaxed Solidification.", *Metallurgical and Materials Transactions B*, 1995, vol. 26B, pp. 111-119.

9. Wang, C.Y, and C. Beckermann: "A Multiphase Solute Diffusion Model for Dendritic Alloy Solidification.", *Metallurgical and Materials Transactions A*, 1993, vol. 24A, pp. 2787-2802.

10. Huang, S.C., and M.E. Glicksman: *Acta Metallurgica*, 1981, vol. 29, pp. 701-715.

11. Ananth, R., and W.N. Gill: *Journal of Crystal Growth*, 1991, vol. 108, pp. 173-189.

12. Cantor, B., and A. Vogel: "Dendritic Solidification and Fluid Flow.", *Journal of Crystal Growth*, 1977, vol. 41, pp. 109-123.

13. Wang, C.Y, and C. Beckermann: "Equiaxed Dendritic Solidification With Convection: Part I. Multiscale/multiphase Modeling.", *Metallurgical and Materials Transactions A*, 1996, vol. 27A, pp. 2754-2764.

14. Lipton, J., M.E. Glicksman, and W. Kurz: "Dendritic Growth Into Undercooled Alloy Melts.", *Materials Science and Engineering*, 1984, vol. 65, pp. 57-63.

15. Gandin, Ch.-A., et al.: "Boundary Layer Correlation for Dendrite Tip Growth With Fluid Flow.", *Materials Science and Engineering*, 2003, vol. A342, pp. 44-50.

16. Burmeister, L.C. Convective Heat Transfer. . 2nd ed. New York: Wiley, 1993.

17. Beckermann, C., and C.Y Wang: "Equiaxed Dendritic Solidification With Convection: Part Iii. Comparison With Nh4cl- H2o Experiments.", *Metallurgical and Materials Transactions A*, 1996, vol. 27A, pp. 2784-2795.

18. Jackson, K.A., et al.: "On the Origin of the Equiaxed Zone in Castings.", *Transactions of the metallurgical society of AIME*, 1966, vol. 236, pp. 149-158.

19. Martorano, M. A., C. Beckermann, and Ch.-A. Gandin: "A Solutal Interaction Mechanism for the Columnar-To-Equiaxed Transition in Alloy Solidification.", *Metallurgical and Materials Transactions A*, 2003, vol. 34A, pp. 1657-1674.

20. Hunt, J.D.: "Cellular and Primary Dendrite Spacings.", *Solidification and casting of metals - Metals Society, London*, 1979, pp. 3-9.

21. Kurz, W., and D.J. Fisher: "Dendrite Growth at the Limit of Stability: Tip Radius and Spacing.", *Acta Metallurgica*, 1981, vol. 29, pp. 11-20.

22. Ciobanas, A.I., A. Bejan, and Y. Fautrelle: "Dendritic solidification morphology viewed from the perspective of constructal theory.", *Physical Review E*, (Submitted 2006).

23. Bejan, A. Shape and Structure, From Engineering to Nature. . New York: Cambridge University Press, 2000.

24. Ciobanas, A.I., and Y. Fautrelle: "Ensemble Averaged Two-Phase Eulerian Model for Columnar/equiaxed Solidification of a Binary Alloy. Part II. Simulation of the Columnar-To-Equiaxed Transition.", *Materials Science and Engineering A*, (Submitted 2006).

25. Browne, D.J., and J.D. Hunt: "An Interface Tracking Model of Moving Boundaries in Multi-Phase Systems: Application to Solidification.", *Archives of thermodynamics*, 2003, vol. 24.1, pp. 25-35.

26. Wu, M., and A. Ludwig: "Volumne Averaging Concept for Mixed Columnar-Equiaxed Solidification.", *Proceedings of McWASP XI*, 2006.

27. Drew, D.A.: "Mathematical Modeling of Two-Phase Flow.", *Ann. Rev. Fluid Mech.*, 1983, vol. 15, pp. 261-291.

28. Ishii, M. Thermo-Fluid Dynamic Theory of Two-Phase Flow. . Paris: Eyrolles, 1975.

29. Ni, J., and C. Beckermann: "A Volume-Averaged Two-Phase Model for Transport Phenomena During Solidification.", *Metallurgical Transactions B*, 1991, vol. 22B, pp. 349-361.

30. Krieger, I.M.: *Adv. Colloid Interface Sci.*, 1972, vol. 3, pp. 111-136.